Ionized and Photodissociation Regions toward a New Sample of Massive Star-forming Clumps

Dissertation

zur

Erlangung des Doktorgrades (Dr. rer. nat.)

der

Mathematisch-Naturwissenschaftlichen Fakultät

der

Rheinischen Friedrich–Wilhelms–Universität Bonn

vorgelegt von

Wonju KIM

aus

Gyeongju, Republic of Korea

Bonn, 2018

Abstract

HII regions are an excellent indicator of high-mass star-forming regions and ongoing star formation in galaxies. Powerful outflows from O/B stars in their early stages and, during their whole life, intense UV radiation and stellar winds appreciably alter the chemical composition of the ISM in their vicinity and turn the surfaces of molecular clouds into photodissociation regions. To investigate the feedback of young high-mass stars, a comprehensive sample of regions is necessarily to cover different evolutionary stages and molecular environments.

This thesis presents a study of HII regions and PDRs in a sample of 967 compact dust clumps selected from catalogs of ∼10,000 sources identified by the APEX Telescope Large Area Survey of the Galaxy (ATLASGAL). This sample includes star-forming and quiescent clumps to ensure a variety of different evolutionary stages. The primary goal of this thesis is to understand the physical properties and kinematics of HII regions and their influence on the natal dense dust clumps, especially in form of PDRs. The analysis of molecular line surveys conducted toward ATLASGAL dust clumps focuses, first, on radio recombination lines in HII regions and continues with an investigation of PDR tracers.

In particular, millimeter radio recombination lines (mm-RRLs) observed with the IRAM 30m and Mopra 22m telescopes are analyzed. Several RRLs at 3 mm wavelength were covered with principal quantum number n ranging from 39 to 65 and Δn = 1, 2, 3, and 4 (H$n\alpha$, H$n\beta$, H$n\gamma$, and H$n\delta$). This is the largest published sample of mm-RRLs detections: H$n\alpha$, H$n\beta$, H$n\gamma$, and H$n\delta$ mm-RRLs were detected toward 178, 65, 23, and 22 clumps, respectively. Compact radio continuum counterparts were identified for 134 of the clumps with RRL detections showing that the mm-RRLs are associated with known compact and ultra-compact HII regions. Besides, eight detections represent potentially new HII regions found exclusively from this study. Based on the good agreement of the measured mm-RRL and molecular line velocities, associations of the young HII regions with dense molecular clumps were established. Furthermore, H^{13}CO$^+$ linewidths from clumps with mm-RRLs are broader than in those without them. This indicates a physical connection between the embedded HII region and their natal environments. Nine clumps show broad RRL linewidths ($> 40\,\mathrm{km\,s^{-1}}$) that reveal pronounced turbulent motions within the ionized gas. By using the mm-RRLs and radio continuum emission, the estimated electron densities and diameters of the HII regions are $n_e < 10^5\,\mathrm{cm^{-3}}$ and $D > 0.03\,\mathrm{pc}$, respectively.

A dedicated RRL survey was observed with the APEX 12m telescope, covering a variety of (sub)millimeter radio recombination lines (submm-RRLs) with principal quantum numbers ranging from 25 to 30. RRLs observed at different wavelengths allow us to investigate the excitation conditions of ionized gas within HII regions. Comparing mm- and submm-RRLs shows that these RRLs are emitted in local thermodynamic equilibrium (LTE). The average ratio (0.31) of the measured H35β/H28α fluxes is close to the LTE value of 0.28. Furthermore, the submm-RRL luminosities show excellent

correlations with the Lyman photon flux and bolometric luminosities of the embedded O/B stars. The H$\textsc{ii}$ regions are associated with the most massive and luminous clumps of the sample. The production rate of ionizing photons, Q, was estimated using the H28α line. The measured Q is consistent with the Lyman continuum photon flux determined by $5\,\mathrm{GHz}$ radio continuum emission. This allows RRLs to be used to measure star formation rates in galaxies. Six RRL sources show a combination of a narrow and a broad Gaussian line feature that suggest a link to high-velocity ionized flows.

In a study of the ISM surrounding H$\textsc{ii}$ regions, in 409 ATLASGAL clumps eight molecules (HCO, HOC$^+$, C$_2$H, c-C$_3$H$_2$, CN, H^{13}CN, HC^{15}N, HN^{13}C) as PDR tracers are investigated plus C^{18}O and H^{13}CO$^+$ molecular lines as reference molecules tracing dense molecular gas. Most molecules show detection rates of above 94% except for HCO, H^{13}CN, and HC^{15}N. These three molecules are mostly detected in H$\textsc{ii}$ regions. Interestingly, 40 clumps also show CN self-absorption profiles, indicating potential infalling or expanding motions within the clumps. These lines are broader and brighter toward more evolved clumps. Also, abundances of HCO as well as HCO/H^{13}CO$^+$ column density ratios significantly drop with increasing H$_2$ column density. This shows that the HCO molecule is more abundant in PDRs illuminated by FUV radiation than inside molecular clouds. On the other hand, small hydrocarbons (c-C$_3$H$_2$ and C$_2$H) known as typical PDR tracers do not show significant abundance changes over a range of H$_2$ column density, while toward H$\textsc{ii}$ regions the column density ratio of the two molecules shows a moderate increase with dust temperature.

List of publications related to the PhD thesis:
"Ionized and Photodissociation Regions toward a New Sample of Massive Star-forming Clumps"
Wonju Kim

1. **ATLASGAL-selected massive clumps in the inner Galaxy. IV. Millimeter hydrogen recombination lines from associated HII regions**
   Kim, W.-J.; Wyrowski, F.; Urquhart, J. S.; Menten, K. M.; Csengeri, T. (2017)
   A&A, 602, A37.
   DOI:10.1051/0004-6361/201629764 [arXiv:1702.02062]

2. **New detections of (sub)millimeter hydrogen radio recombination lines towards high-mass star-forming clumps**
   Kim, W.-J.; Urquhart, J. S.; Wyrowski, F.; Menten, K. M.; Csengeri, T. (2017)
   A&A, submitted.

3. **ATLASGAL — Molecular fingerprints of an unbiased sample of massive star forming clumps**
   Urquhart, J. S.; Figura, C.; Wyrowski, F.; Giannetti, A.; **Kim, W.-J.**; Wienen, M.; Leurini, S.; Pillai, T.; Csengeri, T.; Gibson, S. J.; Menten, K. M.; Moore, T. J. T.; Thompson, M. A., in prep.

Acknowledgements

The long journal that I have gone since 2014 June was a miracle and marvelous time. I stepped on Germany with excitement and fear about the new place. One day, I told my friends about my first feeling about my journal. That was so new and strange because I never had such experiences like living people who have the different faces, in different cultures and environments. From time to time, the unknown feeling overwhelmed me. At that time, I couldn't imagine that I would eventually finish all of these and meet people who I can never forget.

Here, I would like to thank the people who made all me these as beautiful memories. There is no doubt that it would be impossible to make such great journal without the blessing of God and all the people.

My first and hugest thanks are to my lovely family and especially to my mother, sister, and brother, Yongsoon Kwon, Sojung Kim and Seobgu Kim. Each of them is my precious treasure and my strength ever I have had in my life. They are always beside me and provide a shelter where I can rest and relieve all the concerns from the world. I could go anywhere because of their support, and current me can be here. I also thank my father, Sangrak Kim, who looks down me from Heaven. He was the best supporter of my dream ever and always proud of me.

I want to give a very special thank to Alessandro Ridolfi. He is the best company and supporter after my family. Thanks to him, I have gotten all the motivations and strengths to keep going on my PhD projects for last years. Again, I cannot imagine how I would go through all the difficulties without him.

Another special thank is for James Urquhart. Expressing him with a single word is difficult. He is the best collaborator, a faithful friend, and an excellent teacher. More than all the words, I am willing to call him my mentor without hesitating. I have gotten a big inspiration from him as an astronomer and felt such wonderful supports from him that let me pursue my dream with happiness. I always appreciate that I met him such wonderful person as my mentor.

I am profoundly grateful to my advisor, Friedrich Wyrowski. He is the first person who allowed and guided me to explore my ideas and to develop these. His kind supervision from beginning to end encouraged me to challenge new works. I sincerely appreciate that he listened to me with patience and dedicated his time to me. I am glad he was my PhD advisor.

A very special thank is for my supervisor, Karl M. Menten. I gratefully thank him for his support for all the last years. It would be hard and difficult without his constant support to complete my PhD. It is always the honor of being his student, and it will be forever.

Great thanks to my special friends, Carsten König, Ka Tat Wong, Dario Colombo, Hans Nguyen, Maitraiyee Tiwari, Veselina Kalinova, Dhanya G Nair, Marion Wienen, Amit Bansod! Friends! I want to give a special friendship thanks to all of you. This friendship is one of the beautiful things I received a gift during my German life. I will

remember your faithful friendship more than this thesis when I recall the memories about Bonn in Germany. Thanks to my fellow Ph.D. and Master's students! I would also like to mention Nina Brinkmann, Eleni Graikou, Joey Martinez, Jason Wu, Vivien Thiel, Fetema Kamali, Lure Bouscasse, Arshia Jacob!

Thanks to the post-docs who gave me supportive advice, Rosie Chen, Thushara Pillai, Minyoung Lee, Ann Mao, Timea Csengeri, Maria Massi. In particular, I would like to mention Rosie Chen and Thushara Pillai. Their warm advice gave comfort to me every time.

A special thank to Tuyet-Le Tran, Barbara Menten, Eva Schmelmer. They made that my life in Bonn was able to be without any problems. Thanks to them, I could make beautiful memories in Bonn.

Contents

List of Figures

List of Tables

Introduction

Contents

When looking up at the night sky, most of the space appears empty. In fact, the empty space is filled with material, the so-called *interstellar medium* (ISM). To understand the appearance and evolution of our Milky Way and galaxies in general, it is crucial to study the cyclic processes by which stars inject energy and enrich the ISM. These processes change the chemistry and kinematics of the birthplaces of the next generation of stars. During the life cycle of stars, constant recycling and enhancement of heavier elements lead to the chemical evolution of galaxies. Furthermore, the cyclic processes regulate the star formation rate in galaxies through feedback, especially from *high-mass star formation.*

High-mass stars are representative of the present star formation rate in galaxies, and control the rate via their formation and dissolution. They regulate the turbulent and thermal pressure in the ISM through the injection of mechanical energy into the ISM, via stellar winds, supernova explosions, and formation of the hot coronal gas. In particular, the generation of turbulent pressure counteracts the self-gravity within clouds.
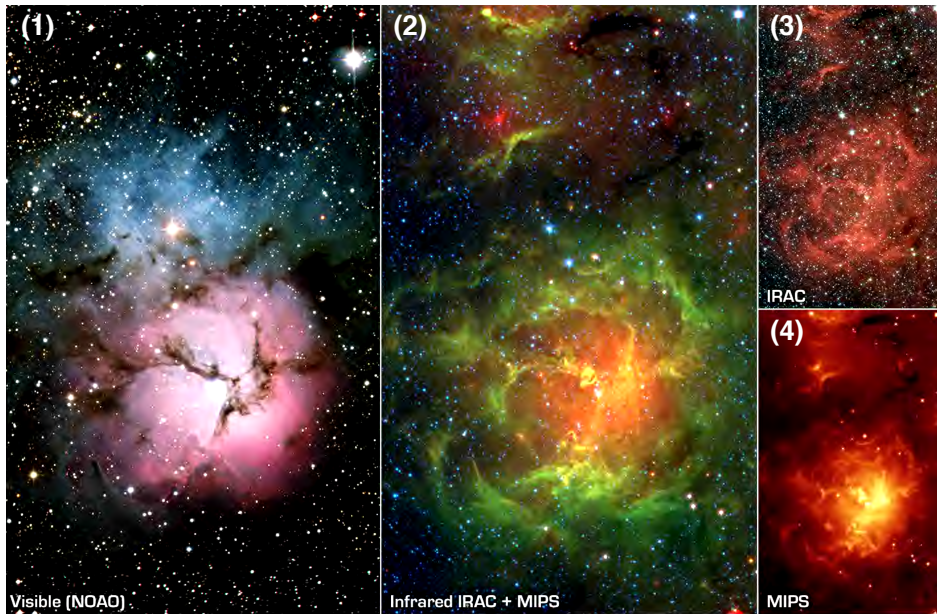
Figure 1.1: Trifid Nebula (Messier 20). (1): the visible-light image clearly shows the bright Hɪɪ regions (pink color) and reflection nebula (blue). (2), (3), and (4): the infrared images from Spitzer Space Telescope well represent 30 high-mass stars and 120 newborn stars in the nebula. (2): a three-color composite of $4.5\,\mu$m (blue), $8.0\,\mu$m (green) and $24\,\mu$m (red) wavelengths. (3) and (4) are $8.0\,\mu$m and $24\,\mu$m images, respectively. (Credit: National Optical Astronomy Observatory/NASA/JPL-Caltech/J.Rho (SSC/Caltech))

Also, high-mass stars are vital sources of far-ultraviolet (FUV) photons ($6\,\mathrm{eV} < \text{photon energy} < 13.6\,\mathrm{eV}$) and possibly as supernovae responsible for cosmic-rays. FUV photons and cosmic-rays control the heating, ionization, and dissociation in the ISM, and play a crucial role in heating the dust. Regulating those processes through shielding by dust permits formation and survival of molecules in clouds. The molecules and dust allow cooling of the ISM through various molecular line and continuum emission processes. Eventually, they also lead to gravitational instabilities by cooling clouds from which further generations of stars will form. As such, high-mass star formation is the primary source of FUV radiation and chemical enrichment in the Milky Way and is, therefore, an essential part to understand the origin and evolution of other galaxies. However, it is hard to find high-mass star-forming regions because high-mass star formation occurs in dense parts of molecular clouds and is obscured at visible wavelengths (sometimes even at short infrared (IR) wavelengths).

Ionized gas surrounding newly born high-mass stars (O and B type stars) is a good signpost of high-mass star formation and a good indicator of the current star formation rate. These regions are called *H*ɪɪ *regions* because the gas exists mostly in the form of ionized hydrogen, which is the most abundant element in the Universe. Hɪɪ regions

in the Milky Way are among the brightest objects at various wavelengths including visible, infrared, and radio wavelengths. Figure 1.1 shows the famous Trifid Nebula (Messier 20) in the constellation Sagittarius. We can clearly see a visible bright HII region (pink color in image (1)) with a reflection nebula next to it. In the IR hot dust is seen in the HII region as well as warm dust at the edges of the HII where the HII region heats and compresses the remnant molecular cloud from which it was formed.

HII regions are not only important as a tracer of high-mass star-forming regions, but also as sources of feedback that can influence the ISM throughout their evolution. FUV photons from bright O/B stars give rise to dissociation regions that are formed between the ionized and molecular gas. We refer to these regions as *photodissociation regions* (*PDRs*; also called photon-dominated regions): these are intense interface regions that emit strongly at mid-infrared (mid-IR) wavelengths (e.g., $8\,\mu$m wavelengths; see green color in image (2) and red color in image (3) of Figure 1.1).

In this thesis, we utilize radio recombination lines emitted from the recombination of ions and electrons in HII regions, as these lines allow us to study both the dynamical and physical properties of the HII regions. Furthermore, several molecular lines known as tracers of PDRs are used to probe the kinematic properties and chemical processes associated with these interaction/transition regions. We will use a combination of radio continuum, recombination, and molecular lines to study HII regions and their local environments. In this chapter, we will provide an overview of these regions and an outline of the study in detail.

1.1 The interstellar medium in the Milky Way

The Milky Way (MW), our Galaxy, is a gas-rich spiral galaxy. One of its most notable characteristics is its flat-disk shape whose size is roughly $\geq 20\,$kpc in length and $\geq 250\,$pc in height (Sparke & Gallagher 2000). The local thickness of the disk is systematically variable with the spectral type of stars. O and B stars are more concentrated toward the Galactic plane than G stars, like the Sun. The central $3\,$kpc region of the Galaxy, the so-called central bar-shaped bulge, has the densest concentration of stars, gas, and dust. Our Sun orbits at a radius of $8.5\,$kpc, or about halfway to the outer edge. The local rotation speed is $220\,$km s^{-1}, corresponding to a period of 2.4×10^8 years (Stahler & Palla 2005).

The composition of the ISM between stars consists of a mixture of gas and dust. Its composition is not very different from the time when it was formed. However, it is continuously reformed through ongoing star formation, nucleosynthesis, and stellar mass loss. The recycling processes eject newly formed elements into the MW and heat the surrounding medium. In fact, the stars, known as population II, in the halo of the Galaxy are the oldest with only 1 percent of heavy elements. In contract, the stars, known as population I, contain more of the heavy elements and are found in the Galactic plane (disk) where currently stars are forming. When high-mass stars die, a large portion of their mass is returned to the ISM enriched by nucleosynthesis and approximately 20 percent of the mass are used for star formation (Schulz 2005).

Table 1.1: Phases of the ISM in the Milky Way (Mathis 1990).

Medium	Phase	Density (cm^{-3})	Temperature (K)	Heating signature
HI cloud	Cold	30	100	Dust
Warm HI	Warm	0.5	$8{\times}10^3$	Dust
Warm HII	Warm	0.03	10^4	Photoionization
HII region	Warm	>100	10^4	Photoionization
Hot ISM	Hot	10^{-3}	$10^{6.5}$	SNe shocks
Molecular cloud	Cold	$>1{,}000$	10-50	Cosmic rays

Interstellar dust is approximately 1% of the ISM in solid form. This means that only a few dust particles are found in one billion cubic centimeters of space. Even though the shape of dust grains is not well known, their structure is considered to be cores surrounded by icy mantles. The cores are mainly silicates and carbonaceous material (Draine 2003). The mantles are composed of a mixture of iced water and other molecules that freeze out from ambient gas. Such mantles form within cold interstellar clouds and evaporate when the grain temperature exceeds about 100 K. Typical sizes of dust grains are about 0.01 to 1 μm, with evidence of grain growth in molecular clouds. Dust grains cause reddening through extinction and polarization because of the elongated shape of dust grains. The existence of dust grains is considered an essential requirement for the formation of molecular hydrogen (H_2).

Interstellar gas contributes to the remaining 99% of the ISM in mass (Hildebrand 1983). The interstellar gas is composed of 90.8% hydrogen, 9.1% helium and tiny amounts of carbon, oxygen, iron, and other heavier elements formed by the previous generations of stars. Interstellar gas exists in different phases in the MW as shown in Table 1.1.

The thermally stable state of the neutral gas is predicted to be separated into two phases, the *cold neutral* and *warm neutral media* (CNM and WNM). The CNM mostly exists as *atomic hydrogen clouds* (HI clouds). The HI clouds are spread throughout the MW and extend far beyond the visible stars in the Galactic disk. Typical number densities span a range of 10 to 100 cm^{-3}, and the diameter range is from 1 to 100 pc. The distribution of HI surface density in the Galaxy is shallow within the central bulge but rises to a reasonably uniform level between radii of 4 to 14 kpc. The WNM is also distributed widely throughout the Galactic disk, with a scale height twice of that of the CNM. The number density of this gas is about 0.5 cm^{-3} and its temperature is estimated at $8{\times}10^3$ K. However, observations do not support the strict segregation into cold and warm stable phases and suggest that roughly 48% of the WNM may be in a thermally unstable phase (Heiles & Troland 2003). The *warm ionized medium* (WIM) is widespread, and its diffuse emission is detectable with Hα lines. The WIM shares the same density and temperature as the WNM, but its hydrogen content is mostly ionized. In the MW, half of the volume is filled by some combination of WIM and

WNM (Cox 2005).

The other half of the volume of the MW is filled by the *hot ionized medium* (hot ISM) with density $< 10^{-3}\,\mathrm{cm}^{-3}$, and $T > 10^5\,\mathrm{K}$. The hot ISM is produced by supernova explosions. The extremely hot gas produced in these events very slowly cools down, and thus the newly formed remnants unavoidably pass through older ones. *Ionized hydrogen regions* (HII regions) are another form of ionized interstellar gas, which is another important ISM phase studied in this thesis. They are formed around individual O and B stars. The peak of the HII gas distribution is at a galactic radius near $5\,\mathrm{kpc}$, coincident with a dense ring of molecular material where much of the star formation is concentrated (Jackson et al. 2006). Since HII regions are created by young, high-mass stars, the distribution of HII gas is closely related to star formation activity in molecular gas. The presence of emission lines from the heavier elements in HII regions allows us to reconstruct the chemical composition of interstellar gas (Stahler & Palla 2005). The properties of HII regions vary broadly and will be described in Section 1.3, in more detail.

The *molecular gas* resides in clouds with a complex classification in size, density, temperature, and mass. According to the global distribution of H_2 probed by CO measurements, molecular gas is more closely limited to the Galactic plane (Stahler & Palla 2005). It occupies only about one percent of the accessible volume. Table 1.2 summarizes the properties of different molecular regions and is ordered by their typical visual extinction (A_V) along the line of sight.

Diffuse clouds are isolated and contain a similar amount of atomic, and molecular hydrogen gas. They can last for long periods through the balance of pressure between the internal gas and the surrounding rarefied warmer medium. However, signposts of star formation are never found in the diffuse clouds, and the latter just contribute a small fraction to the mass of the ISM.

Giant molecular clouds (GMCs) are important for star formation in the MW. GMCs have a hierarchical density structure; on large scales, they consist of low-density gas but on small scales, high density clumps are present and within these even smaller, higher density core structures are found. In GMCs, over 80% of molecular hydrogen gas in the MW is found and sustains for millions of years. On average, 3% of the GMC's mass turns into stars during star formation, and its star formation rate (averaged over the total H_2 mass in the Galactic disk of $2 \times 10^9\,\mathrm{M_\odot}$) is about $2\,\mathrm{M_\odot}$ year^{-1} (Stahler & Palla 2005).

Many GMCs show filamentary shapes which can be easily found in dust continuum emission maps (Molinari et al. 2010b; Li et al. 2016). GMCs frequently show clumpy structures rather than being homogeneous. The clumps in Table 1.2 are sub-structures of molecular clouds. Most of those clumps are picked up by the $870\,\mu$m dust emission maps of the ATLASGAL survey (Schuller et al. 2009; Urquhart et al. 2014a; Csengeri et al. 2014) which will be explained in Section 1.2.1. The clumps also can be separated into several dense cores. The dense cores trace single or small groups of high-mass stars. The places where high-mass stars form in the GMCs will be discussed in the

Table 1.2:   Different molecular regions and their typical properties (Stahler & Palla 2005).

Regions	Diameter (pc)	Density (cm^{-3})	Temperature (K)	Mass $(\mathrm{M}_\odot)$
Diffuse Clouds	3	500	50	50
Giant Molecular Clouds	50	100	15	10^5
Clumps	1.5	550	10	250

next section.

1.2   High-mass star formation

Stars can be classified into three groups by their mass: low-mass stars ($M_{\mathrm{star}} < 3\,\mathrm{M}_\odot$) (Shu et al. 1999), intermediate-mass ($3\,\mathrm{M}_\odot < M_{\mathrm{star}} < 8\,\mathrm{M}_\odot$), high-mass (also so-called massive) stars ($M_{\mathrm{star}} > 8\,\mathrm{M}_\odot$) (Zinnecker & Yorke 2007). The high-mass stars correspond to O and B spectral types based on their temperature. In this thesis, we will only focus on the high-mass stars and their evolutionary sequence, in particular, the HII region stage. The formation of low- and high-mass stars differ in their Kelvin−Helmholtz and free-fall time scales.

The Kelvin−Helmholtz timescale estimates how fast a protostar radiates away its binding energy and contracts before hydrogen burning begins (the pre-main sequence lifetime) (Stahler & Palla 2005; McKee & Ostriker 2007). The Kelvin−Helmholtz timescale ($t_{\mathrm{KH}} = GM^2/RL$) is determined by mass (M), radius (R) and luminosity (L) of a protostar. On the other hand, the free-fall timescale (t_{ff}) determines the accretion timescale for the envelope of dense molecular core and is calculated as $t_{ff} \simeq (3\pi/32G\rho)^{1/2}$, where ρ is density.

The formation time scales (t_{SF}) of high-mass stars are $t_{\mathrm{SF}} \gtrsim t_{\mathrm{KH}}$, whereas the free-fall timescale of material is longer than the Kelvin−Helmholtz timescale ($t_{\mathrm{KH}} \ll t_{ff}$). Therefore, accretion continues while hydrogen burning starts inside stars (Kahn 1974; Palla et al. 1993). In contrast, the t_{KH} of low-mass stars is much larger than the t_{ff} and thus they obtain their mass before nuclear reactions begin.

The luminosities of low-mass protostars are dominated by accretion in cores with masses of the order of the thermal Jeans masses (critical masses). On the other hand, the luminosities of high-mass protostars are mostly due to nuclear reactions, and the high-mass protostars are born in molecular cores with greater than their thermal Jeans masses (McKee & Ostriker 2007).

The evolutionary sequence of high-mass star formation is derived from numerical and observational studies over the past decade. A model describing the sequence can be divided into four stages (Zinnecker & Yorke 2007; Kurtz et al. 2000; Garay & Lizano 1999; Urquhart et al. 2014a, 2017). High-mass star formation takes place in a massive, dense clump in a clumpy molecular cloud. In the beginning, the clump is gravitationally bound without any embedded sources (see leftmost drawing in Figure 1.2).
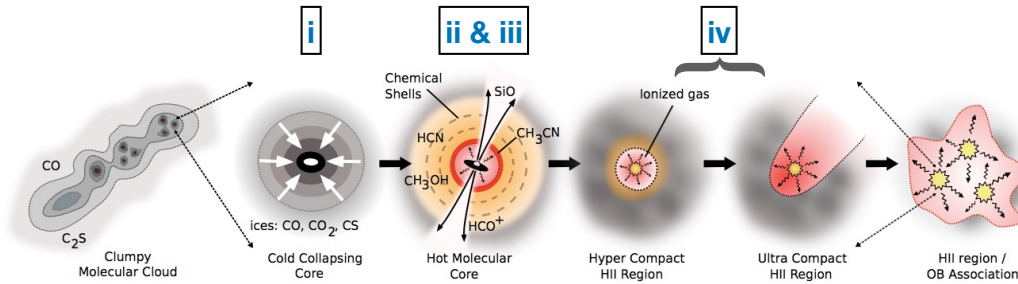
Figure 1.2: This illustration shows the formation of a cluster of high-mass stars from inside molecular clouds (Credit: Cormac Purcell). The sequence corresponds to classes on a approximately timescale. These classes are classified by observational results.

(i) The first stage corresponds to the second drawing of Figure 1.2. Formation of high-mass stars begins when individual cores are gravitationally unstable. The cores start to collapse isothermally inward, and the free-fall timescale is $\sim 10^5$ years.

(ii) The gas and dust become optically thick due to the increasing densities. A central protostar gains its mass by accretion through a disk which is surrounded by the infalling natal envelope. The central protostar increases the temperature of the envelope and excites Class II methanol-maser emission via radiative pumping in the disk (Sobolev et al. 2007). This stage occurs at some point between the cold collapsing core and hot molecular core as shown in Figure 1.2. This evolutionary stage is on the Kelvin−Helmholtz timescale of order 10^4 years.

(iii) In this stage, due to high accretion rates (Hosokawa & Omukai 2009; Hosokawa et al. 2010), the mass of a protostar grows from 5 to 10 $M_\odot$, and its internal density and temperature decrease due to the increasing radius of the protostar (Hoare et al. 2007). Thus, nuclear reactions in the protostar are postponed (Hoare et al. 2007). Above 10 $M_\odot$, the Kelvin−Helmholtz timescales (t_{KH}) is lower than the accretion timescale (t_{ff}). At this stage, the protostar releases angular momentum through collimated jets and molecular outflows. Also, the molecular surrounding of the protostar becomes significantly contracted and warmed up forming a hot molecular core (density of $n_{H_2} \geq 10^7\,cm^{-3}$ and temperature $T \geq 100\,K$). Although the timescale for this stage is unclear, a conceivable timescale is approximately 10^4 years (Kurtz et al. 2000). As seen in Figure 1.2, emission from a variety of molecules released from the ice mantles of dust grains become detectable. These molecular lines are very useful tools to trace the physical and chemical conditions in the cores. The HII region has not yet formed, but the luminosities of protostars are between 10^3 and $10^5\,L_\odot$. These objects are referred to as massive young stellar objects (MYSOs) or high-mass young stellar objects (HMYSOs) (Mottram et al. 2011; Lumsden et al. 2013; Urquhart et al. 2014a).

(iv) In this stage, high-mass stars reach the zero-age main sequence (ZAMS). Their luminosity increase due to starting hydrogen burning. Finally, the high-mass stars produce significant UV radiation photons and strong stellar winds, which will appreciably change the physical and chemical conditions as well as the structure of their

environment. The energetic UV photons ionize material and create an ionized region (HII region) that surrounds the high-mass protostar. HII regions are also classified into different classes dependent on compactness of the ionized region (i.e., hyper-compact, ultra-compact and compact HII regions as seen the last three stages in Figure 1.2) (Wood & Churchwell 1989; Kurtz et al. 1994; Churchwell 2002; Hoare et al. 2007). While HII regions expand inside their natal molecular clouds, they can either trigger further star formation or destroy the natal molecular clouds. Therefore, this stage is very important to understand the influence of high-mass stars on their environment, besides being interesting in its own right. The different classes of young HII regions and the importance of this stage to understand feedback from high-mass stars will be discussed further in Section 1.3. The evolution and lifetimes of high-mass stars are very short. Therefore, a large sample of massive molecular clumps is required to study this evolutionary sequence and to determine statistical properties of the various stages.

1.2.1   The birthplaces of high-mass stars

The appearance of the MW varies at different wavelengths as demonstrated by Figure 1.3, which shows the central region of the Galaxy. In fact, the dark areas are highly obscured at optical and near-infrared wavelengths (bottom panels) but are visible at mid-infrared and (sub)millimeter wavelengths (upper panels).

To study the evolutionary sequence of high-mass star formation, we need a large and comprehensive sample of high-mass star-forming sites. Many observational studies to identify high-mass objects in their early stages have been conducted using various tracers, such as maser emission (Walsh et al. 1997, 2014; Pestalozzi et al. 2005; Beuther et al. 2002), infrared colors (Palla et al. 1991; Molinari et al. 1996; Sridharan et al. 2002; Lumsden et al. 2002, 2013), radio continuum emission (Wood & Churchwell 1989; Kurtz et al. 1994) and high-density molecular tracers (Bronfman et al. 1996; Molinari et al. 1996). Dense, compact regions were sometimes seen in extinction at infrared wavelengths; these are referred to as Infrared Dark Clouds (IRDCs) (Rathborne et al. 2006). These objects were, therefore, considered to be an alternative criterion to identify a large unbiased sample of high-mass star forming-regions (Menten et al. 2005; Wyrowski 2008). However, those samples tend to target specific stages, and thus an unbiased sample was still missing. Alternatively, dust continuum emission in the (sub)millimeter regime, from cold dust grains can be used as a tracer of all the early stages of high-mass star (clusters) formation. Besides, the dust emission can be used to measure the dust mass and eventually total mass of the emitting cloud because the dust emission is in general optically thin.

For these reasons, the APEX Telescope Large Area Survey of the Galaxy (ATLAS-GAL) project was carried out (see the upper panel of Figure 1.3; Schuller et al. 2009). This survey is the largest and most sensitive ground-based (sub)millimeter survey yet conducted of the inner Galactic plane, with the primary goal to comprehensively cover a large sample of high-mass star-forming regions, involving all the stages displayed in Figure 1.2, in a systemic way.

This survey provides ∼10,000 dense clumps (the ATLASGAL Compact Source Cat-

alogue, CSC; Contreras et al. 2013; Urquhart et al. 2014a) which are ∼ 90 % of all dense molecular clumps (≥ 1000 $M_\odot$) in the Galaxy up to a distance of 20 kpc (Urquhart et al. 2014d, 2017). For this reason, the ATLASGAL CSC includes the vast majority of all potential high-mass forming clumps in the Galaxy (Urquhart et al. 2017). This fact is the major reason for observations of molecular and radio recombination lines toward ATLASGAL dust clumps presented in this thesis.

Complementary, a large number of Galactic plane surveys, which span near-infrared to radio wavelengths (e.g., GLIMPSE, Benjamin et al. 2003; WISE, Cutri et al. 2012; MSX, Price et al. 2001; MIPSGAL, Carey et al. 2009 ; Herschel Hi-GAL, Molinari et al. 2010a); and the Co-ordinated Radio and In- frared Survey for High-Mass Star Formation Hoare et al. 2012; Purcell et al. 2013), are available for the area covered by the ATLASGAL survey and provide a means to probe the proposed evolutionary sequence of high-mass star formation. However, these surveys only measure continuum emission, which cannot probe the dynamics of the objects and their surroundings, which can be obtained through spectral line observations as presented in this thesis. The most common way to identify HII regions is observing the thermal bremsstrahlung emission from ionized gas at radio (mostly centimeter) wavelengths (e.g., Wood & Churchwell 1989; Kurtz et al. 1994; Urquhart et al. 2007, 2009; Hoare et al. 2012; Purcell et al. 2013). Furthermore, radio continuum observations are important to distinguish between MYSOs and HII regions because MYSOs do not emit strong UV radiation that ionizes their surroundings (Hoare et al. 2007). The ionized gas within HII regions does emit not only free-free continuum emission but also spectral line emission via the recombination process. In addition, recombination lines at (sub)millimeter wavelengths do not suffer from the optical depth and extinction effects as compared to infrared spectral lines.

We will discuss the details of recombination line observations in Section 1.4. In the next section, we will explore the importance of HII regions for understanding high-mass star formation and the influence on their environments.

1.3   HII regions

If we assume an ionizing star is formed in uniform HI gas, it will completely ionize the HI gas within a sphere with Strömgen radius (R_s), in which ionization and recombination are in equilibrium. The Strömgen sphere will have a partially HI and HII ionized thin boundary with a thickness of about 10^{14} cm. Real HII regions are not formed in pure HI gas but are still embedded deep inside clumpy massive molecular clouds, complicating their detailed morphology. In this section, we will describe in detail the properties of small and dense HII regions found within the GMCs. Studies of these small and dense HII regions not only provide properties of recently formed high-mass stars but can also probe the dynamics and morphologies of their environment allowing us to investigate the density distribution and kinematics of their immediate surroundings.
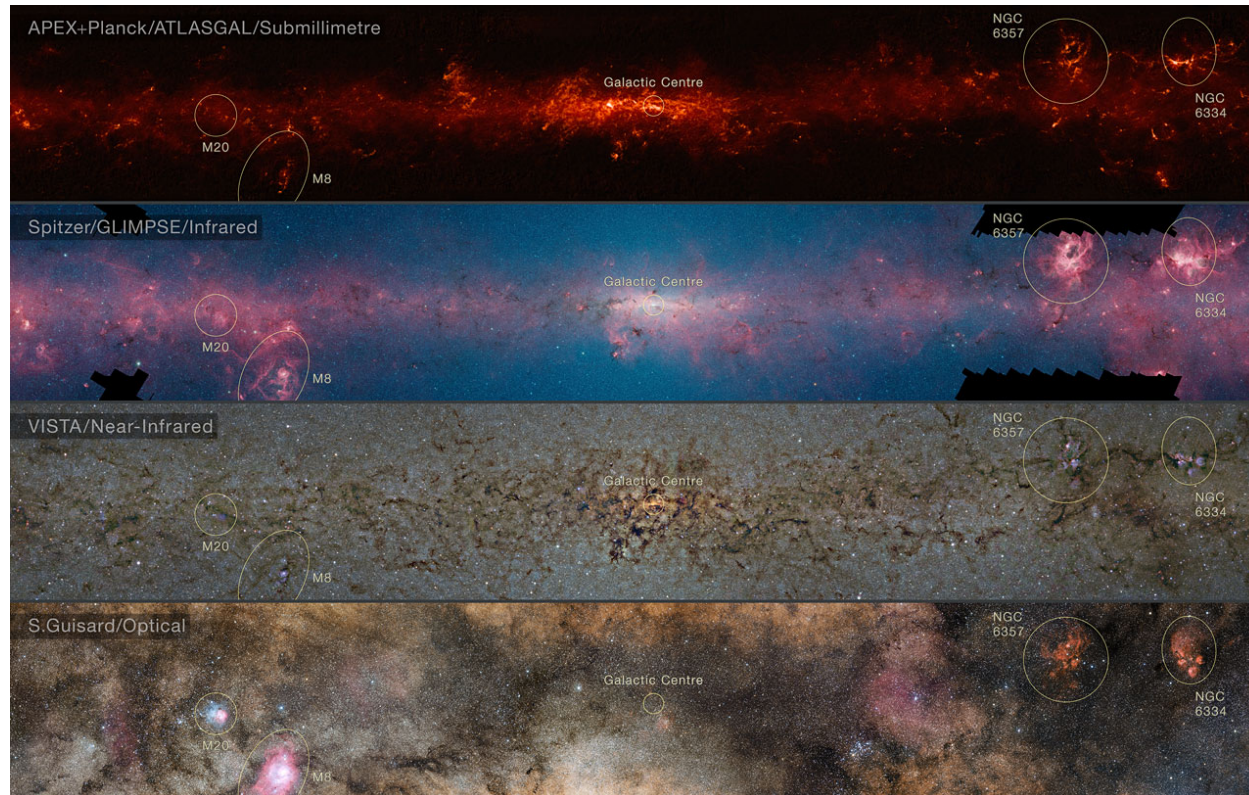
Figure 1.3: The central regions of the Milky Way observed at different wavelengths; from top to bottom, (sub)millimeter (ATLASGAL), mid-infrared (GLIMPSE), near-infrared (VISTA), and visible light. These images show the different ISM phase presented by several large continuum surveys (Credit: ESO/ATLASGAL consortium/NASA/GLIMPSE consortium/VVV Survey/ESA/Planck/D. Minniti/S. Guisard Acknowledgement: Ignacio Toledo, Martin Kornmesser).

Table 1.3: Physical properties of HII regions (Kurtz & Franco 2002).

Class of Regions	Diameter (pc)	Density (cm^{-3})	EM (pc cm^{-6})	Ionized Mass $(\text{M}_\odot)$
Hyper-compact	~ 0.03	$\geq 10^6$	$\geq 10^{10}$	$\sim 10^{-3}$
Ultra-compact	≤ 0.10	$\geq 10^4$	$\geq 10^7$	$\sim 10^{-2}$
Compact	≤ 0.50	$\geq 5 \times 10^3$	$\geq 10^7$	~ 1
Classic	~ 10.00	$\sim 1 \times 10^2$	$\geq 10^2$	$\sim 10^5$

Since the properties of the environment control their evolution, we will have a closer look at their evolution inside dense molecular clumps and their classification based on their observational properties.

1.3.1 Observational stages

Many observations have shown that young HII regions do evolve over their lifetime in dense molecular clumps. Stages of HII regions are classified in terms of their density and size, which are linked to their evolution (Table 1.3). HII regions are usually divided into *hypercompact* (HC HII), *ultracompact* (UC HII), *compact* and *extended* (or classic) HII regions (Wood & Churchwell 1989; Garay et al. 1993; Kurtz et al. 1994; Becker et al. 1994; Mezger & Henderson 1967; Habing & Israel 1979).

Historically, HC HII regions were discovered last after the other classes of HII regions because of their compactness (Gaume et al. 1995). At their densities, they are optically thick below 20 GHz and so were not detected in the early surveys conducted at frequencies $1-10$ GHz (see Figure 1.4). Their properties characterized by observations are ~ 0.03 pc in size, $\geq 10^6 \text{ cm}^{-3}$ in density, and $\geq 10^{10}$ pc cm^{-6} in emission measure (Kurtz et al. 2000; Hoare et al. 2007). After the HC HII stage, HII regions evolve to the UC HII stage and are more than an order of magnitude larger and two orders of magnitude less dense than the HC HII regions (see Table 1.3). The UC HII stage is still located in the inner, high-pressure parts of molecular clouds (Kurtz et al. 2000; Churchwell 2002). Compact HII regions have larger sizes (0.5 pc) and lower densities, and are located in more evolved zones of the clouds. However, they still have not entirely dispersed their natal molecular clouds.

There has recently been a strong interest in *HC HII* regions because they are considered to be extremely young HII regions thought to directly follow the MYSO stage. As mentioned above, HC HII are optically thick at centimeter radio wavelengths and so have been found mostly at millimeter wavelengths. Their high densities, emission measures, and compactness (see Table 1.3) point to the transition stage where the young stars rapidly finish their Kelvin$-$Helmholtz contraction and ionize their surroundings to create HC HII regions (see Figure 1.2) (Norberg & Maeder 2000; Keto & Wood 2006). If molecular material is still accreted via a disk during this HC HII stage, the disk prevents ionized gas expanding toward it, and thus the HII region will develop into the polar regions (Keto 2007).

Indeed, some HC HII regions are associated with high column density $(N(\text{H}_2) >$
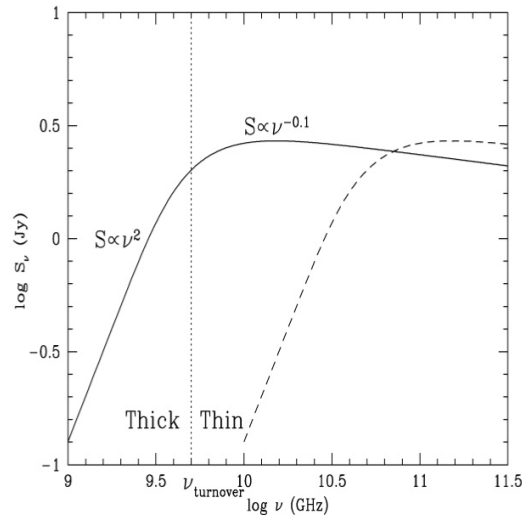
Figure 1.4: Radio spectrum of free-free emission from a spherical, homogeneous and isothermal H<small>II</small> region (Kurtz 2005). The solid line represents the free-free emission from a UC H<small>II</small> region whereas the dashed line indicates the free-free emission from a HC H<small>II</small> region. The vertical dotted line corresponds to a turnover frequency of $5\,\mathrm{GHz}$. At the turnover frequency, lower frequencies are optically thick and the higher ones are optically thin.

10^{23} cm^{-2}) clumps with infalling motion, molecular outflows, rotating flattened molecular envelopes, and time-varying radio continuum fluxes (Keto & Klaassen 2008; Galván-Madrid et al. 2008; Klassen et al. 2012). Also, this stage is very interesting to study with radio recombination lines as these lines probe the kinematics of the ionized gas; which will be discussed in the next Section 1.4.

The most interesting parts of the UCHII stage are its morphology and age. Wood & Churchwell (1989) first classified the morphologies of UC H<small>II</small> regions as cometary, core-halo, shell, and irregular-multiple peaked structures. An additional morphology, the bipolar type, was added later and is very rare. Figure 1.5 shows examples of all the morphologies except for the irregular-multiple peaked type, which appears to consist of sources surrounded by extended ionized gas. Since an UC H<small>II</small> region does not evolve in a uniform HI cloud, its morphology is likely to result from a combination of age, dynamics of ionized and molecular gas, the density structure of its immediate surroundings, and the motion of the central star relative to the ambient medium. Therefore, a simple isolated H<small>II</small> region model cannot explain the morphologies and long lifetimes of UC H<small>II</small> regions ($\sim 10^5$ years). Currently, there are six proposed hypotheses to solve the lifetime problem and different morphologies (e.g., Churchwell 1999 and references therein). Those hypotheses are the champagne flow (or blister) model; infall model; photo-evaporating disk model; pressure-confined H<small>II</small> region; stellar wind-supported bow shock model; and mass-loaded stellar wind model. Apart from the bow shock model, none of the other models can explain both the morphology and the long lifetime together. The
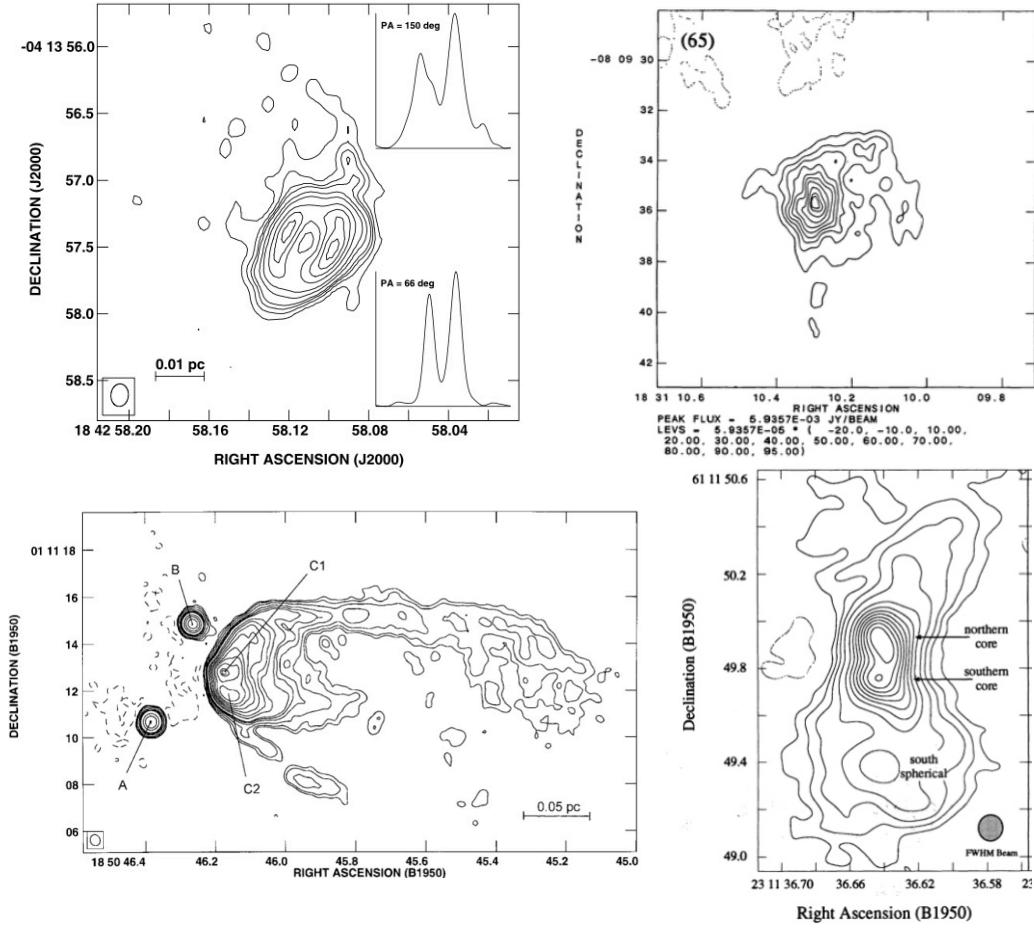
Figure 1.5: Four typical morphologies of HC HII and UC HII regions. *Upper panels*: shell HII region (left, Sewiło et al. 2008) and core-halo HII region (right, Wood & Churchwell 1989) from left to right. *Lower panels*: cometary HII region (with unresolved core HC HII regions) (left, Sewilo et al. 2004b) and bipolar HII region (right, Gaume et al. 1995) from left to right.

bow shock model can resolve both issues, but it needs detailed information about the ambient density, stellar velocity with respect to the surroundings, and the viewing angle of the observations. Although a single hypothesis cannot explain all cases, different ones may be applicable at different stages of the evolution of UC H II regions (Churchwell 1999). To confirm predictions from these hypotheses, it is necessary to measure the kinematics of the ionized gas within UC H II regions because each predicts different kinematics.

The UC H II regions found by Wood & Churchwell (1989) and Kurtz et al. (1994) showed *extended lower density ionized halos* (Garay et al. 1993; Kurtz et al. 1999; Kim & Koo 2001) surrounding the UC H II regions. Radio recombination line studies toward these extended ionized gas of the UC H II regions (Kim & Koo 2001) have revealed that the extended emission regions are not only chance projections with the UC H II regions, but also many of them are physically associated with the UC H II regions. The measured energy flux from the extended regions requires ionization by a high-mass stellar cluster rather than a single high-mass star. One possible explanation was proposed by Franco et al. (2000) and Kim & Koo (2001) for these associations of both extended ionized gas and their UC H II regions. They suggested that the existence of both UC H II and extended emission is caused by a champagne flow combined with the clumpy structure of the molecular core. To confirm this explanation, determining physical parameters of both the ionized and molecular emission and comparing these with theoretical models are required.

1.4   Radio recombination lines in the Milky Way

In the previous sections, we have explored the different stages of H II regions in the MW and have discussed open questions concerning these objects. In this section, we will demonstrate how recombination lines can be used as an important tool to address some of these open questions.

From an ionized gas region, we can detect spectral lines that result from transitions between highly excited hydrogen atomic levels after the recombination of ions and electrons into atoms. After electrons have recombined, they cascade downwards from an upper level to a lower level. When these lines appear in the radio regime, they are called *radio recombination lines* or *RRLs*. In this thesis, we will use RRLs emitted at millimeter and submillimeter wavelengths. In this section, we will explain why we chose the RRLs at the short wavelengths to study H II regions which are associated with dense dust clumps.

1.4.1   First detection of radio recombination lines

In 1945, van de Hulst suggested the possibility of radiation from transitions between highly excited levels of atoms in the radio regime. The detection of such RRLs depends upon the shape of the emission lines. Stark broadening due to high electron densities was expected as a major broadening effect reducing peak intensities.
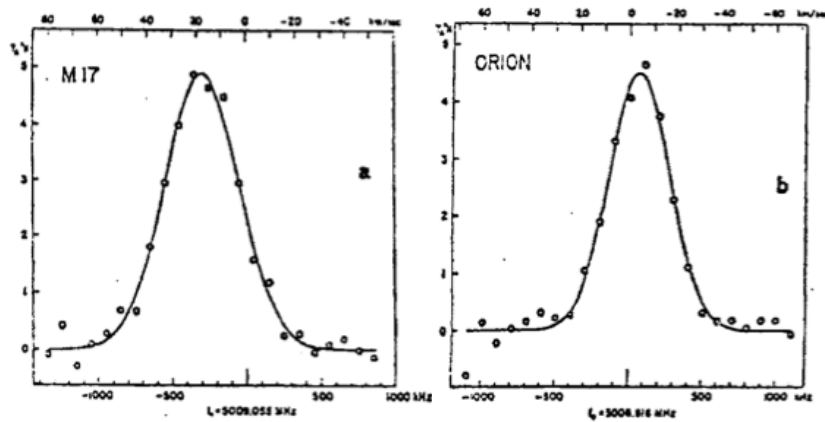
Figure 1.6: The first detection of RRLs (H109α) with a significant signal-to-noise level toward M17 and Orion HII regions, by Hoglund & Mezger (1965).

Therefore, at that time, van de Hulst and other astronomers were pessimistic about detecting recombination lines at radio wavelengths. However, Kardashev (1959) suggested the opposite conclusion and made detailed calculations of the expected line widths and intensities of excited hydrogen RRLs in HII regions. Based on the new calculation by Kardashev, Dravskikh & Dravskikh (1964) detected the H104α RRLs in the Omega nebula. However, this detection was too weak to unambiguously confirm the presence of an RRL. In 1965, the H90α and H104α RRLs were detected with a reasonable signal-to-noise by Sorochenko & Borodzich (1965) and Dravskikh et al. (1965). After their detections, Hoglund & Mezger (1965) detected the H109α RRLs shown in Figure 1.6 with a significantly good signal-to-noise level using the 43 m telescope of the National Radio Astronomy Observatory in Green Bank. These early efforts resulted in the discovery of spectral lines in the radio regime from the process of recombination of ions and electrons and paved the way for RRLs to become a powerful tool to study ionized gas in the Galaxy.

1.4.2 Radio recombination lines from HII regions

Radio continuum emission provides a means to derive many properties of ionized gas from HII regions in the MW. Nevertheless, observing RRLs is necessary to measure the kinematics of the ionized gas to address the unsolved problems of age and morphology of young HII regions, and physical association of compact HII regions and extended ionized halo emission.

As discussed in the previous section, it is still an open question at which stage the HC HII regions form. Not only their extraordinary compactness is evidence for their young age, but also observations of particularly broad RRLs support that they are a stage between MYSOs and UC HIIs. Frequently, HC HII regions were associated with extremely broad RRLs (FWHM ~ 50 to $180 \, \mathrm{km \, s^{-1}}$), while UC HII regions are considered young, but more evolved HII regions associated with narrower linewidths of

RRLs, $\sim 30\,\mathrm{km\,s^{-1}}$ (Kurtz et al. 2000; Hoare et al. 2007). Also, rare bipolar Hɪɪ regions showed the existence of broad RRLs with strong velocity gradients along the pole axes. The broad RRLs toward some HC Hɪɪ and bipolar Hɪɪ regions were considered to trace the high-velocity ionized flows of rapidly expanding young Hɪɪ regions (Gaume et al. 1994; Churchwell 2002). In addition, RRLs provide kinematics and electron temperature of evolving Hɪɪ regions. Several hypothesis (e.g., bow-shock or champagne flow, Hoare et al. 2007) offer reasonable explanations for the evolution of Hɪɪ region, but the predicted kinematics of the ionized gas has to be confirmed through observations. IR fine structure lines and recombination lines are often used to probe the ionized gas from different morphologies of Hɪɪ regions (Zhu et al. 2008). IR fine-structure lines are difficult to observe toward high extinction regions, whereas RRLs do not suffer from extinction.

RRLs from Hɪɪ regions have also played a remarkable role in helping to determine the structure of the Galaxy. The strongest emitting sources of RRLs are Hɪɪ regions which directly trace current high-mass star-forming regions. Reifenstein et al. (1970) and Wilson et al. (1970) carried out RRL observations in the northern ($l = 348° \sim 209°$) and southern ($l = 189° \sim 49.5°$) hemispheres, respectively, to understand the distribution of Hɪɪ regions in the Galaxy. They superposed the locations of the Hɪɪ regions on the Galactic plane with kinematic distances determined using a rotation curve of the Galaxy. However, they could not estimate the distance of sources located within the inner Galaxy. Later, Downes et al. (1980) and Caswell & Haynes (1987) simultaneously observed RRLs and H_2CO absorption lines to resolve the distance ambiguity towards the inner Galactic Hɪɪ regions. Taylor & Cordes (1993) plotted the distribution of Hɪɪ regions using the RRL data from Downes et al. (1980) and Caswell & Haynes (1987) with the spiral structure model of Georgelin & Georgelin (1976), adopting a value of 8.5 kpc of the distance between the Galactic center and the Sun. The distribution of Hɪɪ regions is well described by the Galactic spiral structure, and observation of RRLs provide good measurements of distances for the high-mass star-forming regions. Large surveys of RRLs have been mostly conducted at centimeter wavelengths (e.g., Caswell & Haynes 1987; Lockman 1989; Araya et al. 2002; Watson et al. 2003; Quireza et al. 2006; Anderson et al. 2011, 2014; Alves et al. 2015) whereas observation of RRLs at shorter wavelengths (e.g., Churchwell et al. 2010) have only been made toward relatively a few source sample.

1.5 Photodissociation regions

Photodissociation regions (PDRs) occur at the interface between Hɪɪ regions and molecular clouds and are caused by energetic FUV radiation from the ionizing stars of the Hɪɪ regions that dissociate molecules into atoms and ionizes certain atoms (e.g., Hollenbach & Tielens 1997). Early observations using the fine structure lines of [Cɪɪ] 158 μm and [Oɪ] 63 μm towards massive star-forming regions such as Orion A and M17 (Melnick et al. 1979; Storey et al. 1979; Russell et al. 1980, 1981) revealed predominately neutral IR-luminous regions lying outside Hɪɪ regions. Figure 1.7 shows an astonishing
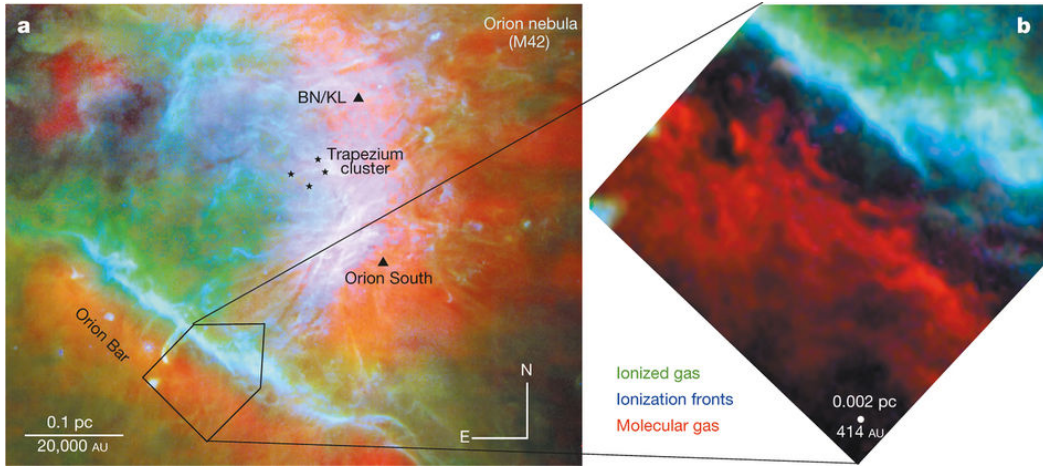
Figure 1.7: The Orion bar as a prototype PDR. These images show a multiphase ISM view of the Orion nebula and molecular cloud (Goicoechea et al. 2016). The three colors present different phases of the ISM in this region. The red color shows the extended molecular cloud traced by HCO^+ emission with ALMA interferometer. The green color is the hot ionized gas surrounding the stars probed by the [SII] 6,731 Å line and the interface region is detected by the [OI] 6,300 Å line (blue). Those fine structure lines were mapped with VLT/MUSE.

image of the Orion PDR region where we can see an evidently layered appearance of the PDR between the ionization front and molecular gas zone. In the PDR interfaces, the ultraviolet radiation field is continuously attenuated with distance from the stars as it penetrates into the molecular cloud (red color in Figure 1.7). Such PDRs are one of the main targets of this thesis, but the general concept of PDRs includes all places where FUV ($6\,\mathrm{eV} < h\nu < 13.6\,\mathrm{eV}$) photons influence the ISM. The FUV photons illuminate the star-forming regions as seen in the mid-infrared GLIMPSE image of Figure 1.3 and excite complex molecules such as polycyclic aromatic hydrocarbons (PAHs) which emit strongly at mid-IR wavelengths. Studying PDRs allows us to investigate the influence of FUV radiation photons mostly emitted from high-mass stars on the structure, chemistry, thermal balance, and evolution of the neutral interstellar medium of galaxies. Overall, PDR studies help to investigate the role of UV radiation in affecting the ISM physical conditions and its role in regulating the star formation process in galaxies.

1.5.1 Physical structure

We here will have a close look at the structure of PDRs in the standard PDR model with a plane parallel structure (Figure 1.8). The incident UV flux from the interstellar radiation field or high-mass O/B stars penetrates into molecular clouds. Due to strong UV radiation with energies above 13.6 eV, hydrogen atoms are ionized, and a HII region is formed. H^+ recombines into atomic hydrogen after the ionization front. Just beyond
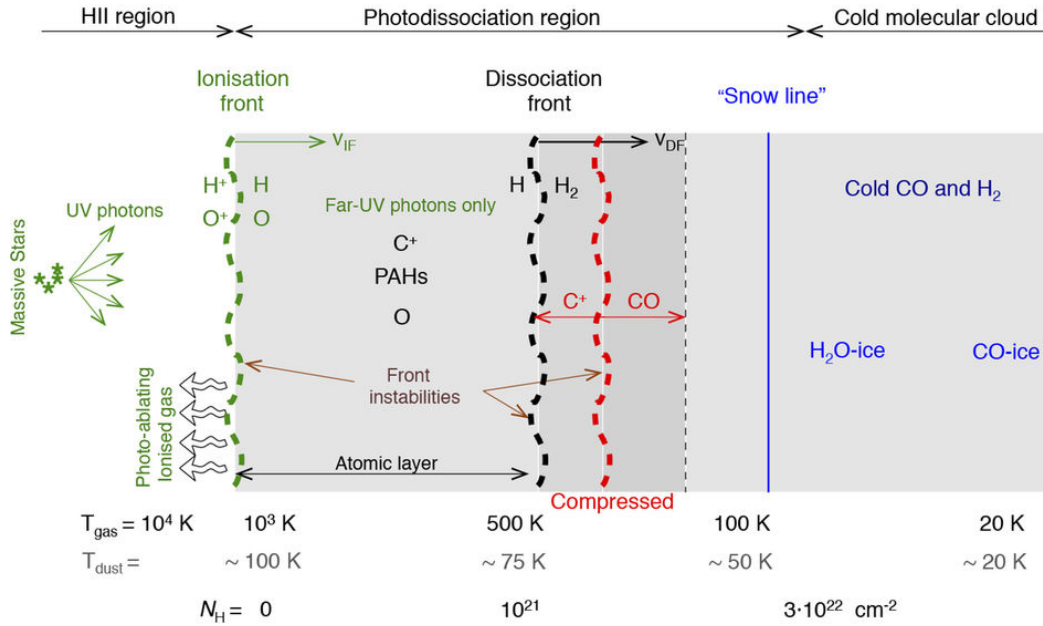
Figure 1.8: Diagram of a plane parallel photodissociation region and molecular cloud
(Credit: Goicoechea et al. 2016). The high-mass stars provide the incident UV radiation
into the molecular cloud from left to right. V_{IF} and V_{DF} are the velocity of the
advancing ionization and dissociation fronts. The "Snow line" represents inner cloud
layers where molecular gases start to freeze.

the ionization front, a PDR starts, but it does not sharply separate from the HII region.
Both regions overlap in a thin HII/HI interface where the Lyman continuum photons
are absorbed. The FUV radiation with energy less than the $13.6\,\text{eV}$ continues into
the molecular cloud. That energy can still ionize heavier atoms such as carbon; C$\rightarrow$
C$^+$. Therefore, C$^+$ coexists in PDRs with atomic hydrogen. If the FUV flux is strong
enough in the molecular clouds, oxygen (O) and carbon are not bound in CO molecules,
but molecules are photodissociated.

    The strength of the FUV flux can be measured in units of the average interstellar
FUV flux ($1.6 \times 10^{-3}\,\text{erg}\,\text{cm}^{-2}\,\text{s}^{-1}$, Habing 1968). The incident FUV radiation field
(G_0) can be much higher ($G_0 \gtrsim 10^6$) in the vicinity ($0.1\,\text{pc}$) of an O star. The visual
extinction, A_V, is often used for measuring the depth into PDRs. C$^+$ lies at the outer
part of PDRs, and after the dissociation front the H$_2$ layer begins, but as we have
mentioned above, these layers overlap each other (C$^+$/H$_2$). The transition from H
to H$_2$ happens at $A_V \approx 2$ ($A_V \approx 1$ corresponds to $N_H \simeq 1.87 \times 10^{21}$ cm^{-2}). The
layer of C$^+$ can expand to $A_V \sim 2-4$, and the layer of atomic oxygen can reach up to
$A_V \sim 10$. Further into the cloud, the UV radiation is shielded, and thus the physical
and chemical conditions are those of a cold and dense molecular cloud. The exact
depths of the layers of H/C$^+$/O (or PDRs) depend on the FUV photodissociation of
molecules and the FUV photoionization of carbon.

The attenuation of the FUV flux is significant for the structure of PDRs. The propagation of FUV radiation is governed by dust absorption and scattering, and the global geometric structure of the molecular clouds. Many of the previous studies (e.g., Roberge et al. 1981, 1991) considered the structure of PDRs as a homogeneous plane parallel slab like the diagram shown in Figure 1.8. However, it has been revealed interstellar clouds are not homogeneous on all scales (Falgarone & Phillips 1996). The clumpy structure in the PDRs needs to be considered for the penetration of FUV radiation (e.g., Stutzki et al. 1988; Boisse 1990). The penetration of FUV radiation will vary because of the clump filling factor and density difference between clump and interclump gas. FUV radiation passing through such clumpy PDRs raises large fluctuations in the mean intensity of relevant molecules when each clump is optically thick, scattering in clump or interclump gas is not critical, and its radiation field irradiate the molecular clouds from any direction (Monteiro 1991; Störzer 1997). One important reason to study PDRs is that most of the molecular gas in the Galaxy exists in them (at $A_V \lesssim 10$ in GMCs) except for the molecular gas in dense star-forming cores (Hollenbach & Tielens 1997). In addition, PDRs are bright IR radiation sources because the large carbon molecules (known as polycyclic aromatic hydrocarbons) emit IR feature at IR wavelengths and dust grains emit at mid- and far-infrared wavelengths after absorbing the incident starlight inside PDRs at a depth of $A_V \sim 1$ (Wright et al. 1991; Hollenbach & Tielens 1997).

1.5.2 Chemistry in photodissociation regions

Chemistry in a (dense) PDR almost resembles that in diffuse clouds. In particular, photoreaction, electron recombination, self-shielding of H_2/CO, and dust absorption are very important, and the combination of them change the structure of PDRs shown in Figure 1.8 (e.g., Tielens & Hollenbach 1985; Hollenbach et al. 1991; Fuente et al. 1993, 1995).

The emission from vibrationally excited H_2 is strong in PDRs with high gas temperature ($\gtrsim 500\,\mathrm{K}$). As a result, reactions between atoms and radicals (e.g., C^+, O, OH) with H_2 can easily happen and become dominant (see Hollenbach & Tielens 1997 and references therein). Photodissociation of H_2 is driven by H_2 absorbing FUV in the Lyman, and Werner transitions in a range of the 912 - 1100 Å(Draine & Bertoldi 1996, Hollenbach & Tielens 1997 and references therein). However, when H_2 column density becomes high ($> 10^{14}\,\mathrm{cm}^2$), the self-shielding of H_2 creates a sharp HI/H_2 transition zone. In PDRs with strong FUV fields, the transitions zone is significantly affected by dust absorption and forms at $A_V \sim 2$. The dust absorption largely controls the location of the C^+/C/CO transition in the bright PDRs (Eidelsberg et al. 1992, van Dishoeck & Black 1988, Hollenbach & Tielens 1997 and references therein). Furthermore, reactions of H_2 with C^+, O, N, S^+, and Si^+ are especially crucial to initiate chemical reactions (Wagner & Graff 1987).

A simple model is the *steady-state stationary PDR model* to explain the chemistry in PDRs. It assumes no time-dependent effects and ignores flows through the PDR. Many studies (e.g., Tielens & Hollenbach 1985; Sternberg & Dalgarno 1989; Hollenbach et al.

1991) modeled PDRs assuming that the timescale of H_2 formation on grains is shorter than the dynamical timescales or the time scales of a change in the FUV flux. These models considered the simple structure of a PDR as shown in Figure 1.8. Recently, models have taken into account clumpy PDRs to investigate the C+/C/CO transitions (e.g., Burton et al. 1990; Tauber & Goldsmith 1990; Meixner & Tielens 1993; Stoerzer et al. 1996).

1.6 About this thesis

1.6.1 Goal of the thesis

The presence of H<small>II</small> regions is a clear signpost of ongoing high-mass star formation in molecular clouds. In addition, H<small>II</small> regions dramatically alter the physical and chemical conditions of their surroundings. As a result, layers (PDRs) of ionized and dissociated gas are formed around H<small>II</small> regions due to UV radiation from O and B type stars. The properties (e.g., kinematics, chemistry, etc.) of these regions allow us to understand the processes of high-mass star formation and the evolution of molecular clouds (eventually, the evolution of the Galaxy). The ATLASGAL survey provides a large and comprehensive sample covering sources without biases of any evolutionary phases. This sample contains the most active star-forming regions in the inner part of the Galaxy. The ATLASGAL clumps provide an excellent sample to study the influence of evolving H<small>II</small> regions inside dense molecular clumps on their environments. Therefore, the principal goal of this thesis is to characterize the physical properties (e.g., electron density, photoionization rate, etc.) of H<small>II</small> regions associated with the clumps, and to investigate how PDRs change their chemistry.

To conduct this study, we have utilized large-sample molecular line surveys toward $\sim 1,000$ ATLASGAL clumps, covering the whole 3 millimeter (mm) wavelength band with the IRAM 30 m telescope and a large fraction of the band with the Mopra 22 m telescope. In addition to the 3 mm observations, we also used the APEX 12 m telescope to observe (sub)millimeter (submm) RRLs toward a well-selected sample of clumps.

We have used specific emission lines among the observed atoms and molecular species from the observation data sets. As introduced in previous sections, hydrogen RRLs (Chapters 4 and 5) are an excellent tool to study H<small>II</small> regions. Therefore, we used these RRLs to identify H<small>II</small> regions and to characterize the properties of them for this thesis. In addition, we also studied the detailed properties of RRLs using those observations from millimeter to (sub)millimeter wavelengths (Chapter 5).

To investigate the chemical influence of the H<small>II</small> regions on their surroundings, we selected $C^{18}O$, HCO, $H^{13}CO^+$, HOC^+, C_2H, c-C_3H_2, CN, $HC^{15}N$, $H^{13}CN$ and $HN^{13}C$ from the same observations with the IRAM 30 m telescope. From these molecular lines, we measured physical parameters (e.g., column density and abundance rates) to compare their quantity to other PDRs such as the Orion bar and Horsehead nebula.

1.6.2   Outline of the thesis

This thesis consist of three parts: the first covers in Chapters 2 and 3 important theoretical background needed for the scientific analysis. The second part presents the observational results and their analysis in Chapters 4, 5, and 6. The last part consists of summary and outlook in Chapter 7. Here follows a short outline of the thesis:

• **In Chapter 2** we give the reader a general background of radio continuum and recombination line emission processes and applications of those to study HII regions. We first describe radiative transfer for continuum and recombination emission including maser emission. Then, three broadening effects on the profile of radio recombination lines are presented. Finally, we present how physical parameters of HII regions are derived.

• **In Chapter 3** we introduce the physics of molecular lines for different types of molecules, including their hyperfine structure. Especially, we describe the derivation of molecular column densities for different types of molecules.

• **In Chapter 4** we present results of hydrogen radio recombination observations at millimeter wavelength using the IRAM 30 m and Mopra 22 m telescopes. We identify HII regions toward clumps and investigate characteristics of these regions by means of mm-RRLs.

• **In Chapter 5** we show results of hydrogen radio recombination observations at (sub)millimeter wavelength using the APEX 12 m telescope. We also compare the submm-RRL to mm-RRLs from the previous chapter.

• **In Chapter 6** we present results of the molecular line analysis using the same observations from the IRAM 30 m telescope and investigate how PDRs associated with the HII regions, studied in the previous chapters, affects the chemistry of the molecular clumps.

• **In Chapter 7** we summarize our results and propose future investigations using interferometers such as ALMA, NOEMA, and JVLA to obtain high-resolution observations toward some interesting sources.

Radio continuum and recombination emission from HII regions

Contents

Thermal bremsstrahlung emission, also referred to as free-free emission, and spectral emission lines of hydrogen atoms deliver important information (e.g., density, brightness, structure, and so on) about ionized gas clouds (HII regions) in the Milky Way. They are essential tools for identifying HII regions and characterizing their properties.

Table 2.1: Properties of the most abundant atoms of RRL and their Rydberg constants.

Atom	Atomic mass (a.m.u)	Ionization potential (eV)	Rydberg Constant (cm^{-1})	Δv $(v_\mathrm{X}$ - $v_\mathrm{H})$ $(\mathrm{km\,s}^{-1})$
H^1	1.007825	13.6	109,677.58	000.0
He^4	4.002603	24.6	109,722.27	-122.1
C^{12}	12.000000	11.4	109,732.30	-149.5
N^{14}	14.003074	14.5	109,733.01	-151.5
O^{16}	15.994915	13.6	109,733.55	-152.9
S^{32}	31.972070	10.3	109,735.43	-158.0

In this chapter, we will present the theoretical background of radio continuum emission and recombination lines (RRLs), and their applications to study the properties of astronomical objects in the MW.

The hydrogen atom is the most common atom in the Universe that gives rise to recombination lines, but other abundant heavier atoms, like helium (He), carbon (C), and oxygen (O), also produce observable recombination lines. The frequency of each atomic recombination line is described by the following equation,

$$
\begin{aligned}
\nu_{\mathrm{n_1+\Delta n \to n_1}} &= \frac{2\pi^2 m Z^2 e^4}{h^3}\left(\frac{1}{n_1^2} - \frac{1}{(n_1+\Delta n)^2}\right) \\
&= RcZ^2\left(\frac{1}{n_1^2} - \frac{1}{(n_1+\Delta n)^2}\right),
\end{aligned}
\tag{2.1}
$$

where Z and e are the nuclear and electronic charge, respectively, and c is the speed of light. Here, we notate upper and lower levels as $(n_1 + \Delta n)$ and n_1 because RRLs are generated by cascading between principal quantum number (n) levels. This notation of the energy levels for RRLs is used to prevent confusion with the notation for number densities (in the upper level, n_u, and in the lower level, n_l) of atoms or molecules in energy levels. R is the Rydberg constant for atoms, derived by $R = 109737.3(1 + m/M)^{-1}$ $[\mathrm{cm}^{-1}]$, where M is mass of the nucleus and m is the electronic mass. Δn is the notation for the cascade order between transition levels. $\Delta n = 1, 2, 3, 4, \cdots$ and so on are called as α, β, γ, δ line and so on. For instance, H42α line refers to the hydrogen radio transition from level $n_{43} \to n_{42}$ and H52β line is from $n_{54} \to n_{52}$. Table 2.1 presents the Rydberg constant and properties of the most abundant atoms.

As mentioned above, other elements also have RRLs although their abundance in the ISM is much lower. Figure 2.1 shows the RRLs of the heavier elements compared to the hydrogen atom, separated in frequency. The frequencies of those RRLs are given by Eq. (2.1). As seen in Figure 2.1, the RRLs of He, C, and X atoms are shifted from the H RRL in velocity with the fixed separations listed in Table 2.1. Frequencies of the C RRL and other heavier RRLs (so-called X RRLs) are very close and often blended with each other. The X RRLs represent RRLs of N, O, S, and etc. but it is generally difficult to separate them because their frequencies are too close to each other. Except for hydrogen and helium, the other atoms do not require high ionization energy, but
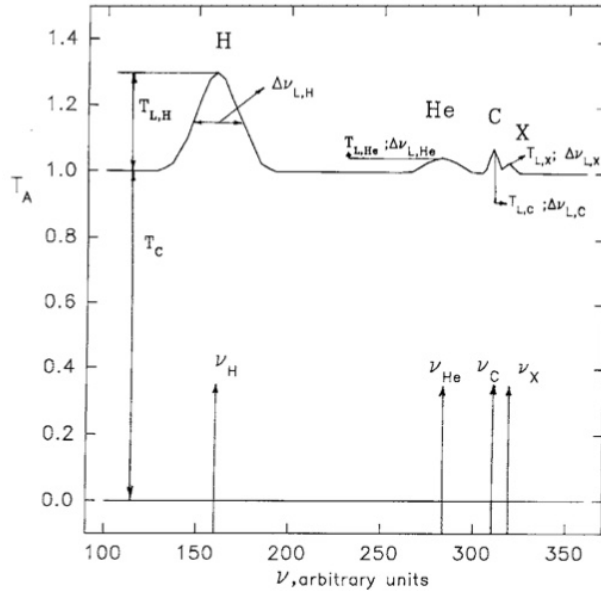
Figure 2.1: Hypothetical spectra of radio recombination lines of hydrogen, helium, carbon and X atoms, which indicate the merged RRL from heavier atoms such as N, O, S and etc (Credit: Gordon & Sorochenko 2002).

their abundances are much smaller than those of hydrogen and helium. As a result, the intensities of those RRLs in HII regions become much weaker and the detection of these RRLs requires high sensitivity. We will discuss the physical conditions and applications of the most common RRLs (hydrogen and helium RRLs) in Section 2.6.

2.1 Radiative transfer

To understand the complex emission processes in the ISM, we first have to introduce the particular physics involved in the radiative transfer.

To start, we consider loss and gain mechanisms in stationary condition. When the specific intensity, I_ν, from sources pass through a typical cloud from the back to the front, the specific intensity changes due to radiative loss (absorption and scattering) and gain (radiating elements) mechanisms. The change of I_ν can be expressed by the following equation,

$$dI_\nu = -I_\nu \kappa_\nu dx + \varepsilon_\nu dx. \tag{2.2}$$

It describes the change in I_ν through a slab of material in an interstellar cloud of thickness dx. κ_ν is the line absorption coefficient and takes into account the attenuation of the radiation in the direction of the observer. ε_ν is called the line emission coefficient and accounts for all gains in intensity.

In thermodynamic equilibrium (TE), radiation is in equilibrium with matter, isotropic, and prescribed by a blackbody energy distribution. I_ν is conserved along

a ray ($dI_\nu/dx = 0$ and $I_\nu = B_\nu(T)$), resulting in

$$\frac{dI_\nu}{dx} = 0 = -\kappa_\nu B_\nu(T) + \varepsilon_\nu. \tag{2.3}$$

Here, $B_\nu(T)$ is known as the Planck Function and can be written as,

$$B_\nu(T) \equiv \frac{2h\nu^3}{c^2} \frac{1}{e^{h\nu/k_B T} - 1}. \tag{2.4}$$

From Eq. (2.3), we can obtain Kirchoff's law which states the ratio of emission and absorption coefficients, for a system in TE:

$$\frac{\varepsilon_\nu(T)}{\kappa_\nu(T)} = B_\nu(T). \tag{2.5}$$

Before integrating Eq. (2.2) along the path crossing through the cloud, we can define τ_ν, called the optical depth or opacity as

$$\tau_\nu = -\int_{x0}^{x} \kappa_\nu(x)dx \quad \text{or} \quad d\tau_\nu = -\kappa_\nu dx. \tag{2.6}$$

Note if $d\tau_\nu \ll 1$, the emission from the cloud is optically thin; if $d\tau_\nu \gg 1$, optically thick.

Finally, the intensity seen by the observer is given by integrating Eq. (2.2) along the cloud, as

$$I_\nu(x) = I_\nu(0)e^{-\tau_\nu(x)} + \int_0^{\tau_\nu(x)} B_\nu(T(\tau))e^{-\tau}d\tau. \tag{2.7}$$

If the medium in the cloud is isothermal, and that is $T(\tau_\nu) = T = \text{constant}$, Eq. (2.7) can be computed explicitly resulting in

$$I_\nu(x) = I_\nu(0)e^{-\tau_\nu(x)} + B_\nu(T)(1 - e^{-\tau_\nu(x)}). \tag{2.8}$$

In the radio regime where $h\nu \ll k_B T$, the "Rayleigh-Jeans approximation" approximates the Planck Function, and it becomes $B_\nu(T) \approx 2\nu^2 k_B T/c^2$. On the other hand, in the optical range where $h\nu \gg k_B T$, the "Wien approximation" approximates the Planck Function, $B_\nu(T) \approx \frac{2h\nu^2}{c^2} \exp(-h\nu/k_B T)$.

Since B_ν is proportional to T in the Rayleigh-Jeans approximation, the specific intensity is often expressed as the equivalent blackbody brightness temperature, T_b: $T_b(\nu) \equiv I_\nu c^2/2k_B \nu^2$. We can rewrite Eq. (2.8), assuming the Rayleigh-Jeans approximation in terms of temperatures:

$$T_b(x) = T_b(0)e^{-\tau_\nu(x)} + T(1 - e^{-\tau_\nu(x)}). \tag{2.9}$$

Under the specific conditions when there is no background radiation, such that $T_b(0) = 0$, we can even simplify this equation. It becomes in the optically thin case, $\tau_\nu \ll 1$,

$$T_b = \tau_\nu T, \tag{2.10}$$

and in optically thick case, $\tau_\nu \gg 1$,

$$T_b = T. \tag{2.11}$$
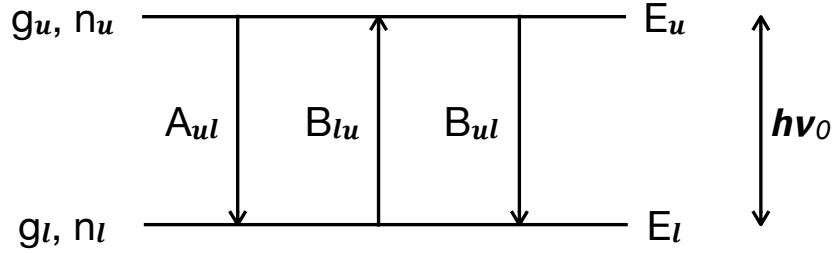
Figure 2.2: Three possible processes between an upper energy level (E_u) and a lower energy level (E_l). The three processes are described by their Einstein coefficients A_{ul}, B_{lu}, and B_{ul} which are spontaneous, absorption, and stimulated coefficients, respectively. n_u and n_l indicate the number density of atoms or molecules in the levels, and g_u and g_l are the statistical weights of those energy levels.

2.2 Spectral line radiative transfer with Einstein coefficients

The intensity measured from an object depends on the temperature of the cloud, the temperature of the background, and the optical depth through the cloud. To compute the optical depth, we first need to describe the three coefficients related to the electromagnetic properties of radiation.

Figure 2.2 presents for a simple two level system the absorption and emission processes. The spontaneous emission coefficient, A_{ul}, is the average photon emission rate (s^{-1}) for an atom or a molecule transiting from an upper energy level (u) to a lower energy level (l) without interference of the surrounding radiation field. On the other hand, the other two Einstein coefficients, B_{lu} and B_{ul}, describe emission and absorption stimulated by the surrounding radiation field. Absorption processes can be described by the absorption Einstein coefficient, $B_{lu}\bar{u}$, which represents the average rate of absorbed photons by a single atomic or molecular system in its lower energy level. Here, $\bar{u}$ is the profile-weighted mean energy density of the surrounding radiation field, $\bar{u} = \int_0^\infty u_\nu(\nu)\phi(\nu)d\nu$ because the energy levels have finite widths. The opposite process of the absorption, the so-called negative absorption, is stimulated emission which results from a photon with the energy of $h\nu_0$ stimulating the system to yield a second photon with the same energy and direction. There, ν_0 is the center frequency. Then the rate of stimulated emission is defined as $B_{ul}\bar{u}$.

At local thermodynamic equilibrium (LTE), the average rate of photons created by both spontaneous and stimulated emission must be in balance with the average rate of photons absorbed,

$$n_u A_{ul} + n_u B_{ul}\bar{u} = n_l B_{lu}\bar{u} \tag{2.12}$$

where n_u and n_l are the number densities of atoms or molecules in the upper and lower levels, respectively. Also, at LTE the ratio of n_u to n_l can be described by the

Boltzmann equation,

$$\frac{n_u}{n_l} = \frac{g_u}{g_l} e^{-\frac{E_u - E_l}{k_B T}} = \frac{g_u}{g_l} e^{-\frac{h\nu_0}{k_B T}}. \tag{2.13}$$

From Eq. (2.12), the average energy density $\bar{u}$ can be written as,

$$\bar{u} = A_{ul} \left[\frac{g_l}{g_u} \exp\left(\frac{h\nu_0}{k_B T}\right) (B_{lu} - B_{ul}) \right]^{-1} \tag{2.14}$$

In TE, $\bar{u}$ is described by the Planck radiation law, $\bar{u} = \frac{4\pi}{c} B_{\nu_0}$:

$$\bar{u} \approx \frac{8\pi h\nu_0^3}{c^3} \left[\exp\left(\frac{h\nu_0}{k_B T}\right) - 1 \right]^{-1}. \tag{2.15}$$

Eq. (2.14) must agree with Eq. (2.15), therefore:

$$\frac{A_{ul}}{B_{ul}} \left[\frac{g_l}{g_u} \frac{B_{lu}}{B_{ul}} \exp\left(\frac{h\nu_0}{k_B T}\right) - 1 \right]^{-1} = \frac{8\pi h\nu_0^3}{c^3} \left[\exp\left(\frac{h\nu_0}{k_B T}\right) - 1 \right]^{-1} \tag{2.16}$$

From which follows

$$\frac{g_l}{g_u} \frac{B_{lu}}{B_{ul}} = 1 \tag{2.17}$$

and

$$
\begin{aligned}
A_{ul} &= \frac{8\pi h\nu_0^3}{c^3} B_{ul} \quad \text{(energy density)} \quad \text{or} \\
&= \frac{2h\nu_0^2}{c^2} B_{ul} \quad \text{(specific density)}.
\end{aligned}
\tag{2.18}
$$

Eqs. (2.17) and (2.18) are called the Einstein relations.

For dipole emission, the spontaneous emission coefficient A_{ul} can be expressed by the dipole matrix element $|\mu_{ul}|^2$,

$$A_{ul} = \frac{64\pi^4}{3hc^3} \nu_{ul}^3 |\mu_{ul}|^2 \tag{2.19}$$

In the previous section, material properties were described by macroscopic parameters, while the emission coefficient and the absorption coefficient are associated with atomic properties of the matter. The processes described by the Einstein coefficients contribute to the I_ν passing through a slab of its thickness dx. Therefore, the three processes transiting between E_u and E_l contribute to the energy $h\nu_0$ distributed over the entire solid angle 4π. The total amount of energy absorbed, and emitted by both stimulated and spontaneous emission are defined by,

$$dE_a(\nu) = h\nu_0 n_l B_{lu} \frac{4\pi}{c} I_\nu \phi_e(\nu) dV \frac{d\Omega}{4\pi} d\nu dt. \tag{2.20}$$

$$dE_s(\nu) = h\nu_0 n_u B_{ul} \frac{4\pi}{c} I_\nu \phi_a(\nu) dV \frac{d\Omega}{4\pi} d\nu dt. \tag{2.21}$$

$$dE_e(\nu) = h\nu_0 n_u A_{ul} \phi_e(\nu) dV \frac{d\Omega}{4\pi} d\nu dt. \tag{2.22}$$

where $\phi_a(\nu)$ and $\phi_e(\nu)$ are the line profiles for the absorbed and emitted radiation and here, those line profiles are considered to be equal, $\phi_a(\nu) = \phi_e(\nu) = \phi(\nu)$. The volume element dV corresponds to $d\sigma ds$.

Hence, the energy providing the intensity in a frequency range, $d\nu$, solid angle, $d\Omega$, time, dt, and unit area, $d\sigma$, perpendicular to the beam direction is given by,

$$dI_\nu d\Omega d\sigma d\nu dt$$
$$= \frac{h\nu_0}{4\pi}\left[n_u B_{ul}\frac{4\pi}{c}I_\nu - n_l B_{lu}\frac{4\pi}{c}I_\nu + n_u A_{ul}\right]\phi(\nu)d\Omega d\sigma ds d\nu dt. \tag{2.23}$$

The full equation of spectral line radiative transfer with Einstein coefficients is thus

$$\frac{dI_\nu}{ds} = -\frac{h\nu_0}{c}(n_l B_{lu} - n_u B_{ul})I_\nu\phi(\nu) + \frac{h\nu_0}{4\pi}n_u A_{ul}\phi(\nu). \tag{2.24}$$

We can obtain the absorption and emission coefficients by comparing withe Eq. (2.3), resulting in

$$\kappa_\nu = \frac{h\nu_0}{c}n_l B_{lu}\left(1 - \frac{g_l}{g_u}\frac{n_u}{n_l}\right)\phi(\nu) \tag{2.25}$$

and

$$\varepsilon_\nu = \frac{h\nu_0}{4\pi}n_u A_{ul}\phi(\nu). \tag{2.26}$$

In LTE, the energy levels are populated according to the Boltzmann distribution at a temperature T using Eqs. (2.17) and (2.18). The absorption coefficient in Eq. (2.25) can then be rewritten as,

$$\kappa_\nu = \frac{c^2}{8\pi\nu_0^2}\frac{g_u}{g_l}n_l A_{ul}\left[1 - \exp\left(-\frac{h\nu_0}{k_B T}\right)\right]\phi(\nu). \tag{2.27}$$

2.3   Continuum free-free emission

Continuum radiation from HII regions is a mixture of thermal emission from dust grains in associated clouds and "free-free" emission or Bremsstrahlung from unbounded charged particles. In the (far) infrared and submillimeter regimes, the emission from dust can be more intense than the free-free emission, but at millimeter and centimeter wavelengths the radiation is dominated by free-free emission. Regarding RRLs, the free-free emission measuring the amount of ionization in HII regions is very important. The ratio of RRLs to free-free continuum emission can be a good measure of the thermodynamic state of ionized gas because it yields the ratio of unbound to bound electrons in the HII regions.

To calculate the continuum absorption coefficient, κ_C, one has to account for both the Coulomb interactions between two charged particles and the velocity distribution of the particles. The continuum absorption coefficient is determined by integrating the emission produced during each encounter over the velocity distribution of the particles. The velocity distribution of the particles can be described by the non-relativistic Maxwellian distribution of particle speeds in LTE as,

$$f(v) = \frac{4\nu^2}{\sqrt{\pi}} \left(\frac{m_e}{2k_BT} \right)^{3/2} \exp\left(-\frac{m_e\nu^2}{2k_BT} \right). \tag{2.28}$$

By integrating Eq. (2.28), we can obtain the continuum emission coefficient, ε_ν,

$$\varepsilon_\nu = \frac{\pi^2 Z^2 e^6 n_e n_i}{4c^3 m_e^2} \left(\frac{2m_e}{\pi k_BT} \right)^{1/2} \ln\left(\frac{b_{\max}}{b_{\min}} \right), \tag{2.29}$$

where $b_{\max}$ and $b_{\min}$ are the minimum and maximum impact parameters of a free-free interaction, respectively.

By using the emission coefficient, the absorption coefficient can be computed using Kirchhoff's law (Eq. 2.5). Oster (1961) derived an expression for the absorption coefficient, which is valid for the radio regime after applying the Rayleigh-Jeans approximation ($h\nu \ll k_BT$):

$$\kappa_C = \left(\frac{n_e n_i}{\nu^2} \right) \left(\frac{8Z^2 e^6}{3\sqrt{3}m^3 c} \right) \left(\frac{\pi}{2} \right)^{1/2} \left(\frac{m}{k_BT} \right)^{3/2} \langle g \rangle, \tag{2.30}$$

where n_e and n_i are volume densities of electrons and ions, respectively. The quantity $\langle g \rangle$ is the Gaunt factor averaged over a Maxwellian velocity distribution defined by the kinetic temperature T. Furthermore, if electron temperature, T_e, is constant along the line of sight and $n_i(x) = n_e(x)$, then Eq. (2.30) can be expressed as the continuum optical depth,

$$\tau_C = 3.014 \times 10^{-2} \left(\frac{T_e}{\mathrm{K}} \right)^{-3/2} \left(\frac{\nu}{\mathrm{GHz}} \right)^{-2} \left(\frac{\mathrm{EM}}{\mathrm{pc\,cm^{-6}}} \right) \langle g \rangle, \tag{2.31}$$

where EM is the emission measure and is given by

$$\frac{\mathrm{EM}}{\mathrm{pc\,cm^{-6}}} = \int_0^{x/\mathrm{pc}} \left(\frac{n_e}{\mathrm{cm^{-3}}} \right)^2 d\left(\frac{x}{\mathrm{pc}} \right). \tag{2.32}$$

Alternatively, a simpler expression of the continuum optical depth given by Altenhoff (1960) approximating the Gaunt factor is

$$\tau_C = 8.235 \times 10^{-2} \left(\frac{T_e}{\mathrm{K}} \right)^{-1.35} \left(\frac{\nu}{\mathrm{GHz}} \right)^{-2.1} \left(\frac{\mathrm{EM}}{\mathrm{pc\,cm^{-6}}} \right) a(\nu, T), \tag{2.33}$$

where the a factor is the ratio of the optical depths derived by Oster (1961) and Altenhoff (1960). Mezger & Henderson (1967) provided a relation for the a factors at different frequencies and electron temperatures. The a factor is given by:

$$a = \frac{\tau_{C(\mathrm{Oster})}}{\tau_C(\mathrm{AMWW})} = 0.366 \left(\frac{\nu}{\mathrm{GHz}} \right)^{0.1} \left(\frac{T_e}{\mathrm{K}} \right)^{-0.15}$$
$$\times \left\{ \ln\left[4.995 \times 10^{-2} \left(\frac{\nu}{\mathrm{GHz}} \right)^{-1} \right] + 1.5 \ln\left(\frac{T_e}{\mathrm{K}} \right) \right\}. \tag{2.34}$$

From κ_C and ε_C in the Rayleigh-Jeans approximation and the general form of radiation transfer, we can obtain the intensity of the free-free emission from a HII region

at a given frequency. If we assume that the HII region is homogeneous in density and temperature without foreground emission, then we can express the intensity of free-free emission as

$$T(x) = T(0)e^{-\tau_C(0)} + T(1 - e^{-\tau_C}),$$ (2.35)

where $T(0)$ refers to the background emission attenuated by the HII region.

2.4 Radio recombination lines

Adopting concepts discussed in Section 2.2,

$$\kappa_L \approx \frac{h^2\nu^2}{4\pi k_B T} \phi_\nu N_{n_1} B_{n_1,n_2}.$$ (2.36)

Note these approximated expressions are underestimated by about $(h\nu/k_B T)^2/2$. The Einstein coefficient can be rewritten with the oscillator absorption and emission strengths, f_{n_1,n_2} and f_{n_2,n_1} (the emission oscillator strength is negative) respectively as,

$$f_{n_1,n_2} = -\frac{g_{n_2}}{g_{n_1}} f_{n_2,n_1} = \frac{mch\nu}{4\pi^2 e^2} B_{n_1,n_2}$$ (2.37)

With the approximation given by Menzel (1968), the absorption oscillator strengths can written as

$$f_{n_1,n_2} \approx n_1 M_{\Delta n} \left(1 + 1.5\frac{\Delta n}{n_1}\right).$$ (2.38)

where $M_{\Delta n} = 0.190775, 0.026332, 0.0081056$, and 0.0034918 for $\Delta n = 1, 2, 3$, and 4 (H$n\alpha$, H$n\beta$, H$n\gamma$, and H$n\delta$), respectively. Note, for hydrogen RRLs, appropriate oscillator strengths are given by Goldwire (1968) and Menzel (1969).

Using the Saha-Boltzmann ionization equation, we can obtain the number density of atoms (N_{n_1}) in the lower bound level related to the population of the electrons and ions of the unbound states, n_e and n_i,

$$N_{n_1} = \frac{n_e n_i}{T^{3/2}} \frac{n_1^2 h^3}{(2\pi m k_B)^{3/2}} \exp\left(\frac{Z^2 E_{n1}}{k_B T}\right),$$ (2.39)

where E_{n_1} is the energy of level n_1.

For hydrogen, $E_n/k_B T$ is $1.579 \times 10^5/n^2/T$. In the the Rayleigh-Jeans regime, the general absorption coefficient becomes,

$$\kappa_L \approx 3.469 \times 10^{-12} \phi_\nu Z^2 \Delta n \frac{f_{n_1,n_2}}{n_1} \left(1 - \frac{3\Delta n}{2n_1}\right) \frac{n_e n_i}{T^{5/2}} \exp\left(\frac{Z^2 E_{n_1}}{k_B T}\right),$$ (2.40)

where the unit of κ_L is in cm^{-1} if n_e and n_i are in cm^{-3}. The temperature T is in Kelvins and E_{n_1} is in ergs. The value of κ_L increases roughly as n^3 but decreases as $T^{5/2}$. In addition, the κ_L directly varies with the term $N_e N_i$.

Since the intensity of the RRL depends on the free-free continuum, to obtain pure RRL intensities, we need both coefficients of line and continuum emission. Using both linear opacities of the line and continuum emission, the intensity of the RRL becomes,

$$I_L = I - I_C = B_\nu(T)e^{-\tau_C}(1 - e^{\tau_L}) \approx B_\nu \tau_L, \qquad (2.41)$$

where $\tau_L \ll 1$. Note that in usual HII region gas at cm wavelengths, τ_C and τ_L are much less than 1. However, if τ_C is not optically thin anymore at a given frequency, RRL intensities are reduced because the exponential term in Eq. (2.41) is close to zero. In the $\tau_C \gg 1$ case, no RRL can be detected even at cm wavelengths. In general, radio continuum emission become optically thick within HII regions surrounding young stellar objects inside dense molecular clumps. To detect RRLs toward such HII regions, we need to observe them at shorter than cm wavelengths.

2.4.1 RRL intensities under LTE conditions

For the hydrogen atom, it is possible to determine the Einstein coefficient A_{n_2,n_1} by considering the classical electric dipole. At radio wavelengths, when $n \gg 1$, $h\nu_0 \ll k_B T_e$, and $g_2 \approx g_{n_1}$, the spontaneous Einstein coefficient is given by

$$A_{n_2,n_1} = \frac{64\pi^6 me^{10}}{3h^6 c^3} \frac{1}{n^5} = \frac{5.36 \times 10^9}{n^5} \quad [\text{s}^{-1}]. \qquad (2.42)$$

From Eqs. (2.39) and (2.42), for large n in the radio regime, we can determine the τ_L at the center frequency (ν_0) of a line emitted in a region for an H$n\alpha$ line using,

$$\tau_L = 1.92 \times 10^3 \left(\frac{T_e}{\text{K}}\right)^{-5/2} \left(\frac{\text{EM}}{\text{cm}^{-6}\text{pc}}\right) \left(\frac{\Delta\nu}{\text{kHz}}\right)^{-1}. \qquad (2.43)$$

In practice, τ_L can be rewritten in temperature units when $\tau_L \ll 1$ and $T_L = T_e \tau_L$ as,

$$
\begin{aligned}
T_L &= 1.92 \times 10^3 \left(\frac{T_e}{\text{K}}\right)^{-3/2} \left(\frac{\text{EM}}{\text{cm}^{-6}\text{pc}}\right) \left(\frac{\Delta\nu}{\text{kHz}}\right)^{-1} \\
&= 576 \times \left(\frac{T_e}{\text{K}}\right)^{-3/2} \left(\frac{\text{EM}}{\text{cm}^{-6}\text{pc}}\right) \left(\frac{\nu_0}{\text{GHz}}\right)^{-1} \left(\frac{\Delta v_{FWHM}}{\text{km s}^{-1}}\right)^{-1},
\end{aligned}
\qquad (2.44)
$$

where v_{FWHM} is the full width of the Gaussian line at half intensity in units of km s^{-1}.

Under conditions with $\tau_C, \tau_L \ll 1$, hence $I_C \approx B_\nu \tau_C$ and $I_L \approx B_\nu \tau_L$, the ratio of the line to continuum emission for the same source will be,

$$\int_{line} \frac{I_L}{I_C} d\nu = \int_{line} \frac{\tau_L}{\tau_C} d\nu = \int_{line} \frac{\kappa_L}{\kappa_C} d\nu. \qquad (2.45)$$

Therefore, we can express this general form of the intensity ratio by substituting κ_L and κ_C for hydrogen RRLs emitted in LTE as,

$$\int_{line} \frac{I_L}{I_C} d\nu \approx 1.301 \times 10^5 \Delta n \frac{f_{n1,n2}}{n_1} \frac{\nu^{2.1}}{T_e^{1.15}} F \exp\left(\frac{1.579 \times 10^5}{n_1^2 T_e}\right), \qquad (2.46)$$

where the factor F corrects the observed free-free emission for the distribution of ionized helium, $F \equiv 1 - (N_{He}/N_H)$. In the left term, the integration element, $d\nu$, is in kHz and in right term, ν, is in GHz.

For an H$n\alpha$ line, we can obtain the intensity ratio of line to free-free continuum from Eqs. (2.33) and (2.43),

$$\frac{T_L}{T_C} \left(\frac{\Delta v_{FWHM}}{\mathrm{km\,s^{-1}}} \right) = \frac{6.985 \times 10^3}{a(\nu, T_e)} \left[\frac{\nu}{\mathrm{GHz}} \right]^{1.1} \left[\frac{T_e}{\mathrm{K}} \right]^{-1.15} \frac{1}{1 + N_{He}/N_H}. \tag{2.47}$$

2.4.2 RRL intensities when LTE conditions do not apply

We have discussed the RRL intensities under LTE which assumes a single temperature to describe the statistical state of bound and unbound levels of atoms.

Radiative and collisional rates level exactly balance each other:

$$e^{h\nu/k_B T_{ex}} = \frac{b_{n_2}}{b_{n_1}} e^{h\nu/k_B T_e}. \tag{2.48}$$

where the departure coefficient, b_n, is the ratio of the actual population of atoms in a level n to the theoretically expected population of atoms in LTE. In LTE, the departure coefficients for the levels are by definition 1.

However, Goldberg (1966) noted that the T_{ex} that represents the relative population of the bound quantum levels is not exactly the same as the T_e of the ionized gas. As a result, a correction factor (departure coefficient, b_n) is required to account for the difference due to the non-LTE amount of stimulated emission. Therefore, the actual κ_L corrected for non-LTE is defined as,

$$\begin{aligned}
\kappa_L &= \kappa_L^* b_{n1} \left[\frac{1 - (b_2/b_1)e^{-h\nu/k_B T_e}}{1 - e^{-h\nu/k_B T_e}} \right] \\
&= \kappa_L^* b_{n1} \beta \\
&\approx \kappa_L^* b_{n1} \left(1 - \frac{k_B T_e}{h\nu} \frac{d\mathrm{ln}b_{n2}}{dn} \Delta n \right), \quad h\nu \ll k_B T_e,
\end{aligned} \tag{2.49}$$

where κ_L^* refers to the LTE form of linear absorption coefficient.

The β is a cofactor of b_{n2} given by Goldberg (1968),

$$\begin{aligned}
\beta &= \left(1 - \frac{k_B T_e}{h\nu} \frac{d\mathrm{ln}b_{n2}}{dn} \Delta n \right) \\
&= 1 - 20.836 \left(\frac{T_e}{\mathrm{K}} \right) \left(\frac{\nu}{\mathrm{GHz}} \right)^{-1} \frac{d\mathrm{ln}b_n}{dn} \Delta n.
\end{aligned} \tag{2.50}$$

Figure 2.3 shows that the estimated b_n and the (1- β_n) factor in a range of electron densities of $10^4 - 10^8 \,\mathrm{cm^{-3}}$ for a fixed T_e of $10^4 \,\mathrm{K}$.

Furthermore, the non-LTE emission coefficient is

$$\varepsilon_L = \kappa_L^* b_{n2} B_\nu(T_e) \tag{2.51}$$
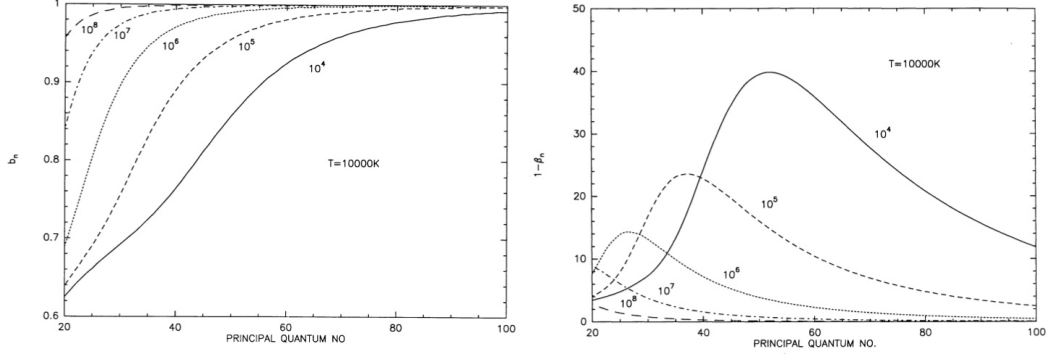
Figure 2.3: b_n and β as functions of principal quantum numbers for high frequency H$n\alpha$ lines at different densities and $T_e = 10^4$ K (Credit: Walmsley 1990).

And, the intensity of the line in non-LTE is given using the actual κ_L and ε_L.

$$
\begin{aligned}
I &= I_L + I_C \\
&= \frac{\varepsilon_C + \varepsilon_L}{\kappa_C + \kappa_L}\left[1 - e^{-(\tau_C+\tau_L)}\right] \\
&= \frac{\kappa_C + \kappa_L^* b_{n2}}{\kappa_C + \kappa_L^* b_{n1}\beta}B_\nu(T_e)\left[1 - e^{-(\tau_C+\tau_L)}\right] \\
&= \eta B_\nu(T_e)\left[1 - e^{-(\tau_C+\tau_L)}\right].
\end{aligned}
\tag{2.52}
$$

where the η factor summarizes the correction to the Planck function due to the departure from LTE,

$$
\eta = \frac{1 + b_{n2}(\kappa_L^*/\kappa_C)}{1 + b_{n1}(\kappa_L^*/\kappa_C)\beta}.
\tag{2.53}
$$

All these non-LTE correction factors must be applied only for the line coefficients because T_e describes the thermodynamic state of the ionized gas, and thus the continuum coefficient does not need any correction.

Therefore, the intensity ratio of the line to the continuum can be written as,

$$
\frac{I_L}{I_C} = \frac{I - I_C}{I_C} = \frac{I}{I_C} - 1 = \left[\frac{\eta\left(1 - e^{-(\tau_C+\tau_L^* b_{n1}\beta)}\right)}{1 - e^{-\tau_C}}\right] - 1.
\tag{2.54}
$$

In the radio wavelength regime, if τ_C and τ_L are much smaller than 1, we can approximate $I_L \approx I_L^*(1 - \frac{\tau_C}{2}\beta)$ and therefore, Eq. (2.45) becomes for non-LTE,

$$
\int_{line} \frac{I_L}{I_C}d\nu \approx \int_{line} \frac{I_L^* b_{n2}(1 - \frac{\tau_C}{2}\beta)d\nu}{I_C}.
\tag{2.55}
$$

2.4.3   Maser emission

For maser action to arise in RRLs, population inversion has to occur. This means that opacity of RRL is smaller than 0, $\tau_L < 0$. However, that condition is not enough for
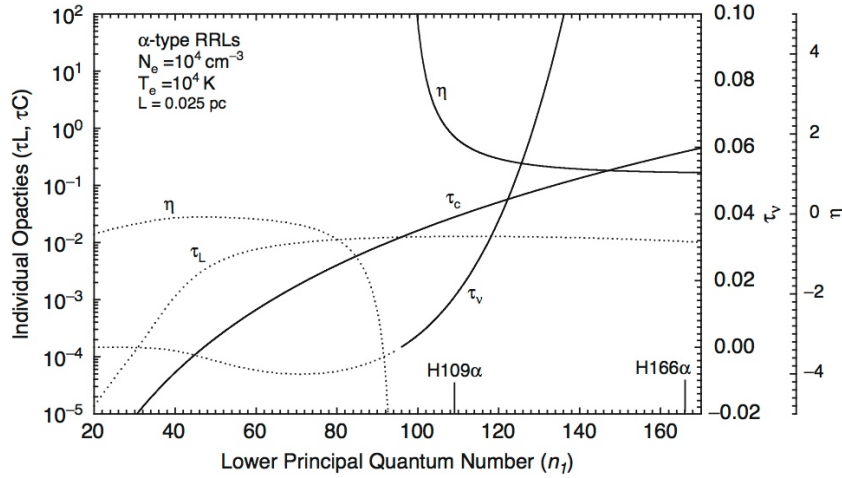
Figure 2.4: Left axis refers to the variation of the radio continuum and actual RRL opacities as a function of the principal quantum number for the HII region. The inner right axis indicates the sum of opacities (τ_ν) and the outer right axis corresponds to the Planck function for stimulated emission (η). Dotted lines are where the quantities (τ_ν, τ_L, and η) are negative (Credit: Gordon & Sorochenko 2002).

maser amplification because RRL and radio continuum emission are produced together in HII region. Hence, the opacity of continuum emission has to be considered. This implies that the τ_L must be negative and at same time the absolute value of τ_L , $|\tau_L|$, also must be larger than τ_C. As a result, the net opacity ($\tau_\nu \equiv \tau_C + \tau_L$) becomes smaller than zero (Ponomarev et al. 1994; Strelnitski et al. 1996), and consequently, RRL maser action can arise in ionized gas.

Figure 2.4 shows the relationships of τ_C, τ_L, τ_ν and the Planck function correction factor, η, as functions of quantum number (n) for an HII region which has $n_e = 10^4\,\mathrm{cm}^{-3}$, $T_e = 10^4\,\mathrm{K}$, and a size of $0.025\,\mathrm{pc}$. The solid lines always indicate positive values, whereas the dotted lines are negative. The τ_L values are only negative in Figure 2.4 as mentioned above, but the τ_C is always positive. However, for quantum numbers $n < 95$ the absolute value of τ_L takes over that value of τ_C. Therefore, all the conditions for RRL masers are fulfilled for $n < 95$ such that $\tau_L < 0$, $|\tau_L| > \tau_C$, and $\tau_\nu < 0$. The most noteworthy case of strong maser emission is only found from the source MWC349, which suggests that the RRL masers are very rare (Martin-Pintado et al. 1989; Thum et al. 1995; Martín-Pintado 2002). In spite of a lot of attempts to find other sources with RRL masers, the dearth of RRL masers still remains an unsolved problem.

The non-LTE radiative transfer theory explains the behavior of RRL intensities as a function of the quantum number when inhomogeneities of the ionized gas such as temperature gradients, geometry of HII regions, and inhomogeneous density structures are considered (Goldberg 1966; Simpson 1973; Shaver 1980). The most significant evidence of departure from LTE have been attained by the intensity ratio of $n\alpha$ and

higher-order lines (i.e., $\Delta m = 2, 3, 4$, and so on, which are called as β, γ, δ and so on) (Dupree & Goldberg 1970). The higher-order lines can be observed at approximately the same frequency. Furthermore, the beam size of the antenna has the same beam width for the transitions. In non-LTE conditions, the β/α line ratio shows a deviation from the LTE value. The line ratio of peak intensities under LTE conditions can be estimates by the following equation (Dupree & Goldberg 1970),

$$\rho_{\mathrm{LTE}} = \frac{m^2 f_{m,m+\Delta m}}{n^2 f_{n,n+1}}, \tag{2.56}$$

where ρ_{LTE} is the line ratio of peak intensities of higher-order line to α line in LTE. The m and Δm indicate the quantum number and the order of hydrogen higher-order transitions. The n is the quantum number of a given hydrogen α line.

In non-LTE conditions, changes in the β/α ratio are due to some effects such as pressure broadening, stimulated emission, and Lyman line pumping (Cersosimo & Magnani 1990). Since the β line is stronger affected by pressure broadening than the α line, the peak intensity of β lines decrease relative to the case without pressure broadening. Alternatively, the intensity of the α lines can be stimulated by external radiation fields. Last, the absorption of stellar Lyman line photons may significantly affect the intensities of RRLs in HII regions by stars of spectral type later than O6 (Beigman & Chichkov 1980; Hoang-Binh 1983). This effect is most conspicuous at high frequency, for example (sub)millimeter wavelengths (Hoang-Binh 1983; Cersosimo & Magnani 1990; Gordon & Walmsley 1990).

The majority of Galactic HII regions show β/α values close to the LTE ratios (Gordon & Walmsley 1990; Thum et al. 1995). However, the prominent RRL maser source, MWC349, shows low β/α ratios that are due to enhancement of the α lines by stimulated emission (Thum et al. 1995). The stimulated emission results from the high free-free continuum opacity in the ionized wind of MWC 349A (Thum et al. 1995).

2.5 The profile of radio recombination lines

In general, the line profiles of RRLs are determined by several effects: natural and Stark (or "pressure") broadenings lead to Lorentz profiles with prominent line wings, while thermal/micro-turbulence and dynamical broadenings show Gaussian profiles. The combined profile is called a Voigt profile. Figure 2.5 shows the three line profiles, Gaussian (solid line), Lorentz (dotted line), and Voigt (dashed-line) profiles.

2.5.1 Natural broadening: Lorentz profiles

Natural broadening results from the finite length of the emitted wave train and the variation of its amplitude over the emission time. It is an intrinsic property of the atom and the quantum uncertainty (ΔE) of an energy level (E). The full width of the line at half maximum derived by Weisskopf & Wigner (1930) is,

$$\frac{\Delta\nu}{\nu_0} \approx \frac{1}{\pi\nu_0}\sum_{n1=1}^{n_2-1} A_{n_2,n_1} \tag{2.57}$$

Sobel'Man et al. (1995) provided a useful approximation to calculate the sum of the spontaneous transition probabilities, A_n, out of level n for $(n+1) > 20$,

$$A_n \approx 2.4 \times 10^{10}\frac{\ln n}{n^5} \ \ [\text{cm}^{-1}]. \tag{2.58}$$

Therefore, we get the expression for the natural width of RRLs ($n > 20$) by substituting $\nu_H = 6.58 \times 10^{15}\frac{1}{n^3}$ Hz and putting Eq. (2.58) into Eq. (2.57). In velocity units, we have

$$\Delta v_{\text{natural}} \approx 1.2 \times 10^{-6}\, c\, \frac{\ln(n+1)}{(n+1)^2} \ \ [\text{km s}^{-1}]. \tag{2.59}$$

For H25α and H42α, $\Delta v_{\text{natural}}$ is 1.7×10^{-3} km s^{-1} and 7.3×10^{-4} km s^{-1}, respectively. These natural broadening width is negligible for RRLs from centimeter to (sub)millimeter wavelengths.

2.5.2 Doppler broadening: Gaussian profiles

Doppler broadening of a spectral line is the result of the Doppler effect caused by a distribution of velocities of atoms or molecules. Random motions of the emitting particles yield different Doppler shifts, corresponding to stochastical red- and blueshifts of the observed frequency.

Thermal broadening

If the distribution of particle velocities is governed by collisions without any large scale turbulence, the emitting gas particles follow a Maxwell-Boltzmann velocity distribution for a given kinetic temperature:

$$N(v_x)dv_x = N\left(\frac{M}{2\pi k_B T}\right)^{1/2}\exp\left(-\frac{Mv_x^2}{2k_B T}\right)dv_x. \tag{2.60}$$

The left hand side represents the probability, $N(v_x)$, of an atom having a velocity component in infinitesimal length (dx) along the line of sight, and on the right hand side, N, is the total number of atoms contributing to a line. M is the mass of a atom.

The profile $\phi_G(\nu)$ of the Doppler broadened line is,

$$\phi_G(\nu) = \left(\frac{4\ln 2}{\pi}\right)^{1/2}\frac{1}{\Delta\nu_G}\exp\left[-4\ln 2\left(\frac{\nu_0 - \nu}{\Delta\nu_G}\right)\right]. \tag{2.61}$$

where $\Delta\nu_G$ is the full width of the Gaussian line at half intensity in frequency unit.

By assuming that the total intensity I in the RRL is proportional to the total number of atoms N and using $dv_x = -\frac{c}{\nu_0}d\nu$, we can obtain the full width of the

thermally broadened Gaussian line at half of maximum intensity from Eqs. (2.60) and (2.61).

$$\Delta v_{\text{thermal}} = (4\ln 2)^{1/2} \left(\frac{2k_B T_e}{M}\right)^{1/2} \quad [\text{km s}^{-1}].$$

(2.62)

Turbulence broadening

The Doppler profile of the RRLs is not only determined by the kinetic temperature of the gas, but microturbulence also causes part of the Doppler profile.

Therefore, the total Doppler broadened line width is obtained simply by adding the thermal and turbulent widths in quadrature,

$$(\Delta v_G) = \sqrt{(\Delta v_{\text{thermal}})^2 + (\Delta v_{\text{turbulence}})^2}$$
$$= (4\ln 2)^{1/2} \left(\frac{2k_B T_e}{m} + v_{turbulence}^2\right)^{1/2} \quad [\text{km s}^{-1}].$$

(2.63)

2.5.3   Stark (pressure) broadening: Lorentz profiles

Of the possible broadening effects, Stark broadening, the so-called pressure broadening, is not important for mm/submm-RRLs, only for cm-RRLs. It consists of the splitting and displacement of atomic energy levels by superposition of an external electric field.

Collisions of ions and electrons contribute separately to the Stark broadening. A simple approximation for the RRL pressure broadening by electrons and ions was obtained by Smirnov (1985):

(i) electron contribution

$$\Delta v_{\text{pressure,e}} = 8.2 n_e \frac{c}{\nu_0} \left(\frac{n+1}{100}\right)^{\gamma_e} \left(1 + \frac{\gamma_e}{2}\frac{\Delta n}{n+1}\right) \quad [\text{km s}^{-1}]$$

(2.64)

where the factor γ_e is the growth rate of RRL collisional broadening by electrons and its average value is 4.5.

(ii) ion contribution

$$\Delta v_{\text{pressure,i}} = (0.06 + 2.5 \times 10^{-4} T_e) n_i \frac{c}{\nu_0} \left(\frac{n+1}{100}\right)^{\gamma_i} \left(1 + \frac{2.8\Delta n}{n+1}\right) \quad [\text{km s}^{-1}]$$

(2.65)

where γ_i is $6 - 2.7 \times 10^{-5} T_e - 0.13(n/100)$.

The broadening by electrons is more significant than that by ions. Therefore, the Stark broadening is mainly attributed to collisions by electrons.
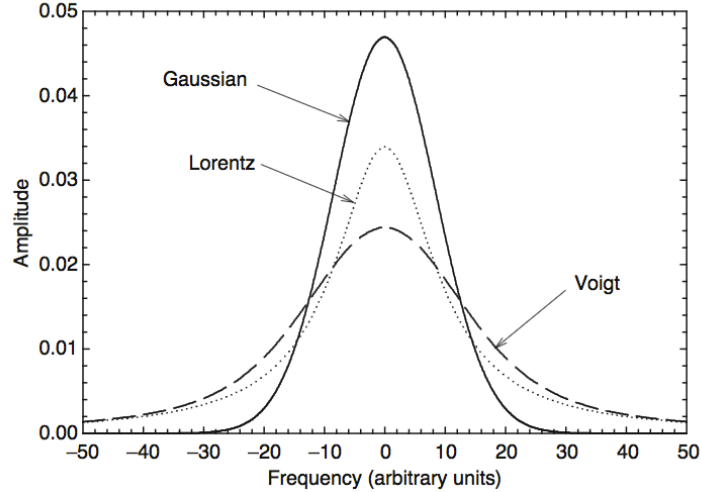
Figure 2.5: Gaussian, Lorentz and Voigt line profiles. The Voigt profile is a convolution of the Gaussian and Lorentz profiles (Credit: Gordon & Sorochenko 2002).

2.5.4 Voigt profiles: observed profiles

Figure 2.5 shows the three different line profiles, Gaussian, Lorentz and Voigt profiles. The Gaussian and Lorentz profiles are considered to be independent, and we see the core of the Voigt profile behaves like a Gaussian profile, while wings well away from the core follow the characteristic of the wings of a Lorentz profile.

A useful simple approximation for the line width of the Voigt profile as a superposition of Gaussian and Lorentz profiles is given by Smirnov (1985),

$$\Delta v_{\mathrm{V}} = 0.534 \Delta v_{\mathrm{L}} + \sqrt{(\Delta v_G^2 + 0.217 \Delta v_{\mathrm{L}}^2)} \quad [\mathrm{km\,s^{-1}}] \tag{2.66}$$

where the line width of the Voigt profile, Δv_{V}, is the full width of line at half intensity (FWHM). If the contribution of the Lorentzian is significant, the width of an observed line refers the Δv_{V}. The Δv_G contains conributions from turbulence and thermal broadenings as described by $\Delta v_G^2 = \Delta v_{\mathrm{turbulence}}^2 + \Delta v_{\mathrm{thermal}}^2$.

We can also test the fraction of Doppler and Stark broadening on the line widths. The line width ratios of Doppler and pressure broadenings are, as derived by Brocklehurst & Seaton (1972),

$$\frac{\Delta \nu_{\mathrm{Pressure}}}{\Delta \nu_{\mathrm{Doppler}}} = 0.142 \left(\frac{n}{100}\right)^{7.4} \left(\frac{n_e}{10^4}\right) \tag{2.67}$$

Figure 2.6 shows the line widths of RRLs toward H<small>II</small> regions as a function of principal quantum numbers. As seen in Eq. (2.67), the pressure broadening effect increases for RRLs with large n and, therefore, the line width caused by a Lorentz profile rapidly
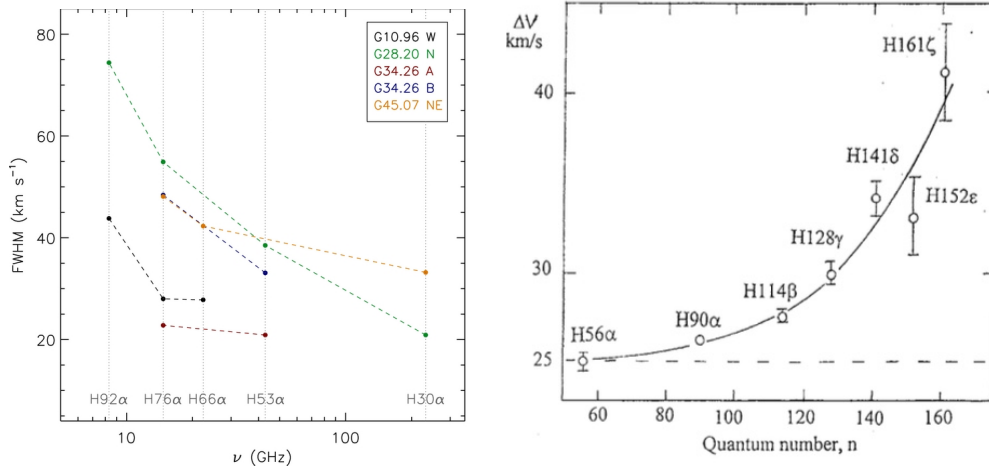
Figure 2.6: Line width (FWHM) as a function of principle quantum number. *Left*: RRL VLA observations toward ultra- and hyper compact HII regions (Sewiło et al. 2011). *Right*: Line width of Voigt profiles observed toward the Orion Nebula as a function of principal quantum number (Smirnov et al. 1984).

grows as well. However, at short wavelengths the pressure broadening is reduced, and the line widths of RRLs are mostly attributed to Gaussian broadening.

2.6 RRL observations of HII regions

The UV photons ($h\nu > 13.6\,\mathrm{eV}$) emitted from newly born high-mass stars (O4-B9) or O/B star clusters are energetic enough to ionize hydrogen in the regions surrounding the stars. Figure 2.7 shows different structures of ionized gas regions associated with RRLs from hydrogen, helium, and carbon atoms. Since the ionization potential energy of these atoms differ as seen in Table 2.1, we can find their RRLs in different environments. Ionizing helium atoms needs higher ionization potential ($h\nu > 24.6\,\mathrm{eV}$). Thus, the sizes of ionized He zones are generally smaller than the sizes of the corresponding ionized H zones. There are other atoms with ionization potentials below 13.6 eV (or $\lambda > 912$ Å), for example, the case of the carbon atom (11.3 eV). As a result, observing RRLs from different atoms allows us to study the properties of the exciting stars and the chemical composition of the ISM.

2.6.1 Hydrogen RRL profiles from inhomogeneous HII regions

Owing to the high angular and velocity resolution of facilities such as the JVLA, ALMA, and NOEMA interferometers, it is possible to resolve the internal structure of young HII regions such as ultra- and even hypercompact HII. In particular, using low-n quantum number RRLs at mm/submm wavelengths has advantage because the regions are optically thin at these wavelengths. In addition to the improved instruments, recently,
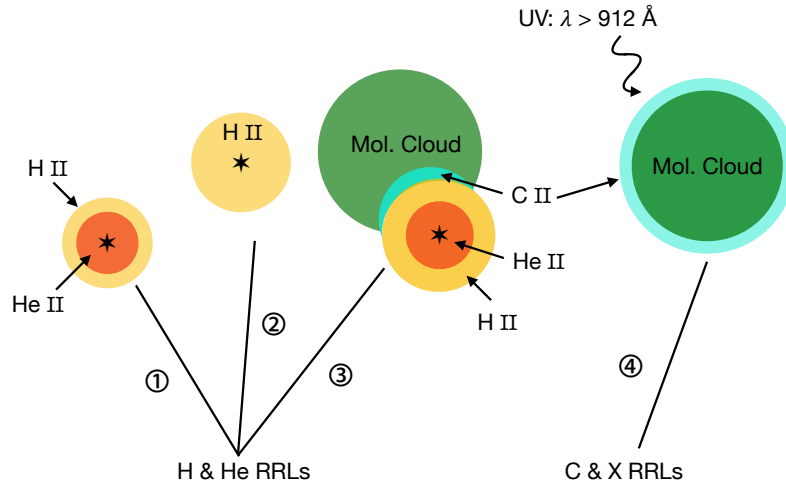
Figure 2.7: Different types of ionized gas in the ISM. (1) a dense and bright HII region or a planetary nebula. (2) an extended and low electron density HII region. (3) A dense and bright HII region with an ionized carbon region created between molecular cloud and the HII region. (4) An ionized carbon region at the molecular boundary which is irradiated by UV radiation from distant radiating sources (adapted from Gordon & Sorochenko 2002).

detailed and sophisticated simulation results deliver information on the physical conditions probed by radio continuum and recombination line emission.

In Figure 2.8, the image shows simulated results of line profiles under LTE and non-LTE conditions within HII regions with velocity gradients. The LTE line profiles are symmetric and identical for different velocity gradients. On the other hand, non-LTE profiles show different asymmetries as a result of optical depth effects (Viner et al. 1979) and show different profiles with changing velocities. As seen by the higher intensities in non-LTE profiles, the non-LTE conditions can give rise to maser amplification in recombination line emission (Gordon & Sorochenko 2002). As shown by examples of simulated non-LTE line profiles in the plot of Figure 2.8, observing asymmetric line profiles caused by non-LTE conditions will offer an opportunity to search for systematic motion in the ionized gas.

2.6.2   Helium RRLs: abundance of He in the Milky Way

Detections of helium RRLs not only allows us to investigate the structure within HII regions, but also to study the chemical evolution of the Galaxy and the primordial helium abundance in the universe (Gordon & Sorochenko 2002). Helium (^{4}He), the second most abundant element, is believed to be formed during the era of primordial nucleosynthesis (Peebles 1966). The only other significant source of producing ^{4}He is the synthesis in stars (Burbidge et al. 1957). Optical recombination lines were used as the primary diagnostic for measuring the abundance of ^{4}He, indirectly.

Although the RRLs are weaker than optical recombination lines, they are simpler
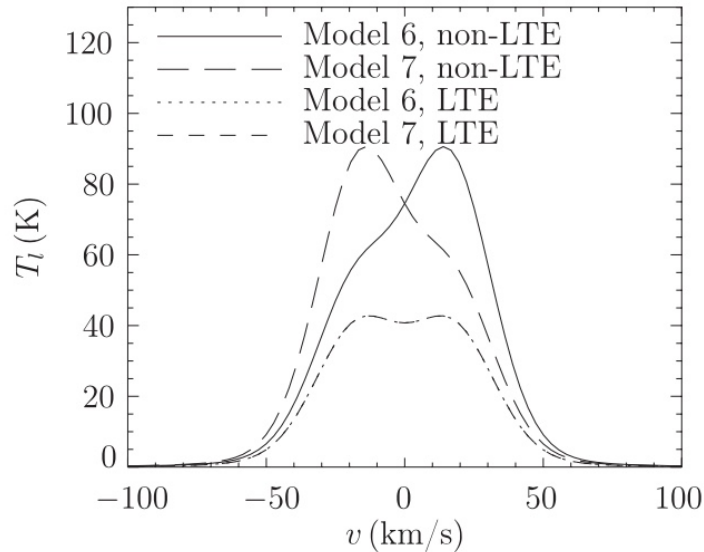
Figure 2.8: These H85α RRL profiles are simulated results for a line of sight through the center of a spherical H II region with changing velocity along a radius of the H II region for different velocity gradients (Peters et al. 2012).

to interpret. The ratio ($y^+ = {}^4\mathrm{He}^+/\mathrm{H}^+$) of the intensities of hydrogen and helium corresponds to the abundance ratio ($y = {}^4\mathrm{He}/\mathrm{H}$). The y^+ values were measured by RRLs and optical recombination lines toward extrataglactic objects ($y^+ = 0.01$, Peimbert & Spinrad 1970) and Galactic H II regions ($0.06 \leq y^+ \leq 0.10$, Churchwell et al. 1974).

Figure 2.9 shows a recent study of y^+ ($<y^+> = 0.068\pm0.007$) using the Green Bank telescope (Wenger et al. 2013) presenting a similar range of y^+ as earlier surveys. According to Osterbrock (1989), y^+ of 0.10 indicates a single star with an effective temperature greater than $\sim 39{,}000\,\mathrm{K}$ which is equivalent to spectral type $\sim$O8V or earlier (Sternberg et al. 2003) if the He II and H II Strömgren zones are coinciding. The actual helium abundance within an H II region is, however, the sum of the relative number densities of the neutral, singly-ionized, and doubly-ionized forms of helium, $y = y^0 + y^+ + y^{++}$. Since ordinary O-type stars cannot produce the enormous amount of energy ($h\nu > 54.4\,\mathrm{eV}$) required to make doubly ionized helium, the amounts of y^{++} can be neglected. Only if neutral helium does not exist within H II regions, y^+ can be used to measure y. However, all of the helium is not always ionized. As mentioned before, the size of the ionized helium region can change, which depends on several factors such as the spectral type of the exciting stars, line profiles, departure from LTE conditions, and continuum opacity contributed by dust.

In early observations, the y^+ measured by RRLs towards bright H II regions varied with n (Lockman & Brown 1982). These variations were considered to be caused by the different departure of hydrogen and helium (Baldwin et al. 1991), geometric effects (Mezger 1980), and poor spectral baselines (Lockman & Brown 1982). Also,
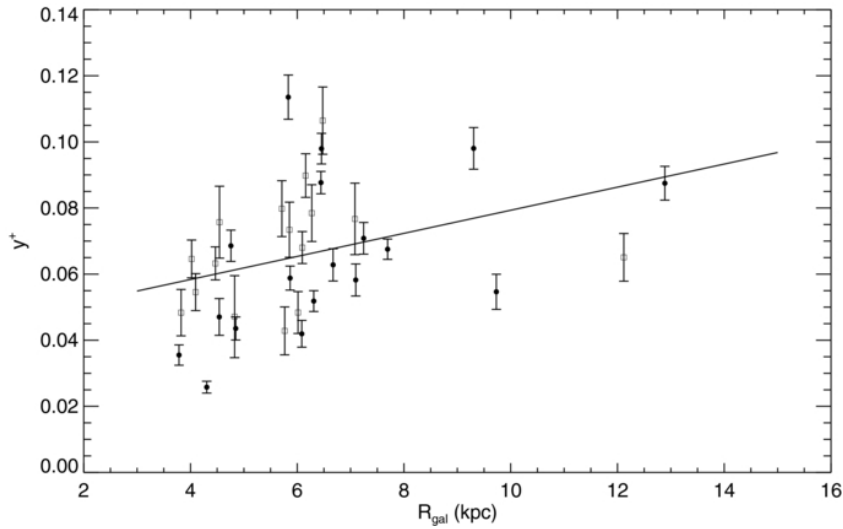
Figure 2.9: ^{4}He$^+$/H$^+$ abundance ratio (y$^+$) as a function of Galactocentric radius (R$_{gal}$) (Wenger et al. 2013).

enhancement of y^+ values have been found in the outer parts of HII regions, for example W3A (Roelfsema et al. 1992; Adler et al. 1996), W49A/M (De Pree et al. 1997), and NGC 6334A and K3−50A (Balser et al. 2001).

There are some possible explanations to explain the enhanced y^+ values (Balser et al. 2001; Wenger et al. 2013). High-mass stars eject helium-rich material toward the outer parts of HII regions. Also, the helium strömgren zone might be larger than the hydrogen zone (so-called inverse zone, Ershov et al. 1998; Gulyaev et al. 1997), because of a hard radiation field (or other radiative transfer effects). Furthermore, helium lines contaminated by carbon lines could increase the measurement of y^+. In the case of the Orion nebula, the measurements of y^+ by Pankonin et al. (1980) and Tsivilev et al. (1986) showed different trends. Pankonin et al. (1980) presented a decrease of y^+ from 10% near the center to 6% toward the edge. On the other hand, Tsivilev et al. (1986) found an increase of y$^+$ from ∼8% at the center to ∼11% at the edge. Later, Poppi et al. (2007) investigated the trends within the Orion nebula, and they also found a decrease from the center core to the outer envelope for different direction from the center. Their derived line velocities, widths and y^+ support the well-known "blister-type" structure of this HII region which was also proposed in the study of Tsivilev et al. (1986).

2.7 Derived physical parameters of HII regions

2.7.1 Electron temperature

Simultaneous observations of hydrogen RRLs and radio continuum emission at the same frequency provide the most precise measurement of T_e in HII regions even if they are optically obscured.
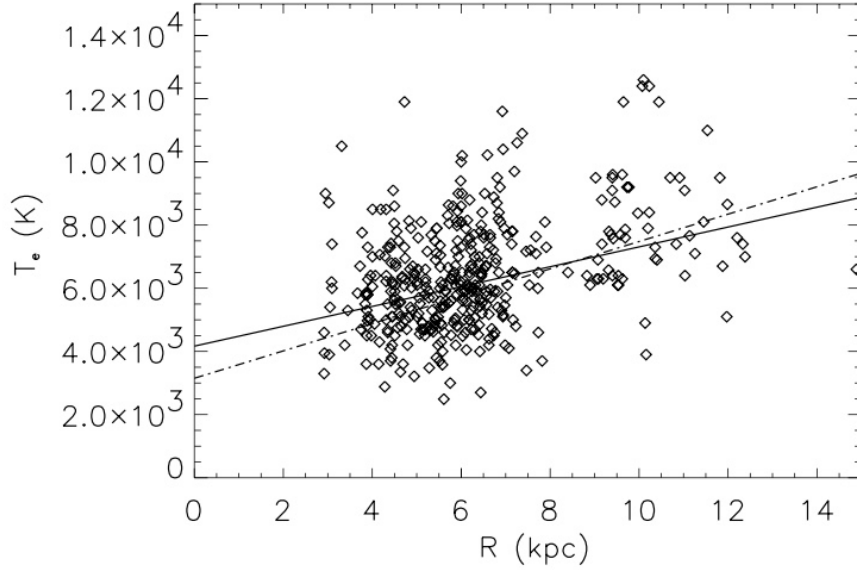
Figure 2.10: Electron temperature as a function of Galactocentric distance (Paladini et al. 2004). The solid line and the dot-dashed line are the least-squares linear fits of Paladini et al. (2004) and Shaver et al. (1983), respectively.

T_e can be calculated in a rather complicated way, which requires knowledge of the HII region structure, T_L/T_c, $\langle n_e \rangle$, EM and Δv. However, we can obtain its value through a simpler method with some assumptions: 1) the structure of the HII region is considered to be plane-parallel, homogeneous and isothermal; 2) all optical depths are small: $|\tau_L + \tau_C| \ll 1$ and $\tau_C \ll 1$; 3) the lines can be treated as if they were formed under LTE: $b_n = 1$, $\beta = 1$. We can then re-write Eq. (2.47) for the ratio of integrated line intensity to radio continuum emission.

Then, the LTE electron temperature, T_e^*, can be estimated with,

$$\frac{T_e^*}{K} = \left[\frac{6.985 \times 10^3}{a(\nu, T)} \left(\frac{\nu}{GHz} \right)^{1.1} \frac{1}{1 + N_{He}/N_H} \left(\frac{\Delta v}{km\,s^{-1}} \right) \left(\frac{T_C}{T_K} \right) \right]^{0.87}. \tag{2.68}$$

At frequencies of approximately $\nu \approx 10 - 40\,GHz$, T_e^* can give a good approximation of the actual electron temperature, T_e, with better than 20% accuracy. As mentioned in the previous section, if non-LTE effects become large within HII regions, we need to correct for the non-LTE effect to T_e^* to get the actual temperature.

We can correct T_e^* with values of b, β and τ_C as,

$$T_e = T_e^* \left[b \left(1 - \frac{\tau_C}{2} \beta \right) \right]^{0.87}. \tag{2.69}$$

Most hydrogen RRLs observed from typical HII regions seem to be formed under LTE conditions. Therefore, it is not necessarily required to correct the non-LTE effects

in general. Figure 2.10 shows the relation between T_e^* with Galactocentric distance from Paladini et al. (2004) using 404 Galactic HII regions from a source catalog of Paladini et al. (2003). As seen in the figure, a decrease of T_e^* with Galactocentric distance is found confirming the trend first been shown by Churchwell & Walmsley (1975). The relationship ($T_e[\text{K}] = (4166 \pm 124) + (314 \pm 20)R_{\text{Gal}}[\text{kpc}])$ in Paladini et al. (2004) was quite similar to the previously well-measured result ($T_e[\text{K}] = (3150 \pm 110) + (433 \pm 40)R_{\text{Gal}}[\text{kpc}])$ of Shaver et al. (1983). A recent RRL survey at $1.4\,\text{GHz}$ (Alves et al. 2015) also shows the gradient as $T_e[\text{K}] = (3609 \pm 479) + (496 \pm 100)R_{\text{Gal}}$ [kpc].

The presence of this gradient was explained by Shaver et al. (1983) as a result of the Galactocentric gradient of metallic elements in the Galaxy. In particular, the most abundant are oxygen and nitrogen, which cool HII regions using radiating spectral lines. This is due to the fact that the collisions with free electrons in HII regions excite easily metastable levels in these atoms. Consequently, this process leads to the cooling down of a HII regions at a faster rate and results in a lower electron temperature. Since the inner parts of the Galaxy have high star formation rates, T_e should decrease as a result of the increase of metallicity. Also, the abundance gradient of heavier elements such as oxygen and nitrogen shows a decrease with increasing Galactocentric radius (Shaver et al. 1983; Afflerbach et al. 1996).
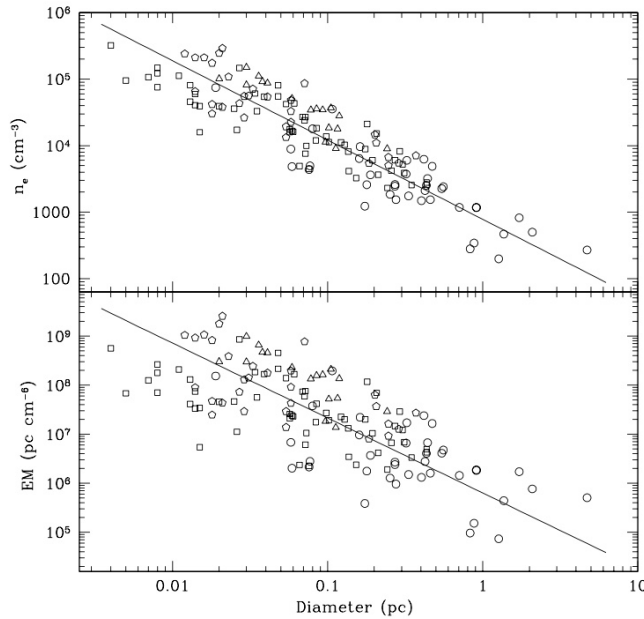
Figure 2.11: These show relationship between physical parameters of compact and UC HII regions. *upper* : Electron density as a function of diameter. *lower* : Emission measure as a function of diameter. The different symbols represent different samples from different studies (Wood & Churchwell 1989; Garay et al. 1993; Gaume et al. 1995; De Pree et al. 1997).

2.7.2 Electron density

The Electron density, n_e, is one of the most important properties for HII regions. The n_e is used as the threshold for classifying HII regions as mentioned in Chapter 1.3. To measure electron densities, we generally use radio continuum emission, but RRL can also be utilized for it. Since the n_e is $\sqrt{\frac{\text{EM}}{\Delta s}}$ where Δs is the diameter of a HII region in pc, we need to first obtain the emission measure (EM).

We can re-write Eqs. (2.33) and (2.44) for emission measure as

$$\text{EM}_C = \frac{\tau_C}{8.235 \times 10^{-2} a(\nu, T_e) T_e^{-1.35} \nu^{-2.1}} \quad [\text{cm}^{-6}\,\text{pc}] \qquad (2.70)$$

and

$$\text{EM}_L = \frac{T_e^{3/2}}{576} \nu T_L \Delta v_{\text{FWHM}} \quad [\text{cm}^{-6}\,\text{pc}], \qquad (2.71)$$

where ν is the rest observed frequency in GHz.

When we measure the T_e using Eq. (2.69), we can estimate the n_e for individual sources. Otherwise, we can use a typical electron temperature of 10^4 K.

Figure 2.11 shows the n_e and EM as a function of diameter of HII regions (Garay & Lizano 1999). The electron densities and emission measures are inversely proportional to sizes of HII regions. This relationship implies that small HII regions have high electron densities, showing that the compactness of HII regions seems to be related to the evolutionary stage of young HII regions as we have discussed in Chapter 1.3.

2.7.3 Photoionizing photon production rate, Q

If ionization equilibrium is satisfied in a HII region, we can measure the photonionizing photon production rates, Q, from measurements of RRLs. The photonizing photon production rate is related to the emission measure EM_{H+} over the volume of the ionized region as (Osterbrock 1989; Scoville & Murchikova 2013),

$$Q(\text{H}^+) = \int_{\nu_{th}}^{\infty} \frac{L}{h\nu} \, d\nu = \text{EM}_{H+} \alpha_B. \qquad (2.72)$$

when $h\nu \geq 13.6\,\text{eV}$ and then $h\nu_{thermal}$ is equal to $h\nu_0 = 13.6\,\text{eV}$. α_B ($= \sum_2^{\infty} \alpha_n$) is the total recombination coefficient as the sum over all levels with principal quantum number n except for the ground level. This case is called Case B. For Case B ionizing photons generated by recombinations to the ground level are absorbed in optically thick nebulae, and thus there is no contribution of the ground level to the ionization balance (Osterbrock 1989). The total recombination coefficient is a function of density and temperature. Storey & Hummer (1995) calculated total recombination coefficients at different electron densities and temperatures.

Since we can use measurements of RRLs to derive Q (e.g., Scoville & Murchikova 2013; Bendo et al. 2017), we modify Eq. (2.72) in observational units,

$$\frac{Q(\mathrm{H}n\alpha)}{\mathrm{s}^{-1}} = 3.99 \times 10^{24} \left(\frac{\alpha_B}{\mathrm{cm}^3\,\mathrm{s}^{-1}} \right)$$
$$\times \left(\frac{\varepsilon_\nu}{\mathrm{erg\,s}^{-1}\,\mathrm{cm}^{-3}} \right)^{-1} \left(\frac{\nu}{\mathrm{GHz}} \right) \left(\frac{D}{\mathrm{kpc}} \right)^2 \left(\frac{\int F_\nu\, dv}{\mathrm{Jy\,km\,s}^{-1}} \right), \tag{2.73}$$

where ε_ν is the effective emissivity at a frequency ν of observed RRL transition. These α_B and ε_ν parameters vary with the electron density and temperature.

2.7.4 Line widths and velocities

As discussed in Section 2.5, the non-thermal broadening of RRLs is influenced by different processes within H II regions, such as the density structure of the parental molecular cloud, stellar winds, and/or the motion of the exciting star with respect to the ambient medium (Garay & Lizano 1999). Therefore, line profiles and line widths of RRLs directly offer information about the kinematics of compact H II regions.

In the millimeter and short centimeter wavelength regimes ($n \leq 100$), the pressure broadening can be neglected as seen by the ratio of pressure broadening to Doppler broadening in Eq. (2.67). Then, the observed lines have approximately Gaussian profiles and also the RRL measurement can estimate T_e precisely. Finally, the velocity caused by turbulence within the telescope beam can be derived as,
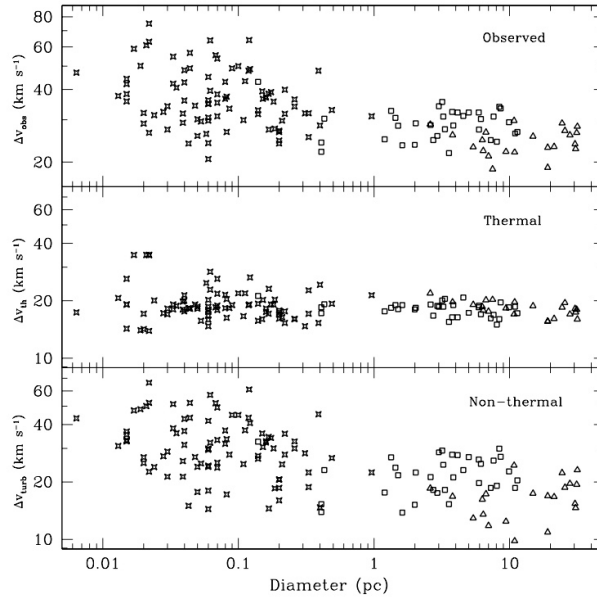
Figure 2.12: Line width as a function of diameter of H II regions (Garay & Lizano 1999). The explanation for the different symbols are same in Figure 2.11. Top, middle, and bottom panels show observed line width, thermal line width, and nonthermal line width (turbulence), respectively.

$$v_{\text{turbulence}} = 0.6\sqrt{(\Delta v_G^2) - 4.55 \times 10^{-2} T_e} \quad [\text{km s}^{-1}]. \tag{2.74}$$

Here, Δv_G is the observed FWHM line width of the Gaussian profile of a hydrogen RRL. Such turbulent velocities depend upon the angular resolution of the telescope and the angular extent of these HII regions (Gordon & Sorochenko 2002).

Also, Garay & Lizano (1999) showed that the line widths due to turbulence broadening are significant in compact HII regions, and the line width of HII regions decreases as the size of the HII regions increases (see Figure 2.12). They considered that the turbulence broadening might be due to either large-scale systematic motions of the ionized gas or the motions of small-scale eddies within the compact HII region. There are two possible models which are photo-evaporation from massive circumstellar disks (Hollenbach et al. 1994; Yorke & Welz 1996; Richling & Yorke 1997) or mass loading from clumps embedded within UC HII regions (Dyson et al. 1995; Lizano et al. 1996) to interpret this broadening. Nevertheless, neither of these models have explicitly predicted the behavior of line widths with distance.

Derivation of molecular abundances

Contents

The emission and absorption processes of molecules depend on the specific conditions in the ISM. This fact allows us to investigate the interstellar medium by measuring the intensities and line profiles of molecular lines.

We can convert observational data into the number of molecules per unit area along the line of sight in a given molecular level. We call this quantity *column density* which is an important measurement to estimate basic physical quantities (i.e., molecular abundance, kinetic temperature, and spatial density) (Mangum & Shirley 2015).

In the previous chapter, we have discussed the basics of radiative transfer and statistical equilibrium. Here, we will describe the necessary background information to determine column densities which will be used in Chapter 6 to measure molecular abundances and their changes in different environments, in particular as a function of the strengths of the UV radiation.

3.1 Types of molecules

A molecule can have three different categories of transitions corresponding to different energies: electronic transitions with energies of a few eV are responsible for lines at visual or UV wavelengths; lines from vibrational transitions with energies of 0.1 - 0.01

eV appear at infrared wavelengths; rotational transitions with energies of $\cong 10^{-3}$ eV correspond to lines at cm and mm wavelengths.

Here, we will focus on rotational lines at millimeter wavelengths since only those are studied in this thesis. Molecules can be divided into four types based on their moments of inertia along the three principal axes (I_a, I_b and I_c). These molecules are called linear, spherical, symmetric, and asymmetric top molecules. The moment of inertia (I_c) along the "c" axis has the maximum value, while the moment of inertia (I_a) along the "a" axis has the minimum value. The "b" axis is perpendicular to the other two axes (a and c). The convention for the naming these principal moments of inertia is $I_c \geq I_b \geq I_a$.

3.1.1 Linear molecules

For a linear molecule, there is no rotation along the I_a axis and the rotation axis is perpendicular to the chemical bond axis (i.e.,$I_b = I_c > I_a \simeq 0$).

Linear molecules normally consist of two or more atoms, and thus the diatomic molecules are a typical example of linear molecules. In this thesis, the linear molecules C_2H, $H^{13}CO^+$, $H^{13}CN$, $HC^{15}N$, $HN^{13}C$, HOC^+, $C^{18}O$, CN are studied in Chapter 6.

The rotational kinetic energy is given by

$$E_{\text{rot}} = \frac{L^2}{2I} \tag{3.1}$$

where L is the total angular momentum and I is the moment of inertia of a given molecule. The moment of inertia for a rigid molecule with two atoms A and B about any axis through the center of gravity is $I = m_A r_A^2 + m_B r_B^2 = m r_e^2$ with $r_e = r_A + r_B$ and $m = (m_A m_B)/(m_A + m_B)$, where m_A and m_B, and r_A and r_B are the masses and distances of the atoms from the axis.

In the case of a linear/diatomic molecule in the rigid rotor approximation, the rotational energy can be expressed as the solution of the Schrödinger equation,

$$\begin{aligned} \frac{E_{\text{rot}}}{h} = \frac{W(J)}{h} &= \frac{\hbar^2}{h2I} J(J+1) \\ &= \frac{h}{8\pi^2 I} J(J+1), \end{aligned} \tag{3.2}$$

where the eigenvalue of L^2 is driven by $\hbar^2 J(J+1)$ and $\hbar$ $(= h/2\pi)$ is the Planck constant. J is the quantum number of angular momentum and is integer (i.e., $J = 0, 1, 2, ...$). The term $\frac{h}{8\pi^2 I}$ can be expressed as the rotational constant, B.

Because of centrifugal stretching for a slightly elastic molecule, the rotational energy will increase with the radius of the bond axis. Therefore, the rotational energy of an elastic molecules is modified as

$$\frac{E_{\text{rot}}}{h} = \frac{W(J)}{h} = \frac{\hbar^2}{h2I} J(J+1) + D[J(J+1)]^2 \tag{3.3}$$

where the centrifugal distortion constant is $D = \frac{4B^3}{\omega_{vib}^2}$. Since the vibrational frequency ω_{vib} is usually much larger than B, the contribution of the centrifugal distortion is small.

The frequency of the molecular transition $(J + 1 \rightarrow J)$ from an upper state $J + 1$ to a lower state J is given by,

$$\nu(J) = \frac{1}{h}[W(J + 1) - W(J)] = 2B(J + 1) - 4D(J + 1)^3. \tag{3.4}$$

The selection rule for an electric dipole transition in a linear/diatomic molecule is $\Delta J = \pm 1$. D has a positive value, and the typical size of D is about 10^{-5} of the magnitude of B for most molecules. The deviation between the perfectly rigid rotor and actual frequencies will become larger with an increase of J. Hence, the actual frequencies will always be lower than the predicted frequencies for a rigid rotator.

3.1.2   Symmetric and asymmetric molecules

Symmetric molecules

For symmetric-rotor or symmetric-top molecules, two of the principal moments of inertia are equal by symmetry, and the third should be non-zero. If $I_c = I_b > I_a$, the molecule is said to be prolate symmetric and is elongated. On the other hand, if $I_c > I_b = I_a$, the molecule is referred to have oblate symmetry, and it has a flattened disk shape. Additionally, if the three principal moments of inertia are identical, $I_c = I_b = I_a$, then the molecule is called a spherical molecule.

The rotational energy for a symmetric molecule is

$$\frac{E_{\text{rot}}}{h} = BJ(J + 1) + s_0 K^2 - D_J J^2 (J + 1)^2 - D_{JK}(J + 1)K^2 - D_K K^4, \tag{3.5}$$

where for a prolate symmetric-top molecule $s_0 \equiv A - B$ and for an oblate symmetric-top molecule $s_0 \equiv C - B$. A, B, and C are the three rotational coefficients: $A = \frac{h}{8\pi^2 I_a}$, $B = \frac{h}{8\pi^2 I_b}$, and $C = \frac{h}{8\pi^2 I_c}$. The quantum number K (K = 0, ..., $\pm J$) in symmetric and asymmetric (near-symmetric) molecules describes the projection of the total angular momentum number J onto the molecular symmetry axis: for an oblate, the c-axis; for a prolate, the a-axis.

Asymmetric molecules

In the case of asymmetric molecules, the three principal moments of inertia are unequal, $I_c \neq I_b \neq I_a$. Most nonlinear molecules found in the ISM belong to this asymmetric molecule type. The majority of the molecules are asymmetric rotors which exist as either a prolate near-symmetric rotor $(I_c \simeq I_b > I_a)$ or an oblate near-symmetric rotor $(I_c > I_b \simeq I_a)$.

$$
\begin{aligned}
\frac{E_{\text{rot}}}{h} &\simeq \bar{B}J(J + 1) + (A - \bar{B})K_a^2 \quad \text{(for a prolate)} \\
&\simeq \bar{B}J(J + 1) + (C - \bar{B})K_c^2 \quad \text{(for an oblate)}
\end{aligned}
\tag{3.6}
$$

where for a prolate rotor $\bar{B} = \frac{1}{2}(B+C)$ and for an oblate rotor $\bar{B} = \frac{1}{2}(A+B)$. The rotational energy levels are labeled J_{K_a,K_c}. Therefore, for a prolate molecule, J and K_a are good quantum numbers, whereas, for an oblate molecule, J and K_c are good numbers. Cyclic C_3H_2 ($J_{K_a,K_x} = 2_{1,2} - 1_{0,1}$), which is analyzed in this thesis, is an example of an oblate slightly asymmetric molecule.

3.2 Fine and hyperfine structure

In some of the molecules (C_2H, CN, HCO, and $H^{13}CN$) in this thesis, the rotational transitions are split into fine/hyperfine structures. If unpaired electrons and/or a non-zero orbital angular momentum of its electrons exist in a molecule, spin doubling ($J = N + S$) occurs due to the coupling between the angular momentum of rotation of the molecule (N) and the unpaired electron spin (S). This process produces the fine structure. C_2H, CN, and HCO have an electronic state which is described by the projection of its orbital angular momentum onto the molecular axis, Λ and the total electron spin of S. Each electronic state is expressed as $^{2S+1}\Lambda$. The $\Lambda = 0, 1$, and 2 states are noted as Σ, Π, Δ, respectively. Therefore, The electron spin multiplicity ($2S + 1$) is appended as a left superscript to Σ, Π, and Δ. For example, C_2H has the electronic state with $\Lambda = 0, S = 1/2$, and a positive plane symmetry and thus its electronic state can be denoted as $^2\Sigma^+$.

On the other hand, the hyperfine structure is caused by the magnetic dipole or electric quadrupole of nuclei interacting with electrons or other nuclei if one or more nuclei in a molecule have non-zero nuclear spin. The hyperfine interactions are divided into two groups where the interaction is either due to the magnetic origin or the nuclear quadrupole moment. The hyperfine interaction by the magnetic dipole in a diamagnetic molecule is, in general, negligible. In contrast, the so-called nuclear quadrupole interaction is the main reason that produces the hyperfine structure of the aforementioned molecules.

The interaction is produced when the electric quadrupole moment interacts with the electric field gradient around the nucleus when a nucleus has a nuclear spin of one or larger. In other words, this hyperfine structure ($F = J + I$) is produced by the coupling of the angular momentum (J) and the spin of the nucleus (I). The molecules in this thesis are those with ^1H ($I = 1/2$), ^{13}C ($I = 1/2$), ^{14}N ($I = 1$), and ^{15}N ($I = 1/2$) that have non-zero spin nuclei. For instance, the ^{14}N nucleus has a nuclear spin of one, and therefore it has hyperfine splitting in the low$-J$ transitions of $HC^{14}N$ and $H^{13}C^{14}N$. Conversely, hyperfine splitting of $HC^{15}N$ is not significant and small since ^{15}N has a nuclear spin of $1/2$ (less than one). The selection rule for the hyperfine structure is $\Delta F = \pm 1, 0$ but $\Delta F = 0 \to 0$ does not have allowed transitions.

3.3 Column density

Measuring the number of molecules per unit area along the line of sight allows an understanding of the physical conditions in the ISM such as spatial density, molecular

abundance, and kinetic temperature if several lines with different upper energies are observed.

This quantity is known as "column density" and can be derived from a two-state system. The column density of molecules in an upper state is obtained by integrating the number density over the path length dx,

$$N_u \equiv \int n_u dx. \tag{3.7}$$

The column density defined in Eq. (3.7) is related to τ_ν. We used the Eqs. (2.6), (2.13), (2.18), (2.19), and (2.25) defined in the previous Chapter 2 to derive N_u as

$$
\begin{aligned}
N_u &= \frac{8\pi\nu^3}{c^3 A_{ul}} \left[\exp\left(\frac{h\nu}{k_{\mathrm{B}}T_{\mathrm{ex}}}\right) - 1 \right]^{-1} \int \tau_\nu dv \\
&= \frac{3h}{8\pi^3 |\mu_{lu}|^2} \left[\exp\left(\frac{h\nu}{k_B T_{ex}}\right) - 1 \right]^{-1} \int \tau_\nu dv,
\end{aligned} \tag{3.8}
$$

where we integrated over the line profile ($\int \phi_\nu = 1$) and converted frequency to velocity. T_{ex} is the excitation temperature that will be discussed in Section 3.3.3. The dipole matrix element, $|\mu_{lu}|^2$, is equal to $S\mu^2$ where S is the line strength of the transition, and μ is the dipole moment of the molecule.

N_u only takes into account the number of molecules in the upper state and thus we have to relate N_u to the total population of all energy levels

$$\frac{N_{\mathrm{tot}}}{N_u} = \frac{Q_{\mathrm{rot}}}{g_u} \exp\left(\frac{E_u}{k_{\mathrm{B}}T_{\mathrm{ex}}}\right), \tag{3.9}$$

$$N_{\mathrm{tot}} = \frac{8\pi\nu^3}{c^3 A_{ul}} \frac{Q_{\mathrm{rot}}}{g_u} \exp\left(\frac{E_u}{k_{\mathrm{B}}T_{\mathrm{ex}}}\right) \left[\exp\left(\frac{h\nu}{k_{\mathrm{B}}T_{\mathrm{ex}}}\right) - 1 \right]^{-1} \int \tau_\nu dv, \tag{3.10}$$

here, we express N_{tot} with A_{ul} instead of $S\mu^2$.

3.3.1 Degeneracies (g_u)

The total degeneracy, g_u, for an energy level of a transition is given by the product of rotational (g_J and g_K) and spin (g_I) degeneracies: $g_u \equiv g_J g_K g_I$. The rotational degeneracy, g_J occurs due to the projection of the angular momentum on the rotation axis and so all molecules have g_J. The degeneracy related with the internal quantum number K is g_K. For linear and asymmetric molecules, g_K is 1 and for $K \neq 0$ in symmetric molecules $g_K = 2$. The nuclear spin degeneracy (g_I) is considered mainly for *nonlinear molecules or hyperfine splitting* since it describes the statistical weights related with identical nuclei in a nonlinear molecule with symmetry. g_I is $\frac{g_{\mathrm{nuclear}}}{g_n}$, where $g_n = (2I+1)^\sigma$ and σ is the number of identical nuclei (Mangum & Shirley 2015).

3.3.2 Rotational partition function ($Q_{\rm rot}$)

The partition function, Q, describes the relative population of states in the gas. For molecules, the partition function is a function of four states of the molecule: electronic, vibrational, rotational, and nuclear spin. Since in the cold ISM only the ground electronic and vibrational states of most molecules are populated, we only take into account rotational and nuclear spin partition functions as,

$$Q_{\rm rot} = \sum_{J,K,I} g_J g_K g_I \exp\left(-\frac{E_{JK}}{k_{\rm B} T_{\rm ex}}\right). \tag{3.11}$$

For diatomic and linear molecules in case of $g_J = 2J + 1$, $g_K = 1$, and $g_I = 1$,

$$\begin{aligned} Q_{\rm rot} &= \sum_{J=0}^{\infty} (2J + 1)\exp\left(-\frac{E_J}{k_{\rm B} T_{\rm ex}}\right) \\ &\simeq \frac{k_{\rm B} T_{\rm ex}}{hB} + \frac{1}{3}. \end{aligned} \tag{3.12}$$

For symmetric and slightly asymmetric rotor molecule in case of $g_J = 2J + 1$, $g_K = 1(K = 0)$ or $2(K \neq 0)$ for symmetric rotors (for all asymmetric rotors, $g_K = 1$), and $g_I = g_{\rm nuclear}/(2I + 1)^{\sigma}$,

$$\begin{aligned} Q_{\rm rot} &= \sum_{J=0}^{\infty} \sum_{K=-J}^{+J} g_K g_I (2J + 1)\exp\left(-\frac{E_{JK}}{k_{\rm B} T_{\rm ex}}\right) \\ &\simeq \frac{\sqrt{m\pi}}{\sigma}\left(\frac{k_{\rm B} T_{\rm ex}}{hB}\right)^{3/2}, \end{aligned} \tag{3.13}$$

where $m = \frac{B}{A}$ for a prolate symmetric rotor molecule, $m = \frac{B}{C}$ for a oblate symmetric molecule and $m = \frac{B^2}{AC}$ for a slightly asymmetric rotor molecule.

3.3.3 Excitation temperature ($T_{\rm ex}$)

The excitation temperature, T_{ex} for the transition from an upper to a lower state can be defined by the populations of the upper and lower states,

$$\begin{aligned} \frac{n_u}{n_l} &= \frac{g_u}{g_l}\exp\left(-\frac{(E_u - E_l)}{k_{\rm B} T_{\rm ex}}\right) \qquad \text{(in general)} \\ &= \frac{g_u}{g_l}\exp\left(-\frac{h\nu}{k_{\rm B} T_{\rm kin}}\right) \qquad \text{(for LTE excitation).} \end{aligned} \tag{3.14}$$

The excitation temperature in the two-level system is defined by the balance between radiative and collisional excitation and de-excitation.

$$n_u(A_{ul} + B_{ul}\bar{u} + C_{ul}) = n_l(B_{lu}\bar{u} + C_{lu}), \tag{3.15}$$

where $n_l C_{lu}$ gives the number of collisional excitations per unit volume per unit time from the lower state to the upper state and $n_u C_{ul}$ indicates the number of collisional de-excitation from the upper state to the lower state.

The collisional excitation and de-excitation are related via

$$C_{lu} = \frac{g_u}{g_l} \exp\left(-\frac{h\nu}{k_B T_{ex}}\right) C_{ul}.$$
(3.16)

The excitation temperature only governs the ratio of n_u to n_l and is not necessarily the kinetic temperature,

$$\frac{n_u}{n_l} = \frac{B_{lu}\bar{u} + C_{lu}}{A_{ul} + B_{ul}\bar{u} + C_{ul}}.$$
(3.17)

Using Eqs. (2.15, 2.17, and 2.18) we can express Eq. (3.17) again as

$$\frac{n_u}{n_l} = \frac{g_u}{g_l} \frac{A_{ul}\left[\exp\left(\frac{h\nu}{k_B T_b}\right) - 1\right]^{-1} + C_{ul}\exp\left(-\frac{h\nu}{k_B T_k}\right)}{A_{ul}\exp\left(\frac{h\nu}{k_B T_b}\right)\left[\exp\left(\frac{h\nu}{k_B T_b}\right)\right]^{-1} + C_{ul}},$$
(3.18)

re-arranging the degeneracies to the right and using Eq. (3.14), the right hand side reduces to $\exp\left(-\frac{h\nu}{k_B T_{ex}}\right)$. The spontaneous emission rate (A_{ul}) is more dominant in comparison to the collisional rates (C_{ul}) if the H_2 densities is low. In this case, the excitation temperature is equal to the the ambient radiation brightness temperature (T_b): $T_{ex} \to T_b$. In contrast, for high H_2 density C_{ul} is much higher than A_{ul} and thus the excitation temperature becomes equal to the kinetic temperature (T_{kin}): $T_{ex} \to T_{kin}$.

3.4   Approximations to the column density equation

The measured molecular spectral line intensity is the difference between the intensity toward a reference position that has only background emission and the intensity toward the target source as described by Eq (2.8),

$$\delta I_\nu \equiv I_\nu - I_\nu(0)$$
$$[B_\nu(T_{ex}) - B_\nu(T_{bg}))]\left[1 - \exp(-\tau_\nu)\right]$$
(3.19)

The specific intensity I_ν is substituted by the Rayleigh-Jeans temperature $J_\nu(T)$, which is equivalent to a given temperature of the black body. B_ν is related with $J_\nu(T)$ as follows: $\frac{c^2 B_\nu(T)}{2k\nu^2} = J_\nu(T)$ and $J_\nu(T) \equiv \frac{h\nu/k_B}{\exp(h\nu/k_B T) - 1}$.

$$T_R = \frac{c^2}{2k_B \nu^2}\Delta I_\nu$$
$$= f\left[J_\nu(T_{ex}) - J_\nu(T_{bg}))\right]\left[1 - \exp(-\tau_\nu)\right],$$
(3.20)

where the T_R is the radiation temperature of the observed source. f is the so-called beam filling factor which is the fraction of the beam filled by the source.

3.4.1 Optically thin case

If the optical depth is low along the line of sight ($\tau_\nu \ll 1$), the exponential term $[1 - \exp(-\tau_\nu)]$ reduces to τ at the rest frequency and thus Eq. (3.20) for the optical thin case becomes,

$$T_R = f[J(T_{\mathrm{ex}}) - J(T_{\mathrm{bg}})]\tau. \tag{3.21}$$

Substituting Eq. (3.21) to the column density Eq. (3.10),

$$
N_{\mathrm{tot}}^{\mathrm{thin}} = \left(\frac{8\pi\nu^3}{c^3 A_{ul}}\right)\left(\frac{Q_{\mathrm{rot}}}{g_u}\right)\frac{\exp\left(\frac{E_u}{k_{\mathrm{B}}T_{\mathrm{ex}}}\right)}{\exp\left(\frac{h\nu}{k_{\mathrm{B}}T_{\mathrm{ex}}}\right) - 1}
$$
$$
\times \frac{1}{[J_\nu(T_{\mathrm{ex}}) - J_\nu(T_{\mathrm{bg}})]}\int \frac{T_R}{f}dv \tag{3.22}
$$

The intensity is proportional to the optical depth and consequently so is the column density. In the optically thin case, all emitted photons escape without being absorbed in the cloud. If we assume that $h\nu/k_{\mathrm{B}}T_{\mathrm{ex}} \ll 1$ and $T_{\mathrm{ex}} \gg T_{\mathrm{bg}}$ under LTE conditions, we obtain the following equation

$$\ln\frac{3k_{\mathrm{B}}\int T_R dv}{8\pi^3\nu S\mu^2} = \ln\frac{N_{\mathrm{tot}}}{Q_{\mathrm{rot}}} - \frac{E_u}{k_{\mathrm{B}}T_{\mathrm{rot}}} \tag{3.23}$$

The relation should be linear if we observe multiple transitions for the same species which are under LTE condition. The slope of a plot of $\ln(N_{\mathrm{tot}}/Q_{\mathrm{rot}})$ versus E_u/k_{B} provides $1/k_{\mathrm{B}}T_{\mathrm{rot}}$ and $N_{\mathrm{tot}}/Q_{\mathrm{rot}}$ can be obtained from the intercept. This method is called the rotation diagram method (RD). RD is very useful to derive the column density and rotation temperature for molecules in warm and dense clouds, for example, in star-forming cores where the assumptions required for this method are reasonably satisfied. In real cases, the RD fit is not always successful since multiple components in the observed cloud do not share the same physical conditions and LTE does not apply to their excitation. If the collisions are adequately frequent in comparison with radiation probabilities, rotation temperature (T_{rot}) is satisfied and becomes close to the kinetic temperature of H_2. On the other hand, if collisions happen less frequently, the level populations deviates from LTE and the line is said to be subthermally excited. Therefore, the excitation temperature is different from transition to transition and a single Boltzmann distribution cannot fully represent the level population.

3.4.2 Optically thick case

If the optical depth is high ($\tau_\nu \geq 1$), then we cannot directly obtain the column density as in the optically thin case.

However, we can estimate the column density in the optically thick case as a function of the column density in the optically thin case using the optical depth correction factor $C_\tau = \frac{\tau}{1-\exp(-\tau)}$ (Goldsmith & Langer 1999), where we argue $h\nu \ll k_{\mathrm{B}}T_{\mathrm{ex}}$ and $T_{\mathrm{bg}} \ll T_{\mathrm{ex}}$,

$$N_{\text{tot}}^{\text{thick}} = N_{\text{tot}}^{\text{thin}} \frac{\tau}{1 - \exp(-\tau)}, \tag{3.24}$$

where the optical depth can be derived by observations of other isotopologues or hyperfine ratios. RD can also be used as a diagnostic tool for calculating the optical depth of the emission which we will describe later.

Since $\tau_\nu \geq 1$, $[1 - \exp(-\tau_\nu)] \simeq 1$ and thus Eq. (3.20) becomes the optically thick case,

$$T_R^{\text{thick}} = f[J(T_{\text{ex}}) - J(T_{\text{bg}})]. \tag{3.25}$$

Therefore, we can estimate the excitation temperature for optically thick molecular lines using Eq. (3.25),

$$T_{\text{ex}} = \frac{h\nu}{k_{\text{B}}} \left[\ln \left(1 + \frac{(h\nu/k_{\text{B}})}{T_{\text{thick}} + J(T_{\text{bg}})} \right) \right]^{-1}. \tag{3.26}$$

As we have briefly mentioned above, the optical depth can also be derived by hyperfine structure fitting, but it is sometimes not reliable in the presence of anomalous hyperfine excitation are dominant due to non-LTE effects.

3.5　Application: cyclic-C_3H_2

Most molecular species ($C^{18}O$, $H^{13}CO^+$, $HN^{13}C$, $H^{13}CN$, $HC^{15}N$, C_2H), which are analyzed in this thesis, are linear. On the other hand, cyclopropenylidene (c-C_3H_2) is a cyclic, slightly oblate asymmetric molecule and has two nuclei with identical spin $1/2$.

Therefore, here we will describe how to derive the column density for c-C_3H_2 for measurements of its $2_{1,2} \rightarrow 1_{0,1}$ transition (the ortho species) using Eq. (3.22) in the optical thin case. However, we can also utilize Eq.(3.23) to calculate its column density.

The parameters used to estimate the column density and are obtained from the CDMS database[1]:

$$S = 4.85$$
$$\mu = 3.27 \,\text{Debye} = 3.27 \times 10^{-18} \,\text{esu cm}$$
$$A_0 = 35092.57 \,\text{MHz}$$
$$B_0 = 32212.95 \,\text{MHz}$$
$$C_0 = 16749.03 \,\text{MHz}$$
$$g_u = 15$$
$$T_{ex} = 18.75 \,\text{K}$$
$$Q_{\text{rot}}(18.75 \,\text{K}) = 201.8429$$
$$E_u = 6.44539 \,\text{K}$$
$$\nu = 85.338893 \,\text{GHz}$$

---

[1]https://www.astro.uni-koeln.de/cdms
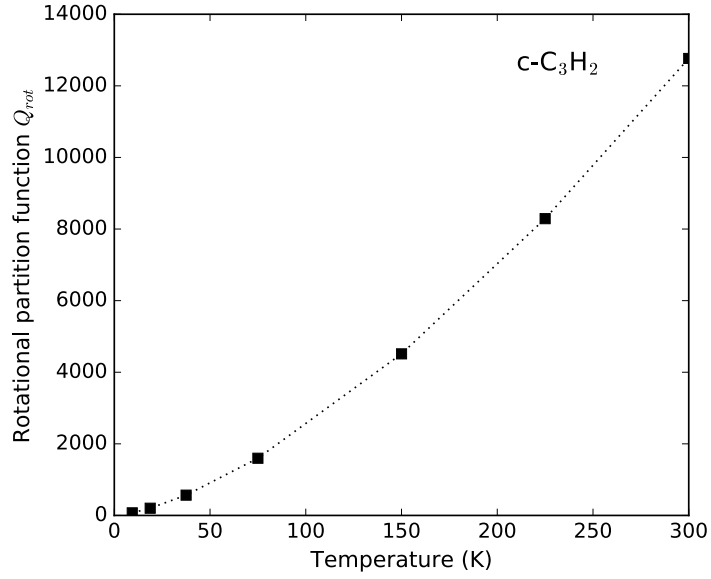
Figure 3.1: The rotational partition function as a function of the temperature for c-C_3H_2 molecule.

If we fix $T_{ex} = 18.75\,\text{K}$ and assume that the emission is optically thin, Eq.(3.22) for the total column density of c-C_3H_2 becomes:

$$N_{tot}(c - C_3H_2) = 7.53 \times 10^{12} \int T_{MB}\, dv \quad [\text{cm}^{-2}]. \tag{3.27}$$

As we have seen that the rotational partition function is a function of temperature, we need to choose a proper value for the temperature. Figure 3.1 shows the change of the partition function with temperature. In this thesis, different values of the rotational partition function are applied for calculating column densities toward individual sources.

Millimeter hydrogen radio recombination line surveys

Contents

4.1 Introduction

High-mass star formation plays a critical part in the evolution of galaxies and an important role in the chemical enrichment of the interstellar medium (ISM) in the Milky Way (Zinnecker & Yorke 2007). High-mass star formation starts in massive cold and dense gravitationally bound clumps that are still infrared-quiet and subsequently collapse and

fragment into cores. The cores contain protostars called massive young stellar objects (MYSOs) that gain their mass with high accretion rates (Urquhart et al. 2014d). Finally, the formation of an HII region that is first hypercompact and then ultracompact signifies the arrival of the embedded MYSO on to the main sequence and it is therefore a key stage in the evolution of massive stars. The massive stars reach the main sequence while still deeply embedded in their natal cloud and continue to accrete material even after the HII region has begun to form (Zinnecker & Yorke 2007; Churchwell 1990, 2002; Kurtz et al. 2000; Kurtz & Hofner 2005). Investigating HII regions in their earliest stages while they are still embedded in their parental dense molecular clouds allows us to determine at what evolutionary stage high-mass stars stop accumulating their mass $M > 10 \, M_\odot$ and how the accretion and outflow processes evolve after the protostar arrives on the main sequence (Keto & Klaassen 2008; Churchwell et al. 2010).

The embedded HII regions are surrounded by dust cocoons, but are bright from mid- and far-infrared (mid- and far-IR) to radio wavelength since the dust absorbs ultraviolet radiation from the HII regions and re-emits it at infrared wavelengths (Wood & Churchwell 1989). Far-IR colors, interstellar masers, and molecular lines have all been employed to identify HII region candidates, and radio continuum surveys have since confirmed many of them and derived their physical parameters (Forster & Caswell 1989; Wood & Churchwell 1989; Kurtz et al. 1994; Hofner & Churchwell 1996; Shepherd & Churchwell 1996; Urquhart et al. 2009; Walsh et al. 2014). A class of the densest and most compact, optically thick ionized nebula known as hyper-compact HII regions (HC HIIs), have been revealed by observations conducted at high radio frequencies (e.g., 43 or 50 GHz; Carral et al. 1997; Kurtz 2005).

These surveys have been very successful in identifying a large number of young embedded compact and ultra-compact HII regions (UC HIIs; Lumsden et al. 2013); to date ∼600 have been cataloged. However, they tend to target HII regions with specific properties or evolutionary stages and may not provide a complete picture of the full evolutionary sequence. For example, the properties of the earliest hyper-compact phase are based on a few tens of sources; these sources are likely to be some of the most extreme and are therefore probably not representative of the general population of these objects.

Dust continuum emission in the submillimeter wavelength range (submm) can directly trace high column density regions in which high-mass stars form. Moreover, the cold dust absorbs IR emission from objects at different evolutionary stages and then emits thermal emission through the submm. The APEX Telescope Large Area Survey of the Galaxy (ATLASGAL; Schuller et al. 2009) is a dust continuum survey at $870 \, \mu m$ that provides an unbiased view of the dense gas located throughout the mid-plane of the inner Galaxy ($-60° \leq \ell \leq +60°$ and $|b| \leq 1.5°$; Schuller et al. 2009). ATLASGAL has identified ∼10,000 dense clumps (Compact Source Catalogue (CSC; Contreras et al. 2013; Urquhart et al. 2014a), GaussClump Source Catalogue (GCSC; Csengeri et al. 2014)), many of which are in the pre-stellar, protostellar, and HII region stages. This sample is therefore ideal for the study of the whole embedded evolutionary sequence of massive stars.

We selected dust clumps based on flux limits at $870 \, \mu m$ continuum emission for

follow-up molecular line surveys in the 3 mm atmospheric window using the IRAM
30m and Mopra 22m telescopes. The clumps were originally selected as the brightest
870 μm clumps being mid-IR dark and bright, respectively, and later divided into three
photometric categories (i.e., 22 μm dark, bright, and H II regions; Csengeri et al. 2016).
The clump photometric categories were determined from their association with mid-IR
emission from the all-sky Wide-field Infrared Survey Explorer (WISE; Wright et al.
2010) and the Galactic Legacy Infrared Mid-Plane Survey Extraordinaire (GLIMPSE ;
Benjamin et al. 2003). Furthermore, the flux limited selection of clumps with different
infrared properties ensures that for the different evolutionary stages the most massive
clumps were observed (Giannetti et al. 2014; Csengeri et al. 2016).

Although the mid-IR surveys are useful for distinguishing between IR bright (pro-
tostellar) and IR dark (starless) sources, they cannot identify H II regions and therefore
additional information is required. The hot ionized regions emit strongly at radio
wavelengths and can be identified using radio continuum observations. The CORNISH
survey (Hoare et al. 2012; Purcell et al. 2013) has been used to identify ∼200 H II re-
gions associated with ATLASGAL clumps (Urquhart et al. 2013b) and the targeted
radio continuum observations conducted as part of the RMS survey (Urquhart et al.
2007, 2009) have identified several hundreds more; a catalog of these matches and a
summary of their properties is given in Urquhart et al. (2014d). All of these H II regions
have been identified from 5-9 GHz radio continuum observations. These observations
are sensitive to compact and ultra-compact (UC) H II regions that are generally op-
tically thin at these frequencies, while they are not sensitive to the more embedded,
optically thick, hyper-compact (HC) H II regions. However, these regions are optically
thin at millimeter wavelengths and so mm-RRLs offer an opportunity to identify a
younger generation of embedded H II regions that may have been missed from radio
continuum surveys.

Most of the previous radio recombination line surveys have been made with single-
dish telescopes at centimeter (cm) wavelengths. The cm-RRLs have principal quan-
tum numbers (n) $\geq$ 85 and were mostly observed with angular resolutions of a few
arc-minutes (e.g., Lockman 1989; Caswell & Haynes 1987; Anderson & Bania 2009;
Anderson et al. 2014; Alves et al. 2015). There are a number of higher resolution
studies of individual sources (Gaume et al. 1995; De Pree et al. 2004a; Sewilo et al.
2004a; Sewiło et al. 2008; Keto et al. 2008). These studies have provided some insight
into the properties of H II regions, and have revealed that they have significant broad
linewidths that decrease as the H II region expands. The broadest linewidths are found
toward the youngest H II regions (HC H IIs > 40 km s^{-1}), while the slightly more evolved
UC H IIs have typical linewidths between $30 - 40$ km s^{-1}.

The Mopra and IRAM molecular line surveys cover the frequencies of a number of
mm-RRL transition. Such RRLs have been observed in a few targeted studies (e.g.,
Jaffe & Martín-Pintado 1999; Churchwell et al. 2010). These tend to focus on indi-
vidual or small samples of sources. In this chapter we use the mm-RRLs observed in
our line surveys to conduct a search for deeply embedded H II regions in an untargeted
and relatively unbiased way given that the clumps were selected based on their sub-
millimeter and mid-infrared properties alone and not specifically with H II regions in

Table 4.1: Summary of the observational setup of the telescopes, coverage, and the number of sources observed.

Surveys	Southern survey	Northern survey
Frequency (GHz)	$85.6 - 88.4$	$85.6 - 110.6$
Telescope	Mopra 22m	IRAM 30m
Date (mm/yy)	05/08, 08/09 & 09/09	04/11 & 10/12
l (deg)	$-60° \leq \ell \leq 0°$	$0° \leq \ell \leq +60°$
Number of sources	566	410
rms (Jy)	0.20	0.05
Δv resolution ($\mathrm{km\,s^{-1}}$)	3.5∼3.8	3.7∼4.1
Beam size ($''$)	∼36	∼29
K to Jy ($\mathrm{Jy\,K^{-1}}$)	22.0	5.9

mind. These observation, therefore, have the potential to identify new HII regions and provide information on the kinematics of the ionized gas and their interaction with the molecular gas of their natal clump; this in turn will improve our understanding of how the HII regions impact the physical structure and dynamics of their local environment.

Since mm-RRL sources have so far not been studied in a systematic way, the low sample statistics makes it difficult to compare their properties with those determined from cm-RRL studies. In fact, cm- and mm-RRLs are likely to be probing different evolutionary stages and/or different physical conditions. For example, the linewidths of cm-RRLs are affected by pressure broadening caused by high electron density; this leads to a significant broadening of the line profile (Gordon & Sorochenko 2002; Sewiło et al. 2008). However, the impact of pressure broadening for mm-RRLs is negligible and thus the mm-RRLs linewidths are dominated by thermal and turbulent motions within the gas (Gordon & Sorochenko 2002). Therefore, mm-RRLs provide a useful probe for the study of the intrinsic motions and physical properties of compact HII regions. Furthermore, observations of different order transitions (e.g., $\Delta n = 1, 2, 3,$ ..., denoted H$n\alpha$, H$n\beta$, H$n\gamma$, and so on) allow us to determine whether the mm-RRL emission departs from non-LTE or LTE conditions since the degree of such departures may change with quantum number and order (Thum et al. 1995).

In this chapter we present a new mm-RRL survey to find embedded HII regions in ATLASGAL clumps and derive the properties of the HII regions detected. This mm-RRL survey provides the largest sample of mm-RRL detections and an unbiased way to search for HII regions. The structure of the paper is as follows. The observations and data reduction is described in Section 4.2. The general results of detected mm-RRLs and association with molecular clumps, radio continuum, and mid-IR counterparts are presented in Section 4.3. The relationships with the radio continuum counterparts and calculated physical parameters are discussed in Section 4.5. Finally, we summarize our main results in Section 4.6.

4.2   Observations and data reduction

4.2.1   Source selection

The selection of the sources for the Mopra and IRAM surveys was based on their $870\,\mu$m continuum peak flux. We applied different flux limits to clumps with different infrared properties, to cover a range of evolutionary stages, and observed all sources above the flux limits. For the earlier Mopra survey, we used the $21\,\mu$m emission properties, $21\,\mu$m-bright and -dark, of the Midcourse Space Experiment (MSX; Price et al. 2001), and when Spitzer data became available, we used their 8 and $24\,\mu$m emission properties for the IRAM survey (see Giannetti et al. 2014 and Csengeri et al. 2016 for details).

As the results, the $870\,\mu$m peak flux thresholds are different for the Mopra and IRAM surveys. Nevertheless, both surveys can be considered to cover all different evolutionary stages and differ slightly by the mass ranges they cover. We use all the sources of both surveys as a single sample for all the data analysis, and the number of sources (976) are large enough to reduce potential biases.

4.2.2   Observational setups

We used the Mopra 22m and IRAM 30m telescopes to observe a sample of ATLASGAL source distributed across the inner Galactic plane. The beam sizes and frequency coverage results in different angular resolutions and sensitivities for the two telescopes; they are summarized in Table 5.2. Since we have stacked the mm-RRLs to improve the signal-to-noise ratio (S/N) of the observations, in the following we use the beam size of the lowest frequency transition; this is the value given in Table 5.2. The number of sources observed in different longitude ranges by the Mopra 22m and the IRAM 30m telescopes (see next section) are also summarized in Table 5.2.

4.2.2.1   Mopra 22m telescope observations

The mm-RRL data for the southern hemisphere were obtained from targeted molecular line observations with the Mopra 22m telescope (Project IDs: M327-2008 and M327-2009; Wyrowski et al. 2008, 2009).[1] As previously mentioned, the sources were selected based on their mid-IR emission properties (mid-IR bright or mid-IR dark) to ensure that a range of evolutionary stages was probed. The $870\,\mu$m peak flux threshold was based on the IR properties of the clumps; for mid-IR bright clumps a value of $1.75\,\mathrm{Jy\,beam^{-1}}$ was used, while for the mid-IR dark clumps flux limit of $1.2\,\mathrm{Jy\,beam^{-1}}$ was used. In total, 566 ATLASGAL dust clumps were observed within the longitude ranges $-60° \leq \ell \leq 0°$. The Mopra observations used the MOPS spectrometer[2], which has a bandwidth coverage of $8\,\mathrm{GHz}$ and was tuned to 89.3 GHz providing coverage of $85.2 - 93.4\,\mathrm{GHz}$ with a velocity resolution of $\sim 0.9\,\mathrm{km\,s^{-1}}$ and angular resolution of

---

[1]The Mopra radio telescope is part of the Australia Telescope National Facility which is funded by the Australian Government for operation as a National Facility managed by CSIRO.

[2]The University of New South Wales Digital Filter Bank used for the observations with the Mopra Telescope was provided with support from the Australian Research Council.
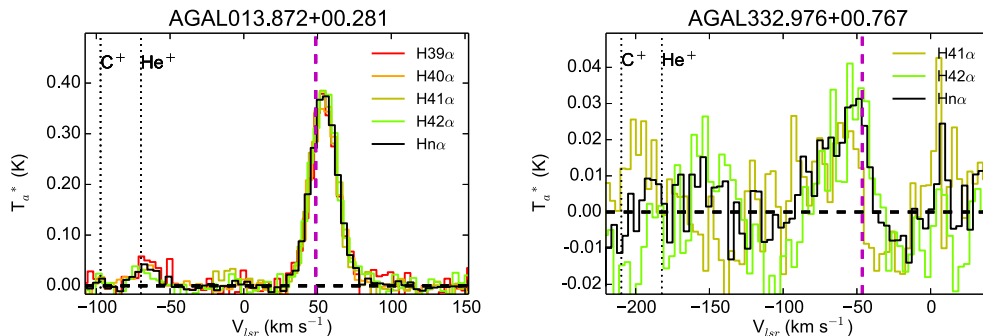
Figure 4.1: For two sources in our sample, each color represents an observed RRL H$n\alpha$ transition and the black line shows the stacked spectrum. The purple dashed lines indicate the systemic local standard of rest (lsr) velocity of the clump determined from the H^{13}CO$^+$ transition and the two vertical black dotted lines indicate expected positions of helium and carbon RRLs.

$\sim 36'' \pm 3''$ at 86 GHz (Ladd et al. 2005). This frequency range includes three mm-RRL transitions, H41α, H42α, and H52β. We have scaled the measured antenna temperatures, $T_{\rm a}^*$, to the main-beam brightness temperatures, $T_{\rm MB}$, using the Mopra main-beam efficiency ($\eta_{\rm MB} = 0.49$; Ladd et al. 2005).

4.2.2.2 IRAM 30m telescope observations

For the northern hemisphere the mm-RRL data were obtained from targeted molecular line observations with the IRAM 30m telescope (Project IDs: 181-10 and 037-12) (see Csengeri et al. 2016 for more details).[3] The 870 μm peak flux thresholds of mid-bright and mid-IR dark clumps for the IRAM 30m observations were 0.6 Jy beam^{-1} and 0.3 Jy beam^{-1}, respectively. In total, 410 ATLASGAL dust clumps were observed within the longitude ranges $0° \leq \ell \leq +60°$. The IRAM observations used the EMIR receiver, which covers almost the whole 3 mm atmospheric window with a velocity resolution of $\sim 0.5\,{\rm km\,s^{-1}}$. These observations were therefore able to observe twenty mm-RRL transitions including the three observed with Mopra. The observed mm-RRL transitions, rest frequencies, and absorption oscillator strengths are listed in the first three columns of Table 4.2. We used the forward efficiency ($\eta_l = 0.95$) and the main-beam efficiency ($\eta_{\rm MB} = 0.81$) to convert the $T_{\rm a}^*$ to the $T_{\rm MB}$ for the IRAM 30m observations[4].

---

[3]IRAM is supported by INSU/CNRS (France), MPG (Germany), and IGN (Spain).
[4]http://www.iram.es/IRAMES/mainWiki/Iram30mEfficiencies

Table 4.2: Frequency, absorption oscillator strength, and detection rates of observed hydrogen millimeter recombination lines.

mm-RRL Transition	Rest frequency (MHz)	Absorption oscillator strength*	Number of Observed sources	Number of Detected sources[a]	Detection Rate[b]
H$n\alpha$	–	–	976	178	18 ± 1
H39α	106737.4	7.725489	385	58	15 ± 2
H40α	99023.0	7.916287	366	57	16 ± 2
H41α[†]	92034.4	8.107084	972	146[c]	15 ± 1
H42α[†]	85688.4	8.297880	972	136	14 ± 1
H$n\beta$	–	–	976	65	7 ± 1
H48β	111885.1	1.342709	366	20	5 ± 1
H49β	105301.9	1.369046	385	26	7 ± 1
H50β	99225.2	1.395383	366	28	8 ± 1
H51β	93607.3	1.421720	366	28	8 ± 1
H52β[†]	88405.7	1.448056	971	47	5 ± 1
H$n\gamma$	–	–	389	23	6 ± 1
H55γ	109536.0	0.482179	366	17	5 ± 1
H56γ	103914.8	0.490287	385	17	4 ± 1
H57γ	98671.9	0.498395	366	18	5 ± 1
H58γ	93775.9	0.506503	366	19	5 ± 1
H60γ	84914.4	0.522718	385	15	4 ± 1
H$n\delta$	–	–	389	22	6 ± 1
H60δ	110600.7	0.230388	366	9	2 ± 1
H61δ	105410.2	0.233881	385	9	2 ± 1
H62δ	100539.6	0.237374	385	11	3 ± 1
H63δ	95964.6	0.240867	366	10	3 ± 1
H64δ	91663.1	0.244359	384	11	3 ± 1
H65δ	87615.0	0.247852	383	7	2 ± 1

Notes. The H$n\beta$, H$n\gamma$, and H$n\delta$ mm-RRLs are only detected toward clumps where the peak intensities of H$n\alpha$ mm-RRLs are brighter than 0.24, 0.62, and 0.54 Jy, respectively. Column 1 is mm-RRLs increasing transition, in Cols. 2 and 3 we give the numbers of observed and detected sources, respectively. The last column shows the detection rates. Line parameters and rms levels of the stacked and individual transitions are available in electronic form at the CDS. [†] Mopra 22m covered only these three transitions. [a] A detection requires a stacked signal above 3σ. [b] The statistical errors of detection rates are obtained assuming binomial statistics. [c] Some H41α spectra are located at an edge or beyond observed band width.

References. (*) Goldwire (1968); Menzel (1969)

4.2.3 Data reduction

The data reduction was performed using the CLASS program of the GILDAS package[5]. Since the RRLs with the adjacent principal quantum numbers (n) and the same Δn have similar energy levels and absorption oscillator strengths, resulting in similar intensities, it is possible to stack the spectra to improve the S/N of the emission. This technique has been successfully used in cm-RRLs surveys (e.g., Alves et al. 2010; Anderson et al. 2011). We show two examples of the stacked spectra in Figure 4.1; the upper panel shows the four H$n\alpha$ transitions ($n = 39, 40, 41,$ and 42) of AGAL013.872+00.281, while the lower panel shows the H$n\alpha$ transitions ($n = 41$ and 42) emission detect toward AGAL332.976+00.767. In both panels we show the profile of the combined stacked spectra (black line). The emission seen toward AGAL013.872+00.281 is clearly detected; however, the emission toward AGAL332.976+00.767 is ambiguous in the individual transitions but is detected at a significant level in the stacked line ($> 3\sigma$). After stacking all transitions, a polynomial baseline of order 1 to 3 fitted to a $200\,\mathrm{km\,s^{-1}}$ wide line-free velocity range was subtracted from the spectra.

In addition to the mm-RRLs, we also used the high number density and high column density tracing H^{13}CO$^+$ ($\nu = 86754.330\,\mathrm{MHz}$) and N$_2H^+$ (1−0) ($\nu = 93173.772\,\mathrm{MHz}$) transitions to determine the systemic radial velocities of the associated dense molecular clumps. The velocities of the peak emission in the H^{13}CO$^+$ and N$_2$H$^+$ (1−0) line spectra were determined using CLASS and are indicated in Figure 4.1 by the vertical purple dashed line.

4.3 Results

4.3.1 Detection rates

Fitting Gaussian profiles to spectra of the stacked and individual transitions provided line parameters and rms levels. We used a peak intensity greater than $3\,\sigma$ as a threshold for detections. In total, we detected H$n\alpha$ emission toward 178 clumps and H$n\beta$, H$n\gamma$, and H$n\delta$ RRLs toward 65, 23, and 22 clumps, which represent 18%, 7%, 6%, and 6% of the full sample, respectively. Figure 4.2 shows one object in the sample where mm-RRL emission is detected in H$n\alpha$, H$n\beta$, H$n\gamma$, and H$n\delta$ transitions. The numbers of observed and detected sources, and detection rates of stacked lines (H$n\alpha$, H$n\beta$, H$n\gamma$, and H$n\delta$) and individual transition lines are summarized in Table 4.2. Variations in the numbers of observed sources in the individual transition lines occur because the IRAM 30m observation did not cover all transitions toward all clumps targeted. Clumps with detected mm-RRL are listed in Table 4.3 which also provides flags to indicate their association with mid-IR and radio continuum emission (these associations are discussed in more detail in a later section).

In general, the relative intensity of RRL emission changes with Δn of the RRL. The intensities of small Δn RRLs (i.e., H$n\alpha$ transition) are higher than the intensities of larger Δn RRLs (i.e., H$n\beta$, H$n\gamma$, and H$n\delta$ transitions) (Towle et al. 1996). This

---

[5]https://www.iram.fr/IRAMFR/GILDAS/doc/html/class-html/class.html

explains the lower detection rates of $\Delta n > 1$ RRLs for a given sensitivity. Furthermore, the H$n\alpha$ transition can be stimulated more easily by maser emission than higher-order transitions under non-LTE conditions, which can lead to an increase in their intensity and detection rate. In Section 4.3.2.1, we discuss whether the H$n\alpha$ mm-RRLs depart from LTE.
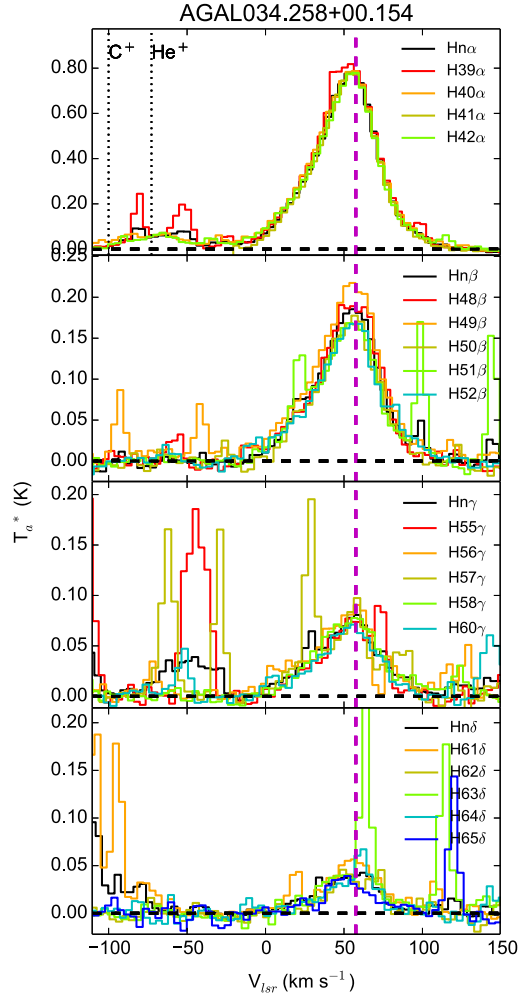
Figure 4.2:   One of the mm-RRL spectra detected toward the ATLASGAL sources. Each color represents a different transition. The black lines are stacked mm-RRLs and the purple dashed lines indicate the velocity of the H^{13}CO$^+$ emission line. The vertical black dotted lines indicate positions of expected helium and carbon RRLs. Other emission lines are an unidentified molecular emission.

Table 4.3: Clumps detected with mm-RRLs.

ID No.	ATLASGAL clump name	RA α(J2000)	Dec. δ(J2000)	Dist (kpc)	Log(M_{clump}) (M$_\odot$)	Log(L_{bol}) (L$_\odot$)	H$n\alpha$ v$_{\mathrm{lsr}}$ (km s^{-1})	Systemic v$_{\mathrm{lsr}}$ (km s^{-1})	WISE mid-IR	Radio emission	Comments
1	AGAL008.671−00.356	18:06:19.0	−21:37:28	−−	−	−	+44	+35	IR-bright	Y	EGO
2	AGAL010.151−00.344	18:09:21.2	−20:19:28	1.6	2.11	−	+20	+9	Complex	Y	
3	AGAL010.168−00.362	18:09:26.7	−20:19:03	3.6	3.01	−	+10	+14	Complex	Y	W31
4	AGAL010.323−00.161	18:09:01.4	−20:05:12	3.5	3.60	4.62	+5	+12	IR-bright	Y	
5	AGAL010.472+00.027	18:08:37.9	−19:51:48	8.6	4.55	5.34	+60	+67	IR-bright	Y	
6	AGAL010.624−00.384	18:10:28.6	−19:55:46	4.9	4.20	5.61	+0	−3	IR-bright	Y	W31
7	AGAL010.957+00.022	18:09:39.2	−19:26:28	13.7	4.15	5.10	+18	+21	IR-bright	Y	
8	AGAL011.034+00.061	18:09:39.7	−19:21:20	14.4	3.84	5.02	+9	+15	IR-bright	Y	
9	AGAL011.936−00.616	18:14:00.8	−18:53:24	4.0	3.61	4.97	+42	+38	IR-bright	Y	
10	AGAL012.208−00.102	18:12:39.6	−18:24:14	13.6	4.58	−	+28	+24	IR-bright	Y	
11	AGAL012.804−00.199	18:14:13.5	−17:55:32	2.4	4.03	5.11	+36	+36	IR-bright	Y	W33
12	AGAL013.209−00.144	18:14:49.3	−17:32:46	4.6	3.55	−	+50	+52	IR-bright	Y	
13	AGAL013.384+00.064	18:14:24.9	−17:17:39	1.9	2.02	−	+14	+14	IR-bright	Y	
14	AGAL013.872+00.281	18:14:35.6	−16:45:39	4.4	3.50	−	+52	+49	IR-bright	Y	
15	AGAL015.013−00.671	18:20:21.3	−16:12:42	2.0	3.84	4.13	+8	+18	Complex	C	M17
16	AGAL015.024−00.654	18:20:17.9	−16:11:30	2.0	2.73	−	+20	+19	Complex	C	M17
17	AGAL015.029−00.669	18:20:22.4	−16:11:44	2.0	3.68	5.17	+10	+19	Complex	C	M17SW
18	AGAL015.051−00.642	18:20:18.7	−16:09:43	2.0	−	−	+21	+18	Complex	C	M17
19	AGAL015.056−00.624	18:20:15.4	−16:08:59	2.0	2.17	−	+22	+18	Complex	C	M17

Notes. Only a portion of the entire table is given here for guidance of content. The full table is available in electronic form at the CDS. Columns, from left to right, are source ID, equatorial coordinates, heliocentric distance, ATLASGAL clump mass, bolometric luminosity of all RMS sources embedded in the ATLASGAL clump, local standard of rest (lsr) velocity of the mm-RRL and the systemic velocity of the dense clump (as determined from the H^{13}CO$^+$ or N$_2$H$^+$ (1−0) transitions), mid-IR property, presence of radio emission, and comments. For radio emission, the flags Y and N indicates whether or not a radio continuum source is found within a radius of 18″. A flag C indicates possible contamination from nearby extended radio sources that are located within a radius of 2′.

Table 4.4: Intensity and linewidth of mm-RRLs.

| Stacked line | No. of sources | S_{peak} (Jy) | | linewidth (km s^{-1}) | | |
Transition		Mean (rms)	Median (rms)	Mean	σ	Standard error
H$n\alpha$	178	1.75 (0.14)	0.91 (0.15)	28.4	7.0	0.52
H$n\beta$	65	1.02 (0.14)	0.70 (0.06)	28.3	7.4	0.92
H$n\gamma$	23	0.37 (0.04)	0.29 (0.04)	28.5	7.5	1.57
H$n\delta$	22	0.25 (0.04)	0.18 (0.04)	27.2	8.4	1.80

4.3.2   General properties of the mm-RRLs

In Table 4.4 we present a summary of the mean intensities and linewidths of the various stacked mm-RRL spectra. The mean and median peak intensities clearly decrease toward higher-order transitions while the mean linewidths for all transitions are similar (linewidth $\sim$30 km s^{-1}). Figure 4.3 shows how pressure broadening affects the observed linewidths as a function of the principal quantum number (n) and electron density. Even though there is a variation in the pressure broadening in the range of our observed transitions (gray filled area) for high electron densities ($\geq 10^5$ cm^{-3}), the pressure broadening of mm-RRLs from UC HIIs with typical density of 10^4 cm^{-3} (Kurtz 2005) is very small and can be neglected. The linewidths of mm-RRLs for all transitions considered here are, therefore, likely to be dominated by unresolved turbulent and thermal motions of the ionized gas. In addition, the linewidth ratio of higher-order to H$n\alpha$ transitions shows whether there is any pressure broadening affecting the mm-RRL (Viner et al. 1979): Mean linewidth ratios of H$n\beta$/H$n\alpha$, H$n\gamma$/H$n\alpha$, and H$n\delta$/H$n\alpha$ are 0.96±0.12, 0.93±0.10, and 0.89±0.15, respectively. Since the pressure broadening effect increases with principal quantum number (n) we expect to find significant variations from unity if there is significant pressure broadening in the gas; however, this is not seen suggesting that this effect is negligible. The relation of peak intensities and the linewidths of the H$n\alpha$ mm-RRLs is shown in Figure 4.4. In general, evolved HII regions such as UC HII and compact HII regions have been found to have linewidths of $\sim$30 km s^{-1}; however, broader RRL have been reported toward HC HIIs (linewidth ≥ 40 km s^{-1}; e.g., Sewilo et al. 2004a). In Figure 4.4, the linewidths of the majority of mm-RRLs are narrower than 40 km s^{-1}, which is consistent with the RRLs being associated with UC HII regions. However, this plot also reveals nine clumps that have broader mm-RRL linewidths (> 40 km s^{-1}), six of which have a S/N > 5 and so are considered to be reliable. Such broad linewidths are normally found toward more compact HII regions making these six sources potential HC HII region candidates (source ID: N32, N49, N51, N62, N73, and N107 in Table 4.3) and we investigate some of these in more detail in Section 4.5.4.

4.3.2.1   Excitation conditions

Comparing peak intensity ratios of H$n\alpha$ and higher-order RRLs is useful in order to diagnose whether the mm-RRLs are emitted under local thermodynamic equilibrium (LTE) or non-LTE conditions. Table 4.5 gives the measured mean ratios from the
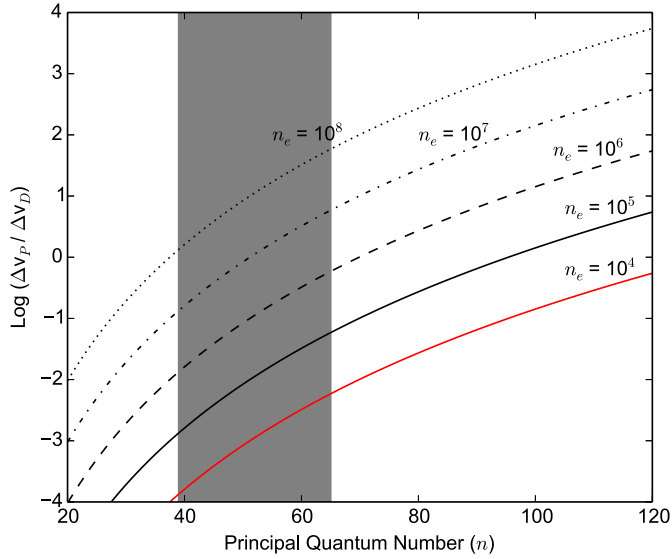
Figure 4.3: Plot of Eq. (4.9) from Brocklehurst & Seaton (1972) with different electron densities (n_e). The gray area indicates observed mm-RRLs transitions ($39 \leq n \leq 65$) in this chapter. The curves show how the relationship between the linewidth ratio and the principal quantum numbers varies as a function of the electron density. The values Δv_P and Δv_D indicate the linewidths produced by pressure broadening and doppler broadening effects, respectively.

mm-RRLs and the expected ratios assuming LTE condition of pairs of transitions. In non-LTE conditions the measured ratio is lower than expected under LTE conditions, due to an increase in the H$n\alpha$ intensity from stimulated maser amplification than the higher-order lines, as seen in MWC349A (Thum et al. 1995).

The peak intensity ratios for the observed mm-RRLs are, on average, consistent with the corresponding LTE ratios (Eq. 2.56) within the 1σ scatter of the observed values. However, we note that the mm-RRLs from AGAL034.258+00.154 (ID: N49) and AGAL043.166+00.011 (ID: N55) show significantly lower peak intensity ratios (e.g., H$n\beta$/H$n\alpha$ (0.236±0.008 and 0.252±0.007), H$n\gamma$/H$n\alpha$ (0.096±0.008 and 0.102±0.007) and H$n\delta$/H$n\alpha$ (0.055±0.005 and 0.064±0.005)). A geometrical effect in a spherical H$\textsc{ii}$ region with variable electron temperature and density could produce these low ratios (Walmsley 1990).

Since these transitions are observed with similar spatial resolution, the geometrical effect is not important. The H$n\alpha$ RRLs of the two sources might be enhanced by weak maser amplification even though their ratios do not deviate from LTE to the same extent as the well-known case of MWC349A (see Thum et al. 1995; Martín-Pintado 2002). Therefore, these two H$\textsc{ii}$ regions are candidates for new RRL maser sources and observations are underway to investigate these sources in more detail. The results of these observations will be reported in next chapter.
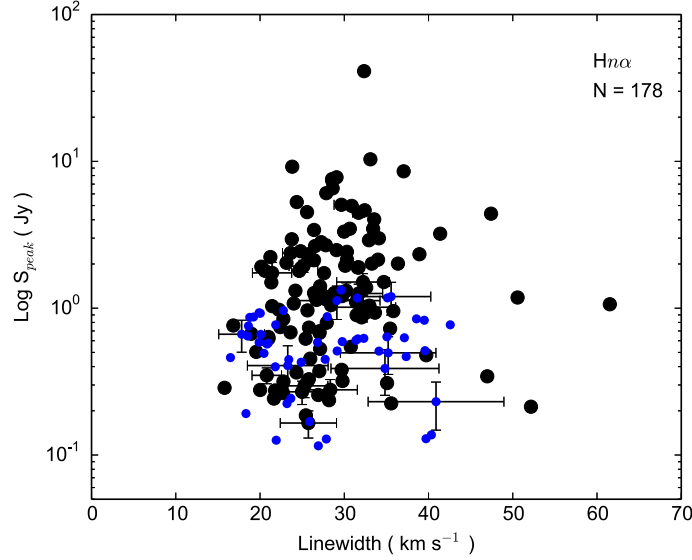
Figure 4.4: Distribution of H$n\alpha$ RRLs peak intensity as a function of linewidth. The blue dots indicate sources with mm-RRLs detected below 5σ. The error bars are plotted for every 7th source chosen at random to show their range.

Table 4.5:   Ratio of mm-RRL transitions.

Pairs (#)	Mean peak intensity ratio	
	Observed	Under LTE
H$n\beta$/H$n\alpha$ (65)	0.31 ± 0.07	0.27
H$n\gamma$/H$n\alpha$ (23)	0.14 ± 0.02	0.13
H$n\delta$/H$n\alpha$ (22)	0.10 ± 0.02	0.07

The (#) indicates the number of sources that are detected in both transitions. These mean values are average values of individually measured ratios of sources in which both lines are detected.
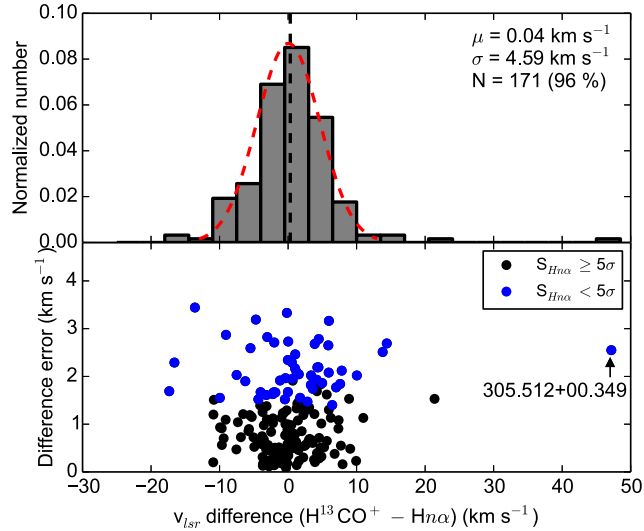
Figure 4.5: Upper panel: Histogram of the v_{lsr} difference between $H^{13}CO^+$ and $Hn\alpha$ RRL. The bin size is $3.5\,\mathrm{km\,s^{-1}}$. Lower panel: Distribution of peak velocity errors with respect to the v_{lsr} differences. The blue dots represent sources with weak mm-RRLs below $5\,\sigma$.

4.3.3 Systematic velocities of the clumps

We used the $H^{13}CO^+$ and N_2H^+ $(1-0)$ transitions as a tracer of the systematic velocity of the dense molecular clumps (Beuther & Sridharan 2007). The $H^{13}CO^+$ emission was detected toward 170 sources, and so the N_2H^+ $(1-0)$ transition was used to determined the velocities for the other eight sources. Both of these transitions were observed simultaneously with the mm-RRL transitions and are available from the IRAM and Mopra data sets.

As seen in all of the examples given in Figures 4.1 and 4.2, the peak velocity of the mm-RRL emission is similar to that of the thermal molecular transition, which indicates that the two emission features are likely to be associated with the same clump. Figure 4.5 shows the differences between $Hn\alpha$ RRL and $H^{13}CO^+$ velocities. The velocity distribution is reasonably well fitted by a Gaussian profile (red dashed line) with a mean and standard error of $0.04 \pm 0.35\,\mathrm{km\,s^{-1}}$. This result is similar to that found in other cm- and mm-RRL studies made toward other samples of compact H II regions (e.g., UC H II; Churchwell et al. 2009) and GLIMPSE IRAC $8\,\mu$m bright H II regions (Anderson et al. 2014). These studies found mean velocity differences in a range of $-1.3\,\mathrm{km\,s^{-1}} \leq \Delta\,v_{lsr} \leq +1.5\,\mathrm{km\,s^{-1}}$. The strong correlation between the velocities of the molecular and ionized gas supports the physical association between the two.

Although the correlation between the mm-RRL and $H^{13}CO^+$ velocities is generally

very good, there are some sources where the velocity difference is larger than $15\,\mathrm{km\,s^{-1}}$, which is more than three times the standard deviation (σ, $4.6\,\mathrm{km\,s^{-1}}$). In particular, the mm-RRL velocity we measure for AGAL305.512+00.349 (ID: N82) is extremely offset with respect to the systematic velocity as marked in the bottom panel of Figure 4.5. We note that in the majority of these cases the mm-RRL emission has a low S/N (see bottom panel of Figure 4.5, blue dots) with the exception of AGAL301.136−00.226 (ID: N73), which is discussed in Section 4.5.4.
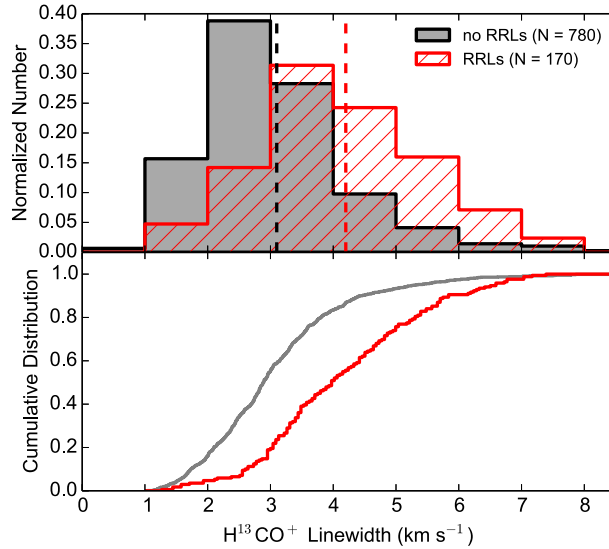
Figure 4.6:   Distributions of $H^{13}CO^+$ linewidth for mm-RRLs associated (red) and mm-RRLs unassociated (gray) sources. Upper panel: Normalized histograms for the sources. The dashed lines represent mean values for each histogram. The bin size is $1.0\,\mathrm{km\,s^{-1}}$. Lower panel: Cumulative distribution functions.

4.3.4   Relation between the molecular clouds and the Hɪɪ regions

To investigate whether there is a dynamic link between the Hɪɪ regions and the associated molecular clumps, we compared the distribution of the mm-RRL and $H^{13}CO^+$ linewidths, and no correlation was found (the Spearman's correlation coefficient, ρ, is 0.09). In Figure 4.6, however, histograms and cumulative distributions of clumps with and without mm-RRL detection show a difference between the $H^{13}CO^+$ linewidths for the two different samples. The linewidths of $H^{13}CO^+$ toward clumps with mm-RRL detection (red curve) are notably broader than those toward clumps without a mm-RRL detection (gray curve), with mean linewidths of 4.18 ± 0.11 (red dashed line) and $3.08 \pm 0.04\,\mathrm{km\,s^{-1}}$ (black dashed line) for clumps with and without mm-RRL detection, respectively. A Kolmogorov-Smirnov (KS) test shows that the null hypothesis that the two samples are drawn from the same parent population is rejected with a $p-$value $\ll$

0.001, implying that the existence of H II regions traced by the mm-RRL detection contributes to the turbulence of the associated molecular clumps. This trend of molecular linewidth broadening with clump evolution is also confirmed by the results of Wienen et al. (2012) and Urquhart et al. (2013b); both of these studies find a mean linewidth of the NH_3 transition $(2.8\,km\,s^{-1})$ toward ATLASGAL clumps associated with radio continuum sources, which is significantly broader than that found toward clumps without an embedded mid-IR sources (a mean linewidth of $1.9\,km\,s^{-1}$).

4.4   Comparison of cm- and mm-RRLs detected toward H II regions

So far, RRL studies with single-dish telescopes and interferometers have mostly focused on RRLs at cm wavelength. There are only a few mm-RRL surveys that were conducted toward small samples biased toward a specific evolutionary phase such as UC H II or HC H II regions. Our new survey investigates for the first time the general properties of mm-RRLs toward a large sample and in this section, we take a look at the overall properties of mm-RRLs in comparison with cm-RRLs of previous large surveys.

Table 4.6 is a summary of cm- and mm-RRL surveys used in this comparison. The RRLs surveys were carried out at different wavelengths with various beam sizes and targeted on different evolutionary phases of H II regions, from UC H II to extended H II regions. The H II regions of Caswell & Haynes (1987) and Lockman (1989) were classified by 6 cm radio continuum surveys with single-dish telescopes, which have a poor spatial resolution for identifying small H II regions. These H II regions could be in different evolutionary phases of H II region. Therefore, in comparisons they are considered to be general H II regions that are denoted by H IIs here. Figure 4.7 shows the cumulative distributions of RRL linewidths, in which the H IIs (a black distribution) combines cm-RRLs from Lockman (1989) and Caswell & Haynes (1987).

In Figure 4.7, there is an obvious difference between linewidths of RRLs of the WISE selected H IIs (WISE H IIs) from Anderson et al. (2011) and the other samples. The linewidths of WISE H IIs are significantly narrower (mean width of $22.3\,km\,s^{-1}$) than the other surveys with mean values between 26.8 and $33.4\,km\,s^{-1}$. Kolmogorov-Smirnov tests are able to reject the null hypothesis, that the linewidths of the WISE H II regions are similar to the other surveys, with very small $p-$values $\ll 0.001$, implying differences in the properties of the H II regions samples. In fact, the WISE H IIs, which

Table 4.6: Hydrogen radio recombination line surveys.

Survey	H$n\alpha$ transition	λ	Beam size	No.
This work	H39α − H42α	3 mm	$29'' - 36''$	178
Churchwell+10	H30α	1.3 mm	$12''$	25
Lockman+89	H87α − H88α	3 cm	$180''$	462
Anderson+11	H88α − H93α	4 cm	$73'' - 89''$	603
Caswell+87	H109α − H110α	6 cm	$264''$	317
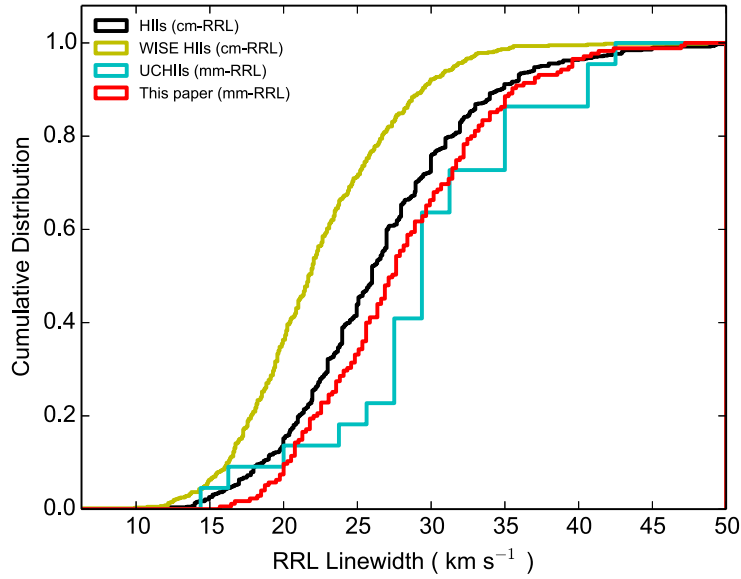
Figure 4.7:   Cumulative distributions of RRL linewidths for this work (red line) and previous surveys (yellow line: Anderson et al. 2011; black line: Lockman 1989; Caswell & Haynes 1987; and cyan line: Churchwell et al. 2010).

are classified by $8\,\mu m$ emission in GLIMPSE IRAC maps, include ionized bubbles, as well as more evolved HII regions (Anderson et al. 2011). The sample (UC HIIs) of Churchwell et al. (2010) seems to be offset from the cm HIIs and from the sources discussed in this chapter. However, the size of the sample is too small to be reliable and a null hypothesis that all of three samples are similar cannot be rejected because of a $p-$value (0.03) greater than 1%.

In Figure 4.7, the cm-RRLs of HIIs and the mm-RRLs from this work show similar linewidth distributions, although the cm-RRLs can be significantly affected by pressure broadening. The histogram in the upper panel of Figure 4.8 shows velocity differences that are less than $15\,\mathrm{km\,s^{-1}}$ toward the majority of sources (120 clumps) and therefore suggest that the cm- and mm-RRLs are tracing on common HII regions. In the bottom plot of the upper panel the scatter dots show the distribution of offsets between observed positions of cm- and mm-RRLs as a function of the velocity difference. The scatter is homogeneous and further supports the idea that the cm- and mm-RRLs are emitted from the same region.

The cumulative distributions in the lower panel of the Figure 4.8 show RRL linewidths of HIIs and this work toward common HII region which match in observed positions and velocities. In addition, the distribution for all sources are also displayed. The distribution of selected mm-RRLs from this work (orange, with a mean linewidth of 28.5 ± 0.5 $\mathrm{km\,s^{-1}}$) does not change much compared to the total sample of mm-RRLs (red, mean linewidth of $28.4\pm0.5\,\mathrm{km\,s^{-1}}$). However, the distribution of selected cm-RRLs from the HIIs sample (gray, mean linewidth of $29.6\pm0.4\,\mathrm{km\,s^{-1}}$) moves toward broader linewidths compared with the distribution of the whole HIIs sample (black,
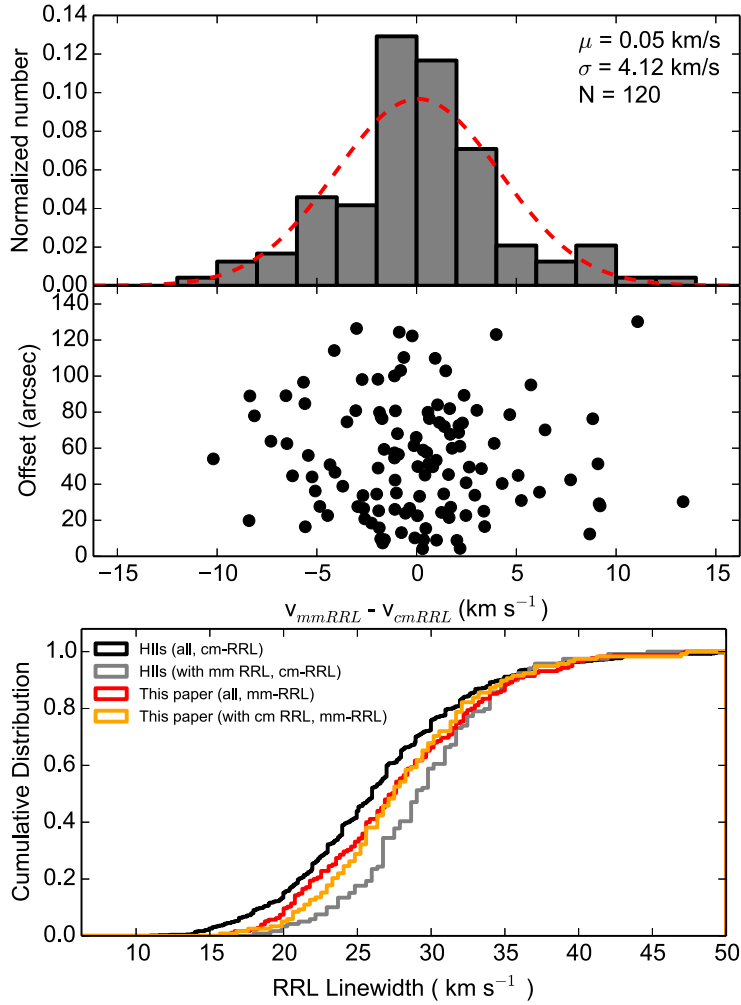
Figure 4.8:   Upper panel: Velocity difference between mm-RRL and cm-RRL for sources where the beams of the surveys overlap (top plot). The velocity difference as a function of an offset between the mm-RRL and cm-RRL pointing centers (bottom plot). Lower panel: Cumulative distributions of cm- (gray) and mm-RRLs (orange) for clumps where the velocity difference between the cm- and mm-RRLs is within $15 \, \mathrm{km \, s^{-1}}$.

mean linewidth of $26.8 \pm 0.3 \mathrm{km \, s^{-1}}$). A KS test for the linewidths of the selected cm- and mm-RRLs samples also shows that a null hypothesis is invalid with a $p-$value $\ll 0.001$. This suggests that the selected cm-RRLs are likely suffering from pressure broadening.

However, the cm-RRL surveys were carried out with $2 \sim 6$ times larger beams than ours. The broader cm-RRLs can also be affected by larger scale motions of the ionized gas in the larger beams. Our beams cover gas with a size of $1 \, \mathrm{pc}$ at typical distance of $5 \, \mathrm{kpc}$. On the other hand, the beams of the cm-RRL surveys can capture gas with a

size of about $4 \sim 6\,\mathrm{pc}$. Therefore, the linewidths of the cm-RRLs could also be a result of the blending of more than one H II region leading to the observed broader linewidths.

4.4.1   Radio continuum and mid-IR counterparts

To further investigate the origin of the mm-RRLs, we examined mid-IR images and searched for embedded radio continuum sources coincident with the clumps. For example, because of its compactness a HC H II region only emits weak radio emission that is optically thick throughout the radio range (i.e., $\nu < 50\,\mathrm{GHz}$ where its flux density varies as ν^2). Given this weak emission, they might not have been detected in past shallow radio surveys that were conducted at longer cm wavelengths.

We extracted mid-IR maps from the WISE and GLIMPSE surveys and created three-color images centered on the observed position. The mid-IR three-color images of three sources that are representative of compact, extended, and complex mid-IR emission are presented in Figure 4.9. These images provides a useful way to identify embedded protostellar objects and to investigate their local environments. We searched WISE point source catalogs (Cutri et al. 2012) and identified mid-IR counterparts within a radius of $18''$ (approximately the size of the ATLASGAL telescope beam) for 118 clumps[6]. However, visual inspection of the three-color images reveals that many of the maps are affected by saturation indicating the presence of very bright sources within them. In total, we find mid-IR emission toward 127 clumps (including some sources that are saturated and that are not included in the WISE catalogs). We also find that the saturation in the maps toward 43 sources is so bad that they cannot be used to evaluate the distribution of the mid-IR emission; many of these are found toward well known star-forming regions such as M17 and G305 (Povich et al. 2007 and Hindson et al. 2012, respectively). We find no significant mid-IR emission associated with eight clumps.

We also utilized several large continuum surveys at wavelengths of 3, 6, and 20 cm (Zoonematkermani et al. 1990; Becker et al. 1994; Condon et al. 1998; Walsh et al. 1998; Giveon et al. 2005; White et al. 2005; Helfand et al. 2006; Urquhart et al. 2007, 2009; Purcell et al. 2013) to identify embedded compact and UC H II regions. Using the same radius ($18''$) used to search for WISE counterparts, we identified 116 compact radio sources that are positionally coincident with clumps associated with mm-RRLs.

There is a possibility that radio sources other than H II regions are the origin of the radio continuum, in particular extragalactic sources. The radio sources considered here are associated with the peak of the dust emission and are often extended, which is very unlikely for extragalactic sources. In addition, the extragalactic source counts are much lower at 5 GHz than at 1-2 GHz and hence the number of extragalactic sources, and the possibility of chance alignments with dust, is very low (Urquhart et al. 2013b). H II regions, even smaller UC H IIs, clearly show counterparts in mid-IR data (e.g., GLIMPSE data), whereas extragalactic sources are not normally associated with

---

[6] WISE point sources with the following quality flags "D", "P", "H", or "O" are likely to suffer from contamination or confusion and are not reliable, and so have been excluded.
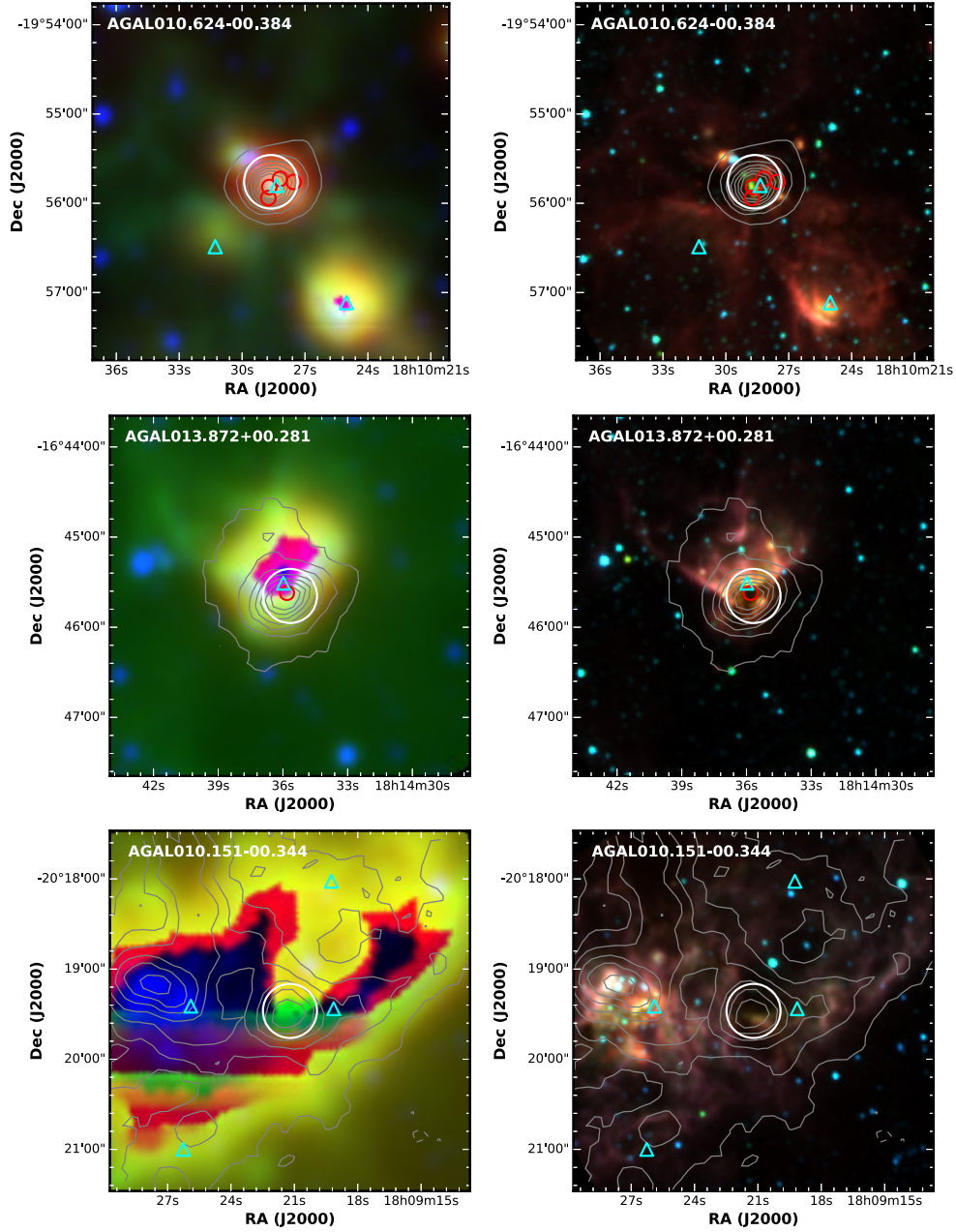
Figure 4.9: Clumps representative of the three typical mid-IR morphologies discussed in the text (from left to right: compact, extended, and complex.) Upper panel: WISE three-color composite images (4.6 (blue), 12 (green), and 22 μm (red)). Lower panel: GLIMPSE IRAC three-color composite images (3.6 (blue), 4.6 (green), and 8 μm (red)). Gray contour lines indicate 870 μm dust continuum emission from the ATLASGAL survey. The red circles and cyan triangles are 5 GHz CORNISH sources and 1.4 GHz NVSS sources. The white circles are centered on the pointing positions used for our Mopra and IRAM observations and their diameters approximate the FWHM beams size of these telescopes in the 85–100 GHz range. The ATLASGAL beam has a size of 19″ FWHM.

any mid-IR emission (Hoare et al. 2012; Purcell et al. 2013; Urquhart et al. 2013b). Since all of the matched radio sources have an association with mid-IR emission, they can be classified as Hɪɪ regions.

In addition to the above-mentioned radio continuum surveys, 13 more clumps with mm-RRL detection have a 18 GHz radio counterpart in the AT20G survey (Ricci et al. 2004). In spite of the poor resolution and positional accuracy of the AT20G survey, these sources are associated with the clumps and mm-RRLs and so are likely to be Hɪɪ regions. Radio counterparts for five other clumps are also found in the literature (Kuchar & Clark 1997; Hindson et al. 2012, 2013). In total, compact radio emission is found to be associated with ∼75% of the whole mm-RRL associated sample. The positions of these radio sources are indicated in the images presented in Figure 4.9. All of the radio sources are associated with clumps that are also associated with mid-IR emission, although ten of these are badly saturated in WISE 12 and 22 μm maps, but are recognizable in the GLIMPSE IRAC maps without any saturation. The positional correlation of the mid-IR source, the radio continuum emission, and the detection of the mm-RRL emission in 134 cases is consistent with the hypothesis that the ATLASGAL clumps are harboring compact Hɪɪ regions.

We are left with 44 clumps toward which mm-RRL emission is detected, but which are not associated with a compact radio source. There are three possible explanations for these sources: 1) the mm-RRL emission is coming from a nearby evolved Hɪɪ region, 2) the mm-RRL is associated with an optically thick Hɪɪ region at cm wavelengths whose flux density is below the limits of the exiting cm-wavelength surveys, or 3) the clump has not been included in any high-resolution radio continuum surveys.

Almost certainly, the 127 clumps with a compact mid-IR source are undergoing star formation. Conversely, the absence of a potential embedded source suggests that the mm-RRL emission is likely to be associated with nearby Hɪɪ regions. In addition, we have already found large differences between the velocity of mm-RRL and the systemic velocity of the molecular gas for a number of associations which might be due to such contamination (Section 4.3.3). As previously mentioned, no mid-IR emission is detected toward eight of these clumps, one of which (N82) has a significant difference between the velocity of the mm-RRL and the systemic velocity of the clump, as have been marked in Figure 4.5, and it is therefore likely that this association is due to contamination. We note that 3 of the 134 compact radio sources (N59, N73, N104) are matched to mm-RRL emission where the velocities of the mm-RRLs with respect to the molecular gas are larger than 15 km s^{-1}. Therefore, they are likely unassociated with molecular clumps and the result of contamination from nearby Hɪɪ regions. Nevertheless, they also have compact radio and mid-IR sources. It means that we cannot fully exclude the possibility that the large velocity difference is caused by other reasons such as internal turbulent motions of the Hɪɪ regions.

Owing to the relatively large size of the Mopra and IRAM beams, it is possible that some of the mm-RRL detections originate from large-scale Hɪɪ regions in close proximity to a significant number of clumps and not the star-forming regions associated with the ATLASGAL clumps. Bright and extended Hɪɪ regions might even be picked up by the sidelobes of the telescopes.
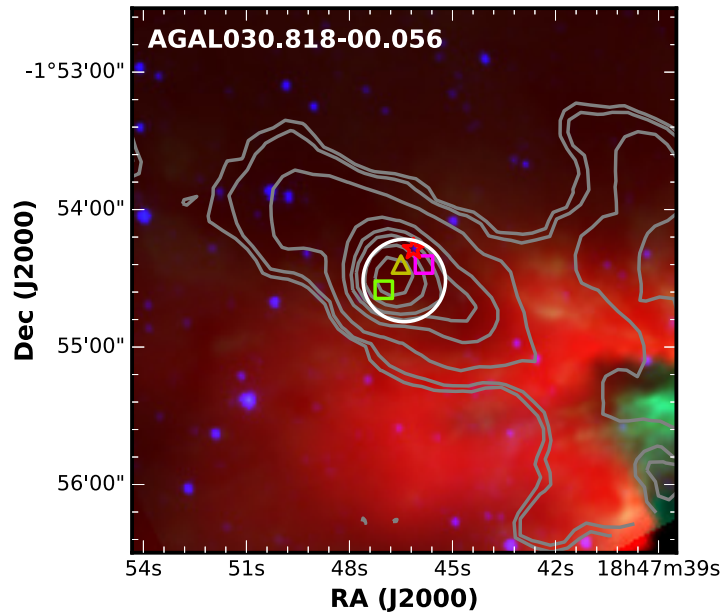
Figure 4.10:   Potential HC H<small>II</small> region candidate W43-MM1. It is one of the bright dust continuum peak of the W43 "mini-starburst" region (Sridharan et al. 2014). Mid-IR three-color composite images (GLIMPSE IRAC $3.6\,\mu$m (blue), $8\,\mu$m (green), and WISE $22\,\mu$m (red)). The gray contours trace the $870\,\mu$m dust continuum emission. The white circles are centered on the pointing position used for IRAM observation. The red star symbol indicates a WISE $22\,\mu$m point source. The yellow triangle is an OH maser (Szymczak & Gérard 2004). The green and purple squares indicate Class I and II CH$_3$OH masers (Larionov & Val'tts 2007; Szymczak et al. 2012).

The radio counterparts found for the northern hemisphere clumps are drawn primarily from the CORNISH survey which is an unbiased 5 GHz radio continuum survey (Hoare et al. 2012), and so the third possibility that a particular clump has not been included in any high-resolution radio continuum surveys can be discarded. In this region of the plane we find 11 mm-RRL detections not associated with a compact radio source. Of these, nine are located near the intense star-forming regions M17, G34, W49, and W51. Their mid-IR images are almost completely saturated in the WISE 22 μm band and show complex GLIMPSE IRAC 8 μm emission. The non-detection of any compact radio continuum and the close proximity to star-forming complexes lead us to conclude that the mm-RRL emission is due to contamination and is not associated with the clumps. The remaining two sources, AGAL029.911−00.042 (ID: N30) and AGAL030.818−00.056 (ID: N37; see also Figure 4.10), are associated with compact mid-IR emission. Source N30 is related to SiO molecular emission with high-velocity line wings, which indicates the presence of outflows from deeply embedded MYSOs (Csengeri et al. 2016). Source N37 is associated with masers (e.g., Class I & II methanol and OH masers) that also indicate an earlier stage than an evolved HII region. Therefore, these two sources are good potential HC HII region candidates.

The radio associations identified for clumps located in the southern hemisphere have largely been drawn from targeted observations of an MSX color selected sample of MYSOs (Urquhart et al. 2007) and methanol masers (Walsh et al. 1997). A consequence of this is that not all mm-RRL emitting clumps have been observed. Therefore, the detection of a mm-RRL may be revealing the location of HII regions that have not previously been discovered at radio wavelengths. There are 25 mm-RRL sources detected in the fourth Quadrant that have not previously discussed; 19 are located near the edges of large complexes where mm-RRL emission is likely to be the result of contamination from evolved HII regions; however, the remaining 6 detections are all associated with compact mid-IR emission and are likely to be good HII region candidates.

Figure 4.11 visualizes in a Venn diagram the association of the mm-RRL detected clumps with radio and infrared WISE 22 μm emission. It also provides average values of integrated 6 cm continuum (blue text) and mm-RRL (red text) intensities. In summary, we identify 44 sources that show mm-RRLs and are not matched to a compact radio source. Of these, 28 are located near some of the most intense star-forming regions in the Galaxy where the nature of the emission cannot be reliably determined. In addition, eight clumps are found to be mid-IR dark and therefore unlikely to harbor HII regions; in all of these cases there is evidence of a nearby HII region that is likely to be the source of the observed mm-RRL emission. Nevertheless, the fact that a mid-IR dark clump may contain an HII region cannot be completely excluded in order to explain the mm-RRL detection toward the mid-IR dark clump. Finally, there are eight clumps that are associated with bright mid-IR emission, many of which are also associated with methanol masers; these are considered to be good HII region candidates.
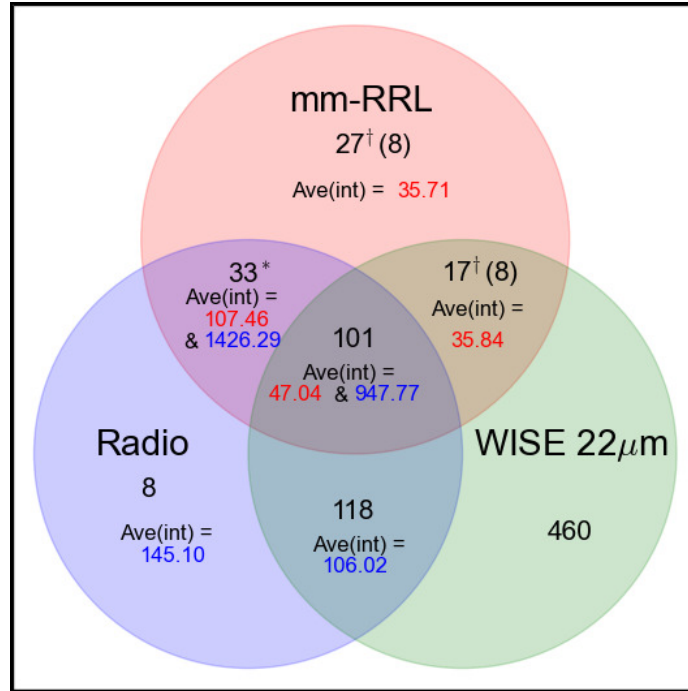
Figure 4.11: Venn diagram illustrating the distributions of ATLASGAL clumps (black numbers) that are in association with mm-RRL detection, radio continuum sources (only considering large continuum surveys for clumps without mm-RRL detection, while the number of radio sources with mm-RRL is based on complete, individual searches), and WISE $22\,\mu$m emission (only considering association with WISE $22\,\mu$m point sources). In addition, average integrated fluxes of total H$n\alpha$ and 6 cm radio continuum are given as red and blue numbers in Jy km s^{-1} and mJy, respectively. The star (*) indicates that these 33 sources are saturated in WISE $22\,\mu$m emission and the dagger (†) indicates that contaminated sources have been included. The numbers in parentheses represent 8 mid-IR dark sources among the 27 clumps with only mm-RRL and 8 potential HII candidates among the 17 clumps with both the mm-RRL and the WISE $22\,\mu$m point source.

4.5 Analysis and discussion

4.5.1 Comparison of the mid-IR and radio properties

In the previous section we discussed the radio and mid-IR counterparts that are associated with clumps with mm-RRL detection. We found that the vast majority of the mm-RRL emission sources are associated with strong mid-IR emission and compact radio emission sources and these are therefore associated with compact Hɪɪ regions. The full sample of 976 observed ATLASGAL clumps also includes clumps associated with radio and mid-IR emission but toward which no mm-RRL emission has been detected. In this section we compare the mid-IR and radio properties of the Hɪɪ region with and without detectable mm-RRL emission in an effort to understand the differences between the two samples.

Compact radio sources have been matched to 242 clumps (only considering the main large radio continuum surveys that we used when searching for radio counterparts) from the whole sample of 976 clumps (∼25% of the sample), but mm-RRL emission is only detected toward slightly less than half of these. In Figure 4.12 we compare the 6 cm continuum luminosity and Hɪɪ region diameter of radio sources with and without mm-RRL emission association. The information regarding radio sources, parental clumps, and heliocentric distances is provided in Table 4.7.

It is clear from the upper panel of Figure 4.12 that the radio sources associated with mm-RRL emission are significantly brighter than those without. Such a clear difference is not found for the Hɪɪ region diameters, which are similar for both source groups. This suggests that the mm-RRL detectability is mainly sensitive to the radio continuum brightness of the Hɪɪ regions. We note that we only use the 6 cm continuum detections for the analysis presented here and the rest of the paper, as this data is available for the majority of the clumps and all of the surveys have a similar angular resolution and sensitivity leading to a consistent data set to study the continuum association.

Within a search radius of $18''$ at a observed position, WISE $22\,\mu$m point sources are matched to 696 clumps in the sample (∼70%) with 118 being associated with mm-RRL detections and 578 associated with mm-RRL quiet clumps. This would suggest that the majority of the sources observed are actively forming stars, with approximately 35% (242/696) of these already harboring young stellar objects and/or compact Hɪɪ regions. Figure 4.13 shows the cumulative flux distributions[7] of the WISE $22\,\mu$m counterparts for various associations with the mm-RRL detection and radio continuum counterpart. The WISE point sources without the bad flags are valid, but their fluxes brighter than 330 Jy are not reliable (see Csengeri et al. 2014 for more details). Therefore, the plots for fluxes of the WISE $22\,\mu$m counterparts have only used the WISE $22\,\mu$m point sources with a flux less than 330 Jy. It is clear that the mm-RRL samples (red and orange curves) are associated with the brightest WISE sources and the flux distributions are

---

[7]The $22\,\mu$m magnitudes were converted to flux in Jy units. A zero point magnitude of 8.2839, a color correction factor of 1.0 for $22\,\mu$m, and an additional correction factor of 0.9 due to an uncertainty in the calibration were used to calculate the conversion factor (Wright et al. 2010).
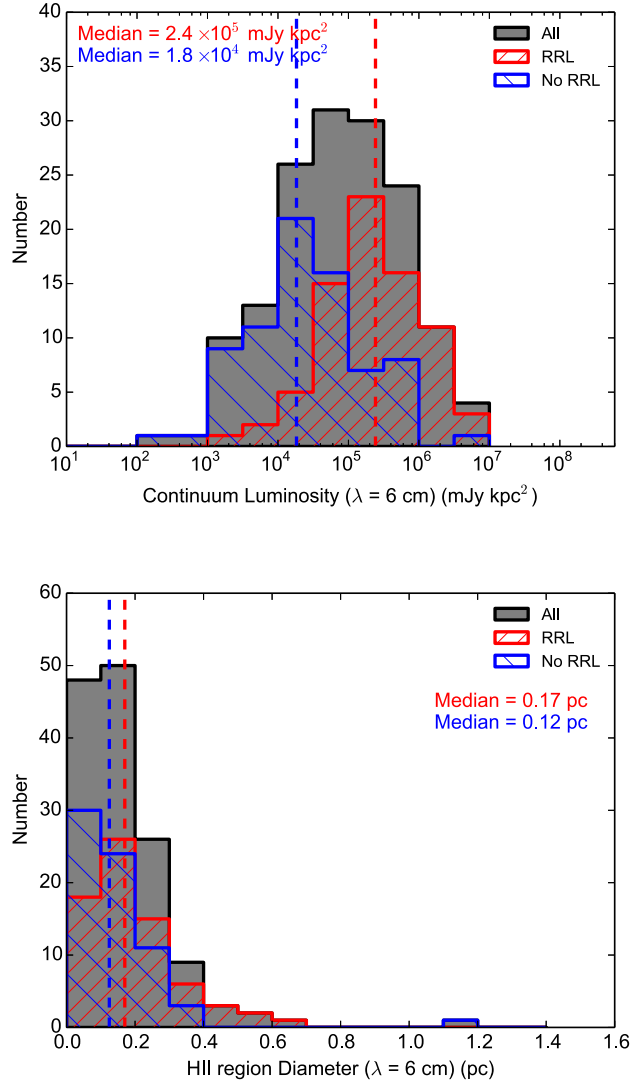
Figure 4.12: Upper panel: Radio continuum luminosity for sources with and without mm-RRL emission. The bin size is 0.5 dex. Lower panel: HII region diameters. The bin size is 0.1 pc. The blue and red dashed lines indicate median values of the radio continuum luminosity and HII region diameter for mm-RRL and non mm-RRL sources. The gray histograms of both plots show the distributions of the full sample
.

Table 4.7: WISE 22 μm point sources and radio continuum sources matched with mm-RRLs detection.

| | 6 cm radio continuum | | | WISE 22 μm | |
No.	$S_{6\,cm}$ (mJy/beam)	$\int S_{6\,cm}$ (mJy)	Angular diameter ($''$)	$F^{\dagger}_{22\,\mu m}$ (Jy)	Distance (kpc)
1	667.5	795.0	3.6	12.3	–
4	13.8	170.3	19.0	–	3.5
5	34.6	57.7	2.2	–	8.6
6	360.6	2060.9	4.9	–	4.9
7	109.1	196.0	1.6	17.2	13.7
8	21.7	50.2	5.2	28.6	14.4
9	163.9	1155.9	5.7	186.9	4.0
10	72.2	207.9	2.4	4.2	13.6
11	287.9	12616.4	16.2	–	2.4
12	40.7	946.8	8.2	38.8	4.6
13	10.5	603.9	19.1	59.3	1.9
14	24.7	1447.6	15.4	–	4.4
21	97.7	519.3	3.1	40.9	17.1
23	48.0	1277.9	14.6	–	3.0
24	121.6	342.1	2.3	31.1	12.1
25	86.4	510.2	8.6	–	4.5
27	33.0	49.0	1.5	–	9.1

Notes. A portion of the entire table is given here for simplicity. The entire table is available at the CDS. Regarding the displayed values of 6 cm radio continuum emission, explanations of how to determine the values are available in Sections 4.5.2 and 4.5.3. [†] The $F_{22\,\mu m}$ is a measured flux of a point source from the WISE point source catalog, which is the closest one without a bad flag within a searching radius of $18''$. WISE 22 μm point sources with fluxes over 330 Jy are excluded as the detectors saturate and the fluxes are unreliable.

References. 6 cm radio continuum emission: Becker et al. (1994); White et al. (2005); Urquhart et al. (2007, 2009); Purcell et al. (2013). WISE 22 μm point source: Cutri et al. (2012). Distance: Urquhart et al. (2014d); Csengeri et al. (2016)
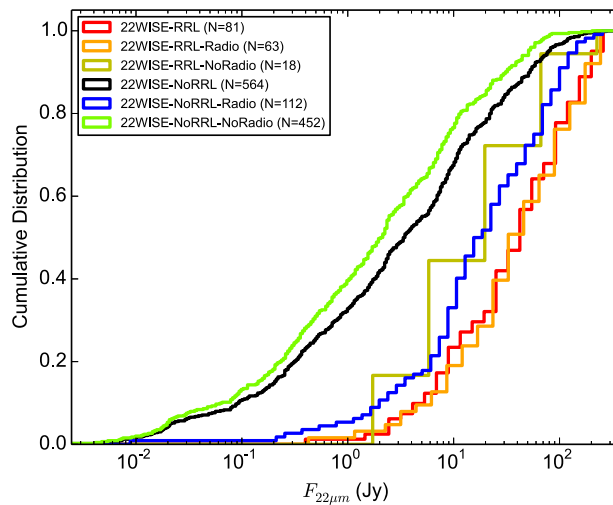
Figure 4.13: Cumulative flux distributions of WISE 22 μm point sources. The colors indicate associations with a detection of a mm-RRL and a radio continuum counterpart. WISE 22 μm point sources with fluxes over 330 Jy are excluded as the detectors saturate and the fluxes are unreliable.

significantly different from WISE sources not associated with a mm-RRL (black curve). The distribution of the radio and mid-IR associated clumps (blue curve) is significantly different from both the radio quiet clumps and the radio loud and mm-RRL associated clumps (the KS test is able to reject the null hypothesis that these are drawn from the same parent population with a $p-$value $\ll 0.001$).

We have previously shown that radio sources not associated with mm-RRL emission tend to have weaker continuum luminosities. The distribution of their mid-infrared fluxes shown in Figure 4.13 reveals that they also tend to have significantly lower mid-IR emission. Both the radio and mid-IR emission are distance dependent quantities and it is therefore possible that these trends are due to a physical difference in the properties of the embedded objects or due to a distance bias. If these trends arise from physical differences in the embedded objects, we would expect to see separation between both radio source groups with mm-RRL and without, in radio and mid-IR flux distributions. To minimize the potential for bias we only use clumps associated with a single radio source in a searching radius; this ensures that the flux of the radio source is compared with a flux of the closest WISE point source and that the radio and mid-IR emission are related to the same ionizing star. The WISE 22 μm fluxes of 25 point sources matched with the radio sources are severely saturated. Therefore, we used the MSX 21 μm flux for those saturated sources instead of excluding them from the radio and mid-IR flux distributions. Fig. 4.14 shows a scatter plot of integrated 6 cm radio continuum flux as a function of the WISE 22 μm point source flux in association with mm-RRL detection. It is clear from this plot that the mm-RRLs are associated with the
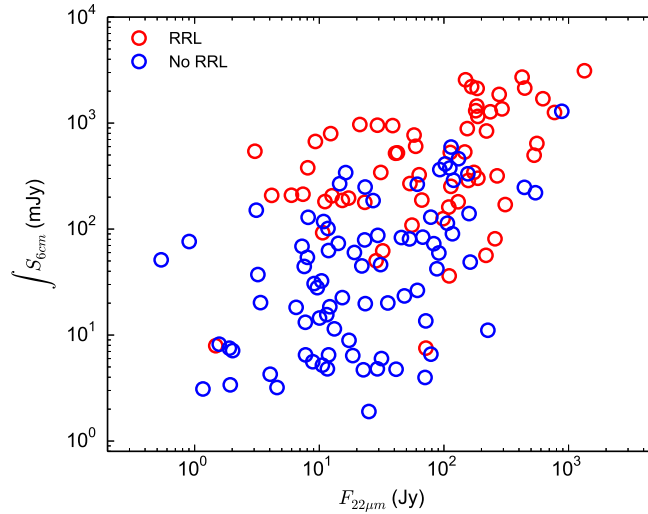
Figure 4.14: Integrated 6 cm radio continuum flux as a function of 22 μm flux for the mm-RRL quiet and bright radio sources.

brightest radio sources and that this trend is largely independent of the mid-infrared emission. This is confirmed by a KS test ($p-$value $\ll 0.001$). In other words, these two populations are likely to have different physical conditions and are not the result of a distance bias. In spite of the small $p-$value of the KS test, however, these two populations are not obviously separated in the distributions.

Figure 4.15 shows the Lyman continuum flux as a function of the heliocentric distance for radio continuum sources associated with ATLASGAL clumps. In this plot the mm-RRL associated and mm-RRL quiet radio sources are indicated as red and blue circles, respectively. The Lyman continuum fluxes are calculated using

$$\left(\frac{N_i}{\mathrm{photon\,s^{-1}}} \right) = 9 \times 10^{43} \; \left(\frac{\int S_\nu}{\mathrm{mJy}} \right) \; \left(\frac{D^2}{\mathrm{kpc}} \right) \; \left(\frac{\nu^{0.1}}{5\,\mathrm{GHz}} \right), \qquad (4.1)$$

where $\int S_\nu$ is the integrated radio flux density measured at frequency ν and D is the heliocentric distance to the source (Urquhart et al. 2013b). This assumes the H$\textsc{ii}$ regions are optically thin. This significantly underestimates the Lyman continuum flux for more compact H$\textsc{ii}$ regions, but this assumption is justified (see next two sections). Radio continuum sources with mm-RRL mostly show Lyman continuum fluxes of $\geq$ $10^{47}\,\mathrm{photon\,s^{-1}}$, whereas the distribution of mm-RRL quiet radio sources tends to be associated with weaker H$\textsc{ii}$ regions ($\sim 10^{46}\,\mathrm{photon\,s^{-1}}$). The median of the Lyman continuum flux distribution for radio sources with mm-RRL (red dot-dashed line) is close to $10^{48}\,\mathrm{photon\,s^{-1}}$, while the median of the Lyman continuum flux distribution for mm-RRL quiet radio sources (blue dot-dashed line) is less than $\sim 10^{46.5}\,\mathrm{photon\,s^{-1}}$.

The Lyman continuum fluxes of a large fraction of the radio sources with mm-RRL correspond well to the expected fluxes of late O-type stars. H$\textsc{ii}$ regions ionized by O-
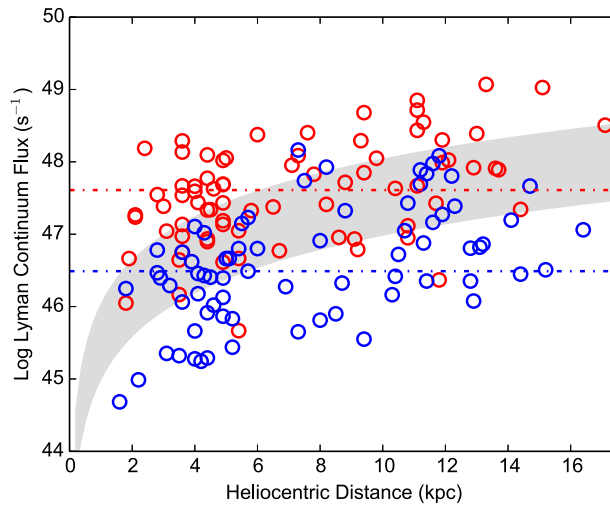
Figure 4.15: Lyman continuum flux as a function of heliocentric distance. The red and blue circles represent 6 cm radio continuum sources associated with and without mm-RRL sources. The gray area is filled between Lyman continuum fluxes estimated with median 6 cm integrated fluxes of radio sources associated with and without mm-RRL. The red and blue dot-dashed lines show median values in the Lyman continuum flux distributions for those sources, respectively.

type stars have Lyman continuum fluxes of $> 10^{48}$ photon s^{-1} and tend to have larger Hii region diameters than Hii regions associated with B-type stars that have fluxes $< 10^{48}$ photon s^{-1} (Urquhart et al. 2013b). The sensitivity of the Mopra and IRAM observations appears to be limited to the detection of mm-RRL from the brightest late O-type stars.

4.5.2 The recombination line and radio continuum emission

The radio continuum sources are smaller than the beam size of the Mopra and IRAM observations and so in some cases there are two or more radio sources located within the beam. It is thus likely that the observed mm-RRL emission has contributions from several radio continuum sources. To account for this we have summed the flux of all radio sources within the beam to obtain the total integrated radio flux. In Figure 4.16 we plot spatially integrated 6 cm continuum flux density versus velocity-integrated mm-RRL flux. The mm-RRL detection thresholds are estimated from $\Delta w = \sigma \delta v \sqrt{N}$, where δv is the channel width in units of km s^{-1} and N is the number of channels over which the emission is found (we have used a value of 10). Comparing the continuum and line fluxes we find them to be strongly correlated (the Spearman's correlation coefficient, ρ, is 0.70 with a $p-$value $\ll 0.001$). An xy-bisector fit to these data results in a slope of 0.86 ± 0.06.
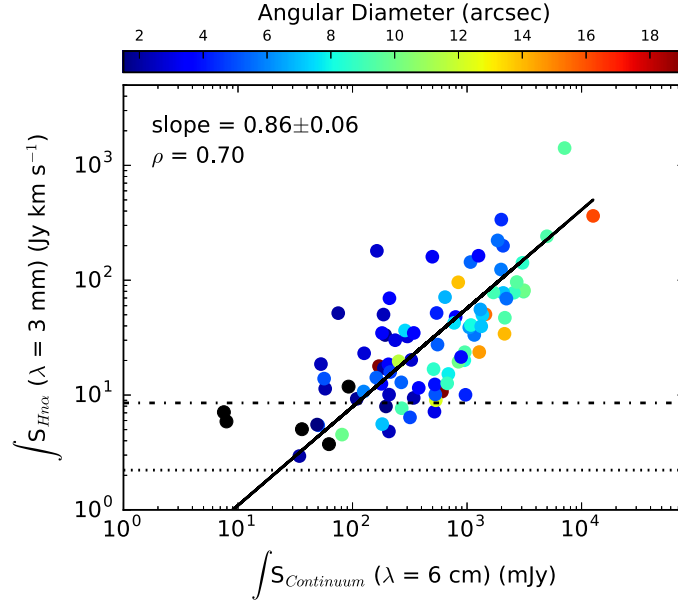
Figure 4.16:   Integrated flux of radio continuum at 6 cm versus integrated flux of mm-RRLs at 3 mm. The black solid line indicates the best-fit line determined by a xy-bisector fit to the data. The black dot-dashed and dotted lines indicate 3σ integrated fluxes for IRAM 30m $(2.22 \, \mathrm{Jy \, km \, s^{-1}})$ and Mopra 22m $(8.54 \, \mathrm{Jy \, km \, s^{-1}})$. The color bar represents an angular diameter of continuum source in units of arc second. The black filled-circles show no angular size for unresolved radio sources. The errors on the integrated fluxes of mm-RRLs are $1.82 \, \mathrm{Jy \, km \, s^{-1}}$ on average.

Given that the mm-RRLs and radio continuum emission are tracing the same volume of gas, we would expect to find a linear relationship if the HII regions continuum emission were optically thin. However, if it were optically thick at 6 cm we would expect the mm-RRL and continuum flux to deviate significantly from a linear relationship. The most compact HII regions are the most likely to have optically thick emission (blue filled circles in Figure 4.16); however, these regions do not deviate from the linear relationship. The fit to the fluxes shown in Figure 4.16 is close to linear, which suggests that all of the HII regions are broadly optically thin.

In Figure 4.17 we show the relationship between the bolometric luminosity of all embedded HII regions identified by the RMS survey (Lumsden et al. 2013) in each clump (Urquhart et al. 2014d) and the mass of the host clump. In this plot we also indicate the luminosity of the associated mm-RRL emission. When we calculated the luminosities of the mm-RRLs for the clumps with mm-RRL detections, we only used a subsample of the clumps with 6 cm radio continuum sources in order to reduce potential contamination by nearby HII regions unassociated with the clumps, which is more of an issue for the lower resolution 20 cm NVSS survey.

There is a strong correlation between these three parameters with a clear trend for more luminous HII regions giving rise to stronger mm-RRL emission and being associ-
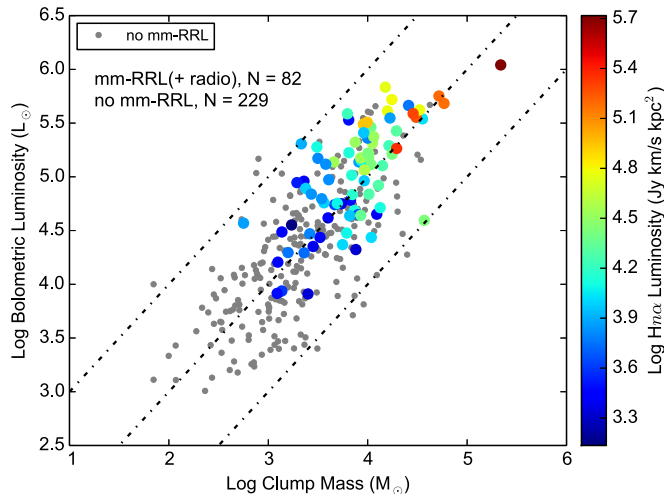
Figure 4.17: Bolometric luminosity as a function of clump mass for HII regions presented in Urquhart et al. (2014d). The colors represent the mm-RRL luminosity. The gray dots indicate clumps without mm-RRL detection. The lower, middle and upper diagonal dot-dashed lines represent the $L_{bol}/M_{clump} = 1$, 10, and $100 \, L_\odot/M_\odot$, respectively.

ated with more massive clumps. We evaluated a Spearman's correlation coefficient (ρ) for clumps with mm-RRL detection, without detection, and all clumps and obtained 0.67, 0.70, and 0.76 with $p-$values $\ll 0.0001$, respectively. These results are higher than the partial Spearman's correlation coefficient ($r = 0.64$) of the MYSO, HII region, and multiphase subsamples in Urquhart et al. (2014d).

The Spearman's correlation coefficient ($\rho = 0.67$) of the clumps with mm-RRL detection is significantly higher than the partial Spearman's correlation coefficient ($r = 0.53$) for the HII region subsample which are CORNISH HII regions of Urquhart et al. (2013b). The clumps with mm-RRL detection are not only associated with mm-RRLs, but also have compact radio continuum sources. The clumps are therefore a subsample of the CORNISH HII regions with a brighter flux than those of Urquhart et al. (2013b). The fact that the mm-RRLs are associated with brighter radio continuum sources is also supported by the distribution seen in Figure 4.14.

Clumps without a mm-RRL detection (gray dots) show a broad distribution from low to high masses and bolometric luminosities. On the contrary, clumps that are detected mm-RRLs (colored circles) tend to be associated with a large mass and bolometric luminosity. Similarly, the $H^{13}CO^+$ linewidths increase in clumps with the mm-RRL detection, as was shown in Section 4.3.4, although no clear correlation exists between the linewidth of $H^{13}CO^+$ and mm-RRLs for the mm-RRL luminosity in Figure 4.17. It seems that the clumps with mm-RRL detection are more massive and have larger $H^{13}CO^+$ linewidths, the latter also implying that they are in virial equilibrium.

A possible reason for the lack of correlation between the linewidths of mm-RRL

and $H^{13}CO^+$ may be that different size scales are involved; the linewidths of mm-RRL are linked to the small scales of the HII regions, whereas the linewidths of $H^{13}CO^+$ are averages over the larger scale molecular clumps. However, we found by comparing samples with and without HII regions that the HII regions detected by mm-RRLs show enhanced turbulent motions in their environments, either directly or indirectly. This mm-RRL luminosity gradient and the $H^{13}CO^+$ linewidths reveal that the most massive clumps that host HII regions and that are associated with strong mm-RRLs also have broader molecular linewidths.

4.5.3 Emission measure and electron density

In order to compare the physical parameters estimated by mm-RRL emission and 6 cm radio continuum, we need to calculate the emission measure (EM) of the continuum sources. The synthesized beam brightness temperature is calculated by Eq. 2 in Wood & Churchwell (1989)

$$T_b = \frac{S_\nu 10^{-29} c^2}{2\nu^2 k \Omega_b},\qquad(4.2)$$

where S_ν is the peak flux density (mJy beam^{-1}), Ω_b is the solid angle of synthesized beam, k_b is the Boltzmann constant, ν is the rest frequency in Hz, and c is the speed of light in m s^{-1}. The solid angle Ω_b is calculated from $\Omega_b = 1.133\theta_b^2$ (sr), where θ_b is $1''5$ for the CORNISH sources (Purcell et al. 2013), $2''5$ for the RMS sources (Urquhart et al. 2007), and $4''0$ for the sources identified by Becker et al. (1994). We assume $\tau_C \ll 1$ at 5 GHz and the Rayleigh-Jeans approximation, and thus τ_C becomes $-\ln(1 - T_b/T_e)$. Emission measure is determined using τ_C and Eq. (2.70), where a is a correction factor of order unity (Mezger & Henderson 1967), which is 0.9938 at an electron density (T_e) of 10,000 K (Wood & Churchwell 1989) and $\nu = 5$ GHz.

Finally, in order to estimate an electron density (n_e), we use the physical diameters of the 6 cm radio continuum sources. If there are multiple continuum sources within the Mopra/IRAM beams, we estimate a new HII region diameter from the combined area of radio continuum sources, i.e., $\Delta s = \sqrt{\sum_{n=1}^{n} \Delta s_n^2}$, in $n_e = \sqrt{\frac{EM}{\Delta s}}$.

Since we confirmed that the linewidths of detected mm-RRLs are dominated by Doppler broadening (i.e., in LTE) (Section 4.3.2) and that the mm-RRLs seem to be optically thin (Section 4.5.2), we can determine the EM from the velocity-integrated intensity of the measured mm-RRL (Rohlfs & Wilson 2000). We estimate the EM using the following equation that takes account of the beam dilution effect in Eq. (2.71),

$$EM_{RRL}\ (cm^{-6}\ pc) = \frac{T_e^{3/2}}{576}\left(\frac{\theta_{MB}^2 + \theta_s^2}{\theta_s^2}\right)\left(\frac{\nu_0}{GHz}\right)\left(\frac{\int T_{MB}\,\Delta V}{K\ km\ s^{-1}}\right),\qquad(4.3)$$

where the beam filling factor, f_{beam}, is given by $\theta_s^2/(\theta_{MB}^2 + \theta_s^2)$ in which θ_s is the angular diameter of the radio continuum source and θ_{MB} is the antenna main-beam size. The angular diameter also presents a summed size for the physical diameters of radio continuum sources. Here we use the same T_e as with the radio continuum data.
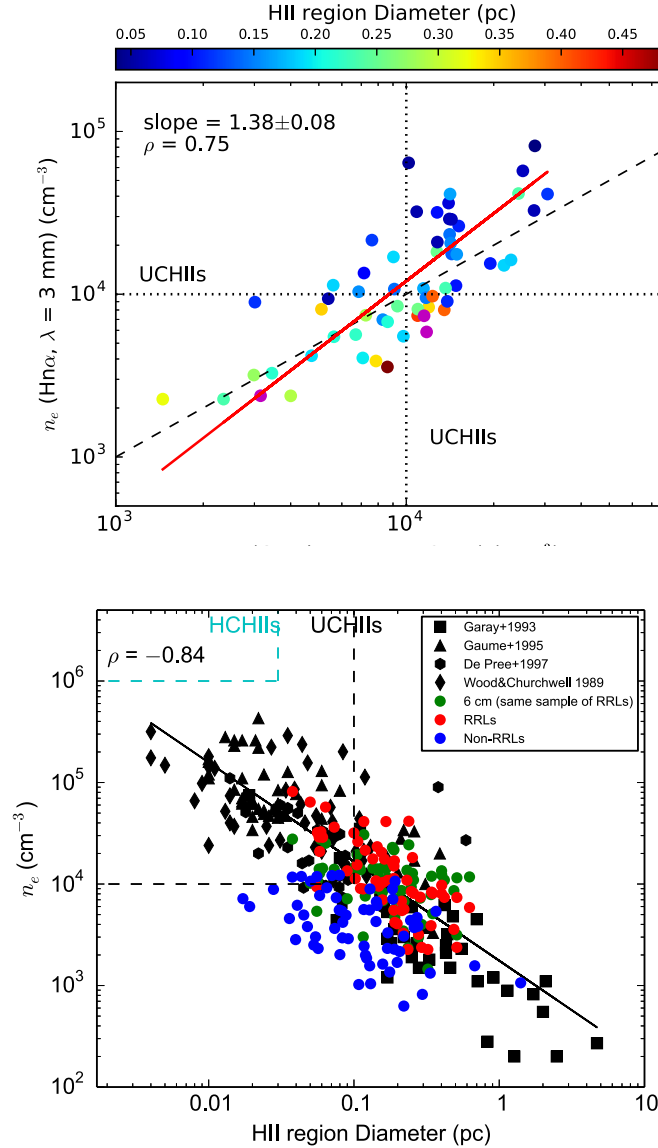
Figure 4.18: Left panel: n_e derived from 6 cm radio continuum emission versus n_e from mm-RRLs. Equality is indicated by the black dashed line. The dotted lines show the thresholds of electron density for UC HII. The colors represent HII region physical diameters in units of pc (see color bar) and the purple circles mark regions with diameter over 0.5 pc. The red line represents the best-fit line determined by an xy-bisector fit to the data. Right panel: n_e as a function of HII region diameter. The red and green symbols show the distribution of the same sample of mm-RRL detections but where the election densities are derived from the the mm-RRL emission and 6 cm radio continuum emission, respectively. The black symbols indicate data from previous radio continuum surveys and the blue circles are radio sources toward which no mm-RRL emission is detected and where the electron density has been estimated from the of 6 cm radio continuum emission. The black solid line represents the best-fit line determined by a least-squares polynomial fit with one degree to the data of the previous radio continuum surveys (black symbols) and this mm-RRL surveys (red symbols).

In the left panel of Figure 4.18 we present a comparison of the n_e calculated independently from the radio continuum and mm-RRL emission. There is a strong correlation between these two measurements with a correlation coefficient of $\rho = 0.75$ with $p-$value $\ll 0.001$. The xy-bisector fit to these data gives a slope of 1.38 ± 0.08. There is a noticeable trend for the more compact radio sources to have higher n_e in the measurement by the mm-RRL emission, which is expected since they are likely to be less optically thin.

In the right panel of Figure 4.18 we show the relationship between n_e and the H II region diameter. The black symbols indicate the distribution of H II regions reported in the literature, while the red and blue symbols show the properties of mm-RRL loud and quiet H II regions discussed in this chapter. There is clearly a strong correlation between these parameters ($\rho = -0.84$ with $p-$value $\ll 0.001$).

As previously discussed, we have found that the detected mm-RRLs tend to be associated with brighter H II regions, many of which are driven by O-type stars. Figure 4.18 reveals that the mm-RRLs tend to be associated with H II regions that are more evolved than the UC H II region stage. They also cover a similar range of physical scales to the mm-RRL quiet H II regions, but have significantly higher n_e, which suggests that they are driven by more massive stars. Comparing these results to the typical n_e and diameters of HC H II (cyan dashed line; diameter $\leq 0.03\,\text{pc}$ and $n_e \geq 10^5\ \text{cm}^{-3}$) and UC H II (black dashed line; diameter $\leq 0.1\,\text{pc}$ and $n_e \geq 10^4\ \text{cm}^{-3}$) (Kurtz et al. 2000), we find that most of the mm-RRL sources correspond to compact H II regions with a few located in the UC H II region part of the parameter space. We note that none is located in the HC H IIs parameter space; however, this plot only includes mm-RRL sources that have been matched with $6\,\text{cm}$ radio continuum emission and so may be biased away from HC H II regions as these tend to be optically thick at this frequency and are therefore less likely to be detected. As discussed in Section 4.4.1, we have identified a number of new H II region candidates, and although the nature of these objects needs to be confirmed, this sample does include a few good potential HC H II region candidates.

The results obtained from the mm-RRL parameters are consistent with the results determined from the radio continuum. This demonstrates the feasibility and complementarity of using mm-RRL observations to identify and parameterize compact H II regions. Furthermore, mm-RRL observations have a couple of distinct advantages over conventional searches (e.g., radio continuum and mid-IR color selection) as all H II regions should be optically thin at 3 mm and provide velocity information that can be used to derive distances and identify their natal molecular cloud.

4.5.4 Potential young H II regions

For a while, high-mass stars during their early evolutionary phase as HC H II regions still show activities such as accretion, infall, and outflow. As discussed in Section 4.5.3, although we have found that the properties of most sources are indicative of compact and UC H II regions, we have identified three cases in which broad non-thermal motions mark potential young H II regions.

In Section 4.3.2, we report broad mm-RRLs from nine clumps that have linewidths broader than $40 \, \mathrm{km \, s^{-1}}$. Roughly 30% of UC Hiis and 50% of HC Hiis are known to be associated with such broad RRLs observed at cm-wavelengths (Jaffe & Martín-Pintado 1999). Such broad RRL objects (BRLOs) are thought to be linked to a limited period having ionized outflows before the more evolved UC Hii phase (Jaffe & Martín-Pintado 1999; Sewilo et al. 2004a; Sewiło et al. 2008; Keto et al. 2008; Zhang et al. 2014; Guzmán et al. 2014). Interestingly, one of the nine BRLOs, N73, has a velocity offset of its mm-RRL velocity with respect to its systemic velocity. This could be due to the influence of contamination by nearby Hii regions. Nevertheless, N73 is not only associated with a bright WISE $22 \, \mu\mathrm{m}$ and unresolved radio continuum sources but is also coincident with an ionized outflow candidate reported by Guzmán et al. (2012). The ionized outflow candidate was explained to be an optically thick, expanding HC Hii (Purser et al. 2016). However, there is still no satisfactory explanation that is consistent with the origin of such BRLOs, although ionized outflows, disk winds, bow shocks, champagne flows, and inflows models (Jaffe & Martín-Pintado 1999) have been suggested to explain this phenomenon.

The second piece of evidence for the extreme youth of some Hii regions is the existence of stimulated (maser) emission in the mm-RRLs of N49 and N55. The mm-RRLs of these two clumps seem to be weakly enhanced by maser amplification. Radio recombination line maser emission is a very rare phenomenon and to date only two sources, WMC 349A and Mon R2 (Martin-Pintado et al. 1989; Jiménez-Serra et al. 2013), have been confirmed as RRL maser sources. According to these studies, the RRL maser phenomenon is linked to the structure and kinematics of the internal ionized gas rather than the nature of the source, and therefore the maser emission could be expected toward some young Hii regions showing high internal electron density that are modified by ionized stellar winds. Observing higher frequency, i.e., lower n (sub)mm-RRLs, would also be helpful; such observations toward MWC 349A have revealed that the line shape becomes more and more asymmetric with decreasing n, developing a pronounced double-peaked shape (Thum et al. 1995; Martín-Pintado 2002; Jiménez-Serra et al. 2013). Interferometric observations are needed to confirm the RRL masers, similar to the confirmation of Mon R2 using high-resolution observations (Jiménez-Serra et al. 2013).

We have found mm-RRLs toward eight clumps without a radio counterpart. In particular, some of these (e.g., N37 as shown in Figure 4.10) do not show extended $22 \, \mu\mathrm{m}$ or $8 \, \mu\mathrm{m}$ emission, but are associated with various masers such as OH, H_2O, Class I & II CH_3OH. Source N37, also known as W43-MM1, is considered to be a hot core and has multiple outflows (Motte et al. 2003; Sridharan et al. 2014). In addition, wing features seen in SiO emission, like the case of N30, (Csengeri et al. 2016) support the existence of outflows. Regardless of the absence of radio counterparts, the detections of the maser emission and the wings of SiO suggest that the detected mm-RRLs are produced from embedded young Hii regions in the clumps, but further mm- and submm-RRL observations at the high resolution and sensitivity provided by interferometers are necessary to study their properties in detail.

4.6   Summary and conclusions

We carried out 3 mm spectral line observations toward 976 dense clumps identified by the ATLASGAL survey ($-60° \leq \ell \leq +60°$). The sample was carefully selected to include a wide range of evolutionary stages from starless clumps to protostellar and compact H II region stages. The observed spectra included a number of mm-RRLs and thermal molecular line transitions allowing a range of physical and environmental conditions to be investigated at the same angular resolution.

We have detected H$n\alpha$ mm-RRL emission toward 178 ATLASGAL clumps; H$n\beta$, H$n\gamma$, and H$n\delta$ transitions have been detected toward 65, 23, and 22 clumps, respectively. Inspecting mid-IR images and high-resolution radio continuum surveys, we are able to associate 134 of these mm-RRL detections with compact and UC H II regions previously identified in the literature. This represents the largest mm-RRL sample so far reported and provides a new method of identifying and parameterizing H II regions. Comparing the radio and mid-IR fluxes of the mm-RRL quiet and loud sources, we find that they are associated with the brightest continuum sources. Thus, because of the limited sensitivity of our observations we were not able to detect mm-RRLs toward an additional ∼126 H II regions. Analysis of the ratios of the different mm-RRL transitions reveals that the lines are formed under LTE conditions.

Comparing the systemic velocity of the molecular material and the velocity of the ionized gas traced by the mm-RRL emission ($\sigma < 5\,\mathrm{km\,s^{-1}}$) reveals a strong correlation between the two, which is consistent with the mm-RRL emitting H II regions still being associated with their parental molecular clumps. We expected feedback from the embedded H II regions to have a direct effect on the global turbulent motion in their molecular clumps. Comparing the H^{13}CO$^+$ linewidth of the mm-RRL associated and unassociated clumps, we find that the associated clumps tend to be more turbulent. However, we cannot reject the possibility that this is due to the Larson size-line width relation (Larson 1981).

We find a strong correlation between the integrated 6 cm radio continuum and mm-RRL emissions (the correlation coefficient $\rho = 0.70$). This result implies that the 6 cm continuum and mm-RRL emissions are tracing the same ionized nebula. We also find that the Lyman continuum fluxes for these mm-RRL source are associated with evolved H II regions driven by late O-type stars and the reason for large H II region diameters (∼0.5 pc) is that the H II regions driven by O-type stars expand faster than B-type stars.

Of the remaining 44 mm-RRL detections that are not confirmed with radio counterparts, 36 are thought to be associated with nearby evolved H II regions, while 8 detections are considered to be potential new H II region candidates; these will need to be confirmed by future high-resolution and high-sensitivity radio continuum observations.

In this chapter we have explored a new method of identifying compact H II regions using mm-RRL emission. We have identified 142 genuine H II regions (including the 8 potential H II regions) and analysis of the line parameters has produced results that are consistent with those obtained from the radio continuum emission. We have therefore

demonstrated that mm-RRLs are a viable and complementary method of identifying compact Hɪɪ regions and investigating their physical properties. Furthermore, mm-RRL observations have some inherent advantages over studies that merely analyze continuum emission in that they provide velocity information, which can be used to match the regions to their host clumps and to determine their Galactic locations.

Submillimeter hydrogen radio recombination line survey

This chapter is adapted from the submitted paper of Kim, W.-J., Urquhart, J. S.,
Wyrowski, F., Menten, K. M. and Csengeri, T. 2017, A&A.

Contents

5.1 Introduction

Massive stars affect their environment in various ways, thereby shaping the evolution of galaxies and leading to chemical enrichment of the interstellar medium (Zinnecker & Yorke 2007). All the processes of massive star formation take place while the star or cluster is still deeply embedded in its molecular cloud. Indeed, the high-mass star/cluster is hidden at optical and even near-infrared wavelengths. For these reasons, it is more challenging to make observations of high-mass star formation than those of

low-mass star formation, and also they are rare and located at much larger distances (Schuller et al. 2009; Urquhart et al. 2017). For these reasons, the feedback between young OB stars and their molecular clouds is still not well understood.

Young massive stars are hot and thus create small regions of hot ionized gas around them that expands into their local environment and interacts with the surrounding molecular gas; these are known as compact HII regions. The HII region phase is the last stage of the massive star formation process. Studying this phase is not only important due to the exciting stars' influence on their environment, but it is also key to understand of how high-mass stars obtain masses above $10\,M_\odot$ (Churchwell et al. 2010). Indeed, the youngest and most compact HII regions (hyper- and ultra-compact) are often associated with various star formation signposts such as molecular outflows, infall motions, and methanol and water masers, which themselves are pumped by radiation and shocks (Urquhart et al. 2013b, 2015). These signposts suggest that the mass assembly process is still active.

The gas in HII regions surrounding newly born O/B stars has velocity dispersions of 25-35 km s^{-1} determined by a mix of thermal ($\sim$20 km s^{-1}) and turbulent motions (Wilson et al. 2009). The kinematics in the ionized gas can be investigated using radio recombination lines (RRLs), particularly toward sources that are deeply embedded in dense molecular clumps. In these dense clumps, observations of Lyman α, Hα and other ultraviolet/optical/near-infrared recombination lines are strongly attenuated due to high levels of visual extinction (up to hundreds of mag.) while RRL emission can still escape out of the clumps. Therefore, RRLs are an excellent tool for analyzing the distribution and kinematic of the ionized gas associated with HII regions.

Interestingly, strong maser emission has been observed from submillimeter RRLs towards only a few sources (Thum et al. 1995; Martín-Pintado 2002; Contreras et al. 2017). Therefore it is interesting to investigate how widespread RRL maser emission is towards HII regions.

Submm-RRL observations provide kinematics of HII regions and probe the Lyman continuum photon production rate, which can be used as a measure of star formation rates (SFRs) in external galaxies (Scoville & Murchikova 2013; Bendo et al. 2017). These rates have been compared with those measured by other SFR tracers such as ultraviolet continuum emission, optical/near-infrared recombination lines, mid-/far-infrared continuum emission, and radio continuum emission and have been found to give consistent results (e.g., NGC5253, Bendo et al. 2017).

In our previous study of hydrogen RRLs at millimeter wavelengths (Kim et al. 2017), we identified 178 mm-RRL sources toward 976 compact dust clumps selected from the APEX Telescope Large Area Survey of the Galaxy (ATLASGAL) Compact Source Catalogues and GaussClump Source Catalogue (CSCs; Contreras et al. 2013; Urquhart et al. 2014b, and GCSC; Csengeri et al. 2014). These mm-RRLs were found to be associated with embedded HII regions identified from cm-wavelength radio continuum surveys (e.g., Urquhart et al. 2007, 2013b) and were used to derive the properties of the ionized gas which in turn were compared with the properties of their natal molecular clumps. The properties of the mm-RRLs were found to be consistent with properties derived from the 6 cm radio continuum.

To further characterize the properties of these H II regions, we have re-observed many of these sources targeting RRLs at submillimeter wavelengths, which not only provide brighter flux than mm-RRLs but also allow to investigate the RRL excitation and whether maser emission is influencing the intensity of RRLs. We have, therefore, carried out submillimeter RRL (submm-RRL) observations using the APEX 12m telescope to investigate further the H II regions detected in the course of our mm-RRL survey.

The observations and data reduction are explained in Section 5.2. The general properties of the detected submm-RRLs, including the detection rates, and a comparison between submm-RRL and mm-RRL are presented in Section 5.3. The associations with H II regions and molecular clumps are described in Section 5.4. The derivation of the ionizing Lyman photon production rate from the submm-RRL data is described in Section 5.5. Several sources with peculiar line profiles are discussed in Section 5.6. Lastly, we present a summary of our main results in Section 5.7.

5.2   Observation and data reduction

5.2.1   Source selection and observational setup

The sources for this targeted survey with the Atacama Pathfinder Experiment (APEX) 12 m diameter submillimeter telescope (Güsten et al. 2006) have been selected based only on their peak mm-RRL intensity as measured from our surveys with the IRAM 30 m and the Mopra 22 m telescopes (Kim et al. 2017). For the selection, the intensity threshold was set to 0.2 K of the peak mm-RRL intensity. This threshold was chosen by comparing the intensity of stacked mm-RRL profiles to H26α RRL data that was observed by APEX as part of a different molecular line survey toward the ATLASGAL "Top 100" sample (see Giannetti et al. 2014; König et al. 2017 for details). In total, 104 ATLASGAL sources were selected from the mm-RRL catalog (Kim et al. 2017), and the submm-RRL observations with the APEX 12 m telescope were carried out primarily in 2015 (Project IDs: M0025-95 and M0018-96) with some additional observations being made in 2016.

The APEX observations used the dual frequency FLASH receiver (Klein et al. 2014) for the H25α, H27α, H28α and H35β transitions and the APEX-1 (HET230, Vassilev et al. 2008) receiver for the H29α and H30α transitions. The observations mainly covered the H25α, H28α and H35β transitions. However, the H27α, H29α and H30α transitions were also observed to obtain better line profiles towards some sources for which the other RRL profiles were found to be contaminated by emission from molecular lines. The spectra of the observed submm-RRL transitions, therefore, vary slightly from source to source. In Table 5.1 we provide details of the transitions observed towards each source and indicate where they are detected. In Table 5.2 we give the observed frequency, the oscillator strength of each transition and the FWHM beam widths of the APEX beam at the frequency of the transition, the conversion factor between K and Jy and the telescope's main beam efficiency, η_{MB}[1]. The beam

---

[1]http://www.apex-telescope.org/instruments

Table 5.1: List of observed sources.

ID	ATLASGAL	RA	Dec.	Observed
No.	clump name	α(J2000)	δ(J2000)	transition
1	AGAL010.151−00.344	18:09:21.2	−20:19:28	H25α, H28α, (H35β?)
2	AGAL010.168−00.362	18:09:26.7	−20:19:03	(H25α?), H28α, (H35β)
3	AGAL010.472+00.027	18:08:37.9	−19:51:48	(H26α^c?)
4	AGAL010.624−00.384	18:10:28.6	−19:55:46	H25α, H26α, H28α, H35β
5	AGAL011.936−00.616	18:14:00.8	−18:53:24	H25α, H28α, (H35β?)
6	AGAL012.804−00.199	18:14:13.5	−17:55:32	H25α, H26α, H28α, H35β
7	AGAL013.209−00.144	18:14:49.3	−17:32:46	H25α, H28α, (H35β?)
8	AGAL013.872+00.281	18:14:35.6	−16:45:39	H25α, H28α, H35β
9	AGAL015.024−00.654	18:20:17.9	−16:11:30	H25α, H28α, (H35β)
10	AGAL015.029−00.669	18:20:22.4	−16:11:44	H25α, H26α, H28α, (H35β)
11	AGAL015.051−00.642	18:20:18.7	−16:09:43	(H25α?), H28α, (H35β)
12	AGAL018.301−00.389	18:25:41.8	−13:10:21	H25α, H28α, (H35β)
13	AGAL028.199−00.049	18:42:58.1	−04:13:58	H25α, H28α, (H35β)
14	AGAL029.954−00.016	18:46:03.5	−02:39:24	H25α, H27α, H28α, H35β
15	AGAL030.753−00.051	18:47:38.2	−01:57:51	(H25α), H28α, (H35β)

Notes. Non-detections are given in parentheses. Uncertain detection are marked with a question mark, "?", and are considered as non-detection for all data analysis. A superscripted "c" indicates severe contamination by complex molecules or unidentified lines. The full table is available in Table A.1.

sizes given in the Table. 5.2 are calculated using $\Theta_{\mathrm{FWHM}} = 7.8'' \times (800/\nu)^2$, where ν is a rest frequency of the transition in GHz.

5.2.2 Data reduction and identification of blended molecular lines

In the submillimeter wavelength regime, the spectra of hot molecular cores, i.e. warm, dense regions around embedded massive young stellar objects, are dominated by many lines from complex molecules. As a result, molecular lines can overlap with the submm-RRLs, making the detection and line fitting more complicated, particularly when trying to distinguish between potential RRL maser emission which can have spectral features as narrow as typical molecular lines (Thum et al. 1995; Martín-Pintado 2002). Therefore, it is necessary to identify any molecular line contribution to observed narrow features on a broad profile.

To identify narrow line features, we used WEEDS within the CLASS software of the GILDAS package[3]; CLASS is also used for the RRL data reduction. Figure 5.1 shows an example of identified emission lines of the CH_3OCHO molecule and a submm-RRL (H25α) toward AGAL034.258+00.154. We fit the CH_3OCHO molecular emission assuming local thermal equilibrium (LTE) and that the lines are exposed to the same physical conditions (single value of excitation temperature, H_2 column den-

---

[2]http://www.apex-telescope.org/telescope
[3]https://www.iram.fr/IRAMFR/GILDAS/doc/html/class-html/class.html
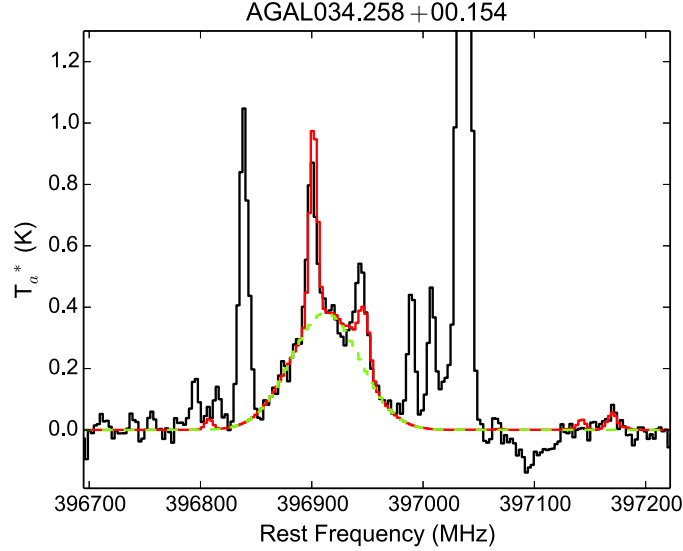
Figure 5.1:   An example of the identification of molecular lines blended with submm-RRL emission (black line) in AGAL034.258+00.154. The red profile shows a combined profile of the modeled profiles of CH_3OCHO lines using WEEDS and a Gaussian profile of the H25α RRL. The latter is also shown as the green dashed line. Other emission lines are an unidentified molecular lines.

Table 5.2:   Observed transitions and observational parameters.

RRL transition	Frequency (MHz)	Oscillator strength*	Observed sources	rms (Jy)	Beam size ($''$)	K to Jy $(Jy\,K^{-1})$	η_{MB}
H25α · · · · · ·	396900.866	5.0541050	85	1.24	15.7	41	0.73
H26α · · · · · ·	353622.776	5.2449384	27	1.64	17.6	41	0.73
H27α · · · · · ·	316415.451	5.4357673	13	0.43	19.7	41	0.73
H28α · · · · · ·	284250.594	5.6265921	85	0.50	22.0	39	0.75
H29α · · · · · ·	256302.056	5.8174132	7	0.44	24.3	39	0.75
H30α · · · · · ·	231900.947	6.0082311	30	0.40	26.9	39	0.75
H35β · · · · · ·	282332.932	1.0002938	85	0.45	22.1	39	0.75

Notes. FLASH receiver: H25α, H26α, H27α, H28α, and H35β. APEX-1 (HET230) receiver: H29α and H30α.

Reference. (*) Goldwire (1968).

Table 5.3: List of detected source numbers and detection rates for each transition.

RRL transition	Observed sources	Detected sources	Detection Rate (%)
H$n\alpha$ ······	104	93	89
H25α······	85	43	51
H26α······	27	16	59
H27α······	13	12	92
H28α······	85	79	93
H29α······	7	5	71
H30α······	30	26	86
H35β······	85	35	41

Notes. The H$n\alpha$ means the staked RRL of the detected submm-RRL transitions for an individual source.

sity, linewidth, and peak velocity to all transitions of this molecule within observed frequency bands). The fits to the CH$_3$OCHO line data obtained from WEEDS and the H25α line are shown in red and green, respectively. The broad profile of the H25α line is consistent with that of other submm-RRL transitions observed towards this source with regard to peak velocity, intensity and linewidth. In addition, we find that, while the H26α transition is not blended with molecular lines nearby in frequency, it is contaminated in several cases by attenuated strong emission from a CS (7−6) transition ($\nu = 342883$ MHz) originating from the other side-band of the receiver.

   All narrow features could be identified as blended complex lines from molecules. The observed broad features originate from hydrogen submm-RRLs. We, therefore, only use the line parameters determined from fits to the broad velocity features for the analysis in this chapter. A polynomial baseline of order 1 to 3 was fitted to the line-free channels in a 300 km s^{-1} wide velocity range and subtracted from the spectrum of each transition. The average rms values for each transition are given in the Table 5.2; these were determined from the line-free channels, which have a velocity resolution of 2.1 km s^{-1}. In some cases the submm-RRLs have been smoothed to a velocity resolution of 4.1 km s^{-1} to increase the signal-to-noise. We find that the majority of the submm-RRLs can be fitted with a single Gaussian component. However, for a handful of sources, the profiles have significant red/blue shifted wings and these were fitted with two components, a narrower component that fits the central portion of the line and a much broader component that fits the high-velocity wings. We will discuss those sources with two Gaussian RRL components in Section 5.6. Furthermore, we re-reduced all data of individual and stacked mm-RRLs presented in Kim et al. (2017) using the same velocity resolution as for the submm-RRLs to facilitate comparisons of the mm- and submm-RRLs (see Figure 5.2 for examples).

Table 5.4:   Gaussian line parameters of the individual submm-RRL transitions and stacked submm-RRLs.

ID No.	RRL transition	v_{Peak} $(\mathrm{km\,s^{-1}})$	Δv $(\mathrm{km\,s^{-1}})$	Area $(\mathrm{Jy\,km\,s^{-1}})$	Peak (Jy)	rms (Jy)
1	H$n\alpha$	+21	32±1	156.5±5.7	4.64	0.46
	H25α	+22	24±9	80.7±20.3	3.21	1.10
	H28α	+20	31±2	165.6±7.7	4.99	0.63
	H35β	−	−	−	−	0.56
2	H$n\alpha$	+11	17±1	71.7±4.2	3.88	0.47
	H25α	−	−	−	−	1.15
	H28α	+11	21±3	77.7±8.0	3.43	0.66
	H35β	−	−	−	−	0.78
3	H26α	−	−	−	−	2.01
4	H$n\alpha$	+0	29±1	310.6±7.7	10.00	0.49
	H25α	+3	33±4	254.2±77.5	7.18	1.23
	H26α	+6	38±3	336.5±28.6	8.36	1.47
	H28α	+0	29±1	314.7±7.0	10.20	0.48
	H35β	+1	30±2	104.0±7.2	3.23	0.60

Notes. All line parameters are available at the CDS via anonymous ftp. ID number corresponds to the ID number in Table. 5.1.

5.3 Results

5.3.1 Detection rate

Since the intensity of RRLs increases with the frequency of the RRL (Gordon & Sorochenko 2002), high detection rates of submm-RRLs were expected from the observed mm-RRL sources. Table 6.5 gives the detection rate for each submm-RRL transition. The detection rates are lower than 100% because our observations are less sensitive than the mm-observations; the non-detections toward six sources might be due to poorer flux sensitivity (for H28α, rms = 0.50 Jy compared to the rms values of the Mopra and IRAM observations, which were 0.20 and 0.05 Jy, respectively). Furthermore, the detection of submm-RRLs towards 11 clumps are ambiguous due to blending from molecular lines that make it difficult to separate the molecular and submm-RRLs profiles; we considered these sources as non-detections which are indicated in Table 5.1.

Furthermore, if the blending is not too severe as in the case of H25α of AGAL034.258+00.154 (Figure 5.1), the molecular emission and RRL can be reliably separated, and the detection of the submm-RRL is considered valid. The H$n\alpha$ and H35β submm-RRL transitions (signal-to-noise (S/N) ratio $\geq 3\sigma$) have been detected towards a large fraction of the observed sources; these are detected towards 93 (89 %) and 34 (40 %) clumps, respectively. The detection rate of the H35β compared with the H$n\alpha$ transitions is consistent with the results of the mm-RRL survey at a similar S/N level.

5.3.2 Properties of submm-RRLs

Figure 5.2 displays examples of detected submm-RRL spectra (upper panels) and the corresponding mm-RRL spectra (lower panel; Kim et al. 2017) toward AGAL037.874−00.399 and AGAL332.156−0.449. The profiles of the submm- and mm-RRLs show good agreement in peak velocity, linewidth and profile shape, however, we note a significant difference in the intensity, with the submm-RRLs being approximately a factor of 2 brighter. Figure 5.3 shows a comparison of the peak flux of the H28α line to the peak fluxes measured for the other submm-RRL transitions (i.e., $n = 25, 26, 27, 29,$ and 30) (upper panel), and also for the H35β transition (lower panel). We chose the H28α transition as the main transition for these comparisons because this transition is mainly covered by all the observations and is detected with a reasonable S/N level toward the observed sources.

Since we observed multiple submm-RRL transitions toward a majority of our sources, we can investigate whether there is a significant flux difference for different quantum numbers. Overall the peak fluxes determined from the different submm-RRLs agree with each other within the uncertainties (as shown in the upper panel of Figure 5.3): the slope determined from a linear xy-bisector fit to the data is 1.00±0.04. In addition to the best-fit, the Pearson correlation coefficient (r) for the whole data set is 0.95 with $p-$value $\ll 0.0001$, revealing that the RRL fluxes are very highly correlated. Although some sources show deviations from the primary trend, their S/N ratio tends to be poor. The consistency of the submm-RRL fluxes indicates that there is
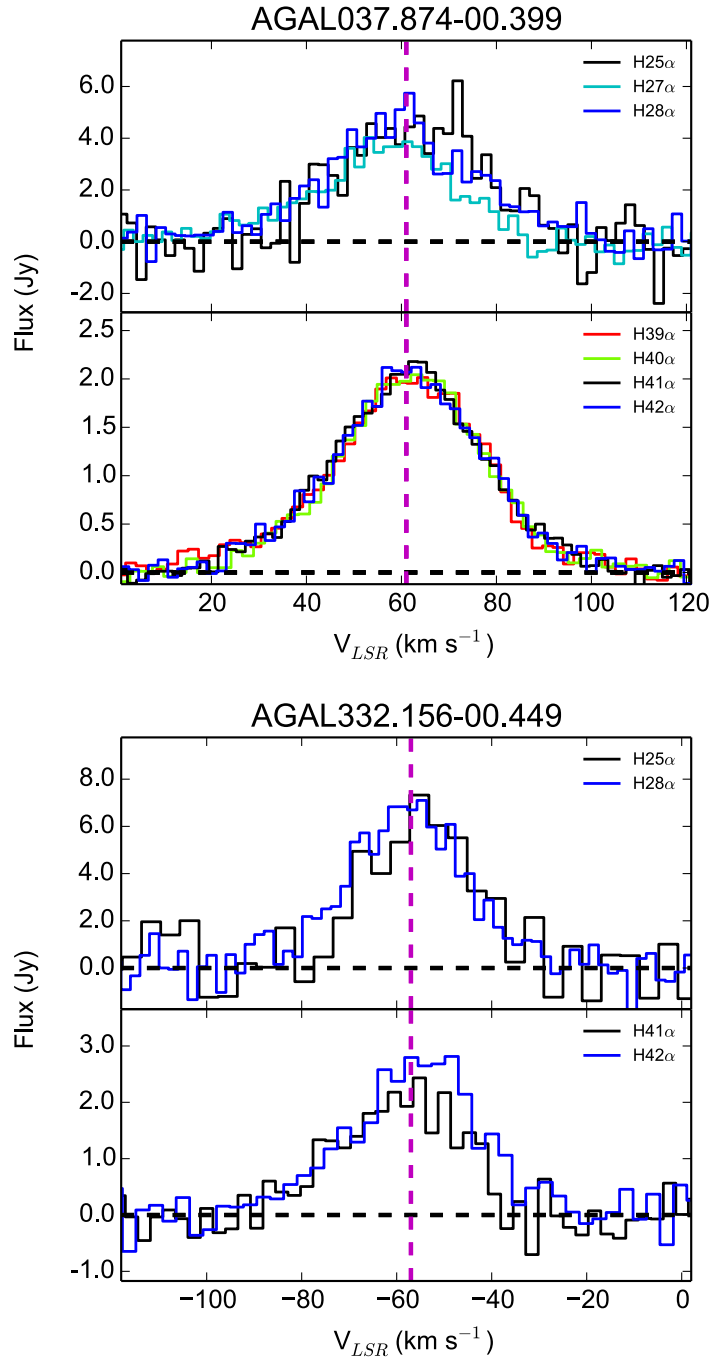
Figure 5.2:   Examples   of   detected   submm-RRLs   (upper   panels)   of AGAL037.874−00.399   and   AGAL332.156−00.449   and   their   corresponding   mm-RRLs (lower panels) from Kim et al. (2017). The vertical purple dashed lines indicates the systemic velocity measured with H^{13}CO$^+$ (1−0) lines. The different colors present different submm/mm-RRL transitions detected in this work and Kim et al. (2017).

no extreme density gradient toward the H$\scriptstyle\rm II$ regions on angular scales of a few tens of arc-seconds which would lead to differences in the measured fluxes (Dupree & Goldberg 1970).

By comparing the linewidths of the various submm-RRLs similarly as we have just done for the fluxes, we also find a moderate correlation ($r = 0.53$ with $p-$value $\ll$ 0.0001). The correlation coefficient is considerable but the uncertainty in the linewidths tends to be significantly higher than for the peak fluxes.

The lower panel of Figure 5.3 shows the comparison of peak fluxes of the H28α and H35β transitions. As we have seen, the detection rate of the H35β line is lower than that of the H28α line (Table 6.5) since the H35β lines are about six times fainter than the H28α lines. The slope from xy-bisector fitting is 0.99 and the correlation coefficient (r) of 0.95 with a small $p-$value $\ll$ 0.0001 reveals a significant correlation between both transitions. If maser excitation contributed to the observed fluxes, a low ratio of H35β/H28α fluxes is expected to be quite similar to the ratio measured in the submillimeter wavelength regime toward MWC349 (H35β/H28α $\sim$ 0.078). The peak flux ratios of H28α and H35β in the lower panel of Figure 5.3 are, however, consistent with the predicted LTE value. The average value of H35β/H28α toward each source, 0.31, is only slightly above the LTE prediction value of 0.28 but close to the value of 0.32 measured from typical H$\scriptstyle\rm II$ regions in the Galaxy (Thum et al. 1995).

In our previous analysis of the mm-RRLs (Kim et al. 2017), we identified two sources in which the observed fluxes could have been the result of maser emission; these were AGAL034.258+00.154 and AGAL043.166+00.011. They were identified by their low Hβ/Hα ratios, which is suggestive of non-LTE conditions due to an increase in the Hα intensity from stimulated maser amplification (as seen in MWC349A; Thum et al. 1995). The submm-RRL profiles for these two sources reveal no features that would indicate the presence of maser emission similar to those seen towards MWC349A at submillimeter wavelengths and their profiles are consistent with pure thermal emission. As discussed in the previous paragraph, the ratio of H35β/H28α of AGAL043.166+00.011 (cyan circle) shown in the lower panel of Figure 5.3 does not show a significant offset from the LTE value. In case of AGAL034.258+00.154, it was impossible to determine this ratio due to contamination of the H35β line. The H$n\alpha$ line profiles of the source, however, already showed no maser emission. We can, therefore, rule out, based on the new submillimeter data, that AGAL034.258+00.154 and AGAL043.166+00.011 are associated with RRL maser emission.

5.3.3 Properties of submm-RRLs in comparison to mm-RRLs

Table 5.5 compares the linewidth ratios of detected H$n\alpha$ lines (i.e., n = 25, 26, 27, 28, 30, 39, 40, 41) to the H42α line (in this table we only consider detections with a S/N ratio $> 8\,\sigma$). The low quantum numbers correspond to higher-frequencies. Here we chose the H42α transition as the main transition to investigate intrinsic linewidths caused by non-thermal motions.

The median ratios are very close to unity for the whole range of transitions (H41α to H25α) and are all within one standard deviation. That is consistent with the transitions
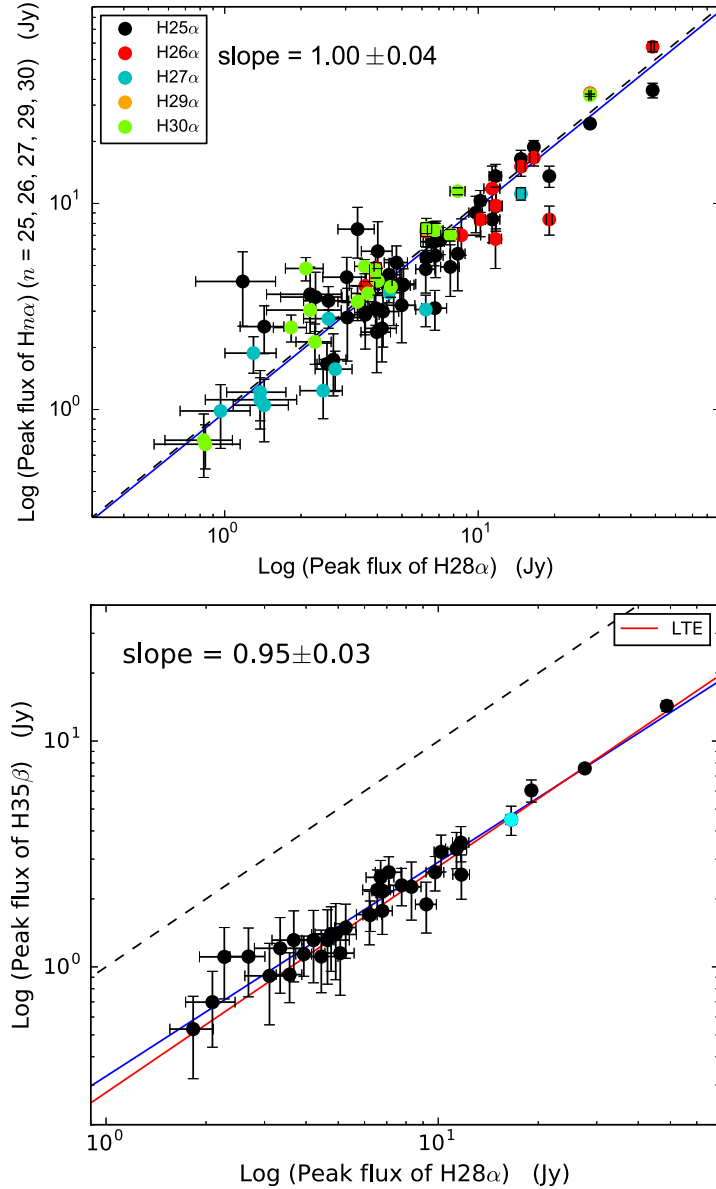
Figure 5.3: *Upper*: Peak flux of the H28α transition versus peak flux of other transitions; H25α (black), H26α (red), H27α (cyan), H29α (orange), and H30α (bright green). All the plotted sources are detected in the H28α transition, and thus there are a few sources missing, which are only detected in other lines. *Lower*: Peak flux of the H28α transition versus peak flux of H35β. In both plots, equal fluxes are indicated by the black dashed line, and blue lines indicate the best-fit determined by xy-bisector fits to all data points. The red line in the right panel presents the predicted LTE value.

Table 5.5: Ratios of the H$n\alpha$ linewidth to the H42α linewidth.

Submm-RRL transition	Linewidth ratio		
	Median (σ) ($\mathrm{km\,s^{-1}}$)	Maximum ($\mathrm{km\,s^{-1}}$)	Minimum ($\mathrm{km\,s^{-1}}$)
H25α/H42α	1.0 (0.08)	1.2	1.0
H26α/H42α	1.0 (0.09)	1.1	0.8
H27α/H42α	0.9 (0.28)	1.5	0.8
H28α/H42α	1.0 (0.13)	1.5	0.8
H30α/H42α	1.0 (0.05)	1.1	0.9
H39α/H42α	1.0 (0.07)	1.2	0.9
H40α/H42α	1.0 (0.09)	1.3	0.9
H41α/H42α	1.0 (0.07)	1.2	0.8

Notes. The H$n\alpha$ means the staked RRL of the detected submm-RRL transitions for an individual source. It only contains sources with peak fluxes greater than $8\,\sigma$. In case of the H29α, there are no sources that have both H29α and H42α detections $\geq 8\,\sigma$.

tracing the same physical conditions and size scales (electron temperature and densities) within the beam areas of these single dish observations. It also indicates that there is no significant turbulence. We note that there are some relative deviations from unity (see maximum and minimum ratios in Table 5.5). However, only a few particular sources seem to be affected, which might be related to micro-turbulence in the inner H$\textsc{ii}$ regions (Jaffe & Martín-Pintado 1999).

Since the linewidths and intensities are comparable in the whole range of submm-RRLs, it is feasible to stack the transitions of adjacent quantum numbers to improve their S/N ratio towards each source. However, even by stacking the RRLs we still found some sources with poor S/N levels. We, therefore, plotted the uncertainties in the linewidth and peak intensity to determine reliable thresholds that can be used to select high S/N sources. From the distribution of the uncertainties, we chose the S/N ratio threshold to be larger than $8\,\sigma$ for both the linewidths and peak fluxes of mm/submm-RRLs to allow for a reliable comparison with the stacked 3mm data.

Figure 5.4 compares the linewidth and peak flux for the stacked mm-RRLs and submm-RRLs. In the upper panel of Figure 5.4, the distribution of high-reliability linewidths of mm-RRLs and submm-RRLs reveals a good correlation (Pearson correlation coefficient $r = 0.7$ with $p-$value $\ll 0.0001$). A linear least square fit to all of the data points is close to the line of equality. The median value and standard deviation of all the linewidth of mm-RRLs are $29.6\,\mathrm{km\,s^{-1}}$ and $5.3\,\mathrm{km\,s^{-1}}$, and those values for submm-RRLs are $28.7\,\mathrm{km\,s^{-1}}$ and $6.2\,\mathrm{km\,s^{-1}}$.
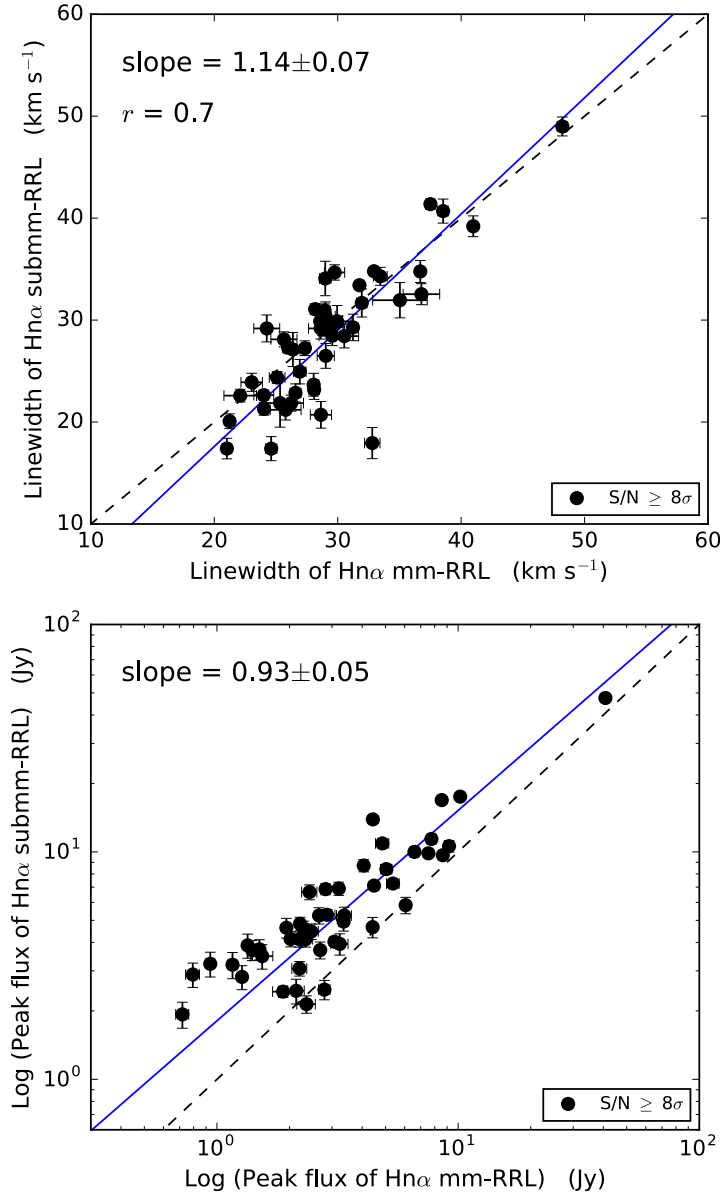
Figure 5.4:   *Upper*: Linewidth comparison of stacked mm- and submm-RRLs. The black filled circles indicate sources with a peak flux with S/N ≥ 8 σ of both RRLs. *Lower*: Peak flux comparison of stacked submm- and mm-RRL. The black symbols are the same as in the upper panel. The black dashed-lines indicate the locus of equal linewidths and fluxes. The blue lines show the best-fit from xy-bisector fitting.

Table 5.6: Summary of properties of molecular clumps and embedded sources associated with RRLs discussed in the text.

ATLASGAL name	v_{sys} ($\mathrm{km\,s^{-1}}$)	1st v ($\mathrm{km\,s^{-1}}$)	1st Δv ($\mathrm{km\,s^{-1}}$)	2nd v ($\mathrm{km\,s^{-1}}$)	2nd Δv ($\mathrm{km\,s^{-1}}$)	Dist. (kpc)	T_{dust} (K)	Log L_{bol} ($L_{\odot}$)	Log M_{clump} ($M_{\odot}$)	Log L/M	Log Ly (photon $\mathrm{s^{-1}}$)
AGAL012.804−00.199	+35.5	+33.4	28.7	+46.1	39.4	2.6	−	−	−	−	48.9
AGAL029.954−00.016	+97.5	+98.7	23.7	+85.8	33.1	5.2	35.5	5.7	3.6	2.1	48.9
AGAL034.258+00.154	+57.5	+54.8	30.6	+40.9	57.6	1.6	29.2	4.8	3.2	1.6	47.6
AGAL043.164−00.029	+16.0	+9.1	33.5	+28.2	46.0	11.1	31.2	6.2	4.5	1.7	49.5
AGAL043.166+00.011	+12.7	+6.7	34.8	+37.9	45.8	11.1	33.3	6.9	5.0	1.9	49.3
AGAL045.121+00.131	+59.0	+62.2	31.0	+58.6	57.3	8.0	34.5	6.0	3.9	2.2	49.2

Notes. The full table for all sources is only available at the CDS via anonymous ftp. The line parameters have been obtained with Gaussian fits to the stacked 3mm RRLs. Columns from the 3rd to 6th are only for these selected sources since the linewidth are obtained from two Gaussian component fit in section 5.6. The 1st v and 2nd v are the local standard of rest velocities of the peaks of narrow and broad RRL components of these sources. The 1st Δv and 2nd Δv are linewidths of the narrow and broad RRL components. From left to right, other columns are the clump name, the systemic velocity (v_{sys}) of the dense clump, heliocentric distance (Dist.), dust temperature (T_{dust}), bolometric luminosity (L_{bol}) of all RMS sources embedded in the ATLASGAL clump, clump mass (M_{clump}) , ratio of bolometric luminosity over clump mass ($L_{\mathrm{bol}}/M_{\mathrm{clump}}$), Lyman photon flux (Ly) from radio continuum emission at 6 cm wavelength.

References. Properties of the ATLASGAL clumps: König et al. (2017); Urquhart et al. (2017). v_{sys}: Kim et al. (2017). 6 cm radio continuum emission: Becker et al. (1994); White et al. (2005); Urquhart et al. (2007, 2009); Purcell et al. (2013).

Those standard deviations of mm-RRLs and submm-RRLs are just a factor of 2-3 more than their velocity resolution ($\sim 2\,\mathrm{km\,s^{-1}}$). In addition, the sources with a good S/N ratio (black circles) are even more tightly clustered around the line of equality. This linewidth comparison and the result in Table 5.5 are consistent with the hypothesis that both the mm-RRLs and submm-RRLs are probing the same ionized gas and that we can discard any significant influence of line broadening on the fitted parameters, which would have affected the mm-RRLs stronger than the submm-RRLs.

In the lower panel of Figure 5.4 we compare the peak fluxes of mm- and submm-RRLs. The linear least squares fit to all of the data reveals the presence of an offset from the line of equality, with the submm-RRL fluxes being significantly higher. The shift in the distribution from the line of equality is approximately a factor of two from mm ($86-100\,\mathrm{GHz}$) to submm ($231-397\,\mathrm{GHz}$) wavelengths. This shift agrees with the estimated difference in line intensities of Fig. 3 of Peters et al. (2012), assuming a HII region with an electron density of $n_e = 5 \times 10^5\,\mathrm{cm^{-3}}$ and a temperature of $T_e = 10^4\,\mathrm{K}$. This difference is due to the increase in the line to continuum ratio with increasing frequency expected for RRLs. Furthermore, the RRL intensity computation by Peters et al. (2012) only considers the line emissivity and does not include stimulated emissions. The good agreement we have found with the theoretical predictions is consistent with the detected mm-RRLs and submm-RRLs being emitted from optically thin HII regions. Nevertheless, there are some sources where the fluxes deviate significantly from the observed trend possibly indicating the presence of some HII regions with different physical conditions.

5.4   Association with molecular clumps

Comparing the velocities of the ionized gas determined from the submm- and mm-RRLs and those of the molecular gas determined from the $H^{13}CO^+$ ($1-0$) transition (Kim et al. 2017), we find velocity differences ($v_{H^{13}CO^+} - v_{RRL}$) of them to be in good agreement with a standard deviation of $4.8\,\mathrm{km\,s^{-1}}$. This is consistent with the hypothesis that the RRLs are associated with young HII regions that are either embedded or still associated with their natal clouds. Thus the properties of these HII regions may be related to the properties of their molecular clumps. We have, therefore, tried to identify correlations between the ionized and molecular gas using properties of radio emission from the CORNISH (Hoare et al. 2012; Purcell et al. 2013) and Red MSX (Lumsden et al. 2013) 5 GHz radio continuum surveys (Urquhart et al. 2007, 2009) and the properties of dust clumps determined from submm-dust emission of ATLASGAL survey (Schuller et al. 2009; König et al. 2017; Urquhart et al. 2017).

In Table 5.6, we provide a summary of the properties of molecular clumps and HII regions towards a small sample of selected sources (the full table is available via CDS). The sources selected for this table are those that are associated with non-Gaussian RRL profiles, which are discussed in Section 5.6. The peak velocities and linewidths for the first and second Gaussian components were obtained from fits to the stacked mm-RRLs. The distance, dust temperature (T_{dust}), bolometric luminosities (L_{bol}) of embedded ob-
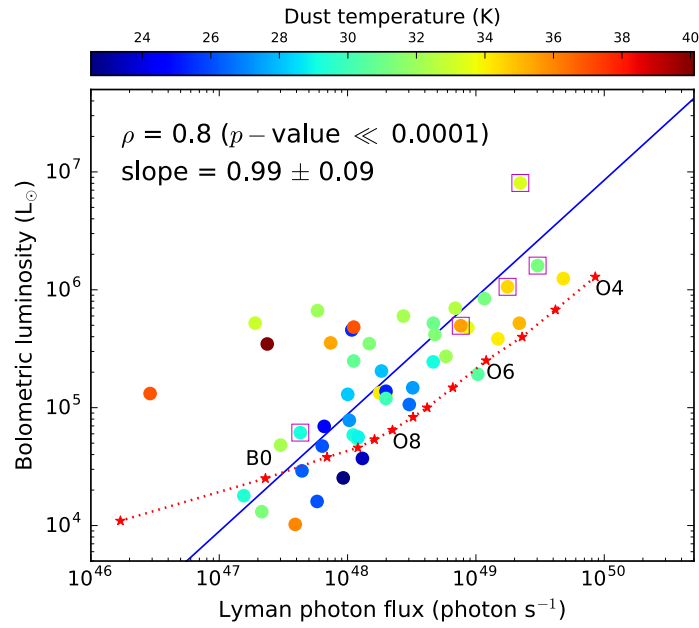
Figure 5.5: Bolometric luminosity (L_{bol}) as a function of Lyman continuum photon flux of 6 cm radio continuum emission integrated over the beam of the 3 mm observations. The colors indicate dust temperatures in the molecular clumps. The blue line shows the result of a fit to the data points using xy-bisector fitting. The purple squares superposed on the circles are particular sources with two Gaussian component RRLs (see Table 5.6 and Sect. 5.6). The red-dotted line and red stars indicate bolometric luminosity and Lyman continuum photon flux corresponding to each spectral type (O4 - B0.5) for ZAMS stars from Panagia (1973).
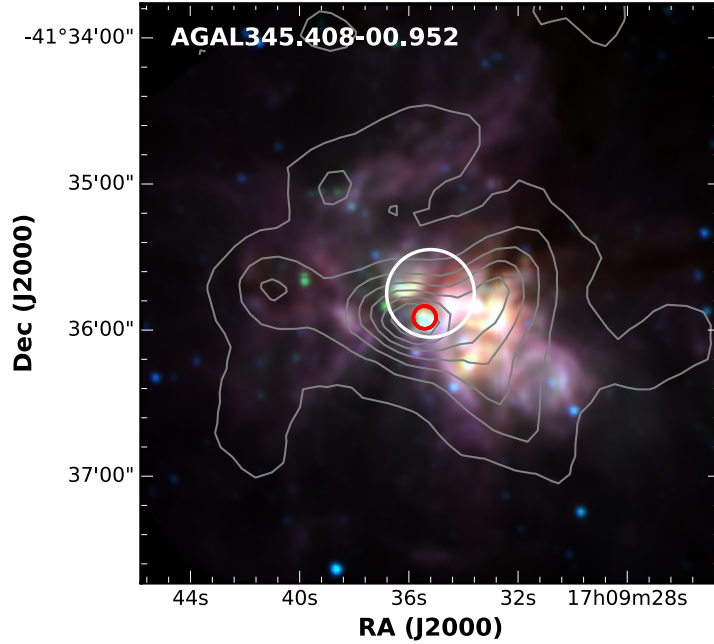
Figure 5.6:   A GLIMPSE IRAC three-color composite image (blue; $3.6\,\mu$m, green; $4.6\,\mu$m, and red; $8\,\mu$m) of one (AGAL345.408$-$00.952) of the three outliers in Fig. 5.5. The white circle indicate a size of Mopra beam (FWHM, $36''$) and the red circle presents a RMS radio continuum source (Urquhart et al. 2007). The gray contours trace the $870\,\mu$m dust continuum emission from the ATLASGAL survey.

jects, clump mass ($M_{\rm clump}$) and $L_{\rm bol}/M_{\rm clump}$ ratio are taken from Urquhart et al. (2017) and the Lyman flux is determined from the 6 cm radio continuum sources correlated with the mm-RRLs (Kim et al. 2017).

Figure 5.5 shows the relation between the Lyman continuum photon flux emitted by the embedded massive star(s) and the bolometric luminosity generated by the whole cluster of protostellar objects embedded in the molecular clumps. The distribution of bolometric luminosities is shifted above the track of the zero-age main sequence (ZAMS) luminosities for the spectral type of a single star (Panagia 1973), likely because the bolometric luminosity measured is the contribution of a whole cluster of embedded objects. Only some sources with lower luminosities lie below the ZAMS values. Lower than expected bolometric luminosities could be due to either a separation between the H II region and molecular material or leakage of UV radiation, which is responsible for the heating of dust grains, out of the dust clumps.

Except for a few outliers, we find a significant correlation between the two parameters (Spearman correlation coefficient excluding the three outliers, $\rho = 0.8$ with $p-$value $\ll 0.0001$). The correlation coefficient and the distribution show a clear correlation, but both bolometric luminosity and Lyman photon flux have a significant distance dependence. We have estimated a partial Spearman correlation ($r_{\rm AB,C}$) test of bolometric
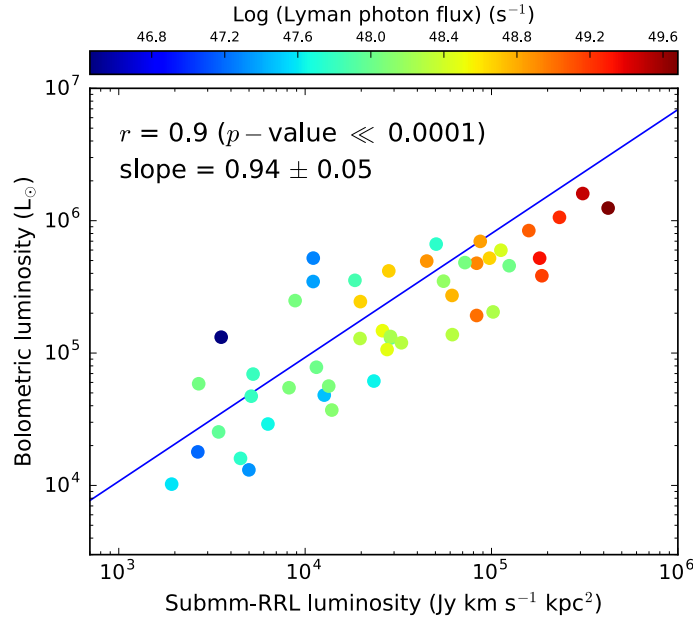
Figure 5.7: Luminosity of the submm-RRLs versus L_{bol} of embedded central objects. The color bar indicates the Lyman photon flux of ionizing stars associated with the dust clumps and the submm-RRLs. The best linear fit is presented with the blue line.

luminosity, Lyman photon flux to eliminate their distance dependence using Eq. 4. of Urquhart et al. (2013a). We obtained a partial Spearman correlation coefficient of 0.5 and Student's $t-$value of 3.8. These results of the partial Spearman correlation test also show there is a reasonable correlation between the two parameters, rejecting the null hypothesis and being independent of distance. The good correlation between the Lyman flux and the bolometric luminosity would suggest that the luminosity of the clumps is dominated by the most massive stars in the forming protocluster (cf. Urquhart et al. 2013b). The sources that are best fitted with two Gaussian components, indicated by the purple squares, tend to be the most luminous in the sample except for one (AGAL034.258+00.154). By looking at the dust temperature, we find they tend to increase with the bolometric luminosity and the Lyman photon fluxes increase, although there are some deviations from this trend. This is consistent with the feedback (radiation, outflows and strong winds) from the embedded HII regions increasing the temperature in surrounding molecular material. The increase in the dust temperature is likely to be linked to the evolutionary status of the central objects and as their luminosities increase so do the temperatures of the natal clumps.

In Figure 5.5, three outliers (AGAL010.168−00.362, AGAL331.546−00.067, AGAL345.408−00.952) significantly deviate to the left from the linear fit. These all have higher bolometric luminosities compared to the Lyman photon flux than the other sources, and we also note that two have a significantly higher dust temperature ($T_{\mathrm{dust}} \geq$
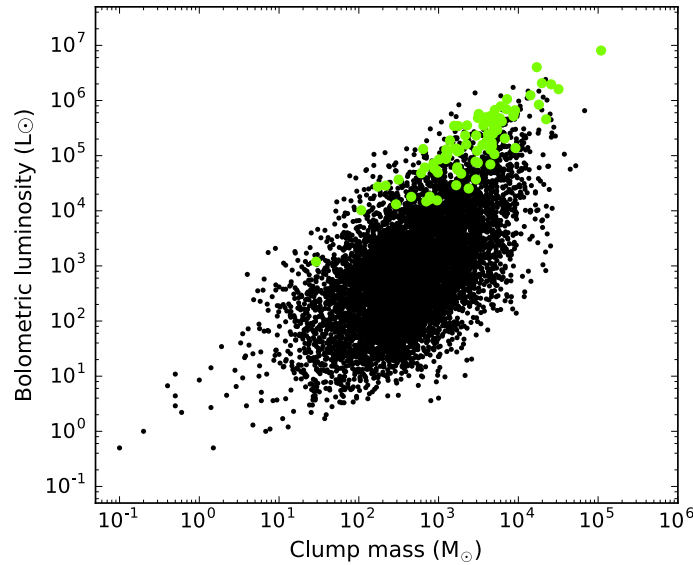
Figure 5.8: L_{bol} as a function of M_{clump} toward the full ATLASGAL sample (Urquhart et al. 2017). The bright green circles indicate sources with a submm-RRL detection.

36.5 K; AGAL010.168−00.362 and AGAL345.408−00.952). The cause of the high dust temperatures toward the outliers is likely that sizes of the radio continuum sources are much smaller than the aperture used for the infrared and submm photometry and subsequent spectral energy distribution (SED) analysis (see König et al. 2017 for details of the photometry and fitting). Indeed, inspection of the GLIMPSE IRAC three-color composite images (3.6 μm, 4.6 μm, and 8 μm) reveals that all three are associated with extended mid-infrared emission (see Figure 5.6 for example). It is also clear from these images that the bolometric luminosity is arising from an extended star formation complex while the radio emission is associated with only a small part of the complex.

Figure 5.7 presents comparisons of three parameters, the luminosity of the submm-RRLs, bolometric luminosity and Lyman photon flux toward the submm-RRL detected clumps. In addition to the strong correlation seen in Figure 5.5, the luminosity of the submm-RRLs shows pronounced correlations with the bolometric luminosity and Lyman photon flux. The Pearson (r) correlation coefficient gives a high correlation (0.9) with a small $p-$value $\ll 0.0001$. The three parameters increase altogether. It means that bright and hot stars emit stronger UV radiation and thus increase brightness of submm-RRLs and furthermore bolometric luminosity.

The good correlations between Lyman photon flux, submm-RRL, and bolometric luminosities, and the high dust temperature ($T_{\mathrm{dust}} > 24$ K) suggest that these submm-RRL sources are already quite evolved. We have plotted the clump mass as a function of the bolometric luminosity for all the ATLASGAL clumps (Urquhart et al. 2017; black dots) and the submm-RRL sources (green circles) in Figure 5.8. It is evident from this plot that the submm-RRL sources are some of the most luminous sources in the
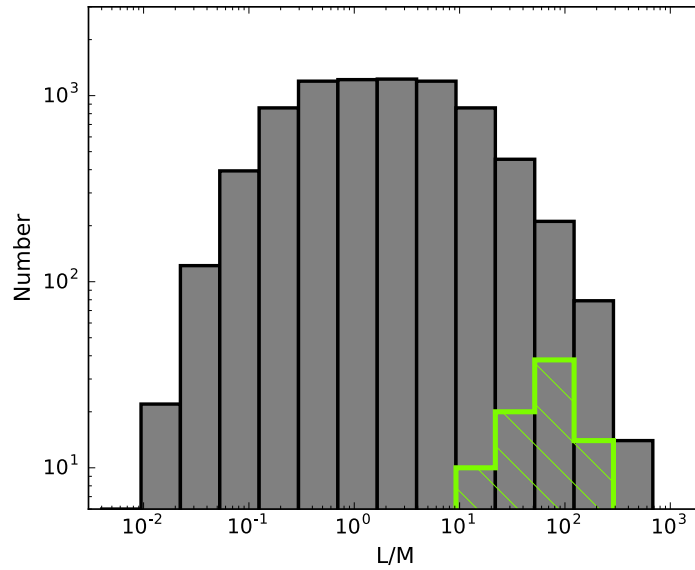
Figure 5.9: Histogram of $L_{\mathrm{bol}}/M_{\mathrm{clump}}$ for the full ATLASGAL sources (gray) and the submm-RRL sources (bright green).

whole inner-Galactic plane mapped by ATLASGAL. Figure 5.9 shows a histogram of the bolometric luminosity to clump mass ratio ($L_{\mathrm{bol}}/M_{\mathrm{clump}}$) for the full ATLASGAL sample with the distribution of the submm-RRL associated clumps over-plotted in green. The $L_{\mathrm{bol}}/M_{\mathrm{clump}}$ ratio is often used as a diagnostic for evolution (e.g., Eden et al. 2013) and shows that the submm-RRL sources are some of the most evolved young stellar objects in the Galaxy. The mm- and submm-RRLs analysis presented here and in Kim et al. (2017) have, therefore, identified and parameterized a sample of some of the most luminous and evolved compact objects in the Galaxy.

5.5 Photoionizing photon production rate, Q

If we assume the detected submm-RRL lines probe most of the photoionizing stars in clumps within the beam of APEX, it is possible to measure the photoionizing photon production rate, Q. In principle, Lyman photon flux and Q measure the same quantity: the number of emitted photons per second. The photoionizing photon production rate, Q can be obtained from the submm-RRL flux using Eq. (2.73).

   We estimated the Q value for the H28α data since this transition is detected toward a majority of the observed sources. The α_B and ε_ν for our calculations are taken from the published values by Storey & Hummer (1995). Figure 5.10 shows the relationship (black circles) between the Lyman photon flux measured by 5 GHz radio continuum emission and the estimated Q(H28α) using the α_B and ε_ν based on the chosen $T_e = 10^4\,\mathrm{K}$ and $n_e = 10^4\,\mathrm{cm}^{-3}$. The cyan and red dashed/dotted-lines present variations
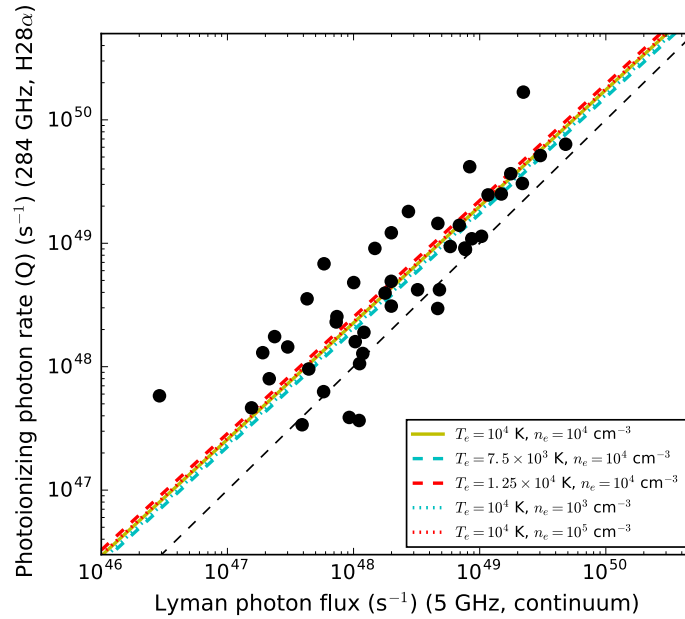
Figure 5.10: Photoionzing photon rate (Q) measured by the submm-RRLs (this chapter) as a function of Lyman photon flux estimated by $5\,\mathrm{GHz}$ radio continuum emission from CORNISH and RMS surveys (Purcell et al. 2013; Urquhart et al. 2007). Those two parameters have the same unit (s^{-1}), the number of photons per time. The equality of both axes is indicated with a black dashed-line. The color dotted- and dashed-lines present the best linear fits to the data points calculated for different electron temperature and density in Eq. (2.73). The black data points are estimated with $T_e = 10^4\,\mathrm{K}$ and $n_e = 10^4\,\mathrm{cm}^{-3}$.

of the fits resulting from Q values computed using different electron densities and temperatures ($T_e = 10^4\,\mathrm{K}$ and $n_e = 10^4\,\mathrm{cm}^{-3}$). The variations are not significant in ranges of electron density ($10^3 - 10^5\,\mathrm{cm}^{-3}$) and temperature ($7.5 \times 10^3 - 1.25 \times 10^4\,\mathrm{K}$). Their is a slight shift between the Lyman photon flux and the photoionizing rate $Q(\mathrm{H}28\alpha)$ indicating that the single dish recombination line measurement pick up more photoionizing photons than the interferometric continuum measurements which might resolve out emission. Overall, these two measurements show good agreement, and it confirms that the H28α lines are thermally excited. Furthermore, it confirms that the Q values measured by mm/submm RRLs are useful to measure star formation rates on extragalactic scales.

5.6   Sources of interest

In Section 5.2, we mentioned six sources where the RRL spectral profile deviates significantly from the expected Gaussian line shape due to the presence of excess emission
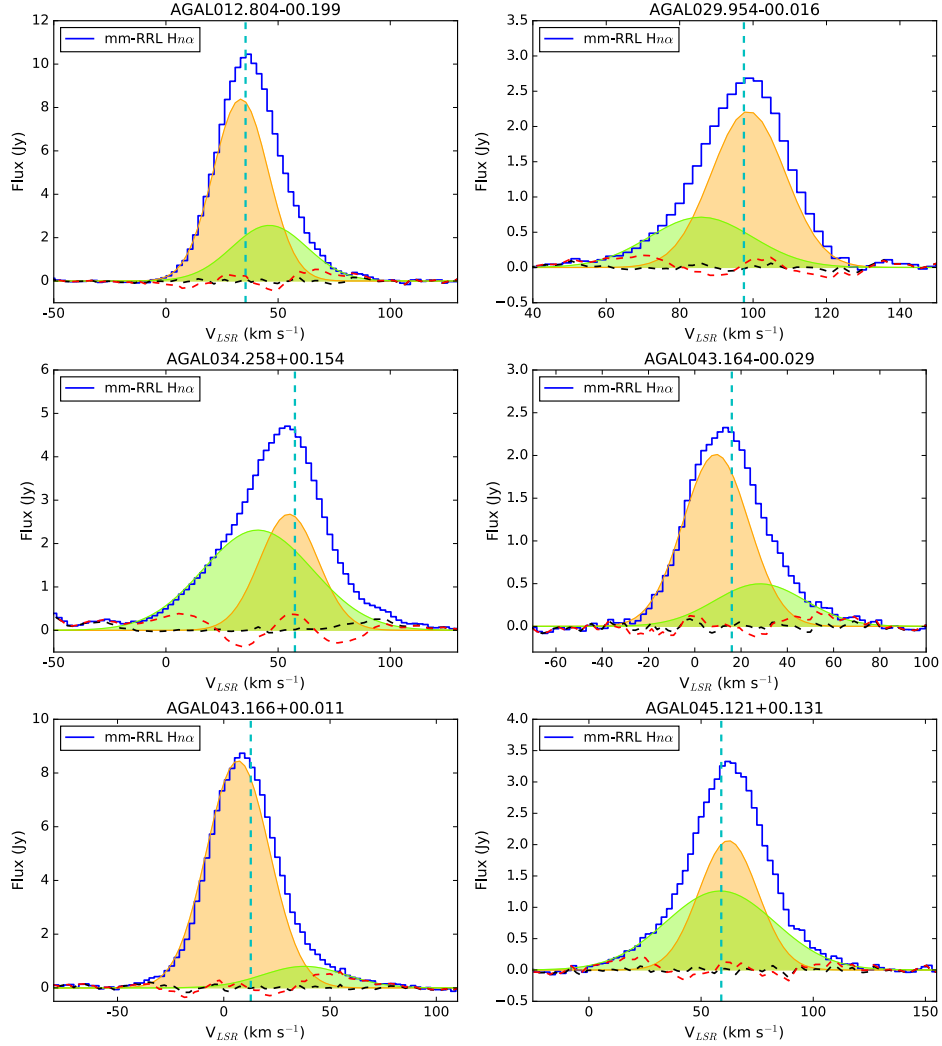
Figure 5.11: The green and yellow filled areas show two Gaussian fitted profiles of the Hnα transition. The black dashed line is a residual noise signal of the two Gaussian profiles. On the other hand, the red dashed line indicates a residual noise from a one component Gaussian fit to the data. The vertical cyan dashed line shows the systemic velocity of the clump measured by H^{13}CO$^+$ (1−0).

seen at higher velocities. We show the stacked mm-RRL spectral profiles for these sources in Figure 5.11. In all of these cases fitting a single Gaussian profile to the RRL results in large residuals. However, the large residuals can be significantly reduced using a two component fit to these data. One component is centered at the systemic velocity of the sources and a second, broader component, is fitted to the emission from the higher velocity gas. The parameters of Gaussian fits of the two components are given in Table 5.6. In this section, we have a more detailed look at these sources to understand the nature of these additional high-velocity components. Although the non-Gaussian profiles are observed in both the submm- and mm-RRLs, we have chosen to fit the mm-RRLs as they tend to have a higher S/N ratio and provide therefore more reliable results.

To facilitate the discussion of these sources we complement the spectra presented in Figure 5.11 with three-color mid-infrared images that show the local environment of these regions in Figure 5.12. It is interesting to note that all of the sources, where a high velocity component has been identified, are located in the 1st Quadrant. However, these sources were all targeted in the observing campaign with the IRAM 30 m telescope, resulting in higher sensitivity observations than the observations of southern targets with the Mopra 22 m telescope, which therefore might have missed the weaker, broader components in many other sources. We also note that three of the sources show red-shifted emission, two show blue-shifted emission, and one appears to have both blue and red-shifted components. The higher-velocity gas is likely due to either an expanding flow away from the Hıı regions (Tenorio-Tagle 1979; Tenorio Tagle et al. 1979) or bow-shock generated by wind-blowing high-mass stars moving at a supersonic velocity (van Buren et al. 1990; van Buren & Mac Low 1992) or possibly the combination of both phenomena.

5.6.1   AGAL012.804−00.199

This Hıı region is part of the W33 star forming complex, and so we have adopted a distance of 2.6 kpc to this clump (Immer et al. 2012). The radio emission consists of two distinct sources, a bipolar structure located towards the center of the clump and a more compact, roughly circular source located to the north. All of the radio emission is correlated with bright mid-infrared emission seen in the GLIMPSE image (see the upper left panel of Figure 5.12). The position of the IRAM beam is slightly offset from the peak of the bipolar radio emission, but the brightest lobe of bipolar structure falls within the FWHM beam size. However, emission from the weaker bipolar lobe and the compact source to the north are also likely to be picked up in the outer part of the beam.

The mm-RRL spectrum is shown in the upper left panel of Figure 5.11; this reveals the presence of a red wing, which might be associated with an ionized flow perhaps arising from one of the bipolar lobes. The systemic velocity of the clump is 35.4 km s^{-1} which is broadly consistent with the velocity of the strongest RRL component and so it is the weaker and broader component that is associated with the faster-moving gas. Bieging et al. (1978) also reported different velocity RRL components at low-frequency
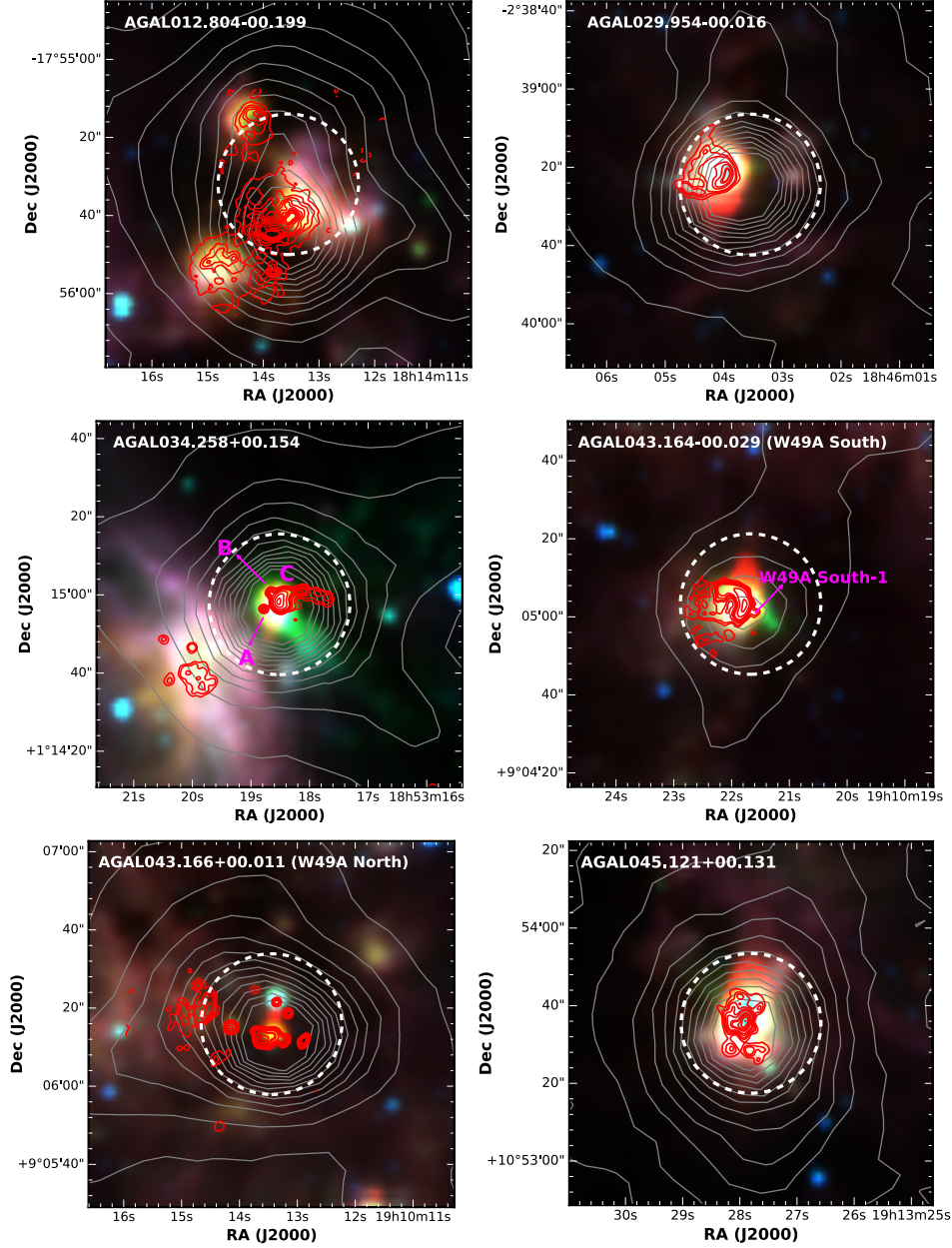
Figure 5.12: GLIMPSE IRAC three-color composite images (blue; $3.6\,\mu$m, green; $4.6\,\mu$m, and red; $8\,\mu$m). The gray contours trace the $870\,\mu$m dust continuum emission from the ATLASGAL survey. The red contours show the $5\,$GHz radio continuum emission from the CORNISH survey. The cyan dashed circles are centered on the pointing positions of the IRAM observation with FWHM of $29''$.

(1.7, 5, and 8.6 GHz) using the Effelsberg 100 m telescope. They suggested that the components with different velocities are associated with flows of ionized gas, which is consistent with our interpretation.

5.6.2   AGAL029.954−00.016

This source is associated with W43 South at a distance of 5.2 kpc (Reid et al. 2014) and has a systemic velocity of 97.2 km s^{-1}. The IRAM beam is centered on the peak of the dust emission, and the radio emission is slightly offset to the west; however, it is fully covered by the beam. The radio emission has a cometary morphology with a bright head pointing towards the center of the clump and a tail-like structure that extends away from the center of the clump into the lower-column density region. The radio emission is correlated both spatially and morphologically with the strong mid-infrared emission (see the upper middle panel of Figure 5.12). The clump has a mass of $\sim 4 \times 10^3$ M$_\odot$ and a dust temperature of 35.5 K and so feedback from the Hii region is having a significant impact on the physical properties of its host clump.

The RRL profile is shown in the upper middle panel of Figure 5.11 and reveals the presence of a high-velocity blue-shifted component; the peak of this component is offset by $\sim$15-20 km s^{-1} from the systemic velocity of the Hii region and the host clump. The high-velocity blue-shifted component corresponds to the velocity range of a Brγ line (around $70 \sim 90$ km s^{-1}) at the position of the head (Martín-Hernández et al. 2003). The linewidth of a Brγ toward the head of the Hii region is also found to be $\sim$20 km s^{-1} broader than that from the tail, but their Brγ observations could not explain it with either bow-shock nor champagne flow models. In addition, they also showed the existence of a velocity gradient toward the tail (Martín-Pintado 2002).

Zhu et al. (2008), however, showed that [Ne ii] line emission and its velocity maps toward this source well agreed with a model of stellar wind pressure-driven Hii regions with a viewing angle of 135°. In this model, the cometary morphology of the Hii region is caused by either a relatively slow motion of the star through the molecular cloud or a density gradient in the cloud (Zhu et al. 2008; Arthur & Hoare 2006). According to the model, emission line forming the ionized gas of a cometary head show a broad linewidth with a negative velocity offset concerning the velocity of molecular gas (Zhu et al. 2008). In fact, our broad RRL also has a negative velocity relative to the systemic velocity although it is not clear the broad RRL comes from the head of this source. Besides, there is a hot core in front of the UC Hii region and HCO$^+$ and SiO molecular lines (Maxia et al. 2001) show the line densities are higher toward the head than the tail. Therefore, our broader RRL component is likely to be associated with accelerated ionized gas toward the tail along the shell created by the relatively slow motion of the star through the the interstellar medium.

5.6.3   AGAL034.258+00.154

This ATLASGAL clump is associated with the G34.26+0.15 Complex. The radio emission consists of three radio continuum components; an extended source that has a

cometary morphology and two compact regions to the west and north-west; these are referred to as C, A, and B, respectively (following Sewiło et al. 2011). The clump has a mass of $\sim 1500\,M_\odot$ and dust temperature of $\sim 30\,K$. The mid-infrared image (upper right panel of Figure 5.12) reveals that this region is located at the edge of a larger HII region located to the south-west (region of extended mid-infrared emission). Besides, the morphologies of radio and mid-IR emissions are not so well correlated with each other towards this source. The reason is likely extinction (Hoare et al. 2007).

The RRL profile shows a strong blue-shifted wing and is fitted with two components with similar intensities but different linewidths. The velocity of the narrowest component corresponds to the systemic velocity of the clump, but it is offset by $\sim 15\,km\,s^{-1}$ from the velocity of the broader component. There is a possibility that some of the RRL emission is coming from the larger HII region located to the south-west given that its falls within the outer part of the IRAM beam. This complex has been observed by Sewiło et al. (2011) at higher-resolution in continuum and the H53α RRL. Their study separated the emission from the three radio sources and determined the velocity of A and C to be $\sim 50\,km\,s^{-1}$ and $\sim 65\,km\,s^{-1}$ for B. All of these are broadly consistent with the systemic velocity of the clump and the narrower RRL component. However, we note that source C has a very broad linewidth ($49\,km\,s^{-1}$) and so may be responsible for the excess seen in the IRAM RRL spectra. Jaffe & Martín-Pintado (1999) also observed 3-mm hydrogen RRLs towards this source with the IRAM 30m telescope and also reported the presence of a similar board linewidth high-velocity component, which is associated with source C.

It is currently unclear from the present data whether the blue-shifted wing seen in the IRAM spectra is the result of contamination from the nearby extended HII region or a combination of the three radio sources identified, however, the latter seems more likely. Furthermore, the cometary shape of the source C has been well explained by the bow-shock model created by wind-blowing massive stars moving at a supersonic velocity with respect to the molecular gas (van Buren et al. 1990).

5.6.4 W49A: AGAL043.164−00.029 and AGAL043.166+00.011

These two HII regions are located in the W49A star forming complex. It is located at a distance of $\sim 11\,kpc$ (Zhang et al. 2013) and is one of the two most active star formation regions in the Galaxy (Urquhart et al. 2014c). AGAL043.164−00.029 has a clump mass of $3 \times 10^4\,M_\odot$, luminosity of $1.6 \times 10^6\,L_\odot$ and systemic velocity of $14.3\,km\,s^{-1}$ while AGAL043.166+00.011 has a clump mass of $11 \times 10^4\,M_\odot$, luminosity of $8 \times 10^6\,L_\odot$ and systemic velocity of $2.9\,km\,s^{-1}$.

5.6.4.1 AGAL043.164−00.029

The radio emission associated with AGAL043.164−00.029 (lower left panel of Figure 5.12) reveals a cometary morphology that is coincident with strong mid-infrared emission; this is known as W49A South. The tail of the cometary structure extends to the west away from the peak submillimeter emission. In front of the head of the cometary

HII region, there is another very weak and compact HII region; this is referred to as W49A South-1 (De Pree et al. 1997).

The clump looks relatively isolated, so all of the RRLs likely arise from the HII regions. The velocity of the strongest RRL component is correlated with the systemic velocity of the clump. The second component is red-shifted with a velocity $12\,\mathrm{km\,s^{-1}}$ larger than the systemic velocity.

This red-shifted component is likely to be associated with high-velocity ionized gas that forms the tail, and that is expanding into the lower-density region away from the head of the cometary structure; the head itself is coincident with the highest column density part of the clump. According to the RRL results of De Pree et al. (1997), however, the velocity gradient over the cometary source and a broad linewidth toward the head supports the bow-shock model and a mass-loaded stellar wind in a molecular cloud with a density gradient, instead of the champagne flow model (De Pree et al. 1997; Zhu et al. 2008). Nevertheless, their RRL velocity resolution was too poor to allow for a detailed investigation of the velocity structure of this source.

5.6.4.2   AGAL043.166+00.011

AGAL043.166+00.011 is the most massive and active clump in the Galaxy; it is known as W49 North. It is perhaps the only example of a young massive protocluster outside of the Galactic center region (Urquhart et al. 2017). The radio emission reveals a cluster of compact sources and this has previously been identified as being associated with the highest density of embedded HII regions in the Galaxy (Urquhart et al. 2013b; De Pree et al. 1997, 2004b). There is a good correlation between the compact sources seen in the mid-infrared image (lower middle panel of Figure 5.12), however, there are few compact radio sources that do not have an infrared counterpart, perhaps due to high extinction.

The RRL spectrum reveals the presence of a relatively modest red-shifted wing that is offset by $\sim30\,\mathrm{km\,s^{-1}}$ from the systemic velocity of the clump. Jaffe & Martín-Pintado (1999) also reported a broad mm-RRL component with an offset velocity from the systemic velocity towards this source. Given the large number of compact radio sources and the poor sensitivity to extended radio emission (due to the large heliocentric distance) it is not possible to investigate the nature of the high-velocity ionized gas associated with this region. Nevertheless, the 7-mm observations by De Pree et al. (2004b) showed that the W49 North region has several broad RRL sources and these may be associated with signatures of ionized disk winds.

Table 5.7: A list of potential ALMA candidates.

| ATLASGAL name | RA α(J2000) | Dec δ(J2000) | Dist. (kpc) | RRL peak flux | | Radio continuum source | | |
				mm (Jy)	submm (Jy)	Size ($''$)	Peak flux (mJy/beam)	Morphology
AGAL010.624−00.384	18:10:28.70	−19:55:49.1	5.0	6.6	10.0	4.6	305.6	core-halo
AGAL012.804−00.199	18:14:13.96	−17:55:44.9	2.6	10.2	17.5	16.2	287.9	bipolar?
AGAL013.872+00.281	18:14:35.81	−16:45:37.2	3.9	2.2	4.8	15.4	24.7	cometary
AGAL032.797+00.191	18:50:30.95	−00:01:56.5	13.0	2.8	6.9	10.0	279.1	cometary or multi-peaks
AGAL037.874−00.399	19:01:53.59	+04:12:51.7	9.7	2.0	4.1	8.9	255.7	cometary?
AGAL043.164−00.029	19:10:22.01	+09:05:03.2	11.3	2.3	4.6	9.6	242.9	cometary
AGAL045.121+00.131	19:13:27.96	+10:53:35.7	8.0	3.2	6.9	7.5	299.7	cometary? or bipolar?
AGAL045.454+00.061	19:14:21.31	+11:09:11.7	8.4	1.4	3.7	7.6	61.8	unresolved
AGAL298.224−00.339	12:10:01.18	−62:49:54.0	11.4	...	6.6	4.1	369.9	cometary
AGAL298.859−00.437	12:15:25.27	−63:01:17.0	10.1	...	4.0	2.6	79.5	unresolved
AGAL324.201+00.121	15:32:53.21	−55:56:11.8	6.8	2.2	4.1	6.1	286.6	cometary (& unresolved)
AGAL330.954−00.182	16:09:52.54	−51:54:54.9	5.3	4.1	8.7	3.9	444.4	unresolved
AGAL332.156−00.449	16:16:40.53	−51:17:08.9	3.6	2.4	6.7	14.0	101.2	irregular
AGAL332.826−00.549	16:20:11.10	−50:53:15.4	3.6	4.9	10.9	3.4	461.6	unresolved(bipolar?)
AGAL333.284−00.387	16:21:31.70	−50:27:00.5	3.6	7.8	11.4	9.4	421.4	irregular (cometary?)
AGAL333.604−00.212	16:22:09.58	−50:05:59.6	3.6	40.8	47.5	10.6	393.6	irregular
AGAL345.649+00.009	17:06:15.99	−40:49:45.4	1.4	2.1	2.5	5.1	627.4	core-halo

Notes. The provided coordinates in here are coordinates of radio continuum sources in the ATLASGAL clumps instead of coordinates of the ATLASGAL clumps.

References. Distance: Urquhart et al. (2013a); Lumsden et al. (2013); Urquhart et al. (2017). Coordinate & radio continuum source: Purcell et al. (2013); Urquhart et al. (2007)

However, it is not clear the broader component of our RRL is related with the broad RRLs of the 7-mm observations due to different spatial and flux sensitivities between both observations.

5.6.4.3   AGAL045.121+00.131

This clump is located at a distance of 8 kpc (Reid et al. 2014) and has a systemic velocity of 58.7 km s^{-1}. The clump as a mass of $\sim$7000 M$_\odot$ and a luminosity of 1×10^6 L$_\odot$. The radio emission appears to have a bipolar structure extending to the north and south. The radio morphology is mirrored in the mid-infrared image (lower right panel of Figure 5.12). We note that discrete compact radio sources do appear in the radio emission instead of one bipolar structure and it is unclear if these indicate the presence of individual HII regions or localized enhancements in the radio emission where the ionization front is impacting on a dense structure in the molecular gas.

The RRL profile shows evidence for both red- and blue-shifted wings, although these are rather modest. The two components fitted to the RRL have similar velocities, both of which are correlated with the systemic velocity of the clump. The broader component is almost twice the linewidth of the narrow component and traces the high-velocity gas. The morphological distribution of the CORNISH continuum emission is correlated with the integrated [Ne II] line emission map presented by Zhu et al. (2008), but the [Ne II] observations did not fully resolve them. The 15.0 km s^{-1} to 92.9 km s^{-1} velocity channel maps of the [Ne II] emission to the north this emission corresponds to the most extended radio continuum and the mid-infrared source (see the lower right panel of Figure 5.12). On the other hand, the southern radio continuum emission structures correspond to the [Ne II] emission seen in the 36.2 km s^{-1} to 71.6 km s^{-1} velocity channels. Comparing the radio continuum emission with the [Ne II] velocity channel maps may indicate that the two Gaussian components do not arise from a bipolar flow, but may instead be the result of discrete radio sources sharing a similar peak velocity. High-resolution observations are required to obtain better understanding of the structure and kinematics of this region.

5.6.5   Identification of an ALMA sample

Despite many previous radio continuum observations, the morphology of many HII regions still cannot be fully explained. Studying both the kinematics of ionized gas and the geometry of HII regions provides some insight into their nature. However, the morphology and RRL profiles change with the orientation of our viewing angle and therefore detailed comparison of the observations with current theoretical models (Zhu et al. 2015; Steggles et al. 2017) are also required to help us understand the different morphologies observed.

Given that most compact HII regions detected have sizes of a few arc-second, high-resolution observations are required. Detailed studies have been previously conducted at cm-wavelengths using the VLA and ATCA (Urquhart et al. 2007, 2009; Purcell et al. 2013), however, cm-RRLs can be significantly affected by pressure broadening
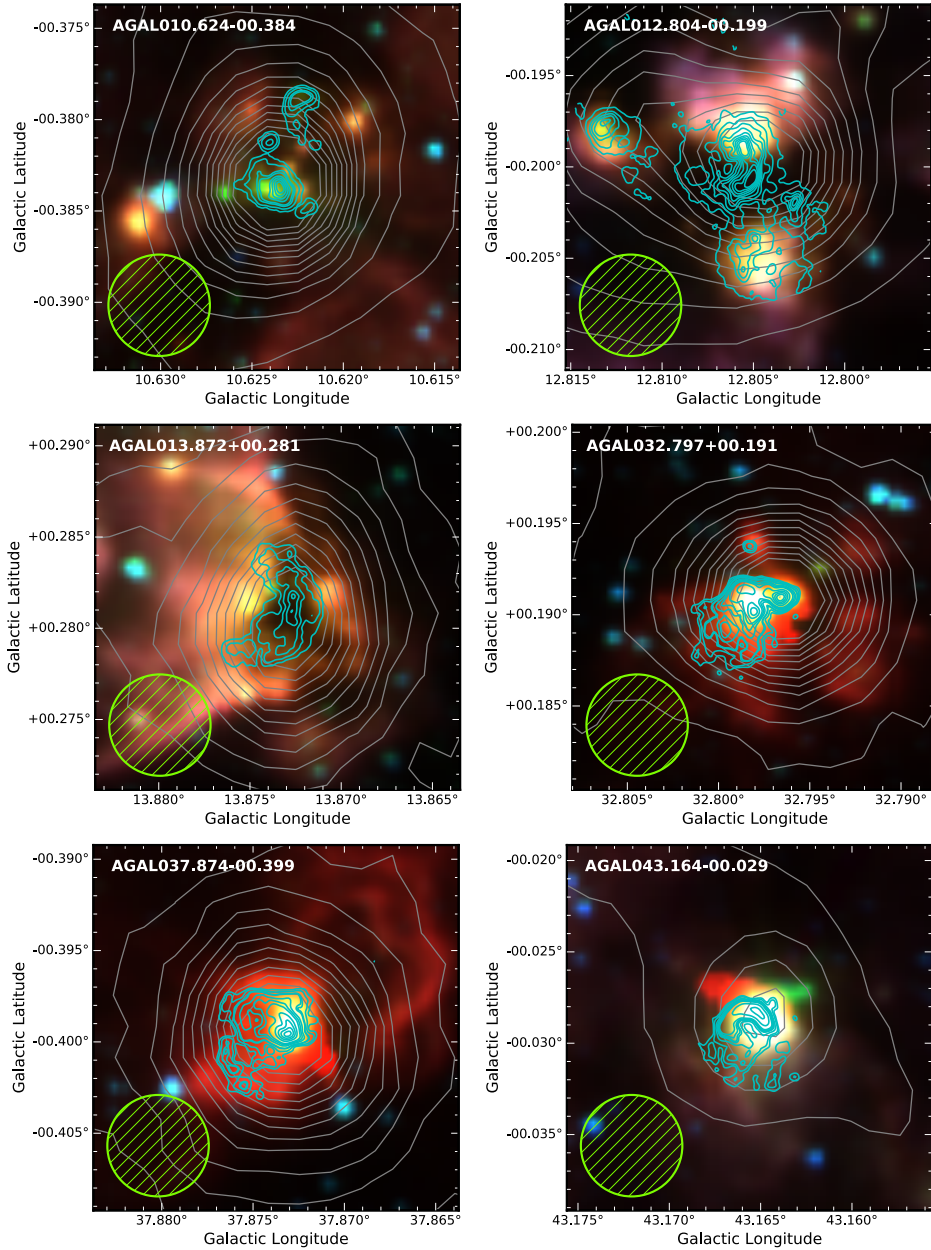
Figure 5.13: GLIMPSE IRAC three-color composite image (blue: $3.6\,\mu$m, green: $4.6\,\mu$m, and red: $8\,\mu$m). Gray contour represents $870\,\mu$m dust continuum emission from the ATLASGAL survey. Cyan and blue contour show $5\,$GHz radio continuum emission from CORNISH and RMS surveys. The arbitrary beam of $20''$ is indicated with a bright green hatched circle in the left-bottom corner.
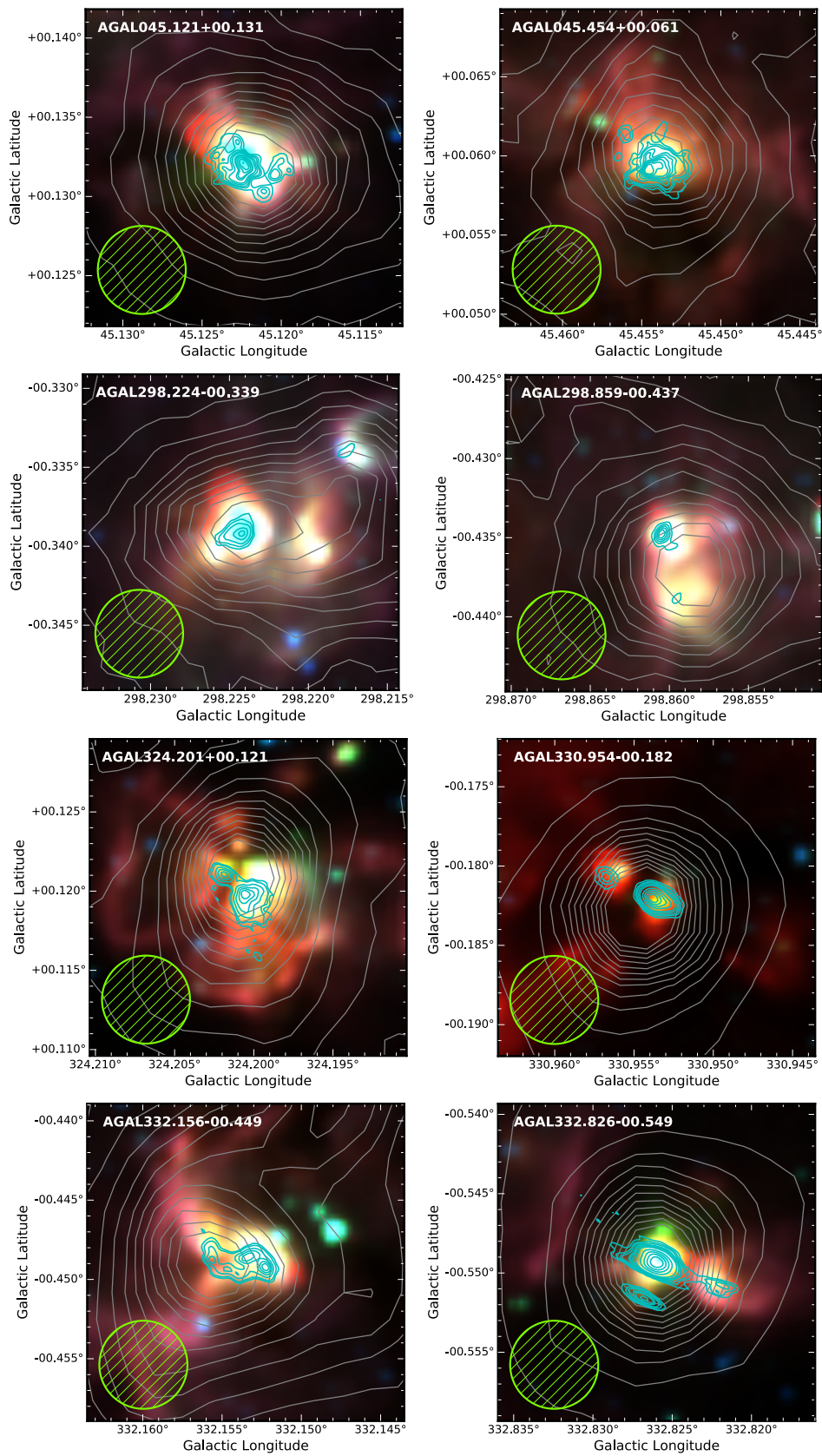
Figure 5.13: Continued.
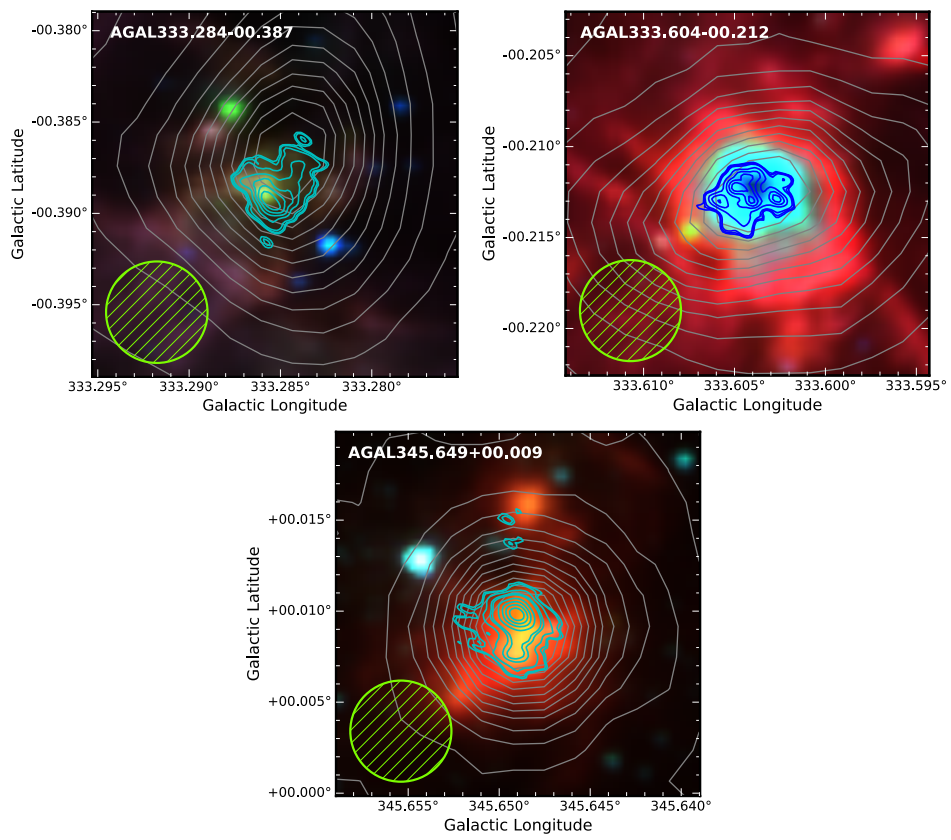
Figure 5.13: Continued.

and the HII regions can often be optically thick resulting in poorly constrained physical parameters. ALMA not only opens up the possibility to observe mm- and submm-RRLs at a similar resolution as the cm-RRLs observed by the VLA but has several additional advantages: 1) the line to continuum ratio increases with frequency and so mm- and submm-RRLs are significantly brighter than at cm-wavelengths; 2) pressure broadening is reduced and is in most cases negligible; 3) the continuum emission of the HII regions is optically thin; 4) there are many thermal molecular transitions that allow the ionized and molecular gas to be traced simultaneously and at a similar resolution.

As previously shown, our sample consists of source of the most massive clumps and most luminous HII regions in the Galaxy and with the radio continuum and mm- and submm-RRL data we can identify a well-characterized sample for follow-up with ALMA. Our selection criteria are:

1. the HII regions should be resolved at high-resolution cm-continuum wavelengths ($\sim$2-3$''$) but smaller than the ALMA primary beam at 850 μm (i.e., $<$18$''$). This ensures that we can investigate the kinematic structure of ionized gas over many beams and the source can be observed in a single pointed observation at the highest frequency.

2. the mm- and submm-RRLs should be bright and relatively isolated from contamination from thermal lines, which can be a significant issue at submillimeter wavelengths.

3. the HII regions should be relatively isolated from nearby evolved HII region which might contribute emission through the side-lobes and make imaging difficult.

Applying these criteria to the sample discussed in this chapter we have identified 17 candidates for further detailed studies with ALMA (see Table 5.7 and Figure 5.13). We excluded several sources which satisfied criteria 2 and 3 above since good quality radio continuum data is not available for them. In Table 5.7 we provide the coordinates of 6 cm radio sources instead of the ATLASGAL dust clumps. Our list of potential ALMA candidates covers radio continuum sources with various radio properties and morphologies. The cometary morphology is the most common in the list, but there is some uncertainty in their morphological classification due to limited sensitivity to angular scales.

These selected sources have clean RRLs profiles at both submm/mm-wavelengths, and thus both wavelengths can be used for observations. Given that the HII regions are optically thin means that both mm- and submm-observations are equally able to probe the properties of the ionized gas. As seen in Table 5.7, their submm-RRLs show brighter peak fluxes than their mm-RRLs. In fact, the line to continuum ratio at submm-wavelengths is a factor of two better at mm-wavelengths (see the lower panel

of Figure 5.4, and figures 3 and 4 in Peters et al. 2012). Observations at submm-wavelengths will also have a factor of 3 higher resolution compared to mm observations for the same configuration, however, the primary beam is also 3 times smaller, and so mm-observations may be more suitable for more extended HII regions. The choice of what frequency to observe a particular source can, therefore, be tailored to ensure the region can be covered in a single pointing and that the same physical scales are probed (i.e., mm-wavelengths for near by and extended HII regions and submm-wavelengths for more distant and compact HII regions).

5.7   Summary and conclusions

We present the results of a set of targeted submillimeter RRL observations of 104 compact HII regions previously identified by Kim et al. (2017). We have observed the H25α, H27α, H28α, H29α and H30α and H35β RRL transitions. The detection rates for the H$n\alpha$ and H$n\beta$ transitions are 89% (93) and 40% (34), respectively. These have been compared with the mm-recombination lines reported by Kim et al. (2017) to investigate the physical properties of the ionized gas and its local environment.

We find that the submm-RRLs are approximately a factor of 2 brighter than the mm-RRLs, which is consistent with LTE and that the RRL line emission from the HII regions is optically thin. We also find a strong correlation between the velocities of the molecular gas and the ionized gas of the HII region still being embedded in their host cloud.

We find a significant correlation between the bolometric luminosity of the embedded clusters in their dust clumps and the ionizing photon flux producing by the stars. This indicates that the stars of the HII regions provide the majority of the clumps luminosity. We also find a trend for increasing dust temperature with the bolometric luminosity consistent with the feedback from the embedded HII regions on its natal environment. Besides, the luminosity of the submm-RRLs presents robust correlations with both bolometric luminosity and Lyman photon flux. Comparing the physical properties of the HII regions and their host clumps to the general population of dust clumps located in the inner-Galaxy, we find the clumps with the submm-RRL detections to be some of the most massive and luminous in the Galaxy.

We used the submm-RRL flux to measure the photoionizing production rate, Q, which corresponds to the Lyman photon flux. The measured Q(H28α) values for H28α lines are consistent with the Lyman photon flux measured from 5 GHz radio continuum emission. This confirms the Q as a tool for measuring star formation rates (SFRs) using submm-RRL observations in external galaxies, without the problems of dust obscuration and influences of evolved star and synchrotron emission to continuum fluxes, encountered by other methods to measure SFRs.

A single Gaussian component well describes the profiles of the majority of RRLs. However, we have identified six HII regions where the spectral profiles show the presence of red and/or blue-shifted wings. These wings reveal the presence of a high-velocity component in the ionized gas. We investigate these sources in detail and find that the

data towards four Hɪɪ regions are consistent with the presence of high-velocity flows associated with the head of cometary or bipolar Hɪɪ regions. The other two clumps are associated with clusters of compact Hɪɪ regions, and so the observed RRL profiles may result from the blending of the emission from several Hɪɪ regions. Higher-resolution observations are required to study the kinematics and physical properties of all of the regions in detail and to disentangle their morphology and long lifetime (about 10^5 years).

Finally, we identify a sample of submm-RRL sources that would be suitable for high-resolution follow-up observations with ALMA. For the potential ALMA candidates, 17 Hɪɪ regions with mm/submm-RRL detections are selected with following criteria: appropriate sizes for the ALMA beam; bright mm/submm-RRLs with no contamination by molecular lines; relatively isolated location of the Hɪɪ regions from nearby evolved Hɪɪ regions.

Molecular line survey of photodissociation regions

Contents

6.1 Introduction

Newly born high-mass stars immensely affect their environment in various ways (i.e., powerful outflows, UV radiation, stellar winds). Especially due to their intense UV

radiation, the surrounding molecular gas is ionized and dissociated. As a result, transition layers (called photodissociation regions; PDRs) are formed between the ionized and cold neutral gas shielded from UV radiation (Tielens & Hollenbach 1985; Tielens 2013). Such PDRs are found in various astrophysical environments at different spatial scales from the illuminated surfaces of protoplanetary disks (e.g., Agúndez et al. 2008) to starburst galaxies and others (e.g., M82; García-Burillo et al. 2002; Fuente et al. 2005 and IC342; Meier & Turner 2005). The chemistry in PDRs is induced by UV photochemistry that determines the thermal and ionization balance in PDRs (Pilleri et al. 2013). Furthermore, many factors (e.g., the strength of UV radiation, the volume density of H_2, turbulence) control the formation and destruction of molecules leading to complex chemistry in PDRs.

So far, most detailed studies of PDRs have focused on nearby regions (e.g., the Horsehead Nebular and the Orion Bar; Cuadrado et al. 2015; Gerin et al. 2009; Teyssier et al. 2004; Rodriguez-Franco et al. 1998; Pety et al. 2005). Some observations have indicated the presence of dense PDRs between the ionized and neutral gas in the Orion Bar and Mon R2 (Rodriguez-Franco et al. 1998; Rizzo et al. 2005). From the detailed molecular excitation studies toward the Orion Bar, the PDR layer consists of at least two components (Hogerheijde et al. 1995; Jansen et al. 1995): low density interclump medium ($n(H_2) \approx 3 \times 10^4 \, \mathrm{cm}^{-3}$) surrounding high density clumps ($n(H_2) \approx 1 \times 10^6 \, \mathrm{cm}^{-3}$) which comprise $\approx 10\%$ of the material in this PDRs. Especially toward Mon R2, high H_2 densities ($> 4 \times 10^6 \mathrm{cm}^{-3}$) were found in its PDR. Mon R2 is the only well-studied source that has PDRs and a UC H_II (Rizzo et al. 2005; Ginard et al. 2012; Pilleri et al. 2013). Its PDRs are illuminated by high UV radiation ($G_0 = 5 \times 10^5$ in units of Habing field; Rizzo et al. 2003) and have a small physical size ($\lesssim 0.1 \, \mathrm{pc}$). Such PDRs surrounding compact H_II or UC H_II regions in molecular clumps have different conditions from the PDRs in the Horsehead nebula. Furthermore, their high densities suggest that the UC H_II region could be pressure-confined by the surrounding high-density molecular gas. The observations toward Mon R2 provided a good understanding of a particular dense PDR illuminated by UV radiation from high-mass stars inside molecular clouds.

To study dense and high UV irradiated PDRs in different conditions, we need a comprehensive sample that is not biased by evolutionary stage and observed molecular species. In general, these PDRs occur in very complex star-forming regions still embedded in their parent molecular clouds. Therefore, it is critical to find molecular tracers whose abundance is primarily driven by PDR chemistry. IR diagnostics (e.g., PAH emission at infrared wavelengths) can give information about PDRs, but they are not easily accessible in the presence of high extinction. Molecular lines also offer additional information on the velocity fields that allow us to investigate turbulence in PDRs. Several molecules are linked to UV photochemistry and can be good tracers of PDRs. Rizzo et al. (2005) identified two groups of molecules as PDR tracers: the first group is related to the surface layers of the PDR (visual extinction $2 \, \mathrm{mag} < A_V < 5 \, \mathrm{mag}$) that are exposed to a high UV field (referred as high UV or HUV). Molecular species in this group are reactive ions (e.g., CO^+ and HOC^+) and small hydrocarbons (e.g., C_2H and c-C_3H_2) (Sternberg & Dalgarno 1995). A second group is found deeper in the PDR

(5 mag $< A_V <$ 10 mag) where they are less exposed to the UV field referred as FUV (i.e., low UV) (Rizzo et al. 2005; Schilke et al. 2001). Radical molecules (e.g., HCO and CN) are considered to belong to this group.

In our previous studies using hydrogen RRLs at (sub)millimeter wavelengths (Kim et al. 2017; Kim et al. submitted; Chapters 4 and 5), we identified HII regions within the observed 976 compact dust clumps (from the ATLASGAL compact source catalogues) using the IRAM 30 m and Mopra 22 m telescopes. We also found radio continuum sources without mm-RRLs. The clumps with RRL detections are associated with stronger UV fields from mostly O-stars, while the clumps with only radio continuum association have weaker UV fields provided by B-stars. Besides, many of the remaining clumps without those signposts have embedded MYSOs that provide even weaker radiation fields. This less energetic radiation cannot ionize hydrogen, but carbon and oxygen atoms, and it can dissociate some molecules. Moreover, finally, some of the clumps (infrared dark clumps) without embedded objects can be affected by cosmic-ray radiation from outside the clumps. Therefore, this sample allows us to investigate PDRs produced by a range of UV radiation strength and physical conditions.

In this chapter, we will use the subsample of dust clumps that were observed with the IRAM 30 m telescope. The observations covered various molecular species by their rotational transitions in the 3 mm wavelength band. Based on previous studies, we selected 8 molecules (HCO, HOC$^+$, C$_2$H, c-C$_3$H$_2$, H^{13}CN, HC^{15}N, HN^{13}C and CN) that are regarded as typical PDR tracers. C^{18}O and H^{13}CO$^+$ were also chosen as general probes of column density and dense gas.

The line selection will be described in Section 6.2. The observations, source type, and data reduction are explained in Section 6.3. The general description of the detected molecular lines and detection rates are presented in Section 6.4, including a description of several sources with CN self-absorption line profile. The measured column density and abundance of the selected molecules and the comparisons of the column densities with the properties of the dust clumps are presented in Sections 6.5 and 6.6. Column density ratios of some of the selected molecular lines (HCO, H^{13}CO$^+$, C$_2$H, and c-C$_3$H$_2$) and their correlations are discussed in Section 6.7. Shortly, we address potential uncertainties in the observed measures in Section 6.8. Lastly, we summarize our main results in Section 6.9.

6.2   Line selection

For our study, we selected 10 molecular species: C^{18}O, H^{13}CO$^+$, HCO, HOC$^+$, CN, C$_2$H, c-C$_3$H$_2$, H^{13}CN, HC^{15}N and HN^{13}C. Rare isotope lines of HCO$^+$, HCN, HNC were chosen to avoid optical depth effects. Information about the selected molecular transition are given in Table 6.1.

C^{18}O: as a rare isotope of carbon monoxide, C^{18}O is a good tracer of the column density toward star-forming regions. It is chemically relatively stable although in very cold regions it can be affected by depletion of CO on dust grain. C^{18}O is used as a ref-

erence molecule to measure the relative abundances of the other molecules in this thesis.

$H^{13}CO^+$, HCO and HOC$^+$: Formylium, $H^{13}CO^+$, is a rare isotopologue of HCO^+ and its lines are mostly optically thin. HCO^+ is a high-density tracer ($\sim 10^5 \, cm^{-3}$), which shows enhanced abundances in regions of higher fractional ionization and toward outflows where shock-generated radiation fields are present (Rawlings et al. 2000). $H^{13}CO^+$ is a linear molecule, but it has six hyperfine components. However, these hyperfine components are very close to each other and in high-mass star-forming regions broad lines are not resolved.

The Formyl radical, HCO, is a triatomic asymmetric-top molecule with an unpaired electron. Although it has a-type and b-type transitions, a-type transitions are more easily detectable due to their stronger dipole moment (1.36 Debye; Landsberg et al. 1977). Previously, HCO has been studied in PDRs toward the Orion Bar, Horsehead nebula, and even the starburst galaxy M82 (Gerin et al. 2009; García-Burillo et al. 2002). Its emission strongly correlates with the PAH and C_2H emission in the Horsehead nebula, and its abundance reaches ($\simeq 1 - 2 \times 10^{-9}$) with respect to H_2 (Gerin et al. 2009). In addition, the column density ratio of $HCO/H^{13}CO^+$ in the PDRs of the H II regions from other studies (Gerin et al. 2009; Schenewerk et al. 1988; Schilke et al. 2001) showed higher values than ratios from other regions without H II regions or any other signpost of star formation.

Hydroxy methylidyne, HOC$^+$, is a reactive ion species and is almost exclusively related to regions with a high ionizing flux (either PDRs or X-ray-dominated regions, Fuente et al. 2003; Rizzo et al. 2003, 2005). However, there are not many **reported** detections of this rare molecule. Toward the UC H II of Mon R2, HOC$^+$ has been detected with the other reactive ion CO$^+$ (Rizzo et al. 2003).

C_2H and c-C_3H_2: The Ethynyl radical, C_2H, and Cyclopropynylidyne, c-C_3H_2, are small hydrocarbon species and are well known to be associated with PAH molecules (Rizzo et al. 2005). These small hydrocarbons are found in PDRs with enhanced abundances related to the presence of intense UV fields (Fuente et al. 2003, 2005; Teyssier et al. 2004; Pety et al. 2005; Ginard et al. 2012; Rizzo et al. 2005). Their spatial distribution is reasonably matched with PAH emission but is slightly different in extent (Pilleri et al. 2013; Cuadrado et al. 2015). In the PDRs of Mon R2 and the Orion Bar, the abundance of C_2H is constant in a broad range of incident UV radiation, but the abundance of c-C_3H_2 appeared high in low UV PDRs (Cuadrado et al. 2015). In addition, C_2H shows higher column densities in high-UV irradiated PDRs, whereas column densities of c-C_3H_2 is predicted to decrease for such PDRs (Cuadrado et al. 2015).

Table 6.1: The transitions of the observed molecules. (†) S_{ij} is the line strength taken from the JPL and CDMS catalogs. (b) Expected relative intensities $(S_{ij}/\sum S_{ij})$, assuming that lines are optically thin ($\tau_\nu < 1$). The sum of relative intensities of the hyperfine lines is normalized to 1.

Group	Species	Transition	Frequency [MHz]	g_u	E_{up} [K]	μ [Debye]	$S_{ij}^\dagger$	Relative I^b	A_{ij} [s^{-1}]
C-O	C^{18}O	$J = 1 - 0$	109782.173	3.0	5.3	0.11	1.000		6.27×10^{-8}
	HCO	$N_{K_-,K_+} = 1_{0,1} - 0_{0,0}, J = 3/2 - 1/2, F = 2 - 1$	86670.760	5.0	4.2	1.36	1.666	0.421	4.69×10^{-6}
	HCO	$N_{K_-,K_+} = 1_{0,1} - 0_{0,0}, J = 3/2 - 1/2, F = 1 - 0$	86708.360	3.0	4.2		0.979	0.247	4.60×10^{-6}
	HCO	$N_{K_-,K_+} = 1_{0,1} - 0_{0,0}, J = 1/2 - 1/2, F = 1 - 1$	86777.460	3.0	4.2		0.979	0.247	4.61×10^{-6}
	HCO	$N_{K_-,K_+} = 1_{0,1} - 0_{0,0}, J = 1/2 - 1/2, F = 0 - 1$	86805.780	1.0	4.2		0.333	0.084	4.71×10^{-6}
Ions	H^{13}CO$^+$	$J = 1 - 0$	86754.288	3.0	4.2	3.90	1.000		3.85×10^{-5}
	HOC$^+$	$J = 1 - 0$	89487.414	3.0	4.3	2.77	3.400		7.20×10^{-5}
C-H	C$_2$H	$N = 1 - 0, J = 3/2 - 1/2, F = 1 - 1$	87284.156	3.0	4.2	0.77	0.170	0.043	2.81×10^{-7}
	C$_2$H	$N = 1 - 0, J = 3/2 - 1/2, F = 2 - 1$	87316.925	5.0	4.2		1.667	0.417	1.65×10^{-6}
	C$_2$H	$N = 1 - 0, J = 3/2 - 1/2, F = 1 - 0$	87328.624	3.0	4.2		0.830	0.208	1.37×10^{-6}
	C$_2$H	$N = 1 - 0, J = 1/2 - 1/2, F = 1 - 1$	87402.004	3.0	4.2		0.830	0.208	1.38×10^{-6}
	C$_2$H	$N = 1 - 0, J = 1/2 - 1/2, F = 0 - 1$	87407.165	1.0	4.2		0.333	0.083	1.66×10^{-6}
	C$_2$H	$N = 1 - 0, J = 1/2 - 1/2, F = 1 - 0$	87446.512	3.0	4.2		0.170	0.043	2.82×10^{-7}
	c-C$_3$H$_2$	$J_{K_a,K_c} = 2_{1,2} - 1_{0,1}$	85338.894	15.0	6.4	3.27	4.503		2.32×10^{-5}
N	H^{13}CN	$J = 1 - 0, F = 1 - 1$	86338.767	3.0	4.1	2.99	1.067	0.333	2.22×10^{-5}
	H^{13}CN	$J = 1 - 0, F = 2 - 1$	86340.184	5.0	4.1		1.778	0.555	2.22×10^{-5}
	H^{13}CN	$J = 1 - 0, F = 0 - 1$	86342.274	1.0	4.1		0.356	0.111	2.22×10^{-5}
	HC^{15}N	$J = 1 - 0$	86054.966	3.0	4.1	2.99	1.000		2.20×10^{-5}
	HN^{13}C	$J = 1 - 0$	87090.850	3.0	4.2	2.70	1.000		1.87×10^{-5}
	CN	$N = 1 - 0, J = 1/2 - 1/2, F = 1/2 - 1/2$	113123.370	2.0	5.4	1.45	0.073	0.037	1.29×10^{-6}
	CN	$N = 1 - 0, J = 1/2 - 1/2, F = 1/2 - 3/2$	113144.157	2.0	5.4		0.594	0.297	1.05×10^{-5}
	CN	$N = 1 - 0, J = 1/2 - 1/2, F = 3/2 - 1/2$	113170.492	4.0	5.4		0.580	0.290	5.15×10^{-6}
	CN	$N = 1 - 0, J = 1/2 - 1/2, F = 3/2 - 3/2$	113191.279	4.0	5.4		0.753	0.377	6.68×10^{-6}

HN^{13}C, H^{13}CN (HC^{15}N), and CN: Hydrogen cyanide, HCN, and hydrogen isocyanide, HNC, are used as tracers of dense gas within molecular clouds (e.g., Vasyunina et al. 2011). The column density ratio HCN/HNC significantly depends on the temperature of the cloud as has been found in the Orion molecular cloud and several high-mass star-forming regions (Goldsmith et al. 1986; Schilke et al. 1992; Jin et al. 2015).

Cyanide Radical, CN, at millimeter wavelengths is popularly used as a probe of dense gas and PDRs in the Galactic ISM (Rodriguez-Franco et al. 1998; Boger & Sternberg 2005). Previous observational and theoretical studies showed that CN abundances are enhanced in PDRs (Fuente et al. 1993; Rodriguez-Franco et al. 1998). In particular, the observations toward the Orion Bar PDRs (Jansen et al. 1995; Rodriguez-Franco et al. 1998) showed that the CN emission is located between the molecular ridge and the ionization fronts. Rodriguez-Franco et al. (1998) suggested that the CN emission arises from a thin ($\sim 1.2 \times 10^{15}$ cm), dense ($> 6 \times 10^6$ cm^{-3}) layer in the Orion Bar. These authors proposed that the molecular region traced by CN has been compressed by the expansion of the H$\textsc{ii}$ region. CN and HCN are also used to study PDRs in Galactic high-mass star-forming regions (Boger & Sternberg 2005 and therein) and external galaxies (e.g., M82) (Fuente et al. 2005; Meier & Turner 2005). The CN/HCN intensity ratios were found to be largest near FUV radiation fields which are behind extreme UV radiation fields.

6.3 Observations, source type, and data reduction

6.3.1 Observations and source type

The molecular line data were taken from unbiased spectral line surveys covering a frequency range of $\sim$84$-$115 GHz (see Csengeri et al. 2016 for details). They contain many molecular lines from different rotational energy levels. The line surveys were observed with the EMIR receiver of the IRAM 30 m telescope (Project IR: 181-10 and 037-12) toward 409 clumps selected from the ATLASGAL compact source catalog. The original velocity resolution of these spectral line data is ~ 0.5 km s^{-1}. The largest beam size in the 3 mm atmospheric window is $\sim$29$''$. We applied the forward efficiency ($\eta_l = 0.95$) and the main-beam efficiency ($\eta_{\mathrm{MB}} = 0.81$) to convert T_a^* to T_{MB}.

Here, we divide the whole sample into two groups according to the presence of H$\textsc{ii}$ regions based on detection of mm-RRL and radio continuum emission from previous large radio continuum surveys (see Chapter 4 for details). Table 6.2 displays information about the observed sources and the clump classification from Urquhart et al. (2017). This classification is used to further divided the group of non-H$\textsc{ii}$ region sources into IR-bright non-H$\textsc{ii}$ and IR-dark non-H$\textsc{ii}$ regions.

Table 6.2: List of observed sources. This table is a part of the whole list of the observed sources. Full table will be provided in Table B.1

ATLASGAL name	RA. α(J2000)	Dec. δ(J2000)	Dist. (kpc)	T_{dust} (K)	Type	Classification†	Comments
AGAL006.216−00.609	18:02:02.9	−23:53:13	3.0	14.6	non-HII	24 dark	
AGAL008.049−00.242	18:04:35.2	−22:06:40	10.9	18.2	non-HII	IR bright or HII	
AGAL008.671−00.356	18:06:19.0	−21:37:28	4.4	25.9	HII	IR bright or HII	no $C^{18}O$, CN, $H^{13}CN$, $HC^{15}N$ data
AGAL008.684−00.367	18:06:23.0	−21:37:11	4.4	24.5	non-HII	24 dark	no C_2H data
AGAL008.706−00.414	18:06:36.6	−21:37:16	4.4	11.9	non-HII	IR bright or HII	
AGAL010.079−00.196	18:08:38.5	−20:18:56	3.5	19.8	non-HII	IR bright or HII	
AGAL010.104−00.416	18:09:31.7	−20:23:58	3.5	20.0	non-HII	24 dark	
AGAL010.151−00.344	18:09:21.2	−20:19:28	3.5	38.6	HII	IR bright or HII	
AGAL010.168−00.362	18:09:26.7	−20:19:03	3.5	40.1	HII	IR bright or HII	
AGAL010.213−00.322	18:09:24.3	−20:15:39	3.5	25.5	non-HII	IR bright or HII	
AGAL010.214−00.306	18:09:20.4	−20:15:02	3.5	19.1	non-HII	70 dark	
AGAL010.284−00.114	18:08:46.6	−20:05:52	3.5	19.3	non-HII	IR bright or HII	
AGAL010.288−00.124	18:08:48.2	−20:05:54	3.5	25.7	non-HII	IR bright or HII	
AGAL010.321−00.231	18:09:17.3	−20:07:14	3.0	22.0	non-HII	IR bright or HII	
AGAL010.323−00.161	18:09:01.4	−20:05:12	3.5	32.1	HII	IR bright or HII	
AGAL010.342−00.142	18:09:00.0	−20:03:36	3.5	26.3	non-HII	IR bright or HII	
AGAL010.444−00.017	18:08:44.7	−19:54:33	8.5	20.0	non-HII	24 dark	
AGAL010.472+00.027	18:08:37.9	−19:51:48	8.5	25.1	HII	IR bright or HII	no C_2H data
AGAL010.579−00.349	18:10:15.1	−19:57:12	5.0	20.6	non-HII	IR bright or HII	
AGAL010.618−00.031	18:09:08.5	−19:45:55	8.5	16.6	non-HII	IR bright or HII	
AGAL010.619−00.422	18:10:36.8	−19:57:01	5.0	17.4	non-HII	70 dark	
AGAL010.624−00.384	18:10:28.6	−19:55:46	5.0	31.0	HII	IR bright or HII	
AGAL010.626−00.337	18:10:18.5	−19:54:17	5.0	22.9	non-HII	IR bright or HII	

($\dagger$) The classification is defined by Urquhart et al. (2017).

6.3.2   Data reduction

For the reduction of the molecular line data, we utilized the CLASS software of the GILDAS package. Since this molecular line survey was conducted without the bias of any specific lines, we needed to identify the selected molecular lines with WEEDS of the CLASS software.

A polynomial baseline of order 1 to 3 was subtracted within a velocity range of $250\,\mathrm{km\,s^{-1}}$ width. Exceptionally, we subtracted the polynomial baseline for C_2H ($N = 1 - 0$) within a velocity range of a $600\,\mathrm{km\,s^{-1}}$ width to cover all six hyperfine lines at once. The hyperfine structures of the C_2H ($N = 1 - 0$) and $H^{13}CN$ ($J = 1 - 0$) transitions were fitted with the hyperfine structure (HFS) fit method[1] of the CLASS software. The HFS fit method assumes that all hyperfine components share a single excitation temperature and that local thermodynamic equilibrium (LTE) is valid. The HFS fit yields the radial velocity (v_{LSR}), the line width (Δv) at the full-width of half maximum, and the total opacity (τ_{tot}). The HFS fit also determines the intrinsic linewidth. The obtained total opacity is not that of an individual component since the HFS relative intensities were normalized to 1.

To obtain the opacity of an individual component, the relative intensity, r_i, in Table 6.1 should be applied to the total opacity as $\tau_i = \tau_{\mathrm{tot}} r_i$ where i indicates the selected ith component. The estimated opacity can be used to derive the peak intensity ($T_{\mathrm{MB},i}$) of the ith component. The line parameters of the other molecular lines were fitted with multi-Gaussian components if one Gaussian fit was insufficient.

Table 6.3: The line parameters of hyperfine lines of C_2H ($N = 1 - 0$) and $H^{13}CN$ ($J = 1 - 0$). We only provide here the first ten of the whole table which is provided in Table B.2. T_{MB} is the peak intensity of the brightest component of a given molecular hyperfine lines. The listed C_2H peak intensity indicates the transition $NJF = 1(3/2)2 - 0(1/2)1$, and the peak intensity of $H^{13}CN$ is the transition $JF = 12 - 01$.

ATLASGAL name	Line	v_{LSR} $(\mathrm{km\,s^{-1}})$	Δv $(\mathrm{km\,s^{-1}})$	τ_{tot}	T_{MB} (K)	rms (K)
AGAL008.671−00.356	C_2H	35.03±0.02	4.39±0.05	2.09±0.12	3.14	0.06
AGAL010.151−00.344	C_2H	9.55±0.01	5.10±0.02	0.54±0.03	2.44	0.04
	$H^{13}CN$	9.70±0.16	4.93±0.37	3.05±0.64	0.43	0.04
AGAL010.168−00.362	C_2H	14.30±0.03	6.50±0.07	1.04±0.13	1.78	0.04
	$H^{13}CN$	14.02±0.09	5.86±0.31	0.84±0.35	0.68	0.04
AGAL010.323−00.161	C_2H	12.31±0.02	3.20±0.04	0.10±0.01	1.43	0.05
	$H^{13}CN$	12.23±0.05	3.14±0.10	0.10±0.55	1.00	0.05
AGAL010.624−00.384	C_2H	-2.90±0.01	5.60±0.04	1.60±0.10	4.22	0.06
	$H^{13}CN$	-4.06±0.01	7.16±0.02	0.10±0.00	1.61	0.06

---

[1] http://www.iram.es/IRAMES/otherDocuments/postscripts/classHFS.ps

6.4 Results

6.4.1 Line parameters

The central velocity was fixed at a v_{LSR} of $0\,\mathrm{km\,s^{-1}}$ for all the sources during the observations. Thus, the frequencies of some molecular lines fall out of the fixed bandwidth for cases with a significantly different LSR velocity (see Chapter 4 for a detailed description). As a result, the numbers of observed and detected sources are slightly different for each molecular line, and unobserved molecules are indicated in Table 6.2.

Tables 6.3 and 6.4 provide examples of the HFS fitted and Gaussian fitted line parameters of the HII region source group. In cases where several velocity components were found, we selected the component with a common velocity in all detected lines. The spectral lines and fitted profiles of two example sources (AGAL011.936−00.616 and AGAL015.013−00.671) are displayed in Figures 6.1 and 6.2.

For CN and HCO, we performed a single Gaussian fit although several hyperfine lines of these molecules have been observed. In case of the CN hyperfine lines, strong deviations of their relative intensity from LTE are found. The deviations made it difficult to get reliable hyperfine fitted results. In particular, this effect is stronger toward the bright three components than toward the weakest one which is considered to be optically thin. To reduce optical depth effects, we used the weakest component of CN ($NJF = 1(1/2)3/2 - 0(1/2)3/2$) for all analysis in this thesis. In addition, some sources show self-absorption in the three bright components, which will be discussed in Section 6.4.2. The four HCO hyperfine lines are considerably weaker than the other molecular lines. The brightest component ($NJF = 1(3/2)2 - 0(1/2)1$) is detected, and just a few sources show all the four HCO hyperfine components. As seen in Figure 6.2, the three hyperfine components of $H^{13}CN$ toward the clumps hosting HII regions are often blended. As a result, the measured line parameter of $H^{13}CN$ toward some sources are associated with high uncertainties, and we will discuss this in later sections. In Figure 6.2, the other molecular line profiles (i.e., $c\text{-}C_3H_2$, $HC^{15}N$, $HN^{13}C$, and $H^{13}CO^+$) show similarity with $C^{18}O$ indicating that they originate mostly from the same gas.

Table 6.4: Gaussian line parameters of $C^{18}O$, HCO, $c\text{-}C_3H_2$, CN, $HC^{15}N$, and $HN^{13}C$. For multiple velocity components, we only tabulate line parameters of the component detected in all molecular species. The full table is provided in Table B.3.

ATLASGAL Name	Line	Area (K km s^{-1})	v_{LSR} (km s^{-1})	Δv (km s^{-1})	T_{MB} (K)	rms (K)
AGAL008.671−00.356	HCO	0.49±0.06	36.43±0.48	6.57±0.78	0.07	0.02
	$H^{13}CO^+$	11.93±0.91	34.20±0.06	3.07±0.10	3.65	0.05
	$c\text{-}C_3H_2$	5.40±0.33	36.29±0.18	5.73±0.26	0.88	0.05
	$HN^{13}C$	10.12±0.14	35.25±0.03	4.47±0.07	2.13	0.05
AGAL010.151−00.344	$C^{18}O$	17.65±0.09	9.19±0.01	5.48±0.03	3.03	0.03
	HCO	0.51±0.05	8.70±0.36	7.42±0.75	0.06	0.01
	$H^{13}CO^+$	7.98±0.11	9.50±0.04	5.26±0.09	1.43	0.04

Table 6.4: continued.

ATLASGAL Name	Line	Area (K km s^{-1})	v_{LRS} (km s^{-1})	Δv (km s^{-1})	T_{MB} (K)	rms (K)
	c-C$_3$H$_2$	8.24±0.10	9.48±0.03	4.99±0.07	1.55	0.03
	CN	5.06±0.16	9.34±0.08	5.18±0.19	0.92	0.06
	HC^{15}N	0.35±0.09	10.65±0.33	2.99±1.07	0.11	0.04
	HN^{13}C	3.13±0.10	9.49±0.07	4.43±0.16	0.66	0.04
AGAL010.168−00.362	C^{18}O	19.18±0.08	14.07±0.02	7.30±0.04	2.47	0.03
	HCO	0.31±0.04	13.95±0.33	4.89±0.63	0.06	0.02
	H^{13}CO$^+$	9.98±0.11	14.14±0.04	6.68±0.09	1.40	0.04
	c-C$_3$H$_2$	7.59±0.11	13.97±0.05	6.65±0.11	1.07	0.04
	CN	4.40±0.16	13.90±0.12	6.40±0.26	0.65	0.06
	HC^{15}N	1.15±0.13	15.39±0.41	7.58±1.04	0.14	0.04
	HN^{13}C	3.30±0.20	13.33±0.12	4.11±0.25	0.75	0.03
AGAL010.323−00.161	C^{18}O	8.27±0.09	11.93±0.02	2.95±0.04	2.63	0.05
	HCO	0.31±0.06	13.66±0.61	6.37±1.21	0.05	0.02
	H^{13}CO$^+$	3.22±0.10	12.06±0.04	2.99±0.11	1.01	0.04
	c-C$_3$H$_2$	1.27±0.09	11.94±0.10	2.75±0.26	0.44	0.04
	CN	1.67±0.15	12.26±0.10	2.51±0.29	0.62	0.08
	HC^{15}N	0.33±0.07	12.27±0.09	0.99±0.33	0.31	0.05
	HN^{13}C	2.21±0.09	12.15±0.05	2.46±0.13	0.85	0.04
AGAL010.472+00.027	C^{18}O	41.22±0.28	66.79±0.02	6.15±0.05	6.30	0.11
	HCO	0.64±0.09	67.62±0.49	7.24±1.30	0.08	0.02
	H^{13}CO$^+$	14.22±0.22	66.65±0.05	6.75±0.12	1.98	0.07
	c-C$_3$H$_2$	4.37±0.23	66.79±0.20	7.41±0.45	0.55	0.07
	CN	3.92±0.35	66.20±0.25	5.73±0.56	0.64	0.14
	HC^{15}N	11.05±0.24	66.82±0.10	8.98±0.23	1.16	0.06
	HN^{13}C	8.32±0.20	66.98±0.07	6.39±0.18	1.22	0.06

6.4.2   Self-absorption profiles of CN emission lines

We have found self-absorption features of the three strong CN lines ($N = 1 - 0$). In total, self-absorption features are found toward 25 H$\textsc{ii}$ and 15 non-H$\textsc{ii}$ region clumps. These molecular clumps likely have a molecular gas structure with temperature and density gradients. As a result, diffuse and low-temperature gas in the foreground absorbs the emitted radiation from these CN molecules along the line of sight.

Figure 6.3 displays two examples of the sources with self-absorption features. These line profiles represent different kinds of gas motions within the clumps. Besides, CN spectral lines of all the sources with self-absorption feature will be provided in Figure B.1. In the left panels of Figure 6.3, AGAL011.936−00.616 shows red-skewed emission features with self-absorption, which might be caused by expansion (Smith et al. 2012). Indeed, its 8 μm emission shows a bipolar morphology with extended emission in the IRAC three color-composite image in the upper left panel of Figure 6.3. However, high-angular resolution observations are needed to confirm this interpretation.
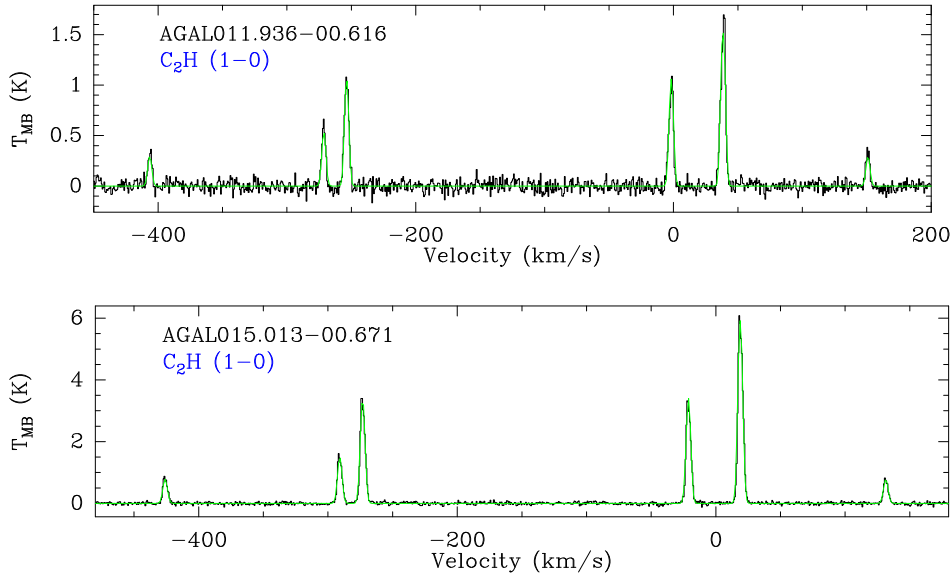
Figure 6.1: Spectra of C_2H hyperfine lines toward two example sources (AGAL011.936−00.616 and AGAL015.013−00.671). The green lines are the fitted profiles by the HFS fits. The fitted profiles of C_2H are the results of HFS fits.

Interestingly, we also find blue-skewed emission features with self-absorption toward AGAL031.261+00.062 (right panels of Figure 6.3). This clump hosts a compact H II region, and there is no extended $8\,\mu m$ emission seen toward AGAL011.936−00.616. Blue-skewed profiles indicate potential infall motions within the clump (Wyrowski et al. 2016; Smith et al. 2012). This blue-skewed profile is not as apparent as seen toward AGAL034.258+00.154. Furthermore, AGAL034.258+00.154 shows an inverse P-Cygni profiles for all the four CN hyperfine components (see Figure B.1). In fact, this clump is already known to have infall motions and hosts two HC H II and one UC H II regions (Liu et al. 2013).

Therefore, these sources with self-absorption features are excellent candidates to investigate in more detail with high-angular resolution infall or expansion motions associated with embedded young H II regions. As discussed in previous chapters, taking into account the conditions of molecular gas in the vicinity of young H II regions is necessary to understand the evolution of the H II regions and their feedback on the parental molecular clouds.

6.4.3   Detection rates

After the identification of the selected molecular species, we confirmed the detection of these molecules by applying a $3\,\sigma$ threshold. Table 6.5 shows the detection rates toward the whole sample including H II and non-H II regions. Since the C_2H ($NJF = 1(3/2)2−0(1/2)1$) and $H^{13}CN$ ($JF = 12 − 01$) transitions are the brightest HFS components of these two molecules, we counted their detection rates with these transitions. The
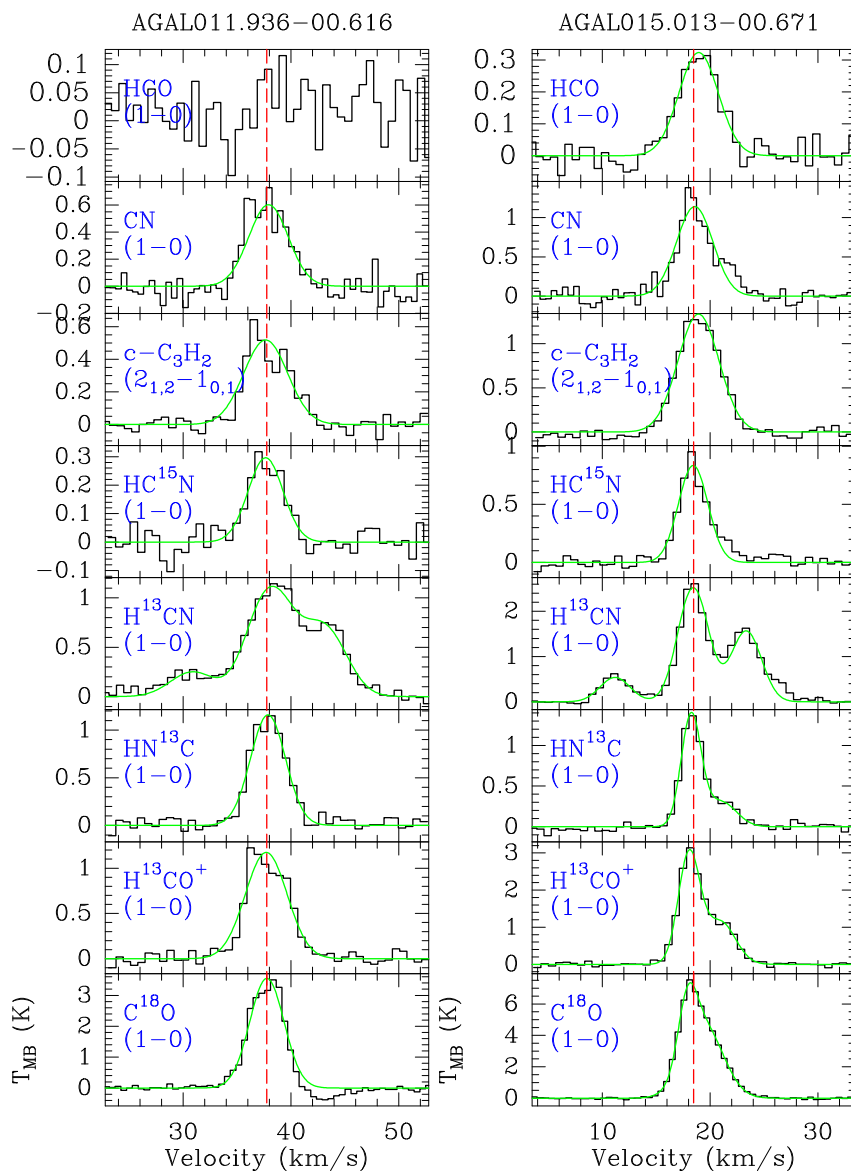
Figure 6.2:   Spectra of HCO, CN, c-C$_3$H$_2$, HC^{15}N, H^{13}CN, HN^{13}C, H^{13}CO$^+$, and C^{18}O. Except for H^{13}CN, all the molecular lines are fitted by Gaussians. For H^{13}CN, HFS fits were used. HCO HFS is not detected toward AGAL011.936−00.616.
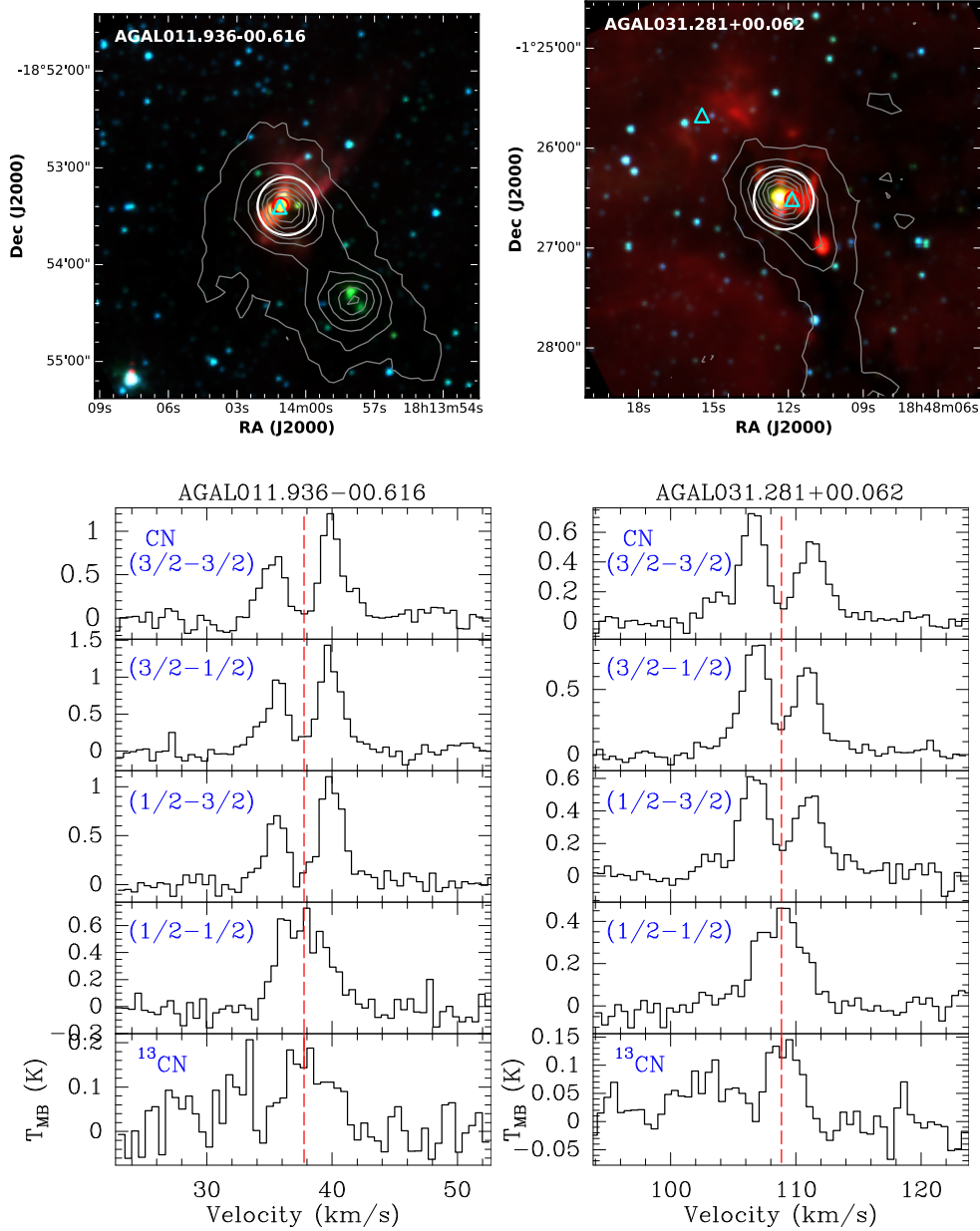
Figure 6.3: The self-absorption of CN lines of AGAL011.936−00.616 (left) and AGAL031.281+0.062 (left). *Upper*: IRAC three-color composite images (blue; 3.6 μm, green; 4.6 μm, and red; 8 μm). The white circles indicate the beam size of the IRAM 30 m telescope. The red circles and cyan triangles mark radio continuum sources from CORNISH and NVSS surveys, respectively. The grey contours represent the 870 μm dust continuum emission from the ATLASGAL survey. *Lower*: Spectral lines of CN $(NJ = 1(1/2) − 0(1/2))$ and ^{13}CN $(N = 1 − 0, J = 3/2 − 1/2, F_1 = 2 − 1, F = 3 − 2)$ transitions. The red vertical lines indicate the systemic velocities measured by H^{13}CO$^+$ lines.

Table 6.5: Detection rates. For all observed sources, the rms of the line survey varies with observing frequency and is given for each molecule. The uncertainties of the detection rates are obtained assuming binomial statistics.

Molecule	rms (K)	Number of Observed sources	Number of Detected sources	Detection Rate (%)
$C^{18}O$	0.050	385	385	100±0
HCO	0.017	405	131	32±2
$H^{13}CO^+$	0.041	403	400	99±0
HOC^+	0.041	403	5	1±1
C_2H	0.039	403	399	99±0
$c-C_3H_2$	0.038	404	403	99±0
CN	0.069	386	363	94±1
$HN^{13}C$	0.040	405	384	94±1
$H^{13}CN$	0.040	403	305	75±2
$HC^{15}N$	0.038	405	161	39±2

detection rates of HCO are based on stacked spectra of HCO. For the stacking, each HFS component is weighted and scaled by its relative intensity. The stacking increased the S/N by a factor of 2.

We detect $C^{18}O$ lines toward all the observed clumps (100%). This result obviously shows that the ATLASGAL dust clumps trace the high column density parts of molecular clouds. In addition, we also find high detection rates for $H^{13}CO^+$ (99%), C_2H (99%), $c-C_3H_2$ (99%), CN (94%), and $HN^{13}C$ (94%). In particular, $H^{13}CO^+$ and $HN^{13}C$ are often detected although these are rare isotopologues. We find a reasonably high detection rate for $H^{13}CN$ (75%). Even the rare isotopologue $HC^{15}N$ is detected with a rate of 39%. However, the other cation, HOC^+ is rarely detected with only a tentative detections (below 3σ) toward five clumps due to its low abundance and dipole moment (the spectra will be provided in Figure B.2). Thus, we exclude HOC^+ line from all statistical analyses in this thesis.

Figure 6.4 shows detection rates of the selected molecules for HII (orange bars) and non-HII (cyan bars) region sources. As seen in Table 6.2, the non-HII region sources from the classification can also host early stages of star formation. However, these sources do not show centimeter free-free emission or mm-RRLs. We assume that bright PDRs are only found in the HII region sources. In Figure 6.4, we can see differences in detection rates for some molecular transitions toward the two groups, in particular, $H^{13}CN$, $HC^{15}N$, and HCO which show higher detection rates toward the HII regions. For $H^{13}CO^+$, C_2H, CN, $HN^{13}C$, the detection rate differences between the two regions are negligible within their uncertainties.

High detection rates toward the HII region group can be related to higher column densities. Figure 6.5 displays cumulative distributions of H_2 column densities toward three groups of the observed sources, HII, and IR bright non-HII and dark non-HII region sources. Their distributions and a Kolmogorov-Smirnov test indicate that the HII region
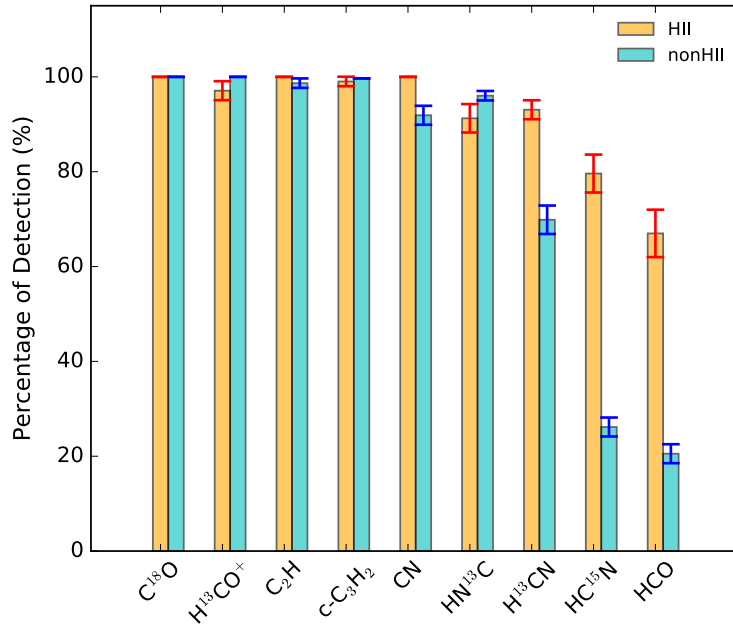
Figure 6.4: Detection rates of typical PDR tracer molecules and $C^{18}O$ as a reference molecule. We used binomial statistics to estimate the red and blue error bars for uncertainties.

sources have somewhat higher H_2 column densities, but median values determined for this group are not significantly different, within $\sim 4 - 6 \times 10^{22}\,\mathrm{cm}^{-2}$ from the overall range of values fro all three groups. Even if there is some effect of H_2 column density, such large differences in the detection rate may be associated with abundance enhancements rather than caused by higher H_2 column density. We still can consider a distance effect, leading to weaker molecular lines for more distant sources. However, it can be presumably excluded because the detection rates for all the molecules between distances of $3 - 5\,\mathrm{kpc}$ are approximately the same (see Figure B.3). Therefore, the high detection rates of $H^{13}CN$, $HC^{15}N$ and HCO toward the HII region group can be related to the abundances of these molecules in PDRs surrounding the HII regions.

6.4.4 Linewidths

To study whether different molecular lines are originating from the same gas or whether different lines show different amounts of turbulence, we determined the mean, median, and standard deviations of the measured line widths. $C^{18}O$ is utilized as a reference molecule.

Figure 6.6 shows the values of mean, median, σ (standard deviation of linewidth) with their error, and the median values of linewidth ratios ($\Delta v_{\mathrm{mol}}/\Delta v_{C^{18}O}$). To search for trends between groups, we plot here linewidths of HII (orange), and IR bright (green) and IR dark (black) non-HII regions. According to the results shown in Figure 6.6, there are manifest differences of linewidths among the three groups. From less evolved
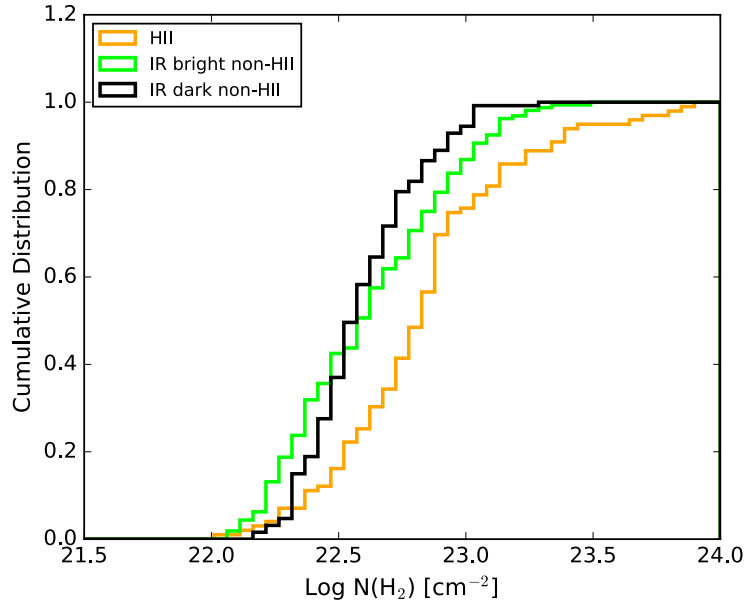
Figure 6.5: Cumulative distributions of H$_2$ column densities toward H$_{\mathrm{II}}$ (orange), and IR bright non-H$_{\mathrm{II}}$ (green) and dark (black) non-H$_{\mathrm{II}}$ regions.

clumps to more evolved clumps, the linewidths of the molecular lines increases. Broader molecular lines toward the evolved stages of clumps were found for ammonia (Wienen et al. 2012; Urquhart et al. 2013c) and H^{13}CO^{+} (Kim et al. 2017). In the mean and median values, the differences of linewidths of H^{13}CN, HC^{15}N, and HN^{13}C among the three groups are small. For the other molecules, the differences of linewidths, however, become more obvious. Due to the weak intensities of HCO lines, the HCO linewidths have large fitting uncertainties compared to other molecular linewidths. Nevertheless, broad linewidths are often found toward the H$_{\mathrm{II}}$ regions. For HCO, H^{13}CN, and HC^{15}N, the linewidths toward IR dark non-H$_{\mathrm{II}}$ regions seems to be broader than the other molecules, but again their errors are higher than those for H$_{\mathrm{II}}$ regions. Indeed, these molecules are weaker and have low S/N levels.

The lower middle panel from top of Figure 6.6 exhibits the standard deviations (σ) of the linewidth and its associated uncertainty. These values represent the 1σ value of the distributions of the linewidths of the three groups. Except for C$_2$H, HC^{15}N, and CN, the other molecular lines have a broader range of distributions of linewidth toward the H$_{\mathrm{II}}$ region sources compared with those toward non-H$_{\mathrm{II}}$ region sources. The bottom panel shows median values of the linewidth ratios ($\Delta v_{\mathrm{ratio}}$) of each molecular line relative to the C^{18}O line. If linewidth ratios are close to 1, this means that C^{18}O and the compared molecular line trace similar molecular gas regions within clumps. The H$_{\mathrm{II}}$ region group (orange) has median values of $\Delta v_{\mathrm{ratio}}$ close to 1 whereas the median values of $\Delta v_{\mathrm{ratio}}$ toward the two non-H$_{\mathrm{II}}$ region groups show small offsets from 1. In general, these molecular lines are weaker toward the non-H$_{\mathrm{II}}$ regions, and thus their S/N levels are lower, especially for the IR dark non-H$_{\mathrm{II}}$ regions.
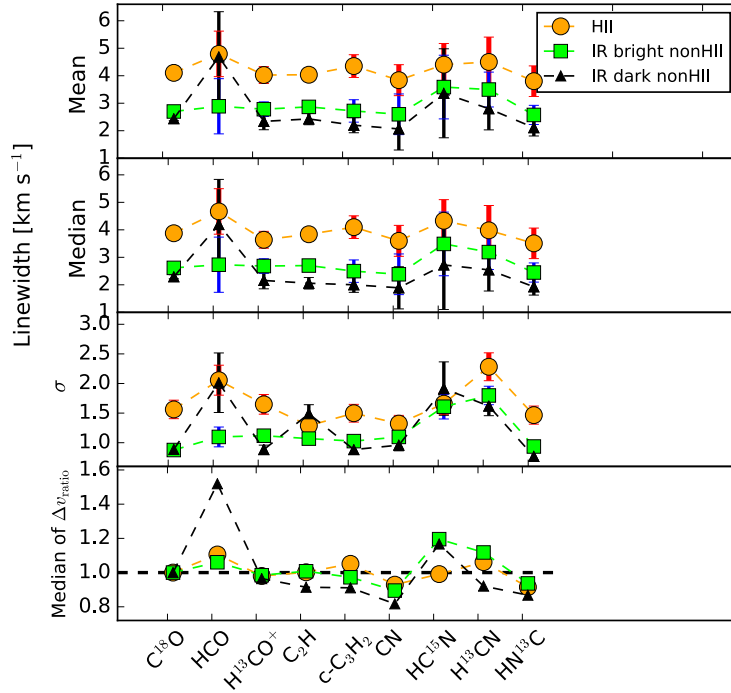
Figure 6.6: Mean, median, standard deviation (σ) of linewidths of the selected molecular lines. The median value of linewidth ratios ($\Delta v_{\rm ratio}$) is a median of the line width ratios of these molecular lines to $C^{18}O$ ($\Delta v_{\rm mol}/\Delta v_{C^{18}O}$) for a given molecule. The σ shows variations from source to source. The error bars for the mean and median values are based on typical Gaussian fit errors with 2σ. The error bars of the standard deviation of linewidths is the standard deviation error.

Figure 6.7 shows scatter plots of linewidths of the selected molecules to that of $C^{18}O$. The orange and cyan circles represent HII and non-HII region groups without separation into subgroups of the non-HII region sources. The red (HII) and blue (non-HII) ellipses visualize the distributions of data points for each group measured with Principal Component Analysis (PCA). Overall, the ellipses and data points are closely located to equality for all the molecules. In particular, the ellipses and data points of $H^{13}CO^+$ and $C^{18}O$ display pronounced correlations and perfectly align on the equality line. In the case of $HN^{13}C$, the ellipses for the two groups are also significantly closer to equality, and their linewidths are slightly narrower than that of $C^{18}O$ as seen in the bottom panel of Figure 6.6. According to the scatter distributions of the HCO, $H^{13}CN$, and $HC^{15}N$ in Figure 6.7, their large offsets in line ratios ($\Delta v_{\rm ratio}$) in Figure 6.6 might be a result of fitting uncertainties. Some sources have remarkably broader linewidths in $H^{13}CN$. Such broadening can be a result of high optical depth, leading to a blending of the HFS lines. If internal turbulence within clumps causes these broad linewidths, we expect to find such a trend also in $HC^{15}N$. There are, however, no sources with notably broader linewidths in Figure 6.7.

To identify similarity of linewidths between these regions, we performed KS tests
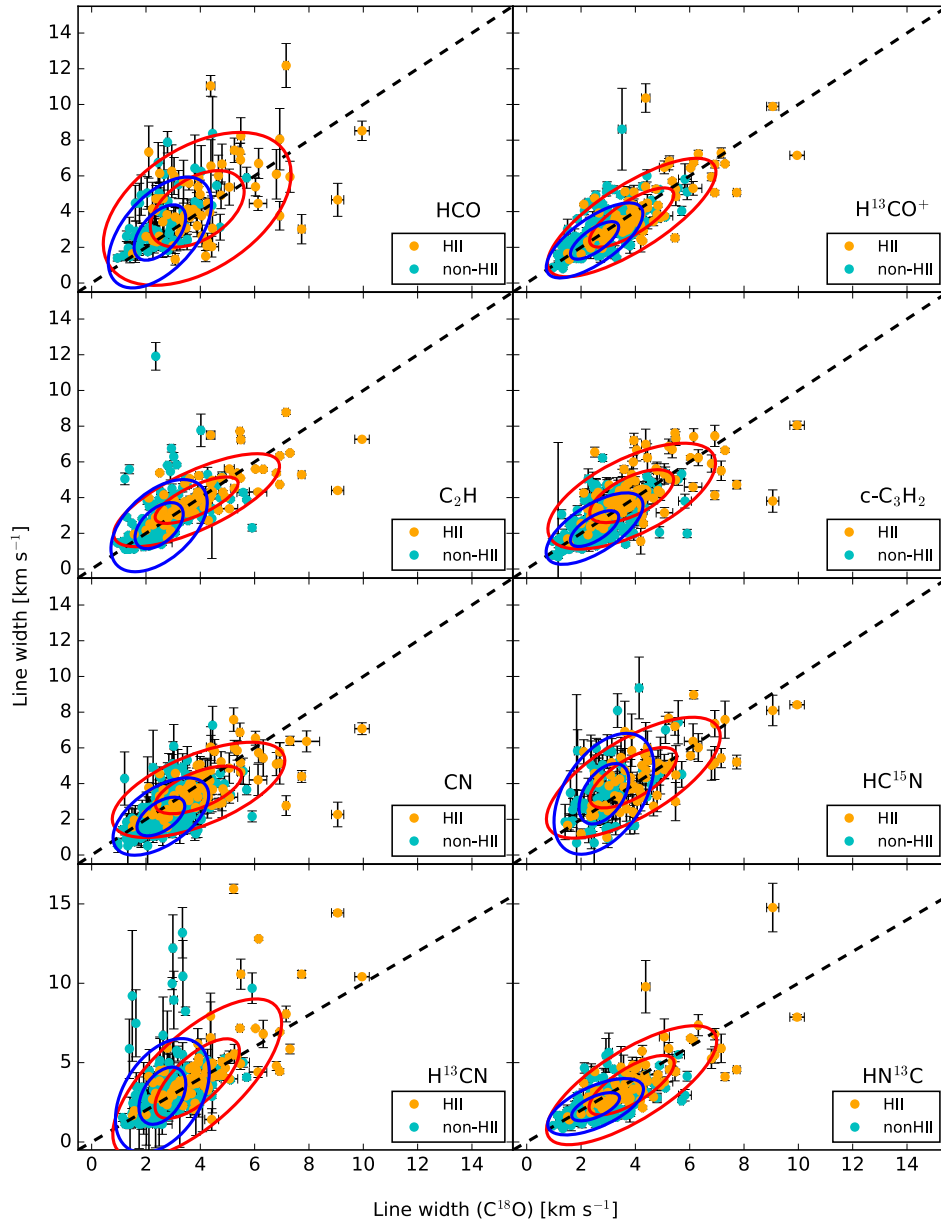
Figure 6.7: The orange circles indicate the ATLASGAL clumps containing Hıı regions and the cyan circles represent the clumps without the presence of Hıı regions, which consist of IR bright non-Hıı and dark non-Hıı regions. The back dashed lines indicate equality. The error bars are obtained from the Gaussian or HFS fits. The red and blue ellipses are probability ellipses with 1σ (inner ellipse) and 2σ (outer ellipse) for the two groups. The probability ellipses were derived with a Principal Component Analysis (PCA).
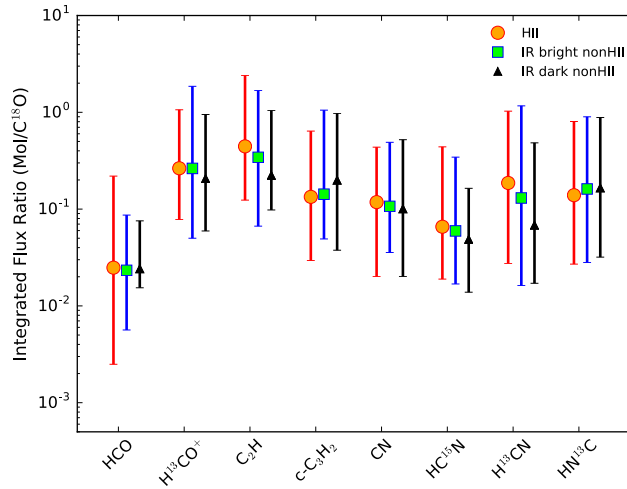
Figure 6.8: The orange, green, and black symbols indicate median values of the integrated flux ratios of the molecular lines to $C^{18}O$ line toward HII (orange), IR bright non-HII (green) and IR dark non-HII (black) regions. Each color error bar represents the full range of the integrated flux ratios (minimum and maximum) for each group.

for the molecular linewidths toward the regions. The null hypotheses can be rejected with a small $p-$values $\ll 0.0001$. It means that the linewidths are statistically larger toward the HII regions than toward the non-HII regions, consistent with the results in Figure 6.6. One possible cause of this may be due to a distance bias. To clarify this, we compared molecular linewidths and distances of the clumps (see Figure B.4), but there are no substantial correlations with an increase of their distances. The distance effect cannot explain such broad line widths toward the HII region group. We also plotted the linewidths of those molecular lines against RRL linewidths. If the molecular lines are mainly emitted in PDRs, we might find some correlations between them due to the dynamical interaction between ionized and photodissociated gas. However, we could not find any significant correlations between them (see Figure B.5) although the HCO line widths seem to show a weak anti-correlation to RRL line widths.

We also calculated the thermal line broadening widths using Eq. (2.62) at temperatures of 10, 20, and 40 K because the clumps including HII regions are hotter than those without. The estimated thermal linewidths at the given temperatures are in a range of $0.13 - 0.26 \, \mathrm{km \, s^{-1}}$. It means that thermal broadening is not the main cause of the broad lines. We suggest that the broad linewidths of the molecular lines are associated with the star forming-activity within the clumps with HII regions.

6.4.5 Integrated fluxes

Assuming optically thin emission for the observed transitions and that $C^{18}O$ is a good tracer of H_2 column density with a constant abundance, integrated flux ratios of the selected molecules to $C^{18}O$ are a measure of the relative abundance of a given molecule within the clump. Figure 6.8 shows ratios of integrated fluxes of the selected molecules
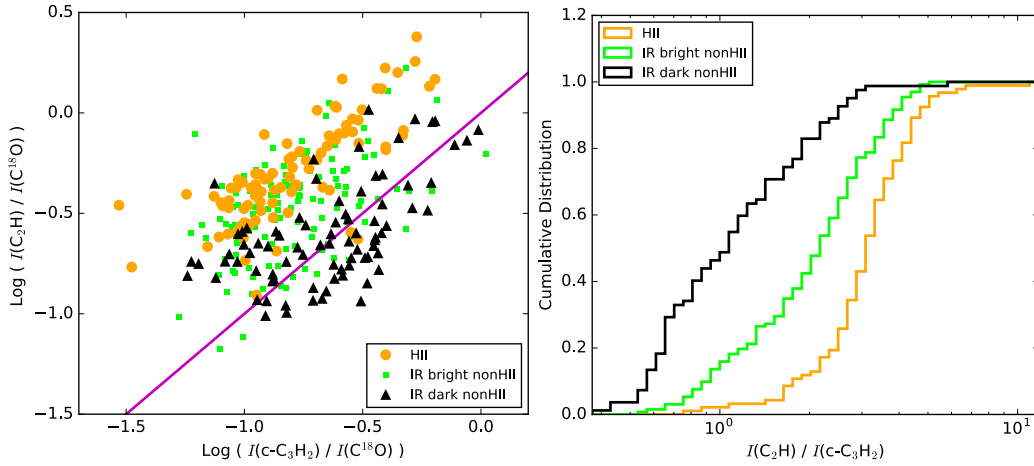
Figure 6.9: *Left*: Integrated intensity of C_2H normalized with $C^{18}O$ as a function of the normalized integrated intensity of $c\text{-}C_3H_2$. The orange circles are HII regions. The green and black symbols indicate IR bright non-HII and dark non-HII regions. The purple line shows equality. *Right*: Cumulative distributions of integrated flux ratios of C_2H to $c\text{-}C_3H_2$ for each group.

to integrated fluxes of $C^{18}O$ (a scatter plot of the ratios is shown in Figure B.6). To obtain a good S/N level, we used the integrated flux of the brightest components for the C_2H and $H^{13}CN$ lines which are obtained from the HFS fitting results. We used the stacked HCO integrated fluxes and the weakest HFS component of the CN transitions due to self-absorption in the other HFS components.

The median value of the C_2H and $H^{13}CN$ flux ratios show some separation among the three groups while the other molecular line ratios of the groups do not seem like the two molecular lines. The three regions are slightly separated by the median value of the C_2H and $H^{13}CN$ flux ratios whereas the other molecule line ratios do not seem different among the regions. Their ratios increase from IR dark non-HII regions to HII regions over IR bright non-HII regions. An abundance enhancement might cause the increase in C_2H flux ratios. On the other hand, the other small hydrocarbon species, $c\text{-}C_3H_2$, does not show such a trend.

If the small hydrocarbons behave differently in these groups, we expect to see differences in their intensity distributions. The left plot of Figure 6.9 shows a comparison of the two molecular lines toward the three groups. Their distributions show significant separations along a diagonal direction from the line of equality (purple line) in the plot. At a given $c\text{-}C_3H_2$ intensity ratio, the HII region sources have brighter C_2H intensity ratio than IR dark non-HII region sources. The IR bright non-HII region sources have the most widespread distributions over IR dark non-HII and HII region sources.

In the right plot of Figure 6.9, we display cumulative distributions of the integrated intensity ratios of C_2H to $c\text{-}C_3H_2$. The differences between the groups become obvious. We performed KS tests for those and found that we can reject the null hypotheses which their integrated flux ratios are same toward the groups, with small $p-$values
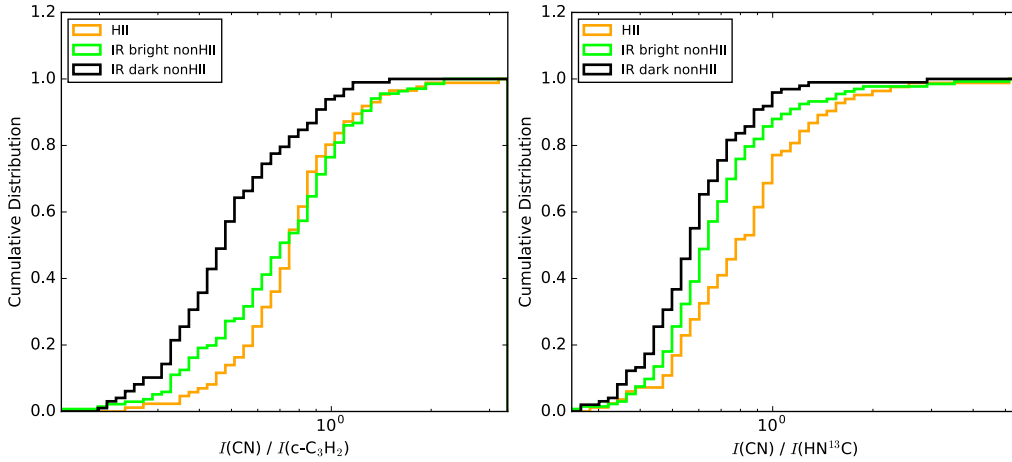
Figure 6.10:   *Left*: cumulative distribution of the integrated intensity ratios of CN to c-C_3H_2 for each group. *Right*: cumulative distribution of the integrated intensity ratios of CN to $HN^{13}C$.

$\ll 0.0001$. The relative intensities of the small hydrocarbons to $C^{18}O$ increase from IR dark non-HII regions via IR bright non-HII region sources to HII region sources, hence during the evolution of high-mass clumps. Figure 6.10 shows cumulative distributions of the integrated intensity ratios of CN to c-C_3H_2 and to $HN^{13}C$. The bright integrated intensities of the CN are associated with the HII region sources. Also, the null hypotheses for the similarity of the CN intensities toward the three groups are invalid with small $p-$values $\ll 0.0001$. To quantify these chemical differences further, we need to estimate absolute abundance of these molecules which will be discussed in later sections.

6.5   Analysis

6.5.1   Column densities

To obtain abundances of the selected molecules to H_2, derivation of their column densities is the first step. Since we observed only a single energy level of the selected molecules, we use several assumptions to measure column density: 1) the molecular lines are emitted under LTE because the critical densities of the observed molecular transitions are lower than the H_2 densities ($> 10^5 \, \mathrm{cm^{-3}}$) in high-mass star-forming regions; 2) at these high densities, the gas and dust temperatures are in equilibrium; 3) the observed line emission is considered to be optically thin. The latter condition is valid for $C^{18}O$, HCO, $H^{13}CO^+$, c-C_3H_2, CN, $HC^{15}N$ and $HN^{13}C$. Therefore, integrated intensities of these molecules were used to derive column densities using Eq. (3.22). For C_2H and $H^{13}CN$, we could obtain the optical depths of the lines by fitting their hyperfine components. In this case, the column densities of C_2H and $H^{13}CN$ were estimated by multiplying Eq. (3.22) by a factor of $\tau/(1 - e^{-\tau})$; 4) calculated column densities

Table 6.6: Column density of molecules in units of cm^{-2}. This table shows a portion of the full table (Table B.4).

ATLASGAL Name	C^{18}O $\times 10^{16}$	HCO $\times 10^{13}$	H^{13}CO$^+$ $\times 10^{13}$	C$_2$H $\times 10^{15}$	c-C$_3$H$_2$ $\times 10^{13}$	CN $\times 10^{15}$	HC^{15}N $\times 10^{13}$	H^{13}CN $\times 10^{13}$	HN^{13}C $\times 10^{14}$
AGAL006.216−00.609	1.08	⋯	0.41	0.79	2.56	0.86	0.05	0.67	0.07
AGAL008.049−00.242	0.37	⋯	0.08	0.12	0.57	0.23	cdots	0.16	0.02
AGAL008.671−00.356	⋯	1.26	0.96	1.73	3.67	⋯	⋯	⋯	0.17
AGAL008.684−00.367	2.90	⋯	1.00	⋯	2.42	1.31	0.21	3.37	0.13
AGAL008.706−00.414	1.26	⋯	0.31	0.42	1.81	0.61	⋯	0.98	0.06
AGAL010.079−00.196	0.69	0.35	0.07	0.38	0.47	0.20	⋯	0.15	0.01
AGAL010.104−00.416	0.66	⋯	0.14	0.17	0.37	0.23	⋯	0.06	0.01
AGAL010.151−00.344	1.34	1.48	0.61	0.75	6.23	1.78	0.05	1.54	0.05
AGAL010.168−00.362	1.45	0.92	0.76	0.88	5.81	1.55	0.15	1.35	0.01
AGAL010.213−00.322	1.65	0.64	0.31	1.91	1.84	1.13	0.06	2.64	0.07
AGAL010.214−00.306	1.22	0.52	0.17	0.39	0.84	0.46	⋯	1.14	0.03
AGAL010.284−00.114	0.99	0.27	0.33	0.47	0.77	0.70	0.06	0.82	0.05
AGAL010.288−00.124	0.80	0.56	0.22	0.72	0.67	0.64	0.07	0.83	0.04
AGAL010.323−00.161	0.64	0.85	0.25	0.22	0.92	0.60	0.04	0.79	0.04
AGAL010.321−00.231	0.54	⋯	0.10	0.16	0.42	0.39	⋯	⋯	0.02
AGAL010.342−00.142	1.03	⋯	0.34	0.49	1.48	0.74	0.12	1.56	0.05
AGAL010.444−00.017	1.20	⋯	0.23	0.13	0.57	0.32	⋯	1.22	0.02
AGAL010.472+00.027	3.34	1.62	1.16	⋯	2.95	1.48	1.54	5.56	0.14
AGAL010.579−00.349	0.89	⋯	0.09	0.15	0.36	0.15	⋯	⋯	0.01
AGAL010.618−00.031	0.54	⋯	0.07	0.05	0.28	⋯	⋯	0.56	0.01
AGAL010.624−00.384	7.51	2.11	2.71	2.40	6.84	2.81	0.83	6.09	0.22
AGAL010.957+00.022	0.72	⋯	0.28	0.22	0.68	0.20	0.07	0.44	0.02
AGAL011.034+00.061	0.71	⋯	0.13	0.30	0.55	0.22	⋯	0.30	0.01

were beam-averaged values; 5) the medium is spatially homogeneous and is larger than the size of the beam.

We note that in some cases we could not obtain proper measurements of τ_{tot}, either because their hyperfine components are not separated sufficiently (e.g., the H^{13}CN spectral line of AGAL011.936−00.616 in Figure 6.2) or their relative intensities have strong deviations from the predicted LTE values. Consequently, we only estimated column densities of these molecules using their opacity when the uncertainty of the fit was below 50 %. For the remaining sources with high τ_{tot} uncertainties, we calculated their column densities as lower limit using the optically thin approximation (Eq. 3.22) and only provide these measurements in Table 6.6 and did not use them in the following analysis.

The dust temperatures used in the analysis were taken from Urquhart et al. (2017) (using the method for the dust temperature determination from König et al. 2017). We estimated the partition function for an individual source and molecule by interpolating the data provided by the CDMS and JPL line databases for a given temperature (e.g., Figure 3.1). The partition functions obtained from CDMS and JPL take into account the hyperfine splitting and ortho- and para-transitions. The measured column densities of a portion of all the observed clumps are tabulated in Table 6.6. As mentioned before, not all lines were observed in all sources, and thus some column densities are missing in Table 6.6 (see Table 6.2 for missing observational data).

Figure 6.11 shows median values with full ranges (as error bars) of the column densities for all of the selected molecules toward different groups. These median values for the three groups are summarized in Table 6.7 and will be discussed later. As expected, C^{18}O column densities averaged over our beam are higher than the column
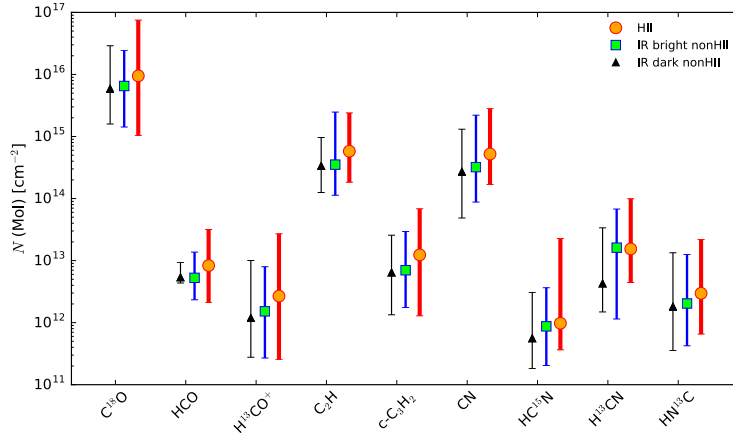
Figure 6.11: The symbols indicate median values of a given molecular column density of a given group. The orange circles represent the HII regions. The green and black symbols are IR bright and dark non-HII regions. The color error bars indicate the total range of all detections.

densities of the other transitions, since CO is after H_2 the most abundant molecule. Furthermore, its critical density (a few $10^3 \, \mathrm{cm}^{-3}$) is lower than the others. Besides, $C^{18}O$ probes the extended envelope surrounding the dense molecular cores.

Column densities of C_2H and CN are the second highest. The other molecules have lower but similar column densities. Overall, the column densities of all molecules are higher in HII regions than in the other groups. High column densities of the C_2H and $H^{13}CO^+$ toward more evolved clumps have already been reported by Sanhueza et al. (2012). In our results, the column density of the $HN^{13}C$ is also higher toward HII regions, but this trend was not apparent in the results of Sanhueza et al. (2012).

Figure 6.12 shows a comparison of column densities of $C^{18}O$ and H_2 toward the different groups. The column densities of H_2 are taken from König et al. (2017), and Urquhart et al. (2017) and were derived using dust continuum emission. Since the rare isotopologue $C^{18}O$ is considered to be a good column density tracer, these two quantities show a reasonable correlation toward HII regions and non-HII regions, respectively ($r = 0.6$ for HII region and $r = 0.5$ for non-HII region). The HII regions have higher column densities of $C^{18}O$ and H_2 than the non-HII regions. In fact, these two regions can be considered different according to results of KS test, with high confidence of $p-$values $\ll 0.0001$.

Figure 6.13 shows scatter plots of column densities of H_2 and the selected molecules. $H^{13}CO^+$ and $HC^{15}N$ exhibit excellent correlations (Pearson correlation coefficient, r, ≥ 0.8 with $p-$value $\ll 0.0001$) toward both HII and non-HII region groups. In addition, C_2H, c-C_3H_2, CN, $H^{13}CN$ and $HN^{13}C$ also show considerably good correlation ($r \sim 0.6$ - 0.7 with $p-$values $\ll 0.0001$). On the other hand, the column density of HCO has poor correlations for both groups ($r = 0.3$ for HII and $r = 0.2$ for non-HII regions) with the H_2 column density. HCO is a typical PDR tracer found to be enhanced in PDRs rather than in cold dense molecular regions toward both Galactic objects (Schilke
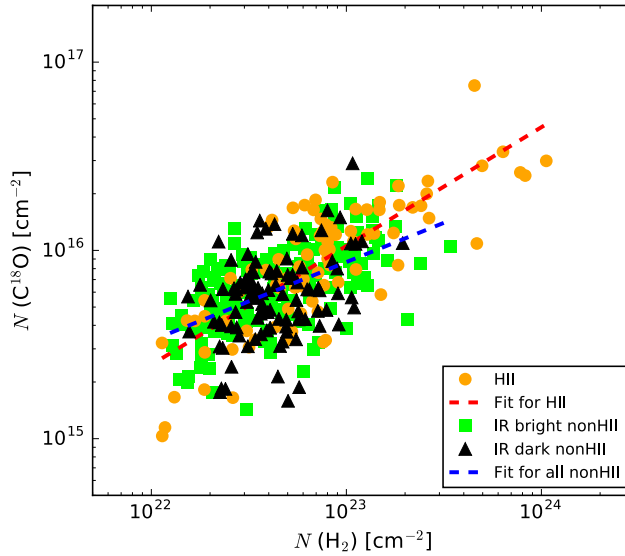
Figure 6.12: Column density of $C^{18}O$ as a function of H_2 column density. The color symbols are the same as in Figure 6.11. The red and blue dashed lines are the best-linear regression fits to data points of Hɪɪ and non-Hɪɪ regions.

et al. 2001; Gerin et al. 2009), and extragalactic sources (García-Burillo et al. 2002). The poor correlation supports a hypothesis that the emission of the HCO toward the detected clumps is associated with PDRs in clumps and not their colder envelopes. For $H^{13}CO^+$, c-C_3H_2, CN, and $HN^{13}C$, KS tests support with small $p-$values ($\ll 0.0001$) that the column densities of these molecules of the two groups are drawn from different samples.

The column density of HCO^+ can be obtained from the column density of $H^{13}CO^+$using the $^{12}C/^{13}C$ ratio. Therefore, we can consider that a trend in $H^{13}CO^+$ is similar to a trend of HCO^+. Indeed, such an increase of column density for HCO^+ was found from less evolved to more evolved sources (Sanhueza et al. 2012; Purcell et al. 2006). For HCO, $H^{13}CN$ and $HC^{15}N$, we cannot find significant differences between these groups according to KS tests toward them. According to the KS tests, the groups have similar properties in column density comparisons, with $p-$values $\gtrsim 0.004$. There is a marginal difference in C_2H column density toward these groups, with $p-$value of 0.00015. The results of Sanhueza et al. (2012) also did not show any increasing trend for C_2H column density over evolutionary stages.

As discussed in the previous section, column densities increase toward Hɪɪ regions. To see whether this trend is directly related to the evolutionary stage of the clumps, we compare the column densities with the dust temperatures of the clumps in Figure 6.14. The displayed Pearson correlation coefficients are estimated for only Hɪɪ and non-Hɪɪ regions. The dust temperature has been found to increase from less evolved to more evolved clumps (Giannetti et al. 2017; Urquhart et al. 2017). The column densities of HCO, $H^{13}CO^+$ and c-C_3H_2 molecules gradually increase with the dust temperature.
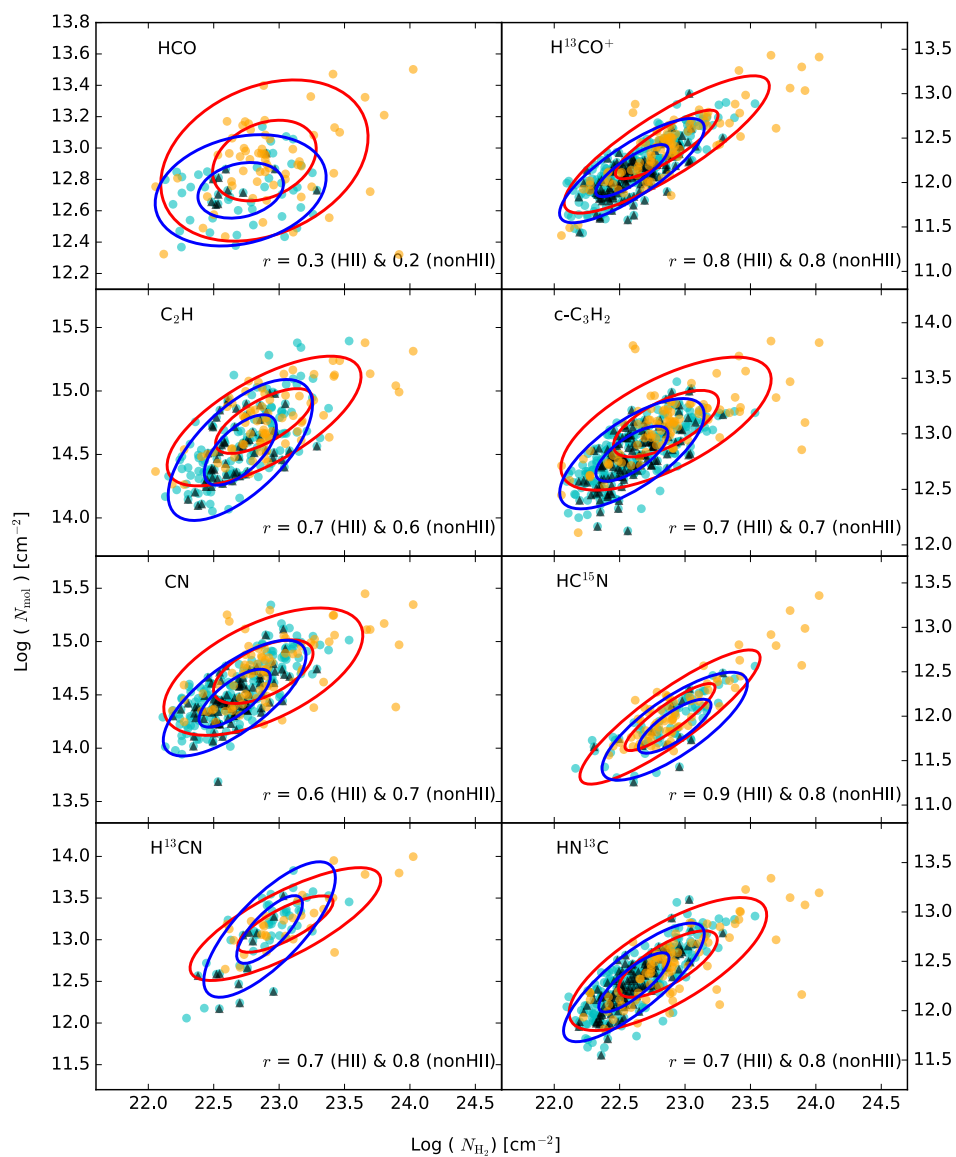
Figure 6.13: Column density of a given molecule as a function of H_2 column density toward HII and non-HII regions with IR dark non-HII regions superposed with black triangles. The ellipses show similar PCA contours as in Figure 6.7. r indicates Pearson correlation coefficients toward HII and non-HII regions.
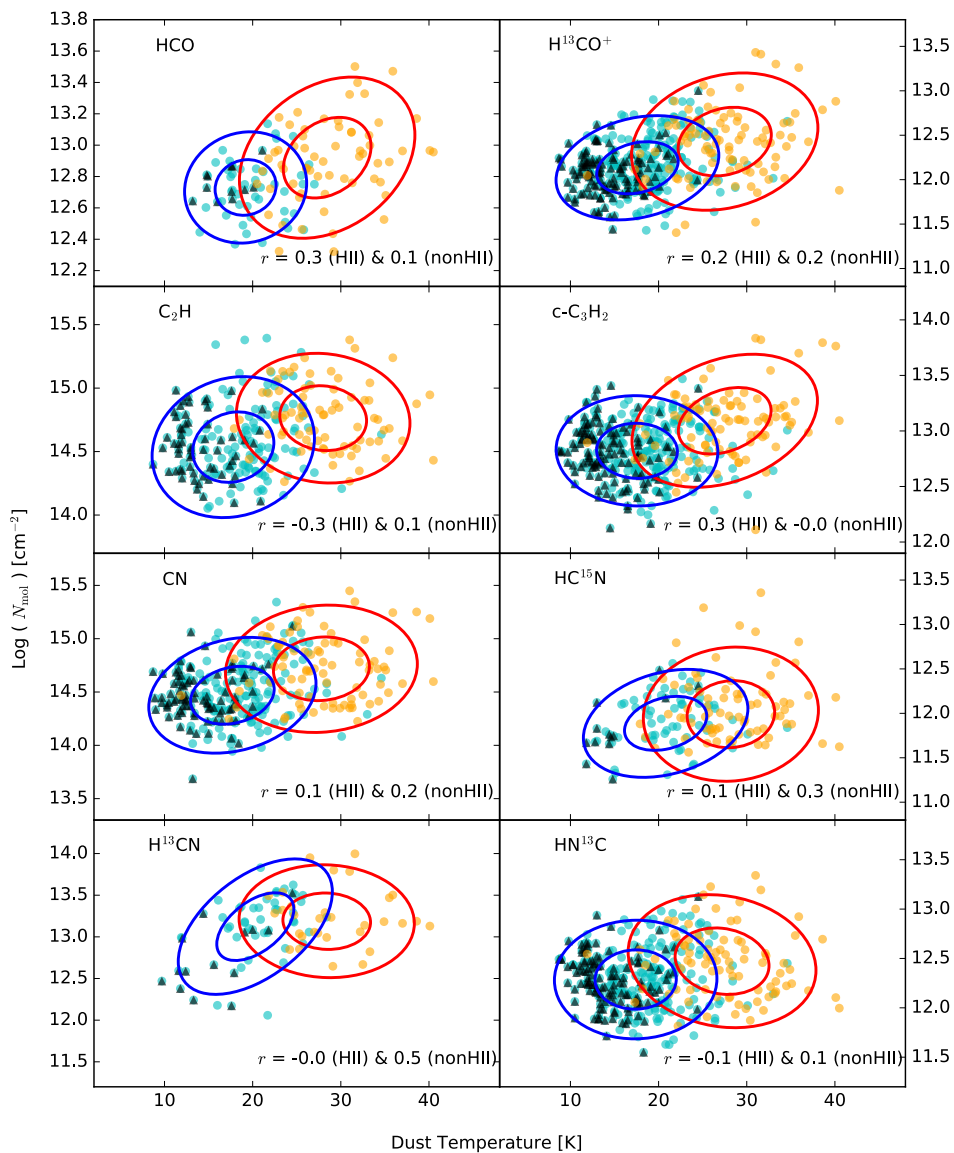
Figure 6.14:   Column density of molecules as a function of dust temperature. The explanations of the symbols and ellipses are the same with Figure 6.13.
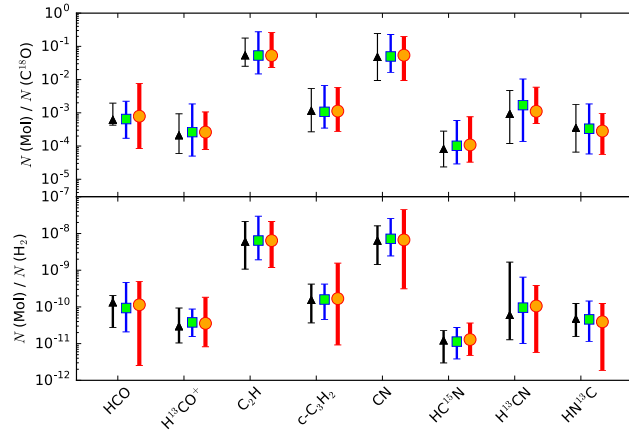
Figure 6.15: The abundance of the selected molecular species. *Upper*: Relative abundances normalized by $C^{18}O$ column density. *Lower*: Absolute abundances to H_2. The red circles, cyan squares, and black triangles indicate HII, IR bright non-HII, and IR dark non-HII regions, respectively. The error bars show full ranges of column densities for each molecule.

A weaker trend is seen for C_2H and CN. Although these trends are not conclusive, such weak trends were also reported by Sanhueza et al. (2012). In most cases, the data are poorly correlated with low confidence $p-$values whereas r for the HCO toward HII regions is also 0.4 but the $p-$value is 0.003, which is a reasonable confidence but not significant. Furthermore, a slight correlation is expected since the dust temperatures were used to compute the column densities.

6.6 Molecular abundances

Figure 6.15 shows abundances relative to $C^{18}O$ and H_2 for the selected molecules toward the three groups. The symbols represent median values of the molecular abundances, and the error bars show the full range of the abundances. These median abundances are listed in Table 6.7 together with column densities. Overall, there are no significant differences among the abundances of the three groups in Figure 6.15. When considering the uncertainties in the calculations, these results are not significantly different from the results of Gerner et al. (2014) who assumed higher temperatures for evolved sources. We will discuss abundances of HCO, C_2H, and c-C_3H_2 in Section 6.7 since they have been known to change in different environments according to previous studies toward prototype PDRs such as the Orion Bar or Mon R2 (Gerin et al. 2009; Cuadrado et al. 2015; Pilleri et al. 2013).

In Figure 6.16, we also plot the relationships of abundances relative to H_2 and H_2 column density of the observed clumps for the HCO, CN, C_2H and c-C_3H_2 molecules; these molecules have been found to show good spatial correlations with some PDRs such as the Horsehead Nebula, the Orion Bar and Mon R2 (Teyssier et al. 2004; Rizzo et al. 2005; Gerin et al. 2009; Ginard et al. 2012; Cuadrado et al. 2015). In addition,

Table 6.7: Column densities and abundances relative to H_2 and $C^{18}O$ for HII, IR bright and dark non-HII regions in $a(x) = a \times 10^x$. These values are median values for a given molecule.

Molecule	HII			IR bright non-HII			IR dark non-HII		
	N [cm^{-2}]	$X(H_2)$	$f(C^{18}O)$	N[cm^{-2}]	$X(H_2)$	$f(C^{18}O)$	N[cm^{-2}]	$X(H_2)$	$f(C^{18}O)$
$C^{18}O$	9.5(15)	1.2(−07)	−	6.5(15)	1.5(−07)	−	5.9(15)	1.4(−07)	−
HCO	8.3(12)	1.1(−10)	7.9(−04)	5.3(12)	9.3(−11)	6.5(−04)	5.4(12)	1.3(−10)	6.2(−04)
$H^{13}CO^+$	2.7(12)	3.6(−11)	2.6(−04)	1.5(12)	3.8(−11)	2.6(−04)	1.2(12)	3.0(−11)	2.1(−04)
C_2H	5.8(14)	6.4(−09)	5.3(−02)	3.5(14)	6.4(−09)	5.3(−02)	3.4(14)	6.0(−09)	5.4(−02)
c-C_3H_2	1.2(13)	1.7(−10)	1.1(−03)	7.0(12)	1.6(−10)	1.1(−03)	6.4(12)	1.6(−10)	1.1(−03)
CN	5.2(14)	6.7(−09)	5.4(−02)	3.2(14)	7.2(−09)	5.0(−02)	2.7(14)	6.4(−09)	4.8(−02)
$HC^{15}N$	9.8(11)	1.3(−11)	1.1(−04)	8.7(11)	1.1(−11)	1.0(−04)	5.6(11)	1.2(−11)	8.2(−05)
$H^{13}CN$	1.5(13)	1.1(−10)	1.1(−03)	1.6(13)	9.6(−11)	1.7(−03)	4.3(12)	6.0(−11)	9.3(−04)
$HN^{13}C$	3.0(12)	3.9(−11)	2.8(−04)	2.0(12)	4.6(−11)	3.3(−04)	1.8(12)	4.7(−11)	3.5(−04)

we show $H^{13}CO^+$ and $HC^{15}N$ abundances as dense gas tracers as well.

The $H^{13}CO^+$ and $HC^{15}N$ abundances (bottom panels in Figure 6.16), show no correlations with H_2 column density and are almost constant with H_2 column density. On the other hand, the HCO abundance significantly drops toward the clumps with high H_2 column density corresponding to a large A_V. The CN, C_2H and c-C_3H_2 column densities also exhibit similar trends, however, less pronounced. The abundance decrease of these molecules might be associated with the strength of the UV radiation. This may explain the low detection rates of HCO toward the non-HII regions.

Our measured HCO column density may also contain a contribution from HCO molecules inside of molecular clumps, not only from PDRs. To analyze this quantitatively, we use a simple toy model; it assumes a high abundance (2.0×10^{-10}) of HCO $(A_V < 5\,\text{mag})$ in a PDR and a low abundance (5.0×10^{-11}) in the dense molecular region. The resulting average abundance changes as a smooth progression occurs between the PDR and the molecular region. The gray dashed line in the most upper left panel of Figure 6.16 is a result of the model. It fits well our data points and might indicate that the trends of decreasing abundances with H_2 column density are caused by abundance jumps from the PDRs into the clouds.

The HCO molecule is referred to as a good tracer of FUV; its emission in the Horsehead nebula was found in a range $1.5 \lesssim A_V \lesssim 3.0$ (Gerin et al. 2009), but in the Orion Bar HCO emission was found deeper into PDRs toward molecular regions with $5 \lesssim A_V \lesssim 10$ (Schilke et al. 2001). Its abundance decreases when the gas is shielded from the FUV radiation (Gerin et al. 2009). At a given H_2 column density, HCO abundances toward the HII regions seem to be slightly higher. To confirm the enhanced abundances of the HCO toward the HII regions, we need spatial maps of HCO transitions toward a few selected sources from each group with high-angular resolution and to compare those with the distribution of UV radiation.

C_2H and c-C_3H_2 are also known as tracers of the surface layers of PDRs exposed to a strong UV field (their highest abundances have been found at visual extinctions of $2\,\text{mag} < A_V < 5\,\text{mag}$, in typical PDRs) (Rizzo et al. 2005; Pety et al. 2005; Ginard et al. 2012). These small hydrocarbons have also shown good spatial correlations with H_2^* $(\nu = 1 - 0)$ and PAH $8\,\mu\text{m}$ emission toward the Horsehead nebula, the Orion Bar, and Mon R2 (Teyssier et al. 2004; Pety et al. 2005; Pilleri et al. 2013; Cuadrado et al.
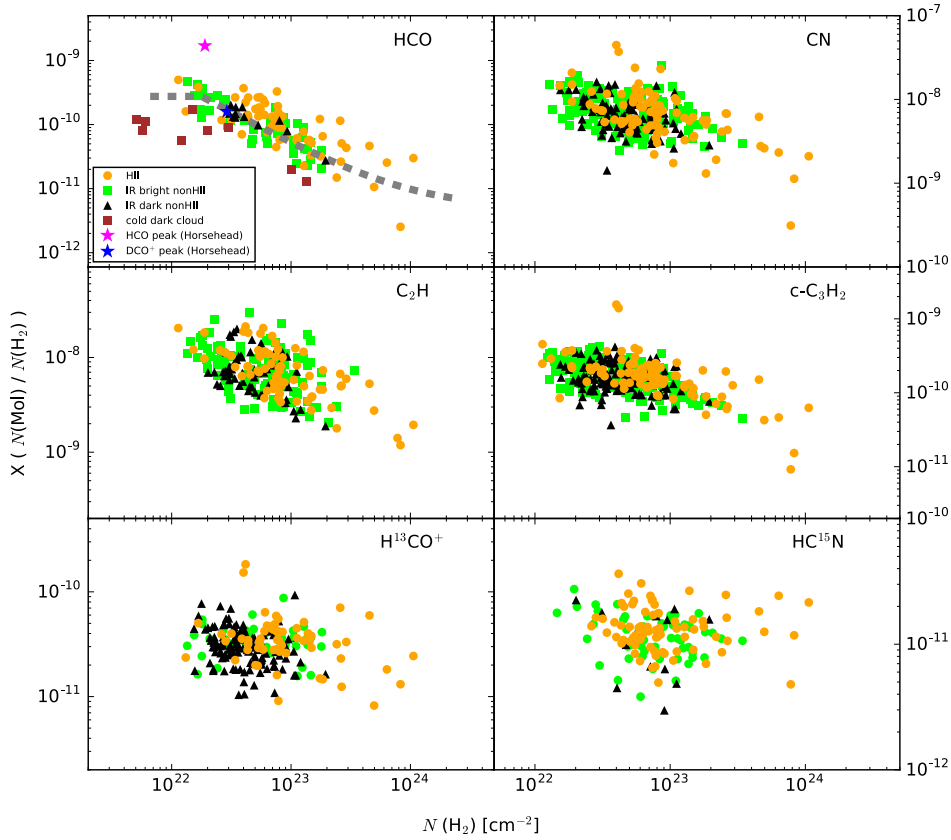
Figure 6.16:   The abundance of HCO, $H^{13}CO^+$, C_2H, c-C_3H_2, $H^{13}CO^+$ and $HC^{15}N$ relative to H_2 as a function of $N(H_2)$. The orange indicates $H{\small II}$ regions while green and black symbols are IR bright and dark non-$H{\small II}$ regions. In the most upper left panel, The brown squares indicate 9 cold dark clouds from Agúndez et al. (2015). The pink and blue asterisks are HCO abundances from a PDR and cold gas region in the Horsehead nebula (Gerin et al. 2009). In the most upper left panel, the gray dashed line indicates a simple abundance jump model.

2015). However, they were also found in UV shielded regions (Beuther et al. 2008). In fact, their abundances decrease with a more moderate slope compared to the HCO decrease. However, it is hard to distinguish the different contributions from PDRs and molecular clouds with our beam size.

6.7   Column density ratios

Relative molecular abundances (with respect to H_2 or $C^{18}O$) are used to quantify the amount of molecules in molecular clumps. However, column density ratios of chemically related molecules are a more direct way to diagnose chemical enhancement of a specific molecule within a clump. Furthermore, these ratios are insensitive to the unknown

beam filling factor and to uncertainties in the assumed physical conditions for molecular species with similar excitation (Ginard et al. 2012). We here focus on column density ratios of two pairs of molecules, $HCO/H^{13}CO^+$ and $c\text{-}C_3H_2/C_2H$. Before the discussion of these column density ratios for each pair, we will briefly explain the formation and destruction of HCO and small hydrocarbons to interpret the column density ratios of these molecules.

6.7.1   Formation of HCO and observational $HCO/H^{13}CO^+$ column density ratio

In previous models (Gerin et al. 2009; Goicoechea et al. 2009), the HCO and $H^{13}CO^+$ abundances in cold gas were constant whereas in PDRs the abundances of these molecules changed due to different chemical reactions. The main destruction process of $H^{13}CO^+$ in PDRs is dissociative recombination with electrons, and this happens quickly: $H^{13}CO^+ + e^- \rightarrow {}^{13}CO + H$.

On the other hand, the formation of HCO is well related to PDRs as described in previous sections. Several formation routes have been proposed to describe the high HCO abundance in PDRs via gas-phase reaction or photodissociation (Gerin et al. 2009).

The gas-phase formation route has two possible chemical reactions. The first one is an important formation route of HCO in FUV shielded regions (Schenewerk et al. 1988; Gerin et al. 2009):

$$\text{Metals (i.e., Mg or Fe)} + HCO^+ \rightarrow HCO + \text{metals}^+ \ (Mg^+ \text{ or } Fe^+) \qquad (6.1)$$

The most plausible pure gas-phase route is a reaction of atomic oxygen with carbon radicals in PDRs (Watt 1983; Leung et al. 1984; Schenewerk et al. 1988):

$$O + CH_2 \rightarrow HCO + H \qquad (6.2)$$

which can enhance the HCO abundance by a factor of $\sim$125 (Gerin et al. 2009).

Another suggested formation route is the gas-grain reaction through FUV radiation: photodissociation of formaldehyde (H_2CO) or grain photodesorption. The first route by FUV has been proposed by Schilke et al. (2001)

$$H_2CO + \text{photon} \rightarrow HCO + H \qquad (6.3)$$

and can increase the HCO abundance by a factor of 5 in PDRs (Gerin et al. 2009).
The second one is by grain photodesorption: HCO forms on the grain mantle and subsequently it is desorted from the grain into the gas-phase (Gerin et al. 2009). Two desorption processes are possible: thermal and photo-desorption. In cold gas regions below $\sim$30 K, thermal desorption does not play a primary role (Gerin et al. 2009) while in warm regions it will contribute to HCO desorption. If thermal desorption is not important, ice-mantle photo-desorption induced by FUV is an alternative process
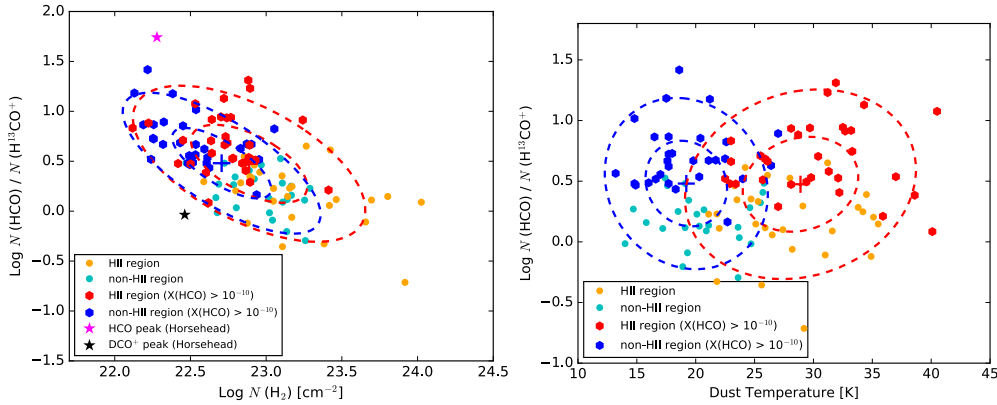
Figure 6.17: Column density ratio of HCO and $H^{13}CO^+$ molecules as a function of $N(H_2)$ (left plot) and T_{dust} (right plot). The red and blue hexagons indicate that sources that their X(HCO) is higher than 10^{-10} and their HCO/$H^{13}CO^+$ column density ratio is higher than 1 (Gerin et al. 2009). The pink and blue asterisks represent HCO/$H^{13}CO^+$ column density ratios from the PDR and cold gas region in the Horsehead nebula (Gerin et al. 2009).

(Willacy & Williams 1993; Bergin et al. 1995). The fact that high HCO abundances are always found in PDRs also supports this photo-desorption process (Schenewerk et al. 1988; Schilke et al. 2001).

Since HCO and $H^{13}CO^+$ molecules have different chemical reactions in PDRs and cold gas regions, we compare column densities of the molecules to constrain the origin of the detected HCO and $H^{13}CO^+$ toward ATLASGAL clumps. In the left plot of Figure 6.17, overall, the column density ratios of HCO/$H^{13}CO^+$ decrease with an increase of H_2 column densities and it is closely related to a decrease of the HCO abundance because the $H^{13}CO^+$ abundances are constant as shown in Figure 6.16. Besides, toward high H_2 column density HII region sources have higher HCO/$H^{13}CO^+$ column density ratios than non-HII region sources.

The black asterisk indicates the ratio measured in cold gas in the Horsehead nebula (Gerin et al. 2009). They concluded that the HCO toward the cold gas region arises from the PDRs vicinity of the surface of the molecular cloud where FUV radiation can still penetrate into the cloud and affect the chemistry. The HCO/$H^{13}CO^+$ ratios of our sources toward HII and non-HII regions are distributed toward higher values than the black asterisk, and thus the detected HCO emission seems to indicate a PDR origin. We also mark sources that have HCO abundances greater than 10^{-10}, and their HCO/$H^{13}CO^+$ ratios are also higher, adopting the measures in the Horsehead nebula PDRs (Gerin et al. 2009). Our sources (red and blue) are found between the values in the PDR and the cold gas of the Hosehead nebula. The enhanced HCO abundance in the PDR of the Horsehead nebula was explained by reaction (6.2). However, our column density ratios might be only explained by reaction (6.3) which can increase the HCO/$H^{13}CO^+$ ratio by 2 orders of magnitude in maximum (Gerin et al. 2009). According to the model results of Ginard et al. (2012), HCO/$H^{13}CO^+$ does not increase

in high UV fields, and the high ratio is found for UV fields $(G_0) < 10^3$ in units of the Habing field which is much lower than the UV field in Mon R2 (5×10^5). It is likely one of the reasons why high HCO abundances and $HCO/H^{13}CO^+$ ratios are not always found toward H$_{II}$ region sources.

In the right plot of Figure 6.17, we compare the column density ratio with dust temperature because one possible HCO formation route is related to thermal grain desorption. It seems that thermal-desorption from grains dose not play an important role since no correlation between the ratios and dust temperatures were found. Even if there are grain photo-desorption processes, it is difficult to probe them with our observational data although H$_{II}$ sources with high HCO abundance $(> 10^{-10})$ are mostly located toward high dust temperatures. If HCO is formed on grain mantles and is desopted by photons, we need to compare HCO with H_2CO, CH_3O and CH_3OH because these molecules are also formed on grain mantles by hydrogenation reactions of CO-ice (Tielens & Whittet 1997; Charnley et al. 1997).

6.7.2 Formation of small hydrocarbons and observational c-C_3H_2/C_2H column density ratio

The formation of small hydrocarbons is still not understood, but several processes have been proposed in PDRs: gas-phase reaction and grain-phase reaction such as photodestruction of PAHs or very small grains (VSGs).

In highly UV-illuminated PDRs with high gas temperatures, within an atomic layer of the PDRs, the gas-phase formation of small hydrocarbon dominates when ionized carbon and electrons are abundant (Cuadrado et al. 2015). Under these conditions, C_2H is formed before forming c-C_3H_2 because c-C_3H_2 needs an additional carbon atom. C_2H is formed in PDRs by

$$C_2H^+ (\text{or } C_2H_2^+ \text{ or } C_2H_3^+) + e^- \rightarrow C_2 \text{ and } C_2H \quad (6.4)$$
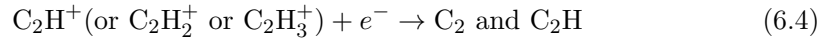
In addition, when gas temperatures are high at about $\sim 1000\,\mathrm{K}$, neutral-neutral reactions especially enhance the abundance of C_2H via barrierless hydrogenation reactions (Pitts et al. 1982) as

$$C_2 + H_2 \rightarrow C_2H + H \quad (6.5)$$

Such production of C_2H is favored in dense and hot PDRs close to highly UV-illuminated regions.

For gas-phase formation of c-C_3H_2, acetylene (C_2H_2) and C^+ form C_3H^+ that reacts with H_2 and then produces the linear and cyclic $C_3H_3^+$ isomers (Maluendes et al. 1993; McEwan et al. 1999). Through dissociative recombination of these molecules (Fossé et al. 2001), linear and cyclic-C_3H_2 are formed as

$$c/l - C_3H_3^+ + e^- \rightarrow c/l - C_3H_2 + H \quad (6.6)$$
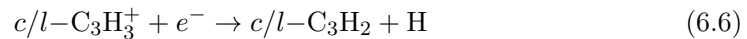
All these reactions for the production of C_2H and c-C_3H_2 require high abundances of C^+ and electrons and high gas temperature. As a consequence, their gas-phase
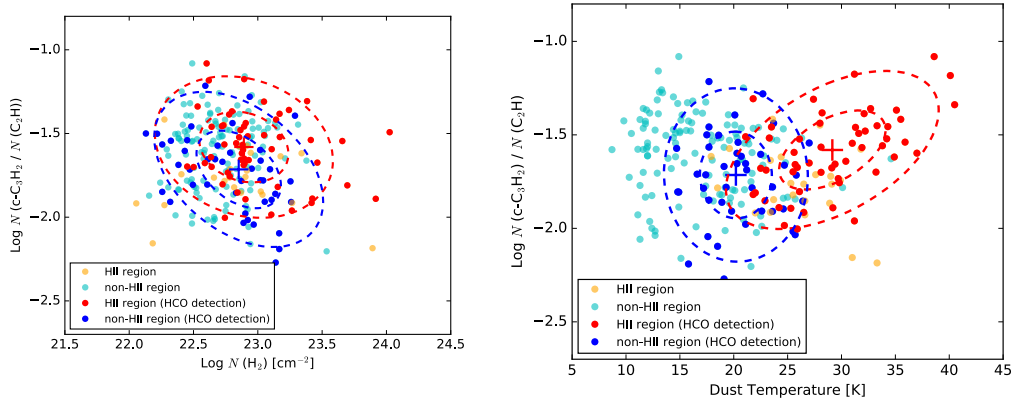
Figure 6.18:   *Left* : Column density ratio of $N(\text{c-C}_3\text{H}_2)/N(\text{C}_2\text{H})$ as a function of T_{clump}. The orange and cyan colors show HII and non-HII regions in logarithmic values. The green and purple dashed line ellipses are PCA ellipses showing distributions of these two populations with 1 and 2σ levels. On the other hand, the red and blue circles only indicate the sources with HCO detections. The red and blue solid ellipses represent the distribution of these selected sources with 1 and 2σ levels.

formation is reduced in cold gas regions ($> A_V \approx 4$) due to lack of C^+/C (locked in CO) and electrons (Pilleri et al. 2013; Cuadrado et al. 2015).

On the other hand, their destruction is caused by photodissociation. Since a strong-UV radiation field destroys small hydrocarbons, their high abundances in such PDRs cannot be explained with only gas-phase reactions. Besides, the $\text{c-C}_3\text{H}_2$ abundances in Mon R2 were found to be higher close to the UV-exposed PDR than the C_2H abundances (Pilleri et al. 2013). The formation sequences mentioned above cannot easily elucidate the high $\text{c-C}_3\text{H}_2$ abundances. Another possible way to produce $\text{c-C}_3\text{H}_2$ is grain-phase formation via photons. The photodissociation of small PAHs or VSGs in PDRs provides fresh small hydrocarbons into highly-illuminated PDRs (Fuente et al. 2003; Pety et al. 2005) and laboratory experiments also showed the production of small hydrocarbons (C_nH_m, $n > m$) from small PAHs (number of carbons ≤ 24) (Useli Bacchitta & Joblin 2007). In particular, PAH-related photochemistry enhances the abundance of $\text{c-C}_3\text{H}_2$ in PDRs via dissociative recombination of C_3H_3^+ with electrons ejected from PAHs or fragmentation of PAHs (Pilleri et al. 2013).

Although those small hydrocarbons are well-known PDR tracers, their abundances vary from one PDR to the other. By investigation how their abundances change toward ATLASGAL clumps, we may gain insight into the origin of the detected small hydro-carbons (C_2H and $\text{c-C}_3\text{H}_2$). In the left plot of Figure 6.18, we compare the column density ratio of $\text{C}_2\text{H}/\text{c-C}_3\text{H}_2$ and H_2 column density toward HII and non-HII region sources. Besides, we mark sources with HCO detection (with dashed-line ellipses) since they indicate the presence of FUV radiation and C^+. As seen in the left plot of Figure 6.17, the distributions of the two regions are not separated. While the $\text{HCO}/\text{H}^{13}\text{CO}^+$ ratios shows the prominent decrease toward high H_2 column densities, such a trend is

Table 6.8: Comparison of C_2H and c-C_3H_2 abundances in different PDRs in $a(x) = a \times 10^x$.

Regions	G_0	n_{H_2} [cm^{-3}]	X(C_2H)	X(c-C_3H_2)	$N_{c-C_3H_2}/N_{C_2H}$
ATLAGAL clumps (This work)					
HII (median)	$\cdots$	$\cdots$	6.4(−09)	1.1(−10)	0.02
HII (full)	$\cdots$	$\cdots$	[0.1 - 2.1](−08)	[0.09 - 15.0](−10)	0.007 − 0.08
IR bright non-HII (median)	$\cdots$	$\cdots$	6.4(−09)	1.6(−10)	0.02
IR bright non-HII (full)	$\cdots$	$\cdots$	[0.2 - 3.0](−08)	[0.5- 4.2](−10)	0.005 − 0.08
IR dark non-HII (median)	$\cdots$	$\cdots$	6.0(−09)	1.5(−10)	0.03
IR dark non-HII (full)	$\cdots$	$\cdots$	[0.1 - 2.1](−08)	[0.4 - 4.2](−10)	0.009 − 0.07
Other PDRs					
MonR2 PDR	5×10^5	3×10^6	1.7(−8)	1.4(−10)	0.008
MonR2 env	$1 − 100$	5×10^4	3.5(−9)	1.4(−11)	0.004
Horsehead	100	1×10^5	1.4(−8)	1.1(−09)	0.08
Oph-W	400	2×10^4	6.0(−9)	6.0(−10)	0.1
IC 63	1500	1×10^5	1.1(−8)	9.0(−10)	0.08
NGC 7023	2600	$10^4 − 10^6$	6.0(−9)	2.0(−10)	0.03
Orion Bar	2×10^4	1×10^5	2.0(−9)	3.8(−11)	0.01−0.03

References: HII and non-HII regions, this work; MonR2 PDR, Pilleri et al. (2013); Horsehead Nebula, Pety et al. (2005); Oph-W, Teyssier et al. (2004); IC 63, Teyssier et al. (2004); NGC 7023, (Fuente et al. 1993, 2003; Pilleri et al. 2012); Orion Bar, Fuente et al. (2003); Ungerechts et al. (1997); Fuente et al. (1996).

not clear in the comparison of the small hydrocarbon ratio and H_2 column density.

Since we could not find evidence of dominant gas-phase reactions, we assume that the observed small hydrocarbon abundances are influence by surrounding molecular clouds where gas-grain reactions and time-dependency may become relevant (Pilleri et al. 2013). We expect that most of the small hydrocarbons are locked on the mantles of dust grains in cold molecular clouds with low kinetic temperature, and then some fraction of them sublimate into the gas-phase during collapse of prestellar cores (Pilleri et al. 2013). The evaporated small hydrocarbons might contribute to the current abundance measured by our observational data. We, therefore, investigated the influences of kinetic temperature on the small hydrocarbon abundances in ALTASGAL clumps.

The right plot of Figure 6.18 shows the N(c-C_3H_2)/N(C_2H) column density ratio versus the dust temperature of the clumps. Without separating different source groups (HII and non-HII regions), the small hydrocarbon ratios seems to be constant in the range $10-35$ K with large scatter. It seems to be consistent with the model results that many molecular species are still on grain mantles below $T_{dust} = 35$ K (Viti et al. 2004; Pilleri et al. 2013). Interestingly, the sources with both detections of the small hydrocarbons and HCO are only seen above 15 K. Since we expect the sources with the HCO detection exposed to FUV radiation, this might indicate the presence of a FUV radiation field toward the source withe dust temperature above 15 K. Despite the large scatter seen in the right plot, these dust temperatures are still much lower than required for pure gas-phase reactions that need temperature of $100-150$ K (Pilleri et al. 2012). The increase of N(c-C_3H_2)/N(C_2H) of HII regions is probably explained via the freeze-out efficiency of small hydrocarbons in clumps and time-dependent effects after the step of molecular sublimation. Indeed, Pilleri et al. (2013) showed that the ratios of c-C_3H_2/C_2H from their models for Mon R2 increase when the freeze-out fraction and evolution time in molecular clouds increase. From our data, it is not clear whether the observed abundances are mostly contributed from the molecular envelope of the HII regions through gas-grain reactions and time-dependent effects, without any PAH-

related chemistry as in the cases of the envelopes of Mon R2 and DR21 (Mookerjea et al. 2012; Pilleri et al. 2013).

Last, we also compared our observational values with the well-measured ratios from nearby PDRs in Table 6.8 because we do not have any information about the strength of the UV radiation fields toward our sources. The UV strength should be related to the emission measures. Large variations of c-C_3H_2/C_2H ratios are seen between sources, and the ratios are independent from G_0, $n(H_2)$, or size of the sources. Overall, our observational results toward all groups of the sources are similar to the known PDRs except for Oph-W which has the highest ratio. The abundances of the small hydrocarbons and their ratios of NGC 7023 are closely matched with the values of our sources. The source is exposed to moderate UV radiation flux, and its volume density range is similar to the PDR and molecular envelope of Mon R2 PDR. As compared with other well-known PDRs, even the abundances and ratios of these small hydrocarbons from the PDRs do not show any trend with any parameters. Some differences in abundances of the molecules may be a complex result of local and initial conditions.

6.8   Uncertainties in the measurements

Overall, our column density measurements agree with those reported in previous studies. However, we could not find clear differences between the sources representative of different evolutionary stages. We used simplifying assumptions such as the optically thin case, equating the dust temperature and gas temperature, and neglecting some factors like source size of the emission. Further uncertainties arise from the assumptions on the used H_2 column densities. In particular, assuming the dust temperature to be equal to the excitation temperature introduces considerable uncertainties toward the HII regions.

6.9   Summary and conclusion

We have investigated 10 molecular transitions from an unbiased molecular line survey in the 3 mm band that was observed using the IRAM 30 m telescope toward 409 ATLASGAL clumps. The ATLASGAL clumps were divided into three groups based on the presence of HII regions and infrared emission: HII, and IR bright non-HII and dark non-HII region sources. The selected molecules were HCO, $H^{13}CO^+$, HOC^+, C_2H, c-C_3H_2, CN, $H^{13}CN$, $HC^{15}N$, $HN^{13}C$ and $C^{18}O$. We find high detection rates (higher than 94 %) for $C^{18}O$, $H^{13}CO^+$, C_2H, c-C_3H_2, CN, and $HN^{13}C$. $H^{13}CN$ is also detected with a good detection rate (75%), and we find HCO and $HC^{15}N$ with detection rates of 32% and 39%, respectively. The non-detection of the HCO, $H^{13}CN$ and $HC^{15}N$ transitions are mostly from the two non-HII region source groups, and we find high detection rates of the molecular transitions toward HII region sources: HCO of 67%, $H^{13}CN$ of 93% and $HC^{15}N$ of 80%.

We also find self-absorption profiles of CN lines. Approximately, half of the cases (40 sources) are observed toward HII region sources (25 clumps), and 15 non-HII region

sources show self-absorption profiles. These self-absorption profiles show blue- and red-skewed emission features that might indicate potential expansion and infall motions in clumps. These clumps with CN self-absorption lines will be good candidates to study further infall motions within the clumps while HII regions are already expanding.

By comparing linewidths of $C^{18}O$ and the selected molecules, we find all the molecular lines become broader from less evolved clumps to more evolved clumps. Such broad linewidths are likely linked to the star-forming activity related to evolutionary stages. In the comparison of C_2H and c-C_3H_2 integrated fluxes, HII region sources have higher integrated flux ratios than IR dark non-HII region sources.

We compared H_2 column densities and determined molecular column densities. Except for HCO, the column densities of the other molecules correlate well with H_2 column densities. The best correlations were obtained from $H^{13}CO^+$ and $HC^{15}N$, which can be considered to be reliable tracers of high column density. Furthermore, we can see the molecular column density increase as embedded objects evolve.

By comparing the molecular abundances and H_2 column density, we find that the abundances of HCO, CN, C_2H and c-C_3H_2 drop with an increase of H_2 column density which corresponds to the visual extinction. However, the abundances of high column density tracers (i.e., $H^{13}CO^+$ and $HC^{15}N$) are almost constant in the range of the H_2 column density. In particular, the HCO abundances are prominently reduced toward high H_2 column density. By comparing with the HCO abundances in cold dark clouds and the Horsehead PDR, the abundances in ATLASGAL clumps are higher than those in the cold dark clouds and the cold gas region in the Horsehead nebula, but lower than the abundance at the Horsehead PDR peak. Furthermore, the HCO abundances in the HII regions seem to be higher than abundances in the non-HII regions at a given H_2 column density. This may be due to an enhancement of HCO molecules in PDRs associated with HII regions.

To minimize uncertainties from unresolved structures and other potential effects, we investigated molecular column density ratios between the molecules chemically related to each other, which are HCO/$H^{13}CO^+$ and c-C_3H_2/C_2H. We found that HCO/$H^{13}CO^+$ ratios decrease as H_2 column density increase. This decrease implies that the detected HCO toward ATLASGAL clumps is likely connected to PDRs. This is also supported by comparing with the ratio of HCO/$H^{13}CO^+$ in the Horsehead Nebula and previous studies. The degree of the difference in the HCO/$H^{13}CO^+$ ratio from high to low H_2 column density is consistent with the model result taking into account photodissociation of H_2CO. Therefore, the measured HCO abundances in the ATLASGAL clumps might be associated with grain-phase reaction because the dust temperatures of the clumps are not hot enough to induce pure gas-phase reactions that efficiently enhance the HCO abundance. To confirm this explanation, we need observational data of H_2CO and CH_3OH molecules to compare with the HCO data. Such molecules are related to hydrogenation reactions of CO-ice on grain mantles.

The results of the c-C_3H_2/C_2H ratios show that the ratios are constant with H_2 column density and dust temperature. The constant ratios toward the H_2 column density can reject the small hydrocarbon formations with the pure gas-phase reaction in PDRs because their abundance in PDRs is very sensitive to A_V according to previous obser-

vational data and models. In addition, no significant change with dust temperature probably indicates that many species are still locked in the dust mantles. However, we found that the c-C_3H_2/C_2H ratios of the H$_{II}$ regions rise from low to high temperature. When the dust temperature increases, molecules are evaporated from dust mantle into the gas-phase. After the sublimation, the released molecules probably react with C^+ and electrons as the central objects evolve. This will cause the small hydrocarbon abundances change in molecular clouds. The c-C_3H_2/C_2H ratios in the molecular envelopes of Mon R2 and DR21 were well interpreted by the models only taking into account gas-grain reaction and time-dependent effects. However, even well-known PDRs also have amply different ratios with no tends. Therefore, we cannot exclude that our measured abundances include some contributions of gas-phase reaction and PAH-related chemical reaction in the embedded small PDRs inside of clumps. We need to clarify which effect is driving the abundance of small hydrocarbons in different molecular circumstances that coexist in the same region. For that reason, high-angular observations of C^+, RRLs, and small hydrocarbons are vital to improve our understanding the small hydrocarbon formations in PDRs and molecular envelopes. In addition, comparing the molecules with PAH emission is also necessary to find additional forming-mechanism of small hydrocarbons.

Summary and future work

Contents

7.1 Summary

Hɪɪ regions formed by O/B-type stars are an excellent signpost for high-mass star-forming regions and demonstrate ongoing star formation in galaxies. Early on, they are still deeply embedded in their natal molecular clumps and obscured at optical wavelengths. Such embedded HII regions are considered the last stage of high-mass star formation. They provide clues how massive stars can obtain a mass $> 10\,\mathrm{M_\odot}$ and affect their ambient ISM in both dynamical and chemical ways. In particular, strong UV radiation and stellar winds from the central high-mass stars and, in their early stages, powerful outflows can significantly alter the chemical composition of the surrounding ISM. It is difficult to understand such complex regions by studying either the HII region or the molecular environment in isolation. Therefore, investigating both is vital to understand the physical connection between the two.

In this thesis, we have studied Hɪɪ and photodissociation regions (PDRs) formed by high-mass O/B stars toward 976 compact dust clumps selected from catalogs of ∼10,000 sources identified by the APEX Telescope Large Area Survey of the Galaxy (ATLAS-GAL. These catalogs ensured a representative mix of star-forming and quiescent clumps such that a variety of different evolutionary stages is represented. Approximately half of the clumps are mid-infrared quiet while the other half are mid-infrared bright. The main goal of this thesis was to understand the physical properties and kinematics of Hɪɪ regions and their influence on the natal dense dust clumps. For this purpose, we utilized radio recombination and molecular emission lines and also combined these lines with continuum emission at infrared and centimeter wavelengths.

Radio recombination lines (RRLs) are very reliable tracers of the ionized gas and can be used to characterize HII regions, as they allow us to investigate the dynamics and physical conditions of the latter directly. The detailed theoretical background of RRLs, for instance emission mechanism under LTE and non-LTE, was described in Chapter 2. In the chapter, we also described how to measure physical properties and excitation conditions of HII regions using RRLs. To investigate properties of surrounding PDRs of HII regions using molecular lines, we explained how physical properties of the molecular gas could be estimated from molecular lines in Chapter 3.

The first part of the scientific analysis has characterized HII regions toward AT-LASGAL dust clumps using RRLs at millimeter and sub-mm wavelengths (Chapters 4 and 5). Until recently, most RRL observations have been carried out at centimeter wavelengths. Owing to instrument improvements, we are now able to perform much more detailed studies of faint RRLs in embedded HII regions and the inner parts of their molecular environments at (sub-)mm wavelengths.

To obtain a large sample of RRLs, we analyzed two large data sets taken from unbiased 3 mm molecular line surveys using the IRAM 30m and Mopra 22m telescopes in Chapter 4. These data covered several RRLs with principle quantum number (n) between 39 and 65, and Δn between 1 and 4 (H$n\alpha$, H$n\beta$, H$n\gamma$, and H$n\delta$). We detected H$n\alpha$ mm-RRL emission toward 178 clumps; H$n\beta$, H$n\gamma$, and H$n\delta$ were also detected toward 65, 23, and 22 clumps, respectively. This is the largest sample of mm-RRLs detections published to date. Comparing the positions of these clumps with radio continuum surveys we identified compact radio counterparts for 134 clumps, confirming their association with known HII regions. The nature of the other 44 detections is unclear, but 8 detections are thought to be potentially new HII regions while the mm-RRL emission from the others may be due to contamination from nearby evolved HII regions. Broad linewidths are seen toward nine clumps (linewidth $> 40 \, \mathrm{km \, s^{-1}}$) revealing significant turbulent motions within the ionized gas; in the past, such wide linewidths were found toward very compact and dense HII regions. We find that the systemic velocity of the associated dense molecular gas, traced by $\mathrm{H^{13}CO^+}$, is consistent with the mm-RRL velocities and confirms them as embedded HII regions. We also find that the linewidth of the $\mathrm{H^{13}CO^+}$ emission is significantly wider than those without mm-RRL detection, indicating a physical connection between the embedded HII region and their natal environments. We also find a correlation between the integrated fluxes of the mm-RRLs and the 6 cm continuum flux densities of their radio counterparts (the correlation coefficient, ρ, is 0.70). By calculating the electron densities we find that the mm-RRL emission is associated with HII regions with electron density $< 10^5 \, \mathrm{cm^{-3}}$ and HII region diameter $> 0.03 \, \mathrm{pc}$.

Based on a large number of RRLs in the 3 mm range (Chapter 4), we aimed at studying their excitation with shorter wavelength (sub)millimeter radio recombination line (submm-RRL) observations (Chapter 5). We proposed and made observations of submm-RRLs with low principal quantum numbers ($n \leq 30$) using the APEX 12 m telescope toward 104 HII regions identified in our 3 mm RRL study. The observations covered the H25α, H28α, and H35β transitions. Toward a small subsample the H26α, H27α, H29α, and H30α lines were observed to avoid contamination by molecular lines

at adjacent frequencies. We have detected submm-RRLs (signal-to-noise $\geq 3\,\sigma$) from compact HII regions embedded within 93 clumps. The submm-RRLs are approximately a factor of 2 brighter than the mm-RRLs and consistent with optically thin emission in local thermodynamic equilibrium (LTE). The average ratio (0.31) of the measured H35β/H28α fluxes is close to the LTE value of 0.28. No indication of RRL maser emission has been found. The Lyman photon flux, bolometric and submm-RRL luminosities toward the submm-RRL detected sources present significant correlations. The trends of dust temperature and the ratio of bolometric luminosity to clump mass, $L_{\rm bol}/M_{\rm clump}$, indicate that the HII regions are related with the most massive and luminous clumps. By estimating the production rate of ionizing photons, Q, from the submm-RRL flux, we find that the Q(H28α) measurements are providing estimates of the Lyman continuum photon flux consistent with those determined from 5 GHz radio continuum emission. Six RRL sources show line profiles that are a combination of a narrow and a broad Gaussian feature. The broad features are likely associated with high-velocity ionized flows.

The second part of this thesis has focused on interface regions (PDRs) between ionized and cold molecular gas using molecular lines observed with the IRAM 30 m telescope at 3 mm (Chapter 6). We selected 8 molecules (HCO, HOC$^+$, C$_2$H, c-C$_3$H$_2$, CN, H^{13}CN, HC^{15}N, HN^{13}C) known as PDR tracers from the 3 mm spectral data. C^{18}O and H^{13}CO$^+$ molecular data were also used as reference molecules tracing dense molecular gas. The molecular lines of 409 ATLASGAL clumps (approximately half of the clumps studied in Chapter 4) were used, and the clumps are classified into three different groups, HII regions, and IR bright non-HII and IR dark non-HII regions. We obtained high detection rates of most molecules, about 94 % except for HCO, H^{13}CN, and HC^{15}N. These three molecules were mostly detected from HII regions (67% for HCO, 93% for H^{13}CN and 80% for HC^{15}N from HII region sources). We also found CN self-absorption profiles toward 40 sources, and of them 25 sources were HII regions. The sources are good candidates to study infalling or expanding motions within the clumps. These molecular lines show that more evolved clumps have broad linewidths and higher integrated flux ratios of C$_2$H/c-C$_3$H$_2$ compared to be less evolved clumps. Also, abundances of HCO as well as HCO/H^{13}CO$^+$ column density ratios significantly drop with increasing H$_2$ column density. In particular, the decrease of the HCO abundance is well matched with a simple toy model that takes into account a significant abundance jump between PDRs and molecular clouds. Comparing HCO/H^{13}CO$^+$ ratios in ATLASGAL clumps and other PDR sources shows similar ratios. All these results suggest that the HCO emission from the clumps is associated with PDRs illuminated by FUV radiation, and the HCO abundance may be related to photodissociation of other molecules such as H$_2$CO. On the other hand, the column density ratios of small hydrocarbons (c-C$_3$H$_2$/C$_2$H) are almost constant in a range of H$_2$ column density and dust temperatures. However, the ratios toward HII regions show a moderate increase with dust temperature.

7.2 Future work

Through our studies of Hɪɪ regions and PDRs toward ATLASGAL dust clumps, we found promising candidates for further investigations of the feedback from Hɪɪ regions onto the ISM and the properties of the last evolutionary stage of high-mass star formation. We here briefly describe our future plan for more detailed follow-up studies.

7.2.1 Dynamics of compact Hɪɪ regions

Through RRL studies at short wavelengths, we identified 17 candidates (Chapters 4 and 5) to study the morphology and evolution of young Hɪɪ regions using high-resolution interferometers. The morphologies of young Hɪɪ regions are closely related to the physical structure of surrounding molecular clouds. Despite many previous efforts, we still do not fully understand the origin of the cometary and bipolar morphologies of Hɪɪ regions. The morphology of Hɪɪ regions is a complicated function of their age, dynamics of both ionized and molecular gas, density structures of the ISM, and relative motions of exciting stars to the ambient ISM (Churchwell 2002). Current models explaining typical morphologies of compact and ultra-compact Hɪɪ regions need to be confronted with measurements of the kinematics of ionized gas (Hoare et al. 2007). The best way to measure velocities of the ionized gas is by observing RRLs (Zhu et al. 2008; Hoare et al. 2012). In particular, those models predict different line profiles and emission characteristics in position-velocity diagrams. Furthermore, RRL observations at mm wavelengths provide reliable measurements of the kinematics since they do not suffer from pressure broadening effects. Observing both radio continuum and mm-RRLs also provide the most precise measurements of the electron temperature and other properties of Hɪɪ regions, without optical depth effects that complicate lower frequency observations. Besides, the identified candidates do not show severe contamination of RRLs with molecular lines.

7.2.2 Study of infalling and expanding motions in the dust clumps using CN lines

We found several clumps with CN self-absorption line profiles indicating either infalling or expanding motions (Chapter 6). In particular, a significant fraction of these cases is found toward the dust clumps hosting Hɪɪ regions. We will propose a detailed study to investigate the dynamical connection between the Hɪɪ region and ambient molecular gas using RRL and CN lines. In combination with the observations proposed in Section 7.2.1, we will obtain a comprehensive kinematical view onto the last evolutionary stage of high-mass star formation and how high-mass stars gain their mass within their natal clumps after forming Hɪɪ regions.

7.2.3 Combining mm/submm-RRLs with centimeter RRLs

The mm/submm-RRLs reported in this thesis are associated with dense dust clumps. Besides, these RRLs were detected toward the clumps with radio continuum counter-

parts which are mostly compact H II or UC H II regions. Their peak velocities are similar to the velocities of molecular lines tracing dense parts of molecular clumps (Chapter 4). These (sub)mm-RRLs originate mostly from dense and young H II regions although RRLs from nearby extended H II regions were picked up within the beam in a few cases. As we briefly introduced in Chapter 1, some radio continuum observations (Kurtz et al. 1999; Kim & Koo 2001) toward UC H II regions showed extended structures of ionized gas surrounding the compact ionized gas. However, there is no clear evidence of their physical connection. To prove the association of the different ionized gas structures, it is necessary to obtain velocity information of the ionized gas using RRLs. We are now observing cm-RRL maps toward the Galactic plane using the Effelsberg 100 m telescope with a newly developed C-band receiver (covering a wide frequency range of $4-8\,\mathrm{GHz}$). This data will provide large maps of cm-RRLs and radio continuum emission, simultaneously. Most of the covered area coincides with ATLASGAL clumps with (sub)mm-RRL detections. Also, we have already obtained observational data of cm-RRLs and radio continuum in the same frequency range with the VLA interferometer to measure the emission on small angular scales. Combination of (sub)mm- and cm-RRLs will allow us to investigate the connection between dense H II regions and their surrounding extended H II regions.

7.2.4 Systematic study of RRLs of hypercompact H II regions

The molecular line surveys used in this thesis were not sensitive enough for a systematic study of RRLs toward HC H II regions. As discussed in Chapters 4 and 5, HC H II regions have weak RRL and radio continuum emission in comparison to UC H II regions. Since they are optically thick at long wavelengths, HC H II regions are considered as an early phase of H II regions soon after a massive young stellar object (MYSO) formed, which are still connected with outflows or jets. Sometime broad RRLs (BRLOs $\geq 40\,\mathrm{km\,s^{-1}}$) at cm and mm wavelengths have been found associated with HC H II regions (Jaffe & Martín-Pintado 1999). So far, we do not have well-studied properties of RRLs toward HC H II regions. Therefore, it is a crucial step to conduct a systematic study of HC H II regions with many sources to understand the connection of BRLOs and HC H II regions, and also to measure physical parameters of the latter via RRLs.

7.2.5 Carbon RRLs to study PDRs

As mentioned in Chapters 1 and 6, ionized carbon is an essential part in the formation of carbon-bearing molecules in PDRs. Ionized carbon regions are created in PDRs immediately away from H II regions. Other PDR molecular tracers studied in Chapter 6 are often also associated with the molecular gas in the clouds. However, observing ionized carbon always traces the PDRs without a doubt. We can trace such regions using carbon RRLs. In general, the ionized carbon regions are very thin. As a result, we need observations with high-angular resolution to resolve the regions. Our observational data was not sensitive enough to detect carbon RRLs toward dust clumps. However, the study of molecular lines in Chapter 6 provides a good sample of PDR

candidates. Therefore, we can conduct more sensitive carbon RRL observations toward these candidates with large single-dish telescopes (i.e., the Effelsberg 100m or IRAM 30m telescopes) or interferometers (i.e., NOEMA or JVLA). Ultimately, combining such carbon RRL observations with SOFIA observations of the $158\,\mu$m Cɪɪ fine structure lines allows to constrain densities and temperatures in the PDRs (Natta et al. 1994).

Submillimeter recombination line surveys

A.1 List of observed sources for submm-RRLs

Table A.1: List of Observed sources for submm-RRLs

ID No.	ATLASGAL clump name	RA α(J2000)	Dec. δ(J2000)	Observed transition
16	AGAL030.818−00.056	18:47:46.4	−01:54:31	(H26α)
17	AGAL030.866+00.114	18:47:15.5	−01:47:14	(H25α), H28α, (H35β)
18	AGAL031.243−00.111	18:48:45.1	−01:33:13	(H25α), H28α, (H35β)
19	AGAL031.281+00.062	18:48:12.1	−01:26:31	H30α
20	AGAL031.412+00.307	18:47:34.2	−01:12:45	(H25α^c?), (H26α^c?), (H28α^c?), (H35β^c?)
21	AGAL032.149+00.134	18:49:31.8	−00:38:08	H30α
22	AGAL032.797+00.191	18:50:30.7	−00:02:01	H25α, H28α, H35β
23	AGAL033.133−00.092	18:52:08.3	+00:08:12	H30α
24	AGAL033.914+00.109	18:52:50.6	+00:55:29	(H25α), H28α, (H35β)
25	AGAL034.258+00.154	18:53:18.5	+01:14:58	H25α, H26α, H27α,H28α,(H35β^c?)
26	AGAL035.466+00.141	18:55:33.7	+02:19:12	H30α
27	AGAL035.579−00.031	18:56:22.7	+02:20:27	H30α
28	AGAL037.874−00.399	19:01:53.6	+04:12:52	H25α,H27α,H28α,H35β
29	AGAL043.148+00.014	19:10:11.0	+09:05:25	(H25α?),H28α,H35β
30	AGAL043.164−00.029	19:10:21.6	+09:05:03	H25α,H28α,H35β
31	AGAL043.166+00.011	19:10:13.4	+09:06:16	H25α,H26α,H28α,H35β
32	AGAL043.178−00.011	19:10:18.7	+09:06:06	(H25α),H28α,(H35β)
33	AGAL043.236−00.047	19:10:33.7	+09:08:21	H25α,H28α,(H35β)
34	AGAL043.889−00.786	19:14:26.7	+09:22:31	(H25α),H28α,H30α,(H35β)
35	AGAL045.071+00.132	19:13:22.0	+10:50:53	H30α
36	AGAL045.121+00.131	19:13:27.8	+10:53:35	H25α,H28α,H35β
37	AGAL045.454+00.061	19:14:20.9	+11:09:13	H25α,H28α,(H35β?)
38	AGAL045.474+00.134	19:14:07.4	+11:12:25	(H30α)
39	AGAL048.991−00.299	19:22:26.1	+14:06:37	(H30α)
40	AGAL049.214−00.342	19:23:01.1	+14:17:10	H30α
41	AGAL049.369−00.301	19:23:10.3	+14:26:27	H30α
42	AGAL049.489−00.389	19:23:43.6	+14:30:32	(H25α^c?),H26α,H28α,(H30α^c?),(H35β^c?)
43	AGAL285.264−00.049	10:31:30.2	−58:02:16	H26α
44	AGAL289.881−00.797	11:01:00.6	−60:50:22	H26α
45	AGAL291.272−00.714	11:11:51.3	−61:18:39	H25α,H26α,H28α,H29α,H30α,H35β
46	AGAL298.224−00.339	12:10:01.0	−62:49:53	H25α,H26α,H28α,H29α,H30α,H35β
47	AGAL298.859−00.437	12:15:24.3	−63:01:24	H25α,H26α,H28α,H29α,H30α,H35β
48	AGAL301.116+00.959	12:36:01.9	−61:51:28	(H25α),H27α,H28α,(H35β)
49	AGAL301.136−00.226	12:35:35.0	−63:02:31	H25α,H28α,(H35β)
50	AGAL305.196+00.034	13:11:13.7	−62:45:04	H25α,H28α,H30α,H35β
51	AGAL305.271−00.009	13:11:55.5	−62:47:16	H25α,H27α,H28α,(H35β?)
52	AGAL305.272+00.296	13:11:43.3	−62:29:00	(H25α),H28α,H30α,(H35β)
53	AGAL305.357+00.202	13:12:31.2	−62:34:10	H25α,H28α,H30α,(H35β?)
54	AGAL305.361+00.186	13:12:33.5	−62:35:03	(H25α),(H28α^c?),(H35β)
55	AGAL305.367+00.212	13:12:35.6	−62:33:33	(H25α),H27α,H28α,(H35β)
56	AGAL311.899+00.084	14:07:35.3	−61:27:20	(H25α),H27α,H28α,(H35β)
57	AGAL312.108+00.309	14:08:41.7	−61:10:45	(H25α?),H28α,H30α,H35β
58	AGAL316.786−00.037	14:45:11.3	−59:48:49	(H25α),H28α,(H35β)
59	AGAL316.799−00.056	14:45:20.5	−59:49:31	H25α,H28α,H30α,H35β
60	AGAL316.811−00.059	14:45:27.8	−59:49:22	(H25α),H28α,H30α,H35β
61	AGAL318.914−00.164	15:00:34.7	−58:58:10	H25α,H28α,H30α,H35β
62	AGAL320.319−00.176	15:10:01.4	−58:17:29	(H25α),H27α,H28α,(H35β)
63	AGAL321.719+01.176	15:13:48.4	−56:24:44	(H25α),H28α,(H35β)
64	AGAL322.158+00.636	15:18:37.3	−56:38:11	(H25α),(H27α),H28α,(H35β)
65	AGAL322.164+00.622	15:18:39.6	−56:38:59	H25α,H28α,H30α,H35β
66	AGAL323.459−00.079	15:29:19.6	−56:31:28	(H25α),H27α,H28α,(H35β)
67	AGAL324.201+00.121	15:32:53.2	−55:56:10	(H25α),H28α,H30α,H35β
68	AGAL326.446+00.907	15:42:16.5	−53:58:27	(H25α),H28α,H30α,(H35β)
69	AGAL326.657+00.594	15:44:42.8	−54:05:43	H25α,H28α,H30α,H35β
70	AGAL327.293−00.579	15:53:08.7	−54:37:08	(H25α^c?),(H28α^c?),(H35β^c?)
71	AGAL327.301−00.552	15:53:02.6	−54:35:42	H25α,H28α,H30α,H35β

Table A.1: continued.

ID No.	ATLASGAL clump name	RA α(J2000)	Dec. δ(J2000)	Observed transition
72	AGAL328.308+00.431	15:54:08.4	−53:11:40	(H25α),H28α,H30α,H35β
73	AGAL328.566−00.534	15:59:37.4	−53:45:58	(H25α),H27α,H28α,(H35β?)
74	AGAL328.809+00.632	15:55:49.6	−52:42:60	H25α,H26α,H28α,H30α,(H35β)
75	AGAL330.294−00.394	16:07:38.8	−52:31:06	(H25α),H28α,(H35β)
76	AGAL330.879−00.367	16:10:20.3	−52:06:15	H25α,H26α,(H28α^c?),(H29α^c?),(H30α^c?),(H35β)
77	AGAL330.954−00.182	16:09:52.9	−51:55:01	H25α,H26α,H28α,H35β
78	AGAL331.521−00.081	16:12:06.3	−51:27:13	(H25α?),H28α,(H35β)
79	AGAL331.546−00.067	16:12:10.6	−51:25:45	(H25α),H28α,(H35β)
80	AGAL332.156−00.449	16:16:40.0	−51:17:06	H25α,H28α,H35β
81	AGAL332.647−00.609	16:19:37.6	−51:03:20	H25α,H28α,(H35β)
82	AGAL332.826−00.549	16:20:11.4	−50:53:19	H25α,H26α,H28α,H35β
83	AGAL333.018−00.449	16:20:36.4	−50:40:56	(H25α),H28α,(H35β)
84	AGAL333.134−00.431	16:21:02.6	−50:35:13	H25α,(H26α?),H27α,H28α,H35β
85	AGAL333.284−00.387	16:21:31.5	−50:27:02	H25α,H26α,H28α,H35β
86	AGAL333.308−00.366	16:21:32.2	−50:25:09	H25α,H28α,H35β
87	AGAL333.604−00.212	16:22:09.9	−50:06:07	H25α,H26α,H28α,H35β
88	AGAL337.121−00.174	16:36:42.9	−47:31:34	(H25α),H28α,(H35β?)
89	AGAL337.922−00.456	16:41:06.1	−47:07:01	(H29α^c?)
90	AGAL338.074+00.011	16:39:38.7	−46:41:33	(H25α),H28α,(H35β)
91	AGAL338.332+00.131	16:40:07.1	−46:25:10	(H25α),H28α,(H35β)
92	AGAL338.434+00.012	16:41:02.0	−46:25:19	H29α
93	AGAL340.784−01.016	16:54:19.7	−45:17:22	H29α
94	AGAL344.424+00.046	17:02:09.0	−41:46:59	(H25α?),H28α,(H35β?)
95	AGAL345.408−00.952	17:09:35.2	−41:35:45	H25α,H28α, (H35β?)
96	AGAL345.488+00.314	17:04:27.7	−40:46:21	H25α,(H26α?),H28α,H35β
97	AGAL345.649+00.009	17:06:16.5	−40:49:39	H25α,H28α,H35β
98	AGAL348.698−01.027	17:19:59.3	−38:57:56	(H25α),(H28α),(H35β)
99	AGAL351.161+00.697	17:19:56.2	−35:57:45	(H26α)
100	AGAL351.244+00.669	17:20:18.9	−35:54:38	H25α,H26α,H28α,H35β
101	AGAL351.416+00.646	17:20:52.3	−35:46:50	(H25α^c?),(H26α^c?),(H28α^c?),(H35β^c?)
102	AGAL351.581−00.352	17:25:25.2	−36:12:45	H26α
103	AGAL353.189+00.899	17:24:44.9	−34:10:36	H25α,H28α,H35β
104	AGAL353.409−00.361	17:30:26.8	−34:41:51	H25α,(H26α),H28α,H35β

Molecular line surveys

B.1 Full list of observed sources

Table B.1: Full list of observed sources.

ATLASGAL name	RA. α(J2000)	Dec. δ(J2000)	Dist. (kpc)	T_{dust} (K)	Type	Classification[†]	Comments
AGAL010.634−00.511	18:10:57.7	−19:59:04	5.0	19.2	non-HII	IR bright or HII	
AGAL010.659+00.079	18:08:49.7	−19:40:23	2.9	9.0	non-HII	70 dark	
AGAL010.669−00.221	18:09:58.1	−19:48:40	2.9	19.5	non-HII	IR bright or HII	
AGAL010.684−00.307	18:10:19.2	−19:50:22	2.9	16.5	non-HII	70 dark	
AGAL010.742−00.126	18:09:45.7	−19:42:08	2.9	11.3	non-HII	24 dark	
AGAL010.747+00.016	18:09:14.4	−19:37:44	2.9	15.6	non-HII	IR bright or HII	
AGAL010.752−00.197	18:10:03.1	−19:43:39	2.9	10.3	non-HII	24 dark	
AGAL010.827−00.022	18:09:32.5	−19:34:28	10.6	18.9	non-HII	IR bright or HII	
AGAL010.957+00.022	18:09:39.2	−19:26:28	2.9	26.9	HII	IR bright or HII	
AGAL010.972−00.094	18:10:07.1	−19:29:03	2.9	11.6	non-HII	IR bright or HII	
AGAL010.982−00.367	18:11:09.4	−19:36:26	5.0	19.8	non-HII	IR bright or HII	
AGAL010.991−00.082	18:10:06.4	−19:27:46	2.9	11.9	non-HII	24 dark	
AGAL011.001−00.372	18:11:12.0	−19:35:43	5.0	20.7	non-HII	IR bright or HII	
AGAL011.034+00.061	18:09:39.7	−19:21:20	2.9	29.9	HII	IR bright or HII	
AGAL011.064−00.099	18:10:19.8	−19:24:12	2.9	11.1	non-HII	24 dark	
AGAL011.082−00.534	18:11:58.7	−19:36:01	3.0	11.8	non-HII	24 dark	
AGAL011.126−00.127	18:10:33.6	−19:21:55	2.9	11.3	non-HII	24 dark	
AGAL011.304−00.059	18:10:40.0	−19:10:36	2.9	12.9	non-HII	70 dark	
AGAL011.344+00.796	18:07:35.1	−18:43:39	2.8	13.4	non-HII	24 dark	
AGAL011.381+00.811	18:07:36.4	−18:41:18	2.8	12.0	non-HII	70 dark	
AGAL011.902−00.141	18:12:11.0	−18:41:30	3.1	19.6	non-HII	IR bright or HII	
AGAL011.917−00.612	18:13:58.0	−18:54:19	3.4	22.8	non-HII	IR bright or HII	
AGAL011.936−00.616	18:14:00.8	−18:53:24	3.4	28.9	HII	IR bright or HII	
AGAL011.942−00.156	18:12:19.3	−18:39:53	3.1	21.5	non-HII	IR bright or HII	
AGAL012.024−00.031	18:12:01.8	−18:31:56	9.4	24.3	non-HII	IR bright or HII	
AGAL012.198−00.034	18:12:23.4	−18:22:48	11.9	28.4	non-HII	IR bright or HII	
AGAL012.208−00.102	18:12:39.6	−18:24:14	13.4	24.4	HII	IR bright or HII	
AGAL012.418+00.506	18:10:50.5	−17:55:45	1.8	25.6	non-HII	IR bright or HII	
AGAL012.496−00.222	18:13:41.4	−18:12:36	2.6	13.0	non-HII	70 dark	
AGAL012.679−00.181	18:13:54.1	−18:01:46	4.8	22.6	non-HII	IR bright or HII	
AGAL012.804−00.199	18:14:13.5	−17:55:32	2.6	−	HII	−	
AGAL012.818+00.322	18:12:19.3	−17:39:53	1.8	14.9	non-HII	24 dark	
AGAL012.853−00.226	18:14:25.1	−17:53:55	2.6	21.7	non-HII	IR bright or HII	
AGAL012.888+00.489	18:11:51.0	−17:31:27	2.5	23.4	non-HII	IR bright or HII	
AGAL012.893−00.282	18:14:42.2	−17:53:22	2.6	18.8	non-HII	IR bright or HII	
AGAL012.899−00.241	18:14:34.6	−17:51:49	2.6	17.6	non-HII	24 dark	
AGAL012.904−00.031	18:13:48.0	−17:45:34	4.8	19.1	non-HII	IR bright or HII	
AGAL012.908−00.259	18:14:39.5	−17:52:02	2.6	23.6	non-HII	IR bright or HII	
AGAL012.914−00.336	18:14:56.6	−17:53:43	2.6	14.2	non-HII	IR bright or HII	
AGAL013.119−00.096	18:14:27.8	−17:36:02	2.6	12.6	non-HII	24 dark	
AGAL013.169+00.077	18:13:56.4	−17:28:33	2.6	17.7	non-HII	24 dark	
AGAL013.178+00.059	18:14:00.5	−17:28:39	2.6	20.3	non-HII	IR bright or HII	
AGAL013.209−00.144	18:14:49.3	−17:32:46	2.6	26.1	HII	IR bright or HII	
AGAL013.276−00.334	18:15:39.5	−17:34:45	2.6	12.2	non-HII	70 dark	
AGAL013.384+00.064	18:14:24.9	−17:17:39	1.9	31.0	HII	IR bright or HII	
AGAL013.658−00.599	18:17:24.0	−17:22:10	4.5	25.7	non-HII	IR bright or HII	
AGAL013.872+00.281	18:14:35.6	−16:45:39	3.9	33.8	HII	IR bright or HII	
AGAL013.882−00.144	18:16:10.1	−16:57:15	1.8	17.8	non-HII	IR bright or HII	
AGAL013.902−00.516	18:17:34.5	−17:06:41	1.5	12.8	non-HII	24 dark	
AGAL013.951−00.407	18:17:16.7	−17:01:12	1.5	14.9	non-HII	24 dark	
AGAL014.084−00.554	18:18:05.2	−16:58:50	1.5	14.8	non-HII	70 dark	
AGAL014.114−00.574	18:18:13.0	−16:57:19	1.5	15.8	non-HII	IR bright or HII	
AGAL014.131−00.522	18:18:03.4	−16:54:58	1.5	11.8	non-HII	24 dark	
AGAL014.181−00.529	18:18:11.2	−16:52:29	1.5	14.7	non-HII	IR bright or HII	
AGAL014.194−00.194	18:16:58.6	−16:42:16	0	0	non-HII		
AGAL014.197−00.214	18:17:03.5	−16:42:44	3.1	12.1	non-HII	24 dark	
AGAL014.204−00.207	18:17:02.9	−16:42:04	3.1	13.0	non-HII	IR bright or HII	
AGAL014.227−00.511	18:18:12.5	−16:49:35	1.5	17.2	non-HII	IR bright or HII	
AGAL014.246−00.071	18:16:37.7	−16:36:05	10.6	17.9	non-HII	IR bright or HII	
AGAL014.327−00.532	18:18:29.3	−16:44:52	1.5	8.7	non-HII	70 dark	
AGAL014.331−00.644	18:18:54.4	−16:47:50	1.5	21.6	non-HII	IR bright or HII	

Table B.1: continued.

ATLASGAL name	RA. α(J2000)	Dec. δ(J2000)	Dist. (kpc)	T_{dust} (K)	Type	Classification†	Comments
AGAL014.434−00.699	18:19:18.2	−16:43:56	1.5	22.5	non-H$_{\text{II}}$	IR bright or H$_{\text{II}}$	
AGAL014.492−00.139	18:17:22.0	−16:25:01	3.1	16.6	non-H$_{\text{II}}$	IR bright or H$_{\text{II}}$	
AGAL014.617+00.332	18:15:53.4	−16:04:57	2.9	16.0	non-H$_{\text{II}}$	24 dark	
AGAL014.632−00.577	18:19:14.6	−16:30:03	1.5	19.1	non-H$_{\text{II}}$	IR bright or H$_{\text{II}}$	
AGAL014.644−00.117	18:17:35.4	−16:16:16	3.1	12.0	non-H$_{\text{II}}$	IR bright or H$_{\text{II}}$	
AGAL014.686−00.222	18:18:03.5	−16:17:11	3.1	14.5	non-H$_{\text{II}}$	24 dark	
AGAL014.711−00.224	18:18:06.5	−16:15:49	3.1	9.7	non-H$_{\text{II}}$	24 dark	
AGAL014.771−00.356	18:18:42.5	−16:16:27	3.1	19.6	non-H$_{\text{II}}$	24 dark	
AGAL014.777−00.334	18:18:38.8	−16:15:29	3.1	23.6	non-H$_{\text{II}}$	IR bright or H$_{\text{II}}$	
AGAL014.777−00.487	18:19:12.3	−16:19:47	2.0	17.9	non-H$_{\text{II}}$	24 dark	
AGAL014.851−00.990	18:21:12.2	−16:30:12	1.9	16.8	non-H$_{\text{II}}$	IR bright or H$_{\text{II}}$	
AGAL015.006+00.009	18:17:50.4	−15:53:38	2.6	14.8	non-H$_{\text{II}}$	24 dark	
AGAL015.013−00.671	18:20:21.3	−16:12:42	2.0	31.5	H$_{\text{II}}$	IR bright or H$_{\text{II}}$	
AGAL015.021−00.621	18:20:10.7	−16:10:43	2.0	26.4	non-H$_{\text{II}}$	IR bright or H$_{\text{II}}$	
AGAL015.024−00.654	18:20:17.9	−16:11:30	2.0	32.7	H$_{\text{II}}$	IR bright or H$_{\text{II}}$	
AGAL015.029−00.669	18:20:22.4	−16:11:44	2.0	35.9	H$_{\text{II}}$	IR bright or H$_{\text{II}}$	
AGAL015.051−00.642	18:20:18.7	−16:09:43	2.0	40.5	H$_{\text{II}}$	IR bright or H$_{\text{II}}$	
AGAL015.053+00.089	18:17:38.9	−15:48:54	2.6	14.4	non-H$_{\text{II}}$	24 dark	
AGAL015.056−00.624	18:20:15.4	−16:08:59	2.0	29.7	H$_{\text{II}}$	IR bright or H$_{\text{II}}$	
AGAL015.193−00.627	18:20:32.6	−16:01:40	2.0	−	H$_{\text{II}}$	−	
AGAL015.216−00.426	18:19:50.6	−15:54:52	2.0	16.5	non-H$_{\text{II}}$	24 dark	
AGAL015.434+00.192	18:18:00.4	−15:25:53	12.1	15.7	non-H$_{\text{II}}$	24 dark	
AGAL015.503−00.419	18:20:22.9	−15:39:34	3.1	15.2	non-H$_{\text{II}}$	24 dark	
AGAL015.583−00.029	18:19:06.4	−15:24:18	10.5	10.5	non-H$_{\text{II}}$	70 dark	
AGAL015.709−00.581	18:21:22.7	−15:33:09	1.8	15.0	non-H$_{\text{II}}$	70 dark	
AGAL015.718−00.594	18:21:26.7	−15:33:09	1.8	12.1	non-H$_{\text{II}}$	24 dark	
AGAL015.791−00.412	18:20:54.9	−15:24:12	12.2	13.4	non-H$_{\text{II}}$	24 dark	
AGAL016.303−00.524	18:22:19.8	−15:00:12	3.3	14.8	non-H$_{\text{II}}$	24 dark	
AGAL016.336−00.586	18:22:37.2	−15:00:05	3.3	15.7	non-H$_{\text{II}}$	IR bright or H$_{\text{II}}$	
AGAL016.404−00.181	18:21:16.3	−14:45:12	3.5	26.8	non-H$_{\text{II}}$	IR bright or H$_{\text{II}}$	
AGAL016.418−00.634	18:22:57.2	−14:57:09	3.3	12.7	non-H$_{\text{II}}$	70 dark	
AGAL016.432−00.667	18:23:06.7	−14:57:19	3.3	11.5	non-H$_{\text{II}}$	24 dark	
AGAL016.442−00.384	18:22:05.0	−14:48:44	3.6	13.4	non-H$_{\text{II}}$	24 dark	
AGAL016.474−00.641	18:23:05.7	−14:54:11	3.3	12.8	non-H$_{\text{II}}$	24 dark	
AGAL016.502−00.642	18:23:09.0	−14:52:51	3.3	14.8	non-H$_{\text{II}}$	24 dark	
AGAL016.586−00.051	18:21:08.9	−14:31:50	4.7	24.7	non-H$_{\text{II}}$	IR bright or H$_{\text{II}}$	
AGAL016.739−00.089	18:21:35.3	−14:24:54	4.9	13.4	non-H$_{\text{II}}$	24 dark	
AGAL016.889+00.484	18:19:47.8	−14:00:34	1.9	14.1	non-H$_{\text{II}}$	24 dark	
AGAL016.916−00.084	18:21:54.2	−14:15:21	3.6	11.6	non-H$_{\text{II}}$	24 dark	
AGAL016.924+00.284	18:20:35.4	−14:04:16	1.9	18.6	non-H$_{\text{II}}$	IR bright or H$_{\text{II}}$	
AGAL016.927+00.957	18:18:09.2	−13:45:12	1.9	18.9	non-H$_{\text{II}}$	IR bright or H$_{\text{II}}$	
AGAL016.942−00.072	18:21:55.3	−14:13:31	15.9	32.2	H$_{\text{II}}$	IR bright or H$_{\text{II}}$	
AGAL016.951+00.779	18:18:50.4	−13:48:54	1.9	23.4	H$_{\text{II}}$	IR bright or H$_{\text{II}}$	
AGAL016.974−00.222	18:22:31.7	−14:16:03	3.6	12.2	non-H$_{\text{II}}$	24 dark	
AGAL016.986−00.922	18:25:06.4	−14:35:09	3.3	12.2	non-H$_{\text{II}}$	IR bright or H$_{\text{II}}$	
AGAL017.029+00.427	18:20:16.7	−13:54:51	1.9	17.7	non-H$_{\text{II}}$	IR bright or H$_{\text{II}}$	
AGAL017.067+00.682	18:19:25.2	−13:45:35	1.9	21.2	non-H$_{\text{II}}$	IR bright or H$_{\text{II}}$	
AGAL017.454−00.194	18:23:21.7	−13:49:54	3.5	17.3	non-H$_{\text{II}}$	IR bright or H$_{\text{II}}$	
AGAL017.554+00.167	18:22:14.3	−13:34:30	1.9	22.0	non-H$_{\text{II}}$	IR bright or H$_{\text{II}}$	
AGAL017.637+00.154	18:22:26.4	−13:30:23	1.9	34.6	non-H$_{\text{II}}$	IR bright or H$_{\text{II}}$	
AGAL017.652+00.172	18:22:24.6	−13:28:58	1.9	19.7	non-H$_{\text{II}}$	IR bright or H$_{\text{II}}$	
AGAL017.667+00.177	18:22:25.0	−13:28:10	1.9	15.4	non-H$_{\text{II}}$	IR bright or H$_{\text{II}}$	
AGAL017.914−00.489	18:25:18.7	−13:33:46	3.3	13.2	non-H$_{\text{II}}$	24 dark	
AGAL017.990−00.347	18:24:56.9	−13:25:35	3.4	14.6	non-H$_{\text{II}}$	IR bright or H$_{\text{II}}$	
AGAL018.098−00.354	18:25:10.5	−13:20:08	3.4	16.5	non-H$_{\text{II}}$	24 dark	no C^{18}O, CN
AGAL018.139+00.334	18:22:46.2	−12:58:47	1.8	13.7	non-H$_{\text{II}}$	70 dark	no C^{18}O, CN
AGAL018.231+00.652	18:21:47.1	−12:44:49	3.2	14.6	non-H$_{\text{II}}$	IR bright or H$_{\text{II}}$	no C^{18}O, CN
AGAL018.286−00.707	18:26:50.0	−13:20:10	3.4	13.9	non-H$_{\text{II}}$	24 dark	no C^{18}O, CN
AGAL018.301−00.389	18:25:41.8	−13:10:21	3.2	29.8	H$_{\text{II}}$	IR bright or H$_{\text{II}}$	no C^{18}O, CN
AGAL018.371−00.381	18:25:48.2	−13:06:29	3.4	20.9	non-H$_{\text{II}}$	IR bright or H$_{\text{II}}$	no C^{18}O, CN
AGAL018.391−00.834	18:27:29.8	−13:18:08	3.4	13.0	non-H$_{\text{II}}$	70 dark	none
AGAL018.409−00.291	18:25:32.4	−13:01:36	4.9	14.4	non-H$_{\text{II}}$	IR bright or H$_{\text{II}}$	no C^{18}O, CN
AGAL018.461−00.002	18:24:35.7	−12:51:08	11.8	25.5	H$_{\text{II}}$	IR bright or H$_{\text{II}}$	no C^{18}O, CN
AGAL018.493−00.199	18:25:22.4	−12:54:53	3.4	14.6	non-H$_{\text{II}}$	70 dark	no C^{18}O, CN
AGAL018.549+00.036	18:24:37.8	−12:45:17	−	24.4	non-H$_{\text{II}}$	24 dark	no C^{18}O, CN
AGAL018.606−00.074	18:25:08.2	−12:45:24	3.4	13.0	non-H$_{\text{II}}$	24 dark	
AGAL018.661+00.036	18:24:50.4	−12:39:21	10.1	21.7	non-H$_{\text{II}}$	IR bright or H$_{\text{II}}$	no C^{18}O, CN
AGAL018.734−00.226	18:25:56.0	−12:42:50	12.6	18.7	non-H$_{\text{II}}$	IR bright or H$_{\text{II}}$	
AGAL018.789−00.286	18:26:15.6	−12:41:33	5.0	11.3	non-H$_{\text{II}}$	IR bright or H$_{\text{II}}$	no C^{18}O, CN
AGAL018.844−00.376	18:26:40.9	−12:41:18	5.0	14.9	non-H$_{\text{II}}$	24 dark	no C^{18}O, CN
AGAL018.883−00.651	18:27:44.9	−12:46:45	5.0	13.9	non-H$_{\text{II}}$	70 dark	no C^{18}O, CN
AGAL018.888−00.474	18:27:07.4	−12:41:40	5.0	22.7	non-H$_{\text{II}}$	IR bright or H$_{\text{II}}$	
AGAL018.991−00.057	18:25:48.5	−12:24:29	5.0	20.1	non-H$_{\text{II}}$	IR bright or H$_{\text{II}}$	no C^{18}O, CN
AGAL019.076−00.287	18:26:48.6	−12:26:25	5.0	29.4	H$_{\text{II}}$	IR bright or H$_{\text{II}}$	no C^{18}O, CN
AGAL019.248+00.267	18:25:07.9	−12:01:46	1.8	18.8	non-H$_{\text{II}}$	IR bright or H$_{\text{II}}$	no C^{18}O, CN
AGAL019.472+00.171	18:25:54.4	−11:52:35	14.1	21.8	non-H$_{\text{II}}$	IR bright or H$_{\text{II}}$	no C^{18}O, CN, H^{13}CN, HC^{15}N
AGAL019.486−00.199	18:27:16.3	−12:02:11	3.3	19.1	non-H$_{\text{II}}$	IR bright or H$_{\text{II}}$	no C^{18}O, CN
AGAL019.589−00.079	18:27:02.1	−11:53:19	5.1	17.7	non-H$_{\text{II}}$	24 dark	no C^{18}O, CN

Table B.1: continued.

ATLASGAL name	RA. α(J2000)	Dec. δ(J2000)	Dist. (kpc)	T_{dust} (K)	Type	Classification[†]	Comments
AGAL019.732−00.651	18:29:22.8	−12:01:36	1.8	12.7	non-HII	70 dark	no C^{18}O, CN
AGAL020.892−00.179	18:29:51.9	−10:46:49	11.7	13.3	non-HII	24 dark	
AGAL021.561−00.032	18:30:36.0	−10:07:11	7.7	21.7	non-HII	IR bright or HII	
AGAL022.038+00.222	18:30:34.4	−09:34:49	3.5	21.3	non-HII	IR bright or HII	
AGAL022.332−00.154	18:32:29.0	−09:29:37	13.1	19.6	non-HII	IR bright or HII	
AGAL022.376+00.447	18:30:24.0	−09:10:40	3.6	13.1	non-HII	24 dark	
AGAL022.412+00.317	18:30:56.5	−09:12:14	5.4	16.4	non-HII	24 dark	
AGAL022.484−00.936	18:35:34.7	−09:43:05	4.0	16.3	non-HII	24 dark	
AGAL022.531−00.192	18:32:59.6	−09:20:08	4.2	11.6	non-HII	70 dark	
AGAL023.007−00.409	18:34:39.6	−09:00:42	4.6	20.9	non-HII	IR bright or HII	
AGAL023.206−00.377	18:34:54.9	−08:49:19	4.6	20.1	non-HII	24 dark	
AGAL023.277−00.214	18:34:27.8	−08:41:01	4.6	11.7	non-HII	70 dark	
AGAL023.387+00.187	18:33:14.3	−08:23:57	4.6	20.2	non-HII	IR bright or HII	
AGAL023.437−00.182	18:34:38.8	−08:31:38	5.9	24.6	non-HII	IR bright or HII	
AGAL023.656−00.127	18:34:51.6	−08:18:22	6.2	26.3	non-HII	IR bright or HII	
AGAL023.817+00.386	18:33:19.5	−07:55:38	−	24.3	non-HII	IR bright or HII	
AGAL023.964−00.109	18:35:22.0	−08:01:28	6.2	20.1	non-HII	IR bright or HII	
AGAL024.010+00.489	18:33:18.3	−07:42:27	5.8	10.3	non-HII	70 dark	
AGAL024.141+00.127	18:34:50.8	−07:45:35	3.6	19.8	non-HII	IR bright or HII	
AGAL024.416+00.101	18:35:26.1	−07:31:44	7.8	17.7	non-HII	24 dark	
AGAL024.629+00.172	18:35:35.5	−07:18:09	7.4	18.3	non-HII	IR bright or HII	
AGAL024.633−00.324	18:37:22.6	−07:31:41	2.9	21.0	non-HII	IR bright or HII	
AGAL024.651−00.169	18:36:51.5	−07:26:27	6.0	19.0	non-HII	24 dark	
AGAL024.673−00.151	18:36:50.0	−07:24:49	6.0	25.7	HII	IR bright or HII	
AGAL024.728+00.152	18:35:50.9	−07:13:27	6.0	25.0	non-HII	IR bright or HII	
AGAL024.789+00.082	18:36:12.3	−07:12:10	6.0	26.5	HII	IR bright or HII	
AGAL024.796+00.101	18:36:10.4	−07:11:43	6.0	28.1	HII	IR bright or HII	
AGAL025.409+00.106	18:37:16.9	−06:38:25	10.2	21.9	non-HII	IR bright or HII	
AGAL025.649+01.051	18:34:21.0	−05:59:42	2.1	23.4	non-HII	IR bright or HII	
AGAL026.159+00.156	18:38:28.6	−05:57:09	7.6	17.0	non-HII	IR bright or HII	
AGAL026.509+00.282	18:38:40.4	−05:35:01	7.6	24.8	non-HII	IR bright or HII	
AGAL026.652+00.007	18:39:54.9	−05:34:55	7.6	24.0	non-HII	IR bright or HII	
AGAL026.849+00.181	18:39:40.0	−05:19:44	5.5	16.5	non-HII	IR bright or HII	
AGAL027.000−00.296	18:41:38.9	−05:24:48	4.1	18.0	non-HII	IR bright or HII	
AGAL027.184−00.081	18:41:13.3	−05:09:02	13.4	30.4	non-HII	IR bright or HII	
AGAL027.314+00.177	18:40:32.1	−04:55:02	12.5	19.9	non-HII	IR bright or HII	
AGAL027.366−00.166	18:41:51.1	−05:01:43	8.0	21.8	non-HII	IR bright or HII	
AGAL027.464+00.119	18:41:01.3	−04:48:37	8.4	13.3	non-HII	24 dark	
AGAL027.551−00.936	18:44:56.6	−05:12:52	4.4	16.6	non-HII	24 dark	
AGAL027.758+00.051	18:41:48.0	−04:34:53	5.9	18.9	non-HII	IR bright or HII	
AGAL027.796−00.277	18:43:02.3	−04:41:49	2.9	22.6	non-HII	IR bright or HII	
AGAL027.974−00.421	18:43:52.8	−04:36:13	11.9	14.4	non-HII	IR bright or HII	
AGAL028.194−00.074	18:43:02.6	−04:14:52	6.1	17.6	non-HII	70 dark	
AGAL028.199−00.049	18:42:58.1	−04:13:58	6.1	28.2	HII	IR bright or HII	
AGAL028.231+00.041	18:42:42.5	−04:09:46	6.1	−	non-HII	−	
AGAL028.273−00.167	18:43:31.1	−04:13:21	4.5	11.8	non-HII	IR bright or HII	
AGAL028.344+00.061	18:42:50.6	−04:03:20	4.5	9.8	non-HII	24 dark	
AGAL028.354+00.072	18:42:49.0	−04:02:22	4.5	12.0	non-HII	70 dark	
AGAL028.361+00.054	18:42:53.8	−04:02:30	4.5	8.9	non-HII	24 dark	
AGAL028.398+00.081	18:42:52.0	−03:59:56	4.5	18.5	non-HII	IR bright or HII	
AGAL028.564−00.236	18:44:17.7	−03:59:42	4.7	−	non-HII	−	
AGAL028.658+00.144	18:43:07.0	−03:44:09	4.5	9.7	non-HII	70 dark	
AGAL028.677−00.277	18:44:39.7	−03:54:43	4.7	16.5	non-HII	IR bright or HII	
AGAL028.707−00.294	18:44:46.3	−03:53:41	4.7	17.1	non-HII	IR bright or HII	
AGAL028.722−00.296	18:44:48.5	−03:52:58	4.7	16.2	non-HII	IR bright or HII	
AGAL028.831−00.252	18:44:51.0	−03:45:54	4.7	24.6	non-HII	IR bright or HII	
AGAL028.849+00.051	18:43:47.6	−03:36:36	7.4	15.9	non-HII	24 dark	
AGAL028.861+00.066	18:43:46.0	−03:35:30	7.4	27.6	non-HII	IR bright or HII	
AGAL029.117+00.027	18:44:22.1	−03:23:02	5.6	16.0	non-HII	IR bright or HII	
AGAL029.409−00.646	18:47:18.2	−03:25:44	4.0	11.6	non-HII	70 dark	
AGAL029.556+00.186	18:44:36.9	−02:55:08	4.5	12.0	non-HII	70 dark	
AGAL029.591−00.614	18:47:31.7	−03:15:14	4.4	15.8	non-HII	70 dark	
AGAL029.861+00.029	18:45:43.3	−02:43:10	5.2	17.4	non-HII	IR bright or HII	no H^{13}CO$^+$
AGAL029.911−00.042	18:46:04.6	−02:42:29	5.2	23.0	HII	IR bright or HII	
AGAL029.954−00.016	18:46:03.5	−02:39:24	5.2	35.5	HII	IR bright or HII	
AGAL029.976−00.047	18:46:12.5	−02:39:12	5.2	21.8	non-HII	IR bright or HII	no C^{18}O, H^{13}CO$^+$
AGAL030.003−00.269	18:47:03.7	−02:43:39	5.2	18.5	non-HII	IR bright or HII	
AGAL030.198−00.169	18:47:03.0	−02:30:36	5.2	28.7	non-HII	IR bright or HII	
AGAL030.321+00.296	18:45:37.4	−02:11:20	5.2	11.2	non-HII	70 dark	
AGAL030.419−00.231	18:47:40.2	−02:20:29	5.2	20.3	non-HII	IR bright or HII	
AGAL030.429−00.116	18:47:16.8	−02:16:47	5.2	17.6	non-HII	IR bright or HII	
AGAL030.568−00.026	18:47:13.1	−02:06:56	5.2	17.6	non-HII	24 dark	
AGAL030.588−00.042	18:47:18.7	−02:06:23	2.7	25.3	HII	IR bright or HII	
AGAL030.603+00.176	18:46:33.3	−01:59:35	5.2	17.4	non-HII	IR bright or HII	
AGAL030.683−00.074	18:47:35.4	−02:02:11	5.2	25.9	HII	IR bright or HII	
AGAL030.703−00.067	18:47:36.0	−02:00:59	5.2	24.2	HII	IR bright or HII	
AGAL030.718−00.082	18:47:40.9	−02:00:31	5.2	21.6	HII	IR bright or HII	onlyC^{18}O data
AGAL030.731−00.079	18:47:41.3	−01:59:43	5.2	21.1	non-HII	24 dark	
AGAL030.753−00.051	18:47:38.2	−01:57:51	5.2	35.4	HII	IR bright or HII	only C^{18}O data

Table B.1: continued.

ATLASGAL name	RA. α(J2000)	Dec. δ(J2000)	Dist. (kpc)	T_{dust} (K)	Type	Classification[†]	Comments
AGAL030.786+00.204	18:46:47.6	−01:49:02	5.2	20.9	non-H$_{II}$	IR bright or H$_{II}$	
AGAL030.811−00.111	18:47:57.6	−01:56:16	5.2	12.5	non-H$_{II}$	70 dark	
AGAL030.818+00.274	18:46:36.6	−01:45:22	5.2	33.0	non-H$_{II}$	IR bright or H$_{II}$	
AGAL030.818−00.056	18:47:46.4	−01:54:31	5.2	25.1	H$_{II}$	IR bright or H$_{II}$	only C^{18}O data
AGAL030.848−00.081	18:47:55.4	−01:53:36	5.2	18.7	non-H$_{II}$	IR bright or H$_{II}$	
AGAL030.863−00.039	18:47:48.1	−01:51:38	5.2	18.4	non-H$_{II}$	70 dark	
AGAL030.866+00.114	18:47:15.5	−01:47:14	2.7	31.3	H$_{II}$	IR bright or H$_{II}$	
AGAL030.866−00.119	18:48:05.7	−01:53:33	5.2	19.7	non-H$_{II}$	IR bright or H$_{II}$	
AGAL030.893+00.139	18:47:13.5	−01:45:08	5.2	12.9	non-H$_{II}$	70 dark	
AGAL030.898+00.162	18:47:08.6	−01:44:14	5.2	22.3	non-H$_{II}$	IR bright or H$_{II}$	
AGAL030.971−00.141	18:48:22.0	−01:48:30	5.2	14.8	non-H$_{II}$	IR bright or H$_{II}$	
AGAL030.996−00.076	18:48:10.8	−01:45:29	5.2	23.2	non-H$_{II}$	IR bright or H$_{II}$	
AGAL031.024+00.262	18:47:01.0	−01:34:39	5.2	13.2	non-H$_{II}$	IR bright or H$_{II}$	
AGAL031.044+00.261	18:47:03.9	−01:33:40	5.2	13.0	non-H$_{II}$	24 dark	
AGAL031.103+00.261	18:47:10.2	−01:30:29	5.2	16.3	non-H$_{II}$	24 dark	
AGAL031.183−00.147	18:48:46.3	−01:37:28	2.7	20.7	non-H$_{II}$	IR bright or H$_{II}$	
AGAL031.243−00.111	18:48:45.1	−01:33:13	12.9	30.5	H$_{II}$	IR bright or H$_{II}$	
AGAL031.254+00.057	18:48:10.1	−01:28:08	5.2	15.8	non-H$_{II}$	70 dark	
AGAL031.281+00.062	18:48:12.1	−01:26:31	5.2	24.7	H$_{II}$	IR bright or H$_{II}$	
AGAL031.396−00.257	18:49:33.0	−01:29:03	5.2	32.2	H$_{II}$	IR bright or H$_{II}$	
AGAL031.412+00.307	18:47:34.2	−01:12:45	5.2	22.0	H$_{II}$	IR bright or H$_{II}$	
AGAL031.464+00.186	18:48:06.1	−01:13:13	5.2	13.2	non-H$_{II}$	70 dark	
AGAL031.581+00.077	18:48:41.8	−01:10:00	5.2	27.0	non-H$_{II}$	IR bright or H$_{II}$	
AGAL031.584−00.117	18:49:23.8	−01:15:17	2.1	23.9	non-H$_{II}$	IR bright or H$_{II}$	
AGAL031.699−00.494	18:50:56.9	−01:19:16	4.6	10.5	non-H$_{II}$	70 dark	
AGAL031.982+00.064	18:49:28.4	−00:48:53	5.2	12.4	non-H$_{II}$	70 dark	
AGAL032.001−00.197	18:50:26.8	−00:55:15	6.1	15.0	non-H$_{II}$	24 dark	
AGAL032.007+00.062	18:49:32.8	−00:47:25	5.2	14.0	non-H$_{II}$	IR bright or H$_{II}$	
AGAL032.019+00.064	18:49:32.7	−00:47:05	5.2	15.1	non-H$_{II}$	IR bright or H$_{II}$	
AGAL032.044+00.059	18:49:36.2	−00:45:59	5.2	20.7	non-H$_{II}$	IR bright or H$_{II}$	
AGAL032.149+00.134	18:49:31.8	−00:38:08	5.2	23.5	H$_{II}$	IR bright or H$_{II}$	
AGAL032.192+00.192	18:50:22.4	−00:05:12	13.0	17.3	non-H$_{II}$	IR bright or H$_{II}$	
AGAL032.744−00.076	18:51:21.8	−00:12:06	11.7	23.7	H$_{II}$	IR bright or H$_{II}$	
AGAL032.797+00.191	18:50:30.7	−00:02:01	13.0	34.2	H$_{II}$	IR bright or H$_{II}$	
AGAL032.821−00.331	18:52:24.6	−00:14:58	5.1	28.4	non-H$_{II}$	IR bright or H$_{II}$	
AGAL033.133−00.092	18:52:08.3	+00:08:12	9.4	26.6	H$_{II}$	IR bright or H$_{II}$	
AGAL033.238−00.022	18:52:04.0	+00:15:37	6.5	20.3	non-H$_{II}$	IR bright or H$_{II}$	
AGAL033.393+00.011	18:52:14.6	+00:24:55	6.5	19.4	non-H$_{II}$	IR bright or H$_{II}$	
AGAL033.568+00.027	18:52:29.8	+00:34:38	6.5	10.5	non-H$_{II}$	24 dark	
AGAL033.623−00.032	18:52:48.6	+00:35:55	6.5	12.0	non-H$_{II}$	24 dark	
AGAL033.744−00.007	18:52:56.9	+00:42:58	6.5	11.9	non-H$_{II}$	IR bright or H$_{II}$	
AGAL033.851+00.017	18:53:03.2	+00:49:33	10.5	18.3	non-H$_{II}$	24 dark	
AGAL033.914+00.109	18:52:50.6	+00:55:29	6.5	27.4	H$_{II}$	IR bright or H$_{II}$	
AGAL033.979−00.021	18:53:25.2	+00:55:22	1.6	23.0	non-H$_{II}$	24 dark	
AGAL034.089+00.011	18:53:30.5	+01:02:03	1.6	19.2	non-H$_{II}$	IR bright or H$_{II}$	
AGAL034.243+00.132	18:53:21.9	+01:13:36	1.6	33.3	H$_{II}$	IR bright or H$_{II}$	
AGAL034.258+00.154	18:53:18.5	+01:14:58	1.6	29.2	H$_{II}$	IR bright or H$_{II}$	
AGAL034.372−00.664	18:56:25.9	+00:58:39	2.1	14.9	non-H$_{II}$	IR bright or H$_{II}$	
AGAL034.401+00.226	18:53:18.6	+01:24:40	1.6	20.5	non-H$_{II}$	IR bright or H$_{II}$	
AGAL034.411+00.234	18:53:18.1	+01:25:24	1.6	22.7	non-H$_{II}$	IR bright or H$_{II}$	
AGAL034.454+00.006	18:54:11.5	+01:21:26	5.3	18.2	non-H$_{II}$	IR bright or H$_{II}$	
AGAL034.459+00.247	18:53:20.2	+01:28:22	1.6	14.4	non-H$_{II}$	24 dark	
AGAL034.591+00.242	18:53:36.1	+01:35:13	15.0	23.0	non-H$_{II}$	IR bright or H$_{II}$	
AGAL034.712−00.596	18:56:48.2	+01:18:47	2.2	22.1	non-H$_{II}$	IR bright or H$_{II}$	
AGAL034.739−00.119	18:55:09.8	+01:33:16	4.8	11.1	non-H$_{II}$	70 dark	
AGAL034.742−00.132	18:55:12.2	+01:33:02	4.8	12.4	non-H$_{II}$	24 dark	
AGAL034.751−00.092	18:55:05.2	+01:34:40	3.1	20.1	non-H$_{II}$	IR bright or H$_{II}$	
AGAL034.757+00.024	18:54:40.7	+01:38:07	4.8	27.0	non-H$_{II}$	IR bright or H$_{II}$	
AGAL034.821+00.351	18:53:38.1	+01:50:28	10.4	21.6	non-H$_{II}$	IR bright or H$_{II}$	
AGAL035.026+00.349	18:54:00.6	+02:01:22	2.3	31.8	non-H$_{II}$	IR bright or H$_{II}$	
AGAL035.042−00.472	18:56:58.4	+01:39:42	2.4	13.4	non-H$_{II}$	24 dark	
AGAL035.132−00.744	18:58:06.4	+01:37:10	2.2	19.4	non-H$_{II}$	IR bright or H$_{II}$	
AGAL035.144−00.754	18:58:08.8	+01:37:15	2.2	21.7	non-H$_{II}$	IR bright or H$_{II}$	
AGAL035.197−00.742	18:58:12.9	+01:40:41	2.2	−	non-H$_{II}$	−	
AGAL035.297−00.897	18:58:57.2	+01:41:42	2.2	15.4	non-H$_{II}$	IR bright or H$_{II}$	
AGAL035.457−00.179	18:56:41.2	+02:10:02	4.1	22.2	non-H$_{II}$	IR bright or H$_{II}$	
AGAL035.466+00.141	18:55:33.7	+02:19:12	4.7	26.1	H$_{II}$	IR bright or H$_{II}$	
AGAL035.484−00.287	18:57:08.2	+02:08:10	2.7	11.8	non-H$_{II}$	24 dark	
AGAL035.579+00.007	18:56:14.3	+02:21:31	10.4	14.7	non-H$_{II}$	IR bright or H$_{II}$	
AGAL035.579−00.031	18:56:22.7	+02:20:27	10.4	28.0	H$_{II}$	IR bright or H$_{II}$	
AGAL035.681−00.176	18:57:05.0	+02:22:00	2.1	15.6	non-H$_{II}$	24 dark	
AGAL035.794−00.174	18:57:16.9	+02:28:00	3.7	19.6	non-H$_{II}$	IR bright or H$_{II}$	
AGAL036.794−00.204	18:59:13.2	+03:20:39	5.8	19.9	non-H$_{II}$	IR bright or H$_{II}$	
AGAL036.826−00.039	18:58:41.0	+03:26:51	3.6	15.0	non-H$_{II}$	IR bright or H$_{II}$	
AGAL036.839−00.022	18:58:39.3	+03:28:00	3.6	16.9	non-H$_{II}$	24 dark	
AGAL036.878−00.474	19:00:19.8	+03:17:43	9.9	21.2	non-H$_{II}$	IR bright or H$_{II}$	
AGAL036.899−00.409	19:00:08.4	+03:20:36	4.7	16.0	non-H$_{II}$	24 dark	
AGAL037.031−00.039	18:59:03.6	+03:37:48	5.8	18.0	non-H$_{II}$	24 dark	
AGAL037.469−00.102	19:00:06.6	+03:59:46	9.7	24.0	non-H$_{II}$	IR bright or H$_{II}$	
AGAL037.498+00.531	18:57:53.3	+04:18:17	0.7	25.8	non-H$_{II}$	IR bright or H$_{II}$	

Table B.1: continued.

ATLASGAL name	RA. α(J2000)	Dec. δ(J2000)	Dist. (kpc)	$T_{\rm dust}$ (K)	Type	Classification[†]	Comments
AGAL037.554+00.201	18:59:09.9	+04:12:18	4.9	22.5	non-HII	IR bright or HII	
AGAL037.874−00.399	19:01:53.6	+04:12:52	9.7	35.1	HII	IR bright or HII	
AGAL038.119−00.229	19:01:44.1	+04:30:38	6.5	26.6	non-HII	IR bright or HII	
AGAL038.354−00.952	19:04:44.8	+04:23:18	2.1	15.0	non-HII	IR bright or HII	
AGAL038.371−00.149	19:01:54.9	+04:46:22	6.5	17.2	non-HII	IR bright or HII	
AGAL038.957−00.466	19:04:07.6	+05:08:56	1.9	12.7	non-HII	IR bright or HII	
AGAL039.048−00.880	19:05:46.4	+05:02:11	4.2	10.7	non-HII	24 dark	
AGAL039.099+00.492	19:00:58.1	+05:42:46	11.5	26.4	non-HII	IR bright or HII	
AGAL039.903−01.349	19:09:01.6	+05:34:44	1.9	−	non-HII	IR bright or HII	
AGAL040.283−00.219	19:05:41.4	+06:26:15	6.4	24.6	non-HII	IR bright or HII	
AGAL041.049−00.247	19:07:12.5	+07:06:22	8.9	20.1	non-HII	IR bright or HII	
AGAL041.347−00.136	19:07:21.7	+07:25:20	11.7	21.0	non-HII	IR bright or HII	
AGAL042.098+00.351	19:07:00.5	+08:18:44	11.5	28.7	non-HII	IR bright or HII	
AGAL043.038−00.452	19:11:38.9	+08:46:30	−	23.7	non-HII	IR bright or HII	
AGAL043.148+00.014	19:10:11.0	+09:05:25	11.1	31.2	HII	IR bright or HII	
AGAL043.164−00.029	19:10:21.6	+09:05:03	11.1	31.2	HII	IR bright or HII	
AGAL043.166+00.011	19:10:13.4	+09:06:16	11.1	33.3	HII	IR bright or HII	
AGAL043.178−00.011	19:10:18.7	+09:06:06	11.1	31.9	HII	IR bright or HII	
AGAL043.179−00.519	19:12:08.9	+08:52:11	8.5	23.3	HII	IR bright or HII	
AGAL043.236−00.047	19:10:33.7	+09:08:21	11.1	25.3	HII	IR bright or HII	
AGAL043.306−00.212	19:11:17.1	+09:07:29	4.2	26.5	non-HII	IR bright or HII	
AGAL043.794−00.127	19:11:53.8	+09:35:49	6.0	34.9	HII	IR bright or HII	
AGAL043.889−00.786	19:14:26.7	+09:22:31	4.4	22.5	HII	IR bright or HII	
AGAL043.994−00.012	19:11:51.6	+09:49:40	6.0	28.4	non-HII	IR bright or HII	
AGAL044.291+00.034	19:12:15.0	+10:06:44	8.1	15.1	non-HII	IR bright or HII	
AGAL044.309+00.041	19:12:17.8	+10:07:39	8.1	23.5	non-HII	IR bright or HII	
AGAL044.422+00.537	19:10:41.0	+10:27:36	13.8	24.6	non-HII	IR bright or HII	
AGAL045.071+00.132	19:13:22.0	+10:50:53	8.0	37.0	HII	IR bright or HII	
AGAL045.096+00.131	19:13:25.3	+10:52:19	8.0	20.7	non-HII	IR bright or HII	
AGAL045.121+00.131	19:13:27.8	+10:53:35	8.0	34.5	HII	IR bright or HII	
AGAL045.454+00.061	19:14:20.9	+11:09:13	8.4	32.5	HII	IR bright or HII	
AGAL045.466+00.046	19:14:25.4	+11:09:28	8.4	29.0	HII	IR bright or HII	
AGAL045.474+00.134	19:14:07.4	+11:12:25	8.4	33.2	HII	IR bright or HII	
AGAL045.493+00.126	19:14:11.0	+11:13:07	8.4	24.9	non-HII	IR bright or HII	
AGAL045.886−00.509	19:17:13.9	+11:16:18	5.8	12.5	non-HII	24 dark	
AGAL046.174−00.524	19:17:49.8	+11:31:07	3.8	13.6	non-HII	24 dark	
AGAL046.426−00.237	19:17:16.5	+11:52:32	3.7	14.5	non-HII	IR bright or HII	
AGAL048.606+00.022	19:20:31.1	+13:55:24	10.8	34.3	HII	IR bright or HII	
AGAL048.991−00.299	19:22:26.1	+14:06:37	5.3	−	HII	−	
AGAL049.043−01.077	19:25:22.2	+13:47:20	3.2	24.0	non-HII	IR bright or HII	
AGAL049.074−00.352	19:22:47.2	+14:09:32	5.3	17.7	non-HII	24 dark	
AGAL049.214−00.342	19:23:01.1	+14:17:10	5.3	28.0	HII	IR bright or HII	
AGAL049.253−00.411	19:23:21.2	+14:17:25	5.3	20.4	non-HII	IR bright or HII	
AGAL049.268−00.337	19:23:06.9	+14:20:15	5.3	21.1	non-HII	IR bright or HII	
AGAL049.369−00.301	19:23:10.3	+14:26:27	5.3	−	HII	−	
AGAL049.401−00.227	19:22:58.3	+14:30:29	5.3	17.6	non-HII	24 dark	
AGAL049.402−00.212	19:22:55.6	+14:30:50	5.3	18.0	non-HII	IR bright or HII	
AGAL049.489−00.389	19:23:43.6	+14:30:32	5.3	31.6	HII	IR bright or HII	
AGAL049.566−00.274	19:23:27.8	+14:37:45	5.3	19.2	non-HII	IR bright or HII	
AGAL049.599−00.249	19:23:26.4	+14:40:18	5.3	21.0	non-HII	IR bright or HII	
AGAL050.046+00.767	19:20:36.0	+15:32:39	12.8	22.9	non-HII	IR bright or HII	
AGAL050.221−00.606	19:25:57.8	+15:03:00	2.9	20.7	non-HII	IR bright or HII	
AGAL050.777+00.152	19:24:17.4	+15:54:05	3.5	19.6	non-HII	IR bright or HII	
AGAL051.678+00.719	19:23:58.7	+16:57:44	10.9	29.1	non-HII	IR bright or HII	
AGAL052.208+00.687	19:25:08.5	+17:24:48	10.9	19.8	non-HII	IR bright or HII	
AGAL053.141+00.069	19:29:17.3	+17:56:21	4.0	21.8	non-HII	IR bright or HII	
AGAL053.619+00.034	19:30:22.6	+18:20:32	4.0	21.1	non-HII	IR bright or HII	
AGAL055.158−00.299	19:34:45.9	+19:31:38	3.9	25.5	non-HII	IR bright or HII	
AGAL058.469+00.436	19:38:57.8	+22:46:38	3.6	18.5	non-HII	IR bright or HII	
AGAL058.709+00.662	19:38:36.8	+23:05:43	2.2	21.7	non-HII	IR bright or HII	
AGAL058.774+00.644	19:38:49.0	+23:08:41	2.2	28.1	non-HII	IR bright or HII	
AGAL059.187+00.106	19:41:43.9	+23:14:10	2.2	18.0	non-HII	IR bright or HII	
AGAL059.351−00.196	19:43:15.2	+23:13:47	2.2	13.2	non-HII	70 dark	
AGAL059.359−00.207	19:43:18.0	+23:14:01	2.2	21.4	non-HII	IR bright or HII	
AGAL059.497−00.236	19:43:42.5	+23:20:15	2.2	15.8	non-HII	IR bright or HII	
AGAL059.577−00.201	19:43:45.9	+23:25:27	2.2	17.7	non-HII	IR bright or HII	
AGAL059.584−00.146	19:43:33.3	+23:27:23	8.6	16.5	non-HII	IR bright or HII	
AGAL059.602+00.912	19:39:34.6	+23:59:47	3.5	29.1	non-HII	IR bright or HII	
AGAL059.634−00.191	19:43:49.6	+23:28:42	2.2	20.8	non-HII	IR bright or HII	no $C^{18}O$, CN
AGAL059.636−00.252	19:44:04.1	+23:26:54	2.2	17.5	non-HII	IR bright or HII	
AGAL059.782+00.066	19:43:10.9	+23:44:04	2.2	23.6	non-HII	IR bright or HII	
AGAL059.789+00.631	19:41:03.0	+24:01:13	2.2	19.3	non-HII	IR bright or HII	
AGAL059.832+00.672	19:40:59.1	+24:04:41	2.2	30.1	non-HII	IR bright or HII	
AGAL059.894−00.047	19:43:51.4	+23:46:30	−	18.8	non-HII	IR bright or HII	
G011.1012−0.3803	18:11:26.8	−19:30:27	−	−	non-HII	−	
G012.7914−0.1958	18:14:11.0	−17:56:27	−	−	non-HII	−	
G013.2029−0.1352	18:14:47.6	−17:32:55	−	−	non-HII	−	
G014.1007−0.5559	18:18:08.4	−16:57:31	−	−	non-HII	−	
G014.6010−0.5400	18:19:03.8	−16:30:42	−	−	non-HII	−	
G025.1526−0.2906	18:38:12.5	−07:02:58	−	−	non-HII	−	

Table B.1: continued.

ATLASGAL name	RA. α(J2000)	Dec. δ(J2000)	Dist. (kpc)	T_{dust} (K)	Type	Classification[†]	Comments
G027.2546+0.1368	18:40:34.3	−04:59:20	−	−	non-H$_{II}$	−	
G028.5559−0.2260	18:44:15.4	−03:59:49	−	−	non-H$_{II}$	−	
G028.6117+0.0306	18:43:26.1	−03:49:52	−	−	non-H$_{II}$	−	
G030.5946+0.1639	18:46:34.8	−02:00:12	−	−	non-H$_{II}$	−	
G030.7306−0.0604	18:47:38.4	−01:59:11	−	−	H$_{II}$	−	no C^{18}O
G031.0441+0.2742	18:47:01.2	−01:33:20	−	−	non-H$_{II}$	−	
G032.9956+0.0415	18:51:24.4	+00:04:33	−	−	non-H$_{II}$	−	
G059.7948+0.0749	19:43:10.4	+23:44:57	−	−	non-H$_{II}$	−	

(†) The classification is defined by Urquhart et al. (2017).

B.2   HFS line parameters

Table B.2:   The line parameters of hyperfine lines of C_2H ($N = 1 - 0$) and $H^{13}CN$ ($J = 1 - 0$). We only provide here the first entires of the whole table **which is provided in Appendix**. T_{MB} **is the peak intensity of the brightest component of a give molecular hyperfine lines**. For C_2H the peak intensity is of the transition $NJF = 1(3/2)2 - 0(1/2)1$ and for $H^{13}CN$ it is of the transition $JF = 12 - 01$.

ATLASGAL name	Line	v_{LSR} $(km\,s^{-1})$	Δv $(km\,s^{-1})$	τ_{tot}	T_{MB} (K)	rms (K)
AGAL006.216−00.609	C_2H	18.62±0.02	2.16±0.04	2.35±0.24	2.18	0.05
	$H^{13}CN$	18.68±0.06	2.63±0.14	0.10±0.43	0.74	0.05
AGAL008.049−00.242	C_2H	39.33±0.04	1.95±0.11	0.58±0.73	0.87	0.05
	$H^{13}CN$	39.44±0.16	1.97±0.35	0.66±0.67	0.21	0.05
AGAL008.671−00.356	C_2H	35.03±0.02	4.39±0.05	2.09±0.12	3.14	0.06
AGAL008.684−00.367	$H^{13}CN$	38.26±0.10	5.23±0.23	2.18±0.43	1.01	0.06
AGAL008.706−00.414	C_2H	38.85±0.04	2.40±0.12	2.99±0.79	0.73	0.05
	$H^{13}CN$	38.93±0.08	2.24±0.23	3.03±1.45	0.38	0.04
AGAL010.079−00.196	C_2H	28.09±0.12	4.00±0.29	6.12±1.49	0.22	0.03
	$H^{13}CN$	28.41±0.49	3.31±1.02	1.69±4.59	0.08	0.04
AGAL010.104−00.416	C_2H	13.42±0.30	11.91±0.78	0.10±5.19	0.28	0.05
	$H^{13}CN$	11.78±0.23	1.56±0.51	0.10±3.41	0.14	0.05
AGAL010.151−00.344	C_2H	9.55±0.01	5.09±0.02	0.54±0.03	2.44	0.04
	$H^{13}CN$	9.70±0.15	4.93±0.37	3.05±0.64	0.43	0.04
AGAL010.168−00.362	C_2H	14.30±0.03	6.50±0.07	1.04±0.13	1.78	0.04
	$H^{13}CN$	14.02±0.09	5.86±0.31	0.84±0.35	0.68	0.04
AGAL010.213−00.322	C_2H	11.44±0.03	4.18±0.08	5.71±0.42	1.17	0.05
	$H^{13}CN$	10.94±0.19	4.60±0.39	6.73±1.47	0.33	0.05
AGAL010.214−00.306	C_2H	11.58±0.03	3.32±0.10	1.94±0.40	0.88	0.04
	$H^{13}CN$	11.93±0.27	4.70±0.83	3.60±1.33	0.23	0.04
AGAL010.284−00.114	C_2H	14.04±0.01	3.47±0.05	1.56±0.22	1.19	0.03
	$H^{13}CN$	13.76±0.05	3.64±0.11	0.70±0.37	0.58	0.03
AGAL010.288−00.124	C_2H	13.85±0.02	2.61±0.04	3.16±0.28	1.44	0.04
	$H^{13}CN$	13.57±0.05	2.87±0.11	1.15±0.49	0.68	0.04
AGAL010.321−00.231	C_2H	32.44±0.13	4.04±0.40	1.84±1.20	0.34	0.05
AGAL010.323−00.161	C_2H	12.31±0.02	3.19±0.04	0.10±0.01	1.43	0.05
	$H^{13}CN$	12.23±0.05	3.13±0.10	0.10±0.55	1.00	0.05
AGAL010.342−00.142	C_2H	12.35±0.01	3.12±0.03	0.63±0.06	2.40	0.05
	$H^{13}CN$	12.46±0.06	3.92±0.14	0.77±0.39	1.10	0.05
AGAL010.444−00.017	C_2H	74.99±0.25	7.77±0.91	0.10±0.21	0.33	0.06
	$H^{13}CN$	75.39±0.32	5.66±0.84	3.51±1.51	0.21	0.04
AGAL010.472+00.027	$H^{13}CN$	65.89±0.06	12.80±0.10	0.10±0.06	1.61	0.07
AGAL010.579−00.349	C_2H	−2.77±0.09	2.74±0.23	3.02±1.28	0.28	0.03
AGAL010.618−00.031	C_2H	63.56±0.06	2.12±0.17	0.10±0.32	0.41	0.04
	$H^{13}CN$	62.86±0.54	3.49±0.88	7.04±5.40	0.08	0.04
AGAL010.619−00.422	C_2H	−1.68±0.08	3.47±0.19	3.00±0.95	0.35	0.04
	$H^{13}CN$	−1.38±0.29	2.98±0.71	0.10±1.03	0.11	0.03
AGAL010.624−00.384	C_2H	−2.90±0.01	5.60±0.04	1.60±0.10	4.22	0.06
	$H^{13}CN$	−4.06±0.01	7.16±0.02	0.10±0.00	3.36	0.06
AGAL010.626−00.337	C_2H	−4.21±0.02	2.83±0.05	3.78±0.28	1.80	0.05
	$H^{13}CN$	−3.86±0.04	2.96±0.08	0.16±0.12	0.87	0.05
AGAL010.634−00.511	C_2H	−2.86±0.10	3.11±0.32	1.90±1.25	0.38	0.05
AGAL010.659+00.079	C_2H	21.23±0.21	4.27±0.55	0.10±1.96	0.22	0.05
AGAL010.669−00.221	C_2H	29.17±0.03	1.44±0.07	4.08±0.83	0.64	0.03
	$H^{13}CN$	29.08±0.07	1.49±0.24	4.29±1.92	0.29	0.04
AGAL010.684−00.307	C_2H	−2.12±0.08	2.18±0.23	3.71±1.82	0.34	0.05
AGAL010.742−00.126	C_2H	29.07±0.05	1.51±0.13	16.45±3.89	0.34	0.05
	$H^{13}CN$	29.23±0.22	2.48±0.57	4.11±3.41	0.19	0.05
AGAL010.752−00.197	C_2H	32.12±0.06	1.48±0.15	7.47±2.75	0.39	0.05
	$H^{13}CN$	36.39±0.17	1.13±0.65	0.10±1.08	0.15	0.05
AGAL010.827−00.022	C_2H	22.00±0.14	2.26±0.27	10.94±4.17	0.14	0.04
AGAL010.957+00.022	C_2H	21.34±0.04	4.00±0.12	0.22±0.38	1.03	0.05
	$H^{13}CN$	21.54±0.16	4.28±0.34	0.10±1.67	0.39	0.05
AGAL010.972−00.094	C_2H	30.02±0.04	1.68±0.11	8.18±1.62	0.47	0.04
	$H^{13}CN$	30.02±0.11	2.27±0.34	0.10±2.53	0.32	0.05
AGAL010.982−00.367	C_2H	−0.57±0.08	2.50±0.22	2.00±1.30	0.29	0.03
	$H^{13}CN$	−0.34±0.20	2.13±0.52	0.10±3.70	0.14	0.04
AGAL010.991−00.082	C_2H	29.78±0.06	2.11±0.16	5.17±1.47	0.45	0.05
	$H^{13}CN$	29.53±0.14	1.51±0.31	9.27±6.98	0.17	0.05
AGAL011.001−00.372	C_2H	−0.96±0.07	2.35±0.22	2.17±1.27	0.31	0.03
	$H^{13}CN$	−0.74±0.70	6.72±2.42	0.10±1.30	0.08	0.03
AGAL011.034+00.061	C_2H	15.71±0.06	4.05±0.17	1.94±0.61	0.65	0.05
	$H^{13}CN$	15.28±0.19	3.58±0.43	0.46±1.73	0.28	0.05
AGAL011.064−00.099	C_2H	29.39±0.05	1.18±0.10	15.92±4.23	0.33	0.05

Table B.2: continued.

ATLASGAL name	Line	v_{LSR} (km s^{-1})	Δv (km s^{-1})	τ_{tot}	T_{MB} (K)	rms (K)
AGAL011.082−00.534	C$_2$H	29.82±0.03	1.97±0.07	4.32±0.66	0.70	0.03
	H^{13}CN	29.73±0.68	2.00±2.26	0.32±0.10	0.28	0.04
AGAL011.126−00.127	C$_2$H	30.41±0.02	1.42±0.05	8.61±1.28	0.49	0.03
	H^{13}CN	30.54±0.06	1.88±0.14	0.10±2.61	0.28	0.03
AGAL011.304−00.059	C$_2$H	31.73±0.06	1.59±0.14	7.39±2.85	0.23	0.03
AGAL011.344+00.796	C$_2$H	27.86±0.07	1.61±0.18	4.39±2.09	0.35	0.05
	H^{13}CN	28.23±0.13	1.67±0.35	5.08±3.63	0.18	0.05
AGAL011.381+00.811	C$_2$H	26.82±0.07	1.63±0.20	4.73±2.11	0.34	0.04
AGAL011.902−00.141	C$_2$H	37.67±0.06	4.31±0.17	1.63±0.50	0.59	0.04
	H^{13}CN	36.98±0.28	6.19±0.95	1.98±1.10	0.23	0.04
AGAL011.917−00.612	C$_2$H	35.66±0.04	3.52±0.11	2.79±0.43	1.13	0.05
	H^{13}CN	36.16±0.13	9.98±0.38	0.73±0.14	0.56	0.05
AGAL011.936−00.616	C$_2$H	38.48±0.02	3.60±0.06	4.05±0.30	1.53	0.05
	H^{13}CN	38.11±0.06	4.76±0.15	0.63±0.31	1.09	0.05
AGAL011.942−00.156	C$_2$H	43.50±0.11	5.15±0.29	0.10±0.17	0.43	0.05
	H^{13}CN	43.38±0.22	4.30±0.42	0.10±0.80	0.28	0.04
AGAL012.024−00.031	C$_2$H	110.98±0.05	3.07±0.17	1.06±0.64	0.54	0.04
	H^{13}CN	110.16±0.50	5.13±1.48	1.42±2.39	0.14	0.04
AGAL012.198−00.034	C$_2$H	51.19±0.04	4.02±0.07	0.10±0.38	0.63	0.03
	H^{13}CN	51.41±0.20	4.67±0.43	2.70±0.93	0.29	0.04
AGAL012.208−00.102	C$_2$H	24.36±0.04	6.34±0.11	0.94±0.23	1.27	0.05
	H^{13}CN	23.33±0.04	6.93±0.07	1.06±0.01	0.80	0.05
AGAL012.418+00.506	C$_2$H	17.98±0.01	3.09±0.02	1.25±0.04	2.30	0.03
	H^{13}CN	17.77±0.02	2.96±0.05	0.10±0.04	1.28	0.03
AGAL012.496−00.222	C$_2$H	35.87±0.02	1.92±0.06	2.38±0.46	0.94	0.03
	H^{13}CN	35.80±0.08	2.30±0.17	0.55±0.40	0.31	0.03
AGAL012.679−00.181	C$_2$H	56.31±0.03	3.88±0.07	3.97±0.28	1.18	0.04
	H^{13}CN	56.01±0.08	4.08±0.17	3.28±0.50	0.58	0.03
AGAL012.804−00.199	C$_2$H	35.37±0.01	4.37±0.02	0.45±0.02	5.24	0.06
	H^{13}CN	35.37±0.03	4.50±0.04	0.91±0.04	2.29	0.05
AGAL012.818+00.322	C$_2$H	19.79±0.01	1.12±0.04	7.88±0.67	0.97	0.04
	H^{13}CN	19.82±0.11	1.13±0.29	1.72±2.81	0.15	0.04
AGAL012.853−00.226	C$_2$H	36.66±0.02	3.22±0.06	3.43±0.29	1.57	0.05
	H^{13}CN	36.54±0.05	2.51±0.18	0.54±0.80	0.66	0.04
AGAL012.888+00.489	C$_2$H	33.40±0.02	3.15±0.05	4.22±0.31	1.58	0.05
	H^{13}CN	32.96±0.04	3.84±0.09	0.82±0.33	1.41	0.05
AGAL012.893−00.282	C$_2$H	35.42±0.10	4.50±0.26	2.84±1.00	0.45	0.05
	H^{13}CN	34.59±0.46	3.21±0.86	11.29±11.81	0.11	0.06
AGAL012.899−00.241	C$_2$H	36.30±0.08	3.79±0.20	6.17±0.96	0.53	0.05
	H^{13}CN	37.05±0.22	3.64±0.61	0.71±1.67	0.26	0.05
AGAL012.904−00.031	C$_2$H	56.77±0.05	3.51±0.15	1.10±0.55	0.80	0.05
	H^{13}CN	57.01±0.09	3.73±0.20	1.81±0.66	0.66	0.05
AGAL012.908−00.259	C$_2$H	37.02±0.00	3.98±0.02	2.76±0.00	1.89	0.03
	H^{13}CN	37.41±0.03	4.14±0.07	2.66±0.18	1.22	0.03
AGAL012.914−00.336	C$_2$H	37.26±0.12	2.91±0.35	5.33±1.98	0.31	0.05
	H^{13}CN	36.80±0.18	3.01±0.46	3.97±2.74	0.25	0.05
AGAL013.119−00.096	C$_2$H	35.96±0.04	1.54±0.09	1.75±0.99	0.73	0.05
	H^{13}CN	35.95±0.13	1.54±0.25	9.51±6.92	0.19	0.05
AGAL013.169+00.077	C$_2$H	50.59±0.08	3.82±0.19	1.67±0.72	0.43	0.04
	H^{13}CN	49.84±0.16	2.35±0.43	0.10±1.37	0.16	0.04
AGAL013.178+00.059	C$_2$H	49.50±0.02	3.28±0.06	1.27±0.23	2.15	0.06
	H^{13}CN	49.30±0.05	3.89±0.12	0.59±0.37	1.17	0.05
AGAL013.209−00.144	C$_2$H	52.42±0.03	3.31±0.09	2.94±0.41	1.09	0.05
	H^{13}CN	51.72±1.99	4.18±0.19	0.25±0.18	0.32	0.05
AGAL013.276−00.334	C$_2$H	41.19±0.03	1.28±0.09	13.72±2.81	0.42	0.04
	H^{13}CN	41.17±0.15	2.44±0.61	1.47±2.16	0.21	0.04
AGAL013.384+00.064	C$_2$H	14.99±0.19	4.06±0.56	4.51±1.90	0.20	0.04
	H^{13}CN	14.84±0.66	4.36±1.06	0.10±2.11	0.12	0.05
AGAL013.658−00.599	C$_2$H	47.77±0.03	2.95±0.07	2.14±0.33	1.51	0.05
	H^{13}CN	47.53±0.07	4.21±0.15	3.07±0.49	0.92	0.05
AGAL013.872+00.281	C$_2$H	48.86±0.00	2.93±0.04	1.34±0.03	2.16	0.05
	H^{13}CN	48.36±0.05	2.94±0.12	0.10±0.27	0.88	0.05
AGAL013.882−00.144	C$_2$H	18.03±0.08	3.23±0.24	0.10±0.68	0.47	0.05
	H^{13}CN	17.79±0.18	3.36±0.47	0.10±16.00	0.26	0.05
AGAL013.902−00.516	C$_2$H	22.93±0.01	1.39±0.02	4.03±0.31	1.84	0.04
	H^{13}CN	22.94±0.07	1.53±0.15	0.10±2.49	0.35	0.04
AGAL013.951−00.407	C$_2$H	20.22±0.04	2.39±0.10	3.63±0.70	0.86	0.05
	H^{13}CN	19.96±0.09	2.70±0.23	2.26±1.24	0.48	0.05
AGAL014.084−00.554	C$_2$H	22.25±0.02	1.69±0.04	5.97±0.55	1.06	0.04
	H^{13}CN	22.23±0.06	1.50±0.14	0.10±0.71	0.34	0.04
AGAL014.114−00.574	C$_2$H	20.09±0.02	3.17±0.05	6.73±0.40	1.35	0.05
	H^{13}CN	19.87±0.05	3.00±0.08	0.24±0.12	0.91	0.05
AGAL014.131−00.522	C$_2$H	21.22±0.02	1.17±0.05	7.49±1.09	0.91	0.05
	H^{13}CN	21.32±0.10	1.13±1.70	0.10±0.79	0.24	0.05
AGAL014.181−00.529	C$_2$H	21.40±0.01	1.52±0.04	3.37±0.39	1.32	0.04

Table B.2: continued.

ATLASGAL name	Line	v_{LSR} (km s^{-1})	Δv (km s^{-1})	τ_{tot}	T_{MB} (K)	rms (K)
	H^{13}CN	21.39±0.04	1.64±0.09	0.28±0.23	0.48	0.04
AGAL014.194−00.194	C$_2$H	39.63±0.03	3.52±0.08	0.66±0.29	1.72	0.06
AGAL014.194−00.194	H^{13}CN	39.91±0.06	3.94±0.15	1.89±0.41	1.02	0.05
AGAL014.197−00.214	H^{13}CN	39.66±0.19	1.50±0.41	5.58±5.26	0.15	0.05
AGAL014.204−00.207	H^{13}CN	39.19±0.21	2.95±0.49	3.39±2.08	0.17	0.04
AGAL014.227−00.511	C$_2$H	19.59±0.01	2.38±0.03	3.33±0.24	1.64	0.04
	H^{13}CN	19.40±0.02	2.49±0.06	0.76±0.30	1.19	0.03
AGAL014.246−00.071	C$_2$H	60.29±0.08	3.89±0.19	3.29±0.77	0.56	0.05
	H^{13}CN	60.81±0.31	3.99±0.71	3.90±2.67	0.19	0.05
AGAL014.327−00.532	C$_2$H	20.10±0.01	1.12±0.00	3.03±0.49	1.05	0.04
	H^{13}CN	20.19±0.05	1.13±0.12	0.10±1.63	0.33	0.04
AGAL014.331−00.644	C$_2$H	22.43±0.02	2.93±0.05	8.09±0.43	1.44	0.05
	H^{13}CN	22.15±0.03	3.54±0.07	1.19±0.25	1.74	0.05
AGAL014.434−00.699	C$_2$H	17.72±0.02	1.84±0.05	1.88±0.34	1.30	0.04
	H^{13}CN	17.58±0.04	1.69±0.10	0.10±0.53	0.53	0.04
AGAL014.492−00.139	C$_2$H	39.84±0.05	2.99±0.12	6.20±0.86	0.70	0.05
	H^{13}CN	40.05±0.18	4.38±0.40	3.50±1.24	0.36	0.05
AGAL014.617+00.332	C$_2$H	26.81±0.03	1.61±0.07	2.79±0.65	1.03	0.05
	H^{13}CN	26.76±0.14	2.02±0.51	0.10±1.22	0.25	0.05
AGAL014.632−00.577	C$_2$H	18.63±0.01	2.14±0.03	6.85±0.35	2.17	0.05
	H^{13}CN	18.61±0.03	2.67±0.08	0.89±0.40	1.29	0.05
AGAL014.644−00.117	C$_2$H	40.92±0.09	2.61±0.18	0.10±1.21	0.45	0.05
AGAL014.711−00.224	H^{13}CN	36.92±0.68	1.92±2.26	1.55±0.10	0.18	0.06
AGAL014.771−00.356	H^{13}CN	33.98±0.68	10.44±2.26	0.10±0.10	0.14	0.03
AGAL014.777−00.334	C$_2$H	32.73±0.07	1.74±0.17	4.77±1.93	0.36	0.05
	H^{13}CN	32.83±0.66	5.91±2.34	1.78±2.71	0.14	0.05
AGAL014.777−00.487	C$_2$H	21.95±0.02	1.43±0.07	1.28±0.58	0.86	0.04
	H^{13}CN	21.81±0.09	1.13±0.23	7.57±3.14	0.15	0.04
AGAL014.851−00.990	C$_2$H	22.10±0.03	2.27±0.09	0.83±0.45	1.15	0.05
	H^{13}CN	22.02±0.16	2.57±0.35	0.10±0.94	0.26	0.05
AGAL015.006+00.009	C$_2$H	24.48±0.07	2.83±0.20	1.86±0.99	0.39	0.04
	H^{13}CN	24.51±0.20	1.89±0.39	0.10±2.49	0.13	0.04
AGAL015.013−00.671	C$_2$H	18.97±0.00	4.08±0.01	1.48±0.01	5.93	0.04
	H^{13}CN	18.43±0.01	3.27±0.02	0.31±0.03	2.52	0.04
AGAL015.021−00.621	C$_2$H	19.78±0.67	2.83±2.23	2.36±0.10	2.62	0.04
	H^{13}CN	19.48±0.05	2.88±0.13	1.86±0.58	0.71	0.04
AGAL015.024−00.654	C$_2$H	20.36±0.01	7.72±0.03	1.09±0.03	2.37	0.04
	H^{13}CN	20.71±0.06	7.17±0.09	0.10±0.03	0.77	0.04
AGAL015.029−00.669	C$_2$H	19.48±0.00	3.34±0.01	0.10±0.00	10.64	0.11
	H^{13}CN	19.21±0.01	3.82±0.02	0.37±0.03	2.99	0.05
AGAL015.051−00.642	C$_2$H	17.98±0.01	2.17±0.02	0.17±0.05	2.54	0.04
	H^{13}CN	18.16±0.05	1.72±0.11	0.10±0.17	0.57	0.04
AGAL015.053+00.089	C$_2$H	29.73±0.05	1.38±0.11	3.72±1.69	0.36	0.04
AGAL015.056−00.624	C$_2$H	17.43±0.01	3.42±0.01	1.50±0.03	3.48	0.04
	H^{13}CN	17.50±0.07	3.04±0.12	0.10±0.12	0.60	0.04
AGAL015.193−00.627	C$_2$H	20.68±0.01	3.29±0.02	0.71±0.04	2.96	0.04
	H^{13}CN	20.82±0.03	2.50±0.06	0.10±0.12	1.21	0.04
AGAL015.434+00.192	C$_2$H	48.06±0.04	2.40±0.14	1.24±0.69	0.54	0.04
	H^{13}CN	48.12±0.68	2.75±2.26	0.10±0.10	0.15	0.04
AGAL015.503−00.419	C$_2$H	39.56±0.03	1.38±0.07	3.66±0.90	0.67	0.04
	H^{13}CN	39.44±0.09	1.13±0.08	0.10±1.19	0.19	0.04
AGAL015.709−00.581	C$_2$H	17.12±0.02	1.12±0.02	3.10±0.66	0.80	0.04
	H^{13}CN	17.36±0.09	1.26±0.23	0.10±2.69	0.24	0.04
AGAL015.718−00.594	C$_2$H	17.61±0.04	2.18±0.11	1.17±0.69	0.63	0.04
	H^{13}CN	17.37±0.09	2.26±0.18	0.10±0.83	0.33	0.04
AGAL015.791−00.412	C$_2$H	45.91±0.06	1.61±0.16	2.71±1.47	0.41	0.04
AGAL016.336−00.586	C$_2$H	41.41±0.05	2.14±0.14	2.62±0.94	0.53	0.04
	H^{13}CN	41.32±0.15	2.08±0.40	2.94±2.71	0.19	0.04
AGAL016.404−00.181	H^{13}CN	45.68±0.66	4.44±2.08	5.75±5.22	0.13	0.04
AGAL016.418−00.634	C$_2$H	41.37±0.13	1.49±0.19	26.90±8.95	0.18	0.04
AGAL016.442−00.384	C$_2$H	47.73±0.03	1.57±0.10	1.51±0.83	0.65	0.04
AGAL016.586−00.051	C$_2$H	59.38±0.02	3.05±0.06	1.51±0.26	1.46	0.04
	H^{13}CN	59.46±0.05	3.83±0.10	0.98±0.29	0.97	0.04
AGAL016.889+00.484	C$_2$H	26.05±0.19	5.05±0.33	1.46±1.36	0.26	0.04
AGAL016.916−00.084	C$_2$H	40.89±0.01	1.12±0.02	3.84±0.49	1.02	0.04
	H^{13}CN	40.80±0.05	1.13±0.08	2.81±1.32	0.31	0.04
AGAL016.924+00.284	C$_2$H	24.72±0.04	2.92±0.09	1.40±0.49	0.54	0.03
AGAL016.927+00.957	C$_2$H	20.93±0.01	2.48±0.04	4.35±0.29	1.54	0.04
	H^{13}CN	20.83±0.03	2.36±0.11	0.39±0.51	0.90	0.04
AGAL016.942−00.072	C$_2$H	−3.88±0.10	4.20±0.28	1.37±0.87	0.38	0.04
	H^{13}CN	−4.29±0.20	1.42±0.68	0.10±2.05	0.13	0.04
AGAL016.951+00.779	H^{13}CN	24.94±0.04	1.66±0.10	0.10±0.23	0.37	0.03
AGAL016.986−00.922	C$_2$H	40.61±0.05	2.11±0.13	3.30±0.98	0.50	0.04
	H^{13}CN	40.23±0.18	2.64±0.46	2.61±2.70	0.17	0.04

Table B.2: continued.

ATLASGAL name	Line	v_{LSR} (km s^{-1})	Δv (km s^{-1})	τ_{tot}	T_{MB} (K)	rms (K)
AGAL017.029+00.427	C$_2$H	24.82±0.03	1.77±0.07	3.49±0.80	0.65	0.04
AGAL017.067+00.682	C$_2$H	23.62±0.09	5.59±0.25	1.85±0.79	0.43	0.04
	H^{13}CN	25.04±1.23	5.87±1.87	0.10±0.89	0.06	0.04
AGAL017.554+00.167	C$_2$H	20.36±0.07	2.88±0.16	3.17±1.03	0.40	0.04
AGAL017.637+00.154	C$_2$H	22.28±0.01	2.29±0.02	0.77±0.05	2.79	0.04
	H^{13}CN	22.23±0.04	2.17±0.08	0.10±0.12	0.84	0.04
AGAL017.652+00.172	C$_2$H	23.03±0.03	1.69±0.07	3.53±0.69	0.82	0.04
	H^{13}CN	22.87±0.14	1.86±0.29	0.10±2.31	0.21	0.04
AGAL017.667+00.177	C$_2$H	22.29±0.03	1.50±0.11	1.10±0.82	0.68	0.04
AGAL017.990−00.347	C$_2$H	41.97±0.03	1.50±0.08	4.24±0.89	0.71	0.04
	H^{13}CN	41.82±0.07	2.45±0.35	0.10±4.56	0.27	0.04
AGAL018.139+00.334	C$_2$H	22.86±0.02	1.12±0.00	3.31±0.60	0.75	0.03
AGAL018.231+00.652	C$_2$H	38.07±0.02	1.40±0.07	5.26±0.87	0.67	0.03
	H^{13}CN	37.68±0.13	2.14±0.32	2.35±1.87	0.18	0.03
AGAL018.286−00.707	C$_2$H	44.75±0.06	1.85±0.18	2.81±1.46	0.30	0.03
AGAL018.301−00.389	C$_2$H	33.10±0.01	3.15±0.02	1.22±0.03	2.60	0.04
	H^{13}CN	33.14±0.04	3.28±0.09	0.10±0.28	0.79	0.03
AGAL018.371−00.381	C$_2$H	44.57±0.01	2.21±0.03	0.10±0.01	1.08	0.03
	H^{13}CN	44.62±0.07	2.75±0.16	0.10±0.42	0.37	0.03
AGAL018.409−00.291	C$_2$H	68.42±0.04	1.46±0.10	4.08±1.18	0.45	0.03
AGAL018.461−00.002	C$_2$H	51.98±0.04	4.59±0.10	3.70±0.38	0.71	0.03
	H^{13}CN	52.09±0.12	4.49±0.30	0.75±0.67	0.41	0.04
AGAL018.493−00.199	C$_2$H	46.51±0.04	1.24±0.10	4.42±1.61	0.40	0.04
AGAL018.549+00.036	H^{13}CN	35.94±0.69	8.20±2.18	0.10±1.78	0.08	0.04
AGAL018.606−00.074	C$_2$H	45.48±0.03	2.38±0.07	1.17±0.39	1.32	0.05
	H^{13}CN	45.59±0.06	2.91±0.10	0.14±0.13	0.79	0.05
AGAL018.661+00.036	C$_2$H	81.03±0.07	3.73±0.25	1.05±0.76	0.40	0.03
	H^{13}CN	81.08±0.12	3.09±0.27	1.29±1.20	0.29	0.04
AGAL018.734−00.226	C$_2$H	41.16±0.05	4.29±0.15	0.35±0.46	0.86	0.05
	H^{13}CN	40.65±0.12	5.01±0.30	2.01±0.59	0.69	0.05
AGAL018.789−00.286	C$_2$H	65.35±0.06	2.94±0.16	2.26±0.79	0.41	0.03
	H^{13}CN	65.25±0.26	3.75±0.46	0.10±0.45	0.15	0.03
AGAL018.888−00.474	C$_2$H	65.91±0.01	4.69±0.03	0.17±0.10	2.25	0.05
	H^{13}CN	66.10±0.07	4.62±0.19	2.37±0.39	1.10	0.05
AGAL018.991−00.057	H^{13}CN	60.52±0.36	3.38±0.71	3.30±3.05	0.12	0.04
AGAL019.076−00.287	C$_2$H	65.70±0.01	3.42±0.03	2.12±0.12	1.70	0.03
	H^{13}CN	65.46±0.04	4.00±0.07	0.10±0.09	1.01	0.04
AGAL019.248+00.267	C$_2$H	15.33±0.10	4.10±0.27	0.73±0.93	0.30	0.03
	H^{13}CN	15.04±0.24	2.94±0.52	3.42±3.35	0.14	0.04
AGAL019.472+00.171	C$_2$H	19.28±0.03	5.27±0.06	2.49±0.19	1.10	0.03
AGAL019.732−00.651	C$_2$H	23.58±0.03	1.12±0.03	9.26±1.42	0.52	0.04
AGAL021.561−00.032	H^{13}CN	113.52±0.34	4.14±0.64	0.10±1.51	0.19	0.05
AGAL022.038+00.222	C$_2$H	51.45±0.03	2.70±0.10	1.28±0.47	1.04	0.05
	H^{13}CN	51.56±0.12	3.64±0.32	1.98±0.88	0.49	0.05
AGAL022.376+00.447	C$_2$H	52.97±0.06	2.53±0.14	2.81±0.94	0.59	0.05
	H^{13}CN	52.53±0.14	3.26±0.32	1.62±1.27	0.36	0.05
AGAL022.412+00.317	C$_2$H	84.26±0.03	1.83±0.08	4.45±0.84	0.66	0.04
	H^{13}CN	84.11±0.13	2.54±0.31	0.10±7.23	0.24	0.04
AGAL022.484−00.936	H^{13}CN	63.87±0.95	9.20±4.12	0.10±4.18	0.08	0.05
AGAL022.531−00.192	C$_2$H	76.44±0.07	2.46±0.16	5.14±1.50	0.34	0.04
	H^{13}CN	76.67±0.27	2.81±0.53	3.69±3.42	0.15	0.04
AGAL023.007−00.409	C$_2$H	77.31±0.06	6.76±0.21	0.56±0.33	0.99	0.05
	H^{13}CN	76.35±0.40	9.54±0.52	10.59±0.46	0.24	0.05
AGAL023.206−00.377	C$_2$H	77.67±0.05	3.60±0.16	1.80±0.53	0.79	0.05
	H^{13}CN	77.62±0.12	1.81±0.44	6.91±5.93	0.20	0.05
AGAL023.277−00.214	H^{13}CN	78.49±0.28	3.37±0.57	0.10±2.36	0.14	0.04
AGAL023.387+00.187	C$_2$H	75.56±0.03	2.16±0.09	3.61±0.70	0.94	0.05
	H^{13}CN	75.60±0.13	3.08±0.28	0.10±2.06	0.41	0.06
AGAL023.437−00.182	C$_2$H	101.48±0.04	5.07±0.11	2.94±0.30	1.36	0.06
	H^{13}CN	98.47±0.29	10.22±0.40	4.76±0.18	0.33	0.05
AGAL023.817+00.386	H^{13}CN	74.43±0.71	8.94±1.82	0.10±3.15	0.12	0.05
AGAL023.964−00.109	C$_2$H	72.79±0.07	3.64±0.17	4.17±0.81	0.56	0.05
	H^{13}CN	73.10±0.26	4.05±0.56	7.37±2.54	0.27	0.05
AGAL024.010+00.489	H^{13}CN	94.89±0.22	2.17±0.59	7.70±6.74	0.12	0.04
AGAL024.416+00.101	C$_2$H	112.49±0.10	4.55±0.23	3.57±0.99	0.37	0.04
	H^{13}CN	112.40±0.45	5.50±0.77	0.10±0.43	0.13	0.04
AGAL024.629+00.172	H^{13}CN	115.31±0.15	2.94±0.38	0.10±1.22	0.28	0.05
AGAL024.633−00.324	C$_2$H	42.77±0.03	1.79±0.07	2.54±0.56	1.18	0.05
	H^{13}CN	42.77±0.14	2.70±0.28	0.10±0.58	0.31	0.05
AGAL024.651−00.169	H^{13}CN	112.47±0.16	2.06±0.35	7.81±4.43	0.14	0.04
AGAL024.673−00.151	C$_2$H	113.04±0.02	3.36±0.06	2.27±0.25	1.80	0.05
	H^{13}CN	112.90±0.07	3.57±0.19	1.25±0.67	0.76	0.05
AGAL024.728+00.152	C$_2$H	109.36±0.04	2.80±0.12	2.13±0.64	0.85	0.05
	H^{13}CN	109.56±0.23	3.84±0.43	0.10±1.42	0.28	0.05

Table B.2: continued.

ATLASGAL name	Line	$v_{\rm LSR}$ (km s^{-1})	Δv (km s^{-1})	$\tau_{\rm tot}$	$T_{\rm MB}$ (K)	rms (K)
AGAL024.789+00.082	C$_2$H	110.36±0.02	3.97±0.05	2.56±0.17	2.10	0.04
	H^{13}CN	111.27±0.06	4.94±0.14	6.30±0.42	1.13	0.05
AGAL024.796+00.101	C$_2$H	110.37±0.04	5.23±0.10	1.81±0.28	1.03	0.04
	H^{13}CN	110.43±0.22	5.29±0.73	0.75±1.08	0.28	0.04
AGAL025.409+00.106	C$_2$H	95.60±0.04	2.39±0.15	0.81±0.69	0.84	0.05
	H^{13}CN	95.25±0.20	3.90±0.50	0.99±1.23	0.37	0.06
AGAL025.649+01.051	C$_2$H	42.76±0.04	4.16±0.11	1.46±0.33	1.36	0.06
	H^{13}CN	43.12±0.08	4.54±0.19	2.65±0.43	1.01	0.06
AGAL026.159+00.156	H^{13}CN	115.91±0.24	1.42±0.49	0.10±5.23	0.10	0.04
AGAL026.509+00.282	C$_2$H	101.75±0.03	3.95±0.08	1.82±0.32	1.02	0.04
	H^{13}CN	101.69±0.05	3.97±0.10	2.81±0.32	1.05	0.04
AGAL026.849+00.181	H^{13}CN	93.47±0.26	2.69±0.60	0.88±3.15	0.12	0.04
AGAL027.184−00.081	C$_2$H	26.11±0.04	3.62±0.10	2.00±0.40	0.79	0.04
	H^{13}CN	25.94±0.19	2.90±0.41	4.83±2.65	0.18	0.04
AGAL027.314+00.177	H^{13}CN	33.77±0.29	3.99±0.71	0.10±2.30	0.16	0.04
AGAL027.366−00.166	C$_2$H	91.88±0.01	4.33±0.03	0.19±0.04	1.77	0.04
	H^{13}CN	91.89±0.06	4.97±0.17	1.80±0.33	1.08	0.04
AGAL027.464+00.119	C$_2$H	100.31±0.07	3.17±0.20	2.72±1.03	0.35	0.04
	H^{13}CN	100.31±0.68	2.91±2.26	0.37±0.10	0.15	0.04
AGAL027.551−00.936	H^{13}CN	85.48±0.79	7.48±2.11	0.10±1.18	0.08	0.04
AGAL027.758+00.051	C$_2$H	99.43±0.04	2.60±0.12	0.68±0.68	0.56	0.03
	H^{13}CN	99.44±0.17	3.02±0.48	0.78±2.06	0.19	0.04
AGAL027.796−00.277	C$_2$H	45.93±0.03	1.82±0.06	6.43±0.86	0.70	0.04
	H^{13}CN	45.90±0.07	2.13±0.17	0.10±6.22	0.40	0.04
AGAL027.974−00.421	C$_2$H	44.65±0.09	2.72±0.26	1.18±0.82	0.45	0.04
	H^{13}CN	44.30±0.09	1.43±0.25	5.16±3.02	0.19	0.04
AGAL028.194−00.074	H^{13}CN	97.98±0.68	2.67±2.26	0.34±0.10	0.16	0.04
AGAL028.199−00.049	C$_2$H	95.89±0.02	5.29±0.04	0.19±0.03	1.50	0.04
	H^{13}CN	97.37±0.08	10.57±0.23	0.10±0.04	0.71	0.04
AGAL028.231+00.041	C$_2$H	107.30±0.05	3.33±0.17	1.62±0.60	0.56	0.04
	H^{13}CN	107.13±0.17	3.20±0.34	0.10±0.68	0.23	0.04
AGAL028.344+00.061	C$_2$H	79.00±0.04	2.70±0.10	1.97±0.51	0.72	0.04
	H^{13}CN	78.63±0.10	3.47±0.24	1.38±0.93	0.37	0.04
AGAL028.354+00.072	C$_2$H	80.24±0.04	2.03±0.09	5.57±0.94	0.52	0.03
	H^{13}CN	79.96±0.09	2.72±0.21	2.87±1.18	0.32	0.04
AGAL028.361+00.054	H^{13}CN	79.18±0.18	2.94±0.43	3.31±2.12	0.20	0.04
AGAL028.398+00.081	C$_2$H	78.42±0.03	2.88±0.06	7.00±0.51	0.86	0.04
	H^{13}CN	78.20±0.12	4.42±0.24	3.82±0.78	0.44	0.04
AGAL028.564−00.236	C$_2$H	86.64±0.05	3.31±0.13	8.30±1.23	0.59	0.05
	H^{13}CN	86.49±0.17	3.38±0.33	7.40±2.48	0.27	0.05
AGAL028.658+00.144	H^{13}CN	79.12±0.23	1.98±0.40	13.43±10.96	0.10	0.04
AGAL028.677−00.277	C$_2$H	89.11±0.02	1.51±0.07	3.43±0.71	0.76	0.04
	H^{13}CN	88.93±0.08	2.10±0.25	0.10±0.41	0.29	0.03
AGAL028.707−00.294	C$_2$H	88.87±0.04	2.13±0.11	3.13±0.82	0.52	0.04
	H^{13}CN	88.69±0.17	2.68±0.43	2.53±2.03	0.19	0.04
AGAL028.722−00.296	C$_2$H	88.18±0.04	1.76±0.11	1.70±0.78	0.56	0.04
AGAL028.831−00.252	C$_2$H	87.24±0.02	3.34±0.06	2.55±0.24	1.42	0.04
	H^{13}CN	87.20±0.07	3.78±0.14	1.91±0.46	0.71	0.04
AGAL028.861+00.066	C$_2$H	103.55±0.02	3.03±0.05	1.43±0.23	2.25	0.06
	H^{13}CN	103.39±0.06	3.62±0.12	1.25±0.42	1.06	0.05
AGAL029.117+00.027	H^{13}CN	96.99±0.68	4.01±2.26	0.22±0.10	0.11	0.04
AGAL029.409−00.646	C$_2$H	61.02±0.03	2.18±0.07	2.55±0.55	0.71	0.03
	H^{13}CN	61.24±0.12	1.84±0.20	0.78±0.54	0.20	0.04
AGAL029.556+00.186	C$_2$H	80.03±0.04	1.67±0.10	5.61±1.28	0.47	0.04
	H^{13}CN	79.67±0.34	3.01±0.69	3.48±3.99	0.09	0.04
AGAL029.591−00.614	C$_2$H	76.54±0.04	2.54±0.11	2.00±0.59	0.60	0.04
	H^{13}CN	76.94±0.09	2.83±0.19	0.10±1.44	0.35	0.04
AGAL029.861+00.029	C$_2$H	103.12±0.08	4.00±0.21	2.04±0.76	0.39	0.04
	H^{13}CN	103.37±0.30	3.58±0.63	1.35±2.64	0.13	0.04
AGAL029.911−00.042	C$_2$H	100.05±0.03	5.39±0.07	1.98±0.16	1.36	0.04
	H^{13}CN	100.15±0.11	4.50±0.25	0.90±0.60	0.47	0.04
AGAL029.954−00.016	C$_2$H	97.26±0.01	3.18±0.04	0.81±0.16	2.19	0.04
	H^{13}CN	97.47±0.02	3.84±0.05	1.01±0.14	2.07	0.04
AGAL029.976−00.047	H^{13}CN	101.62±0.14	4.19±0.31	3.03±0.84	0.34	0.03
	C$_2$H	101.54±0.04	3.58±0.12	1.93±0.43	0.75	0.04
AGAL030.003−00.269	C$_2$H	103.11±0.05	2.46±0.15	6.99±1.11	0.43	0.04
	H^{13}CN	102.95±0.41	4.43±1.49	2.17±2.89	0.12	0.03
AGAL030.198−00.169	C$_2$H	103.18±0.02	2.87±0.04	0.15±0.09	1.06	0.03
	H^{13}CN	103.25±0.09	3.07±0.18	0.10±1.69	0.31	0.03
AGAL030.419−00.231	C$_2$H	105.21±0.01	3.11±0.03	0.62±0.09	2.08	0.03
	H^{13}CN	105.34±0.05	3.24±0.13	1.08±0.48	0.71	0.04
AGAL030.568−00.026	H^{13}CN	87.65±0.21	1.91±0.44	2.56±4.18	0.10	0.03
AGAL030.588−00.042	C$_2$H	41.82±0.03	3.45±0.08	1.60±0.29	1.17	0.04
	H^{13}CN	41.95±0.06	3.54±0.14	1.69±0.50	0.58	0.03

Table B.2: continued.

ATLASGAL name	Line	v_{LSR} (km s^{-1})	Δv (km s^{-1})	τ_{tot}	T_{MB} (K)	rms (K)
AGAL030.603+00.176	C$_2$H	105.50±0.04	3.91±0.10	4.17±0.47	0.63	0.03
	H^{13}CN	105.43±0.17	4.88±0.45	3.01±0.96	0.29	0.03
AGAL030.683−00.074	C$_2$H	92.08±0.03	3.15±0.07	5.34±0.45	0.90	0.04
	H^{13}CN	91.78±0.06	3.22±0.14	0.33±0.57	0.56	0.03
AGAL030.703−00.067	C$_2$H	90.75±0.03	4.52±0.09	3.68±0.28	1.39	0.05
	H^{13}CN	90.06±0.04	3.13±0.09	0.10±0.03	0.83	0.04
AGAL030.731−00.079	C$_2$H	91.10±0.06	3.38±0.15	4.76±0.71	0.64	0.04
	H^{13}CN	91.10±0.12	3.62±0.23	0.10±0.38	0.38	0.05
AGAL030.786+00.204	C$_2$H	81.84±0.04	2.82±0.10	4.22±0.58	0.75	0.04
	H^{13}CN	81.81±0.15	4.12±0.36	3.30±0.82	0.42	0.04
AGAL030.811−00.111	C$_2$H	94.65±0.06	2.06±0.18	1.64±1.12	0.47	0.04
	H^{13}CN	94.01±0.30	3.06±0.62	0.10±1.04	0.13	0.04
AGAL030.818+00.274	C$_2$H	97.68±0.03	2.58±0.09	0.32±0.48	0.81	0.03
	H^{13}CN	97.86±0.08	2.60±0.18	0.10±1.65	0.32	0.03
AGAL030.848−00.081	C$_2$H	97.27±0.08	6.29±0.23	1.33±0.49	0.67	0.05
	H^{13}CN	97.69±0.68	4.06±2.26	0.21±0.10	0.33	0.05
AGAL030.866+00.114	C$_2$H	39.54±0.03	4.17±0.09	1.08±0.26	1.07	0.04
	H^{13}CN	39.38±0.09	3.96±0.16	0.10±0.64	0.49	0.04
AGAL030.893+00.139	C$_2$H	107.49±0.07	3.58±0.19	1.68±0.77	0.59	0.05
	H^{13}CN	104.58±0.32	3.88±0.28	100.00±84.44	0.13	0.05
AGAL030.898+00.162	C$_2$H	105.59±0.04	3.38±0.11	1.27±0.43	0.89	0.04
	H^{13}CN	105.58±0.12	3.64±0.30	0.78±1.08	0.42	0.05
AGAL030.971−00.141	C$_2$H	77.56±0.03	2.13±0.08	1.15±0.47	0.99	0.04
	H^{13}CN	77.50±0.09	3.06±0.18	0.10±0.32	0.46	0.05
AGAL030.996−00.076	C$_2$H	81.80±0.03	2.32±0.09	0.49±0.46	1.05	0.04
	H^{13}CN	81.61±0.10	2.73±0.21	0.10±0.20	0.33	0.04
AGAL031.044+00.261	C$_2$H	97.27±0.05	2.36±0.15	1.51±0.85	0.62	0.05
AGAL031.183−00.147	C$_2$H	42.82±0.07	2.81±0.19	2.84±1.04	0.42	0.04
AGAL031.243−00.111	C$_2$H	20.69±0.06	4.96±0.17	0.26±0.39	0.72	0.04
	H^{13}CN	21.40±0.68	4.09±2.26	0.10±0.10	0.24	0.04
AGAL031.254+00.057	H^{13}CN	106.76±0.68	4.17±2.26	0.10±0.10	0.11	0.04
AGAL031.281+00.062	C$_2$H	108.83±0.03	4.06±0.06	3.98±0.27	1.40	0.04
	H^{13}CN	108.75±0.07	5.02±0.18	1.04±0.36	0.88	0.04
AGAL031.396−00.257	C$_2$H	87.09±0.02	3.84±0.03	0.34±0.04	1.83	0.03
	H^{13}CN	87.02±0.04	4.10±0.05	0.30±0.06	1.02	0.03
AGAL031.412+00.307	C$_2$H	98.05±0.04	5.25±0.09	3.25±0.31	1.25	0.05
	H^{13}CN	96.50±0.07	2.29±0.14	0.10±1.42	0.44	0.05
AGAL031.464+00.186	H^{13}CN	105.00±0.66	4.09±0.91	0.10±1.82	0.06	0.03
AGAL031.581+00.077	C$_2$H	96.04±0.01	3.35±0.03	0.76±0.05	1.94	0.03
	H^{13}CN	96.05±0.04	3.47±0.10	0.94±0.32	0.85	0.03
AGAL031.584−00.117	H^{13}CN	33.62±0.26	3.10±0.66	1.28±2.70	0.18	0.05
AGAL031.699−00.494	C$_2$H	79.74±0.02	1.12±0.03	4.17±0.81	0.57	0.03
AGAL031.982+00.064	C$_2$H	93.94±0.09	1.88±0.23	7.23±3.46	0.37	0.03
	H^{13}CN	93.61±0.13	2.48±0.39	0.10±1.36	0.21	0.04
AGAL032.001−00.197	C$_2$H	96.39±0.06	1.12±0.09	3.98±3.28	0.39	0.03
	H^{13}CN	96.28±0.14	1.44±0.22	0.77±0.83	0.13	0.03
AGAL032.007+00.062	C$_2$H	97.38±0.17	5.29±0.40	5.08±2.84	0.27	0.03
	H^{13}CN	96.56±0.28	5.14±0.70	1.82±1.07	0.21	0.03
AGAL032.019+00.064	C$_2$H	99.72±0.06	2.31±0.19	3.92±1.87	0.72	0.04
	H^{13}CN	97.91±0.35	9.69±0.97	0.10±1.29	0.16	0.04
AGAL032.044+00.059	C$_2$H	95.32±0.02	3.92±0.07	0.56±0.21	1.26	0.03
	H^{13}CN	94.87±0.05	3.92±0.10	1.91±0.29	0.93	0.04
AGAL032.149+00.134	C$_2$H	93.42±0.04	4.25±0.10	1.57±0.34	0.99	0.04
	H^{13}CN	93.23±0.13	3.99±0.26	0.10±4.94	0.40	0.04
AGAL032.739+00.192	C$_2$H	18.72±0.15	5.47±0.48	0.49±1.01	0.25	0.03
	H^{13}CN	18.82±0.28	2.68±0.57	4.98±5.96	0.09	0.03
AGAL032.744−00.076	C$_2$H	37.08±0.06	4.80±0.15	3.34±0.53	0.60	0.04
	H^{13}CN	36.68±0.22	7.93±1.45	1.25±1.15	0.30	0.04
AGAL032.797+00.191	C$_2$H	14.71±0.03	5.58±0.10	1.14±0.25	1.25	0.04
	H^{13}CN	14.11±0.15	6.81±0.86	1.08±0.79	0.47	0.04
AGAL032.821−00.331	C$_2$H	79.13±0.05	3.63±0.17	0.66±0.50	0.54	0.03
	H^{13}CN	79.42±0.18	4.83±0.39	4.60±0.97	0.31	0.04
AGAL033.133−00.092	C$_2$H	76.37±0.04	4.78±0.12	3.83±0.39	0.90	0.04
	H^{13}CN	76.58±0.13	3.84±0.23	0.10±2.71	0.44	0.05
AGAL033.238−00.022	C$_2$H	100.41±0.03	2.07±0.08	2.42±0.58	0.70	0.03
	H^{13}CN	100.27±0.11	2.25±0.32	1.50±1.88	0.25	0.04
AGAL033.393+00.011	C$_2$H	103.66±0.06	4.15±0.21	0.88±0.52	0.59	0.04
	H^{13}CN	103.91±0.11	2.94±0.24	2.31±1.17	0.31	0.04
AGAL033.568+00.027	C$_2$H	105.59±0.06	1.80±0.20	1.99±1.25	0.33	0.03
AGAL033.623−00.032	C$_2$H	103.43±0.08	3.08±0.20	2.85±1.17	0.29	0.03
	H^{13}CN	103.28±0.20	2.05±0.51	1.70±3.26	0.14	0.04
AGAL033.744−00.007	C$_2$H	106.13±0.06	2.72±0.15	1.07±0.80	0.43	0.03
	H^{13}CN	106.36±0.19	3.42±0.50	0.10±5.27	0.17	0.03
AGAL033.914+00.109	C$_2$H	107.74±0.01	2.95±0.04	0.31±0.11	2.33	0.04

Table B.2: continued.

ATLASGAL name	Line	v_{LSR} (km s^{-1})	Δv (km s^{-1})	τ_{tot}	T_{MB} (K)	rms (K)
	H^{13}CN	107.79±0.03	3.19±0.04	0.10±0.04	1.32	0.05
AGAL033.979−00.021	C$_2$H	61.43±0.06	2.71±0.16	4.42±0.95	0.36	0.03
	H^{13}CN	61.88±0.16	2.65±0.35	0.10±0.77	0.17	0.03
AGAL034.089+00.011	C$_2$H	55.61±0.10	2.92±0.24	6.90±1.81	0.30	0.04
	H^{13}CN	54.90±0.22	3.44±0.32	0.52±0.44	0.21	0.04
AGAL034.243+00.132	C$_2$H	57.07±0.00	2.52±0.01	0.62±0.00	2.35	0.04
	H^{13}CN	57.06±0.02	2.35±0.05	0.10±0.04	1.13	0.04
AGAL034.258+00.154	C$_2$H	57.34±0.01	3.47±0.02	1.29±0.08	3.16	0.04
	H^{13}CN	57.50±0.01	4.40±0.01	1.09±0.01	3.57	0.03
AGAL034.372−00.664	C$_2$H	12.18±0.01	1.12±0.00	1.91±0.41	1.01	0.03
	H^{13}CN	12.22±0.07	1.13±0.05	4.03±2.17	0.23	0.03
AGAL034.401+00.226	C$_2$H	57.66±0.03	3.98±0.06	4.75±0.32	1.44	0.05
	H^{13}CN	57.49±0.04	4.12±0.10	2.30±0.31	1.57	0.05
AGAL034.411+00.234	C$_2$H	57.95±0.02	3.13±0.07	2.31±0.30	1.59	0.05
	H^{13}CN	57.83±0.04	3.66±0.07	1.61±0.20	1.73	0.05
AGAL034.454+00.006	C$_2$H	89.64±0.04	2.83±0.11	0.88±0.54	0.61	0.03
	H^{13}CN	89.64±0.14	3.67±0.29	3.40±1.24	0.26	0.03
AGAL034.459+00.247	C$_2$H	59.40±0.03	3.05±0.09	1.46±0.34	0.95	0.03
	H^{13}CN	59.50±0.08	3.96±0.17	2.58±0.52	0.53	0.03
AGAL034.591+00.242	C$_2$H	−22.23±0.09	3.71±0.24	1.66±0.87	0.38	0.04
AGAL034.712−00.596	C$_2$H	44.60±0.02	2.04±0.05	6.71±0.48	1.33	0.04
	H^{13}CN	44.54±0.05	2.47±0.14	0.63±0.69	0.66	0.04
AGAL034.739−00.119	C$_2$H	78.78±0.05	1.58±0.15	5.42±1.91	0.44	0.05
	H^{13}CN	78.94±0.10	1.68±0.34	0.75±2.39	0.30	0.05
AGAL034.742−00.132	C$_2$H	78.98±0.04	1.41±0.11	10.59±2.44	0.41	0.05
	H^{13}CN	78.88±0.68	1.15±2.26	3.79±0.10	0.24	0.05
AGAL034.751−00.092	C$_2$H	51.28±0.06	2.55±0.20	0.66±0.96	0.41	0.03
	H^{13}CN	51.11±0.22	1.97±0.72	11.85±14.62	0.09	0.04
AGAL034.757+00.024	C$_2$H	76.35±0.05	2.73±0.15	2.20±0.78	0.58	0.04
	H^{13}CN	76.46±0.18	3.31±0.34	0.10±5.30	0.22	0.04
AGAL034.821+00.351	C$_2$H	57.19±0.01	2.67±0.04	2.92±0.29	1.86	0.05
	H^{13}CN	57.12±0.08	3.19±0.22	0.66±0.91	0.59	0.05
AGAL035.026+00.349	C$_2$H	53.16±0.02	3.38±0.06	0.41±0.15	1.68	0.04
	H^{13}CN	53.42±0.05	3.98±0.08	0.20±0.18	1.19	0.04
AGAL035.042−00.472	C$_2$H	51.20±0.03	2.56±0.10	0.41±0.42	0.78	0.03
	H^{13}CN	51.28±0.10	1.80±0.31	0.10±2.38	0.23	0.03
AGAL035.132−00.744	C$_2$H	34.80±0.01	3.28±0.02	0.10±0.00	2.42	0.05
	H^{13}CN	34.40±0.04	4.07±0.05	0.10±0.17	1.44	0.05
AGAL035.144−00.754	C$_2$H	33.99±0.03	5.84±0.08	1.89±0.22	1.45	0.04
	H^{13}CN	33.21±0.02	5.75±0.10	0.13±0.01	0.68	0.04
AGAL035.197−00.742	C$_2$H	33.83±0.01	3.68±0.04	2.78±0.17	2.98	0.05
	H^{13}CN	34.15±0.04	4.72±0.12	0.98±0.29	1.69	0.05
AGAL035.297−00.897	C$_2$H	37.38±0.02	1.25±0.05	5.32±0.90	0.88	0.04
	H^{13}CN	37.41±0.07	1.59±0.22	0.10±4.04	0.35	0.04
AGAL035.457−00.179	C$_2$H	64.90±0.10	3.61±0.27	2.10±1.09	0.32	0.04
	H^{13}CN	64.70±0.15	2.29±0.37	8.55±6.47	0.12	0.04
AGAL035.466+00.141	C$_2$H	77.23±0.01	2.78±0.03	1.00±0.16	1.73	0.03
	H^{13}CN	77.06±0.04	2.73±0.10	0.10±0.83	0.61	0.03
AGAL035.484−00.287	C$_2$H	45.48±0.05	1.82±0.16	2.59±1.12	0.62	0.05
	H^{13}CN	45.51±0.18	1.46±0.53	2.51±4.35	0.16	0.05
AGAL035.579+00.007	H^{13}CN	58.10±0.43	2.31±0.74	0.10±7.34	0.08	0.05
AGAL035.579−00.031	C$_2$H	53.05±0.03	5.08±0.09	0.68±0.21	0.98	0.03
	H^{13}CN	53.32±0.07	4.31±0.09	0.10±0.84	0.49	0.03
AGAL035.681−00.176	C$_2$H	27.99±0.02	1.55±0.07	2.10±0.57	1.03	0.04
	H^{13}CN	28.01±0.06	1.13±0.17	3.67±1.50	0.35	0.04
AGAL035.794−00.174	C$_2$H	61.46±0.07	3.02±0.17	7.14±1.54	0.35	0.04
	H^{13}CN	62.29±0.23	5.00±0.60	2.48±0.92	0.33	0.04
AGAL036.794−00.204	C$_2$H	78.45±0.07	2.08±0.19	5.35±1.85	0.36	0.05
AGAL036.826−00.039	C$_2$H	60.42±0.05	2.01±0.17	1.35±1.09	0.52	0.04
	H^{13}CN	60.33±0.10	1.13±1.50	2.77±2.93	0.23	0.04
AGAL036.839−00.022	C$_2$H	58.16±0.07	3.51±0.19	1.50±0.86	0.48	0.04
	H^{13}CN	58.41±0.62	4.50±1.33	3.01±2.73	0.18	0.05
AGAL036.878−00.474	C$_2$H	61.23±0.07	3.10±0.20	1.40±0.97	0.41	0.04
	H^{13}CN	61.42±0.16	2.44±0.41	0.10±2.19	0.20	0.04
AGAL036.899−00.409	C$_2$H	79.98±0.07	2.05±0.18	2.94±1.48	0.39	0.04
	H^{13}CN	79.43±0.24	3.19±0.49	0.96±2.36	0.17	0.04
AGAL037.031−00.039	C$_2$H	80.52±0.04	1.98±0.10	3.41±0.83	0.44	0.03
	H^{13}CN	80.37±0.16	3.00±0.24	0.41±0.40	0.15	0.03
AGAL037.469−00.102	C$_2$H	58.43±0.04	3.24±0.07	0.10±0.05	0.60	0.03
	H^{13}CN	58.96±0.26	3.03±0.72	0.10±7.88	0.11	0.03
AGAL037.498+00.531	C$_2$H	10.30±0.04	3.08±0.10	2.29±0.51	0.55	0.03
	H^{13}CN	10.67±0.15	3.42±0.26	0.10±0.84	0.21	0.03
AGAL037.554+00.201	C$_2$H	85.22±0.04	3.82±0.11	4.67±0.55	0.87	0.05
	H^{13}CN	84.93±0.11	4.58±0.26	2.84±0.63	0.70	0.05
AGAL037.874−00.399	C$_2$H	60.95±0.03	4.73±0.03	0.10±0.01	1.17	0.03

Table B.2: continued.

ATLASGAL name	Line	v_{LSR} (km s^{-1})	Δv (km s^{-1})	τ_{tot}	T_{MB} (K)	rms (K)
	H^{13}CN	61.11±0.12	4.46±0.16	0.10±2.75	0.33	0.03
AGAL038.119−00.229	C$_2$H	83.21±0.03	2.48±0.07	3.11±0.42	0.76	0.03
	H^{13}CN	83.23±0.08	2.70±0.22	1.59±1.03	0.31	0.03
AGAL038.354−00.952	C$_2$H	16.98±0.01	1.74±0.04	1.44±0.26	1.41	0.03
	H^{13}CN	16.92±0.06	1.53±0.26	0.10±1.05	0.32	0.03
AGAL038.371−00.149	C$_2$H	81.32±0.05	1.79±0.12	9.49±1.85	0.24	0.03
	H^{13}CN	81.57±0.17	2.65±0.35	0.13±1.90	0.13	0.03
AGAL038.957−00.466	C$_2$H	42.23±0.04	2.15±0.09	2.71±0.66	1.03	0.06
	H^{13}CN	42.54±0.12	2.62±0.27	0.14±1.00	0.39	0.06
AGAL039.048−00.880	H^{13}CN	71.42±0.19	1.55±0.35	17.03±15.68	0.13	0.06
AGAL039.099+00.492	H^{13}CN	25.66±0.78	12.21±2.10	0.10±5.13	0.11	0.06
AGAL039.903−01.349	C$_2$H	48.51±0.03	1.99±0.12	0.18±1.71	1.05	0.05
AGAL040.283−00.219	C$_2$H	74.18±0.05	4.68±0.16	0.93±0.40	0.86	0.05
	H^{13}CN	73.89±0.12	4.73±0.31	2.55±0.63	0.58	0.05
AGAL041.049−00.247	C$_2$H	65.59±0.09	2.63±0.21	3.59±1.38	0.48	0.06
	H^{13}CN	65.61±0.20	2.81±0.53	0.75±3.14	0.27	0.06
AGAL043.038−00.452	C$_2$H	57.79±0.02	3.55±0.06	0.82±0.20	1.26	0.03
	H^{13}CN	57.59±0.08	3.72±0.19	1.43±0.62	0.40	0.03
AGAL043.148+00.014	C$_2$H	9.54±0.03	7.24±0.12	0.12±0.03	0.85	0.03
	H^{13}CN	8.93±0.33	10.57±0.95	0.10±0.95	0.13	0.03
AGAL043.164−00.029	C$_2$H	14.69±0.05	8.78±0.12	2.00±0.19	0.79	0.03
	H^{13}CN	15.59±0.16	8.06±0.50	0.10±0.56	0.31	0.03
AGAL043.166+00.011	C$_2$H	11.27±0.05	4.40±0.08	1.83±0.18	2.12	0.07
	H^{13}CN	6.64±0.07	14.43±0.13	0.10±0.06	0.95	0.05
AGAL043.178−00.011	C$_2$H	9.43±0.14	7.50±0.23	1.18±0.20	0.83	0.03
	H^{13}CN	7.52±0.68	10.68±2.26	0.11±0.10	0.13	0.03
AGAL043.179−00.519	C$_2$H	57.89±0.01	3.77±0.02	0.42±0.04	1.81	0.03
	H^{13}CN	57.93±0.06	3.92±0.13	0.41±0.40	0.66	0.03
AGAL043.236−00.047	C$_2$H	6.49±0.04	5.36±0.09	2.27±0.26	0.77	0.03
	H^{13}CN	6.15±0.12	4.79±0.29	1.43±0.61	0.31	0.03
AGAL043.306−00.212	C$_2$H	59.84±0.02	2.14±0.05	3.79±0.35	0.97	0.03
	H^{13}CN	59.51±0.04	3.02±0.12	0.10±1.52	0.59	0.03
AGAL043.794−00.127	C$_2$H	44.08±0.02	5.37±0.06	0.77±0.15	1.26	0.03
	H^{13}CN	44.19±0.07	5.43±0.08	1.51±0.06	0.62	0.03
AGAL043.889−00.786	C$_2$H	53.86±0.03	5.06±0.10	1.83±0.24	1.01	0.03
	H^{13}CN	54.33±0.12	4.63±0.30	3.78±0.72	0.40	0.03
AGAL043.994−00.012	C$_2$H	65.55±0.01	1.81±0.02	0.10±0.07	1.35	0.03
	H^{13}CN	65.46±0.05	1.72±0.11	0.10±0.21	0.40	0.03
AGAL044.291+00.034	C$_2$H	56.77±0.06	2.70±0.17	1.79±0.81	0.33	0.03
	H^{13}CN	57.04±0.12	2.67±0.34	1.49±1.76	0.21	0.03
AGAL044.309+00.041	C$_2$H	55.80±0.09	3.11±0.24	3.29±1.30	0.23	0.03
	H^{13}CN	56.66±0.37	5.57±0.47	2.33±0.32	0.13	0.03
AGAL044.422+00.537	C$_2$H	−51.86±0.08	3.42±0.26	0.35±0.94	0.51	0.05
AGAL045.071+00.132	C$_2$H	59.00±0.05	5.61±0.13	0.87±0.31	0.95	0.04
	H^{13}CN	59.12±0.13	5.34±0.39	1.32±0.56	0.65	0.05
AGAL045.096+00.131	H^{13}CN	58.35±0.23	1.75±0.56	0.21±1.99	0.17	0.05
AGAL045.121+00.131	C$_2$H	59.05±0.04	4.15±0.12	0.39±0.32	1.21	0.05
	H^{13}CN	59.13±0.10	3.69±0.23	0.70±0.83	0.49	0.04
AGAL045.454+00.061	C$_2$H	58.12±0.05	5.12±0.17	0.60±0.34	0.90	0.05
	H^{13}CN	58.66±0.23	5.05±0.27	0.51±0.21	0.30	0.05
AGAL045.466+00.046	C$_2$H	62.02±0.03	4.30±0.10	1.88±0.10	1.33	0.05
	H^{13}CN	62.20±0.10	4.20±0.24	1.09±0.67	0.62	0.05
AGAL045.474+00.134	C$_2$H	61.66±0.02	3.64±0.06	2.21±0.25	1.69	0.05
	H^{13}CN	61.97±0.07	3.64±0.17	0.72±0.63	0.71	0.05
AGAL045.493+00.126	C$_2$H	61.21±0.06	4.32±0.15	4.05±0.67	0.81	0.06
	H^{13}CN	60.39±0.15	3.42±0.31	0.10±0.48	0.37	0.05
AGAL046.174−00.524	H^{13}CN	50.36±0.32	3.56±0.60	0.10±2.52	0.20	0.06
AGAL046.426−00.237	H^{13}CN	52.89±0.25	2.92±0.44	0.10±4.23	0.15	0.04
AGAL048.606+00.022	C$_2$H	18.29±0.02	4.31±0.10	0.71±0.29	1.34	0.03
	H^{13}CN	18.29±0.14	4.41±0.34	1.21±0.77	0.34	0.04
AGAL048.991−00.299	C$_2$H	67.92±0.00	3.55±0.01	0.10±0.00	3.81	0.03
	H^{13}CN	67.90±0.03	3.62±0.07	1.10±0.21	1.39	0.04
AGAL049.043−01.077	C$_2$H	38.99±0.03	2.17±0.09	2.69±0.63	0.57	0.03
	H^{13}CN	38.73±0.16	3.22±0.33	0.10±0.87	0.21	0.03
AGAL049.074−00.352	C$_2$H	66.01±0.02	2.91±0.08	0.71±0.33	1.23	0.04
	H^{13}CN	66.33±0.08	2.35±0.19	0.10±1.39	0.30	0.03
AGAL049.214−00.342	C$_2$H	67.09±0.04	3.17±0.09	2.40±0.42	1.39	0.06
	H^{13}CN	67.16±0.11	2.06±0.28	0.10±3.35	0.41	0.06
AGAL049.253−00.411	C$_2$H	66.68±0.02	1.96±0.03	1.69±0.11	0.98	0.03
	H^{13}CN	66.58±0.09	1.45±0.34	1.02±3.07	0.20	0.03
AGAL049.268−00.337	C$_2$H	68.17±0.03	3.29±0.07	2.27±0.30	1.92	0.06
	H^{13}CN	67.79±0.11	3.69±0.26	0.73±0.93	0.61	0.06
AGAL049.369−00.301	C$_2$H	50.95±0.03	3.87±0.06	0.92±0.10	1.96	0.07
	H^{13}CN	50.87±0.07	3.40±0.11	0.10±0.57	0.86	0.06
AGAL049.401−00.227	C$_2$H	50.47±0.02	2.96±0.06	0.10±0.17	0.95	0.04

Table B.2: continued.

ATLASGAL name	Line	v_{LSR} (km s^{-1})	Δv (km s^{-1})	τ_{tot}	T_{MB} (K)	rms (K)
	H^{13}CN	50.58±0.14	2.53±0.40	0.10±0.35	0.18	0.03
AGAL049.402−00.212	C$_2$H	48.48±0.03	2.41±0.08	2.61±0.46	0.81	0.03
	H^{13}CN	48.58±0.10	2.45±0.20	0.45±0.32	0.25	0.03
AGAL049.489−00.389	C$_2$H	56.16±0.01	7.26±0.02	0.26±0.02	5.27	0.06
	H^{13}CN	55.78±0.01	10.41±0.02	0.10±0.00	3.78	0.05
AGAL049.566−00.274	C$_2$H	52.83±0.03	4.30±0.07	0.10±0.01	0.92	0.04
	H^{13}CN	53.19±0.13	3.34±0.34	0.10±0.20	0.37	0.04
AGAL049.599−00.249	C$_2$H	56.94±0.02	2.16±0.07	0.99±0.44	0.87	0.03
	H^{13}CN	56.93±0.06	2.06±0.15	0.10±0.22	0.37	0.03
AGAL050.046+00.767	C$_2$H	−29.94±0.07	2.52±0.15	0.27±0.33	0.44	0.04
AGAL050.221−00.606	C$_2$H	40.66±0.02	2.82±0.05	1.38±0.27	1.10	0.03
	H^{13}CN	40.06±0.09	3.45±0.17	0.10±0.85	0.36	0.03
AGAL050.777+00.152	C$_2$H	42.64±0.04	2.41±0.11	2.27±0.74	0.63	0.04
	H^{13}CN	42.05±0.35	3.38±0.57	0.10±7.10	0.13	0.04
AGAL051.678+00.719	C$_2$H	3.48±0.04	3.75±0.10	1.59±0.34	0.78	0.03
	H^{13}CN	3.48±0.10	4.51±0.22	0.80±0.52	0.43	0.03
AGAL052.208+00.687	C$_2$H	3.67±0.04	4.20±0.10	0.15±0.14	0.74	0.04
	H^{13}CN	3.59±0.19	4.12±0.37	0.50±0.41	0.27	0.04
AGAL053.141+00.069	C$_2$H	21.57±0.01	2.45±0.02	0.20±0.06	2.57	0.05
	H^{13}CN	21.52±0.04	3.15±0.08	0.10±0.08	1.16	0.05
AGAL053.619+00.034	C$_2$H	23.07±0.01	1.55±0.04	0.99±0.36	1.61	0.04
	H^{13}CN	22.83±0.15	1.78±0.39	1.18±3.26	0.18	0.04
AGAL055.158−00.299	C$_2$H	41.20±0.02	2.73±0.05	1.58±0.27	1.10	0.03
	H^{13}CN	41.22±0.04	2.78±0.12	0.10±0.18	0.43	0.03
AGAL058.469+00.436	C$_2$H	36.64±0.02	2.29±0.06	1.14±0.31	1.04	0.03
	H^{13}CN	36.75±0.05	2.83±0.12	0.10±0.14	0.48	0.03
AGAL058.709+00.662	C$_2$H	30.88±0.03	1.59±0.07	3.21±0.69	0.58	0.03
	H^{13}CN	31.20±0.68	2.06±2.26	0.34±0.10	0.17	0.03
AGAL058.774+00.644	C$_2$H	32.45±0.02	2.73±0.05	1.32±0.22	1.32	0.03
	H^{13}CN	32.31±0.06	2.84±0.12	0.10±0.21	0.49	0.03
AGAL059.187+00.106	C$_2$H	29.55±0.02	1.28±0.07	0.42±0.58	0.64	0.03
AGAL059.351−00.196	C$_2$H	28.59±0.02	2.03±0.04	0.10±0.42	0.78	0.03
	H^{13}CN	28.53±0.12	1.13±0.33	4.56±3.14	0.12	0.03
AGAL059.359−00.207	C$_2$H	29.10±0.01	2.11±0.04	0.65±0.25	1.35	0.03
	H^{13}CN	29.16±0.09	2.01±0.18	0.47±0.38	0.22	0.03
AGAL059.497−00.236	C$_2$H	26.54±0.02	2.67±0.07	0.16±0.13	0.96	0.04
	H^{13}CN	27.01±0.15	2.82±0.31	0.10±0.34	0.25	0.04
AGAL059.577−00.201	C$_2$H	25.81±0.03	1.93±0.06	2.06±0.49	0.92	0.04
	H^{13}CN	26.05±0.14	1.85±0.47	0.10±0.78	0.21	0.04
AGAL059.584−00.146	C$_2$H	27.48±0.03	1.88±0.12	0.72±0.64	0.75	0.04
	H^{13}CN	27.19±0.11	1.13±0.18	0.10±2.77	0.15	0.04
AGAL059.602+00.912	C$_2$H	36.53±0.03	3.96±0.09	0.81±0.29	0.87	0.03
	H^{13}CN	36.51±0.10	3.90±0.13	0.34±0.16	0.39	0.03
AGAL059.634−00.191	C$_2$H	28.12±0.02	3.01±0.06	0.87±0.25	1.96	0.05
	H^{13}CN	27.98±0.06	2.83±0.18	0.41±0.84	0.79	0.06
AGAL059.636−00.252	C$_2$H	27.49±0.02	1.47±0.07	1.31±0.61	0.97	0.04
AGAL059.782+00.066	C$_2$H	22.51±0.01	1.96±0.02	1.25±0.13	3.87	0.05
	H^{13}CN	22.51±0.02	2.06±0.04	0.10±0.05	1.54	0.05
AGAL059.789+00.631	C$_2$H	34.01±0.05	3.62±0.12	2.27±0.51	0.67	0.04
	H^{13}CN	34.15±0.12	3.92±0.30	0.23±2.34	0.41	0.04
AGAL059.832+00.672	C$_2$H	34.76±0.05	2.17±0.13	1.95±0.83	0.65	0.05
	H^{13}CN	34.59±0.13	3.01±0.36	0.93±1.53	0.37	0.05
G011.1012−0.3803	C$_2$H	0.88±0.10	2.44±0.25	7.22±2.30	0.20	0.04
	H^{13}CN	0.36±0.25	2.54±0.58	2.61±3.55	0.11	0.03
G012.7914−0.1958	C$_2$H	35.18±0.01	5.81±0.03	0.95±0.04	1.74	0.03
	H^{13}CN	35.92±0.04	4.41±0.05	0.21±0.05	1.05	0.03
G013.2029−0.1352	C$_2$H	51.73±0.02	2.31±0.04	5.02±0.34	1.36	0.04
	H^{13}CN	51.51±0.05	2.65±0.13	1.15±0.56	0.60	0.04
G014.1007−0.5559	C$_2$H	22.36±0.02	1.79±0.04	7.17±0.53	1.20	0.04
	H^{13}CN	22.34±0.68	1.84±2.26	0.10±0.10	0.27	0.04
G014.6010−0.5400	C$_2$H	17.71±0.03	1.44±0.06	2.92±0.73	0.82	0.04
	H^{13}CN	17.91±0.09	1.22±0.19	3.20±2.80	0.21	0.04
G025.1526−0.2906	H^{13}CN	63.65±0.14	1.81±0.30	0.10±0.85	0.19	0.04
G027.2546+0.1368	H^{13}CN	33.13±0.38	3.23±1.46	2.46±6.30	0.12	0.04
G028.5559−0.2260	C$_2$H	85.52±0.06	2.10±0.16	7.44±1.92	0.32	0.04
	H^{13}CN	85.08±0.32	3.17±0.62	0.10±1.68	0.12	0.04
G028.6117+0.0306	H^{13}CN	100.85±0.12	1.62±0.30	1.84±2.61	0.19	0.04
G030.5946+0.1639	H^{13}CN	105.62±0.28	2.69±0.75	0.10±0.54	0.10	0.03
G032.9956+0.0415	C$_2$H	83.67±0.08	2.48±0.26	1.76±1.27	0.38	0.04
	H^{13}CN	83.39±0.27	3.74±0.58	0.10±0.71	0.16	0.04
G059.7948+0.0749	C$_2$H	21.57±0.02	2.42±0.07	0.55±0.30	1.34	0.04
	H^{13}CN	21.78±0.06	3.00±0.10	0.10±0.19	0.52	0.04

B.3   Gaussian line parameters

Table B.3: Gaussian line parameters of $C^{18}O$, HCO, c-C_3H_2, CN, $HC^{15}N$, and $HN^{13}C$.

ATLASGAL Name	Line	Area (K km s^{-1})	v_{LSR} (km s^{-1})	Δv (km s^{-1})	T_{MB} (K)	rms (K)
AGAL006.216−00.609	$C^{18}O$	11.63 ± 0.10	18.04 ± 0.01	2.98 ± 0.02	3.66	0.06
	$H^{13}CO^+$	4.45 ± 0.10	18.53 ± 0.03	2.43 ± 0.07	1.72	0.05
	c-C_3H_2	4.46 ± 0.09	18.60 ± 0.02	2.22 ± 0.06	1.89	0.05
	CN	1.98 ± 0.15	18.72 ± 0.08	2.24 ± 0.20	0.83	0.09
	$HC^{15}N$	0.34 ± 0.09	18.67 ± 0.37	2.52 ± 0.80	0.13	0.05
	$HN^{13}C$	3.50 ± 0.09	18.77 ± 0.03	2.16 ± 0.07	1.52	0.05
AGAL008.049−00.242	$C^{18}O$	4.29 ± 0.08	39.36 ± 0.01	1.57 ± 0.03	2.57	0.05
	$H^{13}CO^+$	0.96 ± 0.07	39.22 ± 0.05	1.32 ± 0.13	0.68	0.05
	c-C_3H_2	0.92 ± 0.07	39.27 ± 0.05	1.39 ± 0.12	0.62	0.05
	CN	0.56 ± 0.15	39.10 ± 0.26	1.95 ± 0.63	0.27	0.09
	$HN^{13}C$	0.87 ± 0.07	39.43 ± 0.05	1.40 ± 0.12	0.58	0.05
AGAL008.671−00.356	HCO	0.49 ± 0.06	36.43 ± 0.48	6.57 ± 0.78	0.07	0.02
	$H^{13}CO^+$	11.93 ± 0.91	34.20 ± 0.06	3.07 ± 0.10	3.65	0.05
	c-C_3H_2	5.40 ± 0.33	36.29 ± 0.18	5.73 ± 0.26	0.88	0.05
	$HN^{13}C$	10.12 ± 0.14	35.25 ± 0.03	4.47 ± 0.07	2.13	0.05
AGAL008.684−00.367	$C^{18}O$	35.63 ± 0.26	37.27 ± 0.02	4.89 ± 0.04	6.85	0.11
	$H^{13}CO^+$	12.32 ± 0.19	37.17 ± 0.04	5.23 ± 0.09	2.21	0.07
	c-C_3H_2	3.61 ± 0.60	37.81 ± 0.28	3.75 ± 0.60	0.90	0.06
	CN	3.46 ± 0.29	37.62 ± 0.17	3.98 ± 0.43	0.82	0.12
	$HC^{15}N$	1.46 ± 0.17	38.06 ± 0.25	4.56 ± 0.64	0.30	0.06
	$HN^{13}C$	7.94 ± 0.15	37.75 ± 0.05	4.82 ± 0.10	1.55	0.06
AGAL008.706−00.414	$C^{18}O$	12.46 ± 0.17	38.69 ± 0.02	2.90 ± 0.05	4.04	0.09
	$H^{13}CO^+$	3.17 ± 0.09	38.84 ± 0.04	2.87 ± 0.09	1.04	0.04
	c-C_3H_2	3.44 ± 0.09	38.81 ± 0.03	2.63 ± 0.08	1.23	0.04
	CN	1.30 ± 0.18	38.82 ± 0.09	1.40 ± 0.26	0.87	0.12
	$HN^{13}C$	2.71 ± 0.09	39.10 ± 0.04	2.52 ± 0.09	1.01	0.04
AGAL010.079−00.196	$C^{18}O$	8.13 ± 0.08	28.21 ± 0.01	2.81 ± 0.03	2.72	0.05
	HCO	0.15 ± 0.05	28.04 ± 0.45	3.79 ± 1.75	0.04	0.01
	$H^{13}CO^+$	0.87 ± 0.08	28.06 ± 0.13	2.86 ± 0.30	0.29	0.04
	c-C_3H_2	0.74 ± 0.08	28.33 ± 0.17	3.34 ± 0.42	0.21	0.03
	CN	0.50 ± 0.10	28.62 ± 0.39	3.58 ± 0.62	0.13	0.05
	$HN^{13}C$	0.44 ± 0.07	28.41 ± 0.19	2.71 ± 0.58	0.15	0.03
AGAL010.104−00.416	$C^{18}O$	7.71 ± 0.11	11.03 ± 0.02	2.36 ± 0.04	3.07	0.06
	$H^{13}CO^+$	1.62 ± 0.09	11.30 ± 0.06	2.21 ± 0.15	0.69	0.05
	c-C_3H_2	0.58 ± 0.08	11.38 ± 0.15	2.23 ± 0.41	0.24	0.04
	CN	0.59 ± 0.16	11.52 ± 0.49	3.55 ± 1.26	0.15	0.08
	$HN^{13}C$	0.65 ± 0.08	11.84 ± 0.12	1.84 ± 0.25	0.33	0.05
AGAL010.151−00.344	$C^{18}O$	17.65 ± 0.09	9.19 ± 0.01	5.48 ± 0.03	3.03	0.03
	HCO	0.51 ± 0.05	8.70 ± 0.36	7.42 ± 0.75	0.06	0.01
	$H^{13}CO^+$	7.98 ± 0.11	9.50 ± 0.04	5.26 ± 0.09	1.43	0.04
	c-C_3H_2	8.24 ± 0.10	9.48 ± 0.03	4.99 ± 0.07	1.55	0.03
	CN	5.06 ± 0.16	9.36 ± 0.08	5.17 ± 0.19	0.92	0.06
	$HC^{15}N$	0.35 ± 0.09	10.65 ± 0.33	2.99 ± 1.07	0.11	0.04
	$HN^{13}C$	3.13 ± 0.10	9.49 ± 0.07	4.43 ± 0.16	0.66	0.04
AGAL010.168−00.362	$C^{18}O$	19.18 ± 0.08	14.07 ± 0.02	7.30 ± 0.04	2.47	0.03
	HCO	0.31 ± 0.04	13.95 ± 0.33	4.89 ± 0.63	0.06	0.01
	$H^{13}CO^+$	9.97 ± 0.11	14.14 ± 0.04	6.68 ± 0.09	1.40	0.04
	c-C_3H_2	7.59 ± 0.11	13.97 ± 0.05	6.65 ± 0.11	1.07	0.04
	CN	4.40 ± 0.16	13.90 ± 0.12	6.40 ± 0.26	0.65	0.06
	$HC^{15}N$	1.15 ± 0.13	15.39 ± 0.41	7.58 ± 1.04	0.14	0.04
	$HN^{13}C$	0.81 ± 0.19	17.24 ± 0.27	3.09 ± 0.52	0.24	0.03
AGAL010.213−00.322	$C^{18}O$	20.41 ± 0.53	11.85 ± 0.01	3.20 ± 0.04	5.99	0.06
	HCO	0.25 ± 0.05	12.47 ± 0.19	2.36 ± 0.65	0.10	0.02
	$H^{13}CO^+$	3.77 ± 0.13	10.97 ± 0.09	5.24 ± 0.21	0.68	0.05
	c-C_3H_2	2.72 ± 0.12	11.73 ± 0.09	4.29 ± 0.23	0.60	0.04
	CN	3.02 ± 0.17	11.37 ± 0.11	4.03 ± 0.24	0.70	0.08
	$HC^{15}N$	0.46 ± 0.09	11.28 ± 0.26	2.52 ± 0.56	0.17	0.05
	$HN^{13}C$	4.09 ± 0.12	11.41 ± 0.07	4.58 ± 0.16	0.84	0.05
AGAL010.214−00.306	$C^{18}O$	14.23 ± 0.10	11.39 ± 0.01	2.88 ± 0.02	4.64	0.05
	HCO	0.22 ± 0.04	12.29 ± 0.39	4.15 ± 0.92	0.05	0.01
	$H^{13}CO^+$	2.01 ± 0.07	11.72 ± 0.05	2.70 ± 0.11	0.70	0.03
	c-C_3H_2	1.34 ± 0.09	11.66 ± 0.11	3.61 ± 0.33	0.35	0.04
	CN	1.15 ± 0.09	11.73 ± 0.08	2.12 ± 0.20	0.51	0.06
	$HN^{13}C$	1.47 ± 0.07	11.85 ± 0.05	2.47 ± 0.12	0.56	0.03
AGAL010.284−00.114	$C^{18}O$	11.53 ± 0.09	14.53 ± 0.01	3.51 ± 0.03	3.08	0.04
	HCO	0.12 ± 0.02	15.32 ± 0.22	2.52 ± 0.66	0.04	0.01
	$H^{13}CO^+$	3.92 ± 0.06	14.02 ± 0.02	3.15 ± 0.05	1.17	0.03
	c-C_3H_2	1.23 ± 0.06	14.53 ± 0.09	3.76 ± 0.21	0.31	0.02
	CN	1.76 ± 0.17	13.80 ± 0.12	2.76 ± 0.31	0.60	0.09
	$HC^{15}N$	0.38 ± 0.06	13.98 ± 0.33	3.98 ± 0.78	0.09	0.03
	$HN^{13}C$	2.87 ± 0.06	13.88 ± 0.03	2.97 ± 0.07	0.91	0.03
AGAL010.288−00.124	$C^{18}O$	9.91 ± 0.08	13.87 ± 0.01	2.91 ± 0.03	3.20	0.04

Table B.3: continued.

ATLASGAL Name	Line	Area (K km s^{-1})	v_{LRS} (km s^{-1})	Δv (km s^{-1})	T_{MB} (K)	rms (K)
	HCO	0.22 ± 0.03	14.64 ± 0.19	2.90 ± 0.39	0.07	0.01
	H^{13}CO$^+$	2.73 ± 0.07	13.64 ± 0.04	2.64 ± 0.08	0.97	0.04
	c-C$_3$H$_2$	0.98 ± 0.07	13.91 ± 0.10	2.69 ± 0.20	0.34	0.03
	CN	1.70 ± 0.09	13.63 ± 0.06	2.33 ± 0.14	0.69	0.06
	HC^{15}N	0.53 ± 0.09	12.96 ± 0.34	3.82 ± 0.59	0.13	0.04
	HN^{13}C	2.67 ± 0.08	13.81 ± 0.04	2.51 ± 0.08	1.00	0.04
AGAL010.321−00.231	C^{18}O	6.52 ± 0.12	32.84 ± 0.04	4.19 ± 0.10	1.46	0.05
	H^{13}CO$^+$	1.25 ± 0.12	32.30 ± 0.15	3.26 ± 0.41	0.36	0.05
	c-C$_3$H$_2$	0.65 ± 0.12	32.20 ± 0.35	3.78 ± 0.80	0.16	0.05
	CN	1.01 ± 0.17	32.65 ± 0.41	4.57 ± 0.76	0.21	0.08
	HN^{13}C	0.89 ± 0.10	32.80 ± 0.14	2.62 ± 0.36	0.32	0.05
AGAL010.323−00.161	C^{18}O	8.27 ± 0.09	11.93 ± 0.02	2.95 ± 0.04	2.63	0.05
	HCO	0.31 ± 0.06	13.66 ± 0.61	6.37 ± 1.21	0.05	0.02
	H^{13}CO$^+$	3.22 ± 0.10	12.06 ± 0.04	2.99 ± 0.11	1.01	0.04
	c-C$_3$H$_2$	1.27 ± 0.09	11.94 ± 0.10	2.75 ± 0.26	0.43	0.04
	CN	1.67 ± 0.15	12.26 ± 0.10	2.51 ± 0.29	0.62	0.08
	HC^{15}N	0.33 ± 0.07	12.27 ± 0.09	0.99 ± 0.33	0.31	0.05
	HN^{13}C	2.21 ± 0.09	12.15 ± 0.05	2.46 ± 0.13	0.84	0.04
AGAL010.342−00.142	C^{18}O	12.86 ± 0.11	11.90 ± 0.01	2.66 ± 0.03	4.54	0.06
	H^{13}CO$^+$	4.25 ± 0.12	12.31 ± 0.04	2.96 ± 0.10	1.35	0.05
	c-C$_3$H$_2$	2.18 ± 0.12	12.11 ± 0.12	4.39 ± 0.31	0.47	0.05
	CN	1.99 ± 0.14	12.19 ± 0.11	3.06 ± 0.24	0.61	0.08
	HC^{15}N	0.89 ± 0.11	12.05 ± 0.18	3.20 ± 0.52	0.26	0.05
	HN^{13}C	3.24 ± 0.20	12.42 ± 0.08	2.65 ± 0.19	1.15	0.05
AGAL010.444−00.017	C^{18}O	14.13 ± 0.23	75.59 ± 0.03	4.02 ± 0.08	3.30	0.10
	H^{13}CO$^+$	2.70 ± 0.11	75.25 ± 0.07	3.48 ± 0.17	0.73	0.05
	c-C$_3$H$_2$	0.90 ± 0.11	75.22 ± 0.24	4.25 ± 0.62	0.20	0.04
	CN	0.81 ± 0.16	76.21 ± 0.22	2.07 ± 0.43	0.37	0.11
	HN^{13}C	1.39 ± 0.09	75.78 ± 0.12	3.67 ± 0.27	0.35	0.04
AGAL010.472+00.027	C^{18}O	41.22 ± 0.28	66.79 ± 0.02	6.15 ± 0.05	6.30	0.11
	HCO	0.64 ± 0.09	67.62 ± 0.49	7.24 ± 1.30	0.08	0.02
	H^{13}CO$^+$	14.22 ± 0.21	66.65 ± 0.05	6.75 ± 0.12	1.98	0.07
	c-C$_3$H$_2$	4.37 ± 0.23	66.79 ± 0.20	7.41 ± 0.45	0.55	0.07
	CN	3.92 ± 0.34	66.20 ± 0.25	5.73 ± 0.56	0.64	0.14
	HC^{15}N	11.05 ± 0.24	66.82 ± 0.10	8.98 ± 0.23	1.16	0.06
	HN^{13}C	8.32 ± 0.20	66.98 ± 0.07	6.39 ± 0.18	1.22	0.06
AGAL010.579−00.349	C^{18}O	10.53 ± 0.08	−2.98 ± 0.01	2.34 ± 0.02	4.23	0.05
	H^{13}CO$^+$	1.12 ± 0.06	−2.83 ± 0.05	1.83 ± 0.11	0.57	0.04
	c-C$_3$H$_2$	0.56 ± 0.07	−3.01 ± 0.12	2.22 ± 0.36	0.24	0.03
	CN	0.39 ± 0.07	−3.01 ± 0.10	1.28 ± 0.29	0.29	0.05
	HN^{13}C	0.54 ± 0.05	−2.55 ± 0.08	1.66 ± 0.19	0.30	0.03
AGAL010.618−00.031	C^{18}O	6.04 ± 0.05	63.29 ± 0.01	1.64 ± 0.02	3.45	0.04
	H^{13}CO$^+$	0.84 ± 0.06	63.54 ± 0.08	2.04 ± 0.19	0.39	0.04
	c-C$_3$H$_2$	0.47 ± 0.05	63.60 ± 0.06	1.33 ± 0.17	0.33	0.03
	HN^{13}C	0.42 ± 0.06	63.77 ± 0.13	1.89 ± 0.33	0.21	0.04
AGAL010.619−00.422	C^{18}O	7.88 ± 0.08	−1.67 ± 0.02	3.31 ± 0.04	2.23	0.04
	H^{13}CO$^+$	0.87 ± 0.05	−1.70 ± 0.04	1.41 ± 0.10	0.58	0.03
	c-C$_3$H$_2$	0.68 ± 0.08	−2.48 ± 0.27	4.49 ± 0.63	0.14	0.03
	CN	0.53 ± 0.10	−1.65 ± 0.16	1.78 ± 0.46	0.28	0.07
	HN^{13}C	0.68 ± 0.05	−1.60 ± 0.05	1.57 ± 0.15	0.41	0.03
AGAL010.624−00.384	C^{18}O	96.06 ± 0.29	−2.88 ± 0.01	6.03 ± 0.02	15.00	0.10
	HCO	0.78 ± 0.09	−1.91 ± 0.28	5.76 ± 0.88	0.13	0.03
	H^{13}CO$^+$	34.39 ± 0.24	−3.03 ± 0.02	6.45 ± 0.05	5.01	0.08
	c-C$_3$H$_2$	9.60 ± 0.17	−3.04 ± 0.05	6.23 ± 0.13	1.45	0.05
	CN	7.73 ± 0.39	−3.54 ± 0.16	6.54 ± 0.39	1.11	0.14
	HC^{15}N	6.12 ± 0.19	−3.29 ± 0.08	5.56 ± 0.22	1.03	0.05
	HN^{13}C	13.51 ± 0.16	−3.01 ± 0.04	6.54 ± 0.09	1.94	0.05
AGAL010.626−00.337	C^{18}O	22.48 ± 0.08	−4.61 ± 0.00	2.62 ± 0.01	8.06	0.05
	HCO	0.38 ± 0.05	−4.37 ± 0.20	3.45 ± 0.53	0.10	0.02
	H^{13}CO$^+$	3.73 ± 0.09	−4.31 ± 0.03	2.75 ± 0.08	1.27	0.05
	c-C$_3$H$_2$	2.50 ± 0.10	−4.38 ± 0.07	3.40 ± 0.15	0.69	0.04
	CN	2.25 ± 0.14	−4.68 ± 0.07	2.27 ± 0.17	0.93	0.08
	HC^{15}N	0.62 ± 0.13	−4.50 ± 0.39	4.05 ± 1.05	0.14	0.05
	HN^{13}C	2.54 ± 0.10	−4.24 ± 0.06	2.90 ± 0.14	0.82	0.05
AGAL010.634−00.511	C^{18}O	6.96 ± 0.08	−2.64 ± 0.01	2.35 ± 0.03	2.79	0.05
	H^{13}CO$^+$	0.96 ± 0.09	−3.48 ± 0.09	1.95 ± 0.24	0.46	0.05
	c-C$_3$H$_2$	0.91 ± 0.09	−3.40 ± 0.12	2.53 ± 0.32	0.34	0.07
	CN	0.73 ± 0.13	−3.86 ± 0.31	3.17 ± 0.54	0.21	0.07
	HN^{13}C	1.17 ± 0.09	−3.37 ± 0.07	1.83 ± 0.17	0.60	0.05
AGAL010.659+00.079	C^{18}O	5.26 ± 0.10	19.54 ± 0.04	3.91 ± 0.08	1.26	0.05
	H^{13}CO$^+$	1.25 ± 0.10	20.86 ± 0.14	3.30 ± 0.26	0.36	0.05
	c-C$_3$H$_2$	1.58 ± 0.09	21.21 ± 0.09	2.92 ± 0.18	0.51	0.05
	CN	0.40 ± 0.10	21.39 ± 0.18	1.40 ± 0.41	0.27	0.07
	HN^{13}C	1.32 ± 0.11	21.72 ± 0.13	3.10 ± 0.28	0.40	0.05
AGAL010.669−00.221	C^{18}O	7.62 ± 0.05	29.31 ± 0.01	1.73 ± 0.01	4.13	0.03

Table B.3: continued.

ATLASGAL Name	Line	Area (K km s^{-1})	v_{LRS} (km s^{-1})	Δv (km s^{-1})	T_{MB} (K)	rms (K)
	H^{13}CO$^+$	1.23 ± 0.05	29.01 ± 0.03	1.60 ± 0.08	0.72	0.03
	c-C$_3$H$_2$	1.55 ± 0.06	29.12 ± 0.03	1.46 ± 0.07	1.00	0.04
	CN	0.90 ± 0.07	29.17 ± 0.05	1.41 ± 0.13	0.60	0.05
	HN^{13}C	1.46 ± 0.05	29.26 ± 0.02	1.58 ± 0.06	0.87	0.03
AGAL010.684−00.307	C^{18}O	5.94 ± 0.07	−2.01 ± 0.01	2.29 ± 0.03	2.44	0.04
	H^{13}CO$^+$	1.08 ± 0.08	−1.76 ± 0.08	1.92 ± 0.16	0.53	0.05
	c-C$_3$H$_2$	0.35 ± 0.09	−1.44 ± 0.23	1.56 ± 0.57	0.21	0.05
	CN	0.40 ± 0.12	−1.99 ± 0.28	1.73 ± 0.64	0.22	0.08
	HN^{13}C	0.54 ± 0.09	−1.66 ± 0.20	2.36 ± 0.40	0.21	0.05
AGAL010.742−00.126	C^{18}O	8.49 ± 0.11	28.96 ± 0.01	2.21 ± 0.04	3.61	0.06
	H^{13}CO$^+$	1.53 ± 0.10	28.82 ± 0.08	2.60 ± 0.21	0.55	0.05
	c-C$_3$H$_2$	1.66 ± 0.09	29.03 ± 0.06	2.19 ± 0.13	0.71	0.05
	CN	0.56 ± 0.11	29.07 ± 0.15	1.60 ± 0.34	0.33	0.08
	HN^{13}C	1.75 ± 0.10	29.15 ± 0.06	2.29 ± 0.16	0.72	0.05
AGAL010.747+00.016	C^{18}O	4.51 ± 0.08	19.97 ± 0.02	2.08 ± 0.04	2.03	0.05
	H^{13}CO$^+$	0.59 ± 0.09	20.16 ± 0.17	2.21 ± 0.30	0.25	0.05
	c-C$_3$H$_2$	0.46 ± 0.07	20.55 ± 0.16	1.96 ± 0.35	0.22	0.04
	CN	0.49 ± 0.11	20.36 ± 0.19	1.65 ± 0.40	0.28	0.08
	HN^{13}C	0.32 ± 0.09	20.03 ± 0.38	2.59 ± 0.74	0.12	0.05
AGAL010.752−00.197	C^{18}O	4.39 ± 0.74	29.64 ± 0.20	2.60 ± 0.36	1.59	0.06
	H^{13}CO$^+$	1.22 ± 0.10	31.92 ± 0.08	2.22 ± 0.24	0.51	0.05
	c-C$_3$H$_2$	1.61 ± 0.08	31.85 ± 0.05	1.96 ± 0.11	0.77	0.04
	CN	0.45 ± 0.08	31.79 ± 0.11	1.27 ± 0.23	0.34	0.06
	HN^{13}C	1.25 ± 0.08	32.02 ± 0.06	1.83 ± 0.12	0.64	0.05
AGAL010.827−00.022	C^{18}O	6.07 ± 0.07	22.00 ± 0.02	2.92 ± 0.04	1.96	0.04
	H^{13}CO$^+$	0.55 ± 0.07	21.94 ± 0.18	2.73 ± 0.35	0.19	0.04
	c-C$_3$H$_2$	0.60 ± 0.07	21.90 ± 0.15	2.56 ± 0.30	0.22	0.04
	HN^{13}C	0.52 ± 0.10	20.78 ± 0.57	5.44 ± 1.07	0.09	0.04
AGAL010.957+00.022	C^{18}O	8.94 ± 0.11	21.41 ± 0.02	3.83 ± 0.06	2.20	0.05
	H^{13}CO$^+$	3.46 ± 0.12	21.38 ± 0.07	3.95 ± 0.16	0.82	0.05
	c-C$_3$H$_2$	1.00 ± 0.10	21.16 ± 0.18	3.51 ± 0.37	0.27	0.05
	CN	0.55 ± 0.14	21.31 ± 0.31	2.66 ± 0.97	0.19	0.07
	HC^{15}N	0.50 ± 0.12	21.62 ± 0.61	4.33 ± 1.02	0.11	0.05
	HN^{13}C	1.45 ± 0.15	21.70 ± 0.18	4.12 ± 0.58	0.33	0.05
AGAL010.972−00.094	C^{18}O	4.80 ± 0.10	30.12 ± 0.02	2.01 ± 0.05	2.24	0.07
	H^{13}CO$^+$	1.96 ± 0.09	29.85 ± 0.04	2.03 ± 0.11	0.91	0.05
	c-C$_3$H$_2$	2.32 ± 0.08	29.87 ± 0.04	2.04 ± 0.08	1.07	0.05
	CN	1.16 ± 0.12	29.89 ± 0.11	1.99 ± 0.25	0.55	0.08
	HN^{13}C	2.15 ± 0.09	29.95 ± 0.05	2.19 ± 0.11	0.92	0.05
AGAL010.982−00.367	C^{18}O	4.37 ± 0.06	−0.30 ± 0.02	3.01 ± 0.05	1.36	0.03
	H^{13}CO$^+$	0.97 ± 0.06	−0.44 ± 0.06	1.97 ± 0.15	0.46	0.04
	c-C$_3$H$_2$	0.90 ± 0.06	−0.46 ± 0.05	1.77 ± 0.15	0.48	0.03
	CN	0.41 ± 0.07	−0.76 ± 0.16	1.71 ± 0.34	0.23	0.05
	HN^{13}C	0.94 ± 0.05	−0.31 ± 0.05	1.82 ± 0.11	0.48	0.03
AGAL010.991−00.082	C^{18}O	6.15 ± 0.12	29.14 ± 0.02	2.20 ± 0.05	2.63	0.07
	H^{13}CO$^+$	1.61 ± 0.10	29.35 ± 0.09	2.92 ± 0.20	0.52	0.05
	c-C$_3$H$_2$	2.19 ± 0.09	29.64 ± 0.05	2.33 ± 0.12	0.88	0.05
	CN	0.96 ± 0.12	29.55 ± 0.14	2.19 ± 0.31	0.41	0.08
	HN^{13}C	2.04 ± 0.09	29.73 ± 0.06	2.64 ± 0.14	0.72	0.04
AGAL011.001−00.372	C^{18}O	4.38 ± 0.07	−1.12 ± 0.02	2.63 ± 0.05	1.57	0.04
	H^{13}CO$^+$	0.65 ± 0.06	−1.13 ± 0.07	1.62 ± 0.17	0.38	0.04
	c-C$_3$H$_2$	0.56 ± 0.07	−1.27 ± 0.14	2.48 ± 0.41	0.21	0.03
	CN	0.53 ± 0.10	−1.04 ± 0.22	2.35 ± 0.55	0.21	0.06
	HN^{13}C	0.65 ± 0.06	−1.01 ± 0.08	1.69 ± 0.21	0.36	0.04
AGAL011.034+00.061	C^{18}O	9.05 ± 0.11	15.32 ± 0.02	4.26 ± 0.06	2.00	0.05
	H^{13}CO$^+$	1.61 ± 0.12	15.02 ± 0.14	4.10 ± 0.36	0.37	0.05
	c-C$_3$H$_2$	0.78 ± 0.10	15.48 ± 0.24	3.81 ± 0.58	0.19	0.04
	CN	0.61 ± 0.14	15.75 ± 0.34	2.88 ± 0.81	0.20	0.08
	HN^{13}C	0.60 ± 0.12	15.44 ± 0.55	5.02 ± 1.07	0.11	0.05
AGAL011.064−00.099	C^{18}O	4.13 ± 0.06	29.42 ± 0.01	1.32 ± 0.02	2.93	0.04
	H^{13}CO$^+$	1.13 ± 0.08	29.39 ± 0.06	1.68 ± 0.13	0.63	0.05
	c-C$_3$H$_2$	1.53 ± 0.07	29.47 ± 0.03	1.46 ± 0.08	0.98	0.05
	CN	0.53 ± 0.09	29.57 ± 0.10	1.26 ± 0.27	0.40	0.07
	HN^{13}C	1.14 ± 0.08	29.55 ± 0.05	1.46 ± 0.11	0.73	0.05
AGAL011.082−00.534	C^{18}O	5.84 ± 0.05	30.05 ± 0.01	2.48 ± 0.02	2.21	0.03
	H^{13}CO$^+$	2.12 ± 0.07	29.73 ± 0.04	2.53 ± 0.10	0.79	0.03
	c-C$_3$H$_2$	3.48 ± 0.06	29.72 ± 0.02	2.39 ± 0.05	1.37	0.03
	CN	1.31 ± 0.09	29.86 ± 0.07	2.16 ± 0.18	0.57	0.06
	HC^{15}N	0.16 ± 0.04	30.13 ± 0.07	0.68 ± 2.02	0.22	0.03
	HN^{13}C	2.24 ± 0.06	29.85 ± 0.03	2.18 ± 0.07	0.96	0.03
AGAL011.126−00.127	C^{18}O	6.13 ± 0.04	30.31 ± 0.01	2.29 ± 0.02	2.51	0.03
	H^{13}CO$^+$	1.40 ± 0.05	30.40 ± 0.03	1.99 ± 0.07	0.66	0.03
	c-C$_3$H$_2$	1.98 ± 0.04	30.37 ± 0.02	1.96 ± 0.04	0.95	0.02
	CN	1.01 ± 0.06	30.17 ± 0.06	2.04 ± 0.13	0.46	0.04
	HN^{13}C	2.10 ± 0.05	30.59 ± 0.02	2.02 ± 0.05	0.98	0.03

Table B.3: continued.

ATLASGAL Name	Line	Area (K km s^{-1})	v_{LRS} (km s^{-1})	Δv (km s^{-1})	T_{MB} (K)	rms (K)
AGAL011.304−00.059	C^{18}O	5.78 ± 0.06	31.47 ± 0.01	1.92 ± 0.02	2.83	0.04
	H^{13}CO$^+$	0.88 ± 0.06	31.78 ± 0.08	2.27 ± 0.16	0.36	0.03
	c-C$_3$H$_2$	0.87 ± 0.06	31.69 ± 0.07	2.01 ± 0.15	0.41	0.03
	CN	0.30 ± 0.07	31.73 ± 0.20	1.69 ± 0.48	0.17	0.05
	HN^{13}C	0.72 ± 0.07	31.93 ± 0.10	2.30 ± 0.30	0.29	0.03
AGAL011.344+00.796	C^{18}O	5.40 ± 0.08	27.74 ± 0.01	2.56 ± 0.05	1.98	0.04
	H^{13}CO$^+$	1.43 ± 0.09	27.69 ± 0.06	2.04 ± 0.14	0.66	0.05
	c-C$_3$H$_2$	1.79 ± 0.08	27.78 ± 0.04	1.99 ± 0.12	0.84	0.04
	CN	0.62 ± 0.12	28.21 ± 0.23	2.37 ± 0.44	0.24	0.07
	HN^{13}C	1.36 ± 0.08	27.88 ± 0.06	1.88 ± 0.13	0.68	0.05
AGAL011.381+00.811	C^{18}O	4.30 ± 0.06	27.14 ± 0.01	1.61 ± 0.02	2.51	0.04
	H^{13}CO$^+$	0.82 ± 0.07	26.62 ± 0.07	1.61 ± 0.16	0.48	0.05
	c-C$_3$H$_2$	1.22 ± 0.06	26.81 ± 0.04	1.63 ± 0.10	0.70	0.04
	CN	0.43 ± 0.09	27.13 ± 0.14	1.38 ± 0.29	0.29	0.07
	HN^{13}C	0.84 ± 0.06	27.04 ± 0.05	1.31 ± 0.12	0.60	0.05
AGAL011.902−00.141	C^{18}O	11.84 ± 0.22	37.95 ± 0.03	3.91 ± 0.06	2.85	0.04
	H^{13}CO$^+$	2.41 ± 0.10	37.62 ± 0.09	4.39 ± 0.22	0.52	0.04
	c-C$_3$H$_2$	1.17 ± 0.08	38.07 ± 0.12	3.68 ± 0.28	0.30	0.03
	CN	0.97 ± 0.11	37.84 ± 0.17	3.25 ± 0.50	0.28	0.05
	HC^{15}N	0.28 ± 0.08	36.50 ± 0.31	2.42 ± 0.97	0.11	0.04
	HN^{13}C	1.78 ± 0.09	37.98 ± 0.11	4.84 ± 0.30	0.34	0.03
AGAL011.917−00.612	C^{18}O	9.28 ± 0.09	36.25 ± 0.01	2.96 ± 0.04	2.94	0.05
	H^{13}CO$^+$	5.20 ± 0.14	35.74 ± 0.05	4.14 ± 0.14	1.18	0.05
	c-C$_3$H$_2$	2.45 ± 0.10	36.01 ± 0.06	3.07 ± 0.15	0.75	0.04
	CN	1.95 ± 0.16	35.65 ± 0.14	3.74 ± 0.41	0.49	0.07
	HC^{15}N	1.32 ± 0.17	35.67 ± 0.35	5.81 ± 0.93	0.21	0.05
	HN^{13}C	3.64 ± 0.13	36.06 ± 0.06	3.52 ± 0.16	0.97	0.05
AGAL011.936−00.616	C^{18}O	14.12 ± 0.11	37.76 ± 0.01	3.74 ± 0.03	3.55	0.05
	H^{13}CO$^+$	5.71 ± 0.13	37.70 ± 0.05	4.57 ± 0.12	1.17	0.05
	c-C$_3$H$_2$	2.65 ± 0.11	37.65 ± 0.10	4.80 ± 0.22	0.52	0.04
	CN	3.05 ± 0.16	37.63 ± 0.12	4.39 ± 0.24	0.65	0.07
	HC^{15}N	1.20 ± 0.11	37.64 ± 0.18	3.82 ± 0.40	0.30	0.05
	HN^{13}C	4.72 ± 0.12	37.87 ± 0.05	3.83 ± 0.11	1.16	0.05
AGAL011.942−00.156	C^{18}O	9.28 ± 0.26	44.26 ± 0.06	4.80 ± 0.14	1.82	0.05
	H^{13}CO$^+$	2.31 ± 0.11	43.47 ± 0.08	3.62 ± 0.20	0.60	0.05
	c-C$_3$H$_2$	0.82 ± 0.12	43.13 ± 0.34	4.68 ± 0.69	0.16	0.04
	CN	0.60 ± 0.14	44.09 ± 0.32	2.98 ± 0.89	0.19	0.07
	HN^{13}C	0.94 ± 0.09	43.87 ± 0.14	2.77 ± 0.30	0.32	0.05
AGAL012.024−00.031	C^{18}O	8.79 ± 0.12	111.00 ± 0.02	2.51 ± 0.04	3.29	0.06
	H^{13}CO$^+$	1.32 ± 0.08	110.60 ± 0.08	2.78 ± 0.20	0.45	0.04
	c-C$_3$H$_2$	0.81 ± 0.08	110.40 ± 0.16	3.49 ± 0.39	0.22	0.03
	CN	0.50 ± 0.08	111.00 ± 0.16	2.00 ± 0.35	0.24	0.05
	HN^{13}C	0.47 ± 0.07	110.70 ± 0.20	2.59 ± 0.40	0.17	0.04
AGAL012.198−00.034	C^{18}O	11.31 ± 0.09	51.00 ± 0.02	4.92 ± 0.04	2.16	0.04
	H^{13}CO$^+$	2.10 ± 0.08	51.20 ± 0.07	3.67 ± 0.16	0.54	0.03
	c-C$_3$H$_2$	0.88 ± 0.08	51.18 ± 0.21	4.28 ± 0.44	0.19	0.03
	CN	1.05 ± 0.11	51.50 ± 0.18	3.45 ± 0.41	0.29	0.05
	HC^{15}N	0.35 ± 0.10	51.51 ± 0.76	5.01 ± 1.59	0.07	0.04
	HN^{13}C	1.27 ± 0.08	51.08 ± 0.11	3.58 ± 0.31	0.34	0.03
AGAL012.208−00.102	C^{18}O	20.77 ± 0.15	25.03 ± 0.02	6.92 ± 0.05	2.82	0.05
	H^{13}CO$^+$	5.71 ± 0.15	23.92 ± 0.09	6.65 ± 0.20	0.81	0.05
	c-C$_3$H$_2$	2.31 ± 0.16	24.39 ± 0.25	7.46 ± 0.59	0.29	0.05
	CN	1.10 ± 0.20	23.05 ± 0.52	5.13 ± 1.16	0.20	0.08
	HC^{15}N	1.79 ± 0.16	23.58 ± 0.33	7.36 ± 0.74	0.23	0.05
	HN^{13}C	3.26 ± 0.15	24.40 ± 0.16	6.79 ± 0.36	0.45	0.05
AGAL012.418+00.506	C^{18}O	15.05 ± 0.04	17.79 ± 0.00	2.99 ± 0.01	4.73	0.03
	HCO	0.11 ± 0.02	18.59 ± 0.20	2.14 ± 0.34	0.05	0.01
	H^{13}CO$^+$	8.14 ± 0.08	17.84 ± 0.01	3.00 ± 0.03	2.55	0.04
	c-C$_3$H$_2$	2.40 ± 0.08	18.65 ± 0.06	3.71 ± 0.13	0.61	0.03
	CN	1.11 ± 0.10	17.73 ± 0.14	2.93 ± 0.34	0.36	0.05
	HC^{15}N	1.05 ± 0.07	17.81 ± 0.08	2.48 ± 0.19	0.40	0.04
	HN^{13}C	2.34 ± 0.07	18.04 ± 0.05	3.12 ± 0.11	0.71	0.03
AGAL012.496−00.222	C^{18}O	6.37 ± 0.07	35.46 ± 0.01	2.22 ± 0.03	2.70	0.04
	H^{13}CO$^+$	2.83 ± 0.06	35.65 ± 0.02	2.06 ± 0.05	1.29	0.04
	c-C$_3$H$_2$	2.44 ± 0.06	35.67 ± 0.02	2.14 ± 0.05	1.07	0.03
	CN	1.18 ± 0.10	35.81 ± 0.09	2.21 ± 0.27	0.50	0.06
	HN^{13}C	1.69 ± 0.06	35.85 ± 0.03	1.89 ± 0.07	0.84	0.03
AGAL012.679−00.181	C^{18}O	18.40 ± 0.24	54.29 ± 0.03	5.71 ± 0.07	3.03	0.04
	HCO	0.48 ± 0.05	56.02 ± 0.27	5.95 ± 0.82	0.08	0.01
	H^{13}CO$^+$	2.15 ± 0.11	55.85 ± 0.10	4.04 ± 0.26	0.50	0.04
	c-C$_3$H$_2$	2.12 ± 0.10	55.94 ± 0.12	5.33 ± 0.29	0.37	0.03
	CN	1.76 ± 0.12	55.97 ± 0.12	3.66 ± 0.29	0.45	0.06
	HC^{15}N	0.88 ± 0.11	55.45 ± 0.26	4.52 ± 0.72	0.18	0.04
	HN^{13}C	2.17 ± 0.07	55.52 ± 0.04	2.59 ± 0.10	0.79	0.04
AGAL012.804−00.199	C^{18}O	53.96 ± 0.17	34.78 ± 0.01	4.39 ± 0.02	11.50	0.09

Table B.3: continued.

ATLASGAL Name	Line	Area (K km s^{-1})	v_{LRS} (km s^{-1})	Δv (km s^{-1})	T_{MB} (K)	rms (K)
	HCO	0.31 ± 0.09	36.70 ± 0.67	5.24 ± 2.57	0.06	0.02
	H^{13}CO$^+$	23.66 ± 0.15	35.28 ± 0.01	4.40 ± 0.04	5.05	0.05
	c-C$_3$H$_2$	5.11 ± 0.17	35.51 ± 0.06	4.35 ± 0.20	1.10	0.06
	CN	4.50 ± 0.39	35.40 ± 0.24	6.00 ± 0.70	0.70	0.14
	HC^{15}N	3.59 ± 0.13	35.51 ± 0.08	4.74 ± 0.21	0.71	0.05
	HN^{13}C	6.53 ± 0.12	35.48 ± 0.03	3.96 ± 0.09	1.55	0.05
AGAL012.818+00.322	C^{18}O	6.83 ± 0.03	19.45 ± 0.00	1.41 ± 0.01	4.55	0.03
	H^{13}CO$^+$	1.13 ± 0.06	19.64 ± 0.03	1.20 ± 0.07	0.89	0.04
	c-C$_3$H$_2$	1.59 ± 0.05	19.74 ± 0.02	1.21 ± 0.04	1.23	0.03
	CN	0.39 ± 0.05	19.62 ± 0.07	1.13 ± 0.18	0.32	0.04
	HN^{13}C	0.61 ± 0.05	19.82 ± 0.05	1.24 ± 0.11	0.46	0.04
AGAL012.853−00.226	C^{18}O	19.61 ± 0.04	35.86 ± 0.00	3.97 ± 0.01	4.64	0.04
	HCO	0.56 ± 0.05	37.13 ± 0.20	4.41 ± 0.45	0.12	0.02
	H^{13}CO$^+$	3.48 ± 0.10	36.32 ± 0.04	2.81 ± 0.10	1.17	0.05
	c-C$_3$H$_2$	2.72 ± 0.11	36.43 ± 0.08	3.95 ± 0.20	0.65	0.04
	CN	2.47 ± 0.13	36.35 ± 0.07	2.78 ± 0.19	0.84	0.07
	HC^{15}N	0.33 ± 0.08	35.79 ± 0.19	1.65 ± 0.46	0.19	0.05
	HN^{13}C	2.48 ± 0.09	36.51 ± 0.04	2.36 ± 0.10	0.99	0.05
AGAL012.888+00.489	C^{18}O	26.80 ± 0.05	33.38 ± 0.00	3.25 ± 0.01	7.75	0.04
	HCO	0.22 ± 0.04	34.27 ± 0.33	3.48 ± 0.67	0.06	0.02
	H^{13}CO$^+$	5.65 ± 0.10	33.09 ± 0.03	3.61 ± 0.07	1.47	0.04
	c-C$_3$H$_2$	2.49 ± 0.10	33.40 ± 0.07	3.52 ± 0.16	0.67	0.04
	CN	2.43 ± 0.13	33.03 ± 0.10	3.66 ± 0.22	0.62	0.07
	HC^{15}N	2.03 ± 0.12	33.05 ± 0.12	4.11 ± 0.27	0.46	0.05
	HN^{13}C	4.16 ± 0.10	32.97 ± 0.05	3.72 ± 0.10	1.05	0.04
AGAL012.893−00.282	C^{18}O	12.47 ± 0.30	36.63 ± 0.03	2.96 ± 0.05	3.96	0.06
	H^{13}CO$^+$	3.34 ± 0.14	35.24 ± 0.12	5.45 ± 0.22	0.57	0.05
	c-C$_3$H$_2$	1.88 ± 0.12	35.13 ± 0.16	4.71 ± 0.29	0.37	0.05
	CN	1.32 ± 0.14	35.30 ± 0.28	5.07 ± 0.57	0.24	0.06
	HN^{13}C	2.00 ± 0.12	34.92 ± 0.16	4.94 ± 0.31	0.38	0.05
AGAL012.899−00.241	C^{18}O	17.03 ± 0.12	36.76 ± 0.01	2.58 ± 0.02	6.20	0.06
	HCO	0.32 ± 0.05	35.37 ± 0.33	4.23 ± 0.58	0.07	0.02
	H^{13}CO$^+$	2.90 ± 0.10	36.99 ± 0.05	2.78 ± 0.12	0.98	0.05
	c-C$_3$H$_2$	1.41 ± 0.14	37.14 ± 0.12	2.40 ± 0.26	0.55	0.05
	CN	1.28 ± 0.12	36.78 ± 0.10	2.36 ± 0.29	0.51	0.06
	HN^{13}C	2.30 ± 0.10	37.06 ± 0.05	2.35 ± 0.12	0.92	0.05
AGAL012.904−00.031	C^{18}O	9.89 ± 0.11	56.33 ± 0.02	3.33 ± 0.04	2.79	0.06
	H^{13}CO$^+$	4.08 ± 0.12	56.52 ± 0.05	3.17 ± 0.11	1.21	0.06
	c-C$_3$H$_2$	1.07 ± 0.10	56.48 ± 0.15	3.33 ± 0.40	0.30	0.04
	CN	1.01 ± 0.12	56.58 ± 0.19	3.06 ± 0.41	0.31	0.07
	HC^{15}N	0.73 ± 0.12	55.65 ± 0.41	5.14 ± 0.96	0.13	0.04
	HN^{13}C	2.27 ± 0.09	56.73 ± 0.06	2.96 ± 0.14	0.72	0.04
AGAL012.908−00.259	C^{18}O	27.01 ± 0.14	35.85 ± 0.01	4.73 ± 0.03	5.36	0.06
	HCO	0.15 ± 0.02	35.15 ± 0.21	2.86 ± 0.53	0.05	0.01
	H^{13}CO$^+$	9.10 ± 0.08	36.95 ± 0.02	4.01 ± 0.04	2.13	0.03
	c-C$_3$H$_2$	2.33 ± 0.06	36.77 ± 0.06	4.25 ± 0.15	0.52	0.02
	CN	2.94 ± 0.15	36.80 ± 0.11	4.57 ± 0.29	0.61	0.06
	HC^{15}N	1.61 ± 0.05	37.20 ± 0.07	4.31 ± 0.18	0.35	0.02
	HN^{13}C	5.04 ± 0.05	37.27 ± 0.02	3.57 ± 0.04	1.33	0.02
AGAL012.914−00.336	C^{18}O	9.06 ± 0.11	36.69 ± 0.02	4.03 ± 0.05	2.11	0.05
	H^{13}CO$^+$	1.75 ± 0.11	37.22 ± 0.10	3.20 ± 0.22	0.51	0.05
	c-C$_3$H$_2$	1.45 ± 0.10	37.37 ± 0.10	2.84 ± 0.22	0.48	0.05
	CN	0.66 ± 0.11	37.06 ± 0.15	1.99 ± 0.43	0.31	0.06
	HN^{13}C	1.76 ± 0.10	37.26 ± 0.07	2.49 ± 0.17	0.66	0.05
AGAL013.119−00.096	C^{18}O	1.61 ± 0.09	35.94 ± 0.03	1.14 ± 0.08	1.33	0.08
	H^{13}CO$^+$	1.53 ± 0.08	35.89 ± 0.04	1.59 ± 0.09	0.90	0.05
	c-C$_3$H$_2$	1.57 ± 0.07	35.90 ± 0.04	1.60 ± 0.08	0.93	0.05
	CN	0.84 ± 0.08	35.94 ± 0.07	1.42 ± 0.16	0.56	0.07
	HN^{13}C	1.38 ± 0.08	36.19 ± 0.05	1.67 ± 0.10	0.78	0.05
AGAL013.169+00.077	C^{18}O	7.97 ± 0.07	50.15 ± 0.01	2.04 ± 0.02	3.66	0.04
	HCO	0.20 ± 0.04	52.01 ± 0.52	5.29 ± 1.07	0.04	0.01
	H^{13}CO$^+$	1.72 ± 0.08	49.87 ± 0.05	2.58 ± 0.14	0.62	0.04
	c-C$_3$H$_2$	1.00 ± 0.06	49.92 ± 0.06	2.03 ± 0.16	0.46	0.03
	CN	1.00 ± 0.09	49.97 ± 0.08	1.78 ± 0.18	0.53	0.06
	HN^{13}C	1.81 ± 0.07	50.04 ± 0.04	2.31 ± 0.11	0.74	0.04
AGAL013.178+00.059	C^{18}O	10.24 ± 0.25	49.19 ± 0.03	2.66 ± 0.08	3.62	0.14
	HCO	0.25 ± 0.05	50.02 ± 0.31	3.26 ± 0.77	0.07	0.02
	H^{13}CO$^+$	5.25 ± 0.12	49.28 ± 0.04	3.42 ± 0.09	1.44	0.05
	c-C$_3$H$_2$	2.70 ± 0.11	49.40 ± 0.07	3.47 ± 0.17	0.73	0.05
	CN	3.74 ± 0.21	49.08 ± 0.07	2.45 ± 0.16	1.44	0.12
	HC^{15}N	1.10 ± 0.12	49.20 ± 0.24	4.76 ± 0.67	0.22	0.04
	HN^{13}C	5.47 ± 0.11	49.42 ± 0.03	3.17 ± 0.07	1.62	0.05
AGAL013.209−00.144	C^{18}O	20.92 ± 0.10	52.30 ± 0.01	4.67 ± 0.02	4.21	0.05
	HCO	0.28 ± 0.05	52.33 ± 0.49	4.85 ± 1.11	0.05	0.02
	H^{13}CO$^+$	1.92 ± 0.12	51.81 ± 0.10	3.46 ± 0.25	0.52	0.05
	c-C$_3$H$_2$	1.46 ± 0.10	52.30 ± 0.13	3.97 ± 0.32	0.35	0.04

Table B.3: continued.

ATLASGAL Name	Line	Area (K km s^{-1})	v_{LRS} (km s^{-1})	Δv (km s^{-1})	T_{MB} (K)	rms (K)
	CN	1.32 ± 0.12	52.08 ± 0.13	2.88 ± 0.30	0.43	0.06
	HC^{15}N	0.43 ± 0.08	51.65 ± 0.28	2.73 ± 0.54	0.15	0.04
	HN^{13}C	1.41 ± 0.09	51.74 ± 0.09	2.84 ± 0.21	0.47	0.04
AGAL013.276−00.334	C^{18}O	6.77 ± 0.06	41.05 ± 0.01	2.12 ± 0.02	3.01	0.04
	H^{13}CO$^+$	1.26 ± 0.06	41.24 ± 0.05	2.05 ± 0.12	0.58	0.04
	c-C$_3$H$_2$	1.63 ± 0.06	41.05 ± 0.03	1.70 ± 0.07	0.90	0.03
	CN	0.77 ± 0.12	41.08 ± 0.19	2.67 ± 0.52	0.27	0.06
	HN^{13}C	1.47 ± 0.05	41.26 ± 0.03	1.81 ± 0.08	0.76	0.03
AGAL013.384+00.064	C^{18}O	5.42 ± 0.09	14.14 ± 0.04	4.20 ± 0.09	1.21	0.04
	H^{13}CO$^+$	0.42 ± 0.10	14.00 ± 0.29	2.47 ± 0.73	0.16	0.05
	c-C$_3$H$_2$	0.18 ± 0.07	17.42 ± 0.28	1.56 ± 0.72	0.11	0.04
	CN	0.62 ± 0.14	14.50 ± 0.43	3.64 ± 1.05	0.16	0.05
AGAL013.658−00.599	C^{18}O	13.80 ± 0.29	47.80 ± 0.03	2.83 ± 0.07	4.58	0.15
	H^{13}CO$^+$	4.26 ± 0.11	47.66 ± 0.04	3.13 ± 0.10	1.28	0.05
	c-C$_3$H$_2$	1.28 ± 0.12	47.35 ± 0.16	3.30 ± 0.36	0.36	0.06
	CN	2.49 ± 0.24	47.57 ± 0.14	2.95 ± 0.35	0.80	0.12
	HC^{15}N	0.89 ± 0.13	47.60 ± 0.32	4.43 ± 0.78	0.19	0.05
	HN^{13}C	3.66 ± 0.10	47.68 ± 0.05	3.42 ± 0.10	1.00	0.05
AGAL013.872+00.281	C^{18}O	21.25 ± 0.00	48.38 ± 0.00	2.40 ± 0.00	8.32	0.04
	HCO	0.22 ± 0.04	49.23 ± 0.16	1.95 ± 0.38	0.11	0.02
	H^{13}CO$^+$	4.08 ± 0.10	48.68 ± 0.03	2.74 ± 0.08	1.40	0.05
	c-C$_3$H$_2$	2.20 ± 0.10	48.79 ± 0.07	3.25 ± 0.18	0.64	0.04
	CN	1.71 ± 0.12	48.59 ± 0.09	2.86 ± 0.26	0.56	0.06
	HC^{15}N	0.70 ± 0.11	48.34 ± 0.20	2.76 ± 0.55	0.24	0.05
	HN^{13}C	1.39 ± 0.10	48.78 ± 0.11	2.87 ± 0.23	0.46	0.05
AGAL013.882−00.144	C^{18}O	4.82 ± 0.09	18.09 ± 0.03	3.20 ± 0.07	1.41	0.04
	H^{13}CO$^+$	1.44 ± 0.11	17.87 ± 0.11	2.81 ± 0.26	0.48	0.06
	c-C$_3$H$_2$	0.75 ± 0.13	17.92 ± 0.34	3.96 ± 0.82	0.18	0.05
	CN	0.41 ± 0.12	17.89 ± 0.37	2.43 ± 0.79	0.16	0.07
	HN^{13}C	0.87 ± 0.12	17.88 ± 0.24	3.42 ± 0.60	0.24	0.05
AGAL013.902−00.516	C^{18}O	4.88 ± 0.14	22.86 ± 0.02	1.62 ± 0.04	2.82	0.04
	H^{13}CO$^+$	2.88 ± 0.05	22.87 ± 0.01	1.57 ± 0.03	1.72	0.03
	c-C$_3$H$_2$	3.77 ± 0.05	22.91 ± 0.01	1.51 ± 0.02	2.35	0.03
	CN	0.90 ± 0.07	22.89 ± 0.06	1.52 ± 0.14	0.56	0.05
	HC^{15}N	0.29 ± 0.06	22.66 ± 0.18	1.77 ± 0.45	0.15	0.04
	HN^{13}C	1.42 ± 0.05	22.97 ± 0.03	1.47 ± 0.06	0.91	0.04
AGAL013.951−00.407	C^{18}O	10.33 ± 0.10	20.00 ± 0.01	2.58 ± 0.03	3.77	0.05
	HCO	0.30 ± 0.04	20.52 ± 0.17	2.47 ± 0.36	0.11	0.02
	H^{13}CO$^+$	2.37 ± 0.10	19.96 ± 0.04	2.10 ± 0.11	1.06	0.05
	c-C$_3$H$_2$	1.41 ± 0.09	20.05 ± 0.06	1.92 ± 0.15	0.69	0.05
	CN	0.57 ± 0.11	20.03 ± 0.24	2.35 ± 0.44	0.23	0.07
	HC^{15}N	0.36 ± 0.09	20.07 ± 0.31	2.37 ± 0.71	0.14	0.05
	HN^{13}C	1.33 ± 0.10	20.22 ± 0.08	2.21 ± 0.20	0.57	0.06
AGAL014.084−00.554	C^{18}O	8.34 ± 0.07	22.04 ± 0.01	1.84 ± 0.02	4.26	0.05
	HCO	0.25 ± 0.03	21.89 ± 0.14	2.51 ± 0.42	0.09	0.01
	H^{13}CO$^+$	1.94 ± 0.06	22.26 ± 0.03	1.91 ± 0.07	0.95	0.04
	c-C$_3$H$_2$	2.23 ± 0.06	22.33 ± 0.02	1.82 ± 0.06	1.16	0.04
	CN	0.58 ± 0.08	21.94 ± 0.12	1.73 ± 0.24	0.32	0.06
	HC^{15}N	0.12 ± 0.04	22.15 ± 0.09	0.68 ± 8.30	0.16	0.03
	HN^{13}C	1.11 ± 0.05	22.35 ± 0.04	1.76 ± 0.08	0.59	0.03
AGAL014.114−00.574	C^{18}O	19.03 ± 0.22	20.02 ± 0.02	3.52 ± 0.05	5.08	0.11
	HCO	0.36 ± 0.04	19.92 ± 0.12	2.17 ± 0.28	0.15	0.02
	H^{13}CO$^+$	5.98 ± 0.10	19.90 ± 0.03	3.48 ± 0.06	1.62	0.04
	c-C$_3$H$_2$	2.40 ± 0.13	21.46 ± 0.06	2.36 ± 0.14	0.95	0.05
	CN	2.34 ± 0.30	19.58 ± 0.22	3.98 ± 0.75	0.55	0.12
	HC^{15}N	0.82 ± 0.12	20.03 ± 0.24	3.43 ± 0.56	0.22	0.05
	HN^{13}C	3.23 ± 0.11	20.28 ± 0.06	3.62 ± 0.13	0.84	0.05
AGAL014.131−00.522	C^{18}O	5.78 ± 0.08	21.03 ± 0.01	1.41 ± 0.02	3.84	0.06
	H^{13}CO$^+$	1.55 ± 0.06	21.19 ± 0.02	1.14 ± 0.06	1.28	0.05
	c-C$_3$H$_2$	2.05 ± 0.07	21.23 ± 0.02	1.28 ± 0.05	1.50	0.04
	CN	0.45 ± 0.09	21.25 ± 0.12	1.34 ± 0.32	0.32	0.07
	HC^{15}N	0.28 ± 0.11	21.01 ± 0.34	1.85 ± 0.99	0.14	0.05
	HN^{13}C	0.86 ± 0.07	21.33 ± 0.05	1.13 ± 0.09	0.72	0.05
AGAL014.181−00.529	C^{18}O	7.09 ± 0.10	20.98 ± 0.01	1.70 ± 0.03	3.92	0.07
	HCO	0.19 ± 0.03	21.20 ± 0.13	1.91 ± 0.32	0.09	0.01
	H^{13}CO$^+$	2.34 ± 0.06	21.38 ± 0.02	1.74 ± 0.05	1.26	0.04
	c-C$_3$H$_2$	2.21 ± 0.05	21.42 ± 0.02	1.68 ± 0.04	1.24	0.03
	CN	0.66 ± 0.08	21.44 ± 0.09	1.63 ± 0.20	0.38	0.06
	HC^{15}N	0.30 ± 0.06	21.68 ± 0.21	1.91 ± 0.36	0.15	0.04
	HN^{13}C	1.28 ± 0.05	21.52 ± 0.03	1.60 ± 0.07	0.75	0.03
AGAL014.194−00.194	C^{18}O	14.10 ± 0.25	38.69 ± 0.03	2.92 ± 0.06	4.54	0.13
	H^{13}CO$^+$	5.78 ± 0.11	39.37 ± 0.03	3.20 ± 0.07	1.70	0.05
	c-C$_3$H$_2$	2.91 ± 0.11	39.02 ± 0.06	3.21 ± 0.14	0.85	0.05
	CN	2.70 ± 0.21	39.37 ± 0.12	3.02 ± 0.28	0.84	0.11
	HC^{15}N	0.85 ± 0.11	39.64 ± 0.21	3.29 ± 0.44	0.24	0.05

Table B.3: continued.

ATLASGAL Name	Line	Area (K km s^{-1})	v_{LRS} (km s^{-1})	Δv (km s^{-1})	T_{MB} (K)	rms (K)
	HN^{13}C	4.23 ± 0.11	39.69 ± 0.04	3.12 ± 0.09	1.28	0.05
AGAL014.197−00.214	C^{18}O	7.11 ± 0.08	39.41 ± 0.01	1.87 ± 0.03	3.57	0.04
	H^{13}CO$^+$	1.09 ± 0.07	39.44 ± 0.05	1.67 ± 0.13	0.61	0.04
	c-C$_3$H$_2$	1.13 ± 0.07	39.43 ± 0.06	1.77 ± 0.12	0.60	0.04
	CN	0.50 ± 0.11	39.25 ± 0.13	1.35 ± 0.44	0.35	0.07
	HN^{13}C	0.90 ± 0.07	39.58 ± 0.06	1.54 ± 0.11	0.55	0.05
AGAL014.204−00.207	C^{18}O	4.71 ± 0.18	39.38 ± 0.03	1.61 ± 0.04	2.75	0.04
	H^{13}CO$^+$	1.68 ± 0.07	39.05 ± 0.04	2.12 ± 0.12	0.74	0.03
	c-C$_3$H$_2$	1.17 ± 0.07	38.97 ± 0.07	2.38 ± 0.17	0.46	0.03
	CN	0.34 ± 0.10	38.63 ± 0.30	1.96 ± 0.82	0.16	0.06
	HC^{15}N	0.30 ± 0.08	38.93 ± 0.46	3.48 ± 1.24	0.08	0.03
	HN^{13}C	1.01 ± 0.07	39.18 ± 0.05	1.76 ± 0.15	0.54	0.04
AGAL014.227−00.511	C^{18}O	15.19 ± 0.04	19.57 ± 0.00	2.07 ± 0.01	6.91	0.04
	HCO	0.31 ± 0.02	19.95 ± 0.07	1.78 ± 0.15	0.16	0.01
	H^{13}CO$^+$	6.13 ± 0.07	19.36 ± 0.01	2.49 ± 0.03	2.31	0.04
	c-C$_3$H$_2$	2.38 ± 0.05	19.48 ± 0.03	2.71 ± 0.06	0.83	0.03
	CN	1.20 ± 0.09	19.39 ± 0.09	2.37 ± 0.18	0.48	0.05
	HC^{15}N	0.93 ± 0.08	19.43 ± 0.12	2.75 ± 0.28	0.32	0.04
	HN^{13}C	2.39 ± 0.06	19.62 ± 0.03	2.56 ± 0.08	0.87	0.03
AGAL014.246−00.071	C^{18}O	13.85 ± 0.09	60.36 ± 0.01	3.62 ± 0.03	3.59	0.04
	H^{13}CO$^+$	2.25 ± 0.12	61.04 ± 0.14	5.12 ± 0.29	0.41	0.05
	c-C$_3$H$_2$	1.89 ± 0.12	60.67 ± 0.14	4.63 ± 0.35	0.38	0.04
	CN	1.59 ± 0.14	59.92 ± 0.16	3.85 ± 0.40	0.39	0.06
	HC^{15}N	0.51 ± 0.12	60.93 ± 0.58	4.74 ± 1.23	0.10	0.05
	HN^{13}C	2.16 ± 0.11	60.92 ± 0.12	4.41 ± 0.25	0.46	0.04
AGAL014.327−00.532	C^{18}O	4.17 ± 0.05	19.93 ± 0.01	1.27 ± 0.02	3.08	0.04
	H^{13}CO$^+$	1.52 ± 0.05	20.01 ± 0.02	1.23 ± 0.04	1.16	0.03
	c-C$_3$H$_2$	1.67 ± 0.04	20.06 ± 0.02	1.02 ± 0.03	1.54	0.03
	CN	0.88 ± 0.06	19.93 ± 0.03	0.91 ± 0.07	0.91	0.06
	HN^{13}C	1.30 ± 0.05	20.10 ± 0.03	1.31 ± 0.06	0.93	0.04
AGAL014.331−00.644	C^{18}O	12.61 ± 0.10	21.81 ± 0.01	3.14 ± 0.03	3.77	0.05
	H^{13}CO$^+$	9.24 ± 0.11	22.31 ± 0.02	3.58 ± 0.05	2.43	0.05
	c-C$_3$H$_2$	2.39 ± 0.11	22.94 ± 0.09	4.15 ± 0.22	0.54	0.04
	CN	2.66 ± 0.14	22.31 ± 0.08	3.28 ± 0.20	0.76	0.07
	HC^{15}N	2.55 ± 0.14	22.09 ± 0.11	4.36 ± 0.30	0.55	0.05
	HN^{13}C	5.26 ± 0.10	22.50 ± 0.03	3.20 ± 0.07	1.55	0.05
AGAL014.434−00.699	C^{18}O	6.32 ± 0.05	17.69 ± 0.01	1.56 ± 0.01	3.80	0.04
	HCO	0.23 ± 0.03	18.16 ± 0.17	2.63 ± 0.40	0.08	0.01
	H^{13}CO$^+$	1.41 ± 0.05	17.58 ± 0.03	1.45 ± 0.06	0.91	0.03
	c-C$_3$H$_2$	1.07 ± 0.07	17.88 ± 0.08	2.62 ± 0.22	0.38	0.03
	CN	0.42 ± 0.09	17.87 ± 0.11	1.29 ± 0.41	0.31	0.06
	HC^{15}N	0.27 ± 0.06	17.54 ± 0.19	1.86 ± 0.45	0.14	0.03
	HN^{13}C	0.41 ± 0.05	17.54 ± 0.13	1.87 ± 0.25	0.21	0.05
AGAL014.492−00.139	C^{18}O	14.95 ± 0.27	38.72 ± 0.03	3.37 ± 0.07	4.17	0.14
	HCO	0.42 ± 0.11	39.41 ± 0.69	5.69 ± 2.56	0.07	0.02
	H^{13}CO$^+$	3.18 ± 0.12	39.84 ± 0.06	3.34 ± 0.14	0.89	0.05
	c-C$_3$H$_2$	3.18 ± 0.12	39.62 ± 0.06	3.36 ± 0.15	0.89	0.05
	CN	1.94 ± 0.20	39.97 ± 0.15	2.83 ± 0.36	0.64	0.11
	HN^{13}C	3.77 ± 0.13	39.98 ± 0.06	3.77 ± 0.14	0.94	0.05
AGAL014.617+00.332	C^{18}O	7.45 ± 0.05	26.58 ± 0.01	1.61 ± 0.01	4.35	0.04
	H^{13}CO$^+$	1.77 ± 0.08	26.80 ± 0.03	1.63 ± 0.08	1.02	0.05
	c-C$_3$H$_2$	1.81 ± 0.06	26.85 ± 0.02	1.29 ± 0.05	1.32	0.04
	CN	1.10 ± 0.08	26.73 ± 0.06	1.54 ± 0.14	0.67	0.06
	HN^{13}C	1.09 ± 0.07	27.04 ± 0.05	1.39 ± 0.12	0.73	0.05
AGAL014.632−00.577	C^{18}O	11.14 ± 0.18	18.14 ± 0.02	2.30 ± 0.04	4.55	0.11
	HCO	0.24 ± 0.04	18.34 ± 0.17	2.05 ± 0.35	0.11	0.02
	H^{13}CO$^+$	5.01 ± 0.10	18.46 ± 0.02	2.55 ± 0.06	1.84	0.05
	c-C$_3$H$_2$	2.05 ± 0.11	18.57 ± 0.06	2.52 ± 0.16	0.77	0.05
	CN	2.46 ± 0.19	18.56 ± 0.07	2.04 ± 0.19	1.13	0.12
	HC^{15}N	1.32 ± 0.10	18.62 ± 0.09	2.49 ± 0.21	0.50	0.05
	HN^{13}C	3.91 ± 0.09	18.68 ± 0.03	2.24 ± 0.06	1.64	0.05
AGAL014.644−00.117	C^{18}O	3.19 ± 0.17	40.93 ± 0.05	1.93 ± 0.10	1.55	0.06
	H^{13}CO$^+$	1.25 ± 0.10	40.76 ± 0.10	2.46 ± 0.20	0.48	0.06
	c-C$_3$H$_2$	1.58 ± 0.09	40.61 ± 0.07	2.42 ± 0.16	0.61	0.05
	CN	0.89 ± 0.12	40.76 ± 0.16	2.37 ± 0.35	0.35	0.07
	HN^{13}C	1.89 ± 0.10	40.72 ± 0.07	2.63 ± 0.15	0.68	0.05
AGAL014.686−00.222	C^{18}O	3.83 ± 0.05	57.99 ± 0.01	1.16 ± 0.02	3.11	0.04
	H^{13}CO$^+$	0.41 ± 0.07	58.29 ± 0.14	1.54 ± 0.30	0.25	0.05
	c-C$_3$H$_2$	0.23 ± 0.08	58.17 ± 0.07	0.69 ± 6.40	0.32	0.05
AGAL014.711−00.224	C^{18}O	3.53 ± 0.10	37.97 ± 0.05	3.25 ± 0.11	1.02	0.05
	H^{13}CO$^+$	0.58 ± 0.10	37.21 ± 0.13	1.72 ± 0.36	0.32	0.06
	c-C$_3$H$_2$	1.42 ± 0.10	37.08 ± 0.06	1.90 ± 0.17	0.70	0.05
	CN	0.48 ± 0.15	37.11 ± 0.13	1.39 ± 0.74	0.33	0.07
	HN^{13}C	0.80 ± 0.10	37.38 ± 0.10	1.71 ± 0.30	0.44	0.06
AGAL014.771−00.356	C^{18}O	4.70 ± 0.07	34.76 ± 0.02	3.36 ± 0.06	1.31	0.03

Table B.3: continued.

ATLASGAL Name	Line	Area (K km s^{-1})	v_{LRS} (km s^{-1})	Δv (km s^{-1})	T_{MB} (K)	rms (K)
	H^{13}CO$^+$	1.27 ± 0.08	34.04 ± 0.10	3.25 ± 0.26	0.37	0.04
	c-C$_3$H$_2$	0.62 ± 0.06	34.26 ± 0.16	2.93 ± 0.32	0.20	0.03
	CN	0.48 ± 0.09	34.67 ± 0.23	2.53 ± 0.54	0.18	0.05
	HN^{13}C	0.81 ± 0.08	34.42 ± 0.13	2.84 ± 0.33	0.27	0.04
AGAL014.777−00.334	C^{18}O	3.50 ± 0.10	32.61 ± 0.04	2.79 ± 0.10	1.18	0.05
	H^{13}CO$^+$	0.99 ± 0.09	32.49 ± 0.12	2.54 ± 0.26	0.36	0.05
	c-C$_3$H$_2$	1.06 ± 0.09	32.42 ± 0.11	2.70 ± 0.29	0.37	0.04
	CN	0.46 ± 0.08	32.87 ± 0.14	1.54 ± 0.28	0.28	0.06
	HN^{13}C	0.90 ± 0.09	32.74 ± 0.14	2.59 ± 0.31	0.33	0.05
AGAL014.777−00.487	C^{18}O	2.10 ± 0.04	21.77 ± 0.01	1.29 ± 0.03	1.53	0.03
	H^{13}CO$^+$	0.87 ± 0.05	21.70 ± 0.04	1.40 ± 0.10	0.59	0.04
	c-C$_3$H$_2$	0.64 ± 0.05	21.83 ± 0.05	1.41 ± 0.14	0.43	0.03
	CN	0.60 ± 0.09	21.47 ± 0.13	1.84 ± 0.41	0.31	0.06
	HN^{13}C	0.61 ± 0.04	21.84 ± 0.05	1.56 ± 0.12	0.37	0.03
AGAL014.851−00.990	C^{18}O	4.86 ± 0.05	21.89 ± 0.01	1.64 ± 0.02	2.79	0.03
	H^{13}CO$^+$	3.19 ± 0.08	21.89 ± 0.02	1.74 ± 0.05	1.73	0.05
	c-C$_3$H$_2$	1.57 ± 0.08	22.05 ± 0.04	1.71 ± 0.10	0.86	0.05
	CN	0.49 ± 0.08	22.05 ± 0.12	1.38 ± 0.26	0.34	0.06
	HN^{13}C	0.92 ± 0.09	22.00 ± 0.09	2.00 ± 0.24	0.43	0.05
AGAL015.006+00.009	C^{18}O	7.69 ± 0.08	24.40 ± 0.01	2.23 ± 0.03	3.24	0.05
	H^{13}CO$^+$	0.99 ± 0.08	24.41 ± 0.09	2.40 ± 0.23	0.39	0.04
	c-C$_3$H$_2$	0.72 ± 0.07	24.26 ± 0.11	2.24 ± 0.26	0.30	0.04
	CN	0.67 ± 0.14	24.59 ± 0.30	2.67 ± 0.56	0.23	0.09
	HN^{13}C	0.80 ± 0.06	24.63 ± 0.09	2.31 ± 0.21	0.33	0.03
AGAL015.013−00.671	C^{18}O	20.98 ± 0.34	19.38 ± 0.03	4.27 ± 0.03	4.62	0.04
	HCO	0.87 ± 0.04	19.33 ± 0.09	4.38 ± 0.20	0.19	0.01
	H^{13}CO$^+$	7.41 ± 0.28	18.04 ± 0.03	2.36 ± 0.06	2.95	0.04
	c-C$_3$H$_2$	6.37 ± 0.12	18.92 ± 0.04	4.48 ± 0.09	1.34	0.04
	CN	4.82 ± 0.19	18.57 ± 0.07	3.97 ± 0.21	1.14	0.08
	HC^{15}N	2.87 ± 0.09	18.43 ± 0.05	3.23 ± 0.13	0.83	0.04
	HN^{13}C	1.09 ± 0.28	21.01 ± 0.41	3.35 ± 0.76	0.31	0.04
AGAL015.021−00.621	C^{18}O	12.54 ± 0.05	20.45 ± 0.01	4.43 ± 0.02	2.66	0.02
	HCO	0.29 ± 0.04	20.76 ± 0.27	4.10 ± 0.51	0.07	0.02
	H^{13}CO$^+$	2.20 ± 0.12	20.49 ± 0.16	6.00 ± 0.34	0.34	0.04
	c-C$_3$H$_2$	2.19 ± 0.10	20.65 ± 0.12	5.18 ± 0.24	0.40	0.04
	CN	2.44 ± 0.12	20.11 ± 0.12	4.29 ± 0.24	0.53	0.06
	HC^{15}N	0.82 ± 0.09	19.73 ± 0.16	3.26 ± 0.43	0.24	0.04
	HN^{13}C	0.47 ± 0.06	23.05 ± 0.08	1.25 ± 0.14	0.35	0.04
AGAL015.024−00.654	C^{18}O	15.95 ± 0.31	19.81 ± 0.05	5.46 ± 0.10	2.74	0.05
	HCO	0.77 ± 0.05	19.67 ± 0.24	7.14 ± 0.62	0.10	0.02
	H^{13}CO$^+$	3.33 ± 0.18	22.87 ± 0.06	2.53 ± 0.11	1.24	0.04
	c-C$_3$H$_2$	4.85 ± 0.12	20.04 ± 0.09	7.62 ± 0.21	0.60	0.03
	CN	2.71 ± 0.21	20.75 ± 0.27	6.87 ± 0.52	0.37	0.08
	HC^{15}N	1.99 ± 0.13	20.82 ± 0.23	7.21 ± 0.50	0.26	0.04
	HN^{13}C	1.01 ± 0.10	23.14 ± 0.08	2.11 ± 0.21	0.45	0.04
AGAL015.029−00.669	C^{18}O	26.09 ± 0.26	18.98 ± 0.02	3.58 ± 0.05	6.84	0.10
	HCO	1.04 ± 0.07	21.33 ± 0.20	5.59 ± 0.43	0.17	0.03
	H^{13}CO$^+$	23.59 ± 0.14	19.18 ± 0.01	3.36 ± 0.02	6.60	0.07
	c-C$_3$H$_2$	6.76 ± 0.42	20.85 ± 0.16	5.58 ± 0.19	1.14	0.06
	CN	4.93 ± 0.29	19.11 ± 0.08	3.05 ± 0.24	1.52	0.14
	HC^{15}N	4.79 ± 0.15	19.31 ± 0.05	3.81 ± 0.15	1.18	0.06
	HN^{13}C	5.26 ± 0.11	19.31 ± 0.03	3.03 ± 0.08	1.63	0.05
AGAL015.051−00.642	C^{18}O	4.44 ± 0.08	17.78 ± 0.02	2.00 ± 0.04	2.08	0.05
	HCO	0.31 ± 0.04	17.98 ± 0.13	2.35 ± 0.35	0.12	0.02
	H^{13}CO$^+$	1.00 ± 0.08	18.02 ± 0.06	1.62 ± 0.16	0.58	0.05
	c-C$_3$H$_2$	1.61 ± 0.09	17.82 ± 0.07	2.54 ± 0.15	0.60	0.04
	CN	1.13 ± 0.12	17.93 ± 0.13	2.30 ± 0.29	0.46	0.08
	HC^{15}N	0.32 ± 0.06	18.16 ± 0.12	1.19 ± 0.28	0.25	0.04
	HN^{13}C	0.63 ± 0.08	18.39 ± 0.11	1.77 ± 0.24	0.33	0.05
AGAL015.053+00.089	C^{18}O	5.79 ± 0.07	29.84 ± 0.01	1.78 ± 0.03	3.06	0.05
	H^{13}CO$^+$	0.99 ± 0.07	29.55 ± 0.05	1.74 ± 0.14	0.54	0.04
	c-C$_3$H$_2$	1.24 ± 0.05	29.67 ± 0.03	1.54 ± 0.08	0.76	0.03
	CN	0.61 ± 0.13	29.28 ± 0.20	1.85 ± 0.46	0.31	0.09
	HC^{15}N	0.29 ± 0.08	30.80 ± 0.40	2.85 ± 0.82	0.09	0.04
	HN^{13}C	0.68 ± 0.05	29.66 ± 0.06	1.36 ± 0.11	0.47	0.04
AGAL015.056−00.624	C^{18}O	5.87 ± 0.27	16.89 ± 0.08	3.67 ± 0.11	1.50	0.05
	HCO	0.54 ± 0.04	17.94 ± 0.14	3.90 ± 0.37	0.13	0.02
	H^{13}CO$^+$	2.08 ± 0.09	17.66 ± 0.07	2.96 ± 0.16	0.66	0.04
	c-C$_3$H$_2$	3.14 ± 0.09	17.64 ± 0.06	3.73 ± 0.12	0.79	0.04
	CN	2.47 ± 0.17	17.34 ± 0.14	3.99 ± 0.34	0.58	0.08
	HC^{15}N	0.58 ± 0.10	17.27 ± 0.20	2.59 ± 0.70	0.21	0.04
	HN^{13}C	1.90 ± 0.10	17.80 ± 0.09	3.14 ± 0.21	0.57	0.05
AGAL015.193−00.627	C^{18}O	6.42 ± 0.10	20.02 ± 0.02	2.63 ± 0.05	2.29	0.06
	HCO	0.52 ± 0.05	20.95 ± 0.21	4.61 ± 0.52	0.10	0.02
	H^{13}CO$^+$	2.37 ± 0.08	20.48 ± 0.04	2.63 ± 0.11	0.85	0.04

Table B.3: continued.

ATLASGAL Name	Line	Area (K km s^{-1})	v_{LRS} (km s^{-1})	Δv (km s^{-1})	T_{MB} (K)	rms (K)
	c-C$_3$H$_2$	2.53 ± 0.09	20.63 ± 0.08	4.29 ± 0.18	0.55	0.04
	CN	1.95 ± 0.17	20.52 ± 0.15	3.66 ± 0.37	0.50	0.08
	HC^{15}N	0.92 ± 0.09	20.92 ± 0.12	2.80 ± 0.35	0.31	0.04
	HN^{13}C	1.99 ± 0.08	20.83 ± 0.05	2.39 ± 0.11	0.78	0.04
AGAL015.216−00.426	C^{18}O	1.97 ± 0.06	21.96 ± 0.02	0.97 ± 0.04	1.91	0.06
	H^{13}CO$^+$	0.83 ± 0.05	22.00 ± 0.03	0.87 ± 0.10	0.90	0.04
	c-C$_3$H$_2$	0.33 ± 0.05	22.01 ± 0.09	0.78 ± 0.10	0.40	0.04
	CN	0.51 ± 0.07	21.89 ± 0.03	0.52 ± 0.38	0.93	0.09
	HN^{13}C	0.74 ± 0.05	22.15 ± 0.03	1.03 ± 0.11	0.67	0.04
AGAL015.434+00.192	C^{18}O	6.81 ± 0.08	48.14 ± 0.01	1.92 ± 0.03	3.34	0.05
	H^{13}CO$^+$	1.47 ± 0.06	48.20 ± 0.03	1.65 ± 0.08	0.83	0.04
	c-C$_3$H$_2$	1.14 ± 0.06	48.26 ± 0.03	1.34 ± 0.09	0.80	0.04
	HN^{13}C	0.62 ± 0.06	48.34 ± 0.07	1.52 ± 0.16	0.39	0.04
AGAL015.503−00.419	C^{18}O	6.90 ± 0.09	39.93 ± 0.02	2.57 ± 0.04	2.53	0.05
	H^{13}CO$^+$	0.94 ± 0.06	39.46 ± 0.05	1.67 ± 0.13	0.53	0.04
	c-C$_3$H$_2$	1.65 ± 0.06	39.42 ± 0.02	1.30 ± 0.05	1.19	0.04
	CN	0.53 ± 0.12	39.85 ± 0.24	1.90 ± 0.45	0.26	0.08
	HN^{13}C	1.13 ± 0.05	39.53 ± 0.03	1.33 ± 0.07	0.80	0.03
AGAL015.583−00.029	C^{18}O	5.66 ± 0.09	71.43 ± 0.01	1.92 ± 0.04	2.77	0.06
	H^{13}CO$^+$	0.58 ± 0.06	71.31 ± 0.12	2.10 ± 0.24	0.26	0.04
	c-C$_3$H$_2$	0.69 ± 0.06	71.40 ± 0.08	1.81 ± 0.19	0.36	0.04
	CN	0.37 ± 0.12	71.23 ± 0.19	1.22 ± 0.52	0.28	0.09
	HN^{13}C	0.37 ± 0.06	71.54 ± 0.12	1.53 ± 0.30	0.22	0.04
AGAL015.709−00.581	C^{18}O	5.09 ± 0.08	17.06 ± 0.01	1.37 ± 0.02	3.50	0.06
	H^{13}CO$^+$	0.91 ± 0.05	17.13 ± 0.03	1.16 ± 0.10	0.74	0.04
	c-C$_3$H$_2$	1.07 ± 0.05	17.12 ± 0.03	1.06 ± 0.05	0.94	0.04
	CN	0.51 ± 0.15	17.18 ± 0.26	1.88 ± 0.80	0.26	0.09
	HN^{13}C	0.49 ± 0.05	17.33 ± 0.04	1.01 ± 0.18	0.45	0.03
AGAL015.718−00.594	C^{18}O	4.31 ± 0.10	17.23 ± 0.03	2.72 ± 0.07	1.49	0.06
	H^{13}CO$^+$	1.62 ± 0.07	17.59 ± 0.04	2.04 ± 0.10	0.75	0.04
	c-C$_3$H$_2$	1.08 ± 0.05	17.69 ± 0.04	1.74 ± 0.09	0.59	0.03
	HN^{13}C	0.90 ± 0.06	17.83 ± 0.06	1.82 ± 0.15	0.47	0.04
AGAL015.791−00.412	C^{18}O	3.16 ± 0.07	45.90 ± 0.01	1.30 ± 0.04	2.29	0.06
	H^{13}CO$^+$	0.65 ± 0.06	45.74 ± 0.06	1.24 ± 0.11	0.50	0.04
	c-C$_3$H$_2$	0.94 ± 0.06	45.66 ± 0.04	1.23 ± 0.09	0.71	0.04
	HN^{13}C	0.71 ± 0.06	45.82 ± 0.04	1.13 ± 0.12	0.59	0.04
AGAL016.303−00.524	C^{18}O	6.33 ± 0.36	37.48 ± 0.04	1.76 ± 0.06	3.38	0.06
	HCO	0.30 ± 0.04	38.87 ± 0.19	3.42 ± 0.72	0.08	0.02
	H^{13}CO$^+$	0.68 ± 0.09	37.92 ± 0.17	2.62 ± 0.41	0.24	0.04
	c-C$_3$H$_2$	0.81 ± 0.08	38.21 ± 0.13	2.72 ± 0.31	0.28	0.04
	HN^{13}C	0.71 ± 0.08	38.31 ± 0.12	2.27 ± 0.30	0.29	0.04
AGAL016.336−00.586	C^{18}O	5.87 ± 0.11	41.29 ± 0.02	2.26 ± 0.05	2.44	0.05
	H^{13}CO$^+$	1.15 ± 0.07	41.25 ± 0.06	2.04 ± 0.15	0.53	0.04
	c-C$_3$H$_2$	1.65 ± 0.07	41.23 ± 0.04	2.02 ± 0.10	0.77	0.04
	CN	0.50 ± 0.12	41.68 ± 0.21	1.73 ± 0.50	0.27	0.09
	HN^{13}C	1.34 ± 0.08	41.31 ± 0.06	2.05 ± 0.15	0.61	0.05
AGAL016.404−00.181	C^{18}O	6.93 ± 0.09	44.40 ± 0.02	2.51 ± 0.04	2.59	0.05
	H^{13}CO$^+$	1.23 ± 0.09	44.45 ± 0.11	3.07 ± 0.28	0.38	0.04
	c-C$_3$H$_2$	0.54 ± 0.12	44.57 ± 0.30	3.17 ± 1.04	0.16	0.04
	HN^{13}C	0.66 ± 0.10	44.62 ± 0.20	3.00 ± 0.59	0.21	0.04
AGAL016.418−00.634	C^{18}O	4.92 ± 0.09	41.52 ± 0.02	2.33 ± 0.05	1.98	0.06
	H^{13}CO$^+$	0.44 ± 0.07	41.10 ± 0.17	2.05 ± 0.33	0.20	0.04
	c-C$_3$H$_2$	1.53 ± 0.08	41.01 ± 0.07	2.58 ± 0.15	0.56	0.04
	HN^{13}C	0.86 ± 0.08	41.06 ± 0.11	2.33 ± 0.24	0.35	0.04
AGAL016.432−00.667	C^{18}O	3.79 ± 0.09	41.54 ± 0.03	2.62 ± 0.07	1.36	0.05
	H^{13}CO$^+$	0.70 ± 0.06	41.94 ± 0.06	1.52 ± 0.15	0.43	0.04
	c-C$_3$H$_2$	1.00 ± 0.06	42.06 ± 0.05	1.92 ± 0.13	0.49	0.03
	CN	0.40 ± 0.12	42.02 ± 0.14	0.96 ± 0.43	0.39	0.10
	HN^{13}C	1.13 ± 0.05	42.08 ± 0.04	1.77 ± 0.10	0.60	0.03
AGAL016.442−00.384	C^{18}O	6.11 ± 0.09	47.56 ± 0.01	1.63 ± 0.03	3.51	0.06
	H^{13}CO$^+$	1.06 ± 0.06	47.63 ± 0.04	1.50 ± 0.10	0.67	0.04
	c-C$_3$H$_2$	1.08 ± 0.06	47.67 ± 0.04	1.42 ± 0.10	0.72	0.04
	CN	0.70 ± 0.14	47.80 ± 0.18	1.83 ± 0.46	0.36	0.09
	HN^{13}C	0.65 ± 0.06	47.71 ± 0.06	1.50 ± 0.17	0.41	0.04
AGAL016.474−00.641	C^{18}O	3.61 ± 0.10	41.07 ± 0.02	1.77 ± 0.06	1.92	0.06
	H^{13}CO$^+$	0.69 ± 0.08	41.25 ± 0.13	2.32 ± 0.33	0.28	0.04
	c-C$_3$H$_2$	0.93 ± 0.08	41.17 ± 0.08	2.20 ± 0.24	0.40	0.04
	HN^{13}C	0.74 ± 0.06	41.38 ± 0.06	1.45 ± 0.13	0.48	0.04
AGAL016.502−00.642	C^{18}O	4.00 ± 0.08	40.96 ± 0.01	1.50 ± 0.03	2.49	0.06
	H^{13}CO$^+$	0.30 ± 0.06	41.20 ± 0.17	1.65 ± 0.43	0.17	0.04
	c-C$_3$H$_2$	0.44 ± 0.06	41.32 ± 0.09	1.27 ± 0.20	0.32	0.04
	HN^{13}C	0.41 ± 0.07	41.17 ± 0.15	1.82 ± 0.37	0.21	0.04
AGAL016.586−00.051	C^{18}O	21.73 ± 0.07	59.05 ± 0.00	3.13 ± 0.01	6.52	0.04
	HCO	0.15 ± 0.02	59.44 ± 0.19	2.28 ± 0.41	0.06	0.01
	H^{13}CO$^+$	4.67 ± 0.08	59.13 ± 0.03	3.16 ± 0.06	1.39	0.04

Table B.3: continued.

ATLASGAL Name	Line	Area (K km s^{-1})	v_{LRS} (km s^{-1})	Δv (km s^{-1})	T_{MB} (K)	rms (K)
	c-C$_3$H$_2$	1.49 ± 0.07	58.67 ± 0.06	2.72 ± 0.16	0.51	0.03
	CN	1.53 ± 0.14	59.17 ± 0.15	3.34 ± 0.34	0.43	0.07
	HC^{15}N	1.07 ± 0.09	59.60 ± 0.17	4.08 ± 0.40	0.25	0.04
	HN^{13}C	2.30 ± 0.08	59.63 ± 0.06	3.43 ± 0.12	0.63	0.04
AGAL016.739−00.089	C^{18}O	6.55 ± 0.10	69.06 ± 0.02	2.54 ± 0.04	2.43	0.05
	H^{13}CO$^+$	0.65 ± 0.09	68.87 ± 0.15	2.31 ± 0.34	0.27	0.05
	c-C$_3$H$_2$	0.96 ± 0.07	68.78 ± 0.07	2.00 ± 0.17	0.45	0.04
	CN	0.42 ± 0.13	68.66 ± 0.30	1.88 ± 0.58	0.21	0.09
	HN^{13}C	0.56 ± 0.06	68.80 ± 0.12	2.16 ± 0.27	0.24	0.04
AGAL016.889+00.484	C^{18}O	4.19 ± 0.08	22.83 ± 0.01	1.22 ± 0.03	3.22	0.06
	H^{13}CO$^+$	0.84 ± 0.07	23.16 ± 0.05	1.43 ± 0.16	0.55	0.04
	c-C$_3$H$_2$	0.48 ± 0.06	26.93 ± 0.10	1.72 ± 0.26	0.26	0.03
	HN^{13}C	0.27 ± 0.06	23.15 ± 0.12	1.27 ± 0.37	0.20	0.04
AGAL016.916−00.084	C^{18}O	4.30 ± 0.08	40.87 ± 0.01	1.23 ± 0.03	3.28	0.06
	H^{13}CO$^+$	1.39 ± 0.05	40.79 ± 0.02	1.31 ± 0.06	1.00	0.04
	c-C$_3$H$_2$	2.20 ± 0.07	40.85 ± 0.01	1.24 ± 0.04	1.68	0.04
	CN	1.09 ± 0.13	40.60 ± 0.08	1.28 ± 0.16	0.80	0.11
	HN^{13}C	1.77 ± 0.06	40.93 ± 0.02	1.32 ± 0.05	1.26	0.04
AGAL016.924+00.284	C^{18}O	6.24 ± 0.06	24.18 ± 0.01	1.28 ± 0.01	4.56	0.04
	HCO	0.30 ± 0.03	24.62 ± 0.12	2.88 ± 0.37	0.10	0.01
	H^{13}CO$^+$	0.31 ± 0.05	24.66 ± 0.16	2.08 ± 0.35	0.14	0.03
	c-C$_3$H$_2$	0.84 ± 0.06	24.66 ± 0.10	3.07 ± 0.25	0.26	0.03
AGAL016.927+00.957	C^{18}O	17.63 ± 0.08	20.72 ± 0.01	2.81 ± 0.01	5.89	0.04
	HCO	0.13 ± 0.03	20.65 ± 0.20	2.02 ± 0.50	0.06	0.01
	H^{13}CO$^+$	5.75 ± 0.07	20.95 ± 0.02	2.76 ± 0.04	1.96	0.04
	c-C$_3$H$_2$	2.49 ± 0.08	21.16 ± 0.05	3.34 ± 0.13	0.70	0.04
	CN	1.46 ± 0.14	21.04 ± 0.13	2.83 ± 0.34	0.49	0.08
	HC^{15}N	0.65 ± 0.08	20.91 ± 0.14	2.37 ± 0.31	0.26	0.04
	HN^{13}C	2.58 ± 0.07	20.93 ± 0.03	2.43 ± 0.08	1.00	0.04
AGAL016.942−00.072	C^{18}O	2.34 ± 0.11	−4.48 ± 0.10	4.42 ± 0.26	0.50	0.05
	c-C$_3$H$_2$	0.59 ± 0.10	−3.65 ± 0.34	4.37 ± 0.91	0.13	0.03
AGAL016.951+00.779	C^{18}O	2.01 ± 0.03	24.85 ± 0.01	1.51 ± 0.02	1.25	0.02
	HCO	0.12 ± 0.02	25.04 ± 0.14	1.64 ± 0.34	0.07	0.01
	H^{13}CO$^+$	1.25 ± 0.04	24.92 ± 0.02	1.66 ± 0.06	0.71	0.02
	c-C$_3$H$_2$	0.81 ± 0.04	25.01 ± 0.04	1.69 ± 0.10	0.45	0.03
	CN	0.85 ± 0.06	24.80 ± 0.05	1.57 ± 0.12	0.51	0.04
	HC^{15}N	0.26 ± 0.04	24.89 ± 0.13	1.66 ± 0.34	0.15	0.03
	HN^{13}C	0.68 ± 0.04	25.06 ± 0.04	1.58 ± 0.10	0.40	0.02
AGAL016.974−00.222	C^{18}O	2.42 ± 0.36	40.94 ± 0.05	1.50 ± 0.10	1.51	0.06
	H^{13}CO$^+$	0.68 ± 0.09	40.83 ± 0.19	3.01 ± 0.57	0.21	0.04
	c-C$_3$H$_2$	0.75 ± 0.05	40.99 ± 0.06	1.67 ± 0.14	0.42	0.03
	HN^{13}C	0.74 ± 0.07	41.10 ± 0.07	1.67 ± 0.17	0.41	0.04
AGAL016.986−00.922	C^{18}O	3.24 ± 0.25	40.60 ± 0.08	2.67 ± 0.17	1.14	0.05
	H^{13}CO$^+$	1.33 ± 0.10	40.76 ± 0.15	3.81 ± 0.41	0.33	0.04
	c-C$_3$H$_2$	2.01 ± 0.08	40.50 ± 0.05	2.76 ± 0.15	0.68	0.04
	CN	0.83 ± 0.13	40.27 ± 0.20	2.53 ± 0.49	0.31	0.08
	HN^{13}C	1.45 ± 0.07	40.67 ± 0.06	2.51 ± 0.15	0.54	0.04
AGAL017.029+00.427	C^{18}O	6.33 ± 0.07	24.84 ± 0.01	1.82 ± 0.02	3.26	0.05
	HCO	0.29 ± 0.03	24.70 ± 0.11	2.30 ± 0.23	0.12	0.01
	H^{13}CO$^+$	1.02 ± 0.06	24.79 ± 0.05	1.67 ± 0.12	0.57	0.04
	c-C$_3$H$_2$	0.70 ± 0.07	25.01 ± 0.09	1.85 ± 0.21	0.36	0.04
	CN	0.28 ± 0.10	24.14 ± 0.26	1.19 ± 0.48	0.22	0.08
AGAL017.067+00.682	C^{18}O	5.43 ± 0.07	21.53 ± 0.01	1.39 ± 0.02	3.67	0.05
	HCO	0.28 ± 0.03	22.04 ± 0.17	2.88 ± 0.41	0.09	0.02
	H^{13}CO$^+$	0.54 ± 0.06	21.49 ± 0.07	1.31 ± 0.17	0.39	0.04
	c-C$_3$H$_2$	0.50 ± 0.06	21.64 ± 0.12	1.96 ± 0.27	0.24	0.03
	HN^{13}C	0.24 ± 0.06	21.66 ± 0.18	1.42 ± 0.45	0.16	0.04
AGAL017.454−00.194	C^{18}O	8.76 ± 0.10	52.78 ± 0.01	1.99 ± 0.03	4.13	0.07
	H^{13}CO$^+$	0.90 ± 0.07	52.78 ± 0.06	1.71 ± 0.16	0.50	0.04
	c-C$_3$H$_2$	0.71 ± 0.07	52.79 ± 0.07	1.68 ± 0.19	0.40	0.04
	HN^{13}C	0.55 ± 0.06	52.90 ± 0.08	1.51 ± 0.19	0.34	0.04
AGAL017.554+00.167	C^{18}O	3.87 ± 0.09	20.14 ± 0.03	2.35 ± 0.07	1.55	0.05
	H^{13}CO$^+$	0.30 ± 0.08	20.64 ± 0.24	1.97 ± 0.61	0.14	0.04
	c-C$_3$H$_2$	0.43 ± 0.07	20.43 ± 0.21	2.34 ± 0.48	0.17	0.04
AGAL017.637+00.154	C^{18}O	10.43 ± 0.10	22.26 ± 0.01	3.00 ± 0.03	3.26	0.05
	H^{13}CO$^+$	5.85 ± 0.08	22.20 ± 0.02	2.34 ± 0.04	2.35	0.04
	c-C$_3$H$_2$	1.38 ± 0.08	22.05 ± 0.08	2.71 ± 0.19	0.48	0.04
	CN	1.19 ± 0.15	22.21 ± 0.13	2.26 ± 0.36	0.50	0.09
	HC^{15}N	0.52 ± 0.07	22.27 ± 0.10	1.55 ± 0.26	0.31	0.04
	HN^{13}C	1.76 ± 0.08	22.22 ± 0.05	2.30 ± 0.12	0.72	0.04
AGAL017.652+00.172	C^{18}O	6.55 ± 0.10	23.17 ± 0.01	2.04 ± 0.04	3.02	0.06
	H^{13}CO$^+$	1.73 ± 0.07	22.84 ± 0.02	1.38 ± 0.06	1.18	0.04
	c-C$_3$H$_2$	0.68 ± 0.05	22.86 ± 0.04	1.12 ± 0.09	0.57	0.04
	HN^{13}C	0.64 ± 0.07	22.98 ± 0.07	1.38 ± 0.19	0.43	0.04
AGAL017.667+00.177	C^{18}O	4.63 ± 0.10	22.37 ± 0.02	1.69 ± 0.05	2.57	0.06

Table B.3: continued.

ATLASGAL Name	Line	Area (K km s^{-1})	v_{LRS} (km s^{-1})	Δv (km s^{-1})	T_{MB} (K)	rms (K)
	H^{13}CO$^+$	1.22 ± 0.06	22.24 ± 0.03	1.42 ± 0.10	0.81	0.04
	c-C$_3$H$_2$	0.90 ± 0.05	22.19 ± 0.04	1.24 ± 0.08	0.68	0.04
	CN	0.39 ± 0.12	22.47 ± 0.19	1.15 ± 0.41	0.32	0.10
	HC^{15}N	0.35 ± 0.08	22.39 ± 0.33	2.54 ± 0.64	0.13	0.05
	HN^{13}C	0.46 ± 0.07	22.40 ± 0.09	1.41 ± 0.28	0.30	0.04
AGAL017.914−00.489	C^{18}O	3.19 ± 0.11	39.89 ± 0.03	1.75 ± 0.08	1.71	0.07
	H^{13}CO$^+$	0.43 ± 0.07	39.65 ± 0.14	1.68 ± 0.26	0.24	0.04
	c-C$_3$H$_2$	0.46 ± 0.05	39.74 ± 0.07	1.26 ± 0.16	0.34	0.03
	HN^{13}C	0.39 ± 0.08	40.10 ± 0.12	1.45 ± 0.24	0.26	0.04
AGAL017.990−00.347	C^{18}O	4.99 ± 0.07	41.84 ± 0.01	1.52 ± 0.03	3.09	0.05
	H^{13}CO$^+$	1.59 ± 0.06	41.81 ± 0.03	1.57 ± 0.08	0.95	0.04
	c-C$_3$H$_2$	1.62 ± 0.05	41.87 ± 0.02	1.44 ± 0.06	1.06	0.04
	CN	0.92 ± 0.11	41.81 ± 0.08	1.42 ± 0.22	0.60	0.08
	HN^{13}C	1.23 ± 0.07	41.94 ± 0.04	1.49 ± 0.10	0.78	0.04
AGAL018.098−00.354	H^{13}CO$^+$	0.98 ± 0.09	45.52 ± 0.11	2.74 ± 0.33	0.34	0.04
	c-C$_3$H$_2$	0.51 ± 0.06	45.95 ± 0.20	3.11 ± 0.42	0.15	0.03
	HN^{13}C	0.41 ± 0.06	45.65 ± 0.12	1.81 ± 0.29	0.21	0.03
AGAL018.139+00.334	H^{13}CO$^+$	0.90 ± 0.04	22.79 ± 0.03	1.04 ± 0.05	0.81	0.03
	c-C$_3$H$_2$	0.89 ± 0.04	22.82 ± 0.03	0.86 ± 0.06	0.98	0.03
	HN^{13}C	0.50 ± 0.05	23.06 ± 0.06	1.24 ± 0.14	0.38	0.03
AGAL018.231+00.652	H^{13}CO$^+$	1.46 ± 0.05	38.02 ± 0.03	1.55 ± 0.07	0.89	0.03
	c-C$_3$H$_2$	1.67 ± 0.05	37.99 ± 0.02	1.42 ± 0.05	1.11	0.03
	HN^{13}C	1.10 ± 0.05	38.05 ± 0.03	1.45 ± 0.08	0.71	0.04
AGAL018.286−00.707	H^{13}CO$^+$	0.91 ± 0.06	44.64 ± 0.06	2.02 ± 0.14	0.42	0.03
	c-C$_3$H$_2$	1.00 ± 0.05	44.78 ± 0.05	1.91 ± 0.12	0.49	0.03
	HN^{13}C	0.84 ± 0.05	44.90 ± 0.05	1.65 ± 0.12	0.48	0.03
AGAL018.301−00.389	HCO	0.49 ± 0.04	33.49 ± 0.23	6.31 ± 0.54	0.07	0.01
	H^{13}CO$^+$	4.88 ± 0.07	32.81 ± 0.02	2.57 ± 0.04	1.78	0.03
	c-C$_3$H$_2$	1.75 ± 0.17	32.35 ± 0.23	6.91 ± 0.63	0.24	0.03
	HC^{15}N	0.62 ± 0.09	32.88 ± 0.21	3.38 ± 0.73	0.17	0.03
	HN^{13}C	2.37 ± 0.06	32.98 ± 0.03	2.20 ± 0.07	1.01	0.03
AGAL018.371−00.381	H^{13}CO$^+$	2.23 ± 0.06	44.51 ± 0.03	1.97 ± 0.06	1.06	0.03
	c-C$_3$H$_2$	1.13 ± 0.05	44.52 ± 0.05	2.21 ± 0.11	0.48	0.03
	HN^{13}C	1.11 ± 0.06	44.64 ± 0.04	1.75 ± 0.09	0.60	0.04
AGAL018.409−00.291	H^{13}CO$^+$	0.77 ± 0.05	68.34 ± 0.05	1.50 ± 0.12	0.48	0.03
	c-C$_3$H$_2$	1.08 ± 0.05	68.42 ± 0.04	1.62 ± 0.08	0.63	0.03
	HN^{13}C	0.74 ± 0.05	68.63 ± 0.05	1.40 ± 0.12	0.49	0.04
AGAL018.461−00.002	H^{13}CO$^+$	2.93 ± 0.08	51.75 ± 0.06	4.07 ± 0.14	0.68	0.03
	c-C$_3$H$_2$	1.58 ± 0.09	52.15 ± 0.15	5.20 ± 0.38	0.29	0.03
	HC^{15}N	0.85 ± 0.10	52.94 ± 0.39	6.33 ± 0.85	0.13	0.03
	HN^{13}C	1.99 ± 0.09	52.38 ± 0.09	4.29 ± 0.21	0.43	0.04
AGAL018.493−00.199	H^{13}CO$^+$	0.52 ± 0.05	46.50 ± 0.06	1.20 ± 0.13	0.40	0.04
	c-C$_3$H$_2$	0.74 ± 0.05	46.44 ± 0.04	1.27 ± 0.10	0.55	0.03
	HN^{13}C	0.60 ± 0.06	46.56 ± 0.08	1.65 ± 0.19	0.34	0.04
AGAL018.549+00.036	H^{13}CO$^+$	1.21 ± 0.07	36.10 ± 0.08	2.88 ± 0.22	0.40	0.03
	c-C$_3$H$_2$	0.57 ± 0.06	36.51 ± 0.14	2.52 ± 0.33	0.21	0.03
	HN^{13}C	0.57 ± 0.07	36.49 ± 0.14	2.59 ± 0.34	0.21	0.03
AGAL018.606−00.074	C^{18}O	4.96 ± 0.34	44.89 ± 0.06	1.87 ± 0.12	2.49	0.09
	H^{13}CO$^+$	4.35 ± 0.10	45.50 ± 0.03	2.57 ± 0.07	1.59	0.05
	c-C$_3$H$_2$	4.33 ± 0.10	45.54 ± 0.03	2.62 ± 0.07	1.55	0.05
	CN	2.55 ± 0.16	45.58 ± 0.07	2.12 ± 0.16	1.13	0.10
	HC^{15}N	0.81 ± 0.14	45.22 ± 0.52	5.83 ± 1.18	0.13	0.05
	HN^{13}C	4.39 ± 0.09	45.79 ± 0.02	2.53 ± 0.06	1.63	0.04
AGAL018.661+00.036	H^{13}CO$^+$	2.06 ± 0.08	81.10 ± 0.06	3.07 ± 0.15	0.63	0.04
	c-C$_3$H$_2$	1.00 ± 0.08	81.14 ± 0.16	3.86 ± 0.39	0.24	0.03
	HN^{13}C	1.33 ± 0.06	81.18 ± 0.06	2.61 ± 0.13	0.48	0.03
AGAL018.734−00.226	C^{18}O	7.74 ± 0.45	42.49 ± 0.16	5.58 ± 0.23	1.30	0.09
	H^{13}CO$^+$	5.27 ± 0.15	41.21 ± 0.07	5.32 ± 0.18	0.93	0.05
	c-C$_3$H$_2$	2.10 ± 0.13	41.57 ± 0.15	5.03 ± 0.34	0.39	0.05
	CN	1.81 ± 0.24	40.84 ± 0.31	4.69 ± 0.73	0.36	0.10
	HC^{15}N	1.05 ± 0.16	41.27 ± 0.58	7.43 ± 1.21	0.13	0.05
	HN^{13}C	4.42 ± 0.14	41.28 ± 0.08	5.50 ± 0.20	0.75	0.04
AGAL018.789−00.286	H^{13}CO$^+$	1.88 ± 0.07	65.21 ± 0.05	2.80 ± 0.12	0.63	0.03
	c-C$_3$H$_2$	1.67 ± 0.07	65.47 ± 0.05	2.71 ± 0.12	0.58	0.03
	HN^{13}C	1.87 ± 0.07	65.55 ± 0.05	2.89 ± 0.12	0.61	0.03
AGAL018.844−00.376	H^{13}CO$^+$	1.84 ± 0.08	61.74 ± 0.08	3.45 ± 0.16	0.50	0.04
	c-C$_3$H$_2$	1.35 ± 0.07	61.66 ± 0.08	3.08 ± 0.17	0.41	0.03
	HN^{13}C	0.90 ± 0.07	61.52 ± 0.12	3.06 ± 0.29	0.28	0.03
AGAL018.883−00.651	H^{13}CO$^+$	0.82 ± 0.06	64.08 ± 0.09	2.22 ± 0.17	0.35	0.04
	c-C$_3$H$_2$	0.58 ± 0.05	64.13 ± 0.09	1.84 ± 0.19	0.29	0.03
	HN^{13}C	0.39 ± 0.06	64.10 ± 0.11	1.50 ± 0.27	0.24	0.04
AGAL018.888−00.474	C^{18}O	26.13 ± 0.20	65.42 ± 0.02	4.60 ± 0.04	5.34	0.08
	HCO	0.45 ± 0.05	64.80 ± 0.26	4.42 ± 0.61	0.10	0.02
	H^{13}CO$^+$	9.14 ± 0.15	65.72 ± 0.04	4.64 ± 0.09	1.85	0.06
	c-C$_3$H$_2$	4.49 ± 0.15	65.75 ± 0.08	4.87 ± 0.21	0.87	0.05

Table B.3: continued.

ATLASGAL Name	Line	Area (K km s^{-1})	v_{LRS} (km s^{-1})	Δv (km s^{-1})	T_{MB} (K)	rms (K)
	CN	5.74 ± 0.27	65.98 ± 0.09	4.02 ± 0.25	1.34	0.12
	HC^{15}N	0.89 ± 0.12	65.96 ± 0.28	3.93 ± 0.53	0.21	0.05
	HN^{13}C	7.33 ± 0.12	66.12 ± 0.03	3.77 ± 0.07	1.82	0.05
AGAL018.991−00.057	H^{13}CO$^+$	0.99 ± 0.06	60.33 ± 0.04	1.65 ± 0.11	0.56	0.03
	c-C$_3$H$_2$	0.44 ± 0.05	60.44 ± 0.08	1.51 ± 0.21	0.28	0.03
	HN^{13}C	0.88 ± 0.05	60.48 ± 0.05	1.75 ± 0.13	0.47	0.03
AGAL019.076−00.287	HCO	0.37 ± 0.04	64.94 ± 0.27	5.41 ± 0.61	0.06	0.01
	H^{13}CO$^+$	3.98 ± 0.07	65.54 ± 0.03	3.28 ± 0.07	1.14	0.03
	c-C$_3$H$_2$	2.37 ± 0.07	65.73 ± 0.05	3.60 ± 0.13	0.62	0.03
	HC^{15}N	1.22 ± 0.09	65.21 ± 0.16	4.16 ± 0.33	0.28	0.04
	HN^{13}C	2.83 ± 0.07	65.79 ± 0.04	3.27 ± 0.10	0.81	0.03
AGAL019.248+00.267	H^{13}CO$^+$	1.58 ± 0.07	14.84 ± 0.09	3.71 ± 0.20	0.40	0.03
	c-C$_3$H$_2$	0.55 ± 0.08	15.96 ± 0.17	2.35 ± 0.45	0.22	0.03
	HN^{13}C	0.63 ± 0.08	15.28 ± 0.24	3.96 ± 0.61	0.15	0.03
AGAL019.472+00.171	HCO	0.34 ± 0.05	19.42 ± 0.52	7.82 ± 1.57	0.04	0.01
	H^{13}CO$^+$	5.80 ± 0.09	19.82 ± 0.05	6.61 ± 0.12	0.82	0.03
	c-C$_3$H$_2$	2.13 ± 0.09	19.74 ± 0.13	6.18 ± 0.28	0.32	0.03
	HN^{13}C	3.30 ± 0.09	19.70 ± 0.09	6.16 ± 0.19	0.50	0.03
AGAL019.486−00.199	H^{13}CO$^+$	0.86 ± 0.09	39.58 ± 0.16	3.23 ± 0.46	0.25	0.04
	c-C$_3$H$_2$	0.23 ± 0.07	39.33 ± 0.21	1.58 ± 0.46	0.14	0.03
	HN^{13}C	0.93 ± 0.09	38.19 ± 0.24	4.73 ± 0.53	0.18	0.03
AGAL019.589−00.079	H^{13}CO$^+$	1.17 ± 0.10	61.44 ± 0.21	4.84 ± 0.40	0.23	0.04
	c-C$_3$H$_2$	1.21 ± 0.09	61.17 ± 0.19	5.18 ± 0.43	0.22	0.03
	HN^{13}C	0.46 ± 0.07	60.25 ± 0.24	2.80 ± 0.47	0.15	0.03
AGAL019.732−00.651	H^{13}CO$^+$	0.90 ± 0.05	23.58 ± 0.03	1.19 ± 0.07	0.71	0.04
	c-C$_3$H$_2$	0.91 ± 0.05	23.58 ± 0.03	1.32 ± 0.10	0.65	0.03
	HN^{13}C	0.39 ± 0.04	23.54 ± 0.06	1.11 ± 0.14	0.33	0.03
AGAL020.892−00.179	C^{18}O	7.83 ± 0.63	60.51 ± 0.23	5.83 ± 0.24	1.26	0.06
	H^{13}CO$^+$	1.79 ± 0.19	58.58 ± 0.28	5.81 ± 0.86	0.29	0.06
	c-C$_3$H$_2$	1.39 ± 0.12	58.91 ± 0.15	3.80 ± 0.39	0.34	0.05
	HN^{13}C	1.02 ± 0.11	58.40 ± 0.16	2.95 ± 0.36	0.33	0.05
AGAL021.561−00.032	C^{18}O	5.50 ± 0.13	113.80 ± 0.03	2.44 ± 0.07	2.12	0.07
	H^{13}CO$^+$	1.42 ± 0.12	113.50 ± 0.13	3.06 ± 0.29	0.44	0.06
	c-C$_3$H$_2$	0.82 ± 0.10	113.30 ± 0.12	2.14 ± 0.29	0.36	0.05
	HN^{13}C	0.91 ± 0.11	113.90 ± 0.20	3.09 ± 0.48	0.28	0.05
AGAL022.038+00.222	C^{18}O	11.54 ± 0.08	51.26 ± 0.01	2.31 ± 0.02	4.70	0.05
	H^{13}CO$^+$	3.27 ± 0.10	51.14 ± 0.04	2.51 ± 0.10	1.22	0.05
	c-C$_3$H$_2$	1.24 ± 0.08	51.47 ± 0.07	2.15 ± 0.16	0.54	0.05
	CN	1.05 ± 0.13	51.25 ± 0.15	2.51 ± 0.35	0.39	0.07
	HN^{13}C	1.31 ± 0.09	51.29 ± 0.06	1.85 ± 0.15	0.66	0.05
AGAL022.332−00.154	C^{18}O	3.29 ± 0.13	30.20 ± 0.07	3.56 ± 0.16	0.87	0.07
	H^{13}CO$^+$	0.95 ± 0.12	30.41 ± 0.18	3.00 ± 0.47	0.30	0.05
	c-C$_3$H$_2$	0.59 ± 0.13	30.49 ± 0.34	3.31 ± 1.00	0.17	0.05
	HN^{13}C	0.53 ± 0.14	31.28 ± 0.54	4.03 ± 1.44	0.12	0.05
AGAL022.376+00.447	C^{18}O	8.26 ± 0.15	53.47 ± 0.02	2.28 ± 0.05	3.41	0.09
	H^{13}CO$^+$	2.88 ± 0.11	52.93 ± 0.05	2.88 ± 0.12	0.94	0.05
	c-C$_3$H$_2$	2.90 ± 0.11	52.85 ± 0.06	3.11 ± 0.14	0.88	0.05
	HN^{13}C	1.34 ± 0.09	52.86 ± 0.08	2.42 ± 0.17	0.52	0.05
AGAL022.412+00.317	C^{18}O	14.51 ± 0.09	84.22 ± 0.01	2.06 ± 0.02	6.62	0.06
	H^{13}CO$^+$	1.80 ± 0.07	84.08 ± 0.04	2.14 ± 0.09	0.79	0.04
	c-C$_3$H$_2$	1.64 ± 0.07	84.04 ± 0.05	2.22 ± 0.11	0.70	0.04
	CN	0.63 ± 0.12	84.35 ± 0.20	1.93 ± 0.46	0.30	0.08
	HN^{13}C	1.39 ± 0.07	84.07 ± 0.06	2.08 ± 0.12	0.63	0.04
AGAL022.484−00.936	C^{18}O	4.33 ± 0.10	63.99 ± 0.02	1.50 ± 0.04	2.72	0.07
	H^{13}CO$^+$	1.14 ± 0.11	64.18 ± 0.11	2.41 ± 0.29	0.45	0.06
	c-C$_3$H$_2$	0.48 ± 0.08	64.17 ± 0.14	1.67 ± 0.30	0.27	0.05
	HN^{13}C	0.74 ± 0.11	64.28 ± 0.14	1.96 ± 0.38	0.35	0.06
AGAL022.531−00.192	C^{18}O	7.26 ± 0.30	76.64 ± 0.05	2.62 ± 0.09	2.60	0.07
	H^{13}CO$^+$	1.48 ± 0.10	76.44 ± 0.10	2.99 ± 0.24	0.47	0.05
	c-C$_3$H$_2$	1.87 ± 0.10	76.37 ± 0.07	2.75 ± 0.17	0.64	0.04
	CN	0.83 ± 0.15	76.30 ± 0.30	3.27 ± 0.68	0.24	0.08
	HN^{13}C	1.38 ± 0.09	76.30 ± 0.10	3.02 ± 0.21	0.43	0.04
AGAL023.007−00.409	C^{18}O	7.73 ± 0.40	77.70 ± 0.04	2.94 ± 0.08	2.47	0.06
	HCO	0.22 ± 0.04	78.21 ± 0.24	2.73 ± 0.68	0.08	0.02
	H^{13}CO$^+$	5.20 ± 0.17	77.44 ± 0.08	5.09 ± 0.22	0.96	0.06
	c-C$_3$H$_2$	1.71 ± 0.13	77.40 ± 0.18	4.71 ± 0.42	0.34	0.05
	CN	2.26 ± 0.20	77.23 ± 0.20	4.41 ± 0.52	0.48	0.08
	HN^{13}C	4.09 ± 0.13	77.55 ± 0.05	3.49 ± 0.14	1.10	0.05
AGAL023.206−00.377	C^{18}O	12.87 ± 0.19	77.44 ± 0.02	3.34 ± 0.06	3.62	0.09
	HCO	0.23 ± 0.04	77.70 ± 0.39	3.81 ± 0.69	0.06	0.02
	H^{13}CO$^+$	3.76 ± 0.12	77.25 ± 0.07	4.17 ± 0.16	0.85	0.05
	c-C$_3$H$_2$	2.34 ± 0.10	77.61 ± 0.06	2.81 ± 0.13	0.78	0.05
	CN	1.40 ± 0.18	77.77 ± 0.15	2.55 ± 0.40	0.52	0.10
	HC^{15}N	2.11 ± 0.19	77.85 ± 0.33	8.09 ± 0.94	0.24	0.05

Table B.3: continued.

ATLASGAL Name	Line	Area (K km s^{-1})	v_{LRS} (km s^{-1})	Δv (km s^{-1})	T_{MB} (K)	rms (K)
	HN^{13}C	3.50 ± 0.11	77.78 ± 0.05	3.32 ± 0.12	0.99	0.05
AGAL023.277−00.214	C^{18}O	12.58 ± 0.10	78.72 ± 0.01	3.49 ± 0.03	3.38	0.05
	H^{13}CO$^+$	2.00 ± 0.11	78.72 ± 0.10	3.78 ± 0.23	0.50	0.04
	c-C$_3$H$_2$	1.81 ± 0.07	78.79 ± 0.07	3.18 ± 0.14	0.54	0.03
	CN	0.69 ± 0.11	78.76 ± 0.19	2.20 ± 0.39	0.29	0.07
	HN^{13}C	1.93 ± 0.10	78.67 ± 0.08	3.48 ± 0.20	0.52	0.04
AGAL023.387+00.187	C^{18}O	7.97 ± 0.41	75.14 ± 0.02	1.86 ± 0.06	4.02	0.07
	H^{13}CO$^+$	3.64 ± 0.10	75.49 ± 0.03	2.36 ± 0.08	1.45	0.05
	c-C$_3$H$_2$	2.44 ± 0.09	75.47 ± 0.04	2.09 ± 0.10	1.09	0.05
	CN	0.54 ± 0.11	75.50 ± 0.13	1.33 ± 0.34	0.38	0.09
	HN^{13}C	1.43 ± 0.10	75.77 ± 0.07	2.17 ± 0.19	0.62	0.05
AGAL023.437−00.182	C^{18}O	29.77 ± 0.22	100.70 ± 0.01	3.45 ± 0.03	8.10	0.10
	HCO	0.45 ± 0.06	101.10 ± 0.20	3.32 ± 0.62	0.13	0.02
	H^{13}CO$^+$	7.31 ± 0.16	101.20 ± 0.05	4.94 ± 0.13	1.39	0.06
	c-C$_3$H$_2$	2.36 ± 0.13	101.40 ± 0.09	3.88 ± 0.28	0.57	0.05
	CN	2.51 ± 0.24	100.90 ± 0.22	4.55 ± 0.48	0.52	0.11
	HC^{15}N	1.31 ± 0.14	101.20 ± 0.27	5.14 ± 0.72	0.24	0.05
	HN^{13}C	4.18 ± 0.14	101.20 ± 0.07	4.43 ± 0.18	0.89	0.05
AGAL023.656−00.127	C^{18}O	3.87 ± 0.09	80.40 ± 0.02	1.50 ± 0.04	2.42	0.07
	H^{13}CO$^+$	0.54 ± 0.08	80.61 ± 0.11	1.52 ± 0.29	0.33	0.05
	c-C$_3$H$_2$	0.28 ± 0.06	80.98 ± 0.14	1.15 ± 0.23	0.23	0.05
AGAL023.817+00.386	C^{18}O	3.40 ± 0.13	76.12 ± 0.06	3.02 ± 0.13	1.05	0.07
	H^{13}CO$^+$	1.17 ± 0.11	76.74 ± 0.11	2.24 ± 0.24	0.49	0.06
	c-C$_3$H$_2$	0.69 ± 0.10	75.97 ± 0.28	3.51 ± 0.54	0.18	0.05
	CN	0.78 ± 0.19	76.08 ± 0.58	4.68 ± 1.26	0.16	0.08
	HN^{13}C	0.94 ± 0.16	76.08 ± 0.45	5.64 ± 1.22	0.16	0.05
AGAL023.964−00.109	C^{18}O	10.97 ± 0.15	72.39 ± 0.03	3.78 ± 0.06	2.73	0.07
	H^{13}CO$^+$	2.97 ± 0.15	72.59 ± 0.12	5.04 ± 0.33	0.55	0.05
	c-C$_3$H$_2$	1.34 ± 0.14	72.73 ± 0.26	4.95 ± 0.60	0.26	0.05
	CN	1.16 ± 0.17	73.19 ± 0.17	2.57 ± 0.52	0.42	0.09
	HN^{13}C	2.39 ± 0.12	73.15 ± 0.10	4.14 ± 0.23	0.54	0.05
AGAL024.010+00.489	C^{18}O	3.68 ± 0.08	94.64 ± 0.02	1.84 ± 0.05	1.88	0.05
	H^{13}CO$^+$	0.75 ± 0.07	94.34 ± 0.10	2.15 ± 0.20	0.33	0.04
	c-C$_3$H$_2$	1.03 ± 0.07	94.37 ± 0.07	2.23 ± 0.15	0.43	0.04
	CN	0.47 ± 0.11	93.97 ± 0.26	2.11 ± 0.58	0.21	0.07
	HN^{13}C	1.26 ± 0.08	94.70 ± 0.08	2.44 ± 0.16	0.48	0.04
AGAL024.141+00.127	C^{18}O	2.05 ± 0.08	51.92 ± 0.02	1.21 ± 0.06	1.59	0.07
	H^{13}CO$^+$	0.62 ± 0.06	51.95 ± 0.06	1.24 ± 0.13	0.47	0.04
	c-C$_3$H$_2$	0.45 ± 0.06	51.85 ± 0.07	1.18 ± 0.20	0.36	0.04
	CN	1.01 ± 0.33	55.88 ± 0.62	4.28 ± 1.49	0.22	0.09
	HN^{13}C	0.64 ± 0.06	114.40 ± 0.05	1.25 ± 0.13	0.48	0.04
AGAL024.416+00.101	C^{18}O	9.23 ± 0.18	113.30 ± 0.03	3.35 ± 0.08	2.59	0.06
	H^{13}CO$^+$	1.91 ± 0.11	113.10 ± 0.12	4.03 ± 0.27	0.45	0.04
	c-C$_3$H$_2$	1.30 ± 0.10	113.10 ± 0.10	3.08 ± 0.30	0.40	0.04
	CN	1.34 ± 0.17	112.90 ± 0.31	4.93 ± 0.75	0.26	0.07
	HN^{13}C	1.58 ± 0.09	113.60 ± 0.08	2.78 ± 0.19	0.53	0.05
AGAL024.629+00.172	C^{18}O	9.07 ± 0.13	115.30 ± 0.02	2.47 ± 0.04	3.45	0.08
	HCO	0.21 ± 0.02	111.70 ± 0.07	0.90 ± 0.11	0.22	0.02
	H^{13}CO$^+$	2.07 ± 0.11	115.00 ± 0.07	2.73 ± 0.17	0.71	0.05
	c-C$_3$H$_2$	1.01 ± 0.09	115.30 ± 0.08	1.92 ± 0.19	0.49	0.05
	CN	0.97 ± 0.16	115.40 ± 0.15	1.86 ± 0.39	0.49	0.11
	HN^{13}C	1.61 ± 0.08	115.30 ± 0.05	2.03 ± 0.13	0.74	0.05
AGAL024.633−00.324	C^{18}O	7.24 ± 0.11	42.61 ± 0.01	2.14 ± 0.04	3.18	0.06
	H^{13}CO$^+$	2.59 ± 0.08	42.69 ± 0.03	1.84 ± 0.07	1.32	0.05
	c-C$_3$H$_2$	1.53 ± 0.08	42.77 ± 0.04	1.50 ± 0.09	0.95	0.05
	CN	0.59 ± 0.14	42.78 ± 0.17	1.72 ± 0.58	0.33	0.08
	HN^{13}C	1.09 ± 0.10	42.74 ± 0.09	2.07 ± 0.24	0.50	0.05
AGAL024.651−00.169	C^{18}O	16.70 ± 0.14	112.10 ± 0.02	3.82 ± 0.03	4.10	0.07
	H^{13}CO$^+$	1.11 ± 0.08	112.80 ± 0.07	2.13 ± 0.20	0.49	0.04
	c-C$_3$H$_2$	0.87 ± 0.08	112.80 ± 0.12	2.83 ± 0.34	0.29	0.04
	CN	1.08 ± 0.14	112.70 ± 0.17	2.65 ± 0.38	0.38	0.08
	HN^{13}C	0.83 ± 0.07	113.00 ± 0.07	1.79 ± 0.17	0.43	0.04
AGAL024.673−00.151	C^{18}O	28.56 ± 0.13	112.70 ± 0.01	3.08 ± 0.02	8.71	0.07
	HCO	0.45 ± 0.06	112.90 ± 0.25	3.94 ± 0.70	0.11	0.02
	H^{13}CO$^+$	4.35 ± 0.12	113.00 ± 0.04	3.28 ± 0.10	1.25	0.05
	c-C$_3$H$_2$	2.75 ± 0.12	112.80 ± 0.08	3.92 ± 0.20	0.66	0.05
	CN	5.25 ± 0.21	58.49 ± 0.09	4.57 ± 0.22	1.08	0.09
	HC^{15}N	0.73 ± 0.14	112.70 ± 0.42	4.48 ± 1.08	0.15	0.05
	HN^{13}C	3.60 ± 0.11	113.20 ± 0.04	2.97 ± 0.10	1.14	0.05
AGAL024.728+00.152	C^{18}O	10.27 ± 0.10	109.00 ± 0.01	2.69 ± 0.03	3.58	0.05
	H^{13}CO$^+$	1.62 ± 0.11	109.30 ± 0.09	2.74 ± 0.20	0.56	0.05
	c-C$_3$H$_2$	0.68 ± 0.10	109.00 ± 0.19	2.37 ± 0.42	0.27	0.05
	CN	0.78 ± 0.15	108.60 ± 0.24	2.51 ± 0.54	0.29	0.09
	HN^{13}C	1.15 ± 0.12	109.30 ± 0.17	3.14 ± 0.36	0.34	0.06
AGAL024.789+00.082	C^{18}O	29.11 ± 0.15	110.00 ± 0.01	4.35 ± 0.03	6.29	0.07

Table B.3: continued.

ATLASGAL Name	Line	Area (K km s^{-1})	v_{LRS} (km s^{-1})	Δv (km s^{-1})	T_{MB} (K)	rms (K)
	HCO	0.27 ± 0.05	109.30 ± 0.38	3.82 ± 1.10	0.07	0.02
	H^{13}CO$^+$	7.51 ± 0.11	110.40 ± 0.03	4.26 ± 0.07	1.66	0.04
	c-C$_3$H$_2$	2.32 ± 0.10	109.90 ± 0.08	4.21 ± 0.20	0.52	0.04
	CN	4.74 ± 0.19	56.33 ± 0.08	4.15 ± 0.20	1.07	0.08
	HC^{15}N	3.07 ± 0.13	110.70 ± 0.11	5.63 ± 0.28	0.51	0.04
	HN^{13}C	6.11 ± 0.10	110.40 ± 0.03	4.20 ± 0.08	1.37	0.04
AGAL024.796+00.101	C^{18}O	14.61 ± 0.67	110.60 ± 0.08	3.95 ± 0.12	3.48	0.06
	HCO	0.56 ± 0.05	110.40 ± 0.26	5.70 ± 0.56	0.09	0.02
	H^{13}CO$^+$	2.15 ± 0.13	110.20 ± 0.14	5.09 ± 0.38	0.40	0.04
	c-C$_3$H$_2$	2.42 ± 0.12	110.30 ± 0.18	7.20 ± 0.41	0.32	0.04
	CN	3.56 ± 0.19	56.63 ± 0.09	3.75 ± 0.24	0.89	0.09
	HC^{15}N	0.34 ± 0.07	109.60 ± 0.27	2.36 ± 0.55	0.13	0.04
	HN^{13}C	1.48 ± 0.10	110.20 ± 0.13	4.06 ± 0.36	0.34	0.04
AGAL025.409+00.106	C^{18}O	7.14 ± 0.10	95.51 ± 0.02	2.35 ± 0.04	2.86	0.06
	H^{13}CO$^+$	2.63 ± 0.13	95.47 ± 0.07	2.95 ± 0.18	0.84	0.06
	c-C$_3$H$_2$	1.93 ± 0.09	95.48 ± 0.04	2.05 ± 0.11	0.89	0.05
	CN	1.04 ± 0.13	95.28 ± 0.11	1.92 ± 0.35	0.51	0.08
	HN^{13}C	1.53 ± 0.09	95.49 ± 0.07	2.33 ± 0.18	0.62	0.05
AGAL025.649+01.051	C^{18}O	7.09 ± 0.32	42.88 ± 0.02	2.66 ± 0.07	2.51	0.05
	H^{13}CO$^+$	7.53 ± 0.14	42.69 ± 0.04	3.92 ± 0.09	1.80	0.06
	c-C$_3$H$_2$	2.03 ± 0.11	42.89 ± 0.09	3.38 ± 0.21	0.56	0.05
	CN	1.43 ± 0.20	42.50 ± 0.21	3.63 ± 0.71	0.37	0.08
	HC^{15}N	1.39 ± 0.16	42.55 ± 0.21	4.26 ± 0.72	0.31	0.05
	HN^{13}C	2.89 ± 0.11	42.96 ± 0.06	3.21 ± 0.14	0.84	0.05
AGAL026.159+00.156	C^{18}O	8.85 ± 0.10	111.60 ± 0.01	2.38 ± 0.03	3.50	0.06
	HCO	0.16 ± 0.04	111.90 ± 0.33	3.00 ± 0.74	0.05	0.02
	H^{13}CO$^+$	1.12 ± 0.07	111.50 ± 0.06	2.02 ± 0.14	0.52	0.04
	c-C$_3$H$_2$	1.07 ± 0.07	111.60 ± 0.07	2.33 ± 0.19	0.43	0.04
	CN	0.77 ± 0.15	112.20 ± 0.35	3.25 ± 0.76	0.22	0.08
	HN^{13}C	0.82 ± 0.06	111.60 ± 0.07	1.73 ± 0.16	0.45	0.04
AGAL026.509+00.282	C^{18}O	10.82 ± 0.60	100.80 ± 0.06	2.56 ± 0.08	3.97	0.05
	H^{13}CO$^+$	5.41 ± 0.09	102.00 ± 0.04	4.30 ± 0.08	1.18	0.04
	c-C$_3$H$_2$	1.61 ± 0.10	101.60 ± 0.13	4.69 ± 0.34	0.32	0.03
	CN	2.15 ± 0.16	101.30 ± 0.12	3.47 ± 0.34	0.58	0.07
	HC^{15}N	2.05 ± 0.14	101.70 ± 0.19	5.98 ± 0.56	0.32	0.04
	HN^{13}C	4.34 ± 0.09	102.20 ± 0.04	4.08 ± 0.10	1.00	0.04
AGAL026.652+00.007	C^{18}O	7.51 ± 0.07	112.20 ± 0.01	2.53 ± 0.03	2.79	0.04
	H^{13}CO$^+$	0.49 ± 0.07	112.90 ± 0.19	2.55 ± 0.41	0.18	0.04
	c-C$_3$H$_2$	0.39 ± 0.06	112.50 ± 0.14	1.93 ± 0.31	0.19	0.03
	CN	0.33 ± 0.09	112.70 ± 0.28	1.99 ± 0.64	0.16	0.06
	HN^{13}C	0.25 ± 0.05	112.90 ± 0.13	1.14 ± 0.24	0.20	0.04
AGAL026.849+00.181	C^{18}O	7.18 ± 0.09	93.87 ± 0.01	2.06 ± 0.03	3.27	0.05
	H^{13}CO$^+$	0.71 ± 0.06	93.84 ± 0.07	1.79 ± 0.17	0.37	0.04
	c-C$_3$H$_2$	0.84 ± 0.06	93.84 ± 0.07	1.91 ± 0.16	0.41	0.04
	CN	0.29 ± 0.09	93.65 ± 0.05	0.52 ± 4.98	0.53	0.08
	HN^{13}C	0.75 ± 0.06	93.92 ± 0.06	1.55 ± 0.14	0.45	0.04
AGAL027.000−00.296	C^{18}O	7.61 ± 0.07	68.11 ± 0.01	1.54 ± 0.02	4.63	0.05
	H^{13}CO$^+$	0.84 ± 0.07	67.85 ± 0.08	1.99 ± 0.19	0.40	0.04
	c-C$_3$H$_2$	0.37 ± 0.04	67.95 ± 0.08	1.24 ± 0.15	0.28	0.03
	CN	0.40 ± 0.10	67.80 ± 0.24	1.62 ± 0.50	0.23	0.07
	HN^{13}C	0.46 ± 0.06	68.08 ± 0.10	1.56 ± 0.21	0.28	0.04
AGAL027.184−00.081	C^{18}O	5.00 ± 0.10	25.93 ± 0.03	3.47 ± 0.09	1.35	0.05
	HCO	0.23 ± 0.03	26.74 ± 0.21	2.87 ± 0.41	0.07	0.02
	H^{13}CO$^+$	1.53 ± 0.09	25.72 ± 0.10	3.55 ± 0.26	0.41	0.04
	c-C$_3$H$_2$	1.12 ± 0.08	25.99 ± 0.13	3.46 ± 0.31	0.30	0.04
	CN	0.65 ± 0.17	25.40 ± 0.49	3.65 ± 1.23	0.17	0.07
	HC^{15}N	0.45 ± 0.10	24.45 ± 0.63	5.46 ± 1.13	0.08	0.04
	HN^{13}C	0.46 ± 0.10	25.85 ± 0.48	4.71 ± 1.30	0.09	0.04
AGAL027.314+00.177	C^{18}O	5.06 ± 0.09	34.17 ± 0.02	2.80 ± 0.06	1.70	0.05
	H^{13}CO$^+$	1.39 ± 0.08	34.00 ± 0.10	3.54 ± 0.23	0.37	0.03
	c-C$_3$H$_2$	1.26 ± 0.08	34.04 ± 0.11	3.72 ± 0.30	0.32	0.03
	CN	0.93 ± 0.14	34.11 ± 0.21	2.72 ± 0.50	0.32	0.08
	HN^{13}C	1.36 ± 0.08	34.00 ± 0.09	3.28 ± 0.23	0.39	0.03
AGAL027.366−00.166	C^{18}O	20.70 ± 0.09	91.46 ± 0.01	4.45 ± 0.02	4.37	0.05
	HCO	0.15 ± 0.03	91.68 ± 0.34	2.96 ± 0.68	0.05	0.02
	H^{13}CO$^+$	9.16 ± 0.09	91.46 ± 0.02	4.23 ± 0.05	2.04	0.04
	c-C$_3$H$_2$	3.28 ± 0.09	91.14 ± 0.06	4.08 ± 0.13	0.76	0.04
	CN	2.57 ± 0.15	91.24 ± 0.11	3.67 ± 0.27	0.66	0.07
	HC^{15}N	1.46 ± 0.12	92.18 ± 0.20	5.26 ± 0.55	0.26	0.04
	HN^{13}C	4.41 ± 0.09	91.44 ± 0.04	3.83 ± 0.09	1.08	0.04
AGAL027.464+00.119	C^{18}O	7.69 ± 0.09	99.85 ± 0.02	4.08 ± 0.05	1.77	0.04
	H^{13}CO$^+$	1.24 ± 0.08	100.40 ± 0.10	3.06 ± 0.22	0.38	0.04
	c-C$_3$H$_2$	2.13 ± 0.07	100.30 ± 0.05	3.20 ± 0.10	0.63	0.03
	CN	0.90 ± 0.12	99.90 ± 0.24	3.41 ± 0.51	0.25	0.06
	HN^{13}C	1.62 ± 0.07	100.50 ± 0.07	2.94 ± 0.14	0.52	0.04

Table B.3: continued.

ATLASGAL Name	Line	Area (K km s^{-1})	v_{LRS} (km s^{-1})	Δv (km s^{-1})	T_{MB} (K)	rms (K)
AGAL027.551−00.936	C^{18}O	6.96 ± 0.07	85.87 ± 0.01	1.63 ± 0.02	4.01	0.05
	H^{13}CO$^+$	0.84 ± 0.06	85.77 ± 0.07	1.97 ± 0.18	0.40	0.04
	c-C$_3$H$_2$	0.86 ± 0.06	85.78 ± 0.05	1.71 ± 0.14	0.47	0.03
	HN^{13}C	0.50 ± 0.07	86.03 ± 0.13	1.88 ± 0.30	0.25	0.04
AGAL027.758+00.051	C^{18}O	9.47 ± 0.09	99.72 ± 0.02	3.23 ± 0.04	2.76	0.05
	H^{13}CO$^+$	1.35 ± 0.08	99.40 ± 0.11	3.78 ± 0.26	0.34	0.03
	c-C$_3$H$_2$	1.32 ± 0.07	99.38 ± 0.07	2.63 ± 0.17	0.47	0.03
	CN	1.22 ± 0.14	99.43 ± 0.17	3.01 ± 0.45	0.38	0.07
	HN^{13}C	1.26 ± 0.08	99.68 ± 0.07	2.45 ± 0.17	0.48	0.04
AGAL027.796−00.277	C^{18}O	9.71 ± 0.08	45.81 ± 0.01	1.93 ± 0.02	4.73	0.05
	H^{13}CO$^+$	2.15 ± 0.07	45.88 ± 0.03	1.97 ± 0.07	1.03	0.04
	c-C$_3$H$_2$	0.89 ± 0.06	45.69 ± 0.06	1.77 ± 0.15	0.47	0.03
	CN	0.71 ± 0.10	46.00 ± 0.12	1.61 ± 0.23	0.41	0.08
	HN^{13}C	1.42 ± 0.06	45.94 ± 0.05	2.22 ± 0.12	0.60	0.03
AGAL027.974−00.421	C^{18}O	4.00 ± 0.24	44.79 ± 0.07	2.26 ± 0.13	1.66	0.04
	H^{13}CO$^+$	1.23 ± 0.06	44.18 ± 0.04	1.85 ± 0.12	0.63	0.04
	c-C$_3$H$_2$	0.98 ± 0.06	44.29 ± 0.04	1.49 ± 0.11	0.62	0.04
	CN	0.33 ± 0.06	44.11 ± 0.09	1.04 ± 0.19	0.30	0.05
	HN^{13}C	1.20 ± 0.07	44.41 ± 0.06	2.04 ± 0.15	0.55	0.04
AGAL028.194−00.074	C^{18}O	14.16 ± 0.09	97.71 ± 0.01	3.84 ± 0.03	3.47	0.04
	H^{13}CO$^+$	1.48 ± 0.08	97.96 ± 0.07	2.65 ± 0.15	0.52	0.04
	c-C$_3$H$_2$	0.94 ± 0.06	97.99 ± 0.06	2.00 ± 0.15	0.44	0.03
	CN	0.41 ± 0.07	98.12 ± 0.11	1.19 ± 0.24	0.33	0.06
	HN^{13}C	0.70 ± 0.06	98.44 ± 0.08	1.95 ± 0.20	0.34	0.04
AGAL028.199−00.049	C^{18}O	20.69 ± 0.28	96.20 ± 0.02	7.73 ± 0.12	2.51	0.03
	HCO	0.19 ± 0.04	97.16 ± 0.41	3.71 ± 1.10	0.05	0.02
	H^{13}CO$^+$	7.04 ± 0.12	95.68 ± 0.04	5.07 ± 0.11	1.30	0.04
	c-C$_3$H$_2$	2.44 ± 0.09	96.14 ± 0.08	4.73 ± 0.24	0.48	0.03
	CN	2.46 ± 0.14	95.95 ± 0.12	4.40 ± 0.33	0.53	0.06
	HC^{15}N	1.69 ± 0.11	96.18 ± 0.16	5.21 ± 0.39	0.30	0.04
	HN^{13}C	4.61 ± 0.10	95.96 ± 0.05	4.56 ± 0.12	0.95	0.04
AGAL028.231+00.041	C^{18}O	8.13 ± 0.07	107.30 ± 0.01	2.82 ± 0.03	2.71	0.04
	H^{13}CO$^+$	1.66 ± 0.08	107.10 ± 0.07	2.75 ± 0.17	0.57	0.04
	c-C$_3$H$_2$	0.83 ± 0.07	107.10 ± 0.10	2.58 ± 0.28	0.30	0.03
	CN	0.70 ± 0.09	107.10 ± 0.18	2.72 ± 0.43	0.24	0.05
	HN^{13}C	0.91 ± 0.08	107.20 ± 0.11	2.58 ± 0.28	0.33	0.04
AGAL028.273−00.167	C^{18}O	10.11 ± 0.11	79.36 ± 0.01	2.92 ± 0.04	3.25	0.05
	H^{13}CO$^+$	1.15 ± 0.08	79.82 ± 0.12	3.45 ± 0.29	0.31	0.03
	c-C$_3$H$_2$	0.89 ± 0.06	79.62 ± 0.09	2.52 ± 0.20	0.33	0.03
	HN^{13}C	0.86 ± 0.07	79.80 ± 0.12	2.77 ± 0.25	0.29	0.04
AGAL028.344+00.061	C^{18}O	10.07 ± 0.10	79.01 ± 0.02	4.36 ± 0.05	2.17	0.04
	H^{13}CO$^+$	2.38 ± 0.09	78.98 ± 0.07	3.47 ± 0.16	0.64	0.04
	c-C$_3$H$_2$	2.79 ± 0.08	79.13 ± 0.05	3.40 ± 0.12	0.77	0.03
	CN	0.91 ± 0.09	78.90 ± 0.13	2.64 ± 0.29	0.32	0.05
	HN^{13}C	2.13 ± 0.08	79.31 ± 0.06	3.12 ± 0.13	0.64	0.04
AGAL028.354+00.072	C^{18}O	6.18 ± 0.10	80.74 ± 0.03	3.07 ± 0.06	1.89	0.05
	H^{13}CO$^+$	1.18 ± 0.07	79.96 ± 0.06	2.12 ± 0.16	0.52	0.04
	c-C$_3$H$_2$	2.21 ± 0.06	80.17 ± 0.03	2.18 ± 0.07	0.95	0.03
	CN	0.80 ± 0.14	80.21 ± 0.16	1.95 ± 0.43	0.38	0.09
	HN^{13}C	2.19 ± 0.07	80.28 ± 0.04	2.36 ± 0.09	0.87	0.04
AGAL028.361+00.054	C^{18}O	4.79 ± 0.07	80.20 ± 0.03	3.40 ± 0.05	1.32	0.04
	H^{13}CO$^+$	1.50 ± 0.08	79.24 ± 0.07	2.77 ± 0.18	0.51	0.04
	c-C$_3$H$_2$	1.57 ± 0.08	79.38 ± 0.06	2.47 ± 0.13	0.60	0.04
	CN	0.51 ± 0.10	79.57 ± 0.23	2.51 ± 0.62	0.19	0.06
	HN^{13}C	1.35 ± 0.07	79.44 ± 0.05	2.12 ± 0.13	0.60	0.04
AGAL028.398+00.081	C^{18}O	12.97 ± 0.06	78.27 ± 0.01	2.67 ± 0.01	4.56	0.03
	HCO	0.18 ± 0.03	79.04 ± 0.22	2.61 ± 0.52	0.07	0.02
	H^{13}CO$^+$	2.72 ± 0.09	77.93 ± 0.05	3.39 ± 0.13	0.75	0.04
	c-C$_3$H$_2$	1.69 ± 0.07	78.39 ± 0.06	3.09 ± 0.16	0.52	0.03
	CN	1.23 ± 0.08	78.17 ± 0.09	2.65 ± 0.19	0.44	0.05
	HC^{15}N	0.77 ± 0.08	78.10 ± 0.19	3.76 ± 0.47	0.19	0.03
	HN^{13}C	2.23 ± 0.08	78.28 ± 0.06	3.48 ± 0.15	0.60	0.04
AGAL028.564−00.236	C^{18}O	21.01 ± 0.15	86.38 ± 0.01	3.80 ± 0.03	5.20	0.07
	HCO	0.36 ± 0.06	85.87 ± 0.54	6.07 ± 1.19	0.06	0.02
	H^{13}CO$^+$	3.61 ± 0.12	86.43 ± 0.07	4.46 ± 0.15	0.76	0.05
	c-C$_3$H$_2$	2.36 ± 0.20	85.35 ± 0.08	1.96 ± 0.15	1.13	0.05
	CN	1.97 ± 0.20	86.53 ± 0.20	3.84 ± 0.38	0.48	0.10
	HC^{15}N	0.29 ± 0.07	87.38 ± 0.20	1.67 ± 0.50	0.16	0.04
	HN^{13}C	3.73 ± 0.11	86.61 ± 0.06	3.93 ± 0.13	0.89	0.05
AGAL028.658+00.144	C^{18}O	3.02 ± 0.08	78.81 ± 0.04	3.11 ± 0.10	0.91	0.04
	H^{13}CO$^+$	0.86 ± 0.06	79.17 ± 0.06	1.67 ± 0.15	0.48	0.04
	c-C$_3$H$_2$	1.15 ± 0.06	79.08 ± 0.04	1.69 ± 0.11	0.64	0.04
	CN	0.54 ± 0.07	79.04 ± 0.09	1.44 ± 0.20	0.35	0.05
	HN^{13}C	1.16 ± 0.06	79.39 ± 0.05	1.86 ± 0.10	0.59	0.04
AGAL028.677−00.277	C^{18}O	8.20 ± 0.11	88.95 ± 0.01	2.00 ± 0.03	3.84	0.07

Table B.3: continued.

ATLASGAL Name	Line	Area (K km s^{-1})	v_{LRS} (km s^{-1})	Δv (km s^{-1})	T_{MB} (K)	rms (K)
	H^{13}CO$^+$	1.99 ± 0.07	89.01 ± 0.03	1.91 ± 0.08	0.98	0.04
	c-C$_3$H$_2$	1.96 ± 0.05	88.96 ± 0.02	1.64 ± 0.05	1.13	0.03
	CN	0.77 ± 0.12	89.05 ± 0.12	1.54 ± 0.25	0.47	0.09
	HN^{13}C	1.33 ± 0.06	89.23 ± 0.04	1.93 ± 0.10	0.65	0.04
AGAL028.707−00.294	C^{18}O	10.81 ± 0.08	88.89 ± 0.01	2.23 ± 0.02	4.55	0.05
	H^{13}CO$^+$	1.60 ± 0.06	88.67 ± 0.04	2.03 ± 0.09	0.74	0.03
	c-C$_3$H$_2$	1.62 ± 0.06	88.68 ± 0.04	2.06 ± 0.09	0.74	0.03
	CN	0.93 ± 0.12	88.79 ± 0.13	2.02 ± 0.32	0.43	0.08
	HN^{13}C	0.30 ± 0.05	100.70 ± 0.16	1.71 ± 0.38	0.17	0.03
AGAL028.722−00.296	C^{18}O	9.63 ± 0.07	88.13 ± 0.01	1.75 ± 0.02	5.18	0.05
	H^{13}CO$^+$	1.05 ± 0.06	88.01 ± 0.05	1.68 ± 0.12	0.58	0.04
	c-C$_3$H$_2$	1.03 ± 0.05	87.95 ± 0.04	1.55 ± 0.10	0.63	0.03
	CN	0.34 ± 0.10	88.01 ± 0.22	1.51 ± 0.54	0.21	0.08
	HN^{13}C	0.78 ± 0.06	88.04 ± 0.05	1.35 ± 0.11	0.54	0.04
AGAL028.831−00.252	C^{18}O	17.19 ± 0.06	87.05 ± 0.01	2.93 ± 0.01	5.52	0.04
	H^{13}CO$^+$	3.99 ± 0.09	87.02 ± 0.03	3.15 ± 0.08	1.19	0.04
	c-C$_3$H$_2$	1.62 ± 0.08	86.98 ± 0.09	3.65 ± 0.23	0.42	0.03
	CN	2.15 ± 0.10	87.04 ± 0.07	3.17 ± 0.17	0.64	0.05
	HC^{15}N	0.52 ± 0.07	87.30 ± 0.15	2.24 ± 0.32	0.22	0.04
	HN^{13}C	3.23 ± 0.07	87.12 ± 0.03	3.14 ± 0.08	0.97	0.03
AGAL028.849+00.051	C^{18}O	9.82 ± 0.10	100.80 ± 0.02	2.92 ± 0.03	3.16	0.05
	H^{13}CO$^+$	0.77 ± 0.09	100.70 ± 0.14	2.68 ± 0.38	0.27	0.04
	c-C$_3$H$_2$	0.48 ± 0.08	100.70 ± 0.20	2.77 ± 0.65	0.16	0.03
	HN^{13}C	0.38 ± 0.07	101.20 ± 0.15	1.76 ± 0.37	0.20	0.04
AGAL028.861+00.066	C^{18}O	21.84 ± 0.21	103.30 ± 0.01	3.12 ± 0.04	6.57	0.09
	H^{13}CO$^+$	4.67 ± 0.10	103.30 ± 0.03	2.85 ± 0.07	1.54	0.05
	c-C$_3$H$_2$	1.88 ± 0.11	103.60 ± 0.10	3.26 ± 0.23	0.54	0.05
	CN	2.02 ± 0.17	103.70 ± 0.10	2.42 ± 0.25	0.79	0.10
	HC^{15}N	1.35 ± 0.15	103.60 ± 0.27	5.17 ± 0.74	0.25	0.05
	HN^{13}C	2.10 ± 0.10	103.40 ± 0.07	3.25 ± 0.19	0.61	0.04
AGAL029.117+00.027	C^{18}O	12.08 ± 0.10	96.83 ± 0.02	3.86 ± 0.04	2.94	0.05
	H^{13}CO$^+$	1.20 ± 0.09	97.46 ± 0.13	3.68 ± 0.31	0.31	0.04
	c-C$_3$H$_2$	1.30 ± 0.08	97.71 ± 0.12	3.82 ± 0.25	0.32	0.03
	CN	0.82 ± 0.16	98.04 ± 0.28	2.88 ± 0.72	0.27	0.09
	HN^{13}C	1.09 ± 0.08	97.83 ± 0.15	4.09 ± 0.35	0.25	0.03
AGAL029.409−00.646	C^{18}O	4.20 ± 0.08	61.53 ± 0.02	2.20 ± 0.05	1.80	0.05
	H^{13}CO$^+$	1.79 ± 0.07	61.02 ± 0.05	2.55 ± 0.10	0.66	0.03
	c-C$_3$H$_2$	2.59 ± 0.06	61.06 ± 0.03	2.30 ± 0.06	1.06	0.03
	CN	0.95 ± 0.12	61.26 ± 0.13	1.99 ± 0.27	0.45	0.08
	HN^{13}C	1.44 ± 0.06	61.20 ± 0.05	2.24 ± 0.11	0.60	0.04
AGAL029.556+00.186	C^{18}O	4.59 ± 0.08	80.01 ± 0.02	1.84 ± 0.04	2.34	0.05
	H^{13}CO$^+$	1.14 ± 0.07	79.95 ± 0.06	2.06 ± 0.15	0.52	0.04
	c-C$_3$H$_2$	1.74 ± 0.06	79.96 ± 0.03	1.86 ± 0.07	0.88	0.04
	CN	0.61 ± 0.12	79.75 ± 0.19	1.88 ± 0.40	0.30	0.08
	HN^{13}C	0.99 ± 0.06	80.10 ± 0.05	1.69 ± 0.12	0.55	0.04
AGAL029.591−00.614	C^{18}O	8.22 ± 0.09	76.89 ± 0.02	2.99 ± 0.04	2.58	0.05
	H^{13}CO$^+$	1.43 ± 0.07	76.61 ± 0.06	2.41 ± 0.14	0.56	0.04
	c-C$_3$H$_2$	1.35 ± 0.08	76.50 ± 0.07	2.62 ± 0.20	0.48	0.04
	CN	0.91 ± 0.11	76.43 ± 0.11	1.82 ± 0.23	0.47	0.08
	HN^{13}C	1.74 ± 0.06	76.70 ± 0.03	1.94 ± 0.08	0.84	0.04
AGAL029.861+00.029	C^{18}O	14.90 ± 0.11	102.50 ± 0.01	3.81 ± 0.03	3.68	0.05
	c-C$_3$H$_2$	1.78 ± 0.06	103.60 ± 0.05	2.73 ± 0.11	0.61	0.03
	CN	0.67 ± 0.16	102.80 ± 0.39	3.15 ± 0.78	0.20	0.09
	HN^{13}C	1.16 ± 0.08	103.90 ± 0.08	2.52 ± 0.22	0.43	0.04
AGAL029.911−00.042	C^{18}O	12.17 ± 0.21	98.35 ± 0.04	2.50 ± 0.04	4.57	0.05
	HCO	0.61 ± 0.04	99.63 ± 0.21	5.82 ± 0.50	0.10	0.01
	H^{13}CO$^+$	3.97 ± 0.10	99.88 ± 0.06	4.75 ± 0.13	0.79	0.04
	c-C$_3$H$_2$	2.96 ± 0.11	99.93 ± 0.12	6.55 ± 0.28	0.42	0.03
	CN	2.24 ± 0.16	99.61 ± 0.16	4.55 ± 0.38	0.46	0.07
	HC^{15}N	0.36 ± 0.08	98.93 ± 0.30	2.60 ± 0.80	0.13	0.04
	HN^{13}C	2.48 ± 0.16	100.20 ± 0.14	4.44 ± 0.34	0.53	0.04
AGAL029.954−00.016	C^{18}O	16.03 ± 0.09	97.78 ± 0.01	2.50 ± 0.02	6.02	0.05
	HCO	0.28 ± 0.04	96.09 ± 0.39	4.72 ± 0.77	0.06	0.02
	H^{13}CO$^+$	7.20 ± 0.08	97.44 ± 0.02	2.96 ± 0.04	2.28	0.04
	c-C$_3$H$_2$	2.49 ± 0.07	97.03 ± 0.05	3.47 ± 0.12	0.67	0.03
	CN	2.16 ± 0.14	97.25 ± 0.11	3.30 ± 0.26	0.62	0.07
	HC^{15}N	2.77 ± 0.10	97.37 ± 0.08	4.56 ± 0.21	0.57	0.04
	HN^{13}C	3.38 ± 0.08	97.47 ± 0.04	3.25 ± 0.10	0.98	0.04
AGAL029.976−00.047	HCO	0.15 ± 0.04	101.50 ± 0.23	2.46 ± 0.89	0.06	0.01
	c-C$_3$H$_2$	1.44 ± 0.07	101.40 ± 0.06	2.87 ± 0.19	0.47	0.03
	CN	1.49 ± 0.14	101.40 ± 0.12	2.60 ± 0.28	0.54	0.08
	HC^{15}N	0.41 ± 0.15	102.40 ± 1.33	5.52 ± 3.23	0.07	0.04
	HN^{13}C	2.40 ± 0.07	101.50 ± 0.03	2.39 ± 0.09	0.94	0.04
AGAL030.003−00.269	C^{18}O	13.27 ± 0.09	102.80 ± 0.01	2.67 ± 0.02	4.67	0.04
	H^{13}CO$^+$	1.18 ± 0.07	102.90 ± 0.08	2.81 ± 0.20	0.39	0.03

Table B.3: continued.

ATLASGAL Name	Line	Area (K km s^{-1})	v_{LRS} (km s^{-1})	Δv (km s^{-1})	T_{MB} (K)	rms (K)
	c-C$_3$H$_2$	1.49 ± 0.06	103.00 ± 0.05	2.42 ± 0.12	0.58	0.03
	CN	0.80 ± 0.09	103.00 ± 0.10	1.93 ± 0.26	0.39	0.06
	HC^{15}N	0.37 ± 0.10	102.30 ± 0.53	4.10 ± 1.51	0.08	0.04
	HN^{13}C	1.51 ± 0.07	103.10 ± 0.06	2.44 ± 0.14	0.58	0.04
AGAL030.198−00.169	C^{18}O	5.33 ± 0.07	103.00 ± 0.01	2.36 ± 0.04	2.13	0.04
	HCO	0.24 ± 0.04	103.20 ± 0.32	4.33 ± 1.20	0.05	0.01
	H^{13}CO$^+$	1.06 ± 0.06	103.10 ± 0.05	1.98 ± 0.14	0.50	0.03
	c-C$_3$H$_2$	0.85 ± 0.06	103.00 ± 0.09	2.43 ± 0.23	0.33	0.03
	HN^{13}C	0.52 ± 0.06	103.20 ± 0.10	1.85 ± 0.25	0.27	0.03
AGAL030.321+00.296	C^{18}O	4.73 ± 0.08	113.10 ± 0.01	1.52 ± 0.03	2.92	0.06
	H^{13}CO$^+$	0.67 ± 0.06	113.20 ± 0.05	1.37 ± 0.13	0.46	0.04
	c-C$_3$H$_2$	0.94 ± 0.05	113.10 ± 0.03	1.28 ± 0.09	0.69	0.04
	HN^{13}C	0.84 ± 0.06	113.40 ± 0.05	1.44 ± 0.11	0.55	0.04
AGAL030.419−00.231	C^{18}O	14.76 ± 0.07	104.70 ± 0.01	2.61 ± 0.02	5.32	0.04
	H^{13}CO$^+$	4.60 ± 0.07	105.10 ± 0.02	2.88 ± 0.05	1.50	0.03
	c-C$_3$H$_2$	2.22 ± 0.07	105.00 ± 0.05	3.10 ± 0.12	0.67	0.03
	CN	2.23 ± 0.09	105.00 ± 0.05	2.52 ± 0.11	0.83	0.05
	HC^{15}N	0.60 ± 0.07	105.30 ± 0.20	3.14 ± 0.43	0.18	0.03
	HN^{13}C	2.62 ± 0.08	105.40 ± 0.04	2.61 ± 0.10	0.94	0.04
AGAL030.429−00.116	C^{18}O	4.11 ± 0.08	103.50 ± 0.01	1.55 ± 0.04	2.49	0.05
	H^{13}CO$^+$	0.44 ± 0.05	103.60 ± 0.07	1.36 ± 0.18	0.31	0.03
	c-C$_3$H$_2$	0.41 ± 0.05	103.30 ± 0.10	1.77 ± 0.21	0.22	0.03
	HN^{13}C	0.40 ± 0.05	103.50 ± 0.12	1.73 ± 0.22	0.22	0.03
AGAL030.568−00.026	C^{18}O	3.52 ± 0.07	88.23 ± 0.02	2.60 ± 0.06	1.27	0.04
	H^{13}CO$^+$	1.08 ± 0.07	88.17 ± 0.11	3.28 ± 0.25	0.31	0.03
	c-C$_3$H$_2$	0.41 ± 0.06	88.22 ± 0.18	2.41 ± 0.39	0.16	0.03
	CN	0.28 ± 0.07	88.48 ± 0.16	1.20 ± 0.31	0.22	0.06
	HN^{13}C	0.64 ± 0.07	88.17 ± 0.13	2.52 ± 0.29	0.24	0.03
AGAL030.588−00.042	C^{18}O	13.71 ± 0.10	41.91 ± 0.01	4.14 ± 0.04	3.11	0.04
	H^{13}CO$^+$	3.87 ± 0.10	41.74 ± 0.05	4.06 ± 0.13	0.90	0.04
	c-C$_3$H$_2$	1.11 ± 0.09	41.82 ± 0.17	4.44 ± 0.43	0.23	0.03
	CN	0.65 ± 0.11	42.15 ± 0.24	2.80 ± 0.51	0.22	0.06
	HC^{15}N	0.66 ± 0.08	41.87 ± 0.21	3.72 ± 0.57	0.17	0.03
	HN^{13}C	1.65 ± 0.09	41.79 ± 0.09	3.47 ± 0.21	0.45	0.04
AGAL030.603+00.176	C^{18}O	8.16 ± 0.19	106.00 ± 0.02	2.48 ± 0.05	3.09	0.04
	HCO	0.35 ± 0.04	105.60 ± 0.34	5.61 ± 0.75	0.06	0.01
	H^{13}CO$^+$	2.69 ± 0.09	104.70 ± 0.08	4.65 ± 0.17	0.54	0.04
	c-C$_3$H$_2$	2.16 ± 0.09	104.90 ± 0.10	4.53 ± 0.21	0.45	0.04
	CN	2.07 ± 0.11	105.10 ± 0.12	4.50 ± 0.29	0.43	0.05
	HC^{15}N	0.77 ± 0.10	105.10 ± 0.26	4.73 ± 0.87	0.15	0.03
	HN^{13}C	3.25 ± 0.09	105.10 ± 0.06	4.23 ± 0.12	0.72	0.04
AGAL030.683−00.074	C^{18}O	15.05 ± 0.08	92.15 ± 0.01	3.53 ± 0.02	4.00	0.04
	HCO	0.37 ± 0.05	93.06 ± 0.26	4.91 ± 0.84	0.07	0.01
	H^{13}CO$^+$	2.46 ± 0.07	91.71 ± 0.04	2.85 ± 0.10	0.81	0.03
	c-C$_3$H$_2$	1.45 ± 0.08	91.99 ± 0.09	3.15 ± 0.21	0.43	0.04
	CN	2.01 ± 0.13	91.72 ± 0.11	3.77 ± 0.31	0.50	0.06
	HC^{15}N	0.47 ± 0.07	92.09 ± 0.24	2.96 ± 0.53	0.15	0.04
	HN^{13}C	1.96 ± 0.06	91.50 ± 0.05	2.73 ± 0.10	0.67	0.03
AGAL030.703−00.067	C^{18}O	18.19 ± 0.67	91.19 ± 0.09	5.26 ± 0.13	3.25	0.04
	HCO	0.54 ± 0.05	93.07 ± 0.30	6.94 ± 0.73	0.07	0.01
	H^{13}CO$^+$	4.03 ± 0.36	91.65 ± 0.26	6.83 ± 0.29	0.55	0.04
	c-C$_3$H$_2$	2.59 ± 0.10	90.87 ± 0.10	5.07 ± 0.24	0.48	0.03
	CN	3.03 ± 0.17	91.11 ± 0.16	6.00 ± 0.42	0.47	0.06
	HC^{15}N	2.01 ± 0.10	90.17 ± 0.12	4.99 ± 0.29	0.38	0.03
	HN^{13}C	5.95 ± 0.10	90.73 ± 0.04	4.56 ± 0.09	1.22	0.04
AGAL030.718−00.082	C^{18}O	20.80 ± 0.40	93.29 ± 0.04	4.53 ± 0.08	4.32	0.05
	CN	2.71 ± 0.24	93.30 ± 0.25	5.81 ± 0.67	0.44	0.09
AGAL030.731−00.079	C^{18}O	19.42 ± 0.18	91.78 ± 0.02	4.45 ± 0.04	4.10	0.04
	HCO	0.39 ± 0.08	93.70 ± 0.82	8.69 ± 2.39	0.04	0.01
	H^{13}CO$^+$	2.36 ± 0.38	90.91 ± 0.21	3.35 ± 0.32	0.66	0.04
	c-C$_3$H$_2$	1.12 ± 0.18	91.60 ± 0.35	4.40 ± 0.77	0.24	0.04
	CN	1.33 ± 0.18	91.85 ± 0.50	7.27 ± 1.06	0.17	0.06
	HN^{13}C	1.27 ± 0.09	91.33 ± 0.12	3.09 ± 0.26	0.39	0.04
AGAL030.753−00.051	C^{18}O	10.69 ± 0.12	91.81 ± 0.02	3.25 ± 0.04	3.10	0.06
	CN	0.87 ± 0.22	96.94 ± 0.30	2.79 ± 1.02	0.29	0.10
AGAL030.786+00.204	C^{18}O	7.53 ± 0.07	81.71 ± 0.01	2.87 ± 0.03	2.46	0.04
	H^{13}CO$^+$	2.62 ± 0.10	81.71 ± 0.06	3.23 ± 0.15	0.76	0.04
	c-C$_3$H$_2$	1.03 ± 0.09	81.66 ± 0.13	3.24 ± 0.33	0.30	0.04
	CN	1.28 ± 0.12	81.67 ± 0.14	3.20 ± 0.37	0.38	0.06
	HC^{15}N	0.44 ± 0.09	81.97 ± 0.24	2.67 ± 0.75	0.16	0.04
	HN^{13}C	1.99 ± 0.08	81.63 ± 0.05	2.63 ± 0.12	0.71	0.04
AGAL030.811−00.111	C^{18}O	6.62 ± 0.08	94.59 ± 0.01	2.36 ± 0.03	2.64	0.04
	H^{13}CO$^+$	1.58 ± 0.08	94.55 ± 0.05	2.18 ± 0.14	0.68	0.04
	c-C$_3$H$_2$	0.87 ± 0.08	94.58 ± 0.09	2.12 ± 0.23	0.39	0.04
	CN	0.51 ± 0.08	94.40 ± 0.14	1.67 ± 0.29	0.29	0.06

Table B.3: continued.

ATLASGAL Name	Line	Area (K km s^{-1})	v_{LRS} (km s^{-1})	Δv (km s^{-1})	T_{MB} (K)	rms (K)
	HN^{13}C	0.86 ± 0.09	95.08 ± 0.12	2.26 ± 0.30	0.35	0.04
AGAL030.818+00.274	C^{18}O	5.30 ± 0.08	98.11 ± 0.02	3.11 ± 0.06	1.60	0.04
	H^{13}CO$^+$	1.33 ± 0.07	97.66 ± 0.05	2.17 ± 0.12	0.58	0.04
	c-C$_3$H$_2$	0.61 ± 0.05	97.55 ± 0.10	2.17 ± 0.20	0.26	0.03
	CN	0.54 ± 0.08	97.47 ± 0.17	2.17 ± 0.36	0.23	0.05
	HN^{13}C	0.86 ± 0.05	97.57 ± 0.06	1.97 ± 0.14	0.41	0.03
AGAL030.818−00.056	C^{18}O	13.43 ± 1.43	97.82 ± 0.10	7.91 ± 0.48	1.59	0.08
	CN	3.43 ± 0.26	98.30 ± 0.23	6.36 ± 0.59	0.51	0.09
AGAL030.848−00.081	C^{18}O	9.45 ± 0.24	94.51 ± 0.04	3.02 ± 0.09	2.94	0.07
	H^{13}CO$^+$	2.18 ± 0.20	98.07 ± 0.11	3.00 ± 0.28	0.68	0.05
	c-C$_3$H$_2$	1.06 ± 0.16	98.52 ± 0.18	3.06 ± 0.62	0.33	0.05
	CN	1.39 ± 0.24	97.05 ± 0.51	6.09 ± 1.22	0.21	0.09
	HN^{13}C	1.56 ± 0.14	97.97 ± 0.10	2.59 ± 0.27	0.57	0.04
AGAL030.863−00.039	C^{18}O	12.81 ± 0.10	94.50 ± 0.01	3.80 ± 0.04	3.17	0.05
	H^{13}CO$^+$	0.76 ± 0.10	94.14 ± 0.12	2.08 ± 0.42	0.34	0.05
	c-C$_3$H$_2$	0.48 ± 0.08	94.59 ± 0.20	2.41 ± 0.44	0.19	0.04
	CN	0.26 ± 0.07	94.30 ± 0.20	1.27 ± 0.45	0.19	0.06
	HN^{13}C	0.41 ± 0.09	94.09 ± 0.20	1.75 ± 0.49	0.22	0.05
AGAL030.866+00.114	C^{18}O	8.43 ± 0.08	39.63 ± 0.02	4.05 ± 0.05	1.96	0.04
	HCO	0.21 ± 0.05	40.45 ± 0.58	4.59 ± 1.51	0.04	0.02
	H^{13}CO$^+$	1.92 ± 0.09	39.65 ± 0.09	4.00 ± 0.21	0.45	0.04
	c-C$_3$H$_2$	1.71 ± 0.12	39.30 ± 0.22	6.67 ± 0.61	0.24	0.03
	CN	0.62 ± 0.14	38.14 ± 0.43	3.75 ± 1.20	0.15	0.06
	HC^{15}N	0.33 ± 0.08	39.15 ± 0.49	3.72 ± 0.76	0.08	0.04
	HN^{13}C	0.93 ± 0.10	39.42 ± 0.25	4.72 ± 0.61	0.19	0.04
AGAL030.866−00.119	C^{18}O	9.27 ± 0.07	100.90 ± 0.01	2.84 ± 0.03	3.07	0.04
	H^{13}CO$^+$	1.14 ± 0.10	101.00 ± 0.15	3.38 ± 0.30	0.32	0.04
	c-C$_3$H$_2$	0.46 ± 0.10	100.40 ± 0.35	3.47 ± 1.09	0.12	0.04
AGAL030.893+00.139	C^{18}O	11.16 ± 0.17	106.60 ± 0.03	3.68 ± 0.06	2.85	0.08
	H^{13}CO$^+$	2.97 ± 0.11	107.20 ± 0.07	3.78 ± 0.14	0.74	0.05
	c-C$_3$H$_2$	2.55 ± 0.11	107.00 ± 0.08	3.66 ± 0.17	0.66	0.05
	CN	1.21 ± 0.17	107.20 ± 0.15	2.17 ± 0.38	0.53	0.10
	HN^{13}C	2.28 ± 0.10	107.30 ± 0.07	3.22 ± 0.14	0.66	0.04
AGAL030.898+00.162	C^{18}O	9.04 ± 0.10	105.60 ± 0.02	3.28 ± 0.04	2.59	0.05
	H^{13}CO$^+$	2.90 ± 0.10	105.70 ± 0.06	3.20 ± 0.13	0.85	0.05
	c-C$_3$H$_2$	1.53 ± 0.10	105.30 ± 0.09	2.85 ± 0.21	0.51	0.04
	CN	1.58 ± 0.11	105.30 ± 0.06	2.05 ± 0.17	0.73	0.07
	HC^{15}N	0.27 ± 0.07	105.40 ± 0.23	1.59 ± 0.46	0.16	0.04
	HN^{13}C	2.65 ± 0.09	105.50 ± 0.05	2.83 ± 0.12	0.88	0.04
AGAL030.971−00.141	C^{18}O	7.94 ± 0.08	77.67 ± 0.01	2.88 ± 0.04	2.59	0.04
	H^{13}CO$^+$	3.43 ± 0.08	77.46 ± 0.02	2.17 ± 0.06	1.48	0.04
	c-C$_3$H$_2$	1.70 ± 0.08	77.34 ± 0.04	2.14 ± 0.12	0.74	0.04
	CN	1.43 ± 0.10	77.10 ± 0.08	2.29 ± 0.19	0.59	0.06
	HN^{13}C	2.02 ± 0.08	77.44 ± 0.05	2.28 ± 0.11	0.83	0.05
AGAL030.996−00.076	C^{18}O	11.53 ± 0.07	81.33 ± 0.01	2.36 ± 0.02	4.58	0.04
	H^{13}CO$^+$	1.91 ± 0.09	81.29 ± 0.06	2.46 ± 0.13	0.73	0.05
	c-C$_3$H$_2$	1.09 ± 0.07	81.40 ± 0.07	2.12 ± 0.15	0.48	0.04
	CN	1.04 ± 0.09	81.43 ± 0.11	2.37 ± 0.22	0.41	0.06
	HC^{15}N	0.38 ± 0.11	80.98 ± 0.77	5.05 ± 1.67	0.07	0.04
	HN^{13}C	1.12 ± 0.08	81.49 ± 0.07	2.30 ± 0.18	0.46	0.04
AGAL031.024+00.262	C^{18}O	6.48 ± 0.07	96.12 ± 0.01	1.94 ± 0.03	3.14	0.04
	H^{13}CO$^+$	1.04 ± 0.08	96.10 ± 0.08	2.06 ± 0.20	0.48	0.04
	c-C$_3$H$_2$	0.92 ± 0.07	96.26 ± 0.06	1.64 ± 0.14	0.53	0.04
	CN	0.23 ± 0.07	96.23 ± 0.16	1.07 ± 0.37	0.20	0.06
	HN^{13}C	0.66 ± 0.08	96.34 ± 0.09	1.62 ± 0.22	0.39	0.05
AGAL031.044+00.261	C^{18}O	5.61 ± 0.10	97.46 ± 0.02	2.09 ± 0.04	2.53	0.06
	H^{13}CO$^+$	1.65 ± 0.09	97.24 ± 0.05	1.99 ± 0.14	0.78	0.05
	c-C$_3$H$_2$	0.96 ± 0.07	97.36 ± 0.06	1.75 ± 0.15	0.52	0.04
	CN	0.52 ± 0.09	97.02 ± 0.20	2.10 ± 0.39	0.23	0.06
	HC^{15}N	0.41 ± 0.10	110.10 ± 0.30	2.59 ± 0.69	0.15	0.05
	HN^{13}C	0.81 ± 0.09	97.12 ± 0.11	1.98 ± 0.31	0.38	0.05
AGAL031.103+00.261	C^{18}O	6.32 ± 0.08	97.05 ± 0.01	1.90 ± 0.03	3.13	0.06
	H^{13}CO$^+$	0.77 ± 0.07	97.29 ± 0.08	1.53 ± 0.17	0.47	0.05
	c-C$_3$H$_2$	0.62 ± 0.07	97.34 ± 0.06	1.21 ± 0.17	0.49	0.05
	CN	0.48 ± 0.10	97.47 ± 0.26	2.28 ± 0.54	0.20	0.06
	HN^{13}C	0.37 ± 0.08	97.34 ± 0.13	1.28 ± 0.30	0.27	0.05
AGAL031.183−00.147	C^{18}O	5.33 ± 0.07	42.78 ± 0.02	2.71 ± 0.04	1.84	0.04
	H^{13}CO$^+$	0.36 ± 0.07	42.93 ± 0.16	1.54 ± 0.38	0.22	0.05
	c-C$_3$H$_2$	0.45 ± 0.09	42.42 ± 0.23	2.44 ± 0.58	0.17	0.04
AGAL031.243−00.111	C^{18}O	4.27 ± 0.09	20.94 ± 0.05	4.44 ± 0.12	0.90	0.04
	H^{13}CO$^+$	1.06 ± 0.10	20.71 ± 0.22	4.47 ± 0.49	0.22	0.04
	c-C$_3$H$_2$	1.29 ± 0.13	20.84 ± 0.30	6.23 ± 0.78	0.20	0.04
	HC^{15}N	0.91 ± 0.12	21.16 ± 0.42	6.02 ± 0.92	0.14	0.04
AGAL031.254+00.057	C^{18}O	15.17 ± 0.08	107.90 ± 0.01	2.98 ± 0.02	4.79	0.04
	H^{13}CO$^+$	1.33 ± 0.10	107.20 ± 0.11	2.77 ± 0.22	0.45	0.05

Table B.3: continued.

ATLASGAL Name	Line	Area (K km s^{-1})	v_{LRS} (km s^{-1})	Δv (km s^{-1})	T_{MB} (K)	rms (K)
	c-C$_3$H$_2$	0.88 ± 0.09	107.10 ± 0.16	3.02 ± 0.31	0.27	0.04
	CN	0.40 ± 0.07	107.10 ± 0.11	1.20 ± 0.23	0.31	0.06
	HN^{13}C	0.76 ± 0.08	107.20 ± 0.10	1.82 ± 0.23	0.39	0.05
AGAL031.281+00.062	C^{18}O	20.26 ± 0.05	108.80 ± 0.01	3.92 ± 0.01	4.85	0.03
	HCO	0.39 ± 0.05	108.80 ± 0.32	5.17 ± 0.80	0.07	0.02
	H^{13}CO$^+$	5.35 ± 0.10	108.80 ± 0.04	4.24 ± 0.09	1.19	0.04
	c-C$_3$H$_2$	2.26 ± 0.12	108.60 ± 0.15	6.00 ± 0.38	0.35	0.04
	CN	2.03 ± 0.09	108.70 ± 0.10	4.36 ± 0.23	0.44	0.04
	HC^{15}N	1.25 ± 0.09	108.80 ± 0.14	3.87 ± 0.29	0.30	0.04
	HN^{13}C	2.85 ± 0.12	109.30 ± 0.07	3.33 ± 0.18	0.80	0.04
AGAL031.396−00.257	C^{18}O	15.37 ± 0.09	86.87 ± 0.01	3.86 ± 0.03	3.74	0.04
	HCO	0.34 ± 0.05	87.63 ± 0.39	5.65 ± 1.11	0.06	0.02
	H^{13}CO$^+$	4.61 ± 0.09	86.77 ± 0.04	3.72 ± 0.09	1.17	0.04
	c-C$_3$H$_2$	1.79 ± 0.08	87.42 ± 0.09	4.08 ± 0.23	0.41	0.03
	CN	2.03 ± 0.15	86.74 ± 0.15	4.46 ± 0.41	0.43	0.06
	HC^{15}N	1.22 ± 0.14	86.97 ± 0.34	6.75 ± 1.15	0.17	0.04
	HN^{13}C	2.08 ± 0.09	86.90 ± 0.09	4.11 ± 0.21	0.48	0.04
AGAL031.412+00.307	C^{18}O	33.81 ± 0.22	97.02 ± 0.02	5.23 ± 0.04	6.08	0.09
	HCO	0.22 ± 0.04	98.15 ± 0.27	2.90 ± 0.75	0.07	0.02
	H^{13}CO$^+$	4.90 ± 0.18	96.66 ± 0.12	6.65 ± 0.32	0.69	0.05
	c-C$_3$H$_2$	3.25 ± 0.17	96.78 ± 0.18	6.87 ± 0.41	0.45	0.05
	CN	3.35 ± 0.26	97.21 ± 0.29	7.58 ± 0.66	0.41	0.09
	HC^{15}N	4.36 ± 0.16	96.96 ± 0.14	7.66 ± 0.34	0.53	0.05
	HN^{13}C	3.04 ± 0.15	97.02 ± 0.14	5.89 ± 0.38	0.48	0.05
AGAL031.464+00.186	C^{18}O	4.32 ± 0.09	103.50 ± 0.03	2.66 ± 0.07	1.52	0.04
	H^{13}CO$^+$	0.46 ± 0.06	103.50 ± 0.10	1.73 ± 0.28	0.25	0.03
	c-C$_3$H$_2$	0.53 ± 0.05	103.50 ± 0.06	1.47 ± 0.15	0.34	0.03
	HN^{13}C	0.39 ± 0.04	103.60 ± 0.09	1.42 ± 0.16	0.26	0.03
AGAL031.581+00.077	C^{18}O	17.16 ± 0.08	96.17 ± 0.01	3.38 ± 0.02	4.77	0.04
	HCO	0.33 ± 0.05	95.07 ± 0.48	6.93 ± 1.21	0.04	0.01
	H^{13}CO$^+$	5.39 ± 0.08	96.02 ± 0.02	3.25 ± 0.06	1.56	0.04
	c-C$_3$H$_2$	1.51 ± 0.07	95.94 ± 0.07	3.30 ± 0.19	0.43	0.03
	CN	1.41 ± 0.11	96.16 ± 0.13	3.25 ± 0.29	0.41	0.06
	HC^{15}N	0.73 ± 0.07	95.79 ± 0.17	3.26 ± 0.34	0.21	0.03
	HN^{13}C	2.34 ± 0.08	96.29 ± 0.05	3.10 ± 0.12	0.71	0.04
AGAL031.584−00.117	C^{18}O	4.92 ± 0.08	33.31 ± 0.02	2.99 ± 0.06	1.54	0.04
	H^{13}CO$^+$	1.15 ± 0.08	33.87 ± 0.09	2.46 ± 0.21	0.44	0.04
	c-C$_3$H$_2$	0.42 ± 0.11	33.24 ± 0.30	2.45 ± 0.78	0.16	0.04
	HC^{15}N	0.18 ± 0.06	33.08 ± 0.13	0.92 ± 0.50	0.19	0.05
	HN^{13}C	0.47 ± 0.09	33.45 ± 0.20	2.27 ± 0.55	0.20	0.04
AGAL031.699−00.494	C^{18}O	4.39 ± 0.05	79.81 ± 0.01	1.34 ± 0.02	3.08	0.04
	H^{13}CO$^+$	1.09 ± 0.05	79.68 ± 0.03	1.25 ± 0.06	0.82	0.03
	c-C$_3$H$_2$	1.46 ± 0.04	79.69 ± 0.02	1.28 ± 0.04	1.07	0.03
	CN	0.50 ± 0.09	79.95 ± 0.15	1.63 ± 0.38	0.29	0.06
	HN^{13}C	0.71 ± 0.05	79.80 ± 0.03	1.09 ± 0.10	0.62	0.03
AGAL031.982+00.064	C^{18}O	3.13 ± 0.07	93.56 ± 0.02	2.02 ± 0.06	1.46	0.04
	H^{13}CO$^+$	0.99 ± 0.06	93.63 ± 0.05	1.75 ± 0.12	0.53	0.03
	c-C$_3$H$_2$	0.98 ± 0.06	93.75 ± 0.05	1.85 ± 0.12	0.50	0.03
	CN	0.64 ± 0.07	93.62 ± 0.08	1.39 ± 0.17	0.43	0.06
	HN^{13}C	1.06 ± 0.06	93.74 ± 0.05	2.06 ± 0.13	0.48	0.03
AGAL032.001−00.197	C^{18}O	4.49 ± 0.05	96.39 ± 0.01	1.56 ± 0.02	2.70	0.04
	H^{13}CO$^+$	0.43 ± 0.05	96.54 ± 0.08	1.35 ± 0.16	0.30	0.04
	c-C$_3$H$_2$	0.60 ± 0.04	96.47 ± 0.03	1.10 ± 0.12	0.51	0.03
	CN	0.30 ± 0.07	96.15 ± 0.09	0.89 ± 0.24	0.32	0.06
	HN^{13}C	0.47 ± 0.05	96.65 ± 0.07	1.32 ± 0.17	0.34	0.03
AGAL032.007+00.062	C^{18}O	10.50 ± 0.08	97.34 ± 0.02	4.27 ± 0.04	2.31	0.04
	HCO	0.13 ± 0.03	97.53 ± 0.26	2.44 ± 0.58	0.05	0.01
	H^{13}CO$^+$	3.09 ± 0.10	96.58 ± 0.09	5.41 ± 0.20	0.54	0.03
	c-C$_3$H$_2$	1.90 ± 0.08	96.10 ± 0.07	3.65 ± 0.19	0.49	0.03
	CN	1.07 ± 0.15	96.83 ± 0.31	4.61 ± 0.81	0.22	0.06
	HC^{15}N	0.39 ± 0.08	97.31 ± 0.49	4.76 ± 0.88	0.08	0.03
	HN^{13}C	0.57 ± 0.06	100.00 ± 0.10	1.79 ± 0.23	0.30	0.03
AGAL032.019+00.064	C^{18}O	8.28 ± 0.01	96.57 ± 0.01	5.91 ± 0.02	1.32	0.04
	H^{13}CO$^+$	2.15 ± 0.16	95.44 ± 0.21	5.10 ± 0.43	0.40	0.03
	c-C$_3$H$_2$	0.88 ± 0.12	99.84 ± 0.08	1.99 ± 0.23	0.41	0.03
	CN	1.02 ± 0.10	99.98 ± 0.10	2.16 ± 0.31	0.44	0.06
	HN^{13}C	1.24 ± 0.06	99.97 ± 0.04	1.85 ± 0.10	0.63	0.03
AGAL032.044+00.059	C^{18}O	13.81 ± 0.10	95.50 ± 0.02	5.11 ± 0.04	2.54	0.04
	H^{13}CO$^+$	5.58 ± 0.08	94.92 ± 0.02	3.70 ± 0.06	1.42	0.03
	c-C$_3$H$_2$	1.79 ± 0.09	95.67 ± 0.13	5.38 ± 0.34	0.31	0.03
	CN	1.79 ± 0.11	94.89 ± 0.10	3.38 ± 0.23	0.50	0.06
	HC^{15}N	1.33 ± 0.12	96.28 ± 0.31	7.01 ± 0.76	0.18	0.03
	HN^{13}C	3.55 ± 0.07	95.18 ± 0.03	3.41 ± 0.08	0.98	0.03
AGAL032.149+00.134	C^{18}O	15.62 ± 0.08	93.13 ± 0.01	3.99 ± 0.02	3.68	0.04
	HCO	0.28 ± 0.04	93.76 ± 0.35	4.41 ± 0.68	0.06	0.02

Table B.3: continued.

ATLASGAL Name	Line	Area (K km s^{-1})	v_{LRS} (km s^{-1})	Δv (km s^{-1})	T_{MB} (K)	rms (K)
	H^{13}CO$^+$	3.86 ± 0.10	92.84 ± 0.05	4.18 ± 0.12	0.87	0.04
	c-C$_3$H$_2$	2.39 ± 0.10	92.98 ± 0.11	4.92 ± 0.24	0.46	0.04
	CN	1.76 ± 0.14	93.19 ± 0.21	5.07 ± 0.45	0.33	0.06
	HN^{13}C	2.11 ± 0.11	93.21 ± 0.12	4.60 ± 0.27	0.43	0.04
AGAL032.739+00.192	C^{18}O	8.56 ± 0.07	19.55 ± 0.01	2.90 ± 0.03	2.77	0.04
	H^{13}CO$^+$	0.82 ± 0.07	19.56 ± 0.11	2.64 ± 0.29	0.29	0.03
	c-C$_3$H$_2$	0.77 ± 0.07	19.16 ± 0.14	3.07 ± 0.32	0.23	0.03
	CN	0.43 ± 0.09	18.99 ± 0.21	2.12 ± 0.59	0.19	0.06
	HN^{13}C	0.38 ± 0.07	20.24 ± 0.35	3.74 ± 0.80	0.10	0.03
AGAL032.744−00.076	C^{18}O	15.44 ± 0.08	36.97 ± 0.01	4.38 ± 0.03	3.32	0.03
	H^{13}CO$^+$	4.58 ± 0.12	37.03 ± 0.07	5.39 ± 0.16	0.80	0.04
	c-C$_3$H$_2$	1.31 ± 0.10	36.73 ± 0.16	4.44 ± 0.44	0.28	0.04
	CN	0.48 ± 0.13	36.01 ± 0.64	4.73 ± 1.37	0.10	0.04
	HC^{15}N	0.55 ± 0.12	37.06 ± 0.51	4.33 ± 1.21	0.12	0.04
	HN^{13}C	1.68 ± 0.12	36.98 ± 0.17	4.86 ± 0.39	0.32	0.04
AGAL032.797+00.191	C^{18}O	23.38 ± 0.19	14.62 ± 0.02	6.32 ± 0.06	3.48	0.04
	HCO	0.27 ± 0.05	16.07 ± 0.51	5.59 ± 1.19	0.05	0.02
	H^{13}CO$^+$	5.58 ± 0.14	14.83 ± 0.09	7.23 ± 0.21	0.72	0.04
	c-C$_3$H$_2$	2.33 ± 0.15	14.81 ± 0.20	6.23 ± 0.45	0.35	0.05
	CN	1.46 ± 0.19	14.07 ± 0.29	5.43 ± 1.02	0.25	0.06
	HC^{15}N	1.00 ± 0.12	13.10 ± 0.38	6.02 ± 0.78	0.16	0.04
	HN^{13}C	1.77 ± 0.15	14.60 ± 0.31	7.36 ± 0.67	0.23	0.04
AGAL032.821−00.331	C^{18}O	3.64 ± 0.09	79.12 ± 0.05	4.14 ± 0.12	0.82	0.04
	H^{13}CO$^+$	2.06 ± 0.08	79.28 ± 0.06	3.18 ± 0.15	0.61	0.04
	c-C$_3$H$_2$	0.66 ± 0.06	79.14 ± 0.11	2.70 ± 0.26	0.23	0.03
	CN	0.84 ± 0.11	79.24 ± 0.23	3.42 ± 0.50	0.23	0.06
	HC^{15}N	0.62 ± 0.11	78.54 ± 0.82	9.36 ± 1.73	0.06	0.03
	HN^{13}C	1.63 ± 0.08	79.37 ± 0.07	2.86 ± 0.16	0.54	0.04
AGAL033.133−00.092	C^{18}O	18.33 ± 0.08	76.39 ± 0.01	3.43 ± 0.02	5.02	0.04
	H^{13}CO$^+$	3.54 ± 0.10	76.63 ± 0.05	3.43 ± 0.11	0.97	0.04
	c-C$_3$H$_2$	2.15 ± 0.10	76.80 ± 0.09	3.84 ± 0.22	0.53	0.04
	CN	1.90 ± 0.11	76.35 ± 0.10	3.34 ± 0.24	0.54	0.06
	HC^{15}N	0.35 ± 0.09	76.43 ± 0.31	2.38 ± 0.74	0.14	0.05
	HN^{13}C	1.81 ± 0.10	76.52 ± 0.08	3.03 ± 0.19	0.56	0.04
AGAL033.238−00.022	C^{18}O	9.37 ± 0.07	100.20 ± 0.01	2.31 ± 0.02	3.82	0.04
	HCO	0.20 ± 0.03	100.70 ± 0.18	2.44 ± 0.41	0.08	0.02
	H^{13}CO$^+$	1.61 ± 0.06	100.10 ± 0.04	2.10 ± 0.08	0.72	0.03
	c-C$_3$H$_2$	0.77 ± 0.07	100.10 ± 0.09	2.39 ± 0.26	0.30	0.03
	CN	0.67 ± 0.07	100.10 ± 0.09	1.58 ± 0.18	0.40	0.06
	HN^{13}C	1.05 ± 0.06	100.40 ± 0.06	2.04 ± 0.14	0.48	0.04
AGAL033.393+00.011	C^{18}O	8.47 ± 0.08	103.70 ± 0.01	3.03 ± 0.03	2.63	0.04
	HCO	0.17 ± 0.04	102.80 ± 0.39	3.33 ± 0.77	0.05	0.02
	H^{13}CO$^+$	2.17 ± 0.07	103.70 ± 0.05	2.74 ± 0.11	0.74	0.04
	c-C$_3$H$_2$	0.76 ± 0.06	103.70 ± 0.10	2.56 ± 0.27	0.28	0.03
	CN	0.45 ± 0.11	103.60 ± 0.31	2.76 ± 0.94	0.15	0.05
	HC^{15}N	0.34 ± 0.08	103.00 ± 0.42	3.50 ± 0.85	0.09	0.04
	HN^{13}C	1.16 ± 0.06	103.60 ± 0.07	2.48 ± 0.17	0.44	0.03
AGAL033.568+00.027	C^{18}O	7.22 ± 0.10	104.90 ± 0.02	2.84 ± 0.05	2.39	0.04
	H^{13}CO$^+$	0.53 ± 0.05	105.40 ± 0.08	1.71 ± 0.18	0.29	0.03
	c-C$_3$H$_2$	0.89 ± 0.05	105.60 ± 0.04	1.62 ± 0.12	0.51	0.03
	HN^{13}C	0.54 ± 0.04	105.50 ± 0.05	1.29 ± 0.13	0.39	0.03
AGAL033.623−00.032	C^{18}O	7.74 ± 0.07	103.90 ± 0.02	3.64 ± 0.04	2.00	0.04
	H^{13}CO$^+$	1.20 ± 0.08	103.50 ± 0.11	3.57 ± 0.25	0.32	0.03
	c-C$_3$H$_2$	1.02 ± 0.06	102.60 ± 0.04	1.39 ± 0.10	0.69	0.03
	CN	0.58 ± 0.10	103.20 ± 0.27	2.98 ± 0.58	0.18	0.05
	HN^{13}C	1.22 ± 0.07	103.30 ± 0.09	3.18 ± 0.18	0.36	0.03
AGAL033.744−00.007	C^{18}O	5.32 ± 0.08	106.50 ± 0.03	4.29 ± 0.07	1.16	0.03
	H^{13}CO$^+$	1.13 ± 0.07	106.00 ± 0.09	2.92 ± 0.21	0.36	0.03
	c-C$_3$H$_2$	1.50 ± 0.06	106.10 ± 0.05	2.55 ± 0.12	0.55	0.03
	CN	0.63 ± 0.10	106.30 ± 0.28	3.27 ± 0.63	0.18	0.05
	HN^{13}C	1.71 ± 0.07	106.20 ± 0.06	3.07 ± 0.14	0.52	0.03
AGAL033.851+00.017	C^{18}O	2.12 ± 0.06	61.23 ± 0.03	2.18 ± 0.07	0.91	0.04
	H^{13}CO$^+$	0.78 ± 0.07	61.19 ± 0.09	2.16 ± 0.23	0.34	0.04
	c-C$_3$H$_2$	0.54 ± 0.05	61.15 ± 0.09	1.89 ± 0.19	0.27	0.03
	CN	0.60 ± 0.11	61.09 ± 0.23	2.57 ± 0.57	0.22	0.06
	HN^{13}C	0.20 ± 0.06	69.09 ± 0.06	0.67 ± 23.60	0.28	0.03
AGAL033.914+00.109	C^{18}O	20.78 ± 0.12	107.60 ± 0.01	3.24 ± 0.02	6.02	0.06
	HCO	0.24 ± 0.04	108.20 ± 0.26	2.96 ± 0.55	0.08	0.02
	H^{13}CO$^+$	6.27 ± 0.10	107.60 ± 0.02	3.07 ± 0.06	1.92	0.04
	c-C$_3$H$_2$	2.73 ± 0.09	107.40 ± 0.05	2.98 ± 0.11	0.86	0.04
	CN	2.09 ± 0.18	107.80 ± 0.12	2.98 ± 0.34	0.66	0.09
	HC^{15}N	1.08 ± 0.10	107.70 ± 0.14	3.32 ± 0.41	0.31	0.04
	HN^{13}C	2.94 ± 0.10	107.50 ± 0.04	2.79 ± 0.11	0.99	0.05
AGAL033.979−00.021	C^{18}O	8.76 ± 0.09	61.27 ± 0.02	3.55 ± 0.04	2.32	0.04
	H^{13}CO$^+$	1.79 ± 0.06	61.50 ± 0.04	2.48 ± 0.11	0.68	0.03

Table B.3: continued.

ATLASGAL Name	Line	Area (K km s^{-1})	v_{LRS} (km s^{-1})	Δv (km s^{-1})	T_{MB} (K)	rms (K)
	c-C$_3$H$_2$	0.66 ± 0.05	61.71 ± 0.08	2.10 ± 0.18	0.30	0.03
	CN	0.42 ± 0.07	61.55 ± 0.18	1.94 ± 0.34	0.20	0.05
	HN^{13}C	0.93 ± 0.06	61.77 ± 0.06	2.02 ± 0.16	0.43	0.03
AGAL034.089+00.011	C^{18}O	9.75 ± 0.17	55.04 ± 0.02	2.31 ± 0.05	3.96	0.08
	H^{13}CO$^+$	1.55 ± 0.13	55.20 ± 0.14	3.27 ± 0.42	0.45	0.05
	c-C$_3$H$_2$	1.29 ± 0.12	55.31 ± 0.17	3.99 ± 0.45	0.30	0.04
	HN^{13}C	0.79 ± 0.10	55.64 ± 0.23	3.46 ± 0.53	0.21	0.04
AGAL034.243+00.132	C^{18}O	16.43 ± 0.11	56.67 ± 0.01	2.77 ± 0.02	5.56	0.06
	HCO	0.36 ± 0.05	57.16 ± 0.24	4.18 ± 0.68	0.08	0.02
	H^{13}CO$^+$	2.30 ± 0.08	57.13 ± 0.03	1.95 ± 0.08	1.11	0.04
	c-C$_3$H$_2$	1.84 ± 0.10	56.82 ± 0.07	2.92 ± 0.20	0.59	0.04
	CN	1.57 ± 0.17	56.86 ± 0.13	2.54 ± 0.32	0.58	0.10
	HC^{15}N	0.89 ± 0.09	56.89 ± 0.13	2.67 ± 0.30	0.31	0.04
	HN^{13}C	1.15 ± 0.07	57.39 ± 0.07	2.13 ± 0.16	0.51	0.04
AGAL034.258+00.154	C^{18}O	31.64 ± 0.02	57.12 ± 0.00	4.25 ± 0.01	7.00	0.02
	HCO	0.08 ± 0.01	57.37 ± 0.14	1.72 ± 0.22	0.04	0.01
	H^{13}CO$^+$	13.66 ± 0.01	57.13 ± 0.00	4.18 ± 0.01	3.07	0.02
	c-C$_3$H$_2$	1.80 ± 0.03	57.25 ± 0.02	2.97 ± 0.05	0.57	0.01
	CN	2.54 ± 0.07	57.13 ± 0.05	3.56 ± 0.11	0.67	0.04
	HC^{15}N	7.12 ± 0.03	57.60 ± 0.01	5.02 ± 0.03	1.33	0.01
	HN^{13}C	7.20 ± 0.03	58.26 ± 0.01	5.72 ± 0.03	1.18	0.01
AGAL034.372−00.664	C^{18}O	1.54 ± 0.04	12.20 ± 0.02	1.33 ± 0.03	1.08	0.03
	H^{13}CO$^+$	0.62 ± 0.04	12.05 ± 0.04	0.81 ± 0.05	0.72	0.03
	c-C$_3$H$_2$	1.62 ± 0.04	12.22 ± 0.01	1.01 ± 0.04	1.50	0.03
	CN	0.26 ± 0.05	12.11 ± 0.10	0.52 ± 1.81	0.48	0.06
	HN^{13}C	1.02 ± 0.04	12.24 ± 0.02	0.85 ± 0.03	1.13	0.03
AGAL034.401+00.226	C^{18}O	14.21 ± 0.61	55.87 ± 0.01	2.10 ± 0.04	6.35	0.07
	HCO	0.24 ± 0.05	58.48 ± 0.59	5.27 ± 1.14	0.04	0.02
	H^{13}CO$^+$	10.64 ± 0.13	57.28 ± 0.03	4.40 ± 0.06	2.27	0.05
	c-C$_3$H$_2$	3.24 ± 0.14	57.23 ± 0.09	4.25 ± 0.21	0.72	0.05
	CN	2.67 ± 0.18	57.54 ± 0.13	3.77 ± 0.28	0.66	0.09
	HC^{15}N	1.69 ± 0.15	57.54 ± 0.24	5.78 ± 0.68	0.28	0.05
	HN^{13}C	5.38 ± 0.10	57.49 ± 0.03	3.70 ± 0.08	1.37	0.04
AGAL034.411+00.234	C^{18}O	10.36 ± 0.14	57.32 ± 0.02	3.23 ± 0.05	3.01	0.07
	H^{13}CO$^+$	6.48 ± 0.11	57.87 ± 0.02	2.96 ± 0.06	2.06	0.05
	c-C$_3$H$_2$	2.42 ± 0.10	57.93 ± 0.05	2.61 ± 0.12	0.87	0.05
	CN	2.16 ± 0.17	57.87 ± 0.09	2.46 ± 0.24	0.83	0.09
	HC^{15}N	1.86 ± 0.32	57.64 ± 0.27	3.68 ± 0.71	0.47	0.05
	HN^{13}C	4.92 ± 0.10	57.83 ± 0.03	2.73 ± 0.06	1.69	0.05
AGAL034.454+00.006	C^{18}O	6.84 ± 0.08	89.55 ± 0.02	2.70 ± 0.04	2.38	0.05
	H^{13}CO$^+$	2.57 ± 0.07	89.64 ± 0.04	3.02 ± 0.09	0.80	0.03
	c-C$_3$H$_2$	0.97 ± 0.07	89.78 ± 0.09	2.79 ± 0.23	0.33	0.03
	CN	0.57 ± 0.09	89.61 ± 0.16	2.08 ± 0.39	0.26	0.06
	HN^{13}C	1.25 ± 0.07	90.03 ± 0.08	2.97 ± 0.19	0.40	0.03
AGAL034.459+00.247	C^{18}O	4.31 ± 0.07	58.54 ± 0.02	2.64 ± 0.05	1.53	0.04
	H^{13}CO$^+$	2.81 ± 0.07	59.22 ± 0.03	2.48 ± 0.08	1.06	0.04
	c-C$_3$H$_2$	1.94 ± 0.07	59.24 ± 0.04	2.21 ± 0.10	0.82	0.04
	CN	0.94 ± 0.08	59.26 ± 0.08	2.12 ± 0.21	0.42	0.05
	HC^{15}N	0.37 ± 0.10	58.24 ± 0.57	4.67 ± 1.80	0.07	0.03
	HN^{13}C	1.97 ± 0.07	59.49 ± 0.03	2.12 ± 0.09	0.87	0.04
AGAL034.591+00.242	C^{18}O	2.01 ± 0.06	−22.62 ± 0.05	3.08 ± 0.10	0.61	0.03
	HCO	0.09 ± 0.02	−21.36 ± 0.16	1.25 ± 0.30	0.06	0.02
	H^{13}CO$^+$	0.38 ± 0.09	−22.10 ± 0.32	2.79 ± 0.78	0.13	0.04
	c-C$_3$H$_2$	0.58 ± 0.09	−22.53 ± 0.25	3.23 ± 0.55	0.17	0.04
AGAL034.712−00.596	C^{18}O	5.83 ± 0.14	44.89 ± 0.03	2.92 ± 0.09	1.88	0.07
	H^{13}CO$^+$	2.72 ± 0.09	44.56 ± 0.04	2.32 ± 0.09	1.10	0.05
	c-C$_3$H$_2$	1.94 ± 0.08	44.68 ± 0.05	2.22 ± 0.12	0.82	0.04
	CN	0.99 ± 0.17	44.56 ± 0.15	1.88 ± 0.41	0.49	0.11
	HC^{15}N	0.50 ± 0.07	44.49 ± 0.10	1.48 ± 0.25	0.32	0.04
	HN^{13}C	1.57 ± 0.09	44.66 ± 0.06	2.39 ± 0.17	0.61	0.04
AGAL034.739−00.119	C^{18}O	8.69 ± 0.08	78.33 ± 0.01	2.06 ± 0.02	3.96	0.05
	H^{13}CO$^+$	1.20 ± 0.10	78.71 ± 0.09	2.25 ± 0.21	0.50	0.05
	c-C$_3$H$_2$	1.93 ± 0.07	78.73 ± 0.03	1.88 ± 0.09	0.96	0.04
	CN	0.78 ± 0.10	78.66 ± 0.15	2.21 ± 0.35	0.33	0.06
	HN^{13}C	1.26 ± 0.08	79.00 ± 0.06	1.93 ± 0.13	0.62	0.05
AGAL034.742−00.132	C^{18}O	6.65 ± 0.07	78.47 ± 0.01	2.11 ± 0.03	2.96	0.04
	H^{13}CO$^+$	1.19 ± 0.08	78.87 ± 0.06	1.82 ± 0.14	0.61	0.05
	c-C$_3$H$_2$	1.73 ± 0.07	78.86 ± 0.03	1.56 ± 0.08	1.04	0.05
	CN	0.59 ± 0.09	79.09 ± 0.13	1.69 ± 0.30	0.33	0.06
	HN^{13}C	1.25 ± 0.08	78.93 ± 0.04	1.50 ± 0.10	0.78	0.05
AGAL034.751−00.092	C^{18}O	2.77 ± 0.06	51.40 ± 0.02	2.32 ± 0.06	1.12	0.04
	H^{13}CO$^+$	0.90 ± 0.06	51.28 ± 0.07	2.14 ± 0.14	0.40	0.03
	c-C$_3$H$_2$	0.75 ± 0.07	51.33 ± 0.10	2.44 ± 0.30	0.29	0.03
	HN^{13}C	0.45 ± 0.06	51.43 ± 0.12	1.81 ± 0.33	0.23	0.04
AGAL034.757+00.024	C^{18}O	5.32 ± 0.14	76.32 ± 0.03	2.43 ± 0.08	2.06	0.08

Table B.3: continued.

ATLASGAL Name	Line	Area (K km s^{-1})	v_{LRS} (km s^{-1})	Δv (km s^{-1})	T_{MB} (K)	rms (K)
	HCO	0.22 ± 0.05	75.80 ± 0.44	4.35 ± 1.36	0.05	0.01
	H^{13}CO$^+$	0.90 ± 0.10	76.88 ± 0.18	3.48 ± 0.52	0.24	0.04
	c-C$_3$H$_2$	0.90 ± 0.11	76.14 ± 0.30	4.76 ± 0.66	0.18	0.04
	CN	0.91 ± 0.19	76.27 ± 0.32	2.94 ± 0.61	0.29	0.11
	HN^{13}C	0.71 ± 0.09	77.24 ± 0.18	2.81 ± 0.38	0.24	0.04
AGAL034.821+00.351	C^{18}O	15.70 ± 0.15	57.20 ± 0.01	3.15 ± 0.04	4.68	0.08
	H^{13}CO$^+$	5.65 ± 0.12	57.12 ± 0.03	2.81 ± 0.07	1.89	0.06
	c-C$_3$H$_2$	2.55 ± 0.11	57.15 ± 0.06	2.94 ± 0.14	0.81	0.05
	CN	1.72 ± 0.16	57.20 ± 0.12	2.62 ± 0.28	0.61	0.09
	HC^{15}N	0.50 ± 0.11	57.30 ± 0.28	2.53 ± 0.75	0.18	0.05
	HN^{13}C	2.20 ± 0.11	57.07 ± 0.06	2.62 ± 0.15	0.79	0.05
AGAL035.026+00.349	C^{18}O	6.07 ± 0.52	52.67 ± 0.08	5.07 ± 0.31	1.12	0.04
	H^{13}CO$^+$	3.79 ± 0.10	53.05 ± 0.05	3.76 ± 0.12	0.95	0.04
	c-C$_3$H$_2$	1.23 ± 0.10	52.98 ± 0.12	3.15 ± 0.29	0.37	0.04
	CN	0.96 ± 0.10	52.63 ± 0.17	3.24 ± 0.34	0.28	0.05
	HC^{15}N	1.28 ± 0.11	53.50 ± 0.20	4.78 ± 0.52	0.25	0.04
	HN^{13}C	1.77 ± 0.11	53.23 ± 0.11	3.79 ± 0.31	0.44	0.04
AGAL035.042−00.472	C^{18}O	2.22 ± 0.05	50.79 ± 0.02	1.48 ± 0.04	1.41	0.03
	H^{13}CO$^+$	1.30 ± 0.05	51.00 ± 0.03	1.64 ± 0.09	0.74	0.03
	c-C$_3$H$_2$	1.17 ± 0.05	51.01 ± 0.03	1.61 ± 0.08	0.68	0.03
	CN	0.45 ± 0.10	51.46 ± 0.22	2.08 ± 0.51	0.20	0.06
	HN^{13}C	0.50 ± 0.05	51.13 ± 0.10	1.82 ± 0.21	0.26	0.03
AGAL035.132−00.744	C^{18}O	5.02 ± 0.53	33.21 ± 0.22	4.38 ± 0.32	1.08	0.03
	H^{13}CO$^+$	9.31 ± 0.12	33.58 ± 0.03	4.06 ± 0.06	2.16	0.05
	c-C$_3$H$_2$	2.42 ± 0.12	33.84 ± 0.11	4.55 ± 0.24	0.50	0.05
	CN	2.33 ± 0.13	34.61 ± 0.11	3.92 ± 0.27	0.56	0.06
	HC^{15}N	1.73 ± 0.12	34.77 ± 0.15	4.32 ± 0.33	0.38	0.05
	HN^{13}C	4.51 ± 0.12	34.26 ± 0.06	4.24 ± 0.12	1.00	0.05
AGAL035.144−00.754	C^{18}O	4.62 ± 0.08	32.47 ± 0.02	3.13 ± 0.06	1.38	0.03
	H^{13}CO$^+$	6.14 ± 0.18	32.40 ± 0.05	3.35 ± 0.12	1.72	0.05
	c-C$_3$H$_2$	1.87 ± 0.13	32.16 ± 0.09	2.66 ± 0.21	0.66	0.04
	CN	0.78 ± 0.12	35.85 ± 0.12	2.02 ± 0.37	0.36	0.05
	HC^{15}N	1.19 ± 0.12	33.02 ± 0.32	5.80 ± 0.72	0.19	0.04
	HN^{13}C	1.70 ± 0.19	35.32 ± 0.15	2.92 ± 0.34	0.55	0.04
AGAL035.197−00.742	C^{18}O	13.49 ± 0.61	33.85 ± 0.04	4.25 ± 0.18	2.98	0.08
	H^{13}CO$^+$	11.66 ± 0.13	33.90 ± 0.02	4.32 ± 0.06	2.53	0.05
	c-C$_3$H$_2$	4.24 ± 0.12	34.04 ± 0.05	3.28 ± 0.11	1.22	0.05
	CN	2.98 ± 0.19	33.83 ± 0.10	3.34 ± 0.26	0.84	0.10
	HC^{15}N	2.68 ± 0.14	33.96 ± 0.11	4.40 ± 0.28	0.57	0.05
	HN^{13}C	5.83 ± 0.12	33.99 ± 0.03	3.40 ± 0.08	1.61	0.05
AGAL035.297−00.897	C^{18}O	3.60 ± 0.14	37.31 ± 0.04	1.91 ± 0.09	1.77	0.09
	H^{13}CO$^+$	1.55 ± 0.06	37.32 ± 0.03	1.37 ± 0.07	1.07	0.04
	c-C$_3$H$_2$	1.59 ± 0.06	37.25 ± 0.02	1.19 ± 0.05	1.26	0.04
	CN	0.54 ± 0.17	37.83 ± 0.20	1.31 ± 0.55	0.39	0.13
	HN^{13}C	0.83 ± 0.06	37.53 ± 0.05	1.42 ± 0.12	0.55	0.04
AGAL035.457−00.179	C^{18}O	5.08 ± 0.08	64.66 ± 0.03	3.36 ± 0.06	1.42	0.04
	H^{13}CO$^+$	1.22 ± 0.09	64.29 ± 0.12	3.26 ± 0.30	0.35	0.04
	c-C$_3$H$_2$	0.52 ± 0.09	64.91 ± 0.35	4.13 ± 0.84	0.12	0.04
	HN^{13}C	0.38 ± 0.08	63.90 ± 0.29	2.64 ± 0.75	0.14	0.04
AGAL035.466+00.141	C^{18}O	9.46 ± 0.11	77.23 ± 0.01	2.37 ± 0.03	3.75	0.04
	HCO	0.28 ± 0.03	77.69 ± 0.23	4.24 ± 0.73	0.06	0.01
	H^{13}CO$^+$	2.48 ± 0.06	77.07 ± 0.03	2.77 ± 0.07	0.84	0.03
	c-C$_3$H$_2$	1.73 ± 0.06	77.16 ± 0.06	3.26 ± 0.13	0.50	0.03
	CN	1.36 ± 0.09	77.13 ± 0.09	2.72 ± 0.18	0.47	0.05
	HC^{15}N	0.49 ± 0.06	77.02 ± 0.15	2.47 ± 0.39	0.19	0.03
	HN^{13}C	1.81 ± 0.06	77.09 ± 0.04	2.59 ± 0.10	0.66	0.03
AGAL035.484−00.287	C^{18}O	3.24 ± 0.07	45.50 ± 0.01	1.54 ± 0.04	1.98	0.04
	H^{13}CO$^+$	1.48 ± 0.10	45.18 ± 0.06	1.95 ± 0.20	0.71	0.05
	c-C$_3$H$_2$	1.59 ± 0.08	45.49 ± 0.04	1.73 ± 0.10	0.86	0.05
	CN	0.32 ± 0.06	45.54 ± 0.08	0.74 ± 0.15	0.40	0.06
	HN^{13}C	1.14 ± 0.08	45.43 ± 0.06	1.76 ± 0.15	0.60	0.05
AGAL035.579+00.007	C^{18}O	7.08 ± 0.12	52.77 ± 0.03	3.94 ± 0.08	1.69	0.04
	H^{13}CO$^+$	2.04 ± 0.13	53.22 ± 0.10	3.50 ± 0.28	0.55	0.05
	c-C$_3$H$_2$	0.53 ± 0.12	53.01 ± 0.15	1.98 ± 0.37	0.25	0.04
	CN	0.72 ± 0.13	52.79 ± 0.33	3.54 ± 0.73	0.19	0.07
	HN^{13}C	0.96 ± 0.10	52.83 ± 0.15	2.84 ± 0.34	0.32	0.05
AGAL035.579−00.031	C^{18}O	15.13 ± 0.08	52.04 ± 0.01	4.76 ± 0.03	2.98	0.03
	HCO	0.30 ± 0.03	52.93 ± 0.26	4.81 ± 0.63	0.06	0.01
	H^{13}CO$^+$	2.94 ± 0.08	52.55 ± 0.07	5.26 ± 0.18	0.53	0.03
	c-C$_3$H$_2$	1.76 ± 0.07	52.69 ± 0.12	5.62 ± 0.28	0.29	0.02
	CN	1.28 ± 0.12	53.10 ± 0.26	5.22 ± 0.57	0.23	0.05
	HC^{15}N	0.68 ± 0.09	53.73 ± 0.30	4.73 ± 0.80	0.14	0.03
	HN^{13}C	0.76 ± 0.07	52.35 ± 0.16	3.87 ± 0.43	0.18	0.03
AGAL035.681−00.176	C^{18}O	2.06 ± 0.12	27.95 ± 0.05	1.74 ± 0.13	1.11	0.07
	H^{13}CO$^+$	1.49 ± 0.07	27.87 ± 0.03	1.40 ± 0.08	1.00	0.05

Table B.3: continued.

ATLASGAL Name	Line	Area (K km s^{-1})	v_{LRS} (km s^{-1})	Δv (km s^{-1})	T_{MB} (K)	rms (K)
	c-C$_3$H$_2$	1.32 ± 0.06	27.93 ± 0.03	1.30 ± 0.08	0.95	0.04
	CN	0.53 ± 0.19	27.72 ± 0.17	1.15 ± 0.64	0.43	0.13
	HN^{13}C	0.97 ± 0.06	27.96 ± 0.05	1.38 ± 0.10	0.66	0.04
AGAL035.794−00.174	C^{18}O	6.54 ± 0.17	61.17 ± 0.04	2.84 ± 0.09	2.16	0.09
	H^{13}CO$^+$	2.22 ± 0.12	61.42 ± 0.10	4.06 ± 0.28	0.51	0.04
	c-C$_3$H$_2$	1.29 ± 0.08	61.47 ± 0.08	2.83 ± 0.20	0.43	0.04
	CN	1.30 ± 0.29	59.97 ± 0.55	4.66 ± 1.03	0.26	0.13
	HC^{15}N	0.39 ± 0.13	62.14 ± 0.47	3.54 ± 1.75	0.10	0.04
	HN^{13}C	1.33 ± 0.09	61.63 ± 0.10	2.75 ± 0.20	0.46	0.05
AGAL036.794−00.204	C^{18}O	8.62 ± 0.07	78.13 ± 0.01	2.04 ± 0.02	3.97	0.04
	H^{13}CO$^+$	0.86 ± 0.09	78.15 ± 0.11	2.11 ± 0.25	0.38	0.05
	c-C$_3$H$_2$	0.73 ± 0.08	78.27 ± 0.10	1.88 ± 0.24	0.36	0.05
	CN	0.42 ± 0.09	78.53 ± 0.22	1.96 ± 0.46	0.20	0.06
	HN^{13}C	0.41 ± 0.07	78.24 ± 0.09	1.16 ± 0.26	0.34	0.05
AGAL036.826−00.039	C^{18}O	8.56 ± 0.13	60.47 ± 0.02	2.35 ± 0.04	3.42	0.08
	H^{13}CO$^+$	1.57 ± 0.08	60.44 ± 0.05	1.91 ± 0.12	0.77	0.04
	c-C$_3$H$_2$	1.23 ± 0.07	60.43 ± 0.05	1.91 ± 0.12	0.60	0.04
	HN^{13}C	0.69 ± 0.08	60.66 ± 0.11	1.91 ± 0.23	0.34	0.05
AGAL036.839−00.022	C^{18}O	6.92 ± 0.23	57.48 ± 0.03	2.12 ± 0.08	3.06	0.09
	H^{13}CO$^+$	2.19 ± 0.11	58.31 ± 0.10	4.05 ± 0.23	0.51	0.05
	c-C$_3$H$_2$	1.90 ± 0.09	58.14 ± 0.10	3.84 ± 0.20	0.47	0.04
	CN	0.76 ± 0.22	57.42 ± 0.35	2.08 ± 0.62	0.34	0.15
	HN^{13}C	1.63 ± 0.11	58.73 ± 0.17	4.66 ± 0.33	0.33	0.04
AGAL036.878−00.474	C^{18}O	3.55 ± 0.13	61.20 ± 0.07	3.81 ± 0.17	0.88	0.06
	H^{13}CO$^+$	1.57 ± 0.09	61.15 ± 0.09	3.15 ± 0.22	0.47	0.04
	c-C$_3$H$_2$	0.81 ± 0.10	60.80 ± 0.23	4.05 ± 0.64	0.19	0.04
	HN^{13}C	0.80 ± 0.08	61.56 ± 0.14	2.75 ± 0.31	0.27	0.04
AGAL036.899−00.409	C^{18}O	8.55 ± 0.16	80.27 ± 0.03	2.95 ± 0.06	2.72	0.09
	HCO	0.20 ± 0.04	60.49 ± 0.37	3.72 ± 0.92	0.05	0.02
	H^{13}CO$^+$	1.58 ± 0.08	79.91 ± 0.06	2.41 ± 0.15	0.62	0.04
	c-C$_3$H$_2$	1.06 ± 0.08	79.90 ± 0.10	2.61 ± 0.21	0.38	0.04
	HN^{13}C	0.96 ± 0.10	80.04 ± 0.12	2.49 ± 0.31	0.36	0.05
AGAL037.031−00.039	C^{18}O	6.39 ± 0.04	80.59 ± 0.01	1.85 ± 0.01	3.24	0.03
	H^{13}CO$^+$	1.37 ± 0.05	80.49 ± 0.05	2.31 ± 0.10	0.56	0.03
	c-C$_3$H$_2$	0.96 ± 0.05	80.53 ± 0.05	2.02 ± 0.12	0.45	0.03
	CN	0.70 ± 0.06	80.50 ± 0.09	2.16 ± 0.24	0.30	0.04
	HN^{13}C	1.02 ± 0.06	80.48 ± 0.07	2.37 ± 0.17	0.41	0.03
AGAL037.469−00.102	C^{18}O	5.08 ± 0.05	57.90 ± 0.01	3.02 ± 0.03	1.58	0.02
	HCO	0.12 ± 0.02	57.98 ± 0.18	2.19 ± 0.35	0.05	0.01
	H^{13}CO$^+$	1.09 ± 0.07	58.59 ± 0.09	3.04 ± 0.24	0.34	0.03
	c-C$_3$H$_2$	0.66 ± 0.06	57.94 ± 0.15	3.11 ± 0.30	0.20	0.03
	CN	0.50 ± 0.08	58.45 ± 0.19	2.60 ± 0.54	0.18	0.04
	HN^{13}C	0.31 ± 0.05	58.52 ± 0.11	1.57 ± 0.30	0.18	0.03
AGAL037.498+00.531	C^{18}O	7.40 ± 0.05	10.55 ± 0.01	3.25 ± 0.02	2.14	0.02
	HCO	0.11 ± 0.02	10.25 ± 0.18	2.20 ± 0.37	0.05	0.01
	H^{13}CO$^+$	1.17 ± 0.06	10.76 ± 0.09	3.29 ± 0.19	0.34	0.03
	c-C$_3$H$_2$	0.66 ± 0.07	10.07 ± 0.18	3.41 ± 0.45	0.18	0.03
	CN	0.52 ± 0.07	10.33 ± 0.20	3.03 ± 0.47	0.16	0.04
	HN^{13}C	0.63 ± 0.06	11.28 ± 0.17	3.33 ± 0.40	0.18	0.03
AGAL037.554+00.201	C^{18}O	13.35 ± 0.15	85.30 ± 0.02	3.54 ± 0.05	3.54	0.07
	H^{13}CO$^+$	4.93 ± 0.17	85.29 ± 0.07	4.22 ± 0.17	1.10	0.07
	c-C$_3$H$_2$	1.85 ± 0.12	85.33 ± 0.11	3.53 ± 0.26	0.49	0.05
	CN	2.07 ± 0.20	85.22 ± 0.17	3.58 ± 0.42	0.54	0.09
	HC^{15}N	0.99 ± 0.16	84.84 ± 0.34	4.91 ± 1.06	0.19	0.05
	HN^{13}C	0.56 ± 0.21	88.89 ± 0.57	3.43 ± 1.33	0.15	0.04
AGAL037.874−00.399	C^{18}O	12.36 ± 0.10	61.30 ± 0.03	6.92 ± 0.06	1.68	0.03
	HCO	0.17 ± 0.03	60.55 ± 0.38	3.62 ± 0.86	0.04	0.01
	H^{13}CO$^+$	3.86 ± 0.09	60.45 ± 0.06	5.06 ± 0.13	0.72	0.03
	c-C$_3$H$_2$	1.63 ± 0.08	61.04 ± 0.10	4.13 ± 0.25	0.37	0.03
	CN	1.42 ± 0.12	60.81 ± 0.25	5.78 ± 0.51	0.23	0.05
	HC^{15}N	0.57 ± 0.09	61.34 ± 0.39	5.15 ± 0.92	0.10	0.04
	HN^{13}C	1.10 ± 0.08	61.01 ± 0.20	5.48 ± 0.52	0.19	0.03
AGAL038.119−00.229	C^{18}O	5.57 ± 0.14	82.91 ± 0.01	2.24 ± 0.03	2.34	0.02
	H^{13}CO$^+$	1.17 ± 0.05	83.04 ± 0.05	2.32 ± 0.12	0.48	0.03
	c-C$_3$H$_2$	0.60 ± 0.06	83.17 ± 0.17	3.38 ± 0.38	0.17	0.03
	CN	0.76 ± 0.07	82.96 ± 0.09	2.25 ± 0.27	0.32	0.04
	HN^{13}C	0.78 ± 0.05	83.16 ± 0.08	2.42 ± 0.20	0.30	0.03
AGAL038.354−00.952	C^{18}O	2.46 ± 0.04	16.52 ± 0.02	2.38 ± 0.04	0.97	0.02
	H^{13}CO$^+$	1.63 ± 0.05	16.73 ± 0.02	1.78 ± 0.07	0.86	0.03
	c-C$_3$H$_2$	1.60 ± 0.04	16.92 ± 0.02	1.44 ± 0.04	1.04	0.02
	CN	0.58 ± 0.05	16.87 ± 0.04	1.09 ± 0.11	0.50	0.04
	HC^{15}N	0.15 ± 0.05	17.06 ± 0.33	1.96 ± 0.76	0.07	0.03
	HN^{13}C	1.07 ± 0.04	16.99 ± 0.03	1.32 ± 0.06	0.77	0.03
AGAL038.371−00.149	C^{18}O	10.37 ± 0.04	81.11 ± 0.01	2.62 ± 0.01	3.72	0.02
	H^{13}CO$^+$	0.98 ± 0.05	81.22 ± 0.07	2.48 ± 0.15	0.37	0.03

Table B.3: continued.

ATLASGAL Name	Line	Area (K km s^{-1})	v_{LRS} (km s^{-1})	Δv (km s^{-1})	T_{MB} (K)	rms (K)
	c-C$_3$H$_2$	0.82 ± 0.05	81.22 ± 0.08	2.47 ± 0.19	0.31	0.03
	CN	0.51 ± 0.06	81.11 ± 0.14	2.28 ± 0.33	0.21	0.04
	HN^{13}C	0.73 ± 0.05	81.63 ± 0.08	2.34 ± 0.20	0.29	0.03
AGAL038.957−00.466	C^{18}O	12.40 ± 0.18	42.02 ± 0.02	2.85 ± 0.04	4.08	0.10
	H^{13}CO$^+$	3.01 ± 0.11	42.17 ± 0.05	2.37 ± 0.10	1.19	0.06
	c-C$_3$H$_2$	2.79 ± 0.10	42.19 ± 0.04	2.08 ± 0.09	1.26	0.06
	CN	0.95 ± 0.22	41.73 ± 0.26	2.01 ± 0.40	0.44	0.16
	HN^{13}C	1.29 ± 0.11	42.37 ± 0.09	2.19 ± 0.22	0.56	0.06
AGAL039.048−00.880	C^{18}O	3.49 ± 0.18	71.62 ± 0.05	1.92 ± 0.12	1.70	0.10
	H^{13}CO$^+$	0.98 ± 0.10	71.45 ± 0.09	1.73 ± 0.19	0.54	0.06
	c-C$_3$H$_2$	1.99 ± 0.10	71.25 ± 0.05	1.98 ± 0.13	0.94	0.06
	CN	0.62 ± 0.20	71.20 ± 0.22	1.17 ± 0.38	0.50	0.19
	HN^{13}C	1.06 ± 0.09	71.41 ± 0.07	1.64 ± 0.15	0.61	0.06
AGAL039.099+00.492	C^{18}O	3.98 ± 0.08	22.80 ± 0.03	2.99 ± 0.07	1.25	0.04
	H^{13}CO$^+$	1.29 ± 0.13	23.08 ± 0.15	2.91 ± 0.34	0.42	0.06
	CN	0.78 ± 0.15	23.09 ± 0.47	5.11 ± 1.23	0.14	0.06
	HN^{13}C	0.44 ± 0.12	23.89 ± 0.40	2.68 ± 0.87	0.15	0.06
AGAL039.903−01.349	C^{18}O	3.28 ± 0.13	48.14 ± 0.03	1.74 ± 0.08	1.77	0.08
	HCO	0.22 ± 0.03	48.93 ± 0.16	2.06 ± 0.35	0.10	0.02
	H^{13}CO$^+$	0.48 ± 0.09	48.31 ± 0.15	1.56 ± 0.31	0.29	0.06
	c-C$_3$H$_2$	0.79 ± 0.10	48.31 ± 0.12	2.14 ± 0.34	0.35	0.05
	CN	1.58 ± 0.22	−6.79 ± 0.13	1.93 ± 0.30	0.77	0.15
AGAL040.283−00.219	C^{18}O	10.48 ± 0.20	74.02 ± 0.03	3.52 ± 0.08	2.80	0.09
	H^{13}CO$^+$	5.87 ± 0.12	73.68 ± 0.04	3.84 ± 0.09	1.44	0.05
	c-C$_3$H$_2$	1.62 ± 0.12	74.24 ± 0.18	4.75 ± 0.44	0.32	0.05
	CN	3.54 ± 0.42	18.54 ± 0.30	5.31 ± 0.77	0.63	0.16
	HC^{15}N	0.92 ± 0.12	73.84 ± 0.29	4.34 ± 0.64	0.20	0.05
	HN^{13}C	2.05 ± 0.11	73.88 ± 0.10	3.67 ± 0.24	0.53	0.05
AGAL041.049−00.247	C^{18}O	4.16 ± 0.07	66.36 ± 0.02	2.58 ± 0.05	1.52	0.04
	H^{13}CO$^+$	1.59 ± 0.14	65.85 ± 0.14	3.16 ± 0.37	0.47	0.06
	c-C$_3$H$_2$	1.53 ± 0.10	65.96 ± 0.08	2.23 ± 0.17	0.65	0.06
	CN	0.76 ± 0.10	65.76 ± 0.12	1.99 ± 0.30	0.36	0.06
	HN^{13}C	1.42 ± 0.13	66.01 ± 0.10	2.28 ± 0.27	0.58	0.07
AGAL041.347−00.136	C^{18}O	4.50 ± 0.07	12.90 ± 0.02	2.26 ± 0.04	1.87	0.04
	H^{13}CO$^+$	0.90 ± 0.12	12.90 ± 0.13	2.11 ± 0.39	0.40	0.06
	c-C$_3$H$_2$	0.51 ± 0.09	13.11 ± 0.13	1.47 ± 0.30	0.32	0.06
	CN	0.24 ± 0.09	12.72 ± 0.22	1.48 ± 0.78	0.15	0.05
	HN^{13}C	0.58 ± 0.09	13.63 ± 0.17	2.00 ± 0.33	0.27	0.06
AGAL042.098+00.351	C^{18}O	2.59 ± 0.09	20.78 ± 0.06	3.51 ± 0.14	0.69	0.04
	H^{13}CO$^+$	1.02 ± 0.21	21.36 ± 0.81	8.61 ± 2.29	0.11	0.05
	c-C$_3$H$_2$	0.52 ± 0.13	20.83 ± 0.51	4.25 ± 1.34	0.12	0.05
AGAL043.038−00.452	C^{18}O	11.37 ± 0.06	57.64 ± 0.01	3.24 ± 0.02	3.30	0.03
	HCO	0.13 ± 0.03	58.38 ± 0.41	3.29 ± 0.91	0.04	0.01
	H^{13}CO$^+$	3.63 ± 0.07	57.65 ± 0.04	3.82 ± 0.09	0.89	0.03
	c-C$_3$H$_2$	1.84 ± 0.07	57.85 ± 0.08	4.02 ± 0.21	0.43	0.03
	CN	1.25 ± 0.10	57.53 ± 0.14	3.68 ± 0.33	0.32	0.05
	HC^{15}N	0.62 ± 0.08	57.98 ± 0.26	4.04 ± 0.54	0.14	0.03
	HN^{13}C	1.31 ± 0.06	57.77 ± 0.09	3.56 ± 0.19	0.34	0.03
AGAL043.148+00.014	C^{18}O	4.27 ± 0.08	10.70 ± 0.05	5.49 ± 0.12	0.73	0.03
	HCO	0.45 ± 0.04	9.19 ± 0.45	7.82 ± 0.93	0.05	0.01
	H^{13}CO$^+$	0.91 ± 0.08	10.11 ± 0.21	4.84 ± 0.51	0.18	0.03
	c-C$_3$H$_2$	2.73 ± 0.12	9.65 ± 0.15	7.30 ± 0.38	0.35	0.03
	CN	0.75 ± 0.11	11.23 ± 0.38	4.64 ± 0.67	0.15	0.05
	HC^{15}N	0.47 ± 0.11	10.32 ± 0.50	4.48 ± 1.64	0.10	0.03
AGAL043.164−00.029	C^{18}O	10.69 ± 0.11	15.40 ± 0.03	7.16 ± 0.08	1.40	0.04
	HCO	0.45 ± 0.05	12.99 ± 0.63	11.43 ± 1.33	0.04	0.01
	H^{13}CO$^+$	3.42 ± 0.11	16.02 ± 0.11	7.28 ± 0.29	0.44	0.03
	c-C$_3$H$_2$	1.30 ± 0.10	11.33 ± 0.18	5.50 ± 0.55	0.22	0.03
	CN	0.66 ± 0.11	15.85 ± 0.22	2.77 ± 0.56	0.23	0.06
	HC^{15}N	0.95 ± 0.09	16.18 ± 0.26	5.43 ± 0.54	0.17	0.03
	HN^{13}C	0.71 ± 0.09	16.93 ± 0.36	5.90 ± 0.90	0.11	0.03
AGAL043.166+00.011	C^{18}O	33.53 ± 0.91	4.36 ± 0.12	9.06 ± 0.23	3.48	0.07
	H^{13}CO$^+$	25.65 ± 0.50	4.36 ± 0.09	9.89 ± 0.20	2.44	0.05
	c-C$_3$H$_2$	0.99 ± 0.14	9.73 ± 0.29	3.81 ± 0.63	0.24	0.05
	CN	0.68 ± 0.17	11.02 ± 0.31	2.27 ± 0.69	0.28	0.10
	HC^{15}N	2.78 ± 0.48	12.02 ± 0.46	7.05 ± 1.10	0.37	0.05
	HN^{13}C	0.91 ± 0.23	13.10 ± 0.26	3.72 ± 0.66	0.23	0.05
AGAL043.178−00.011	C^{18}O	4.18 ± 0.15	3.80 ± 0.08	4.38 ± 0.16	0.90	0.02
	HCO	0.92 ± 0.04	6.71 ± 0.24	11.09 ± 0.55	0.08	0.01
	H^{13}CO$^+$	1.56 ± 0.11	6.38 ± 0.39	10.36 ± 0.80	0.14	0.03
	c-C$_3$H$_2$	1.86 ± 0.28	10.97 ± 0.50	6.98 ± 0.83	0.25	0.04
	CN	0.46 ± 0.11	11.64 ± 0.37	3.24 ± 0.67	0.13	0.04
	HC^{15}N	0.50 ± 0.12	5.02 ± 0.64	5.69 ± 1.73	0.08	0.03
	HN^{13}C	0.58 ± 0.09	9.84 ± 0.83	9.78 ± 1.65	0.06	0.03
AGAL043.179−00.519	C^{18}O	16.11 ± 0.04	57.93 ± 0.00	3.42 ± 0.01	4.43	0.02

Table B.3: continued.

ATLASGAL Name	Line	Area (K km s^{-1})	v_{LRS} (km s^{-1})	Δv (km s^{-1})	T_{MB} (K)	rms (K)
	HCO	0.30 ± 0.03	58.17 ± 0.17	3.62 ± 0.34	0.08	0.01
	H^{13}CO$^+$	3.13 ± 0.07	58.03 ± 0.04	3.31 ± 0.09	0.89	0.03
	c-C$_3$H$_2$	1.96 ± 0.08	57.73 ± 0.08	4.38 ± 0.20	0.42	0.03
	CN	1.85 ± 0.07	57.80 ± 0.07	3.53 ± 0.16	0.49	0.04
	HC^{15}N	0.79 ± 0.08	58.08 ± 0.21	4.25 ± 0.44	0.17	0.03
	HN^{13}C	1.78 ± 0.07	58.17 ± 0.06	3.30 ± 0.16	0.51	0.03
AGAL043.236−00.047	C^{18}O	11.17 ± 0.06	6.68 ± 0.02	6.80 ± 0.04	1.54	0.02
	HCO	0.18 ± 0.04	7.38 ± 0.79	5.97 ± 1.45	0.03	0.01
	H^{13}CO$^+$	2.66 ± 0.09	6.50 ± 0.10	5.94 ± 0.22	0.42	0.03
	c-C$_3$H$_2$	1.10 ± 0.08	5.92 ± 0.22	5.91 ± 0.48	0.17	0.03
	CN	0.82 ± 0.09	6.44 ± 0.29	5.10 ± 0.65	0.15	0.04
	HC^{15}N	0.49 ± 0.08	6.60 ± 0.45	5.03 ± 0.85	0.09	0.03
	HN^{13}C	0.92 ± 0.08	7.19 ± 0.21	5.24 ± 0.61	0.16	0.03
AGAL043.306−00.212	C^{18}O	8.77 ± 0.04	59.68 ± 0.01	2.91 ± 0.02	2.83	0.02
	H^{13}CO$^+$	3.11 ± 0.06	59.45 ± 0.03	2.73 ± 0.06	1.07	0.03
	c-C$_3$H$_2$	1.16 ± 0.05	59.74 ± 0.06	2.55 ± 0.14	0.43	0.03
	CN	1.33 ± 0.06	59.54 ± 0.06	2.47 ± 0.14	0.51	0.04
	HC^{15}N	0.48 ± 0.06	59.40 ± 0.17	2.79 ± 0.49	0.16	0.03
	HN^{13}C	2.20 ± 0.06	59.64 ± 0.03	2.55 ± 0.08	0.81	0.03
AGAL043.794−00.127	C^{18}O	16.24 ± 0.07	43.92 ± 0.01	5.36 ± 0.03	2.85	0.03
	HCO	0.12 ± 0.02	44.16 ± 0.32	3.38 ± 0.66	0.03	0.01
	H^{13}CO$^+$	5.71 ± 0.09	43.95 ± 0.04	5.70 ± 0.11	0.94	0.03
	c-C$_3$H$_2$	1.53 ± 0.09	43.99 ± 0.19	6.70 ± 0.47	0.21	0.03
	CN	1.52 ± 0.11	43.67 ± 0.21	5.85 ± 0.54	0.24	0.04
	HC^{15}N	0.96 ± 0.08	43.78 ± 0.22	5.19 ± 0.51	0.17	0.03
	HN^{13}C	1.53 ± 0.08	44.09 ± 0.12	5.08 ± 0.29	0.28	0.03
AGAL043.889−00.786	C^{18}O	14.67 ± 0.07	54.28 ± 0.01	3.61 ± 0.02	3.82	0.03
	HCO	0.37 ± 0.03	54.29 ± 0.14	3.84 ± 0.30	0.09	0.01
	H^{13}CO$^+$	3.27 ± 0.07	53.87 ± 0.04	3.54 ± 0.10	0.87	0.03
	c-C$_3$H$_2$	1.96 ± 0.07	53.82 ± 0.07	3.96 ± 0.18	0.47	0.03
	CN	1.42 ± 0.09	54.22 ± 0.12	3.98 ± 0.30	0.34	0.04
	HC^{15}N	0.63 ± 0.11	54.00 ± 0.56	6.91 ± 1.70	0.09	0.03
	HN^{13}C	1.47 ± 0.07	54.22 ± 0.08	3.63 ± 0.21	0.38	0.03
AGAL043.994−00.012	C^{18}O	6.09 ± 0.04	65.32 ± 0.01	2.11 ± 0.02	2.71	0.02
	H^{13}CO$^+$	1.99 ± 0.05	65.53 ± 0.02	1.81 ± 0.05	1.03	0.03
	c-C$_3$H$_2$	1.05 ± 0.04	65.42 ± 0.04	1.93 ± 0.09	0.51	0.02
	CN	1.02 ± 0.06	65.43 ± 0.04	1.65 ± 0.11	0.58	0.04
	HC^{15}N	0.30 ± 0.06	65.26 ± 0.33	2.91 ± 0.73	0.10	0.03
	HN^{13}C	1.13 ± 0.04	65.53 ± 0.03	1.80 ± 0.08	0.59	0.03
AGAL044.291+00.034	C^{18}O	6.02 ± 0.04	56.69 ± 0.01	2.28 ± 0.02	2.48	0.02
	H^{13}CO$^+$	1.73 ± 0.06	56.70 ± 0.05	2.88 ± 0.11	0.57	0.03
	c-C$_3$H$_2$	0.76 ± 0.05	56.62 ± 0.07	2.29 ± 0.17	0.31	0.03
	CN	0.64 ± 0.07	57.02 ± 0.15	2.75 ± 0.32	0.22	0.04
	HC^{15}N	0.14 ± 0.05	58.69 ± 0.21	1.29 ± 0.60	0.10	0.03
	HN^{13}C	0.76 ± 0.05	56.95 ± 0.07	2.28 ± 0.15	0.31	0.03
AGAL044.309+00.041	C^{18}O	5.96 ± 0.05	56.05 ± 0.01	3.17 ± 0.03	1.77	0.02
	H^{13}CO$^+$	1.34 ± 0.07	55.78 ± 0.08	3.32 ± 0.19	0.38	0.03
	c-C$_3$H$_2$	0.65 ± 0.04	55.41 ± 0.08	2.29 ± 0.17	0.27	0.02
	CN	0.44 ± 0.09	54.46 ± 0.54	4.82 ± 1.09	0.09	0.04
	HN^{13}C	0.63 ± 0.06	55.55 ± 0.14	3.02 ± 0.34	0.20	0.03
AGAL044.422+00.537	C^{18}O	1.27 ± 0.07	−51.82 ± 0.07	2.54 ± 0.15	0.47	0.04
	HCO	0.23 ± 0.04	−51.29 ± 0.46	4.30 ± 0.77	0.05	0.02
	c-C$_3$H$_2$	0.77 ± 0.13	−52.28 ± 0.34	4.11 ± 0.95	0.18	0.05
AGAL045.071+00.132	C^{18}O	8.56 ± 0.89	58.94 ± 0.04	5.07 ± 0.18	1.59	0.03
	HCO	0.32 ± 0.05	58.33 ± 0.50	6.01 ± 1.18	0.05	0.02
	H^{13}CO$^+$	3.47 ± 0.16	58.41 ± 0.15	6.48 ± 0.36	0.50	0.05
	c-C$_3$H$_2$	1.30 ± 0.12	59.00 ± 0.24	5.33 ± 0.57	0.23	0.04
	CN	1.07 ± 0.14	59.82 ± 0.29	4.87 ± 0.85	0.21	0.05
	HC^{15}N	1.20 ± 0.13	59.31 ± 0.27	4.96 ± 0.67	0.23	0.05
	HN^{13}C	0.94 ± 0.14	58.82 ± 0.47	6.62 ± 1.13	0.16	0.05
AGAL045.096+00.131	C^{18}O	5.84 ± 0.07	58.61 ± 0.01	2.60 ± 0.04	2.12	0.04
	H^{13}CO$^+$	1.38 ± 0.11	58.52 ± 0.09	2.37 ± 0.23	0.55	0.06
	c-C$_3$H$_2$	0.67 ± 0.13	58.99 ± 0.32	3.44 ± 0.94	0.18	0.05
	CN	0.59 ± 0.14	58.34 ± 0.31	3.32 ± 1.20	0.17	0.06
	HN^{13}C	0.55 ± 0.09	58.95 ± 0.22	2.44 ± 0.43	0.21	0.05
AGAL045.121+00.131	C^{18}O	8.79 ± 0.08	58.97 ± 0.02	3.89 ± 0.04	2.12	0.04
	HCO	0.21 ± 0.05	60.20 ± 0.41	3.54 ± 0.88	0.06	0.01
	H^{13}CO$^+$	3.05 ± 0.11	58.96 ± 0.06	3.35 ± 0.13	0.86	0.05
	c-C$_3$H$_2$	1.86 ± 0.11	59.31 ± 0.15	5.00 ± 0.36	0.35	0.04
	CN	1.04 ± 0.14	59.19 ± 0.36	5.01 ± 0.69	0.20	0.06
	HC^{15}N	0.57 ± 0.12	59.04 ± 0.37	3.71 ± 0.93	0.14	0.05
	HN^{13}C	1.04 ± 0.11	58.94 ± 0.24	4.72 ± 0.62	0.21	0.04
AGAL045.454+00.061	C^{18}O	6.30 ± 0.21	58.43 ± 0.05	4.80 ± 0.13	1.23	0.04
	HCO	0.32 ± 0.07	57.42 ± 0.79	6.83 ± 1.79	0.04	0.02
	H^{13}CO$^+$	1.28 ± 0.11	58.59 ± 0.16	3.84 ± 0.38	0.31	0.04

Table B.3: continued.

ATLASGAL Name	Line	Area (K km s^{-1})	v_{LRS} (km s^{-1})	Δv (km s^{-1})	T_{MB} (K)	rms (K)
	c-C$_3$H$_2$	1.66 ± 0.12	57.99 ± 0.20	5.52 ± 0.47	0.28	0.04
	CN	0.82 ± 0.11	58.22 ± 0.19	2.93 ± 0.45	0.26	0.06
	HC^{15}N	0.39 ± 0.10	58.90 ± 0.46	3.34 ± 0.92	0.11	0.05
	HN^{13}C	0.80 ± 0.10	58.63 ± 0.24	3.76 ± 0.53	0.20	0.04
AGAL045.466+00.046	C^{18}O	10.58 ± 0.11	61.93 ± 0.02	4.83 ± 0.07	2.06	0.04
	H^{13}CO$^+$	6.39 ± 0.12	62.33 ± 0.04	4.34 ± 0.09	1.38	0.05
	c-C$_3$H$_2$	1.81 ± 0.12	62.03 ± 0.14	4.40 ± 0.39	0.39	0.04
	CN	1.53 ± 0.11	62.20 ± 0.13	3.70 ± 0.30	0.39	0.05
	HC^{15}N	1.06 ± 0.13	62.20 ± 0.33	5.14 ± 0.74	0.19	0.05
	HN^{13}C	2.95 ± 0.11	62.19 ± 0.08	4.24 ± 0.18	0.65	0.05
AGAL045.474+00.134	C^{18}O	9.66 ± 0.08	61.63 ± 0.01	3.74 ± 0.03	2.43	0.04
	HCO	0.42 ± 0.05	61.22 ± 0.20	3.47 ± 0.45	0.11	0.02
	H^{13}CO$^+$	1.79 ± 0.11	61.47 ± 0.09	3.02 ± 0.24	0.56	0.05
	c-C$_3$H$_2$	2.20 ± 0.12	61.64 ± 0.11	4.27 ± 0.29	0.48	0.05
	CN	1.41 ± 0.10	62.13 ± 0.13	3.45 ± 0.27	0.38	0.05
	HC^{15}N	0.69 ± 0.11	61.97 ± 0.32	3.67 ± 0.63	0.18	0.05
	HN^{13}C	0.87 ± 0.09	61.13 ± 0.16	2.95 ± 0.31	0.28	0.05
AGAL045.493+00.126	C^{18}O	5.72 ± 0.17	62.42 ± 0.03	2.54 ± 0.07	2.11	0.04
	H^{13}CO$^+$	3.30 ± 0.15	61.12 ± 0.12	4.92 ± 0.23	0.63	0.06
	c-C$_3$H$_2$	1.93 ± 0.14	61.46 ± 0.18	4.72 ± 0.36	0.38	0.05
	CN	1.05 ± 0.11	61.06 ± 0.24	4.33 ± 0.46	0.23	0.05
	HN^{13}C	0.96 ± 0.15	62.95 ± 0.21	2.83 ± 0.53	0.32	0.06
AGAL045.886−00.509	C^{18}O	5.86 ± 0.07	59.86 ± 0.02	3.19 ± 0.04	1.72	0.04
	H^{13}CO$^+$	1.75 ± 0.13	59.77 ± 0.12	3.19 ± 0.25	0.52	0.06
	c-C$_3$H$_2$	2.22 ± 0.11	59.59 ± 0.08	3.25 ± 0.17	0.64	0.05
	CN	0.57 ± 0.11	59.82 ± 0.35	3.40 ± 0.61	0.16	0.06
	HN^{13}C	1.50 ± 0.12	59.66 ± 0.15	3.41 ± 0.30	0.41	0.06
AGAL046.174−00.524	C^{18}O	6.19 ± 0.06	50.44 ± 0.01	2.35 ± 0.02	2.48	0.04
	H^{13}CO$^+$	1.58 ± 0.11	50.68 ± 0.08	2.36 ± 0.19	0.63	0.06
	c-C$_3$H$_2$	1.34 ± 0.10	50.44 ± 0.07	1.91 ± 0.14	0.66	0.06
	CN	0.29 ± 0.07	50.38 ± 0.19	1.51 ± 0.35	0.18	0.06
	HN^{13}C	0.82 ± 0.15	50.98 ± 0.25	3.20 ± 0.83	0.24	0.06
AGAL046.426−00.237	C^{18}O	9.55 ± 0.09	52.59 ± 0.01	2.83 ± 0.04	3.17	0.04
	H^{13}CO$^+$	1.74 ± 0.11	52.72 ± 0.10	3.31 ± 0.24	0.49	0.05
	c-C$_3$H$_2$	0.79 ± 0.08	52.07 ± 0.10	2.21 ± 0.26	0.34	0.04
	HN^{13}C	0.88 ± 0.11	52.64 ± 0.26	4.07 ± 0.57	0.20	0.04
AGAL048.606+00.022	C^{18}O	4.80 ± 0.35	18.49 ± 0.08	6.12 ± 0.32	0.74	0.03
	HCO	0.50 ± 0.04	18.05 ± 0.18	4.96 ± 0.46	0.09	0.01
	H^{13}CO$^+$	1.33 ± 0.09	17.97 ± 0.18	5.30 ± 0.38	0.24	0.03
	c-C$_3$H$_2$	1.82 ± 0.08	18.43 ± 0.09	4.59 ± 0.24	0.37	0.03
	CN	0.72 ± 0.12	18.45 ± 0.35	4.21 ± 0.88	0.16	0.05
	HC^{15}N	0.82 ± 0.10	18.38 ± 0.38	6.36 ± 0.98	0.12	0.03
AGAL048.991−00.299	C^{18}O	8.04 ± 0.08	67.61 ± 0.02	4.20 ± 0.05	1.80	0.03
	HCO	0.12 ± 0.02	67.80 ± 0.13	1.52 ± 0.39	0.07	0.01
	H^{13}CO$^+$	7.85 ± 0.08	67.70 ± 0.02	3.81 ± 0.05	1.93	0.03
	c-C$_3$H$_2$	4.24 ± 0.07	67.71 ± 0.03	3.60 ± 0.08	1.11	0.03
	CN	3.51 ± 0.10	67.65 ± 0.04	2.95 ± 0.10	1.12	0.05
	HC^{15}N	1.66 ± 2.71	67.75 ± 1.00	3.47 ± 1.00	0.45	0.03
	HN^{13}C	6.46 ± 0.07	67.88 ± 0.02	3.20 ± 0.04	1.90	0.03
AGAL049.043−01.077	C^{18}O	5.37 ± 0.05	39.16 ± 0.01	2.43 ± 0.03	2.07	0.03
	H^{13}CO$^+$	1.23 ± 0.06	39.11 ± 0.06	2.63 ± 0.15	0.44	0.03
	c-C$_3$H$_2$	0.90 ± 0.06	39.17 ± 0.08	2.40 ± 0.17	0.35	0.03
	CN	0.32 ± 0.07	38.51 ± 0.21	1.89 ± 0.38	0.16	0.05
	HC^{15}N	0.19 ± 0.05	39.06 ± 0.25	1.74 ± 0.42	0.10	0.03
	HN^{13}C	0.72 ± 0.06	39.25 ± 0.10	2.41 ± 0.23	0.28	0.03
AGAL049.074−00.352	C^{18}O	4.28 ± 0.06	66.40 ± 0.02	2.45 ± 0.04	1.64	0.04
	HCO	0.32 ± 0.04	64.76 ± 0.51	7.88 ± 1.19	0.04	0.01
	H^{13}CO$^+$	2.01 ± 0.06	66.16 ± 0.03	2.36 ± 0.09	0.80	0.03
	c-C$_3$H$_2$	2.67 ± 0.06	66.14 ± 0.03	2.33 ± 0.07	1.08	0.03
	CN	1.45 ± 0.09	66.41 ± 0.05	1.77 ± 0.13	0.77	0.06
	HN^{13}C	1.61 ± 0.05	66.35 ± 0.03	2.20 ± 0.08	0.69	0.03
AGAL049.214−00.342	C^{18}O	7.98 ± 0.08	66.40 ± 0.02	3.75 ± 0.04	2.00	0.04
	H^{13}CO$^+$	2.68 ± 0.14	66.65 ± 0.09	3.48 ± 0.21	0.72	0.06
	c-C$_3$H$_2$	3.16 ± 0.15	67.02 ± 0.08	3.45 ± 0.19	0.86	0.06
	CN	1.64 ± 0.17	67.03 ± 0.17	3.45 ± 0.44	0.45	0.08
	HN^{13}C	1.78 ± 0.13	67.21 ± 0.09	2.49 ± 0.23	0.67	0.06
AGAL049.253−00.411	C^{18}O	5.82 ± 0.06	66.48 ± 0.01	1.91 ± 0.02	2.86	0.04
	HCO	0.30 ± 0.03	66.79 ± 0.13	2.89 ± 0.29	0.10	0.01
	H^{13}CO$^+$	1.17 ± 0.05	66.36 ± 0.04	1.76 ± 0.09	0.62	0.03
	c-C$_3$H$_2$	1.00 ± 0.04	66.54 ± 0.04	1.81 ± 0.09	0.52	0.02
	CN	0.80 ± 0.07	66.50 ± 0.07	1.63 ± 0.18	0.46	0.05
	HN^{13}C	0.68 ± 0.05	66.50 ± 0.05	1.57 ± 0.13	0.41	0.03
AGAL049.268−00.337	C^{18}O	9.43 ± 0.31	67.60 ± 0.04	3.29 ± 0.10	2.69	0.05
	HCO	0.28 ± 0.07	67.73 ± 0.36	3.39 ± 1.12	0.08	0.03
	H^{13}CO$^+$	4.83 ± 0.16	67.90 ± 0.06	3.83 ± 0.15	1.18	0.07

Table B.3: continued.

ATLASGAL Name	Line	Area (K km s^{-1})	v_{LRS} (km s^{-1})	Δv (km s^{-1})	T_{MB} (K)	rms (K)
	c-C$_3$H$_2$	4.43 ± 0.15	67.98 ± 0.06	3.73 ± 0.15	1.12	0.06
	CN	2.75 ± 0.14	67.88 ± 0.08	3.07 ± 0.19	0.84	0.08
	HC^{15}N	0.68 ± 0.12	67.51 ± 0.22	2.53 ± 0.53	0.25	0.06
	HN^{13}C	4.42 ± 0.16	68.22 ± 0.06	3.54 ± 0.14	1.17	0.07
AGAL049.369$-$00.301	C^{18}O	9.82 ± 0.08	50.90 ± 0.01	3.03 ± 0.03	3.04	0.04
	HCO	0.72 ± 0.08	51.69 ± 0.35	6.50 ± 0.77	0.10	0.02
	H^{13}CO$^+$	2.19 ± 0.13	50.84 ± 0.07	2.57 ± 0.18	0.80	0.07
	c-C$_3$H$_2$	2.65 ± 0.18	51.04 ± 0.16	4.71 ± 0.37	0.53	0.07
	CN	1.67 ± 0.17	50.92 ± 0.16	3.33 ± 0.42	0.47	0.08
	HC^{15}N	0.84 ± 0.17	51.54 ± 0.42	3.88 ± 0.96	0.20	0.07
	HN^{13}C	0.81 ± 0.12	50.76 ± 0.17	2.23 ± 0.39	0.34	0.07
AGAL049.401$-$00.227	C^{18}O	9.89 ± 0.07	49.53 ± 0.01	3.64 ± 0.03	2.55	0.04
	HCO	0.22 ± 0.04	49.86 ± 0.38	4.27 ± 1.04	0.05	0.01
	H^{13}CO$^+$	1.25 ± 0.06	50.28 ± 0.05	2.21 ± 0.14	0.53	0.03
	c-C$_3$H$_2$	0.98 ± 0.07	50.15 ± 0.12	3.36 ± 0.34	0.28	0.03
	CN	0.54 ± 0.09	50.36 ± 0.11	1.53 ± 0.35	0.33	0.06
	HN^{13}C	0.61 ± 0.06	50.38 ± 0.07	1.67 ± 0.21	0.34	0.03
AGAL049.402$-$00.212	C^{18}O	6.64 ± 0.06	48.52 ± 0.01	2.23 ± 0.03	2.80	0.04
	H^{13}CO$^+$	1.67 ± 0.06	48.40 ± 0.03	2.10 ± 0.08	0.75	0.03
	c-C$_3$H$_2$	1.30 ± 0.05	48.44 ± 0.05	2.37 ± 0.12	0.52	0.03
	CN	0.65 ± 0.09	48.55 ± 0.13	1.97 ± 0.38	0.31	0.06
	HN^{13}C	1.27 ± 0.05	48.53 ± 0.04	2.13 ± 0.11	0.56	0.03
AGAL049.489$-$00.389	C^{18}O	38.34 ± 1.52	58.68 ± 0.17	9.95 ± 0.27	3.62	0.07
	HCO	1.17 ± 0.11	55.83 ± 0.41	8.16 ± 0.78	0.13	0.03
	H^{13}CO$^+$	32.92 ± 0.19	56.47 ± 0.02	7.15 ± 0.05	4.32	0.06
	c-C$_3$H$_2$	9.25 ± 0.22	55.99 ± 0.09	8.05 ± 0.23	1.08	0.06
	CN	6.13 ± 0.26	55.89 ± 0.15	7.07 ± 0.33	0.81	0.09
	HC^{15}N	16.86 ± 0.19	56.71 ± 0.05	8.41 ± 0.12	1.88	0.05
	HN^{13}C	9.65 ± 0.17	56.48 ± 0.07	7.87 ± 0.16	1.15	0.05
AGAL049.566$-$00.274	C^{18}O	5.47 ± 0.14	53.16 ± 0.03	2.55 ± 0.07	2.02	0.05
	H^{13}CO$^+$	1.78 ± 0.13	53.42 ± 0.09	2.78 ± 0.22	0.60	0.04
	c-C$_3$H$_2$	0.34 ± 0.17	53.78 ± 0.30	1.93 ± 0.71	0.16	0.04
	CN	0.56 ± 0.15	53.35 ± 0.21	1.62 ± 0.56	0.32	0.11
	HC^{15}N	0.53 ± 0.11	52.85 ± 0.70	4.80 ± 1.20	0.10	0.04
	HN^{13}C	1.00 ± 0.09	53.39 ± 0.12	2.84 ± 0.29	0.33	0.04
AGAL049.599$-$00.249	C^{18}O	4.96 ± 0.06	56.74 ± 0.01	2.38 ± 0.04	1.95	0.04
	H^{13}CO$^+$	1.71 ± 0.06	56.83 ± 0.03	1.97 ± 0.08	0.82	0.03
	c-C$_3$H$_2$	0.40 ± 0.05	57.00 ± 0.14	2.23 ± 0.35	0.17	0.03
	CN	0.58 ± 0.09	57.02 ± 0.16	2.18 ± 0.41	0.25	0.05
	HC^{15}N	0.14 ± 0.06	56.94 ± 0.19	1.28 ± 0.93	0.10	0.03
	HN^{13}C	0.75 ± 0.05	57.00 ± 0.06	1.67 ± 0.13	0.42	0.03
AGAL050.046$+$00.767	C^{18}O	1.39 ± 0.05	-29.86 ± 0.04	2.14 ± 0.10	0.61	0.03
AGAL050.221$-$00.606	C^{18}O	7.85 ± 0.26	39.21 ± 0.02	1.86 ± 0.04	3.96	0.03
	HCO	0.19 ± 0.03	39.42 ± 0.23	2.93 ± 0.71	0.06	0.01
	H^{13}CO$^+$	2.92 ± 0.07	40.18 ± 0.05	3.60 ± 0.10	0.76	0.03
	c-C$_3$H$_2$	1.17 ± 0.07	39.86 ± 0.10	3.29 ± 0.26	0.34	0.03
	CN	0.71 ± 0.09	40.36 ± 0.18	2.66 ± 0.41	0.25	0.05
	HC^{15}N	0.41 ± 0.07	39.95 ± 0.30	3.05 ± 0.57	0.13	0.04
	HN^{13}C	1.14 ± 0.07	40.17 ± 0.08	2.93 ± 0.19	0.37	0.03
AGAL050.777$+$00.152	C^{18}O	4.42 ± 0.08	42.54 ± 0.02	2.29 ± 0.05	1.81	0.05
	H^{13}CO$^+$	1.07 ± 0.07	42.37 ± 0.06	1.90 ± 0.13	0.53	0.04
	c-C$_3$H$_2$	1.09 ± 0.08	42.65 ± 0.11	3.01 ± 0.25	0.34	0.04
	CN	0.46 ± 0.14	42.51 ± 0.43	2.76 ± 1.04	0.16	0.08
	HN^{13}C	0.56 ± 0.07	42.54 ± 0.12	1.88 ± 0.25	0.28	0.04
AGAL051.678$+$00.719	C^{18}O	7.99 ± 0.07	3.60 ± 0.02	3.87 ± 0.04	1.94	0.03
	H^{13}CO$^+$	3.52 ± 0.08	3.35 ± 0.05	4.30 ± 0.12	0.77	0.03
	c-C$_3$H$_2$	0.74 ± 0.09	2.84 ± 0.30	5.30 ± 0.74	0.13	0.03
	CN	0.68 ± 0.11	2.87 ± 0.26	3.45 ± 0.70	0.18	0.05
	HC^{15}N	0.67 ± 0.09	3.94 ± 0.40	5.84 ± 0.88	0.11	0.03
	HN^{13}C	1.27 ± 0.07	3.33 ± 0.12	4.05 ± 0.26	0.30	0.03
AGAL052.208$+$00.687	C^{18}O	5.84 ± 0.09	4.22 ± 0.03	4.16 ± 0.08	1.32	0.04
	H^{13}CO$^+$	2.39 ± 0.09	4.03 ± 0.06	3.16 ± 0.13	0.71	0.04
	c-C$_3$H$_2$	0.71 ± 0.08	4.28 ± 0.17	2.85 ± 0.35	0.23	0.04
	HN^{13}C	0.95 ± 0.08	3.60 ± 0.12	2.82 ± 0.29	0.32	0.04
AGAL053.141$+$00.069	C^{18}O	12.12 ± 0.13	21.75 ± 0.01	2.64 ± 0.03	4.32	0.06
	H^{13}CO$^+$	6.05 ± 0.15	21.47 ± 0.03	2.36 ± 0.07	2.40	0.08
	c-C$_3$H$_2$	1.79 ± 0.10	21.62 ± 0.06	2.35 ± 0.17	0.71	0.05
	CN	0.82 ± 0.15	21.39 ± 0.21	2.33 ± 0.53	0.33	0.09
	HC^{15}N	0.79 ± 0.09	21.59 ± 0.13	2.35 ± 0.31	0.32	0.05
	HN^{13}C	1.27 ± 0.07	21.66 ± 0.05	1.71 ± 0.12	0.70	0.04
AGAL053.619$+$00.034	C^{18}O	6.83 ± 0.06	23.09 ± 0.01	1.68 ± 0.02	3.83	0.04
	HCO	0.10 ± 0.03	23.13 ± 0.24	1.65 ± 0.47	0.06	0.02
	H^{13}CO$^+$	2.08 ± 0.06	22.97 ± 0.02	1.48 ± 0.05	1.32	0.04
	c-C$_3$H$_2$	0.72 ± 0.06	23.03 ± 0.07	1.73 ± 0.16	0.39	0.04
	CN	0.50 ± 0.09	22.75 ± 0.11	1.20 ± 0.22	0.39	0.08

Table B.3: continued.

ATLASGAL Name	Line	Area (K km s^{-1})	v_{LRS} (km s^{-1})	Δv (km s^{-1})	T_{MB} (K)	rms (K)
	HN^{13}C	0.65 ± 0.06	23.06 ± 0.07	1.49 ± 0.17	0.41	0.04
AGAL055.158−00.299	C^{18}O	7.46 ± 0.07	40.99 ± 0.01	2.35 ± 0.03	2.98	0.03
	HCO	0.19 ± 0.03	41.44 ± 0.22	2.90 ± 0.49	0.06	0.01
	H^{13}CO^{+}	1.18 ± 0.06	40.95 ± 0.06	2.38 ± 0.13	0.47	0.03
	c-C$_3$H$_2$	0.94 ± 0.06	41.02 ± 0.09	2.92 ± 0.20	0.30	0.03
	CN	0.59 ± 0.08	41.14 ± 0.18	2.46 ± 0.35	0.22	0.05
	HC^{15}N	0.33 ± 0.05	41.04 ± 0.20	2.16 ± 0.36	0.14	0.03
	HN^{13}C	0.48 ± 0.06	41.20 ± 0.16	2.35 ± 0.29	0.19	0.03
AGAL058.469+00.436	C^{18}O	6.21 ± 0.05	36.94 ± 0.01	2.68 ± 0.03	2.18	0.03
	H^{13}CO^{+}	2.86 ± 0.06	36.57 ± 0.02	2.43 ± 0.06	1.11	0.03
	c-C$_3$H$_2$	1.05 ± 0.05	36.58 ± 0.05	2.11 ± 0.12	0.47	0.03
	CN	0.67 ± 0.08	36.42 ± 0.13	2.38 ± 0.35	0.27	0.05
	HC^{15}N	0.35 ± 0.06	36.44 ± 0.19	2.21 ± 0.49	0.15	0.03
	HN^{13}C	1.15 ± 0.06	36.81 ± 0.06	2.37 ± 0.14	0.46	0.03
AGAL058.709+00.662	C^{18}O	6.96 ± 0.06	30.77 ± 0.01	2.01 ± 0.02	3.25	0.04
	H^{13}CO^{+}	1.68 ± 0.05	30.86 ± 0.03	1.84 ± 0.06	0.86	0.03
	c-C$_3$H$_2$	0.72 ± 0.05	30.79 ± 0.07	1.91 ± 0.15	0.36	0.03
	CN	0.35 ± 0.09	30.86 ± 0.33	2.66 ± 0.87	0.12	0.05
	HN^{13}C	0.28 ± 0.05	30.94 ± 0.18	1.90 ± 0.37	0.14	0.03
AGAL058.774+00.644	C^{18}O	3.85 ± 0.06	32.51 ± 0.02	2.49 ± 0.04	1.46	0.03
	HCO	0.14 ± 0.02	32.47 ± 0.21	2.34 ± 0.40	0.06	0.01
	H^{13}CO^{+}	1.59 ± 0.06	32.28 ± 0.05	2.58 ± 0.11	0.58	0.03
	c-C$_3$H$_2$	0.94 ± 0.06	32.47 ± 0.10	2.96 ± 0.25	0.30	0.03
	CN	0.63 ± 0.08	32.56 ± 0.14	2.19 ± 0.33	0.27	0.05
	HC^{15}N	0.37 ± 0.06	32.01 ± 0.19	2.23 ± 0.38	0.15	0.03
	HN^{13}C	0.78 ± 0.07	32.38 ± 0.12	2.71 ± 0.26	0.27	0.03
AGAL059.187+00.106	C^{18}O	2.73 ± 0.04	29.29 ± 0.01	1.17 ± 0.02	2.20	0.03
	HCO	0.10 ± 0.02	29.37 ± 0.13	1.52 ± 0.24	0.06	0.01
	H^{13}CO^{+}	0.50 ± 0.04	29.24 ± 0.03	0.99 ± 0.16	0.47	0.03
	c-C$_3$H$_2$	0.30 ± 0.03	29.44 ± 0.05	0.89 ± 0.30	0.32	0.03
AGAL059.351−00.196	C^{18}O	3.49 ± 0.05	28.74 ± 0.01	1.82 ± 0.03	1.80	0.03
	HCO	0.22 ± 0.04	28.09 ± 0.57	5.54 ± 1.44	0.04	0.01
	H^{13}CO^{+}	1.26 ± 0.05	28.49 ± 0.03	1.59 ± 0.07	0.75	0.03
	c-C$_3$H$_2$	0.70 ± 0.05	28.43 ± 0.05	1.63 ± 0.14	0.41	0.03
	CN	0.11 ± 0.05	28.73 ± 0.34	0.93 ± 0.51	0.11	0.05
	HN^{13}C	0.43 ± 0.05	28.49 ± 0.08	1.60 ± 0.20	0.25	0.03
AGAL059.359−00.207	C^{18}O	5.03 ± 0.05	29.14 ± 0.01	2.31 ± 0.03	2.04	0.03
	H^{13}CO^{+}	1.66 ± 0.05	29.13 ± 0.03	2.07 ± 0.08	0.75	0.03
	c-C$_3$H$_2$	0.88 ± 0.06	29.07 ± 0.07	2.42 ± 0.19	0.34	0.03
	CN	0.55 ± 0.07	29.21 ± 0.15	2.36 ± 0.37	0.22	0.04
	HN^{13}C	0.52 ± 0.06	29.37 ± 0.11	2.09 ± 0.26	0.24	0.03
AGAL059.497−00.236	C^{18}O	4.45 ± 0.07	26.44 ± 0.02	2.45 ± 0.05	1.71	0.04
	H^{13}CO^{+}	3.20 ± 0.08	26.64 ± 0.02	1.96 ± 0.06	1.54	0.04
	c-C$_3$H$_2$	1.57 ± 0.07	26.57 ± 0.03	1.61 ± 0.08	0.92	0.04
	CN	0.52 ± 0.12	26.57 ± 0.34	2.65 ± 0.70	0.19	0.07
	HN^{13}C	0.81 ± 0.08	26.64 ± 0.09	2.11 ± 0.28	0.36	0.04
AGAL059.577−00.201	C^{18}O	4.42 ± 0.07	25.98 ± 0.01	1.64 ± 0.03	2.54	0.05
	HCO	0.23 ± 0.04	25.81 ± 0.24	2.90 ± 0.56	0.07	0.02
	H^{13}CO^{+}	1.12 ± 0.06	25.93 ± 0.05	1.66 ± 0.11	0.63	0.04
	c-C$_3$H$_2$	1.08 ± 0.07	25.97 ± 0.06	1.86 ± 0.15	0.55	0.04
	CN	0.21 ± 0.08	26.08 ± 0.24	1.08 ± 0.41	0.19	0.07
	HN^{13}C	0.28 ± 0.06	26.45 ± 0.10	1.04 ± 0.33	0.26	0.04
AGAL059.584−00.146	C^{18}O	2.39 ± 0.05	27.05 ± 0.01	1.35 ± 0.03	1.66	0.04
	HCO	0.20 ± 0.03	28.05 ± 0.15	1.96 ± 0.36	0.09	0.02
	H^{13}CO^{+}	0.67 ± 0.05	27.04 ± 0.04	1.16 ± 0.12	0.55	0.04
	c-C$_3$H$_2$	0.73 ± 0.06	27.37 ± 0.06	1.55 ± 0.13	0.44	0.04
	CN	0.54 ± 0.10	27.65 ± 0.17	1.65 ± 0.33	0.31	0.07
AGAL059.602+00.912	C^{18}O	9.95 ± 0.06	36.62 ± 0.01	4.07 ± 0.03	2.30	0.03
	HCO	0.10 ± 0.02	37.56 ± 0.20	1.77 ± 0.59	0.05	0.01
	H^{13}CO^{+}	1.74 ± 0.08	36.73 ± 0.08	3.58 ± 0.18	0.46	0.03
	c-C$_3$H$_2$	0.74 ± 0.07	36.43 ± 0.20	4.39 ± 0.52	0.16	0.03
	CN	0.61 ± 0.11	36.39 ± 0.41	4.46 ± 0.95	0.13	0.05
	HC^{15}N	0.42 ± 0.07	36.40 ± 0.26	3.02 ± 0.72	0.13	0.03
	HN^{13}C	0.66 ± 0.08	36.40 ± 0.23	3.93 ± 0.49	0.16	0.03
AGAL059.634−00.191	H^{13}CO^{+}	4.00 ± 0.10	27.91 ± 0.03	2.31 ± 0.07	1.63	0.05
	c-C$_3$H$_2$	1.69 ± 0.10	28.18 ± 0.07	2.57 ± 0.18	0.62	0.05
	HC^{15}N	1.03 ± 0.13	28.35 ± 0.24	3.75 ± 0.53	0.26	0.06
	HN^{13}C	2.27 ± 0.09	28.19 ± 0.04	2.04 ± 0.10	1.04	0.05
AGAL059.636−00.252	C^{18}O	3.20 ± 0.05	27.48 ± 0.01	0.95 ± 0.02	3.17	0.05
	HCO	0.28 ± 0.03	27.54 ± 0.08	1.60 ± 0.20	0.16	0.02
	H^{13}CO^{+}	0.47 ± 0.05	27.44 ± 0.06	0.86 ± 0.09	0.51	0.04
	c-C$_3$H$_2$	0.76 ± 0.06	27.39 ± 0.06	1.56 ± 0.15	0.46	0.04
	CN	0.25 ± 0.07	27.53 ± 0.14	0.71 ± 0.23	0.34	0.08
AGAL059.782+00.066	C^{18}O	7.74 ± 0.10	22.48 ± 0.01	2.06 ± 0.03	3.54	0.06
	HCO	0.20 ± 0.04	23.55 ± 0.29	3.14 ± 0.78	0.06	0.02

Table B.3: continued.

ATLASGAL Name	Line	Area (K km s^{-1})	v_{LRS} (km s^{-1})	Δv (km s^{-1})	T_{MB} (K)	rms (K)
	H^{13}CO$^+$	4.68 ± 0.11	22.47 ± 0.02	2.04 ± 0.06	2.16	0.06
	c-C$_3$H$_2$	1.76 ± 0.10	22.43 ± 0.07	2.52 ± 0.18	0.65	0.05
	CN	1.86 ± 0.12	22.49 ± 0.06	1.94 ± 0.14	0.90	0.08
	HC^{15}N	1.27 ± 0.13	22.31 ± 0.11	2.62 ± 0.35	0.46	0.04
	HN^{13}C	2.45 ± 0.08	22.59 ± 0.03	1.83 ± 0.08	1.25	0.05
AGAL059.789+00.631	C^{18}O	3.49 ± 0.19	35.51 ± 0.05	2.26 ± 0.12	1.45	0.05
	H^{13}CO$^+$	3.31 ± 0.11	34.03 ± 0.07	4.52 ± 0.17	0.69	0.04
	c-C$_3$H$_2$	1.11 ± 0.11	34.69 ± 0.25	5.05 ± 0.56	0.21	0.04
	CN	0.73 ± 0.23	34.11 ± 0.70	4.90 ± 2.09	0.14	0.08
	HC^{15}N	0.52 ± 0.09	33.86 ± 0.34	3.64 ± 0.66	0.13	0.04
	HN^{13}C	1.04 ± 0.11	34.27 ± 0.22	4.24 ± 0.50	0.23	0.04
AGAL059.832+00.672	C^{18}O	6.37 ± 0.07	34.68 ± 0.01	2.38 ± 0.03	2.51	0.04
	H^{13}CO$^+$	1.85 ± 0.11	34.72 ± 0.08	3.01 ± 0.22	0.58	0.05
	c-C$_3$H$_2$	0.38 ± 0.10	34.76 ± 0.29	2.31 ± 0.65	0.15	0.05
	CN	0.33 ± 0.11	35.04 ± 0.47	2.29 ± 1.09	0.14	0.06
	HC^{15}N	0.43 ± 0.18	35.41 ± 0.76	3.75 ± 2.64	0.11	0.05
	HN^{13}C	0.65 ± 0.13	35.62 ± 0.42	4.01 ± 0.91	0.15	0.05
AGAL059.894−00.047	C^{18}O	2.30 ± 0.08	3.52 ± 0.04	2.39 ± 0.10	0.91	0.05
	H^{13}CO$^+$	0.51 ± 0.07	3.71 ± 0.15	2.09 ± 0.31	0.23	0.04
	c-C$_3$H$_2$	0.28 ± 0.07	3.97 ± 0.32	2.44 ± 0.70	0.11	0.04
G011.1012−0.3803	C^{18}O	4.98 ± 0.42	0.34 ± 0.10	2.89 ± 0.15	1.62	0.04
	H^{13}CO$^+$	1.63 ± 0.08	0.88 ± 0.07	3.00 ± 0.17	0.51	0.04
	c-C$_3$H$_2$	0.97 ± 0.06	0.77 ± 0.07	2.47 ± 0.19	0.37	0.03
	CN	0.65 ± 0.11	1.10 ± 0.32	3.72 ± 0.58	0.17	0.05
	HN^{13}C	1.10 ± 0.06	0.99 ± 0.07	2.39 ± 0.16	0.43	0.03
G012.7914−0.1958	C^{18}O	11.05 ± 0.43	37.02 ± 0.04	2.79 ± 0.06	3.72	0.04
	HCO	0.61 ± 0.05	33.79 ± 0.32	8.06 ± 0.65	0.07	0.01
	H^{13}CO$^+$	6.08 ± 0.10	35.72 ± 0.03	4.43 ± 0.09	1.29	0.04
	c-C$_3$H$_2$	3.71 ± 0.10	34.89 ± 0.09	6.22 ± 0.20	0.56	0.03
	CN	2.65 ± 0.13	35.13 ± 0.12	4.87 ± 0.30	0.51	0.05
	HC^{15}N	1.06 ± 0.10	35.71 ± 0.25	5.06 ± 0.55	0.20	0.04
	HN^{13}C	3.59 ± 0.08	35.64 ± 0.04	3.59 ± 0.09	0.94	0.03
G013.2029−0.1352	C^{18}O	16.52 ± 0.12	51.44 ± 0.01	2.86 ± 0.02	5.43	0.06
	HCO	0.25 ± 0.04	51.43 ± 0.18	2.98 ± 0.53	0.08	0.01
	H^{13}CO$^+$	3.14 ± 0.07	51.47 ± 0.03	2.84 ± 0.07	1.04	0.03
	c-C$_3$H$_2$	1.62 ± 0.06	51.65 ± 0.05	2.57 ± 0.12	0.59	0.03
	CN	1.63 ± 0.10	51.43 ± 0.07	2.31 ± 0.17	0.66	0.06
	HC^{15}N	0.47 ± 0.08	51.66 ± 0.14	2.07 ± 0.52	0.21	0.03
	HN^{13}C	2.13 ± 0.06	51.73 ± 0.03	2.33 ± 0.07	0.86	0.03
G014.1007−0.5559	C^{18}O	7.25 ± 0.21	22.12 ± 0.01	1.75 ± 0.03	3.89	0.04
	HCO	0.36 ± 0.03	22.74 ± 0.07	1.92 ± 0.20	0.18	0.02
	H^{13}CO$^+$	1.74 ± 0.06	22.16 ± 0.03	1.71 ± 0.06	0.95	0.04
	c-C$_3$H$_2$	2.60 ± 0.06	22.20 ± 0.02	1.76 ± 0.05	1.39	0.03
	CN	0.99 ± 0.09	22.13 ± 0.08	1.77 ± 0.18	0.52	0.06
	HN^{13}C	1.38 ± 0.05	22.23 ± 0.03	1.65 ± 0.08	0.79	0.03
G014.6010−0.5400	C^{18}O	7.64 ± 0.05	17.66 ± 0.00	1.35 ± 0.01	5.31	0.04
	H^{13}CO$^+$	1.49 ± 0.06	17.77 ± 0.04	1.62 ± 0.07	0.86	0.04
	c-C$_3$H$_2$	0.81 ± 0.05	17.71 ± 0.05	1.51 ± 0.11	0.50	0.03
	CN	0.55 ± 0.08	17.66 ± 0.07	1.09 ± 0.21	0.47	0.06
	HN^{13}C	0.97 ± 0.06	17.73 ± 0.05	1.69 ± 0.13	0.54	0.04
G025.1526−0.2906	C^{18}O	9.65 ± 0.08	63.37 ± 0.01	2.34 ± 0.02	3.87	0.05
	H^{13}CO$^+$	1.39 ± 0.07	63.50 ± 0.05	1.94 ± 0.12	0.67	0.04
	c-C$_3$H$_2$	1.08 ± 0.06	63.60 ± 0.05	1.69 ± 0.11	0.60	0.04
	CN	0.53 ± 0.11	63.40 ± 0.17	1.77 ± 0.50	0.28	0.07
	HN^{13}C	1.04 ± 0.06	63.68 ± 0.04	1.51 ± 0.10	0.65	0.04
G027.2546+0.1368	C^{18}O	3.73 ± 0.11	33.17 ± 0.05	3.38 ± 0.11	1.04	0.05
	H^{13}CO$^+$	1.30 ± 0.08	32.98 ± 0.10	3.41 ± 0.21	0.36	0.03
	c-C$_3$H$_2$	1.16 ± 0.07	32.95 ± 0.09	3.00 ± 0.19	0.36	0.03
	CN	0.32 ± 0.08	33.62 ± 0.19	1.55 ± 0.40	0.19	0.06
	HN^{13}C	1.13 ± 0.07	32.98 ± 0.08	2.68 ± 0.17	0.40	0.03
G028.5559−0.2260	C^{18}O	10.88 ± 0.10	85.52 ± 0.01	2.69 ± 0.03	3.80	0.05
	H^{13}CO$^+$	1.34 ± 0.07	85.48 ± 0.06	2.54 ± 0.17	0.50	0.03
	c-C$_3$H$_2$	1.63 ± 0.08	85.37 ± 0.06	2.54 ± 0.14	0.60	0.04
	CN	0.76 ± 0.15	85.85 ± 0.36	3.58 ± 0.76	0.20	0.08
	HN^{13}C	1.17 ± 0.07	85.49 ± 0.06	2.11 ± 0.17	0.52	0.04
G028.6117+0.0306	C^{18}O	9.48 ± 0.07	100.30 ± 0.01	2.84 ± 0.02	3.14	0.04
	H^{13}CO$^+$	1.42 ± 0.07	100.70 ± 0.07	2.78 ± 0.16	0.48	0.04
	c-C$_3$H$_2$	0.60 ± 0.08	101.00 ± 0.24	3.62 ± 0.57	0.15	0.03
	HN^{13}C	0.62 ± 0.06	101.00 ± 0.10	1.99 ± 0.23	0.29	0.04
G030.5946+0.1639	C^{18}O	9.61 ± 0.08	104.80 ± 0.02	3.77 ± 0.04	2.40	0.04
	H^{13}CO$^+$	1.17 ± 0.09	104.70 ± 0.15	4.08 ± 0.37	0.27	0.03
	c-C$_3$H$_2$	0.86 ± 0.07	104.80 ± 0.15	3.58 ± 0.29	0.23	0.03
	HN^{13}C	0.73 ± 0.07	105.40 ± 0.17	3.75 ± 0.43	0.18	0.03
G030.7306−0.0604	C^{18}O	24.05 ± 0.09	92.05 ± 0.01	4.43 ± 0.02	5.10	0.05
	CN	1.32 ± 0.16	91.78 ± 0.17	2.78 ± 0.35	0.45	0.09

Table B.3: continued.

| ATLASGAL Name	Line	Area (K km s^{-1})	v_{LRS} (km s^{-1})	Δv (km s^{-1})	T_{MB} (K)	rms (K)
G031.0441+0.2742	C^{18}O	4.97 $\pm$ 0.08	78.06 $\pm$ 0.02	2.56 $\pm$ 0.05	1.82	0.04
	H^{13}CO^{+}	0.67 $\pm$ 0.07	77.73 $\pm$ 0.10	1.77 $\pm$ 0.20	0.35	0.05
	c-C$_3$H$_2$	0.98 $\pm$ 0.09	77.83 $\pm$ 0.09	2.06 $\pm$ 0.23	0.45	0.05
	CN	0.50 $\pm$ 0.11	77.98 $\pm$ 0.21	1.81 $\pm$ 0.52	0.26	0.07
	HN^{13}C	0.67 $\pm$ 0.08	77.94 $\pm$ 0.11	1.81 $\pm$ 0.24	0.35	0.05
G032.9956+0.0415	C^{18}O	4.18 $\pm$ 0.13	83.45 $\pm$ 0.04	2.26 $\pm$ 0.09	1.74	0.08
	H^{13}CO^{+}	0.71 $\pm$ 0.08	83.46 $\pm$ 0.12	2.17 $\pm$ 0.28	0.31	0.04
	c-C$_3$H$_2$	0.44 $\pm$ 0.07	83.51 $\pm$ 0.17	1.92 $\pm$ 0.34	0.21	0.04
	HN^{13}C	0.74 $\pm$ 0.09	83.70 $\pm$ 0.15	2.82 $\pm$ 0.44	0.25	0.04
G059.7948+0.0749	C^{18}O	5.99 $\pm$ 0.09	21.89 $\pm$ 0.02	2.48 $\pm$ 0.04	2.27	0.05
	H^{13}CO^{+}	2.95 $\pm$ 0.07	21.39 $\pm$ 0.02	2.16 $\pm$ 0.06	1.28	0.04
	c-C$_3$H$_2$	1.18 $\pm$ 0.06	21.42 $\pm$ 0.05	2.05 $\pm$ 0.13	0.54	0.04
	CN	0.73 $\pm$ 0.12	21.30 $\pm$ 0.19	2.14 $\pm$ 0.37	0.32	0.08
	HC^{15}N	0.41 $\pm$ 0.10	21.31 $\pm$ 0.47	3.97 $\pm$ 1.07	0.10	0.04
	HN^{13}C	1.01 $\pm$ 0.06	21.60 $\pm$ 0.06	1.97 $\pm$ 0.15	0.48	0.04

CN spectral lines
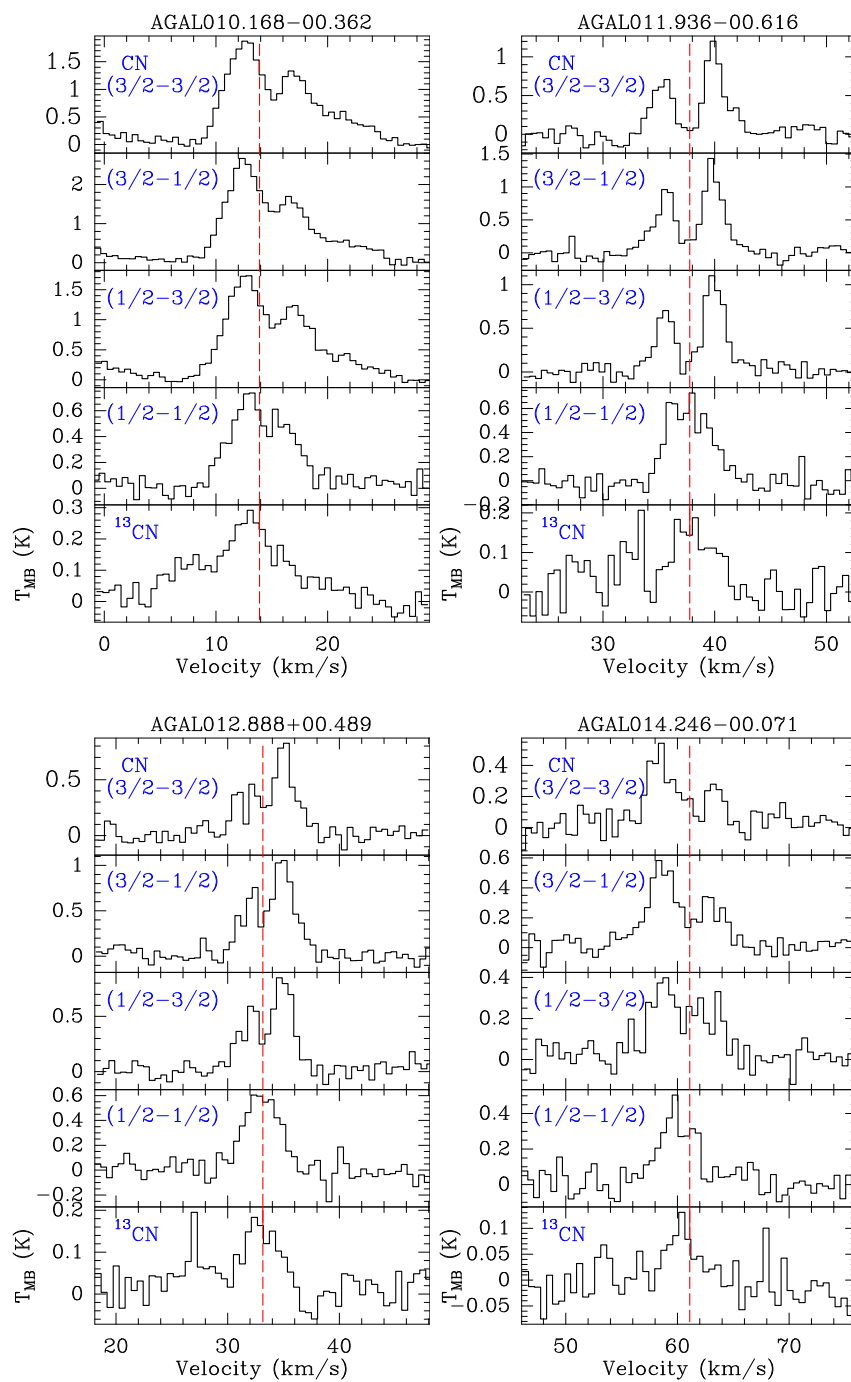
Figure B.1: CN self-absorption toward HII regions
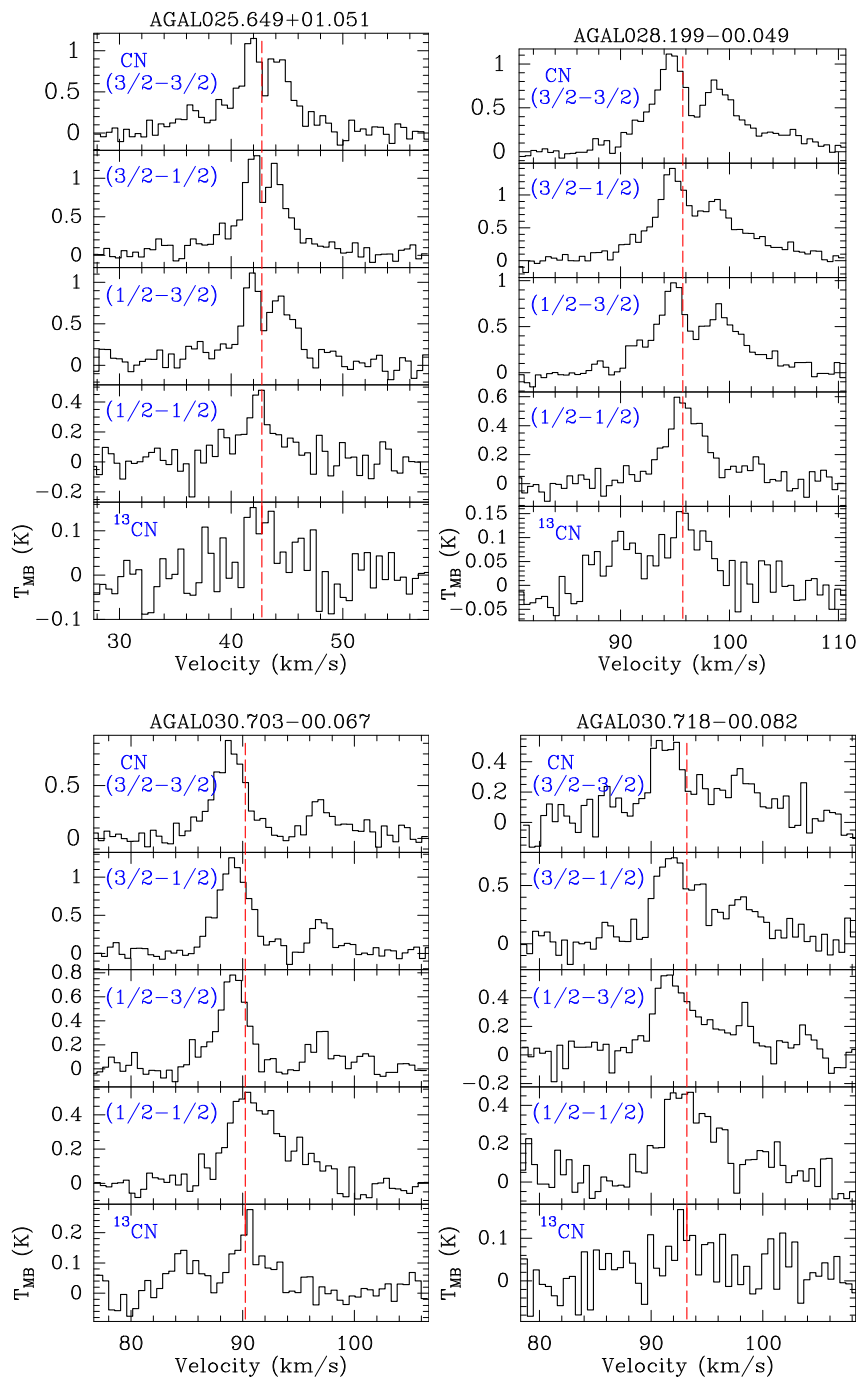
Figure B.1: Continued.
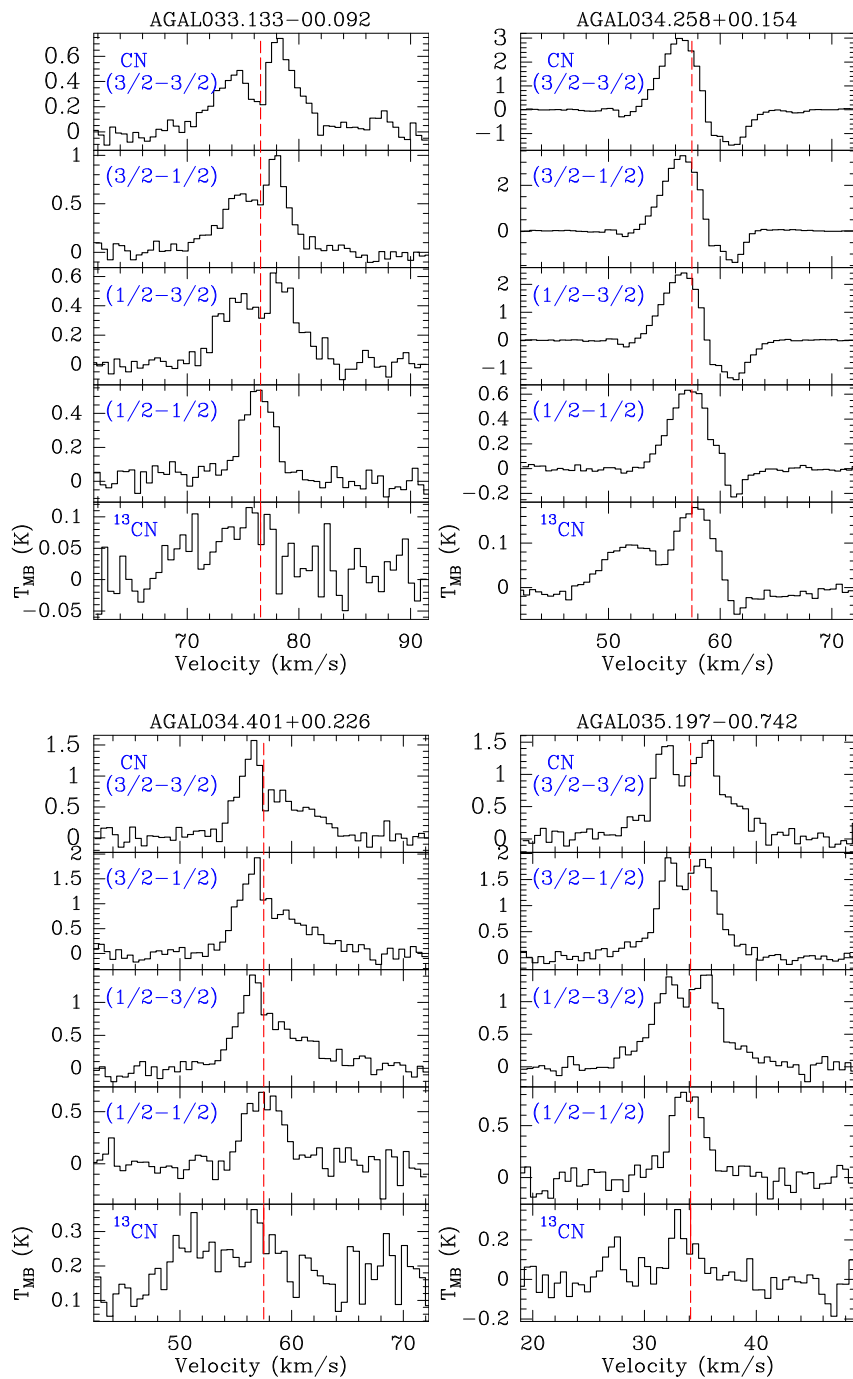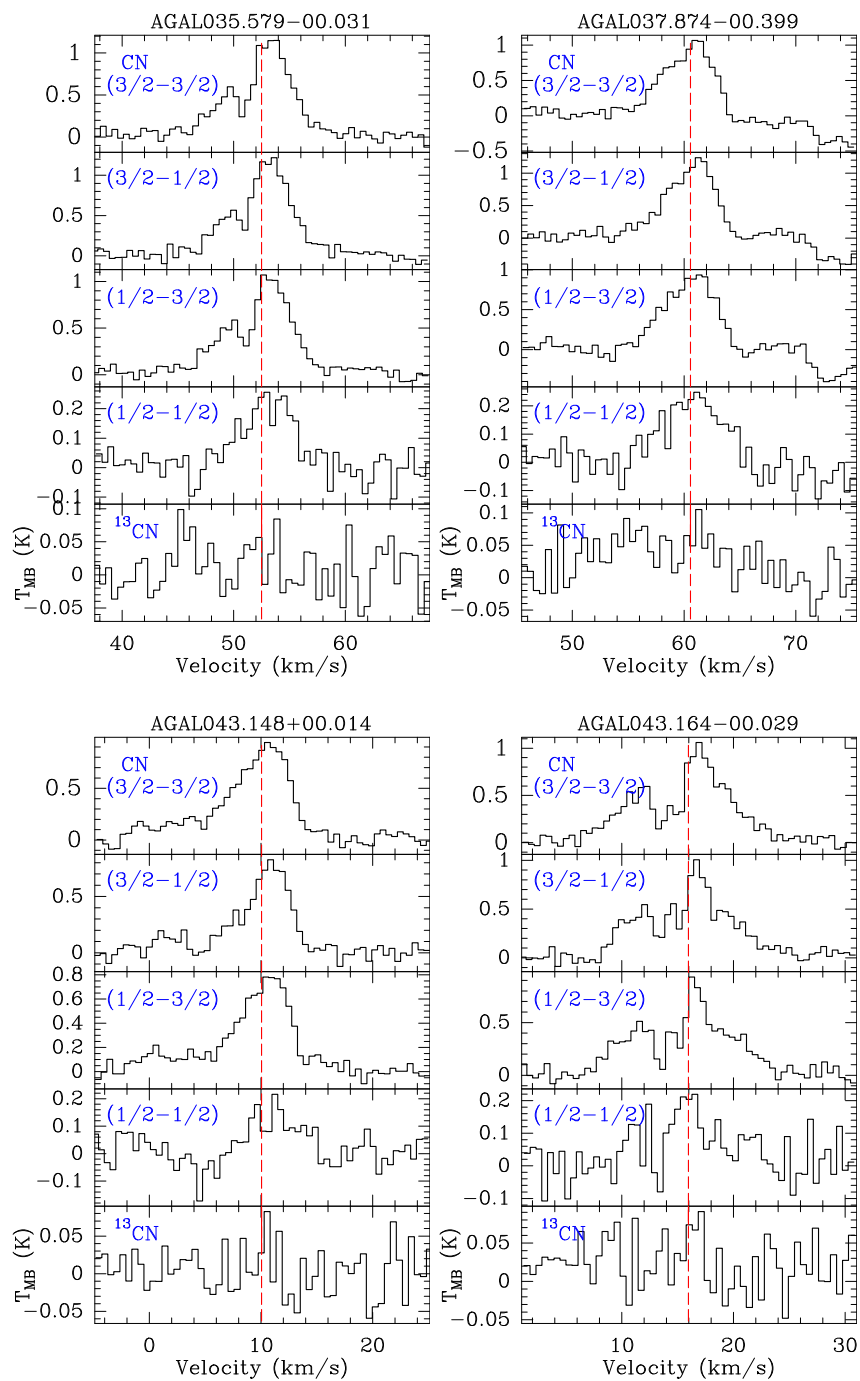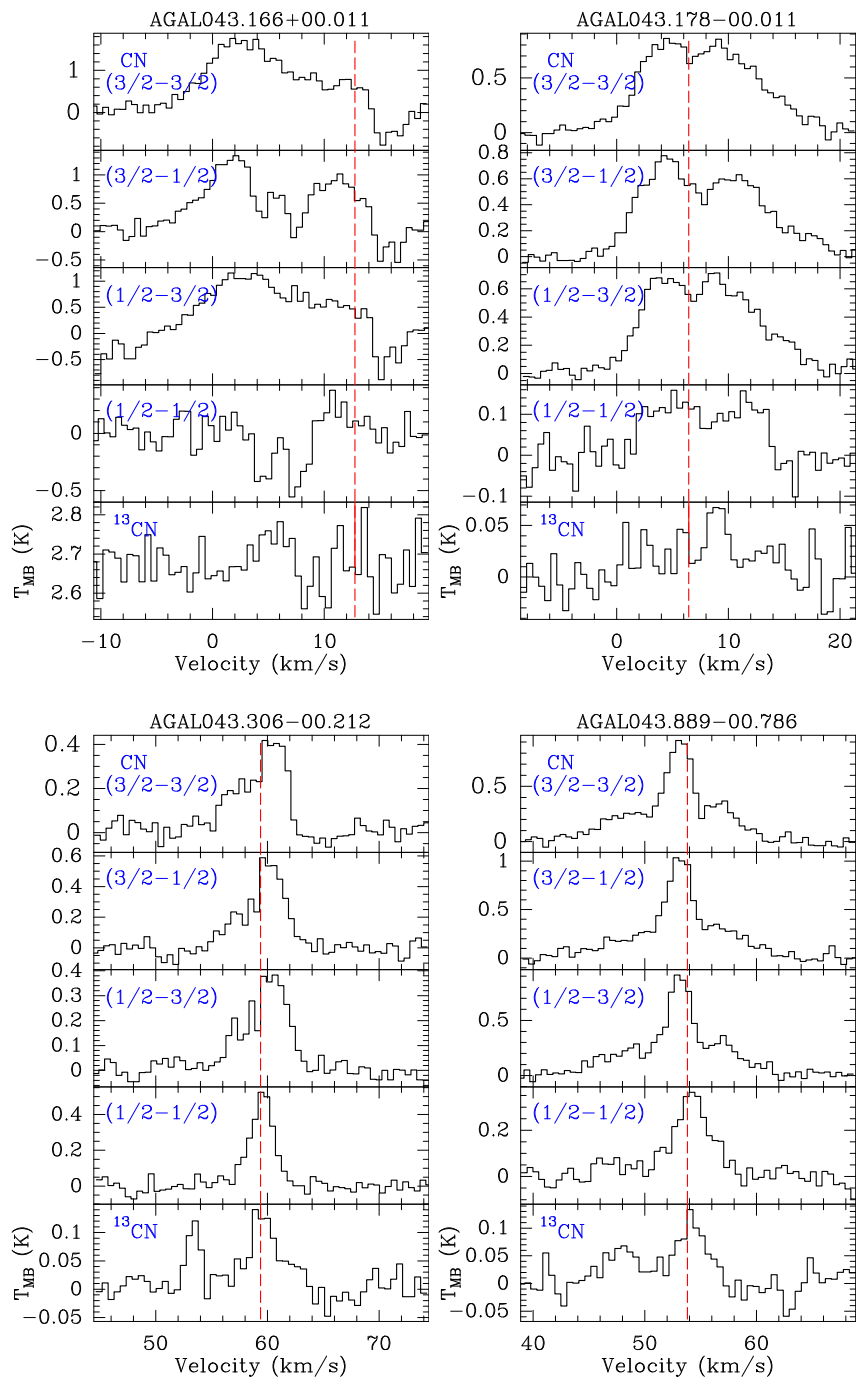
Figure B.1: Continued.

Figure B.1: Continued.

Figure B.1: Continued.

Figure B.1: Continued.
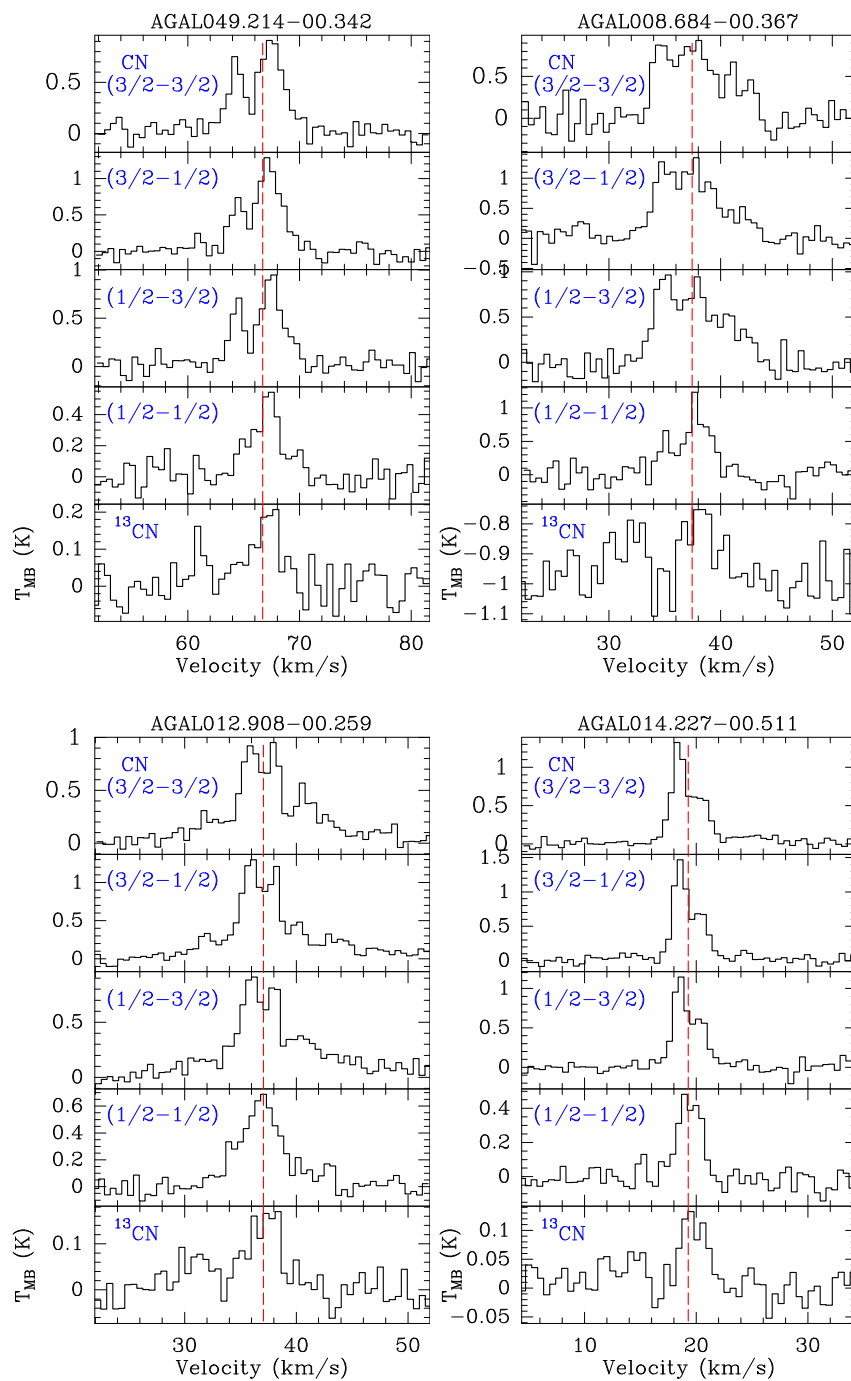
Figure B.1: Continued.
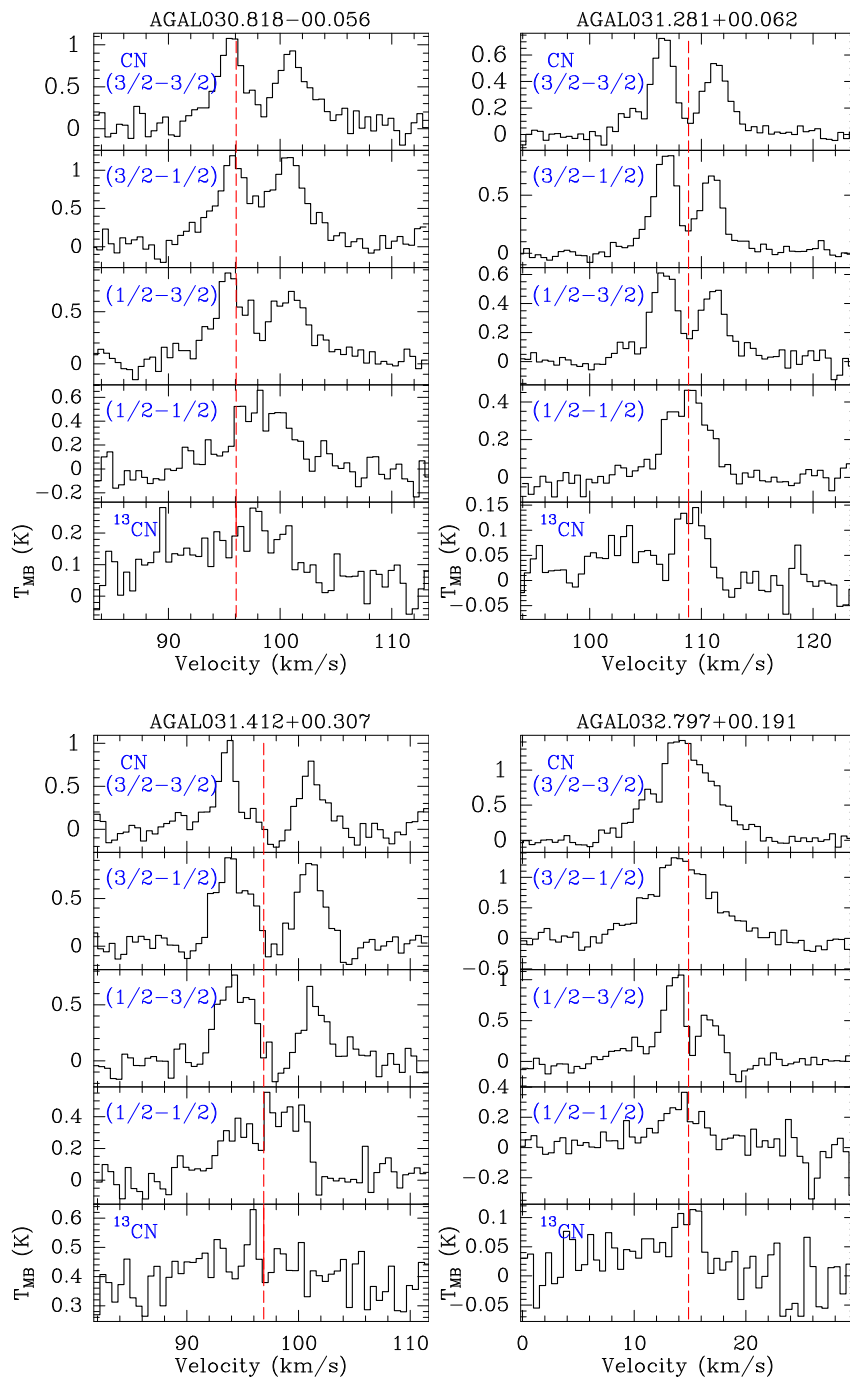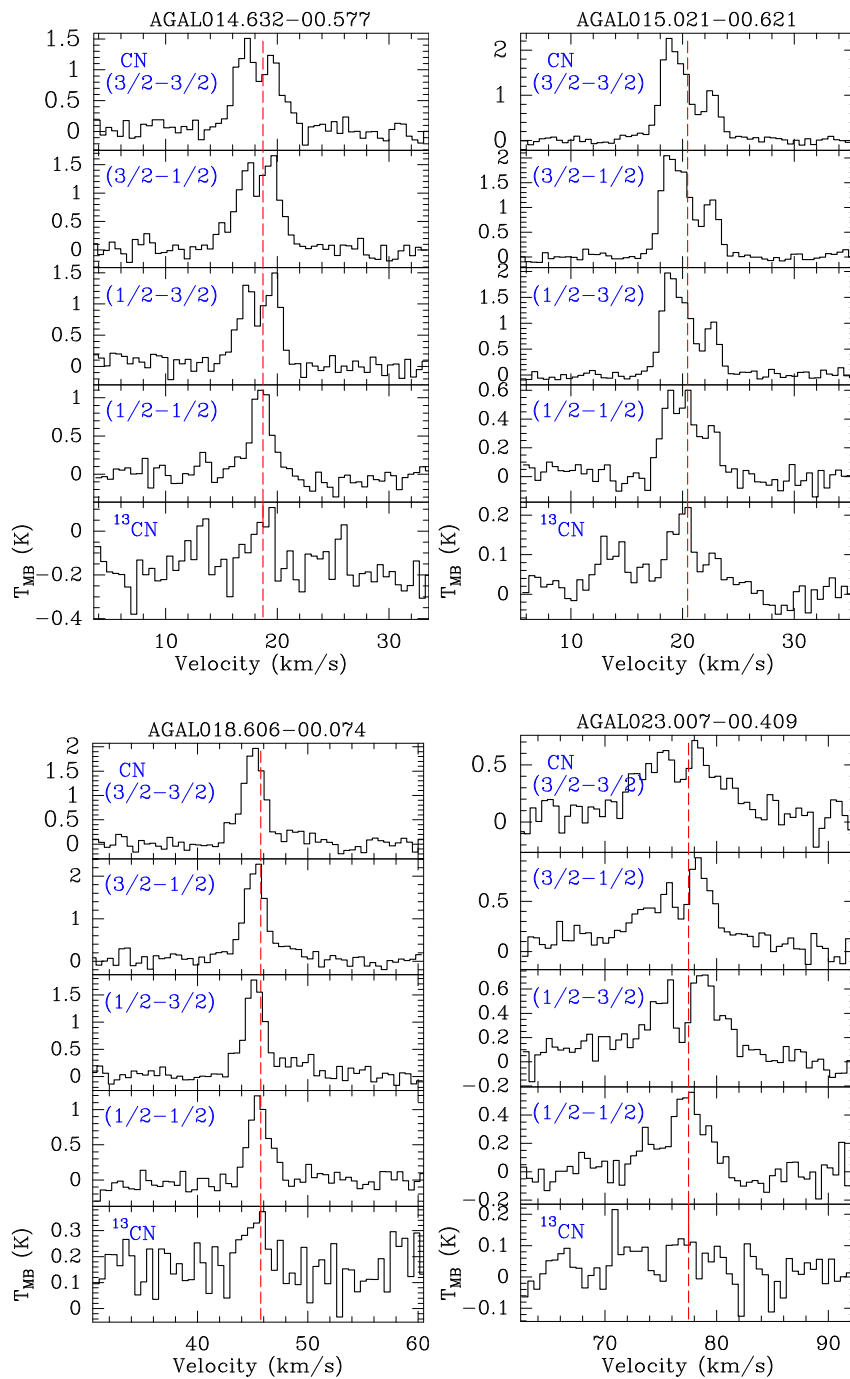
Figure B.1: Continued.
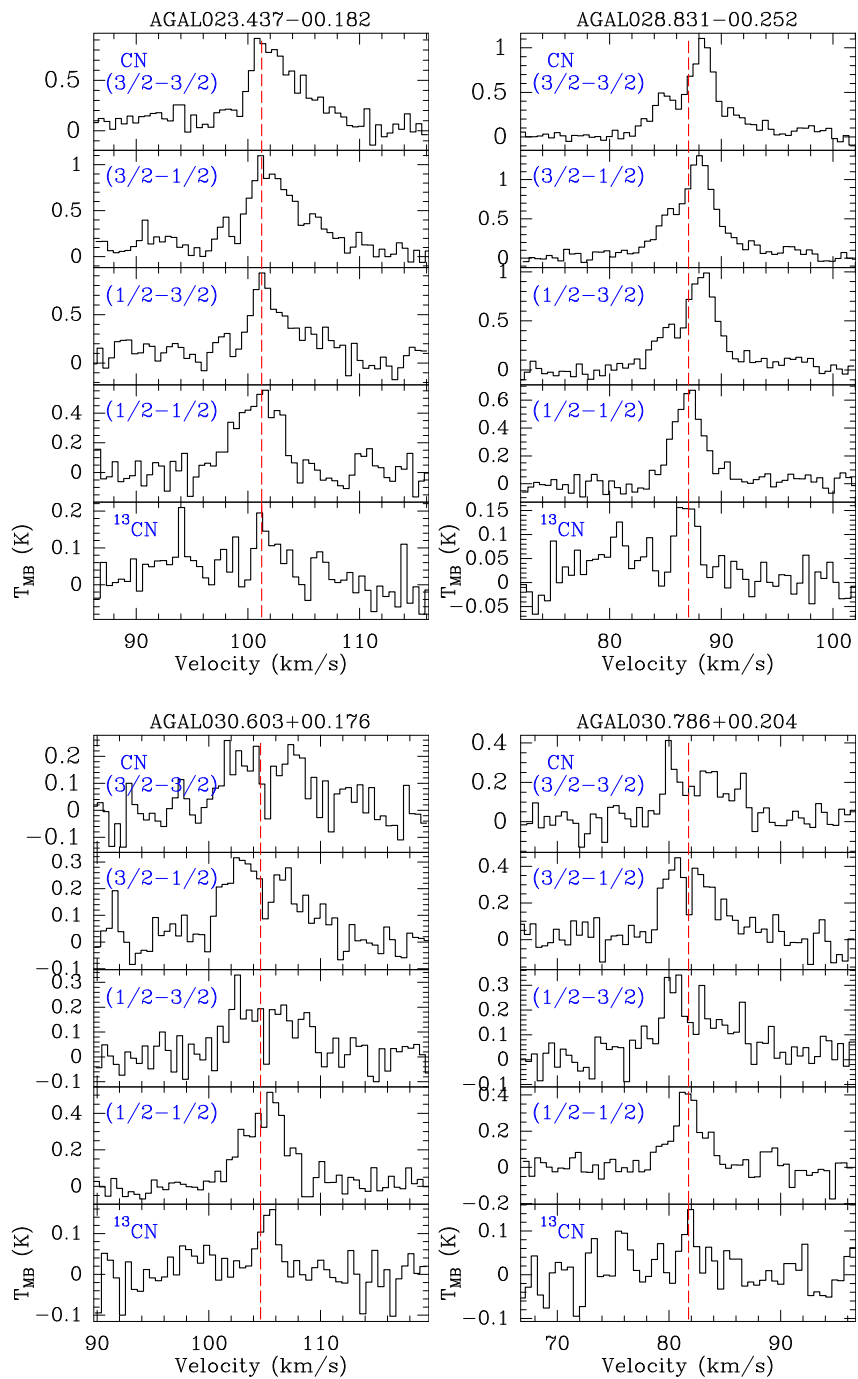
Figure B.1: Continued.
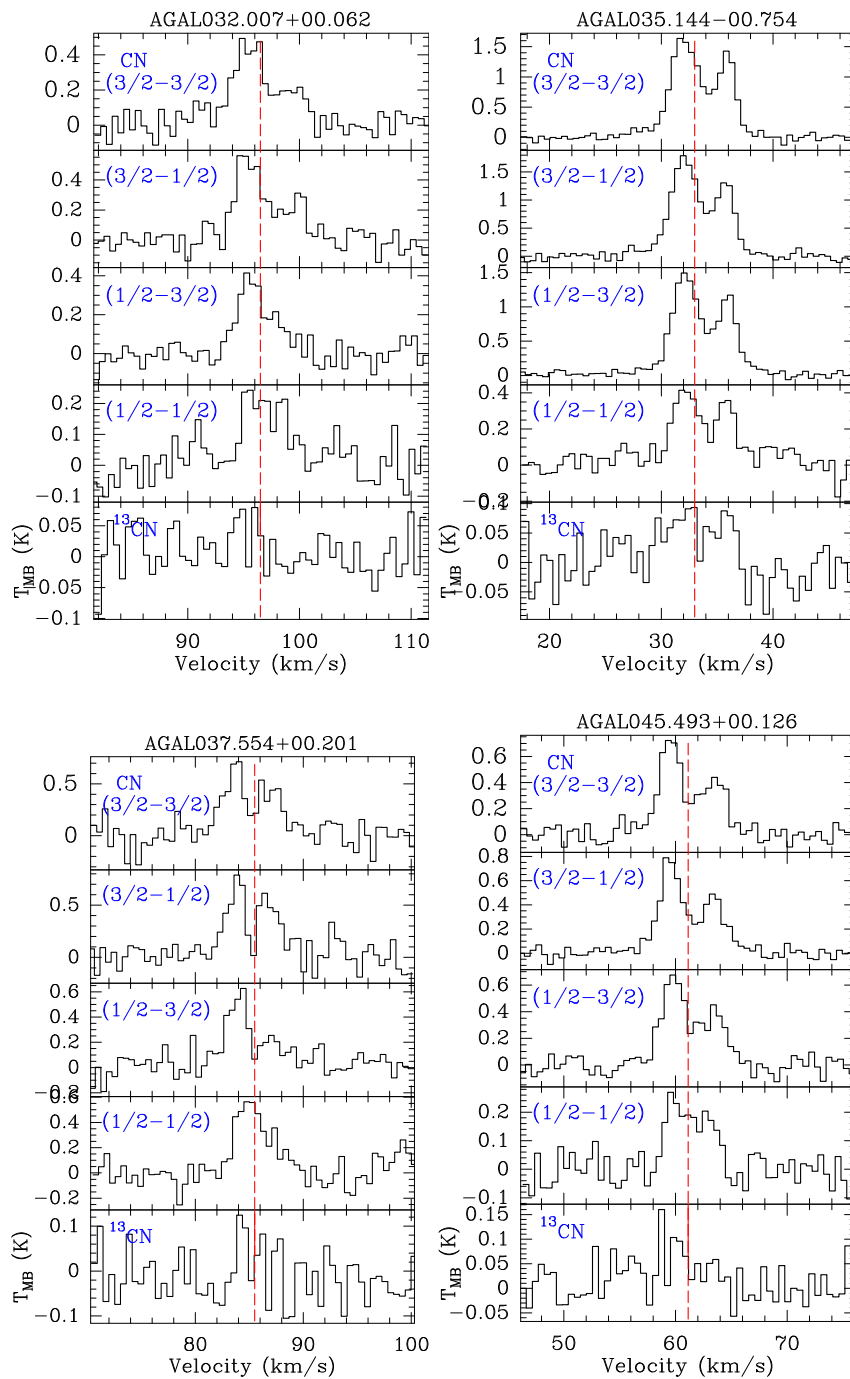
Figure B.1: Continued.

B.4   Spectral lines of Hydroxymethylidyne (HOC$^+$)
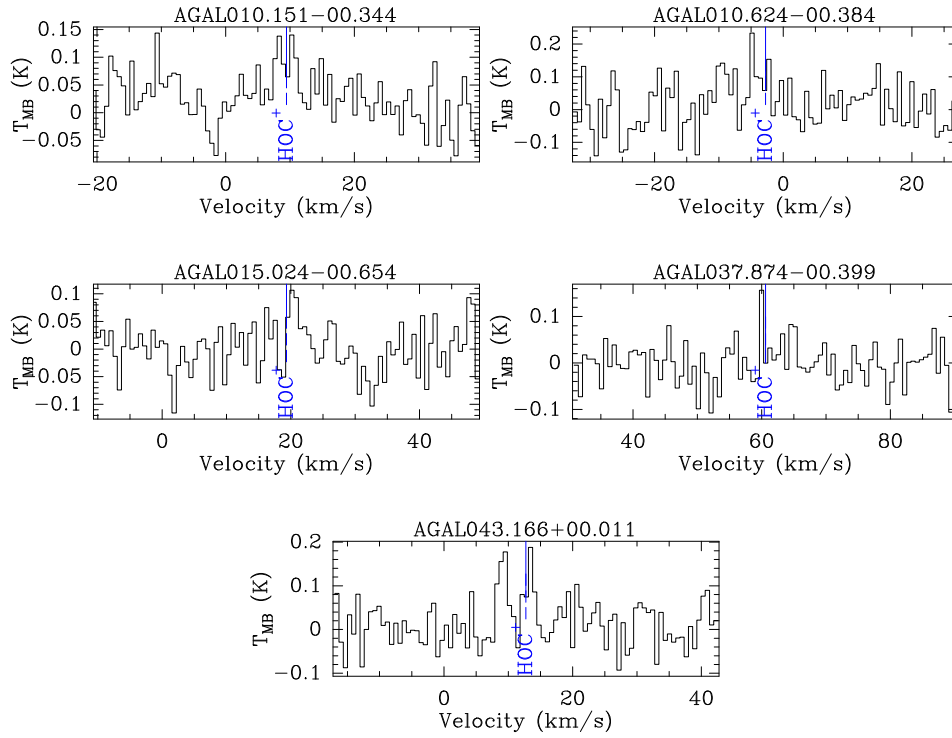
Figure B.2: HOC$^+$ spectral lines.

B.5   Detection rates of molecular lines in distance
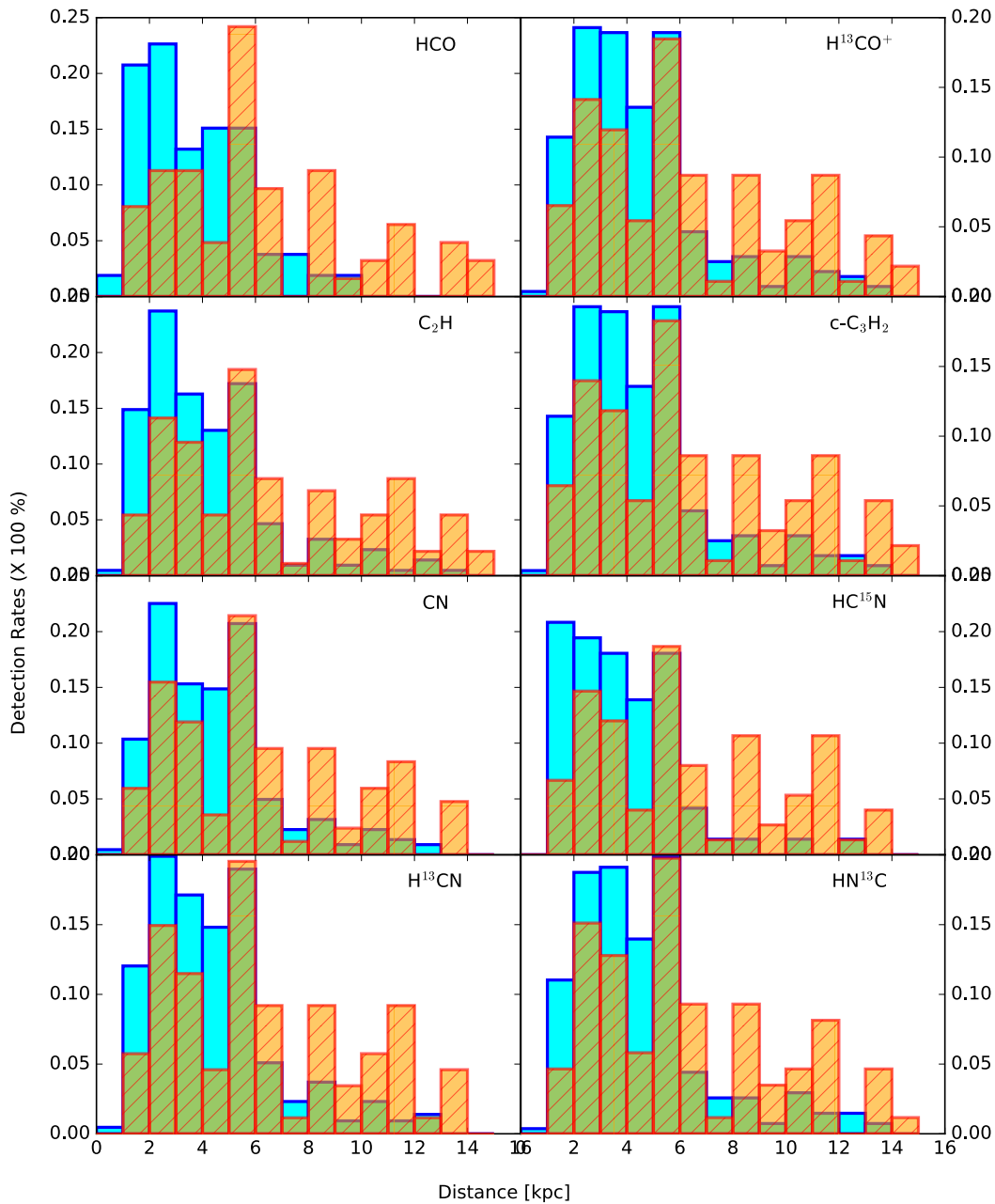
Figure B.3: Detection rate as a function of distance.

B.6   Linewidth of molecular lines with distance
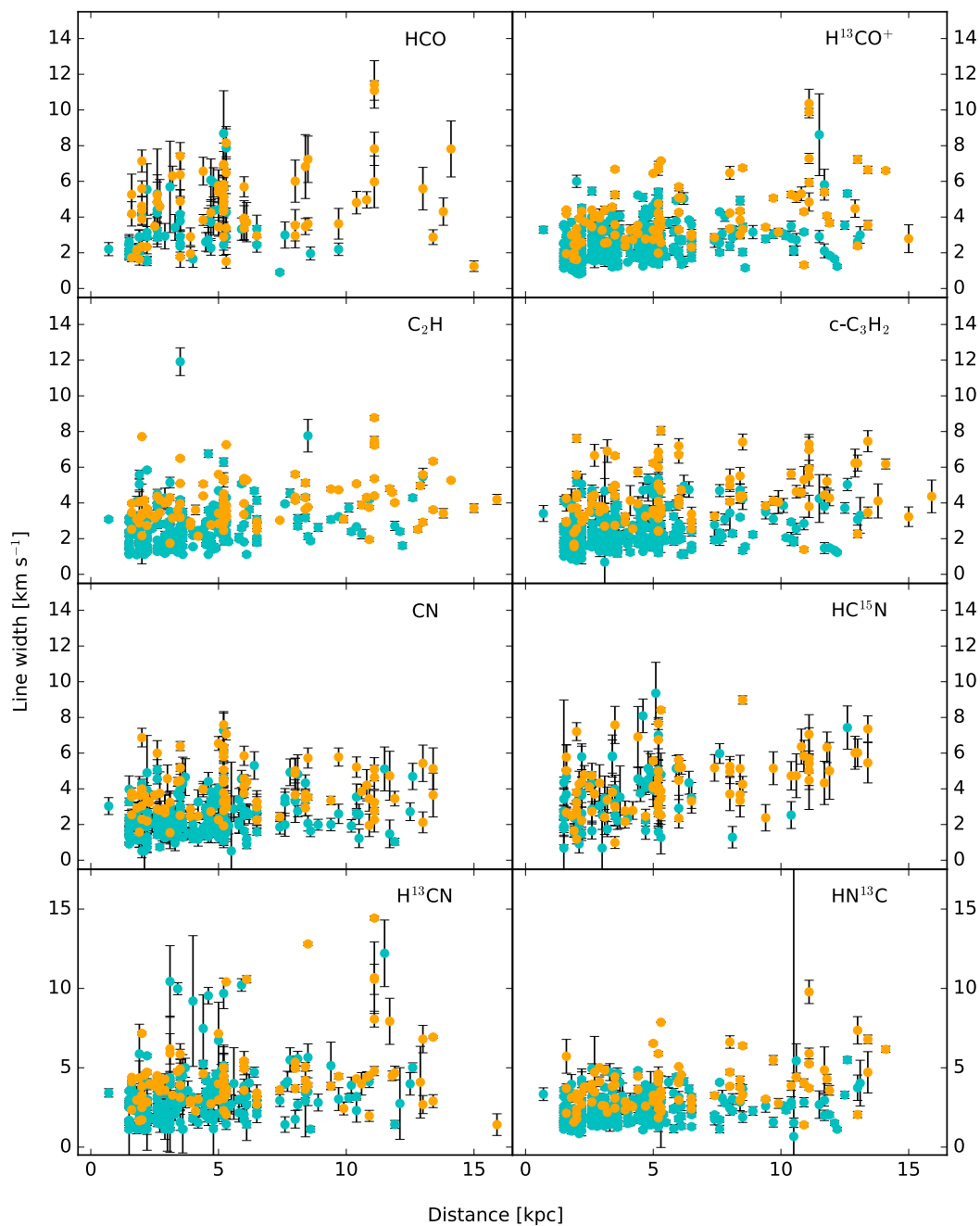
Figure B.4:   Line width as a function of distance.

B.7   Linewidth of molecular lines compared with linewidth of RRLs
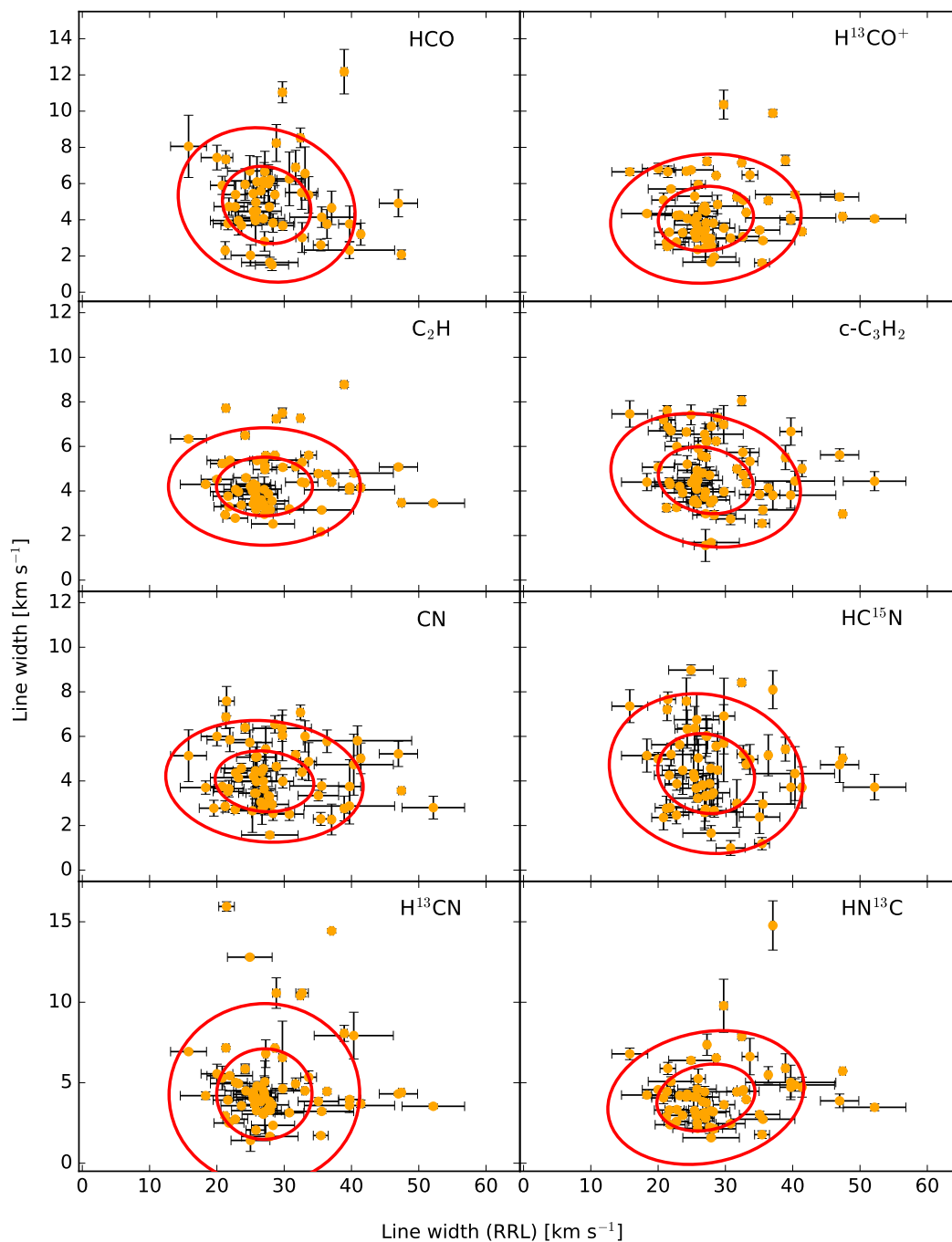
Figure B.5: Line width of the selected molecular species as a function of line width of RRLs.

B.8 Integrated intensity ratios

Figure B.6: Integrated flux ratio of $X/C^{18}O$ as a function of integrated flux of $C^{18}O$. The X refers noted molecular species. The red and cyan colors are same like those in Figure 6.8. The red and blue eclipses represent PCA ellipses showing the distributions of the data points.

B.9   Column density of detected molecules

Table B.4:   Column density of molecules in units of cm^{-2}. This table shows the full table.

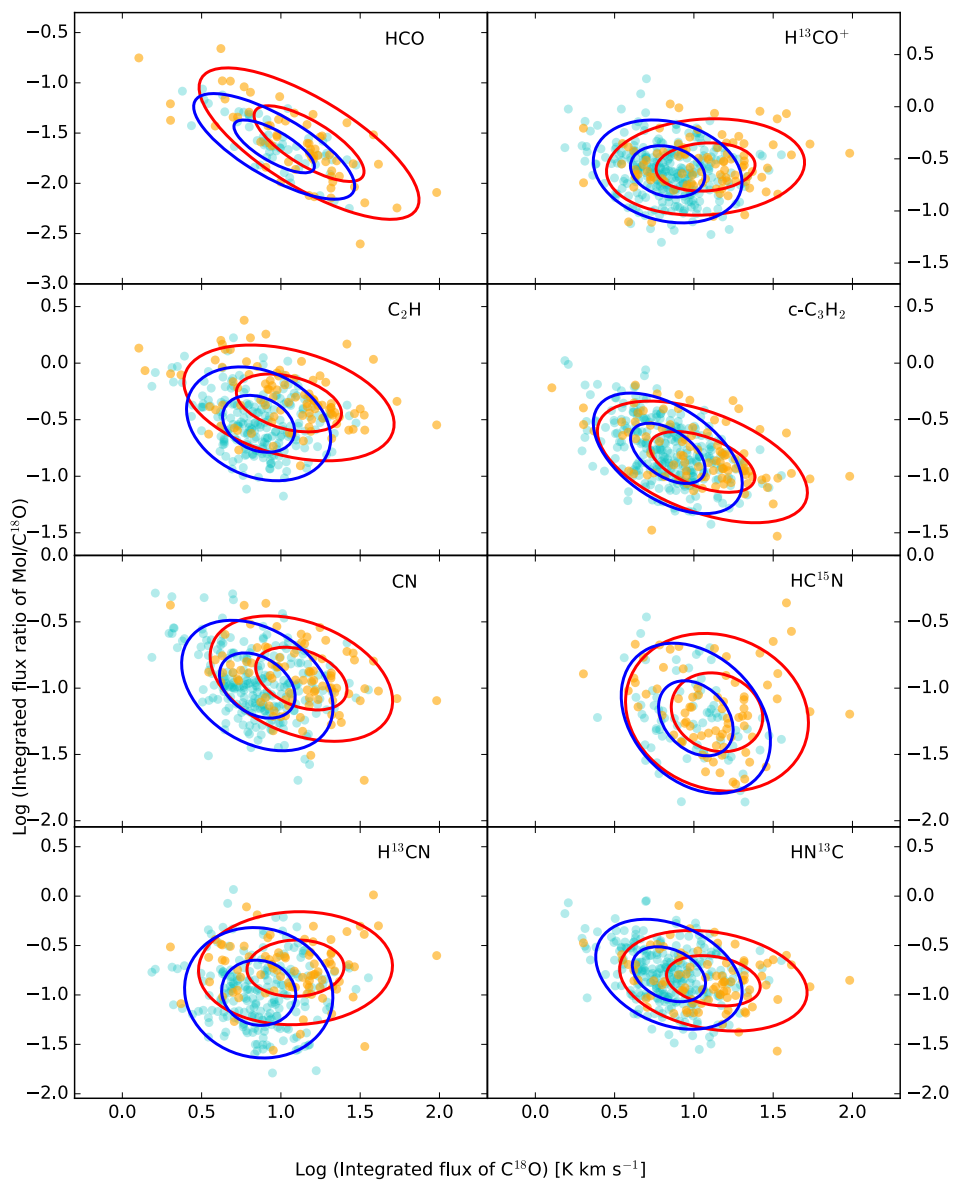| ATLASGAL Name	$C^{18}O$ $\times10^{16}$	HCO $\times10^{13}$	$H^{13}CO^+$ $\times10^{13}$	C_2H $\times10^{15}$	$c\text{-}C_3H_2$ $\times10^{13}$	CN $\times10^{15}$	$HC^{15}N$ $\times10^{13}$	$H^{13}CN$ $\times10^{13}$	$HN^{13}C$ $\times10^{14}$
AGAL006.216−00.609	1.08	−	0.41	0.79	2.56	0.86	0.05	0.67	0.07
AGAL008.049−00.242	0.37	−	0.08	0.12	0.57	0.23	−	0.16	0.02
AGAL008.671−00.356	−	1.26	0.96	1.73	3.67	−	−	−	0.17
AGAL008.684−00.367	2.90	−	1.00	−	2.42	1.31	0.21	3.37	0.13
AGAL008.706−00.414	1.26	−	0.31	0.42	1.81	0.61	−	0.98	0.06
AGAL010.079−00.196	0.69	0.35	0.07	0.38	0.47	0.20	−	0.15	0.01
AGAL010.104−00.416	0.66	−	0.14	0.17	0.37	0.23	−	0.06	0.01
AGAL010.151−00.344	1.34	1.48	0.61	0.75	6.23	1.78	0.05	1.54	0.05
AGAL010.168−00.362	1.45	0.92	0.76	0.88	5.81	1.55	0.15	1.35	0.01
AGAL010.213−00.322	1.65	0.64	0.31	1.91	1.84	1.13	0.06	2.64	0.07
AGAL010.214−00.306	1.22	0.52	0.17	0.39	0.84	0.46	−	1.14	0.03
AGAL010.284−00.114	0.99	0.27	0.33	0.47	0.77	0.70	0.06	0.82	0.05
AGAL010.288−00.124	0.80	0.56	0.22	0.72	0.67	0.64	0.07	0.83	0.04
AGAL010.321−00.231	0.54	−	0.10	0.16	0.42	0.39	−	−	0.02
AGAL010.323−00.161	0.64	0.85	0.25	0.22	0.92	0.60	0.04	0.79	0.04
AGAL010.342−00.142	1.03	−	0.34	0.49	1.48	0.74	0.12	1.56	0.05
AGAL010.444−00.017	1.20	−	0.23	0.13	0.57	0.32	−	1.22	0.02
AGAL010.472+00.027	3.34	1.62	1.16	−	2.95	1.48	1.54	5.56	0.14
AGAL010.579−00.349	0.89	−	0.09	0.15	0.36	0.15	−	−	0.01
AGAL010.618−00.031	0.54	−	0.07	0.05	0.28	−	−	0.56	0.01
AGAL010.619−00.422	0.69	−	0.08	0.25	0.41	0.22	−	0.11	0.01
AGAL010.624−00.384	7.51	2.11	2.71	2.40	6.84	2.81	0.83	6.09	0.22
AGAL010.626−00.337	1.86	0.93	0.31	1.17	1.65	0.86	0.09	0.74	0.04
AGAL010.634−00.511	0.60	−	0.08	0.17	0.57	0.29	−	−	0.02
AGAL010.659+00.079	0.61	−	0.14	0.08	0.66	0.22	−	−	0.03
AGAL010.669−00.221	0.65	−	0.10	0.24	0.98	0.36	−	0.52	0.03
AGAL010.684−00.307	0.53	−	0.10	0.21	0.21	0.17	−	−	0.01
AGAL010.742−00.126	0.88	−	0.15	0.96	0.84	0.27	−	0.75	0.04
AGAL010.747+00.016	0.41	−	0.05	−	0.27	0.21	−	−	0.01
AGAL010.752−00.197	0.47	−	0.13	0.41	0.77	0.23	−	0.07	0.03
AGAL010.827−00.022	0.52	−	0.05	0.25	0.38	−	−	−	0.01
AGAL010.957+00.022	0.72	−	0.28	0.22	0.68	0.20	0.07	0.44	0.02
AGAL010.972−00.094	0.49	−	0.20	0.60	1.20	0.55	−	0.29	0.04
AGAL010.982−00.367	0.37	−	0.08	0.10	0.57	0.16	−	0.09	0.02
AGAL010.991−00.082	0.62	−	0.16	0.43	1.15	0.45	−	0.87	0.04
AGAL011.001−00.372	0.37	−	0.06	0.11	0.36	0.21	−	0.15	0.01
AGAL011.034+00.061	0.71	−	0.13	0.30	0.55	0.22	−	0.30	0.01
AGAL011.064−00.099	0.43	−	0.12	0.65	0.77	0.26	−	−	0.02
AGAL011.082−00.534	0.59	−	0.21	0.49	1.82	0.62	0.03	0.24	0.05
AGAL011.126−00.127	0.63	−	0.14	0.59	1.01	0.49	−	0.21	0.04
AGAL011.304−00.059	0.56	−	0.08	0.24	0.48	0.14	−	−	0.01
AGAL011.344+00.796	0.52	−	0.14	0.19	0.99	0.28	−	0.54	0.03
AGAL011.381+00.811	0.43	−	0.08	0.22	0.64	0.20	−	−	0.02
AGAL011.902−00.141	1.01	−	0.21	0.28	0.74	0.38	0.04	0.92	0.03
AGAL011.917−00.612	0.77	−	0.43	0.66	1.61	0.75	0.19	2.11	0.06
AGAL011.936−00.616	1.12	−	0.45	1.36	1.85	1.12	0.16	1.71	0.08
AGAL011.942−00.156	0.78	−	0.19	0.11	0.53	0.23	−	0.34	0.02
AGAL012.024−00.031	0.72	−	0.11	0.15	0.54	0.19	−	0.35	0.01
AGAL012.198−00.034	0.90	−	0.17	0.13	0.61	0.39	0.05	0.98	0.02
AGAL012.208−00.102	1.69	−	0.47	0.64	1.55	0.42	0.25	2.33	0.05
AGAL012.418+00.506	1.22	0.29	0.66	0.64	1.63	0.42	0.15	1.02	0.04
AGAL012.496−00.222	0.62	−	0.27	0.33	1.34	0.53	−	0.32	0.03
AGAL012.679−00.181	1.52	1.18	0.18	1.13	1.39	0.68	0.13	2.14	0.04
AGAL012.804−00.199	0.00	0.00	0.00	0.00	0.00	0.00	0.00	0.00	0.00
AGAL012.818+00.322	0.63	−	0.10	0.71	0.92	0.17	−	0.12	0.01
AGAL012.853−00.226	1.64	1.37	0.29	1.07	1.77	0.96	0.05	0.58	0.04
AGAL012.888+00.489	2.20	−	0.46	1.35	1.65	0.93	−	2.09	0.07
AGAL012.893−00.282	1.08	−	0.29	0.38	1.17	0.53	−	1.11	0.04
AGAL012.899−00.241	1.50	0.74	0.25	0.95	0.86	0.52	−	0.39	0.04
AGAL012.904−00.031	0.85	−	0.35	0.25	0.67	0.40	0.11	1.52	0.04
AGAL012.908−00.259	2.22	0.38	0.75	1.25	1.54	1.12	0.23	3.78	0.09
AGAL012.914−00.336	0.85	−	0.16	0.39	0.82	0.29	−	1.02	0.03
AGAL013.119−00.096	0.16	−	0.15	0.16	0.85	0.39	−	0.99	0.03
AGAL013.169+00.077	0.70	0.45	0.15	0.18	0.61	0.41	−	0.12	0.03
AGAL013.178+00.059	0.87	0.60	0.44	0.68	1.72	1.47	0.16	1.67	0.10
AGAL013.209−00.144	1.68	0.71	0.15	0.63	0.99	0.49	0.06	0.39	0.02
AGAL013.276−00.334	0.68	−	0.12	0.79	0.86	0.36	−	0.35	0.03
AGAL013.384+00.064	0.42	−	0.03	0.18	0.13	0.22	−	0.13	−
AGAL013.658−00.599	1.11	−	0.34	0.60	0.87	0.93	0.12	3.16	0.06
AGAL013.872+00.281	1.64	0.61	0.32	0.58	1.60	0.61	0.09	0.64	0.02
AGAL013.882−00.144	0.42	−	0.13	0.08	0.46	0.17	−	0.27	0.02
AGAL013.902−00.516	0.48	−	0.28	0.78	2.05	0.41	0.05	0.20	0.03
AGAL013.951−00.407	0.96	0.64	0.22	0.52	0.81	0.25	0.06	1.05	0.03
AGAL014.084−00.554	0.77	0.54	0.18	0.82	1.29	0.25	0.02	0.17	0.02

Table B.4: continued.

ATLASGAL Name	$C^{18}O$ $\times 10^{16}$	HCO $\times 10^{13}$	$H^{13}CO^+$ $\times 10^{13}$	C_2H $\times 10^{15}$	$c\text{-}C_3H_2$ $\times 10^{13}$	CN $\times 10^{15}$	$HC^{15}N$ $\times 10^{13}$	$H^{13}CN$ $\times 10^{13}$	$HN^{13}C$ $\times 10^{14}$
AGAL014.114−00.574	1.73	0.78	0.54	2.20	1.42	0.99	0.13	0.96	0.06
AGAL014.131−00.522	0.59	−	0.15	0.73	1.07	0.21	0.05	0.11	0.02
AGAL014.181−00.529	0.66	0.40	0.21	0.48	1.27	0.29	0.05	0.29	0.02
AGAL014.194−00.194	1.27	−	0.52	0.47	1.73	1.13	0.13	2.75	0.08
AGAL014.197−00.214	0.71	−	0.11	−	0.60	0.23	−	0.46	0.02
AGAL014.204−00.207	0.46	−	0.16	−	0.64	0.15	0.05	0.60	0.02
AGAL014.227−00.511	1.34	0.70	0.54	0.89	1.45	0.49	0.14	1.26	0.04
AGAL014.246−00.071	1.21	−	0.20	0.48	1.16	0.65	0.08	0.90	0.04
AGAL014.327−00.532	0.50	−	0.18	0.25	0.66	0.49	−	0.19	0.03
AGAL014.331−00.644	1.05	−	0.77	2.47	1.55	1.03	0.37	2.84	0.09
AGAL014.434−00.699	0.52	0.56	0.12	0.28	0.70	0.16	0.04	0.25	0.01
AGAL014.492−00.139	1.34	0.93	0.28	0.98	1.91	0.81	−	1.71	0.07
AGAL014.617+00.332	0.67	−	0.16	0.32	1.08	0.46	−	0.17	0.02
AGAL014.632−00.577	0.96	0.56	0.43	2.40	1.28	0.99	0.19	1.48	0.07
AGAL014.644−00.117	0.32	−	0.12	0.08	0.83	0.42	−	−	0.04
AGAL014.686−00.222	0.36	−	0.04	−	0.13	−	−	−	−
AGAL014.711−00.224	0.39	−	0.06	−	0.64	0.25	−	0.29	0.02
AGAL014.771−00.356	0.40	−	0.11	−	0.39	0.19	−	0.43	0.01
AGAL014.777−00.334	0.29	−	0.08	0.18	0.70	0.18	−	0.47	0.02
AGAL014.777−00.487	0.18	−	0.08	0.13	0.39	0.24	−	0.37	0.01
AGAL014.851−00.990	0.42	−	0.27	0.21	0.98	0.20	−	0.20	0.02
AGAL015.006+00.009	0.71	−	0.09	0.16	0.41	0.29	−	0.08	0.02
AGAL015.021−00.621	1.01	0.75	0.18	1.07	1.49	0.91	0.11	1.14	0.01
AGAL015.024−00.654	1.24	2.13	0.26	0.80	3.51	0.98	0.27	1.38	0.02
AGAL015.029−00.669	2.00	2.96	1.82	1.73	5.01	1.76	0.64	3.18	0.08
AGAL015.051−00.642	0.34	0.90	0.08	0.27	1.24	0.40	0.04	0.23	0.01
AGAL015.053+00.089	0.54	−	0.09	0.14	0.71	0.26	0.05	−	0.01
AGAL015.056−00.624	0.46	1.43	0.16	1.20	2.21	0.90	0.08	0.47	0.03
AGAL015.193−00.627	0.00	0.00	0.00	0.00	0.00	0.00	0.00	0.00	0.00
AGAL015.216−00.426	0.18	−	0.07	−	0.20	0.21	−	−	0.01
AGAL015.434+00.192	0.62	−	0.13	0.13	0.67	−	−	0.14	0.01
AGAL015.503−00.419	0.63	−	0.09	0.24	0.96	0.23	−	0.07	0.02
AGAL015.583−00.029	0.60	−	0.06	−	0.33	0.18	−	−	0.01
AGAL015.709−00.581	0.47	−	0.08	0.19	0.62	0.22	−	0.10	0.01
AGAL015.718−00.594	0.43	−	0.16	0.15	0.57	−	−	0.28	0.02
AGAL015.791−00.412	0.30	−	0.06	0.13	0.52	−	−	−	0.01
AGAL016.303−00.524	0.59	0.65	0.06	−	0.47	−	−	−	0.01
AGAL016.336−00.586	0.53	−	0.10	0.21	0.97	0.21	−	0.38	0.02
AGAL016.404−00.181	0.55	−	0.10	−	0.37	−	−	0.81	0.01
AGAL016.418−00.634	0.48	−	0.04	0.86	0.83	−	−	−	0.02
AGAL016.432−00.667	0.39	−	0.07	−	0.51	0.19	−	−	0.02
AGAL016.442−00.384	0.59	−	0.10	0.13	0.60	0.31	−	−	0.01
AGAL016.474−00.641	0.35	−	0.07	−	0.51	−	−	−	0.01
AGAL016.502−00.642	0.37	−	0.03	−	0.25	−	−	−	0.01
AGAL016.586−00.051	1.77	0.37	0.38	0.46	1.00	0.58	0.15	1.50	0.04
AGAL016.739−00.089	0.63	−	0.06	−	0.53	0.19	−	−	0.01
AGAL016.889+00.484	0.40	−	0.08	0.10	0.27	−	−	−	0.01
AGAL016.916−00.084	0.44	−	0.14	0.33	1.14	0.52	−	0.39	0.04
AGAL016.924+00.284	0.54	0.70	0.03	0.17	0.52	−	−	−	−
AGAL016.927+00.957	1.52	0.31	0.49	1.13	1.55	0.59	0.10	0.74	0.05
AGAL016.942−00.072	0.18	−	−	0.15	0.42	−	−	0.05	−
AGAL016.951+00.779	0.17	0.31	0.10	−	0.53	0.32	0.04	0.17	0.01
AGAL016.974−00.222	0.24	−	0.07	−	0.40	−	−	−	0.01
AGAL016.986−00.922	0.32	−	0.13	0.26	1.07	0.39	−	0.45	0.03
AGAL017.029+00.427	0.56	0.65	0.09	0.30	0.43	0.12	−	−	−
AGAL017.067+00.682	0.46	0.68	0.05	0.16	0.32	−	−	0.11	0.00
AGAL017.454−00.194	0.77	−	0.08	−	0.43	−	−	−	0.01
AGAL017.554+00.167	0.32	−	0.03	0.23	0.28	−	−	−	−
AGAL017.637+00.154	0.80	−	0.45	0.43	1.02	0.43	0.07	0.45	0.03
AGAL017.652+00.172	0.56	−	0.15	0.30	0.43	−	−	0.12	0.01
AGAL017.667+00.177	0.42	−	0.11	0.10	0.53	0.16	0.05	−	0.01
AGAL017.914−00.489	0.31	−	0.04	−	0.25	−	−	−	0.01
AGAL017.990−00.347	0.47	−	0.15	0.33	0.93	0.40	−	0.22	0.02
AGAL018.098−00.354	−	−	0.09	−	0.30	−	−	−	0.01
AGAL018.139+00.334	−	−	0.08	0.16	0.50	−	−	−	0.01
AGAL018.231+00.652	−	−	0.13	0.40	0.96	−	−	0.33	0.02
AGAL018.286−00.707	−	−	0.09	0.12	0.56	−	−	−	0.02
AGAL018.301−00.389	−	1.31	0.39	0.70	1.23	−	0.08	0.66	0.04
AGAL018.371−00.381	−	−	0.19	0.13	0.73	−	−	0.29	0.02
AGAL018.409−00.291	−	−	0.07	0.20	0.62	−	−	−	0.01
AGAL018.461−00.002	−	−	0.24	0.71	1.07	−	0.12	0.67	0.03
AGAL018.493−00.199	−	−	0.05	0.18	0.42	−	−	−	0.01
AGAL018.549+00.036	−	−	0.10	−	0.38	−	−	0.17	0.01
AGAL018.606−00.074	0.48	−	0.42	0.34	2.37	1.16	0.13	0.86	0.09
AGAL018.661+00.036	−	−	0.17	0.13	0.65	−	−	0.43	0.02
AGAL018.734−00.226	0.67	−	0.45	0.23	1.31	0.73	0.16	2.31	0.08
AGAL018.789−00.286	−	−	0.19	0.22	0.85	−	−	0.23	0.04
AGAL018.844−00.376	−	−	0.17	−	0.78	−	−	−	0.02
AGAL018.883−00.651	−	−	0.08	−	0.32	−	−	−	0.01
AGAL018.888−00.474	2.16	1.10	0.76	0.56	2.95	2.20	0.13	3.52	0.13

Table B.4: continued.

ATLASGAL Name	C^{18}O ×10^{16}	HCO ×10^{13}	H^{13}CO$^+$ ×10^{13}	C$_2$H ×10^{15}	c-C$_3$H$_2$ ×10^{13}	CN ×10^{15}	HC^{15}N ×10^{13}	H^{13}CN ×10^{13}	HN^{13}C ×10^{14}
AGAL018.991−00.057	−	−	0.08	−	0.28	−	−	0.39	0.02
AGAL019.076−00.287	−	0.99	0.32	0.75	1.66	−	0.17	1.04	0.05
AGAL019.248+00.267	−	−	0.14	0.10	0.35	−	−	0.41	0.01
AGAL019.472+00.171	−	0.82	0.48	0.91	1.38	−	−	−	0.06
AGAL019.486−00.199	−	−	0.07	−	0.15	−	−	−	0.02
AGAL019.589−00.079	−	−	0.10	−	0.74	−	−	−	0.01
AGAL019.732−00.651	−	−	0.09	0.54	0.49	−	−	−	0.01
AGAL020.892−00.179	0.75	−	0.17	−	0.77	−	−	−	0.02
AGAL021.561−00.032	0.46	−	0.12	−	0.53	−	−	0.23	0.02
AGAL022.038+00.222	0.97	−	0.27	0.27	0.80	0.41	−	1.12	0.02
AGAL022.332−00.154	0.28	−	0.08	−	0.37	−	−	−	0.01
AGAL022.376+00.447	0.80	−	0.27	0.30	1.60	−	−	0.81	0.03
AGAL022.412+00.317	1.30	−	0.16	0.39	0.98	0.26	−	0.19	0.03
AGAL022.484−00.936	0.39	−	0.10	−	0.29	−	−	0.24	0.01
AGAL022.531−00.192	0.74	−	0.15	0.36	0.96	0.40	−	0.62	0.03
AGAL023.007−00.409	0.65	0.54	0.44	0.46	1.10	0.89	−	6.77	0.07
AGAL023.206−00.377	1.09	0.54	0.32	0.37	1.49	0.55	0.31	0.70	0.06
AGAL023.277−00.214	1.28	−	0.20	−	0.94	0.32	−	0.18	0.04
AGAL023.387+00.187	0.68	−	0.31	0.48	1.55	0.21	−	0.37	0.03
AGAL023.437−00.182	2.42	1.14	0.60	1.24	1.58	0.95	0.18	4.21	0.07
AGAL023.656−00.127	0.31	−	0.04	−	0.19	−	−	−	−
AGAL023.817+00.386	0.28	−	0.10	−	0.46	0.30	−	0.28	0.02
AGAL023.964−00.109	0.93	−	0.25	0.54	0.85	0.46	−	2.21	0.04
AGAL024.010+00.489	0.40	−	0.08	−	0.49	0.24	−	0.81	0.03
AGAL024.141+00.127	0.18	−	0.05	−	0.29	0.40	−	−	0.01
AGAL024.416+00.101	0.81	−	0.17	0.41	0.79	0.55	−	0.23	0.03
AGAL024.629+00.172	0.79	0.49	0.18	−	0.63	0.39	−	0.25	0.03
AGAL024.633−00.324	0.61	−	0.22	0.34	0.98	0.23	−	0.24	0.02
AGAL024.651−00.169	1.44	−	0.10	−	0.54	0.43	−	0.64	0.01
AGAL024.673−00.151	2.30	1.14	0.35	0.85	1.87	1.97	0.10	1.21	0.06
AGAL024.728+00.152	0.83	−	0.13	0.31	0.46	0.29	−	0.29	0.02
AGAL024.789+00.082	2.34	0.69	0.61	1.30	1.58	1.77	0.43	8.93	0.10
AGAL024.796+00.101	1.16	1.47	0.17	0.62	1.68	1.31	0.05	0.53	0.02
AGAL025.409+00.106	0.59	−	0.22	0.14	1.26	0.40	−	0.61	0.03
AGAL025.649+01.051	0.58	−	0.62	0.58	1.34	0.55	0.20	3.43	0.05
AGAL026.159+00.156	0.79	0.36	0.10	−	0.65	0.32	−	0.05	0.01
AGAL026.509+00.282	0.88	−	0.44	0.48	1.08	0.81	0.29	3.21	0.07
AGAL026.652+00.007	0.63	−	0.04	−	0.25	0.13	−	−	0.00
AGAL026.849+00.181	0.64	−	0.06	−	0.50	0.12	−	0.14	0.01
AGAL027.000−00.296	0.67	−	0.07	−	0.23	0.16	−	−	0.01
AGAL027.184−00.081	0.39	0.61	0.12	0.35	0.79	0.24	0.06	0.63	0.01
AGAL027.314+00.177	0.43	−	0.12	−	0.80	0.37	−	0.19	0.02
AGAL027.366−00.166	1.73	0.36	0.76	0.43	2.13	1.00	0.21	3.12	0.08
AGAL027.464+00.119	0.74	−	0.12	0.21	1.18	0.41	−	0.17	0.03
AGAL027.551−00.936	0.62	−	0.07	−	0.52	−	−	0.18	0.01
AGAL027.758+00.051	0.82	−	0.12	0.11	0.82	0.49	−	0.24	0.02
AGAL027.796−00.277	0.80	−	0.18	0.57	0.59	0.27	−	0.24	0.02
AGAL027.974−00.421	0.37	−	0.11	0.12	0.56	0.14	−	0.46	0.02
AGAL028.194−00.074	1.25	−	0.13	−	0.58	0.17	−	0.15	0.01
AGAL028.199−00.049	1.64	0.49	0.56	0.41	1.70	0.91	0.23	1.95	0.08
AGAL028.231+00.041	0.00	−	0.00	0.00	0.00	0.00	−	0.00	0.00
AGAL028.273−00.167	1.02	−	0.11	−	0.46	−	−	−	0.02
AGAL028.344+00.061	1.12	−	0.26	0.34	1.27	0.47	−	1.00	0.05
AGAL028.354+00.072	0.62	−	0.12	0.48	1.17	0.37	−	0.96	0.04
AGAL028.361+00.054	0.56	−	0.17	−	0.65	0.28	−	0.93	0.03
AGAL028.398+00.081	1.13	0.42	0.23	1.31	1.05	0.50	0.11	2.20	0.04
AGAL028.564−00.236	0.00	0.00	0.00	0.00	0.00	0.00	0.00	0.00	0.00
AGAL028.658+00.144	0.34	−	0.09	−	0.52	0.28	−	1.19	0.03
AGAL028.677−00.277	0.73	−	0.18	0.28	1.18	0.32	−	0.19	0.02
AGAL028.707−00.294	0.96	−	0.14	0.24	0.98	0.38	−	0.41	0.01
AGAL028.722−00.296	0.87	−	0.09	0.13	0.62	0.14	−	−	0.01
AGAL028.831−00.252	1.40	−	0.33	0.75	1.09	0.81	0.07	1.54	0.05
AGAL028.849+00.051	0.89	−	0.07	−	0.28	−	−	−	0.01
AGAL028.861+00.066	1.74	−	0.37	0.67	1.30	0.75	0.19	1.66	0.03
AGAL029.117+00.027	1.09	−	0.11	−	0.77	0.34	−	0.15	0.02
AGAL029.409−00.646	0.43	−	0.18	0.31	1.34	0.45	−	0.20	0.03
AGAL029.556+00.186	0.46	−	0.11	0.38	0.92	0.28	−	0.37	0.02
AGAL029.591−00.614	0.75	−	0.13	0.21	0.80	0.39	−	0.32	0.03
AGAL029.861+00.029	1.31	−	−	0.23	1.09	0.27	−	0.25	0.02
AGAL029.911−00.042	1.00	1.50	0.33	0.95	1.95	0.86	0.05	0.85	0.04
AGAL029.954−00.016	1.23	0.78	0.56	0.48	1.84	0.77	0.37	2.95	0.05
AGAL029.976−00.047	−	−	−	−	−	0.58	−	1.21	0.04
AGAL029.976−00.047a	−	−	−	0.00	0.00	−	0.00	−	−
AGAL030.003−00.269	1.15	−	0.10	0.56	0.93	0.32	0.05	0.38	0.03
AGAL030.198−00.169	0.42	0.64	0.08	0.15	0.59	−	−	0.25	0.01
AGAL030.321+00.296	0.49	−	0.07	−	0.48	−	−	−	0.02
AGAL030.419−00.231	1.25	−	0.39	0.46	1.41	0.88	0.09	1.04	0.05
AGAL030.429−00.116	0.36	−	0.04	−	0.25	−	−	−	0.01
AGAL030.568−00.026	0.31	−	0.09	−	0.25	0.12	−	0.15	0.01
AGAL030.588−00.042	1.11	−	0.31	0.43	0.75	0.24	0.09	1.09	0.03

Table B.4: continued.

ATLASGAL Name	C^{18}O ×10^{16}	HCO ×10^{13}	H^{13}CO$^+$ ×10^{13}	C$_2$H ×10^{15}	c-C$_3$H$_2$ ×10^{13}	CN ×10^{15}	HC^{15}N ×10^{13}	H^{13}CN ×10^{13}	HN^{13}C ×10^{14}
AGAL030.603+00.176	0.72	0.79	0.24	0.68	1.32	0.85	0.12	1.33	0.06
AGAL030.683−00.074	1.21	0.96	0.20	0.99	0.99	0.75	0.07	0.54	0.03
AGAL030.703−00.067	1.48	1.35	0.33	1.34	1.73	1.15	0.28	0.70	0.10
AGAL030.718−00.082	1.74	−	−	−	−	1.05	−	−	−
AGAL030.731−00.079	1.63	0.93	0.20	0.68	0.72	0.52	−	0.39	0.02
AGAL030.753−00.051	0.82	−	−	−	−	0.31	−	−	−
AGAL030.786+00.204	0.63	−	0.22	0.59	0.66	0.50	0.06	1.62	0.03
AGAL030.811−00.111	0.65	−	0.15	0.12	0.47	0.24	−	0.16	0.02
AGAL030.818+00.274	0.41	−	0.10	0.11	0.44	0.20	−	0.21	0.01
AGAL030.818−00.056	1.09	−	−	−	−	1.29	−	−	−
AGAL030.848−00.081	0.82	−	0.19	0.43	0.66	0.56	−	0.43	0.03
AGAL030.863−00.039	1.11	−	0.07	−	0.30	0.10	−	−	0.01
AGAL030.866+00.114	0.66	0.57	0.15	0.35	1.22	0.22	0.04	0.49	0.02
AGAL030.866−00.119	0.79	−	0.10	−	0.29	−	−	−	−
AGAL030.893+00.139	1.09	−	0.29	0.29	1.39	0.55	−	17.53	0.05
AGAL030.898+00.162	0.75	−	0.24	0.29	1.00	0.61	0.04	0.59	0.05
AGAL030.971−00.141	0.74	−	0.31	0.21	0.98	0.62	−	0.48	0.04
AGAL030.996−00.076	0.95	−	0.16	0.16	0.72	0.40	0.05	0.25	0.02
AGAL031.024+00.262	0.63	−	0.10	−	0.51	0.10	−	−	0.01
AGAL031.044+00.261	0.55	−	0.16	0.18	0.53	0.23	0.07	−	0.02
AGAL031.103+00.261	0.57	−	0.07	−	0.37	0.20	−	−	0.01
AGAL031.183−00.147	0.45	−	0.03	0.21	0.29	−	−	−	−
AGAL031.243−00.111	0.33	−	0.08	0.20	0.92	−	0.12	0.25	−
AGAL031.254+00.057	1.38	−	0.12	−	0.52	0.17	−	0.16	0.01
AGAL031.281+00.062	1.65	0.98	0.44	1.46	1.52	0.77	0.17	1.83	0.05
AGAL031.396−00.257	1.20	0.92	0.36	0.39	1.29	0.73	0.16	1.15	0.03
AGAL031.412+00.307	2.81	0.53	0.41	1.37	2.12	1.30	0.62	0.29	0.05
AGAL031.464+00.186	0.42	−	0.04	−	0.29	−	−	0.09	0.01
AGAL031.581+00.077	1.37	0.84	0.43	0.46	1.04	0.52	0.10	1.14	0.04
AGAL031.584−00.117	0.40	−	0.09	−	0.28	−	0.03	0.26	0.01
AGAL031.699−00.494	0.47	−	0.11	0.22	0.71	0.25	−	−	0.02
AGAL031.982+00.064	0.31	−	0.10	0.52	0.52	0.30	−	0.20	0.02
AGAL032.001−00.197	0.41	−	0.04	0.14	0.35	0.13	−	0.09	0.01
AGAL032.007+00.062	0.99	0.28	0.29	0.48	1.07	0.47	0.06	0.77	0.01
AGAL032.019+00.064	0.76	−	0.20	0.74	0.51	0.44	−	0.53	0.02
AGAL032.044+00.059	1.17	−	0.47	0.33	1.15	0.70	0.19	2.24	0.06
AGAL032.149+00.134	1.28	0.70	0.32	0.45	1.58	0.67	−	0.44	0.04
AGAL032.739+00.192	0.76	−	0.07	0.09	0.47	−	−	−	0.01
AGAL032.739+00.192	0.79	−	0.13	0.14	0.55	0.18	−	0.37	0.01
AGAL032.744−00.076	1.27	−	0.38	0.61	0.87	0.18	0.08	1.11	0.03
AGAL032.797+00.191	1.80	0.77	0.43	0.57	1.70	0.52	0.13	1.23	0.03
AGAL032.821−00.331	0.29	−	0.16	0.13	0.46	0.31	0.08	1.73	0.03
AGAL033.133−00.092	1.47	−	0.29	1.05	1.47	0.71	0.05	0.45	0.03
AGAL033.238−00.022	0.79	0.47	0.14	0.22	0.49	0.27	−	0.30	0.02
AGAL033.393+00.011	0.73	0.41	0.19	0.21	0.48	0.18	0.05	0.65	0.02
AGAL033.568+00.027	0.77	−	0.06	0.10	0.43	−	−	−	0.01
AGAL033.623−00.032	0.78	−	0.12	0.20	0.54	0.27	−	0.22	0.02
AGAL033.744−00.007	0.54	−	0.11	0.13	0.79	0.29	−	0.23	0.03
AGAL033.851+00.017	0.18	−	0.07	−	0.34	0.24	−	−	0.00
AGAL033.914+00.109	1.66	0.63	0.50	0.38	1.89	0.78	0.15	1.11	0.05
AGAL033.979−00.021	0.76	−	0.16	0.29	0.41	0.17	−	0.13	0.02
AGAL034.089+00.011	0.84	−	0.13	0.49	0.81	−	−	0.26	0.01
AGAL034.243+00.132	1.27	1.00	0.18	0.38	1.33	0.57	0.12	0.66	0.02
AGAL034.258+00.154	2.50	0.21	1.08	0.98	1.26	0.93	0.97	6.32	0.12
AGAL034.372−00.664	0.14	−	0.06	0.11	0.94	0.11	−	0.34	0.02
AGAL034.401+00.226	−	0.57	−	−	−	−	0.24	−	−
AGAL034.411+00.234	0.86	−	0.54	0.73	1.59	0.83	0.26	3.39	0.08
AGAL034.454+00.006	0.60	−	0.22	0.15	0.60	0.23	−	0.99	0.02
AGAL034.459+00.247	0.40	−	0.26	0.33	1.11	0.41	0.06	1.90	0.04
AGAL034.591+00.242	0.17	0.21	0.03	0.15	0.38	−	−	−	−
AGAL034.712−00.596	0.48	−	0.23	1.33	1.27	0.38	0.07	0.59	0.03
AGAL034.739−00.119	0.90	−	0.12	0.37	0.97	0.38	−	0.27	0.03
AGAL034.742−00.132	0.66	−	0.12	0.62	0.93	0.27	−	0.39	0.03
AGAL034.751−00.092	0.24	−	0.08	0.08	0.48	−	−	0.58	0.01
AGAL034.757+00.024	0.43	0.56	0.07	0.22	0.62	0.34	−	0.20	0.01
AGAL034.821+00.351	1.31	−	0.47	0.93	1.65	0.67	0.07	0.69	0.04
AGAL035.026+00.349	0.47	−	0.30	0.33	0.88	0.35	0.17	1.25	0.03
AGAL035.042−00.472	0.21	−	0.12	0.14	0.65	0.20	−	0.15	0.01
AGAL035.132−00.744	0.43	−	0.80	0.43	1.53	0.93	0.25	1.74	0.08
AGAL035.144−00.754	0.39	−	0.51	0.62	1.22	0.30	0.17	1.12	0.03
AGAL035.197−00.742	0.00	−	0.00	0.00	0.00	0.00	0.00	0.00	0.00
AGAL035.297−00.897	0.33	−	0.14	0.42	0.93	0.23	−	0.19	0.02
AGAL035.457−00.179	0.42	−	0.10	0.15	0.34	−	−	0.63	0.01
AGAL035.466+00.141	0.76	0.71	0.20	0.39	1.18	0.51	0.07	0.45	0.03
AGAL035.484−00.287	0.33	−	0.15	0.23	0.83	0.15	−	0.23	0.02
AGAL035.579+00.007	0.66	−	0.19	−	0.31	0.31	−	0.07	0.02
AGAL035.579−00.031	1.20	0.79	0.23	0.34	1.22	0.47	0.09	0.55	0.01
AGAL035.681−00.176	0.19	−	0.13	0.23	0.78	0.23	−	0.46	0.02
AGAL035.794−00.174	0.56	−	0.19	0.60	0.81	0.52	0.06	1.26	0.02
AGAL036.794−00.204	0.73	−	0.07	0.29	0.46	0.17	−	−	0.01

Table B.4: continued.

ATLASGAL Name	$C^{18}O$ $\times 10^{16}$	HCO $\times 10^{13}$	$H^{13}CO^+$ $\times 10^{13}$	C_2H $\times 10^{15}$	$c\text{-}C_3H_2$ $\times 10^{13}$	CN $\times 10^{15}$	$HC^{15}N$ $\times 10^{13}$	$H^{13}CN$ $\times 10^{13}$	$HN^{13}C$ $\times 10^{14}$
AGAL036.826−00.039	0.79	−	0.14	0.11	0.71	−	−	0.24	0.01
AGAL036.839−00.022	0.62	−	0.19	0.20	1.15	0.32	−	0.75	0.03
AGAL036.878−00.474	0.30	−	0.13	0.13	0.52	−	−	0.14	0.01
AGAL036.899−00.409	0.77	0.44	0.14	0.16	0.63	−	−	0.27	0.02
AGAL037.031−00.039	0.56	−	0.12	0.20	0.59	0.28	−	0.16	0.02
AGAL037.469−00.102	0.42	0.30	0.09	0.11	0.44	0.19	−	0.09	0.01
AGAL037.498+00.531	0.60	0.29	0.09	0.23	0.45	0.19	−	0.19	0.01
AGAL037.554+00.201	1.11	−	0.41	1.04	1.21	0.80	0.14	2.57	0.01
AGAL037.874−00.399	0.95	0.48	0.30	0.28	1.20	0.51	0.08	0.36	0.02
AGAL038.119−00.229	0.45	−	0.09	0.35	0.41	0.28	−	0.42	0.01
AGAL038.354−00.952	0.23	−	0.15	0.28	0.93	0.25	0.02	0.16	0.02
AGAL038.371−00.149	0.92	−	0.09	0.33	0.50	0.21	−	0.11	0.01
AGAL038.957−00.466	1.22	−	0.29	0.45	1.51	0.43	−	0.39	0.03
AGAL039.048−00.880	0.37	−	0.10	−	0.97	0.30	−	1.39	0.02
AGAL039.099+00.492	0.32	−	0.10	−	−	0.29	−	0.36	0.01
AGAL039.903−01.349	0.00	0.00	0.00	0.00	0.00	0.00	−	−	−
AGAL040.283−00.219	0.85	−	0.48	0.32	1.09	1.34	0.13	1.95	0.03
AGAL041.049−00.247	0.35	−	0.13	0.27	0.97	0.30	−	0.30	0.02
AGAL041.347−00.136	0.38	−	0.08	−	0.33	0.10	−	−	0.01
AGAL042.098+00.351	0.21	−	0.08	−	0.37	−	−	−	−
AGAL043.038−00.452	0.93	0.32	0.30	0.33	1.22	0.48	0.09	0.73	0.02
AGAL043.148+00.014	0.33	1.21	0.07	0.29	1.95	0.27	0.06	0.35	−
AGAL043.164−00.029	0.84	1.21	0.27	0.85	0.93	0.24	0.13	0.64	0.01
AGAL043.166+00.011	2.59	−	2.00	1.10	0.72	0.24	0.37	3.42	0.01
AGAL043.178−00.011	0.33	2.50	0.12	0.49	1.34	0.17	0.07	0.35	0.01
AGAL043.179−00.519	1.32	0.75	0.26	0.43	1.30	0.71	0.11	0.83	0.03
AGAL043.236−00.047	0.90	0.46	0.22	0.58	0.74	0.31	0.07	0.71	0.02
AGAL043.306−00.212	0.70	−	0.25	0.46	0.79	0.50	0.07	0.47	0.04
AGAL043.794−00.127	1.25	0.34	0.44	0.47	1.12	0.54	0.13	1.52	0.02
AGAL043.889−00.786	1.22	0.90	0.27	0.61	1.29	0.55	0.09	1.92	0.03
AGAL043.994−00.012	0.48	−	0.16	0.12	0.73	0.38	0.04	0.18	0.02
AGAL044.291+00.034	0.55	−	0.16	0.12	0.44	0.28	0.02	0.34	0.01
AGAL044.309+00.041	0.49	−	0.11	0.14	0.43	0.17	−	0.49	0.01
AGAL044.422+00.537	0.10	0.57	−	0.09	0.52	−	−	−	−
AGAL045.071+00.132	0.65	0.92	0.27	0.38	0.97	0.38	0.16	1.45	0.01
AGAL045.096+00.131	0.49	−	0.12	−	0.43	0.23	−	0.09	0.01
AGAL045.121+00.131	0.68	0.58	0.24	0.29	1.36	0.37	0.08	0.59	0.02
AGAL045.454+00.061	0.49	0.88	0.10	0.29	1.20	0.30	0.05	0.47	0.01
AGAL045.466+00.046	0.84	−	0.51	0.67	1.27	0.56	0.15	1.04	0.05
AGAL045.474+00.134	0.75	1.16	0.14	0.80	1.60	0.51	0.09	0.86	0.01
AGAL045.886−00.509	0.58	−	0.17	−	1.19	0.26	−	−	0.03
AGAL046.174−00.524	0.59	−	0.15	−	0.75	0.13	−	0.25	0.02
AGAL046.426−00.237	0.89	−	0.16	−	0.45	−	−	0.15	0.02
AGAL048.606+00.022	0.37	1.39	0.10	0.38	1.34	0.26	0.11	0.60	−
AGAL048.991−00.299	0.00	0.00	0.00	0.00	0.00	0.00	0.00	0.00	0.00
AGAL049.043−01.077	0.44	−	0.10	0.20	0.60	0.12	0.03	0.18	0.01
AGAL049.074−00.352	0.38	0.73	0.18	0.27	1.64	0.59	−	0.22	0.03
AGAL049.214−00.342	0.63	−	0.21	0.61	2.19	0.60	−	0.22	0.03
AGAL049.253−00.411	0.49	0.71	0.10	0.22	0.64	0.31	−	0.13	0.01
AGAL049.268−00.337	0.79	0.68	0.40	0.92	2.86	1.07	0.10	0.87	0.08
AGAL049.369−00.301	0.00	0.00	0.00	0.00	0.00	0.00	0.00	0.00	0.00
AGAL049.401−00.227	0.87	0.51	0.11	0.11	0.60	0.22	−	0.14	0.01
AGAL049.402−00.212	0.58	−	0.15	0.34	0.80	0.27	−	0.22	0.02
AGAL049.489−00.389	2.99	3.17	2.58	2.06	6.62	2.22	2.28	9.94	0.16
AGAL049.566−00.274	0.47	−	0.15	0.22	0.21	0.22	0.08	0.37	0.02
AGAL049.599−00.249	0.42	−	0.14	0.16	0.26	0.23	0.02	0.22	0.01
AGAL050.046+00.767	0.11	−	−	0.06	−	−	−	−	−
AGAL050.221−00.606	0.66	0.45	0.25	0.31	0.75	0.28	0.06	0.36	0.02
AGAL050.777+00.152	0.38	−	0.09	0.23	0.69	0.18	−	0.13	0.01
AGAL051.678+00.719	0.63	−	0.28	0.30	0.52	0.25	0.09	0.70	0.02
AGAL052.208+00.687	0.50	−	0.20	0.17	0.45	−	−	0.39	0.02
AGAL053.141+00.069	1.01	−	0.50	0.34	1.16	0.32	0.11	1.03	0.02
AGAL053.619+00.034	0.57	0.24	0.17	0.21	0.46	0.19	−	0.15	0.01
AGAL055.158−00.299	0.60	0.49	0.10	0.32	0.64	0.22	0.05	0.32	0.01
AGAL058.469+00.436	0.54	−	0.25	0.22	0.65	0.27	0.05	0.41	0.02
AGAL058.709+00.662	0.58	−	0.14	0.18	0.47	0.14	−	0.11	0.00
AGAL058.774+00.644	0.31	0.38	0.13	0.33	0.66	0.23	0.05	0.37	0.01
AGAL059.187+00.106	0.24	0.23	0.04	0.06	0.19	−	−	−	−
AGAL059.351−00.196	0.34	0.44	0.12	0.10	0.39	0.05	−	0.21	0.01
AGAL059.359−00.207	0.42	−	0.14	0.20	0.57	0.22	−	0.15	0.01
AGAL059.497−00.236	0.40	−	0.29	0.15	0.93	0.22	−	0.23	0.01
AGAL059.577−00.201	0.39	0.52	0.10	0.24	0.66	0.09	−	0.12	0.01
AGAL059.584−00.146	0.21	0.44	0.06	0.11	0.44	0.23	−	0.06	−
AGAL059.602+00.912	0.79	0.27	0.14	0.25	0.52	0.22	0.06	0.44	0.01
AGAL059.634−00.191	−	−	0.34	0.47	1.09	−	0.15	0.75	0.04
AGAL059.636−00.252	0.28	0.63	0.04	0.15	0.47	0.10	−	−	−
AGAL059.782+00.066	0.63	0.51	0.38	0.70	1.16	0.71	0.18	0.87	0.04
AGAL059.789+00.631	0.30	−	0.28	0.36	0.70	0.29	−	0.50	0.02
AGAL059.832+00.672	0.50	−	0.15	0.16	0.27	0.12	0.06	0.41	0.01

Table B.4: continued.

ATLASGAL Name	$C^{18}O$ $\times 10^{16}$	HCO $\times 10^{13}$	$H^{13}CO^+$ $\times 10^{13}$	C_2H $\times 10^{15}$	c-C_3H_2 $\times 10^{13}$	CN $\times 10^{15}$	$HC^{15}N$ $\times 10^{13}$	$H^{13}CN$ $\times 10^{13}$	$HN^{13}C$ $\times 10^{14}$
AGAL059.894−00.047	0.20	−	0.04	−	0.18	−	−	−	−

B.10   Comparison of properties of clumps
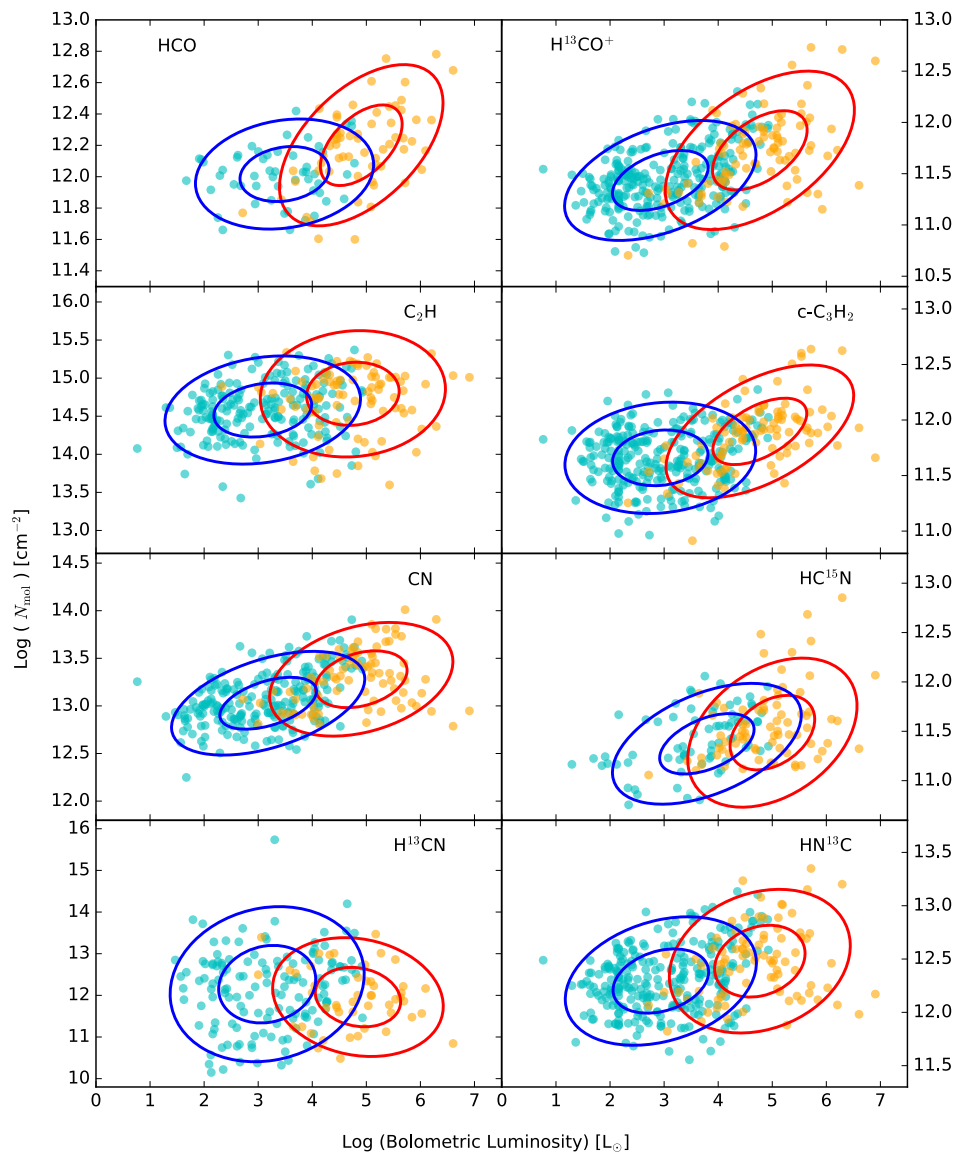
Figure B.7: Bolometric luminosity as a function of column density for molecules.
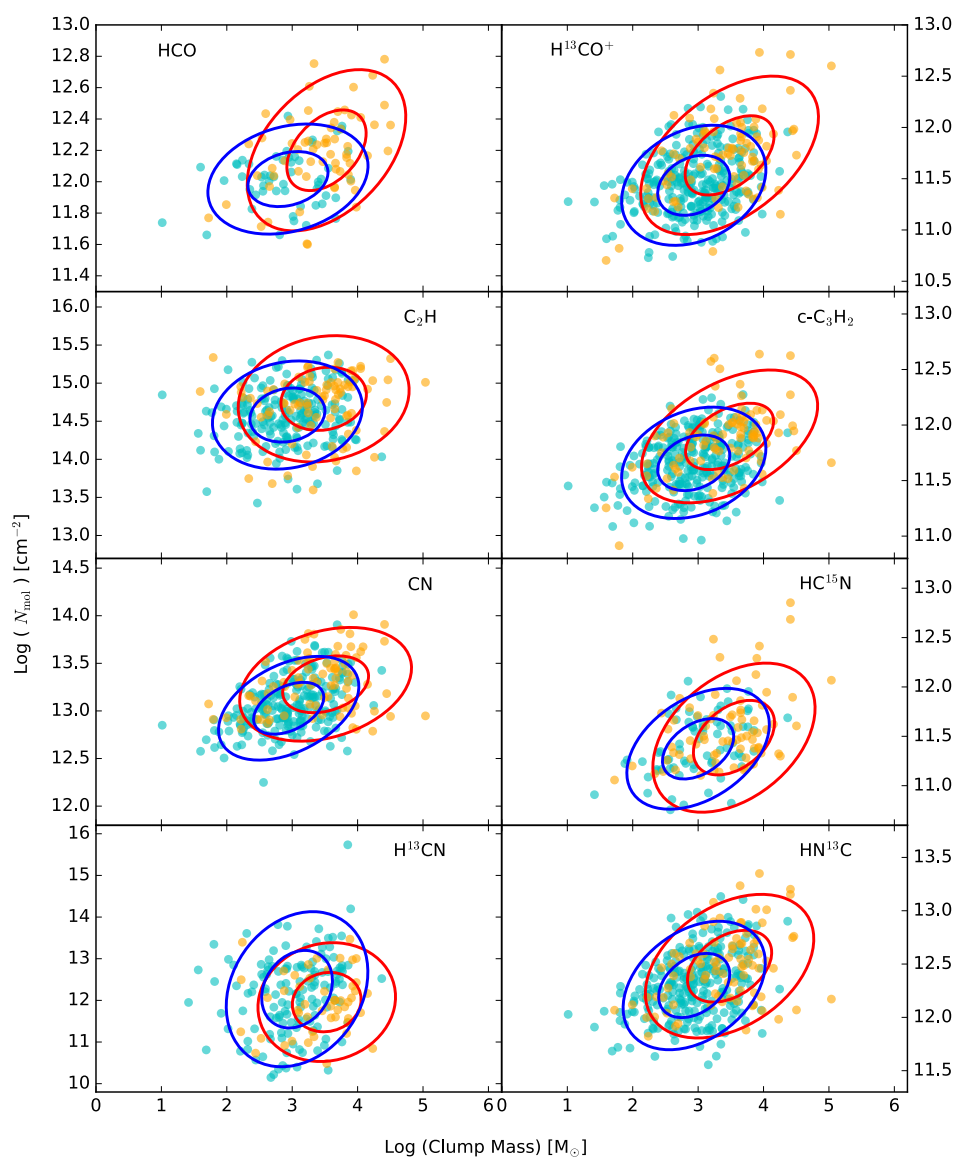
Figure B.8: Mass of clump as a function of column density for molecules.

Bibliography

Adler, D. S., Wood, D. O. S., & Goss, W. M. 1996, ApJ, 471, 871 (Cited on page 42.)

Afflerbach, A., Churchwell, E., Acord, J. M., et al. 1996, ApJS, 106, 423 (Cited on page 44.)

Agúndez, M., Cernicharo, J., & Goicoechea, J. R. 2008, A&A, 483, 831 (Cited on page 132.)

Agúndez, M., Cernicharo, J., & Guélin, M. 2015, A&A, 577, L5 (Cited on page 159.)

Altenhoff. 1960, in Veroff. Sternwarte Bonn No., Vol. 59, 48 (Cited on page 29.)

Alves, M. I. R., Calabretta, M., Davies, R. D., et al. 2015, MNRAS, 450, 2025 (Cited on pages 16, 44 and 60.)

Alves, M. I. R., Davies, R. D., Dickinson, C., et al. 2010, MNRAS, 405, 1654 (Cited on page 65.)

Anderson, L. D. & Bania, T. M. 2009, ApJ, 690, 706 (Cited on page 60.)

Anderson, L. D., Bania, T. M., Balser, D. S., et al. 2014, ApJS, 212, 1 (Cited on pages 16, 60 and 71.)

Anderson, L. D., Bania, T. M., Balser, D. S., & Rood, R. T. 2011, ApJS, 194, 32 (Cited on pages 16, 65, 73 and 74.)

Araya, E., Hofner, P., Churchwell, E., & Kurtz, S. 2002, ApJS, 138, 63 (Cited on page 16.)

Arthur, S. J. & Hoare, M. G. 2006, ApJS, 165, 283 (Cited on page 120.)

Baldwin, J. A., Ferland, G. J., Martin, P. G., et al. 1991, ApJ, 374, 580 (Cited on page 41.)

Balser, D. S., Goss, W. M., & De Pree, C. G. 2001, AJ, 121, 371 (Cited on page 42.)

Becker, R. H., White, R. L., Helfand, D. J., & Zoonematkermani, S. 1994, ApJS, 91, 347 (Cited on pages 11, 76, 84, 90 and 109.)

Beigman, I. L. & Chichkov, B. N. 1980, Journal of Physics B Atomic Molecular Physics, 13, 565 (Cited on page 35.)

Bendo, G. J., Miura, R. E., Espada, D., et al. 2017, ArXiv e-prints (Cited on pages 45 and 97.)

Benjamin, R. A., Churchwell, E., Babler, B. L., et al. 2003, PASP, 115, 953 (Cited on pages 9 and 60.)

Bergin, E. A., Langer, W. D., & Goldsmith, P. F. 1995, ApJ, 441, 222 (Cited on page 161.)

Beuther, H., Semenov, D., Henning, T., & Linz, H. 2008, ApJ, 675, L33 (Cited on page 159.)

Beuther, H. & Sridharan, T. K. 2007, ApJ, 668, 348 (Cited on page 71.)

Beuther, H., Walsh, A., Schilke, P., et al. 2002, A&A, 390, 289 (Cited on page 8.)

Bieging, J. H., Pankonin, V., & Smith, L. F. 1978, A&A, 64, 341 (Cited on page 118.)

Boger, G. I. & Sternberg, A. 2005, ApJ, 632, 302 (Cited on page 136.)

Boisse, P. 1990, A&A, 228, 483 (Cited on page 19.)

Brocklehurst, M. & Seaton, M. J. 1972, MNRAS, 157, 179 (Cited on pages 38 and 69.)

Bronfman, L., Nyman, L.-A., & May, J. 1996, A&AS, 115, 81 (Cited on page 8.)

Burbidge, E. M., Burbidge, G. R., Fowler, W. A., & Hoyle, F. 1957, Reviews of Modern Physics, 29, 547 (Cited on page 40.)

Burton, M. G., Hollenbach, D. J., & Tielens, A. G. G. M. 1990, ApJ, 365, 620 (Cited on page 20.)

Carey, S. J., Noriega-Crespo, A., Mizuno, D. R., et al. 2009, PASP, 121, 76 (Cited on page 9.)

Carral, P., Kurtz, S. E., Rodríguez, L. F., De Pree, C., & Hofner, P. 1997, ApJ, 486, L103 (Cited on page 59.)

Caswell, J. L. & Haynes, R. F. 1987, A&A, 171, 261 (Cited on pages 16, 60, 73 and 74.)

Cersosimo, J. C. & Magnani, L. 1990, A&A, 239, 287 (Cited on page 35.)

Charnley, S. B., Tielens, A. G. G. M., & Rodgers, S. D. 1997, ApJ, 482, L203 (Cited on page 162.)

Churchwell, E. 1990, A&A Rev., 2, 79 (Cited on page 59.)

Churchwell, E. 1999, in NATO Advanced Science Institutes (ASI) Series C, Vol. 540, NATO Advanced Science Institutes (ASI) Series C, ed. C. J. Lada & N. D. Kylafis, 515 (Cited on pages 12 and 14.)

Churchwell, E. 2002, ARA&A, 40, 27 (Cited on pages 8, 11, 16, 59 and 171.)

Churchwell, E., Babler, B. L., Meade, M. R., et al. 2009, PASP, 121, 213 (Cited on page 71.)

Churchwell, E., Mezger, P. G., & Huchtmeier, W. 1974, A&A, 32, 283 (Cited on page 41.)

Churchwell, E., Sievers, A., & Thum, C. 2010, A&A, 513, A9 (Cited on pages 16, 59, 60, 74 and 97.)

Churchwell, E. & Walmsley, C. M. 1975, A&A, 38, 451 (Cited on page 44.)

Condon, J. J., Cotton, W. D., Greisen, E. W., et al. 1998, AJ, 115, 1693 (Cited on page 76.)

Contreras, Y., Rathborne, J. M., Guzman, A., et al. 2017, MNRAS, 466, 340 (Cited on page 97.)

Contreras, Y., Schuller, F., Urquhart, J. S., et al. 2013, A&A, 549, A45 (Cited on pages 9, 59 and 97.)

Cox, D. P. 2005, ARA&A, 43, 337 (Cited on page 5.)

Csengeri, T., Leurini, S., Wyrowski, F., et al. 2016, A&A, 586, A149 (Cited on pages 60, 62, 63, 80, 84, 93 and 136.)

Csengeri, T., Urquhart, J. S., Schuller, F., et al. 2014, A&A, 565, A75 (Cited on pages 5, 59, 82 and 97.)

Cuadrado, S., Goicoechea, J. R., Pilleri, P., et al. 2015, A&A, 575, A82 (Cited on pages 132, 134, 157, 158, 162 and 163.)

Cutri, R. M., Wright, E. L., Conrow, T., et al. 2012, Explanatory Supplement to the WISE All-Sky Data Release Products, Tech. rep. (Cited on pages 9, 76 and 84.)

De Pree, C. G., Mehringer, D. M., & Goss, W. M. 1997, ApJ, 482, 307 (Cited on

pages 42, 44 and 122.)

De Pree, C. G., Wilner, D. J., Mercer, A. J., et al. 2004a, ApJ, 600, 286 (Cited on page 60.)

De Pree, C. G., Wilner, D. J., Mercer, A. J., et al. 2004b, ApJ, 600, 286 (Cited on page 122.)

Downes, D., Wilson, T. L., Bieging, J., & Wink, J. 1980, A&AS, 40, 379 (Cited on page 16.)

Draine, B. T. 2003, ARA&A, 41, 241 (Cited on page 4.)

Draine, B. T. & Bertoldi, F. 1996, ApJ, 468, 269 (Cited on page 19.)

Dravskikh, A. F., Dravskikh, Z. V., Kolbasov, V. A., et al. 1965, Dok. Akad. Nauk SSSR 163, 332. English translation: 1966, Soviet Physics Doklady, 10, 627 (Cited on page 15.)

Dravskikh, Z. V. & Dravskikh, A. F. 1964, Astron. Tsirk., 282, 2 (Cited on page 15.)

Dupree, A. K. & Goldberg, L. 1970, ARA&A, 8, 231 (Cited on pages 35 and 105.)

Dyson, J. E., Williams, R. J. R., & Redman, M. P. 1995, MNRAS, 277, 700 (Cited on page 47.)

Eden, D. J., Moore, T. J. T., Morgan, L. K., Thompson, M. A., & Urquhart, J. S. 2013, MNRAS, 431, 1587 (Cited on page 115.)

Eidelsberg, M., Benayoun, J. J., Viala, Y., et al. 1992, A&A, 265, 839 (Cited on page 19.)

Ershov, D., Gulyaev, S. A., Ivanchik, A., Varshalovich, D. A., & Tsivilev, A. 1998, Astronomical and Astrophysical Transactions, 15, 281 (Cited on page 42.)

Falgarone, E. & Phillips, T. G. 1996, ApJ, 472, 191 (Cited on page 19.)

Forster, J. R. & Caswell, J. L. 1989, A&A, 213, 339 (Cited on page 59.)

Fossé, D., Cernicharo, J., Gerin, M., & Cox, P. 2001, ApJ, 552, 168 (Cited on page 162.)

Franco, J., Kurtz, S. E., García-Segura, G., & Hofner, P. 2000, Ap&SS, 272, 169 (Cited on page 14.)

Fuente, A., García-Burillo, S., Gerin, M., et al. 2005, ApJ, 619, L155 (Cited on pages 132, 134 and 136.)

Fuente, A., Martin-Pintado, J., Cernicharo, J., & Bachiller, R. 1993, A&A, 276, 473 (Cited on pages 19, 136 and 164.)

Fuente, A., Martin-Pintado, J., & Gaume, R. 1995, ApJ, 442, L33 (Cited on page 19.)

Fuente, A., Rodrıguez-Franco, A., Garcıa-Burillo, S., Martın-Pintado, J., & Black, J. H. 2003, A&A, 406, 899 (Cited on pages 134, 163 and 164.)

Fuente, A., Rodriguez-Franco, A., & Martin-Pintado, J. 1996, A&A, 312, 599 (Cited on page 164.)

Galván-Madrid, R., Rodríguez, L. F., Ho, P. T. P., & Keto, E. 2008, ApJ, 674, L33 (Cited on page 12.)

Garay, G. & Lizano, S. 1999, PASP, 111, 1049 (Cited on pages 6, 45, 46 and 47.)

Garay, G., Rodriguez, L. F., Moran, J. M., & Churchwell, E. 1993, ApJ, 418, 368 (Cited on pages 11, 14 and 44.)

García-Burillo, S., Martín-Pintado, J., Fuente, A., Usero, A., & Neri, R. 2002, ApJ,

575, L55 (Cited on pages 132, 134 and 154.)

Gaume, R. A., Claussen, M. J., de Pree, C. G., Goss, W. M., & Mehringer, D. M. 1995, ApJ, 449, 663 (Cited on pages 11, 13, 44 and 60.)

Gaume, R. A., Fey, A. L., & Claussen, M. J. 1994, ApJ, 432, 648 (Cited on page 16.)

Georgelin, Y. M. & Georgelin, Y. P. 1976, A&A, 49, 57 (Cited on page 16.)

Gerin, M., Goicoechea, J. R., Pety, J., & Hily-Blant, P. 2009, A&A, 494, 977 (Cited on pages 132, 134, 154, 157, 158, 159, 160 and 161.)

Gerner, T., Beuther, H., Semenov, D., et al. 2014, A&A, 563, A97 (Cited on page 157.)

Giannetti, A., Leurini, S., Wyrowski, F., et al. 2017, A&A, 603, A33 (Cited on page 154.)

Giannetti, A., Wyrowski, F., Brand, J., et al. 2014, A&A, 570, A65 (Cited on pages 60, 62 and 98.)

Ginard, D., González-García, M., Fuente, A., et al. 2012, A&A, 543, A27 (Cited on pages 132, 134, 157, 158, 160 and 161.)

Giveon, U., Becker, R. H., Helfand, D. J., & White, R. L. 2005, AJ, 130, 156 (Cited on page 76.)

Goicoechea, J. R., Pety, J., Cuadrado, S., et al. 2016, Nature, 537, 207 (Cited on pages 17 and 18.)

Goicoechea, J. R., Pety, J., Gerin, M., Hily-Blant, P., & Le Bourlot, J. 2009, A&A, 498, 771 (Cited on page 160.)

Goldberg, L. 1966, ApJ, 144, 1225 (Cited on pages 32 and 34.)

Goldberg, L. 1968, in Interstellar Ionized hydrogen Proceedings of the Symposium on HII, ed. Y. Terzian, 373 (Cited on page 32.)

Goldsmith, P. F., Irvine, W. M., Hjalmarson, A., & Ellder, J. 1986, ApJ, 310, 383 (Cited on page 136.)

Goldsmith, P. F. & Langer, W. D. 1999, ApJ, 517, 209 (Cited on page 55.)

Goldwire, Jr., H. C. 1968, ApJS, 17, 445 (Cited on pages 30, 64 and 100.)

Gordon, M. A. & Sorochenko, R. L., eds. 2002, Astrophysics and Space Science Library, Vol. 282, Radio Recombination Lines. Their Physics and Astronomical Applications (Cited on pages 24, 34, 38, 40, 47, 61 and 103.)

Gordon, M. A. & Walmsley, C. M. 1990, ApJ, 365, 606 (Cited on page 35.)

Gulyaev, S. A., Sorochenko, R. L., & Tsivilev, A. P. 1997, Astronomy Letters, 23, 165 (Cited on page 42.)

Güsten, R., Nyman, L. Å., Schilke, P., et al. 2006, A&A, 454, L13 (Cited on page 98.)

Guzmán, A. E., Garay, G., Brooks, K. J., & Voronkov, M. A. 2012, ApJ, 753, 51 (Cited on page 93.)

Guzmán, A. E., Garay, G., Rodríguez, L. F., et al. 2014, ApJ, 796, 117 (Cited on page 93.)

Habing, H. J. 1968, Bull. Astron. Inst. Netherlands, 19, 421 (Cited on page 18.)

Habing, H. J. & Israel, F. P. 1979, ARA&A, 17, 345 (Cited on page 11.)

Heiles, C. & Troland, T. H. 2003, ApJ, 586, 1067 (Cited on page 4.)

Helfand, D. J., Becker, R. H., White, R. L., Fallon, A., & Tuttle, S. 2006, AJ, 131,

2525 (Cited on page 76.)

Hildebrand, R. H. 1983, QJRAS, 24, 267 (Cited on page 4.)

Hindson, L., Thompson, M. A., Urquhart, J. S., et al. 2012, MNRAS, 421, 3418 (Cited on pages 76 and 78.)

Hindson, L., Thompson, M. A., Urquhart, J. S., et al. 2013, MNRAS, 435, 2003 (Cited on page 78.)

Hoang-Binh, D. 1983, A&A, 121, L19 (Cited on page 35.)

Hoare, M. G., Kurtz, S. E., Lizano, S., Keto, E., & Hofner, P. 2007, Protostars and Planets V, 181 (Cited on pages 7, 8, 9, 11, 16, 121 and 171.)

Hoare, M. G., Purcell, C. R., Churchwell, E. B., et al. 2012, PASP, 124, 939 (Cited on pages 9, 60, 78, 80, 110 and 171.)

Hofner, P. & Churchwell, E. 1996, A&AS, 120, 283 (Cited on page 59.)

Hogerheijde, M. R., Jansen, D. J., & van Dishoeck, E. F. 1995, A&A, 294, 792 (Cited on page 132.)

Hoglund, B. & Mezger, P. G. 1965, AJ, 70, 678 (Cited on page 15.)

Hollenbach, D., Johnstone, D., Lizano, S., & Shu, F. 1994, ApJ, 428, 654 (Cited on page 47.)

Hollenbach, D. J., Takahashi, T., & Tielens, A. G. G. M. 1991, ApJ, 377, 192 (Cited on page 19.)

Hollenbach, D. J. & Tielens, A. G. G. M. 1997, ARA&A, 35, 179 (Cited on pages 16 and 19.)

Hosokawa, T. & Omukai, K. 2009, ApJ, 691, 823 (Cited on page 7.)

Hosokawa, T., Yorke, H. W., & Omukai, K. 2010, ApJ, 721, 478 (Cited on page 7.)

Immer, K., Menten, K. M., Schuller, F., & Lis, D. C. 2012, A&A, 548, A120 (Cited on page 118.)

Jackson, J. M., Rathborne, J. M., Shah, R. Y., et al. 2006, ApJS, 163, 145 (Cited on page 5.)

Jaffe, D. T. & Martín-Pintado, J. 1999, ApJ, 520, 162 (Cited on pages 60, 93, 107, 121, 122 and 172.)

Jansen, D. J., Spaans, M., Hogerheijde, M. R., & van Dishoeck, E. F. 1995, A&A, 303, 541 (Cited on pages 132 and 136.)

Jiménez-Serra, I., Báez-Rubio, A., Rivilla, V. M., et al. 2013, ApJ, 764, L4 (Cited on page 93.)

Jin, M., Lee, J.-E., & Kim, K.-T. 2015, ApJS, 219, 2 (Cited on page 136.)

Kahn, F. D. 1974, A&A, 37, 149 (Cited on page 6.)

Kardashev, N. S. 1959, Soviet Ast., 3, 813 (Cited on page 15.)

Keto, E. 2007, ApJ, 666, 976 (Cited on page 11.)

Keto, E. & Klaassen, P. 2008, ApJ, 678, L109 (Cited on pages 12 and 59.)

Keto, E. & Wood, K. 2006, ApJ, 637, 850 (Cited on page 11.)

Keto, E., Zhang, Q., & Kurtz, S. 2008, ApJ, 672, 423 (Cited on pages 60 and 93.)

Kim, K.-T. & Koo, B.-C. 2001, ApJ, 549, 979 (Cited on pages 14 and 172.)

Kim, W.-J., Wyrowski, F., Urquhart, J. S., Menten, K. M., & Csengeri, T. 2017, A&A,

602, A37 (Cited on pages 97, 98, 101, 103, 104, 105, 109, 110, 112, 115, 129, 133 and 146.)

Klassen, M., Peters, T., & Pudritz, R. E. 2012, ApJ, 758, 137 (Cited on page 12.)

Klein, T., Ciechanowicz, M., Leinz, C., et al. 2014, IEEE Transactions on Terahertz Science and Technology, 4, 588 (Cited on page 98.)

König, C., Urquhart, J. S., Csengeri, T., et al. 2017, A&A, 599, A139 (Cited on pages 98, 109, 110, 114, 152 and 153.)

Kuchar, T. A. & Clark, F. O. 1997, ApJ, 488, 224 (Cited on page 78.)

Kurtz, S. 2005, in IAU Symposium, Vol. 227, Massive Star Birth: A Crossroads of Astrophysics, ed. R. Cesaroni, M. Felli, E. Churchwell, & M. Walmsley, 111–119 (Cited on pages 12, 59 and 68.)

Kurtz, S., Cesaroni, R., Churchwell, E., Hofner, P., & Walmsley, C. M. 2000, Protostars and Planets IV, 299 (Cited on pages 6, 7, 11, 16, 59 and 92.)

Kurtz, S., Churchwell, E., & Wood, D. O. S. 1994, ApJS, 91, 659 (Cited on pages 8, 9, 11, 14 and 59.)

Kurtz, S. & Franco, J. 2002, in Revista Mexicana de Astronomia y Astrofisica, vol. 27, Vol. 12, Revista Mexicana de Astronomia y Astrofisica Conference Series, ed. W. J. Henney, J. Franco, & M. Martos, 16–21 (Cited on page 11.)

Kurtz, S. & Hofner, P. 2005, AJ, 130, 711 (Cited on page 59.)

Kurtz, S. E., Watson, A. M., Hofner, P., & Otte, B. 1999, ApJ, 514, 232 (Cited on pages 14 and 172.)

Ladd, N., Purcell, C., Wong, T., & Robertson, S. 2005, PASA, 22, 62 (Cited on page 63.)

Landsberg, B. M., Merer, A. J., & Oka, T. 1977, Journal of Molecular Spectroscopy, 67, 459 (Cited on page 134.)

Larionov, G. M. & Val'tts, I. E. 2007, Astronomy Reports, 51, 756 (Cited on page 79.)

Larson, R. B. 1981, MNRAS, 194, 809 (Cited on page 94.)

Leung, C. M., Herbst, E., & Huebner, W. F. 1984, ApJS, 56, 231 (Cited on page 160.)

Li, G.-X., Urquhart, J. S., Leurini, S., et al. 2016, A&A, 591, A5 (Cited on page 5.)

Liu, T., Wu, Y., & Zhang, H. 2013, ApJ, 776, 29 (Cited on page 141.)

Lizano, S., Canto, J., Garay, G., & Hollenbach, D. 1996, ApJ, 468, 739 (Cited on page 47.)

Lockman, F. J. 1989, ApJS, 71, 469 (Cited on pages 16, 60, 73 and 74.)

Lockman, F. J. & Brown, R. L. 1982, ApJ, 259, 595 (Cited on page 41.)

Lumsden, S. L., Hoare, M. G., Oudmaijer, R. D., & Richards, D. 2002, MNRAS, 336, 621 (Cited on page 8.)

Lumsden, S. L., Hoare, M. G., Urquhart, J. S., et al. 2013, ApJS, 208, 11 (Cited on pages 7, 8, 59, 88, 110 and 123.)

Maluendes, S. A., McLean, A. D., Yamashita, K., & Herbst, E. 1993, J. Chem. Phys, 99, 2812 (Cited on page 162.)

Mangum, J. G. & Shirley, Y. L. 2015, PASP, 127, 266 (Cited on pages 48 and 52.)

Martín-Hernández, N. L., Bik, A., Kaper, L., Tielens, A. G. G. M., & Hanson, M. M.

2003, A&A, 405, 175 (Cited on page 120.)

Martín-Pintado, J. 2002, in IAU Symposium, Vol. 206, Cosmic Masers: From Proto-Stars to Black Holes, ed. V. Migenes & M. J. Reid, 226 (Cited on pages 34, 69, 93, 97, 99 and 120.)

Martin-Pintado, J., Bachiller, R., Thum, C., & Walmsley, M. 1989, A&A, 215, L13 (Cited on pages 34 and 93.)

Mathis, J. S. 1990, ARA&A, 28, 37 (Cited on page 4.)

Maxia, C., Testi, L., Cesaroni, R., & Walmsley, C. M. 2001, A&A, 371, 287 (Cited on page 120.)

McEwan, M. J., Scott, G. B. I., Adams, N. G., et al. 1999, ApJ, 513, 287 (Cited on page 162.)

McKee, C. F. & Ostriker, E. C. 2007, ARA&A, 45, 565 (Cited on page 6.)

Meier, D. S. & Turner, J. L. 2005, ApJ, 618, 259 (Cited on pages 132 and 136.)

Meixner, M. & Tielens, A. G. G. M. 1993, ApJ, 405, 216 (Cited on page 20.)

Melnick, G., Gull, G. E., & Harwit, M. 1979, ApJ, 227, L29 (Cited on page 16.)

Menten, K. M., Pillai, T., & Wyrowski, F. 2005, in IAU Symposium, Vol. 227, Massive Star Birth: A Crossroads of Astrophysics, ed. R. Cesaroni, M. Felli, E. Churchwell, & M. Walmsley, 23–34 (Cited on page 8.)

Menzel, D. H. 1968, Nature, 218, 756 (Cited on page 30.)

Menzel, D. H. 1969, ApJS, 18, 221 (Cited on pages 30 and 64.)

Mezger, P. G. 1980, in Astrophysics and Space Science Library, Vol. 80, Radio Recombination Lines, ed. P. A. Shaver, 81–97 (Cited on page 41.)

Mezger, P. G. & Henderson, A. P. 1967, ApJ, 147, 471 (Cited on pages 11, 29 and 90.)

Molinari, S., Brand, J., Cesaroni, R., & Palla, F. 1996, A&A, 308, 573 (Cited on page 8.)

Molinari, S., Swinyard, B., Bally, J., et al. 2010a, A&A, 518, L100 (Cited on page 9.)

Molinari, S., Swinyard, B., Bally, J., et al. 2010b, PASP, 122, 314 (Cited on page 5.)

Monteiro, T. T. 1991, A&A, 241, L5 (Cited on page 19.)

Mookerjea, B., Hassel, G. E., Gerin, M., et al. 2012, A&A, 546, A75 (Cited on page 165.)

Motte, F., Schilke, P., & Lis, D. C. 2003, ApJ, 582, 277 (Cited on page 93.)

Mottram, J. C., Hoare, M. G., Urquhart, J. S., et al. 2011, A&A, 525, A149 (Cited on page 7.)

Natta, A., Walmsley, C. M., & Tielens, A. G. G. M. 1994, ApJ, 428, 209 (Cited on page 173.)

Norberg, P. & Maeder, A. 2000, A&A, 359, 1025 (Cited on page 11.)

Oster, L. 1961, AJ, 66, 50 (Cited on page 29.)

Osterbrock, D. E. 1989, Astrophysics of gaseous nebulae and active galactic nuclei (Cited on pages 41 and 45.)

Paladini, R., Burigana, C., Davies, R. D., et al. 2003, A&A, 397, 213 (Cited on page 44.)

Paladini, R., Davies, R. D., & De Zotti, G. 2004, MNRAS, 347, 237 (Cited on pages 43 and 44.)

Palla, F., Brand, J., Comoretto, G., Felli, M., & Cesaroni, R. 1991, A&A, 246, 249 (Cited on page 8.)

Palla, F., Cesaroni, R., Brand, J., et al. 1993, A&A, 280, 599 (Cited on page 6.)

Panagia, N. 1973, AJ, 78, 929 (Cited on pages 111 and 112.)

Pankonin, V., Walmsley, C. M., & Thum, C. 1980, A&A, 89, 173 (Cited on page 42.)

Peebles, P. J. E. 1966, ApJ, 146, 542 (Cited on page 40.)

Peimbert, M. & Spinrad, H. 1970, ApJ, 159, 809 (Cited on page 41.)

Pestalozzi, M. R., Minier, V., & Booth, R. S. 2005, A&A, 432, 737 (Cited on page 8.)

Peters, T., Longmore, S. N., & Dullemond, C. P. 2012, MNRAS, 425, 2352 (Cited on pages 41, 110 and 129.)

Pety, J., Teyssier, D., Fossé, D., et al. 2005, A&A, 435, 885 (Cited on pages 132, 134, 158, 163 and 164.)

Pilleri, P., Montillaud, J., Berné, O., & Joblin, C. 2012, A&A, 542, A69 (Cited on page 164.)

Pilleri, P., Treviño-Morales, S., Fuente, A., et al. 2013, A&A, 554, A87 (Cited on pages 132, 134, 157, 158, 163, 164 and 165.)

Pitts, W. M., Pasternack, L., & McDonald, J. R. 1982, Chemical Physics, 68, 417 (Cited on page 162.)

Ponomarev, V. O., Smith, H. A., & Strelnitski, V. S. 1994, ApJ, 424, 976 (Cited on page 34.)

Poppi, S., Tsivilev, A. P., Cortiglioni, S., Palumbo, G. G. C., & Sorochenko, R. L. 2007, A&A, 464, 995 (Cited on page 42.)

Povich, M. S., Stone, J. M., Churchwell, E., et al. 2007, ApJ, 660, 346 (Cited on page 76.)

Price, S. D., Egan, M. P., Carey, S. J., Mizuno, D. R., & Kuchar, T. A. 2001, AJ, 121, 2819 (Cited on pages 9 and 62.)

Purcell, C. R., Balasubramanyam, R., Burton, M. G., et al. 2006, MNRAS, 367, 553 (Cited on page 154.)

Purcell, C. R., Hoare, M. G., Cotton, W. D., et al. 2013, ApJS, 205, 1 (Cited on pages 9, 60, 76, 78, 84, 90, 109, 110, 116, 123 and 124.)

Purser, S. J. D., Lumsden, S. L., Hoare, M. G., et al. 2016, MNRAS, 460, 1039 (Cited on page 93.)

Quireza, C., Rood, R. T., Balser, D. S., & Bania, T. M. 2006, ApJS, 165, 338 (Cited on page 16.)

Rathborne, J. M., Jackson, J. M., & Simon, R. 2006, ApJ, 641, 389 (Cited on page 8.)

Rawlings, J. M. C., Taylor, S. D., & Williams, D. A. 2000, MNRAS, 313, 461 (Cited on page 134.)

Reid, M. J., Menten, K. M., Brunthaler, A., et al. 2014, ApJ, 783, 130 (Cited on pages 120 and 124.)

Reifenstein, E. C., Wilson, T. L., Burke, B. F., Mezger, P. G., & Altenhoff, W. J. 1970, A&A, 4, 357 (Cited on page 16.)

Ricci, R., Sadler, E. M., Ekers, R. D., et al. 2004, MNRAS, 354, 305 (Cited on page 78.)

Richling, S. & Yorke, H. W. 1997, A&A, 327, 317 (Cited on page 47.)

Rizzo, J. R., Fuente, A., & García-Burillo, S. 2005, ApJ, 634, 1133 (Cited on pages 132, 133, 134, 157 and 158.)

Rizzo, J. R., Fuente, A., Rodríguez-Franco, A., & García-Burillo, S. 2003, ApJ, 597, L153 (Cited on pages 132 and 134.)

Roberge, W. G., Dalgarno, A., & Flannery, B. P. 1981, ApJ, 243, 817 (Cited on page 19.)

Roberge, W. G., Jones, D., Lepp, S., & Dalgarno, A. 1991, ApJS, 77, 287 (Cited on page 19.)

Rodriguez-Franco, A., Martin-Pintado, J., & Fuente, A. 1998, A&A, 329, 1097 (Cited on pages 132 and 136.)

Roelfsema, P. R., Goss, W. M., & Mallik, D. C. V. 1992, ApJ, 394, 188 (Cited on page 42.)

Rohlfs, K. & Wilson, T. L. 2000, Tools of radio astronomy (Cited on page 90.)

Russell, R. W., Melnick, G., Gull, G. E., & Harwit, M. 1980, ApJ, 240, L99 (Cited on page 16.)

Russell, R. W., Melnick, G., Smyers, S. D., et al. 1981, ApJ, 250, L35 (Cited on page 16.)

Sanhueza, P., Jackson, J. M., Foster, J. B., et al. 2012, ApJ, 756, 60 (Cited on pages 153, 154 and 157.)

Schenewerk, M. S., Jewell, P. R., Snyder, L. E., Hollis, J. M., & Ziurys, L. M. 1988, ApJ, 328, 785 (Cited on pages 134, 160 and 161.)

Schilke, P., Pineau des Forêts, G., Walmsley, C. M., & Martín-Pintado, J. 2001, A&A, 372, 291 (Cited on pages 133, 134, 153, 158, 160 and 161.)

Schilke, P., Walmsley, C. M., Pineau Des Forets, G., et al. 1992, A&A, 256, 595 (Cited on page 136.)

Schuller, F., Menten, K. M., Contreras, Y., et al. 2009, A&A, 504, 415 (Cited on pages 5, 8, 59, 97 and 110.)

Schulz, N. S. 2005, From Dust To Stars Studies of the Formation and Early Evolution of Stars (Cited on page 3.)

Scoville, N. & Murchikova, L. 2013, ApJ, 779, 75 (Cited on pages 45 and 97.)

Sewilo, M., Churchwell, E., Kurtz, S., Goss, W. M., & Hofner, P. 2004a, ApJ, 605, 285 (Cited on pages 60, 68 and 93.)

Sewiło, M., Churchwell, E., Kurtz, S., Goss, W. M., & Hofner, P. 2008, ApJ, 681, 350 (Cited on pages 13, 60, 61 and 93.)

Sewiło, M., Churchwell, E., Kurtz, S., Goss, W. M., & Hofner, P. 2011, ApJS, 194, 44 (Cited on pages 39 and 121.)

Sewilo, M., Watson, C., Araya, E., et al. 2004b, ApJS, 154, 553 (Cited on page 13.)

Shaver, P. A. 1980, A&A, 90, 34 (Cited on page 34.)

Shaver, P. A., McGee, R. X., Newton, L. M., Danks, A. C., & Pottasch, S. R. 1983, MNRAS, 204, 53 (Cited on pages 43 and 44.)

Shepherd, D. S. & Churchwell, E. 1996, ApJ, 472, 225 (Cited on page 59.)

Shu, F. H., Allen, A., Shang, H., Ostriker, E. C., & Li, Z.-Y. 1999, in NATO Advanced Science Institutes (ASI) Series C, Vol. 540, NATO Advanced Science Institutes (ASI) Series C, ed. C. J. Lada & N. D. Kylafis, 193 (Cited on page 6.)

Simpson, J. P. 1973, Ap&SS, 20, 187 (Cited on page 34.)

Smirnov, G. T. 1985, Soviet Astronomy Letters, 11, 7 (Cited on pages 37 and 38.)

Smirnov, G. T., Sorochenko, R. L., & Pankonin, V. 1984, A&A, 135, 116 (Cited on page 39.)

Smith, R. J., Shetty, R., Stutz, A. M., & Klessen, R. S. 2012, ApJ, 750, 64 (Cited on pages 140 and 141.)

Sobel'Man, I. I., Vainshtein, L. A., & Yukov, E. A. 1995, Excitation of Atoms and Broadening of Spectral Lines, 21 (Cited on page 36.)

Sobolev, A. M., Cragg, D. M., Ellingsen, S. P., et al. 2007, in IAU Symposium, Vol. 242, IAU Symposium, ed. J. M. Chapman & W. A. Baan, 81–88 (Cited on page 7.)

Sorochenko, R. L. & Borodzich, É. V. 1965, Dokl. Akad. Nauk SSSR 163, 603. English translation: 1966. Soviet Physics Doklady, 10, 588 (Cited on page 15.)

Sparke, L. S. & Gallagher, III, J. S. 2000, Galaxies in the universe : an introduction, 416 (Cited on page 3.)

Sridharan, T. K., Beuther, H., Schilke, P., Menten, K. M., & Wyrowski, F. 2002, ApJ, 566, 931 (Cited on page 8.)

Sridharan, T. K., Rao, R., Qiu, K., et al. 2014, ApJ, 783, L31 (Cited on pages 79 and 93.)

Stahler, S. W. & Palla, F. 2005, The Formation of Stars, 865 (Cited on pages 3, 5 and 6.)

Steggles, H. G., Hoare, M. G., & Pittard, J. M. 2017, MNRAS, 466, 4573 (Cited on page 124.)

Sternberg, A. & Dalgarno, A. 1989, ApJ, 338, 197 (Cited on page 19.)

Sternberg, A. & Dalgarno, A. 1995, ApJS, 99, 565 (Cited on page 132.)

Sternberg, A., Hoffmann, T. L., & Pauldrach, A. W. A. 2003, ApJ, 599, 1333 (Cited on page 41.)

Stoerzer, H., Stutzki, J., & Sternberg, A. 1996, A&A, 310, 592 (Cited on page 20.)

Storey, J. W. V., Watson, D. M., & Townes, C. H. 1979, ApJ, 233, 109 (Cited on page 16.)

Storey, P. J. & Hummer, D. G. 1995, MNRAS, 272, 41 (Cited on pages 45 and 115.)

Störzer, H. 1997, in IAU Symposium, Vol. 170, IAU Symposium, ed. W. B. Latter, S. J. E. Radford, P. R. Jewell, J. G. Mangum, & J. Bally, 465 (Cited on page 19.)

Strelnitski, V., Haas, M. R., Smith, H. A., et al. 1996, Science, 272, 1459 (Cited on page 34.)

Stutzki, J., Stacey, G. J., Genzel, R., et al. 1988, ApJ, 332, 379 (Cited on page 19.)

Szymczak, M. & Gérard, E. 2004, A&A, 414, 235 (Cited on page 79.)

Szymczak, M., Wolak, P., Bartkiewicz, A., & Borkowski, K. M. 2012, Astronomische Nachrichten, 333, 634 (Cited on page 79.)

Tauber, J. A. & Goldsmith, P. F. 1990, ApJ, 356, L63 (Cited on page 20.)

Taylor, J. H. & Cordes, J. M. 1993, ApJ, 411, 674 (Cited on page 16.)

Tenorio-Tagle, G. 1979, A&A, 71, 59 (Cited on page 118.)

Tenorio Tagle, G., Yorke, H. W., & Bodenheimer, P. 1979, A&A, 80, 110 (Cited on page 118.)

Teyssier, D., Fossé, D., Gerin, M., et al. 2004, A&A, 417, 135 (Cited on pages 132, 134, 157, 158 and 164.)

Thum, C., Strelnitski, V. S., Martin-Pintado, J., Matthews, H. E., & Smith, H. A. 1995, A&A, 300, 843 (Cited on pages 34, 35, 61, 69, 93, 97, 99 and 105.)

Tielens, A. G. G. M. 2013, Interstellar PAHs and Dust, ed. T. D. Oswalt & G. Gilmore, 499 (Cited on page 132.)

Tielens, A. G. G. M. & Hollenbach, D. 1985, ApJ, 291, 722 (Cited on pages 19 and 132.)

Tielens, A. G. G. M. & Whittet, D. C. B. 1997, in IAU Symposium, Vol. 178, IAU Symposium, ed. E. F. van Dishoeck, 45 (Cited on page 162.)

Towle, J. P., Feldman, P. A., & Watson, J. K. G. 1996, ApJS, 107, 747 (Cited on page 65.)

Tsivilev, A. P., Ershov, A. A., Smirnov, G. T., & Sorochenko, R. L. 1986, Soviet Astronomy Letters, 12, 355 (Cited on page 42.)

Ungerechts, H., Bergin, E. A., Goldsmith, P. F., et al. 1997, ApJ, 482, 245 (Cited on page 164.)

Urquhart, J. S., Busfield, A. L., Hoare, M. G., et al. 2007, A&A, 461, 11 (Cited on pages 9, 60, 76, 80, 84, 90, 97, 109, 110, 112, 116, 123 and 124.)

Urquhart, J. S., Csengeri, T., Wyrowski, F., et al. 2014a, A&A, 568, A41 (Cited on pages 5, 6, 7, 9 and 59.)

Urquhart, J. S., Csengeri, T., Wyrowski, F., et al. 2014b, A&A, 568, A41 (Cited on page 97.)

Urquhart, J. S., Figura, C. C., Moore, T. J. T., et al. 2014c, MNRAS, 437, 1791 (Cited on page 121.)

Urquhart, J. S., Hoare, M. G., Purcell, C. R., et al. 2009, A&A, 501, 539 (Cited on pages 9, 59, 60, 76, 84, 109, 110 and 124.)

Urquhart, J. S., Koenig, C., Giannetti, A., et al. 2017, ArXiv e-prints (Cited on pages 6, 9, 97, 109, 110, 112, 114, 122, 123, 136, 137, 152, 153, 154 and 181.)

Urquhart, J. S., Moore, T. J. T., Csengeri, T., et al. 2014d, MNRAS, 443, 1555 (Cited on pages 9, 59, 60, 84, 88 and 89.)

Urquhart, J. S., Moore, T. J. T., Menten, K. M., et al. 2015, MNRAS, 446, 3461 (Cited on page 97.)

Urquhart, J. S., Moore, T. J. T., Schuller, F., et al. 2013a, MNRAS, 431, 1752 (Cited on pages 113 and 123.)

Urquhart, J. S., Thompson, M. A., Moore, T. J. T., et al. 2013b, MNRAS, 435, 400 (Cited on pages 60, 73, 76, 78, 86, 87, 89, 97, 113 and 122.)

Urquhart, J. S., Thompson, M. A., Moore, T. J. T., et al. 2013c, MNRAS, 435, 400 (Cited on page 146.)

Useli Bacchitta, F. & Joblin, C. 2007, in Molecules in Space and Laboratory, 89 (Cited

on page 163.)

van Buren, D. & Mac Low, M.-M. 1992, ApJ, 394, 534 (Cited on page 118.)

van Buren, D., Mac Low, M.-M., Wood, D. O. S., & Churchwell, E. 1990, ApJ, 353, 570 (Cited on pages 118 and 121.)

van Dishoeck, E. F. & Black, J. H. 1988, ApJ, 334, 771 (Cited on page 19.)

Vassilev, V., Meledin, D., Lapkin, I., et al. 2008, A&A, 490, 1157 (Cited on page 98.)

Vasyunina, T., Linz, H., Henning, T., et al. 2011, A&A, 527, A88 (Cited on page 136.)

Viner, M. R., Vallee, J. P., & Hughes, V. A. 1979, ApJS, 39, 405 (Cited on pages 40 and 68.)

Viti, S., Collings, M. P., Dever, J. W., McCoustra, M. R. S., & Williams, D. A. 2004, MNRAS, 354, 1141 (Cited on page 164.)

Wagner, A. F. & Graff, M. M. 1987, ApJ, 317, 423 (Cited on page 19.)

Walmsley, C. M. 1990, A&AS, 82, 201 (Cited on pages 33 and 69.)

Walsh, A. J., Burton, M. G., Hyland, A. R., & Robinson, G. 1998, MNRAS, 301, 640 (Cited on page 76.)

Walsh, A. J., Hyland, A. R., Robinson, G., & Burton, M. G. 1997, MNRAS, 291, 261 (Cited on pages 8 and 80.)

Walsh, A. J., Purcell, C. R., Longmore, S. N., et al. 2014, MNRAS, 442, 2240 (Cited on pages 8 and 59.)

Watson, C., Araya, E., Sewilo, M., et al. 2003, ApJ, 587, 714 (Cited on page 16.)

Watt, G. D. 1983, MNRAS, 205, 321 (Cited on page 160.)

Weisskopf, V. & Wigner, E. 1930, Zeitschrift fur Physik, 63, 54 (Cited on page 35.)

Wenger, T. V., Bania, T. M., Balser, D. S., & Anderson, L. D. 2013, ApJ, 764, 34 (Cited on pages 41 and 42.)

White, R. L., Becker, R. H., & Helfand, D. J. 2005, AJ, 130, 586 (Cited on pages 76, 84 and 109.)

Wienen, M., Wyrowski, F., Schuller, F., et al. 2012, A&A, 544, A146 (Cited on pages 73 and 146.)

Willacy, K. & Williams, D. A. 1993, MNRAS, 260, 635 (Cited on page 161.)

Wilson, T. L., Mezger, P. G., Gardner, F. F., & Milne, D. K. 1970, A&A, 6, 364 (Cited on page 16.)

Wilson, T. L., Rohlfs, K., & Hüttemeister, S. 2009, Tools of Radio Astronomy (Springer-Verlag) (Cited on page 97.)

Wood, D. O. S. & Churchwell, E. 1989, ApJS, 69, 831 (Cited on pages 8, 9, 11, 12, 13, 14, 44, 59 and 90.)

Wright, E. L., Eisenhardt, P. R. M., Mainzer, A. K., et al. 2010, AJ, 140, 1868 (Cited on pages 60 and 82.)

Wright, E. L., Mather, J. C., Bennett, C. L., et al. 1991, ApJ, 381, 200 (Cited on page 19.)

Wyrowski, F. 2008, in Astronomical Society of the Pacific Conference Series, Vol. 387, Massive Star Formation: Observations Confront Theory, ed. H. Beuther, H. Linz, & T. Henning, 3 (Cited on page 8.)

Wyrowski, F., Brooks, K., Beuther, H., et al. 2008, Molecular fingerprints of an unbiased sample of Galactic massive star forming clumps, ATNF Proposal (Cited on page 62.)

Wyrowski, F., Brooks, K., Beuther, H., et al. 2009, Molecular fingerprints of an unbiased sample of Galactic massive star forming clumps II., ATNF Proposal (Cited on page 62.)

Wyrowski, F., Güsten, R., Menten, K. M., et al. 2016, A&A, 585, A149 (Cited on page 141.)

Yorke, H. W. & Welz, A. 1996, A&A, 315, 555 (Cited on page 47.)

Zhang, B., Reid, M. J., Menten, K. M., et al. 2013, ApJ, 775, 79 (Cited on page 121.)

Zhang, C.-P., Wang, J.-J., Xu, J.-L., Wyrowski, F., & Menten, K. M. 2014, ApJ, 784, 107 (Cited on page 93.)

Zhu, F.-Y., Zhu, Q.-F., Li, J., Zhang, J.-S., & Wang, J.-Z. 2015, ApJ, 812, 87 (Cited on page 124.)

Zhu, Q.-F., Lacy, J. H., Jaffe, D. T., Richter, M. J., & Greathouse, T. K. 2008, ApJS, 177, 584 (Cited on pages 16, 120, 122, 124 and 171.)

Zinnecker, H. & Yorke, H. W. 2007, ARA&A, 45, 481 (Cited on pages 6, 58, 59 and 96.)

Zoonematkermani, S., Helfand, D. J., Becker, R. H., White, R. L., & Perley, R. A. 1990, ApJS, 74, 181 (Cited on page 76.)

Wonju Kim – Curriculum Vitae

Personal Information

Date of birth: March 17, 1986
Place of birth: Gyeongju, Republic of Korea
Nationality: Korean
Languages: Korean (native) and English (fluent)
Address: Auf dem Hügel 69, D-53121 Bonn, Germany
E-mail: wjkim@mpifr-bonn.mpg.de

Education & Research Experience

Ph.D. candidate in Astrophysics   June 2014 − present

Max-Planck-Institut für Radioastronomie, Germany

- Thesis title: *"Ionized and photodissociation regions toward a new sample of massive star-forming clumps"*

- Advisors: Prof. Dr. Karl M. Menten and Dr. Friedrich Wyrowski

Research Assistant & VLBI Operator   Mar 2012 − May 2014

Korea VLBI Network (KVN) at Division of Radio Astronomy,
Korea Astronomy and Space Science Institute, South Korea

Research and Observing Assistant   Jan 2010 − Apr 2012

Taeduk Radio Astronomy Observatory (TRAO) and Korea VLBI Network (KVN) at Division of Radio Astronomy, Korea Astronomy and Space Science Institute, South Korea

M.Sc. in Astronomy   Mar 2009 − Feb 2012

Chungnam National University, South Korea

- Thesis title: *"Simultaneous 22 GHz Water and 44 GHz Methanol Masers Survey of Ultracompact H*II *Regions"*

- Advisors: Dr. Kee-Tae Kim and Prof. Kwang-Tae Kim
- Tuition exemption: 3 times

B.Sc. in Astronomy and Space Science   Mar 2005 − Feb 2009

Chungnam National University, South Korea

- Full Scholarship: 1 time
- Tuition exemption: 5 times

Honors and awards

Sep 2015 – Admitted to the Honors branch (H2) program of the Bonn-Cologne Graduate School of Physics and Astronomy: includes a 300 Euros/month scholarship and an additional personal research budget of 500 Euros/year, for a 2-year period.

Research interests

High-mass star formation, hyper-/ultra-compact H$_{II}$ regions, H$_{II}$ bubbles, supernova remnants, bipolar outflows, photo-dissociation regions, dust properties, magnetic field and astrochemistry in the ISM.

Publications

Refereed

J-H. Bae, K-T. Kim, S-Y. Youn, **Won-Ju Kim**, D-Y. Byun, H. Kang and C. S. Oh; *"A multi-epoch, simultaneous water and methanol survey toward intermediate-mass young stellar objects"*, 2011, *ApJS*, 196, 21

S-S. Lee, and 32 coauthors (**Won-Ju Kim**); *"Single-Dish Performance of KVN 21-m Radio Telescopes: Simultaneous Observations at 22 and 43 GHz"*, 2011, *PASP*, 123, 1398L

K-T. Kim, **Won-Ju Kim** and C-H. Kim; *"Molecular Outflows from Newly Formed Massive Stars"*, 2016, *JKAS*, 48, 365

W.-J. Kim, F. Wyrowski, J. S. Urquhart, K. M. Menten, and T. Csengeri; *"ATLASGAL-selected massive clumps in the inner Galaxy IV. Millimeter hydrogen recombination lines from associated H*II *regions"*, 2017, *A&A* in press.

Proceedings

K-T. Kim, D-Y, Byun, J-H. Bae, **Won-Ju Kim**, H-W. Kang, C. S. Oh, S-Y. Youn; *"KVN Single-dish Water and Methanol Maser Line Surveys of Galactic YSOs"*, Proceedings IAU Symposium No. 287, 2012

Won-Ju Kim and K-T. Kim; *"Maser and molecular line surveys of massive star-forming regions"*, Protostars and Planets VI Posters, 22, 2013

Submitted and In preparation

W.-J. Kim, F. Wyrowski, J. S. Urquhart, T. Csengeri and K. M. Menten; *"New detections of (sub)millimeter hydrogen radio recombination lines towards high-mass star-forming clumps"*, 2017, submitted.

W.-J. Kim, F. Wyrowski, J. S. Urquhart, T. Pillai and K. M. Menten; *"ATLASGAL-selected massive clumps in the inner Galaxy — Molecular line survey of photodissociation regions"*, in prep.

W.-J. Kim, K-T. Kim and K-T. Kim; *"Simultaneous 22 GHz water and 44 GHz methanol masers survey of ultracompact H*II *regions"*, in prep.

W.-J. Kim, K-T. Kim, C-H. Kim and S-Y. Youn.; *"43 GHz SiO thermal emission observation for massive star-forming regions"*, in prep.

Successful proposals as Principal-Investigator

Australia Telescope Compact Array (ATCA): TAC racing 3.0, assigned as a backup project (code C3155) —*"A new population of H*II *regions identified by millimeter Radio Recombination Line Sources"*

APEX 12-m sub-millimeter telescope: Grade B, 77.8 hr, Summer-Winter semesters 2015, Project codes M0025-95 and M0018-96 —*"Observation of Sub-mm Hydrogen Recombination α and β Lines toward a New Sample of Massive Star-forming Clumps"*

KVN 21-m single dish telescopes : Grade B, 90 hr, 2012 - 2014 — *"SiO (J=1−0, v=0) and H_2CO ($2_{12}−1_{11}$) Line Survey of Infrared Dark Cores with Star Formation Indicators"*

Computer skills

Proficient in GILDAS software (SIC, GREG, ASTRO, CLASS, WEEDS), Python, IDL, SAOImage ds9 and Unix-based operating systems (Linux, MacOS).

Good knowledge of Fortran 77, AIPS, CASA, Miriad.

Participations and Talks

Cardiff Galactic Star Formation Workshop, Cardiff, The United Kingdom, September 18 - 20, 2017
Talk: *"High-frequency hydrogen radio recombination lines from associated H II regions in ATLASGAL dust clumps: 86 to 397 GHz"*

Visiting Scientist at University of Kent, Canterbury, The United Kingdom, July 31 - August 4, 2017

IMPRS Black Board Lectures on "Machine Learning: the elegant way to extract information from data"; Bonn, Germany, February 13 - 23, 2017

The ISM-SPP Olympian School of Astrophysics; Paralia Katerini, Greece, October 3 - 7, 2016
Poster: *"Hydrogen Recombination Lines: Millimeter hydrogen recombination lines from associated H*II *regions"*

VIALACTEA 2016: The Milky Way as a Star Formation Engine; Rome, Italy, September 26 - 30, 2016
Poster: *"Hydrogen Recombination Lines: Millimeter hydrogen recombination lines from associated H*II *regions"*

IMPRS Black Board Lectures on "Hydrodynamic and magnetohydrodynamic turbulence and dynamos for astrophysicists"; Bonn, Germany, September 20 - 22, 2016

IRAM 30-m Summer School 2015; Pradollano, Spain, September 11 - 18, 2015

"Protostars & Planets VI" Conference; Heidelberg, Germany, July 15 - 20, 2013
Poster: *"Maser and Molecular Line Surveys of Massive Star-forming Regions"*

The 6th East Asia VLBI Workshop; Jeju island, South Korea, June 17 - 19, 2013
Poster: *"Maser and Molecular Line Observations towards Massive Star-forming Regions"*

The Korean Astronomical Society Meeting, Gyeongju, South Korea, April 5 - 6, 2012
Talk: *"Simultaneous 22 GHz Water and 44 GHz Methanol Masers Survey of Ultracompact H*II *Regions"*

The 2nd KVN-VERA Science Workshop; Seoul, South Korea, February 15 - 16, 2012
Talk: *"Simultaneous 22 GHz Water and 44 GHz Methanol Masers Survey of Ultracompact H*II *Regions"*

Memberships

Member of the "APEX Telescope Large Area Survey of the Galaxy" (ATLASGAL) project team

Member of the "Global view of star formation in the Milky Way" (GLOSTAR) project team

Member of the technical commissioning team of the new C-band ($4-8$ GHz) receiver at the Effelsberg 100m telescope

Organizing Experience

Local Organizing Committee Member for the "6th East Asia VLBI Workshop 2013", June 17 - 19, 2013

Local Organizing Committee Member for the "5th KVN-VERA Science Working Group Meeting", June 20 - 21, 2013

Teaching Experience

Teaching Assistant for the course "Galactic Astronomy"; Department of Astronomy and Space Science, Chungnam National University, South Korea, Spring semester 2009

Erklärung

Ich versichere, dass ich die von mir vorgelegte Dissertation selbständig angefertigt, die benutzten Quellen und Hilfsmittel vollständig angegeben und die Stellen der Arbeit- einschlielich Tabellen, Karten und Abbildungen –, die anderen Werken im Wortlaut oder dem Sinn nach entnommen sind, in jedem Einzelfall als Entlehnung kenntlich gemacht habe; dass diese Dissertation noch keiner anderen Fakultät oder Universität zur Prfung vorgelegen hat; dass sie noch nicht verffentlicht worden ist sowie, da ich eine solche Veröffentlichung vor Abschluss des Promotionsverfahrens nicht vornehmen werde. Die Bestimmungen dieser Promotionsordnung sind mir bekannt. Die von mir vorgelegte Dissertation ist von Prof. Dr. Karl M. Menten betreut worden.

Unterschift:
————————————————————————————-
Datum:
————————————————————————————-